Uncovering the cellular and molecular mechanisms of radiotherapy soft tissue injury and fat graft treatment

Lipi Shukla

(MBBS, Dip Anat Surg)

A thesis submitted in total fulfilment of the requirements of the degree of Doctor of Philosophy

School of Exercise Science

Faculty of Health Science

Australian Catholic University

&

Lymphatic and Regenerative Surgery Group

O'Brien Institute Department of St. Vincent's Institute

February 2018

DECLARATION

This is to certify that:

1. this thesis contains no material published elsewhere or extracted in whole or in part from a thesis by which I have qualified for or been awarded another degree or diploma,

2. no parts of this thesis have been submitted towards the award of any other degree or diploma in any other tertiary institution,

3. no other person's work has been used without due acknowledgment in the main text of the thesis,

4. all research procedures reported in the thesis received the approval of the relevant Ethics/Safety Committees (where required).

STATEMENT OF AUTHORSHIP

Components of work included in this Thesis were performed in collaboration with Nicole Harris, Pradyummna Herle and Jason Palmar in the proportions indicated below.

Chapter 3:

3.3.4 Invasion Assays of NHDF performed in conjunction by Nicole Harris (50%)

Chapter 4:

4.2.8 Immunohistochemical ICAM-1 validation and CD68 characterization in arterial samples performed in conjunction with Jason Palmar (20 %)

Chapter 5:

5.2.1.1 Lymphatic staining and quantification in human tissues performed in conjunction with Jason Palmer (25%) and Pradyummna Herle (25%)

5.2.1.5 Prox-1 GFP mouse ear wounding performed in conjunction with Katie Ardipradja (10%), Nicole Harris (10%) and Pradyumna Herle (30%).

5.2.2.3 Validation of CXCR7 expression performed in conjunction with Jason Palmer (20%) and Nicole Harris (20%)

Chapter 7:

7.2.7, 1.1.1 and 7.2.8 VEGFR3 Activation, Proteomic and Exosome Analysis of $ADSC^{CM}$ performed in conjunction with Nicole Harris (50%)

STATEMENT OF COLLABORATIONS

Next Generation Sequencing Bioinformatics – Matthew Ritchie and Monther Alhamdoosh, Australian Genome Research Facility Ltd, The Walter and Eliza Hall Institute

Metabolomic Studies – Konstantinos Kouremenos, Metabolomics Australia, Bio21 Institute

Proteomic Study Design – Ching Seng and Nicholas Williamson, Mass Spectrometry and Proteomics Facility, Bio21 Institute

Exosome Studies – David Greening, Department of Biochemistry and Genetics, La Trobe Institute for Molecular Science

VEGF Neutralising Antibodies and Reagents - Megan Baldwin and Ian Leitch, Opthea Technologies Ltd

Murine Irradiation - Prof Robin Anderson and Jim Hagekyriakou, Peter MacCallum Cancer Centre, Department of Oncology and Physics

Cell Irradiation – Helen Barlow and Anthony Cornelisz, BioResources Centre, St Vincent's Hospital

ACKNOWLEDGEMENTS

I would like to acknowledge the unwavering mentorship and encouragement of my supervisors Ramin Shayan and Wayne Morrison, for choosing to take me on this adventure and supporting the start of my career in Plastic and Reconstructive Surgery.

To all of the Plastic and Reconstructive Surgeons at St. Vincent's Public and Private Hospital for their contributions to tissue sample collection and their invaluable clinical guidance.

To my colleagues in the laboratory Pradyumna Herle, Nicole Harris, Jason Palmer, Tara Karnezis, Caroline Taylor, Effie Keramidaris and Katherine Ardipradja, I thank you all for your technical assistance and expertise in helping me appreciate the true art of science.

This research would not have been possible without the support of Australian Catholic University, the O'Brien Institute, the Hummingbirds and the generous awards made on behalf of the Royal Australian College of Surgeons through the Tour de Cure Foundation for Surgery Research Scholarship.

Above all, I dedicate this thesis to Neil, who is a constant source of love, laughter and motivation, especially when I chose to walk down a more testing path. And to Renu, Naresh and Nupur, whose love, unselfish support and inspiration over many years has laid the foundations for the discipline necessary to face the challenges of this journey successfully.

LIST OF PUBLICATIONS AND AWARDS

PUBLICATIONS

Matthew Thuy, Jeremy K Kam, Geoffrey C Lee, Peter L Tao, Dorothy Q Ling; Melissa Cheng, Su Kah Goh, Alexander J Papachristos, **Lipi Shukla,** Krystal-Leigh Wall, Nicolas R Smoll, Jordan J Jones, Njeri Gikenye, Bob Soh, Brad Moffat, Nick Johnson, Katharine J Drummond. A novel literature-based approach to identify genetic and molecular predictors of survival in GBM: Analysis of 14678 patients using systematic review and meta-analytical tools. *Journal of Clinical Neuroscience 12/2014; 22(5).*

Shukla, L.,* Herle., P,* Morrison, WA., Shayan, R., Preoperative radiation and free flap outcomes for head and neck reconstruction: a systematic review and meta-analysis. * Equal first author contributions. *ANZ Journal of Surgery, 85: 121–127. doi: 10.1111/ans.12888*

Shukla L., Morrison WA., Shayan R, Adipose-Derived Stem Cells in Radiotherapy Injury: A New Frontier. *Frontiers in Surgery. 2015;2:1. doi:10.3389/fsurg.2015.00001.*

Areeb Z, Stylli SS, Ware TM, Harris NC, **Shukla L**, Shayan R, Paradiso L, Li B, Morokoff AP, Kaye AH, Luwor RB. Inhibition of glioblastoma cell proliferation, migration and invasion by the proteasome antagonist carfilzomib. *Med Oncol. 2016 May;33(5):53. doi: 10.1007/s12032-016-0767-3. Epub 2016 Apr 20*

Shukla, L., Herle, P., Palmer, J., Morrison, W., Shayan, R., The role of dermal fibroblasts and keratinocytes in radiotherapy induced bystander effects - a TGFβ-independent process driving tissue fibrosis – novel reversal with fat grafting *(preparation for submission)*

Herle, P., Shukla, N., Willet, J., Ruskin, O., Tomouk, T, **Shukla, L.,** Varigos, G,. Ashton, M., Shayan, R., Recurrence rates in thin melanomas utilizing sentinel node biopsy as a predictive factor– a systematic review and meta-analysis *(preparation for*

submission)

Shukla, L., Harris, N., Herle, P., Karnezis, T,. Shayan, R., Adipose Derived Stem Cells Reverse the anti-lymphangiogenic effects of radiation injury on Lymphatic Endothelial Cells via VEGFR-3 independent pathways *(preparation for submission)*

Shukla, L., Palmar, J., Herle, P., Slavin., J, Karnezis, T,. Shayan, R.,The effect of radiotherapy injury on the macro and microvascular systems – the role of ICAM-1 *(preparation for submission).*

PUBLISHED PROCEEDINGS

Shukla, L., Harris, N., Herle, P., Ardipradja, K., Morrison, WA., Shayan, R Adipose Derived Stem Cells and Fat Grafting: A novel way to reverse the effects of radiotherapy induced lymphoedema. *Plastic Surgery Congress and Annual Scientific Conference, Royal College of Surgeons (RACS) May 2016, Brisbane, Australia.*

Shukla, L., Morrison, WA., Shayan, R. The cellular and molecular effects of radiotherapy on the micro and macrovascular systems – The 'roll' of I-CAM1. *Plastic Surgery Congress, May 2015, Brisbane, Australia.*

Shukla, L., Morrison, WA., Shayan, R. ADSC-Mediated Reversal of Radiation-Induced Soft-Tissue Injury by Fat Grafting. *Plastic Surgery Congress, May 2015, Brisbane, Australia.*

Shukla, L., Morrison, WA., Shayan, R. Radiotherapy Soft Tissue Injury & Fat Grafting: The development of an *in-vitro* model for the investigation & modulation of chronic radiotherapy side effects in normal tissues. *Annual Scientific Conference, Royal Australian College of Surgeons (RACS) May 2014, Singapore*

Shukla, L., Taylor, C., Morrison, WA., Shayan, R. Uncovering the subcellular molecular effects of Radiotherapy in Plastic Surgery.
Plastic Surgery Congress, April 2013, Melbourne Australia.

Shukla, L., Taylor, C., Morrison, WA., Shayan, R. Uncovering the subcellular effects of radiotherapy and its impact on Breast Reconstructive Surgery.
Annual Scientific Conference, RACS, May 2013, Auckland, NZ

AWARDS

Australian Catholic University and O'Brien Institute of Tissue Engineering Center Research Scholarship 2013, 2014

St. Vincent's Hospital Research Prize 2013

Foundation for Surgery Tour De Cure Cancer Research Scholarship, Royal Australian College of Surgeons 2015

Australian Society of Plastic Surgery - Registrar Research Conference - Highly Commended 2016

Australian Society of Plastic Surgery - Registrar Research Conference Prize – 2017

TABLE OF CONTENTS

FIGURES

TABLES

ABSTRACT

Over half of the 120,000 patients diagnosed with a solid tumour in Australia annually require radiotherapy as part of their treatment. Despite significantly enhancing cancer survival, the damage done to healthy native tissues is inevitable and problematic. Radiotherapy soft tissue injury is progressive, may intensify years after treatment and is characterised by pain, contracture, tissue breakdown, recurrent infection and lymphoedema.

Important implications of radiation injury for surgeons are that surgical procedures (whether for functional restoration or cancer recurrence) in irradiated tissues become technically difficult and more hazardous. Direct wound closure or local flaps are restricted by stiff, non-compliant tissue, and even if wound edges are opposable, they are frequently subject to poor wound healing or breakdown. Further, the ability of an irradiated wound bed to accept skin grafts is diminished, necessitating more complex reconstructive procedures such as free microvascular tissue transfer from distant sites, in which radiation injury is also a chief contributing factor to poor patient outcome.

First, essential cell-specific functions were investigated to establish the effects of radiotherapy-injury on the ability of the cells in skin and subcutaneous tissues to survive or respond to subsequent injury or challenge. Next, molecular alterations resulting from irradiation were characterised at mRNA level using next generation sequencing and further investigated using pathway analysis. Finally, the reparative potential of the adipose-derived stem cells (ADSCs) to reduce radiotherapy injury was investigated in using a similar panel of cellular assays. The constituent proteins secreted by these cells that exerted a regenerative effect were then isolated for further analyses.

The results detailed in this thesis demonstrate that each individual component of skin and subcutaneous tissue exhibits a unique response to radiotherapy injury - challenging the traditional dogma that large scale irreversible cell death is responsible for the manifestation of radiotherapy soft tissue injury. Notable findings include radiotherapy-induced hyper-migration of fibroblasts and pericytes, reduced apoptosis

in endothelial and stem cell populations, global suppression of lymphatic endothelial cell (LEC) repair functions and significant alterations in the differentiation capacity of ADSCs.

Next generation gene sequencing revealed key molecular alterations resulting from radiotherapy in a variety of cell types. Significant findings include dysregulation of extracellular matrix proteins and basement membrane collagens – changes likely to contribute to the hypermigratory, adhesive and highly contractile phenotype seen in irradiated fibroblasts. Up-regulation of intercellular adhesion molecule 1 (ICAM-1) in blood vessel endothelial cells found in acute radiotherapy injury was validated in irradiated human tissues and was demonstrated to remain persistently elevated months-to-years after completion of therapy. This finding suggested a key candidate for application to mitigate radiotherapy injury at both the micro and macrovascular level. In order to combat the impaired functions seen in LECs after irradiation, experiments were conducted using stimulation with known potent lymphangiogenic factors VEGF-C and VEGF-D. Irradiated LEC demonstrated an obliterated capacity for response to this stimulation, due to a unique profile of ablated VEGF receptor (VEGFR) -2 signaling and reduced VEGFR-3 activation. Concurrently, up-regulation of interleukin (IL) -8 and chemokine receptor CXCR7 in irradiated LEC was seen and validated in mouse and human tissues to remain upregulated in chronic radiotherapy injury. These two protein candidates, not typically associated with lymphangiogenic properties demonstrated selective lymphangiogenic effect in both normal and irradiated LECs. Together this novel set of data suggest that LECs attempt to regenerate after radiotherapy injury using parallel signaling axes to the traditional VEGF-C and VEGF-D signaling pathways, which are uniquely rendered impotent by radiotherapy injury.

Overall, methods to salvage irradiated tissues to a point to which soft-tissue quality would permit simple wound closure or other tissue repair techniques is desperately needed by clinicians. Fat grafting has been reported as a promising avenue to achieve this when used in previously irradiated areas. It was incidentally noted that irradiated tissue overlying the fat graft became more compliant and less lymphoedematous. The diminished capacity of irradiated ADSC to migrate and differentiate to fat represented significant impairments in their regenerative function. Radiation not only impairs

loco-regional ADSC function, but was also shown to block the recruitment and homing of functional ADSC from sites distant to the injury. This may be due to the mentioned presence of CXCR7 secreted by irradiated LEC. Therefore, to overcome injury and aid in regeneration of tissues the mechanical introduction of healthy ADSC, via fat grafting may be needed to override the failed ADSC recruitment mechanisms.

In the fat grafting model using the introduction of the secretome of ADSCs, ADSC-conditioned media ($ADSC^{CM}$) was able to reverse the effects of radiotherapy injury in both fibroblasts and LEC populations. The final section of this thesis investigated putative therapeutic mechanisms by which ADSCs reverse radiotherapy induced soft tissue injury. Examination of $ADSC^{CM}$ was performed using proteomics, exosome analysis and metabolomics approaches. Several key candidates were identified that may lead to promising therapeutic avenues by which radiotherapy injury can be mitigated.

Understanding of the cellular and molecular mechanisms of radiotherapy induced soft tissue injury, methods by which $ADSC^{CM}$ mediates reversal of the resulting cell dysfunction will provide vital clues and putative therapeutic channels by which to reverse these pathological alterations, thereby reducing the devastating burden of chronic, debilitating side effects of radiotherapy such as fibrosis, lymphoedema and other related diseases, in cancer survivors.

1 CHAPTER 1: LITERATURE REVIEW

1.1 Radiotherapy

Radiation can be classified into two categories; either non-ionizing and ionizing, depending on whether or not the radiation is able to remove electrons from a substance and convert it to a charged ion (1) (2). Therapeutic radiotherapy is categorized as a form of ionizing energy (electromagnetic or particulate in nature), and is used to treat various human malignancies. Ionizing radiation can act directly to ionize tissues through which it crosses, by depositing energy through charged particles (electrons, protons, heavy ions or α-particles) or, alternatively, this process can occur indirectly via neutral particles (photons and neutrons), which subsequently release charged particles on interaction with tissues (3). As this directed beam of radiation makes contact with tissues of the body, it causes orbiting electrons in the atoms of the medium to be excited to higher energy levels, in doing so releasing energy that damages cells and tissues through direct, indirect or radiation induced bystander effects (see section 1.5) (3) (4) (5).

Gamma-rays and X-rays are forms of short wavelengths within the electromagnetic spectrum, that translate to high energy levels, rendering them capable of breaking atomic and molecular bonds, thus ionizing tissues. Other wavelengths on the spectrum include ultraviolet, infrared and radio waves, which are of longer wavelength, lower energy and degree of penetration (3). Both gamma and X-rays release photons after the breakdown of unstable atoms from sources such as Caesium-137 or Cobalt-60, which are collimated to generate high-energy irradiation beams for therapeutic use (3) (6). While the energy within photons is not attenuated by tissue interaction, it is postulated that most of the biological damage caused by radiotherapy is attributed to secondary electron release (3). These principles are utilized within self-contained radiotherapy devices called linear accelerators, first invented by Wideroe in the 1920s (7), which generate therapeutic beams by accelerating electrons through an electromagnetic field (8). The electrons then collide with a target e.g. tungsten to generate therapeutic irradiation beams (6) (for further history and development of radiotherapy techniques see section 1.3). The unit of measurement for radiotherapy is known as the Gray (Gy), which denotes the amount of radiation energy absorbed by a mass, therefore 1 Gy = 1Joule/Kg. However, energy absorption varies with different types of radiation and the concept of linear energy transfer (LET) represents the

amount of energy transferred to a medium per unit length of the path travelled. It is therefore, the energy 'lost' by charged particles as they traverse through the medium colliding with and ionizing the surrounding tissues. In the case of gamma and x-ray radiation, as mentioned, it is the electrons secondarily generated by the photons that are responsible for this energy release and are classically low LET in comparison to neutrons, protons or α-particles that have a higher density of ionizing events. Therefore, high LET radiotherapy does not always translate to optimal biological effect, as an increased density of ionizing events does not yield superior tumour control nor does it minimize normal tissue reactions (2) (9).

The primary target of ionizing radiotherapy is the nuclear DNA in cells, damage to which results in cell death and/or production of non-viable progeny on subsequent division (3). The survival curve for mammalian cells typically depends on factors such as the type of LET, oxygenation levels, temperature, distribution of cells within the cell cycle, dose rate and fractionation regimes used (9). The main aims of radiotherapy are to deliver maximal dose to the tumour, while minimizing normal tissue exposure. Doses used for tumour eradication are dictated by the tolerance of normal 'non-tumour' tissues to radiation injury (see section 1.5) (10).

1.2 Cancer and Radiotherapy in Australia

Over 120,000 cases of cancer are diagnosed in Australia per year, excluding non-melanoma skin cancers. Five year cancer survival rates have dramatically increased from 47% to 66% in the past three decades, predominantly due to a combination of earlier detection and advances in the range of adjuvant therapies, such as radiotherapy (11). Over 50% of patients with malignant solid tumours receive radiotherapy, with either curative or palliative intent, at some stage of their treatment (12). While radiotherapy boasts the benefit of being a non-invasive treatment modality and is potentially organ preserving, its use is limited by the tolerance of surrounding normal tissues, compounded by the fact that these side effects may develop late and do not plateau over time (13) (14). As rates of survivorship from cancer increases, clinicians are frequently confronted with the wide range of chronic morbidities, which diminish patient quality of life and may restrict surgical options available for subsequent surgery such as post-cancer oncological surgery in the case of tumour recurrence.

Cancer survivorship was a concept first described by a physician Fitzhugh Mullan (15). Mullan's idea focused on phases of a patient's life after the immediate diagnosis and treatment. Research pertaining to the conditions that arise as a result of cancer treatment during cancer survivorship, aim to gain a better understanding of the mechanisms that drive the adverse side effects of cancer treatment. It is hoped that more discoveries will help to prevent, control or reduce such side effects in order to improve patient quality of life (16).

Overall, a shift in our approach to understanding underlying molecular mechanisms is required in order to tackle radiotherapy induced soft tissue injury. Redirecting the focus of radiation research from the initial induction injury to address subsequent processes such as; inflammation, angiogenesis, lymphangiogenesis and fibrotic tissue remodeling, will enable investigators to develop fundamental insight into pathological processes that contribute to radiation injury. The ultimate goal is to develop intervention strategies to prevent or reduce the burden of radiotherapy soft tissue injury (14) (17).

1.3 History of Radiotherapy

The history of radiotherapy dates back to a the late 1800s with Röntgen's discovery of X-rays, a "new kind of ray", in 1895 (18). In 1896, Becquerel discovered a natural source of radioactivity (uranium) (19) and Curie isolated radium from the pitchblende ore in 1898 (20). These Nobel Prize winning discoveries formed the foundation from which two radiotherapy delivery techniques (external beam radiotherapy (EBRT) and brachytherapy) were developed (21) (22). These techniques were implemented in clinical practice, initially for the treatment of various dermatological conditions, then adapted for the treatment of solid malignancies. By the early 1900s, successful treatment of skin cancers, gastric carcinomas and laryngeal cancers had been reported (23) (24) (25). It was during this early period that the potential for developing adverse effects of radiotherapy began to emerge. These occurred in the form of inadvertent radiotoxicity, manifesting as soft tissue destruction, exposure of underlying bone and hematological malignancies (24). These effects were noted in experimenting researchers as well as during use in a clinical setting (22) (24).

Several key discoveries in the 1900s formed the foundations of radiotherapy treatment used in clinical practice today. During the 1920s proponents of radiotherapy began to optimize dose and delivery technique, with The International Commission on Radiological Protection (IRCP) founded in 1928 to strategize methods for radioprotection (26). Bergonie and Tribondeau attempted to characterize patterns of radiotherapy injury in both mature cells and stem cells, postulating lower metabolic activity correlated with increased radiosensitivity (27). Coutard developed the concept of protracted dose delivery, known today as fractionation (28). Through detailed observation Coutard analysed the side effects resulting from different doses and fractions of irradiation, particularly pertaining to doses resulting in severe desquamation and oral mucositis. This data led to the titration of radiotherapy dose and timing to successfully treat various head and neck cancers with reduced normal tissue side effects (28). Modern practices have evolved to include fractionation, captitalising on the differences between normal and neoplastic tissue repair mechanisms, the benefits of which, as summarized by Connell include; 1) allowing normal tissue repair of sublethal cell injury, 2) allowing the shift of tumour cells from S-Phase (radio-resistant) to G2/M (radio-sensitive) phases of the cell cycle, 3) providing opportunity for re-oxygenation of hypoxic (radio-resistant) areas of a tumour and 4) recruitment and migration of uninjured cells to repopulate and regenerate normal healthy tissue (24) (29).

In the 1930s a transition was made from radium as a source of radiotherapy to cobalt-60, discovered by Irene and Frederic Joloit-Curie, delivering a superior and more potent source of gamma (γ) – ray radiotherapy (25). This development would facilitate the evolution of a skin sparing dose of 45-60Gy when treating deeply situated tumours, revolutionising EBRT over large areas, while maintaining the constraints of normal tissue tolerance. The initial delivery devices were later superseded by megavoltage linear accelerators, allowing for; generation of higher energy X-rays with superior penetration of tissues, reduction in superficial tissue dose deposition and more effective targeting of deep tumours e.g. located in the pelvis or for treatment of obese patients (30). It also facilitated safer delivery of doses of up to 60-70Gy (31). Meanwhile, the ability of Linear accelerators (LINACs) to generate electron beams became useful to target more superficially located tumours (32).

The invention of ionizing chambers and radiation quantification devices (Geiger-Muller counters), were also an important tool that stemmed from work done by Rutherford (19), on the effects of radioactivity on radon gas. Rutherford's research determined that electricity was conducted by gas through charged ions, which could in turn be used as an indicator of radio-activity enabling measurement of a radiation dosage with the Röntgen Unit (19). Around this time, bony X-Ray imaging became a valuable tool as part of treatment planning algorithms to more accurately direct radiotherapy treatment and dose delivery to the site of the tumour, while improvements in dosimeters also saw the nomenclature of the unit used to quantify radiotherapy doses transition from rad to Gy (joules/kg) (25). With modern day developments in imaging techniques, modalities such as computer tomography and magnetic resonance imaging assist in more accurate imaging and planning (see section 1.6 for further advances in radiotherapy techniques). However, inspite of the advances in understanding and technological improvement in delivery of radiotherapy the adverse effects present a significant clinical problem.

1.4 Mechanisms of therapeutic activity of radiotherapy on tumours

The dose response curve of radiotherapy for cancer control and normal tissue side effects was characterised initially as sigmoidal in nature, with small changes in doses resulting in large changes in effects on both tissue types (33) (34). Therefore, in the early stages of irradiation, tumour eradication was rarely achieved without substantial normal tissue damage (24).

Bergonie and Tribondeau et al. (27) determined that cells with a high mitotic rate and undifferentiated state (a common trait of malignant cells), demonstrated increased radiosensitivity. Also during the 1950s Gray et al. and Puck et al. observed that hypoxia played a significant role in radio-resistance of tumours, especially the necrotic core of the tumour which was at greatest distance from the surrounding vasculature (35). Earlier, Mottram et al. had demonstrated that in the presence of oxygen, cell death increased up to 3.5 fold, likely due to repair of DNA damage induced by reactive oxygen species (36). In the tumour micro-environment, the pattern of hypoxia is often heterogeneous and further insult with radiotherapy is thought to drive up-regulation of factors such as hypoxia induced factor 1α (HIF1α),

which in turn leads to downstream signaling protective against apoptosis, in both tumour and endothelial cell populations (37). Therefore, strategies to counteract hypoxia triggered further research endeavors using hyperbaric oxygen techniques and hypoxic cell sensitisers (33) (38). Another critical concept, introduced by Baclesse, aimed to capitalise on heterogeneous tumour hypoxia in large sized primary lesions. Termed 'target volume shrinking' radiotherapy, it reduced the burden of large cancers to a more resectable size in order to improve the chance of clearance and to minimize the disfigurement of radial extirpative surgery (25) (33). Fletcher et al. also reported that radiotherapy was useful in the control of small/microscopic or subclinical cancers along with additional control achieved by irradiation of clinically uninvolved lymphatic nodal basins (33). In the 1940s, the prevailing concept of the "all or none canceroidal dose" described radiotherapy as a single modality treatment, delivering a homogenous dose tailored to the whole cancer (33). Fletcher's observations in the 1970s challenged this concept, as physicians began to recognize that different tumour tissues and sizes responded differentially to radiotherapy doses (33).

After early anecdotal evidence that irradiation was able to provide a therapeutic benefit in cancer ablation, the need for staging scales and survival analysis to universally evaluate the efficacy of radiotherapy became apparent. Cancer specific staging such as the Tumour/node/metastases (TNM) system, first proposed by Denoix in 1946 (33), was implemented in practice to aid in prognostication and planning of tumour treatment and is the basis of staging systems used today for the majority of solid tumours. Prior to the 1950s, only survival rates had been reported. However, the survival analysis was subsequently refined to include; 1) failure at the primary site, 2) failure of loco-regional control (lymphatic basins), 3) failure of prevention of distant metastases and lastly, 4) new incidence of tumour (33).

The 1970s saw further clinical investigation into the role of radiotherapy in improving cancer survival. In the case of squamous cell carcinomas in the head and neck region, several reports from centers such as M.D. Anderson demonstrated that the use of a conservative cancer resection and limited neck dissection combined with pre or post-operative radiotherapy yielded improved disease free survival rates, in addition to superior functional and cosmetic outcomes (39) (40) (41). In contrast, in the management of breast cancer, irradiation for advanced non-operable tumours lead to

higher failure rates and an initial clinical conclusion that radiotherapy was not useful for treating breast cancer. Instead radiotherapy became considered to be a palliative procedure, in which the fibrotic changes within the surrounding tissue "locked in" cancer cells. In these patients high mortality rates occurred as a result of exophytic recurrence or distant metastases (42). Eventually, however, radiotherapy did gain a place in the management of breast cancers, with its effectiveness demonstrated in improving the survivorship of patients with axillary, supraclavicular or parasternal node-positive disease (43) (44). These findings were an initial indication that lymphatic node disease was a strong prognostic indicator of survival; a concept that has formed the basis of sentinel lymph node biopsy (SLNB) today (45). This method samples the lymph-node (or nodes) most likely to harbor early metastatic tumour as indicated by preoperative injection of either radio-labeled tracer or patent blue dye (or both) (46). Sentinel lymph node biopsy was implemented in the management of melanoma (47), breast carcinoma (48), squamous cell cancers (49) and gastrointestinal tumours (50) (51). Seminal publications such as that by Veronesi et al. demonstrated equivocal survival of early breast cancer patients with breast conservative surgery and radiotherapy, in comparison to the then standard radical and disfiguring mastectomies (52) (53). This concept of treating each patient according to the biological differences in the tumour lead to a progressive change in management of breast cancer worldwide. Randomized trials were also designed to assess radiation for use in rectal cancers and soft tissue sarcomas and demonstrated a clear survival benefit from the concurrent use of radiotherapy and surgery which resulted in a change in the management of many types of cancer. With the options of neoadjuvant and adjuvant treatment, radiotherapy can now be tailored to cater to individual patients, tumour volume and specific tumour types (25) (33).

1.5 Mechanisms of radiotherapy induced soft tissue injury

Radiotherapy impacts all tissues, firstly through the physical effects created by the interaction between radiation and atoms/molecules of recipient cells, which later progress through complex chemical and molecular reactions to produce the biological damage that culminates in the clinical phenomenon of radiotherapy injury (2) (54). The factors that contribute to radiotherapy injury and govern normal tissue tolerance were succinctly summarized by Dorr et al. as being dependent on; 1) inherent tissue

radiosensitivity, 2) rate and dose of radiotherapy fractionation, 3) tissue repopulation and turnover rates, 4) volume of tissue exposure, 5) oxygenation of tissues, 6) redistribution of cells across phases of the cell cycle and lastly, 7) complex molecularly regulated cell signaling (9) (55).

The skin is a vital organ, acting as a barrier against infection and exposure to the external environment while also regulating liquid and electrolyte balance. These functions are all compromised when the barrier is breached as a consequence of radiotherapy (56). Re-establishing total structural integrity after wounding of skin is highly dependent on processes of re-epthelialisation, angiogenesis and lymphangiogenesis, processes which are markedly dysfunctional in a pre-irradiated field (see section 1.7) (56). The epidermis of skin is largely comprised of keratinocytes arranged in a 5 layers (the deepest of which is the basal layer and contains stem cells), as well as a dermal layer which is predominantly constituted of collagen, dermal blood and lymphatic microvascular networks and sebaceous and apocrine structures (9). The clinical issue of normal tissue tolerance arises from the fact that, whilst intended to target cancer cells, a majority of radiotherapy is delivered via external beams, therefore normal skin and underlying subcutaneous tissues are inevitably irradiated and injured, with up to 60-70% of the total dose being absorbed by superficial tissues (Figure 1). This may occur repetitively in the case of multi-beam therapies, which involve both an entry and exit site. Therefore, the challenge in managing these effects still lies in obtaining optimal tumour control, while minimizing normal tissue complications (Figure 2) (2) (9).

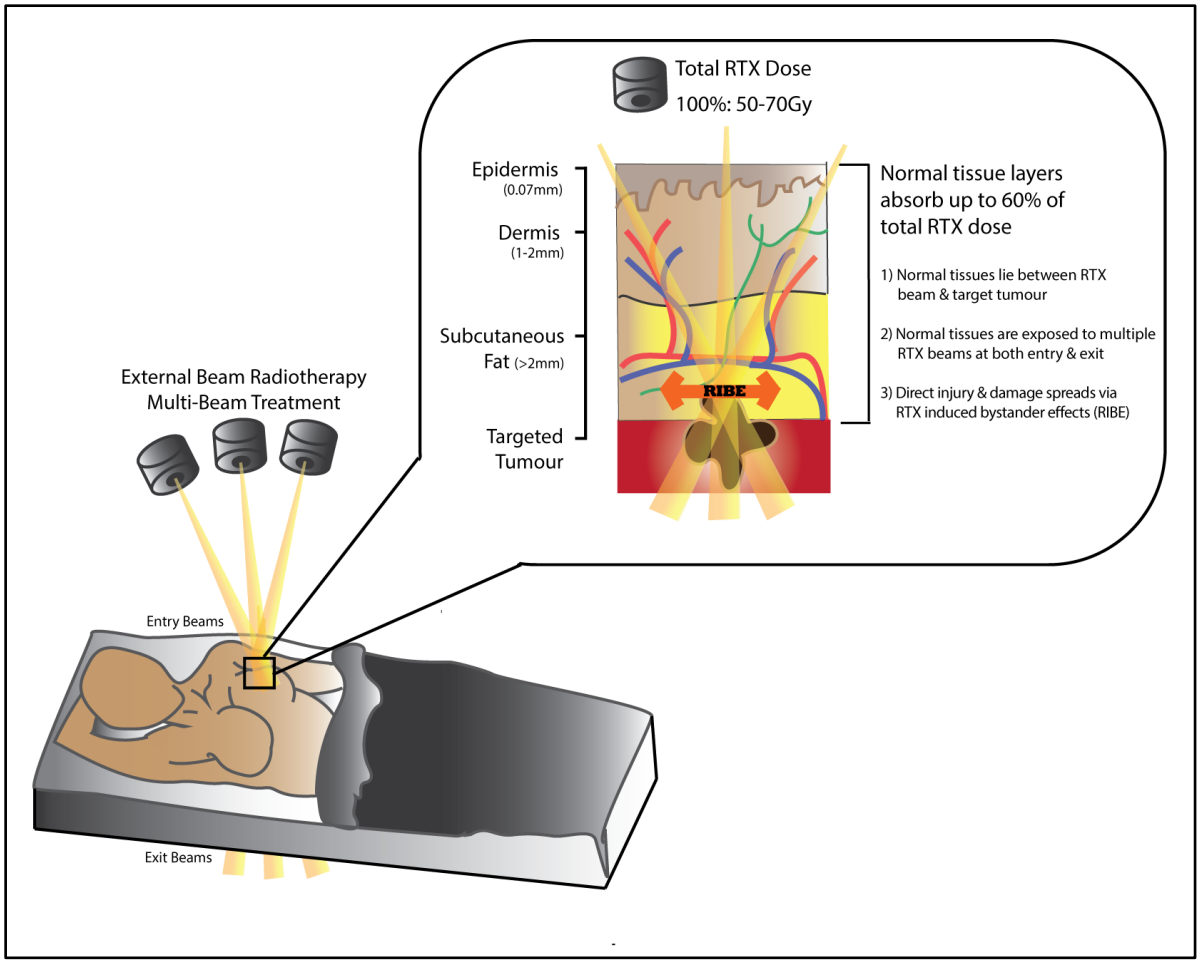

Figure 1

Figure 1 Mechanisms of normal tissue radiotherapy injury

A schematic diagram illustrating tissue absorption of external beam radiation administered radiotherapy (RTX) as it traverses normal skin and subcutaneous tissues on its way to the targeted tumour. The radiotherapy beam interacts with living tissues resulting in electron excitement, release of energy and damage to both tumour and normal tissue cells. Normal tissues can absorb up to 60% of the total radiotherapy dose targeting the tumour.

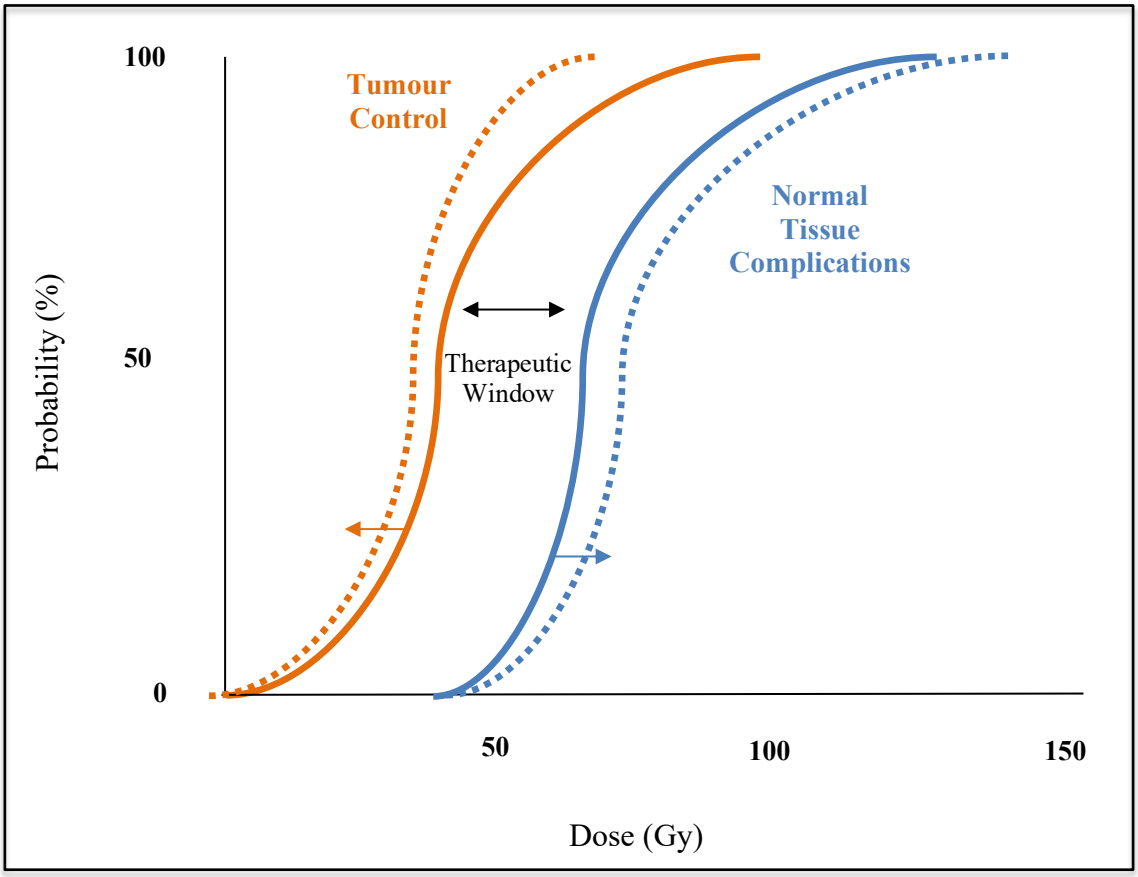

Figure 2

Figure 2 The therapeutic window of radiotherapy – balancing tumour control with normal tissue complications.

This diagram demonstrates the sigmoidal relationship between radiotherapy dose (Gy), tumour control (solid red line) and normal tissue complications (solid blue line). As doses of radiotherapy increase, the percentage of tumour cell control or ablation sharply increases while normal tissue complications lag behind until reaching doses greater than 60Gy. These higher doses lead to an unacceptable level of normal tissue compromise. Therefore, this diagram illustrates the narrow therapeutic window of acceptable radiotherapy doses which are utilized in modern practice. The dotted lines represent potential for shifting these curves, with postulated response rates of tumour control with tumour sensitisers (dotted red line) or increased protection of normal tissues with radioprotectors (dotted blue line). Diagram adapted from (9) (57).

The International Commission on Radiological Protection (IRCP) determined that the basal layer of the epidermis lay at a depth of 0.7mm while structures such as dermal lymphatic capillaries and fibroblasts exist predominantly at 1.0-3.0mm (9). Various groups have investigated methods by which to measure the dose delivered at these levels and the variables that may alter the degree of exposure of superficial tissues to radiotherapy. The key factors that play a significant role in determining the skin surface dose of radiotherapy i.e. the dose that leads to normal tissue side effects include: the irradiation source to surface distance (SSD) (typically 100 cm), obliquity of the beam, beam modifiers, field size, photon scatter, entry and exit site exposure, heterogeneity in tissue density and the use of bolus doses (9) (10) (58). Quach et al. investigated the effect of the skin surface dose on a curved surface, attempting to replicate the hemi cylindrical chest wall, using three modalities of detection: radiochromic film, thermoluminescent dosimeters and a metal oxide semiconductor field effect transistor (MOSFET) dosimeter (58). 50Gy dose administration demonstrated considerable variability in the resulting skin surface dose, with maximal superficial dose found 90^{o} to the angle of exposure. The addition of a bolus to doses demonstrated increases up to 350% at the skin level with only minimal increases in exit doses. This was mechanistically explained by Quach et al., envisaging a buildup of dose on the 'entrance side', while the remainder of the dose traversed deeper tissues, and is subject to the inverse square law; in which the intensity is inversely proportional to the square of the distance from the source (58). Kry et al. concluded that a larger field size, smaller SSD and increased obliquity of the beam >55^{o} (without bolus), increased skin surface dose within the field of treatment, whilst the increased depth of the tumour correlated to a substantial increase in 'out of field' skin exposure, by up to 7 fold via back scatter (10).

Tissue survival has been described as a function of a radiotherapy dose using an equation based on the principles that radiation 'cell kill' results from two components; the initial linear slope (α) and the later quadratic slope (β) (2) (9). Multiple alterations to these equations have been proposed to enable the calculations that predict the normal tissue responses, including various dose fractionation regimes (59). On a basic level the α/β ratio describes the dose at which the non-repairable α component (linear), and repairable β component (quadratic), of cell killing are equal (2). The intrinsic sensitivity of the individual cells and the kinetics of cell turnover are

accounted for by the β component. Rapidly proliferating cells demonstrate increased sensitivity to radiation, therefore the β value is low and the ratio is high, characteristic of early irradiation injury with α/β= 10Gy in mammalian cells. Consequently, if the β value is high, as is the case in slow proliferating populations, in which there is increased time available for repair of sub-lethal damage, repair may occur during injury and the ratio becomes reduced. This is characteristic of late irradiation injury with α/β= 3Gy in mammalian cells (2) (9). The proposed biological mechanisms of injury are detailed in the sections 1.5.1 – 5 below.

1.5.1 Direct and indirect biological mechanisms of radiotherapy injury

The term "direct effects" describes radiation causing irreparable damage to critical targets within the cell, such as lethal double stranded DNA breaks. The term "indirect effects" describes injury to irradiated and surrounding tissues due to the creation of free radicals and an ionizing cascade leading to single stranded breaks, crosslinking, incomplete repair and persistent cellular dysfunction (9) (60). 1Gy of irradiation leads to around 10^5 ionizing events corresponding with 1000-2000 events of base damage, 500-100 single stranded DNA breaks and around 40-50 double stranded breaks (9). Therefore, irradiated tissues exist in a state of chronic inflammation and are constituted by cells that harbor latent potentially lethal DNA damage, which can undergo episodic bouts of radiation-related cell death (61).

Initial hypotheses classically described the effects of radiotherapy as the proportion of cells irreversibly damaged by radiation as a result of lesions in their replicative mechanism. Thus, severity of injury and the time between radiation and manifestation of injury were thought to be dependent on target cell killing (38). However, after assessment of the clinical manifestations of radiotherapy damage, it has been suggested that *direct* cell killing or apoptosis cannot fully account for all the effects of radiotherapy injury. In particular, the late side effects are likely to be a result of the sub-lethal or *indirect* damage with perturbation of molecular signaling, creation of reactive oxygen species (ROS) and a coordinated active biological response, brought about by the early release of chemokines and cytokines (9) (17) (61). The mechanisms of indirect injury are largely driven by the generation of mitochondrial reactive oxygen species (ROS) (62) and they are thought to be responsible for up to 2/3 of the

damage caused by radiotherapy (63). ROS generation results from ionizing energy causing hydrolysis of water, in turn leading to the release of hydrogen (H^+) and hydroxyl radicals ($^\bullet OH$). The combination of two hydroxyl radicals forms hydrogen peroxide (H_2O_2), that is initially volatile and unstable intracellularly, which once stabilised can lead to mutation or cell death (63). Additionally, free radicals such as superoxide (O_2^-) and other organic radicals ($^\bullet R$) may also be formed, themselves subsequently forming organic hydroperoxides ($^\bullet ROOH$), that may undergo Fenton and Haber-Weiss reactions with metals such as Iron (Fe) and Copper (Cu) (64) thus potentially contributing to tissue injury. In addition to ROS, reactive nitrogen species (RNS) such as the peroxynitrite anion ($ONOO^-$) can be produced from nitric oxide (NO), catalyzed by nitric oxide synthases (iNOS) and also contribute radiotherapy injury (64). This injury may also be transmitted to cell progeny or to neighbouring cells. The mitochondria within cells are considered to collectively be the powerhouse responsible for the generation of energy through a set of highly regulated steps that involve the oxidation of ingested carbohydrates, proteins and fat; as well as production and processing of ROS (65). Mitochondria occupy a significant intracellular volume and are therefore highly likely to be targets of radiotherapy injury (62). While the electron transport chain is relatively efficient for oxidation i.e. removal of electrons, in basal conditions about 1-5% of oxygen consumption is still reduced to form O_2^- and H_2O_2, which is thought to markedly increase in response to oxidative stresses such as radiotherapy (64) (65). The increased abundance of highly reactive oxygen or nitrogen species, which saturate counteractive intracellular anti-oxidants, lead to processes such as lipid peroxidation, base damage, crosslinking and telomere dysfunction (65) while further propagating ROS generation. This results in accelerated senescence, injury, mutagenesis or cell death if the damage is incompletely repaired (64). ROS may exert these injurious effects by acting as secondary messengers, by altering activation of phosphatases through conformational change, increasing transcription factor binding and modifying gene expression and/or stability (64). The cumulative effect of these ROS-driven alterations is likely to severely hamper the cell's attempts to modify cellular metabolism in response to the pathological stimulus. At a mitochondrial level, irradiation has been noted to increase pentose phosphate pathway activity, resulting in increased NADPH production, which is a reducing agent and can attempt to combat oxidative stress (64). However,

NADPH oxidases expressed by inflammatory cells or nearby fibroblasts, either recruited or activated in response to irradiation, can also produce O_2^- and H_2O_2 from NADPH, which in turn leads to increased oxidative cell injury (65). Ultimately, if radiotherapy induces significant damage of metabolic regulatory mechanisms, such as components of the electron transport chain, this will lead to a depletion of antioxidant production, an increased rate of 'one electron reductions' of O_2 to form O_2^- and H_2O_2, and eventually contribute to continuing irradiation injury and the development of long-term tissue side effects (64). Multiple studies have explored combatting this form of injury with increasing intracellular or extracellular concentrations of anti-oxidants (such as manganese superoxide dismutase (MnSOD), which specifically targets mitochondria), and have shown that many of the deleterious effects of radiotherapy injury can be reduced (60) (66) (67). This was exemplified by Epperly et al. who demonstrated that the anti-oxidant effects of recruited stem cells to the site of irradiation included reduced esophageal fibrosis which translated to clinical benefits such as reduced stricture formation (68).

The dichotomous response of cells to radiotherapy injury can therefore be characterised by direct cell death (which accounts for depletion of functioning epithelial, endothelial and stromal cell populations) or by indirect, sublethal disruption of the repair mechanisms, activation of premature senescence or accelerated differentiation pathways. Persisting ongoing sub-epithelial inflammation is likely to be potentially responsible for the chronic injury, long after the early tissue reactions have regressed (17) (61). Therefore, "cell death", in the setting of radiotherapy induced soft tissue injury, may represent the loss of a cell's reproductive ability, while it still retains physical viability (9) (69). Thus, the pathogenesis of radiotherapy injury becomes a continuum of events that perpetuates damage to surrounding normal tissues (see section 1.5.5).

1.5.2 Mechanism of radiotherapy injury repair in normal tissues

The ability of a cell to repair DNA damage is dependent on radiotherapy dosing (linear-quadratic curve), phase of the cell cycle, as well as perfusion and oxygenation of tissues (63). Double stranded DNA breaks present the greatest reparative challenge, usually represented by the presence of γ-H2AX which results from relaxation of the

damaged segment of DNA, making the site available for attachment of repair proteins (70). Repair processes are dependent on cell cycle phase with homologous recombination if the cell is in S or G2 and sister chromatids are readily available, or non-homologous end joining (NHEJ) in other phases, particularly G1. Effectively, the process involves an excision of the 5' end of the damaged DNA and the remaining 'overhanging' 3' end is filled by matching a similar (non-homologous) or an identical (homologous) strand of DNA (71). Repair of single stranded breaks occurs via base excision repair, and if the helical structure is damaged, and may also involve nucleotide excision repair (70).

Dorr et al. described three key principles involved in repopulation of cells after irradiation; asymmetrical loss, acceleration of stem-cell division and abortive division (72). They concluded that repopulation of a group of cells in response to an injurious trigger is driven in response to the loss of local stem cells as well as the magnitude of ongoing loss as a result of physiological cell turnover (72). Therefore, an injured environment requires net stem cell production for tissue regeneration. In the case of radiotherapy, there is a shift from asymmetrical stem cell division producing one daughter stem cell and one differentiating daughter cell, to symmetrical division producing two daughter stem cells, compounded with a 50% rate of stem cell sterilization if fractionated therapy is being delivered (72). Therefore, at the very least, this shift allows for a constant stem cell number to be maintained during the treatment phase, allowing for regeneration of tissue on cessation of irradiation. At this time point, there is marked acceleration of stem cell division to allow effective repopulation and restoration of normal tissue, where low survival fractions must be compensated for by more symmetrical division and rapid proliferation of stem cells (55). There is, however, a 'lag-phase' after the initiation of therapy for up to 7-14 days as demonstrated by Turesson et al. who detected suppression of Ki67 proliferative marker and an increase in levels of p53 and p21 (potent cyclin dependent kinase and proliferating cell nuclear antigen inhibitors) in basal keratinocytes after daily 1Gy dosing, with gradual acceleration of proliferation after 2.5 weeks (73). With respect to stem cell populations, Dorr and Weber-Frisch et al. showed that five fractions of 2Gy left only 9% of the original murine mucosal stem cell population alive at 7 days, necessitating 6-8 asymmetrical divisions per day to rapidly regenerate tissue (74). Even with acceleration, the cells would not compensate for a shortened

cell cycle of only a few hours required, therefore the concept of abortive divisions was proposed (75). This theory postulated that the sterilized daughter stem cell (carrying irreversible chromosomal damage) could still undergo limited division prior to terminal differentiation, aiding in the maintenance of a physical barrier and thus minimizing development of side effects such as mucositis (72). Such hypothesis is supported by findings of increased expression of p21 (an inhibitor of cell cycle progression) in irradiated skin samples. p21 is also thought to be responsible for the regulation of keratinocyte stem cell self-renewal, with promotion of terminal differentiation rather than maintenance of stemness (73). However, while the process of abortive division acts as a temporizing measure while the body attempts to find an alternative source of cells for regeneration, the lingering presence of such damaged 'sterilized' cells may allow for propagation of radiotherapy injury through bystander mechanisms (see section 1.5.5).

1.5.3 The effect of radiotherapy during phases of the cell cycle

The series of steps which must be undertaken by a cell to divide are described as the cell cycle; consisting of four phases which are tightly regulated; 1) G1 where cell organelles replicate to prepare for division, 2) S where DNA duplicates itself, 3) G2 where the cell checks for any aberrances in DNA replication and lastly 4) M phase where the process of mitosis (cell division) occurs (63). During the G1 phase, cells may also leave the cycle and enter a G0 phase, a phase of senescence or arrest. As a cell progresses through the cell cycle, the effects of radiotherapy are largely dependent on the predominant activity associated with the phase. Phases involving active replication of cellular machinery, such as G1, G2 and M are particularly radiosensitive, in comparison to S phase where the abundance of DNA replication regulators ensure more stringent detection and correction of any DNA damage (63). Furthermore, transition from one phase to another is controlled by passing through checkpoints, namely from G1/S and G2/M, which are intended to prevent replication of a damaged cell. The effect of ionizing γ-rays on these particular checkpoints can affect multiple regulators genes, activating particular checkpoints and reducing cell proliferation (76). The G1/S phase is governed predominantly by genes such as p53, p21 and retinoblastoma protein (Rb) which in turn control various cyclin dependent kinases (namely CDK4/6-cyclin D and CDK2-cyclin E). Overall these controls only

allow transition to the S phase of DNA replication if the DNA is undamaged (77). When DNA has been damaged by irradiation, p53 accumulation results in activation of p21 and inhibition of Rb phosphorylation, preventing signal translocation to the nucleus and transcription of DNA replication genes required in S-Phase (63). Zhou et al. demonstrated that doses of 1.5Gy administered to human neonatal foreskin derived fibroblasts, resulted in G1 arrest and depletion of cells in S and M phases as early as 6 hours after treatment; and postulated that p53 is largely accountable for trans-repression of cell cycle progression via down-regulation of cell cycle genes CDC2, CCNB1 and Top2a (76). Turreson et al. also demonstrated increasing p53 and p21 using immunohistochemical staining in skin biopsy samples from patients 2-3 weeks after low dose (1-2Gy daily) fractionated radiotherapy treatment (73). Typically, p53 may be associated with apoptosis and removal of non-viable cells from the replicating pool (78). However, in models of radiotherapy injury such as Belyakov et al.'s explant urothelial experiment, the predominant cell cycle response to injury was found to be increased rates of terminal differentiation, rather than large scale apoptosis, a mechanism that the authors suggested may be protective in nature (78). Overall, p53 may increase the lifespan of radiotherapy-damaged cells, which then have the opportunity to initiate bystander signaling propagating irradiation injury to other non-targeted cells (78).

Alternatively, the G2/M checkpoint is responsible for detection of chromosomal abnormalities before mitosis and is thought to be regulated by two main checkpoints one of which is ATM (ataxic telangiectasia mutated)-dependent, and the other is ATM-independent. ATM plays a role in detection of DNA damage, and mutations in these genes in patients are shown to result in extreme radio-sensitivity (79). Through phosphorylation ATM moderates the activity of various CDKs allowing G2/M progression as well as modifying the breakdown of p53. ATM independent pathways involve chk1 and chk2, which through phosphorylation inhibit CDC2 kinase and arrest cells at the G2/M phase (63). Due to the fact that cells all exist in a flux between phases of the cell cycle, Marples et al. proposed the cells in the radiosensitive G2 phase, may progress to mitosis within 30 minutes of irradiation, despite DNA damage; and that these cells therefore carry the injury and a susceptibility to further damage in their post-mitotic phase (80) (81). This observed redistribution of cells within the cell cycle may, increase the genotoxicity of radiotherapy delivered in a

protracted manner. This means that a cell surviving the first fraction is made more radio-sensitive to subsequent fractionated treatment (9).

Zhou et al. studied the early gene profile 6 hours after radiotherapy using human neonatal foreskin derived fibroblasts. The genes suppressed included; BRAC1, MAD2L1, MCM2, MCM3, MCM6, RAD51, RAD54L, RFC4, TIMELESS and TOBP1 (76). Genes repressed at 24 hours irradiation included; BUB1, CCNB1, CCNB2, CDC2, CC20, CDK2, E2F1, KNSL4, PCNA and TOP2A. In contrast genes increased at 24 hours included COLEC12, DCN, F10, FBLN1, LAMB1, LHPP, LXN, SEMA38, SOD3 and SQRDL (76).

1.5.4 Senescence

Senescence is described as a state of cell growth arrest, which is thought to be important in processes of tumour suppression, tumour promotion and aging. It is also pertinent to tissue injury and initially involved with repair and regeneration (82). Senescent cells may still be metabolically active but significantly stunted in their proliferative and differentiation abilities (83). While there is a lack of strict criteria defining a senescent cell, Rodier et al. reviewed and compiled a list of prominent features including: an increase in cell size, expression of β-galactosidase (reflecting increased lysosomal volume), expression of p16INK4a (a tumour suppressor or anti-proliferative gene), DNA damage harbored in the nuclei with expression of proteins such as ATM and Rad3. Finally, the secretion of a multitude of paracrine and autocrine factors by cells with a senescence-associated secretory phenotype (SASP) (82). Igarashi et al. and Oh et al. demonstrated that gamma irradiation doses between 5-15Gy of confluent vascular endothelial cell monolayers exhibited high rates of cellular senescence as detected by β-galactosidase positivity and up-regulation of genes such as CDKN1A. When these cells were trypsinised and re-plated, they demonstrated an increase in their senescence phenotype suggesting that confluent cell DNA repair mechanisms were more robust than cells required to actively divide. Additionally the angiogenic capacity of these senescent irradiated cells was markedly diminished when tested with migration and matrigel tube formation assays (84) (85). Zhi et al. demonstrated similar findings with murine bone-marrow derived stem cells, with greater than 40% increase in senescence detected after 8Gy irradiation at 2

weeks; as well as a marked increase in cell cycle distribution of cells in the G0/1 phase. These findings were all associated with up-regulation of p53 and CDKN1A that was detectable from 24 hours up to the 2-week end point (86).

SASP factors have the potential to facilitate a multitude of processes, including perpetuation of chronic inflammation and spread of tissue injury to adjacent cells in a paracrine fashion; which can impair tissue regeneration or potentially provoke invasion of pre/malignant cells (82) (87). Additionally, this chronic inflammation is also thought to be the basis of numerous age-related diseases (atherosclerosis, osteoporosis, dementia and various cancers). These diseases are thought to be due to persistent oxidative stresses applied by the immune and inflammatory cell infiltrate which lead to remodeling, dysfunction and alterations to the regenerative capacity of tissues by affecting the stem cell niche, or in the case of malignancies, inducing neoplastic transformation (82) (88). Therefore, this intermediary state between proliferation and apoptosis poses a significant issue; as the accumulation of metabolically active senescent cells may contribute considerably to propagation and worsening of cell injury. Further investigations are required into methods by which senescent cells can be cleared from the area of injury if irreversibly damaged, or alternatively how they may be reverted back to the proliferative pool if damage is reversible. These approaches may provide novel avenues to combat some of the unwanted consequences of radiotherapy injury.

1.5.5 Radiation induced bystander effect (RIBE)

The issue of “leakage”, is a phenomenon that is encapsulated by concept known as radiation induced by-stander effect (RIBE). RIBE is a form of radiotherapy damage, in which lethal or non-lethal DNA damage spreads beyond the targeted field and induces cell death and dysfunction in adjacent un-irradiated tissues (89) (90). RIBE has been mostly observed in experiments using high LET α-particle irradiation, rather than low LET X-ray and gamma radiation (91). Double stranded DNA breaks, or other forms of genomic instability such as chromosomal re-arrangements, mutations or the formation of γ-H2AX are thought to be induced in ‘non-targeted’ cells neighbouring those targeted by the radiation, or *in-vitro* in cells grown in culture medium collected from irradiated cells (80) (90) (92) (93) (94). γ-H2AX is the phosphorylated form of the tumour suppressor gene H2AX, which is found on

chromatin adjacent to the site of dSDNA damage; and is involved in DNA repair. γ-H2AX appears transiently within 30 minutes in the target cell, but remains elevated up to 18-48 hours in cells affected by RIBE (80). Zhou et al. used a model of precisely targeted α-particle irradiation with microbeams on confluent cell cultures of human hybrid hamster cells and demonstrated if 10% of cells were irradiated, the observed rate of damage became similar to when the 100% of the identical cell population was irradiated (95). The mechanisms underlying RIBE remain largely unknown, however, proposed hypotheses including generation of ROS, cell-cell gap junction communication or intercellular paracrine effects of cytotoxic factors secreted by injured targeted cells (90) (92) (96).

Blockade of gap junction communication with agents such as Lindane or Octanol, demonstrated reduction in the bystander effect quantified by reduced γ-H2AX staining after irradiation, but only in direct cell co-culture experiments and not in conditioned media models. This suggests that irradiated cells may produce an altered secretome to influence surrounding cells via vesicular release, even when cell-cell signaling is blocked (80) (95). To examine mechanisms of RIBE further, Zhou et al. demonstrated cell-cell communication using Lucifer yellow in wild-type A_L cells or cells overexpressing the protein connexin 43. Dominant negative cells in this experiment showed very little manifestation of the bystander effect, indicating that connexin 43 may be an important target in reducing the ability of cells to utilise cell-cell communication propagating the front of bystander effects (95). Hei et al. proposed a molecular mechanism for signaling pathways that play a role in RIBE which centered around inflammatory cytokines such as TNFα and IL-1β; leading to activation of MAPK pathways and phosphorylation of NFKB. This event in turn leads to transcription of COX-2 (up to 6-fold increase in bystander cells) and Nitric Oxide Synthase (NOS). COX-2 and NOS combined to produce Prostaglandins and Nitric Oxide which lead to the induction and propagation of downstream injury via mechanisms such as chromosomal aberrations, apoptosis, cytokine and ROS production (93) (96). Additionally, a decrease in insulin growth factor binding protein-3 may also be able to initiate downstream signaling, resulting in COX-2 expression. The combined effect of RIBE is thought to provide ongoing free radicals that lead to late radiotherapy-related side effects, independent of p53, and such

induced cytokines may provide excellent therapeutic targets to reduce the manifestations of RIBE (see section 1.9.7) (93).

As previously mentioned, the mitochondria are vital organelles responsible for energy production occurring via regulated oxidation reactions carried out by the cytochromes in the electron transport chain (see section 1.5.1). Leach et al. demonstrated radiation related MAPK up-regulation is linked to the action of ROS, resulting in localised Ca^{2+} release, which is taken up by neighbouring mitochondria, leading to mitochondrial permeability transition (MPT) and further ROS/RNS production (62). Conversely treatment with Ca-chelators and pharmacological blockade of MPT, electron transport or mitochondrial DNA deficient cells exhibited diminished or absent irradiation induced-MAPK expression (62). To further examine the role of mitochondria in RIBE, Zhou et al. elegantly demonstrated that normal human lung fibroblasts depleted of mitochondrial DNA had diminuted tolerance to oxidative stress. The absence of mitochondrial ROS generation lead to overall depletion of intracellular anti-oxidant levels, in turn resulting in a greater likelihood of 'bystander mutagenesis' (93). Mitochondria DNA depleted cells also demonstrated reduced expression of NFKB and downstream targets COX2 and NO synthase (iNOS) after irradiation. Using pharmacological blockade of NFKB with Bay 11-7082 it was determined that NFKB/COX-2/PGE2 and NFKB/iNOS/NO pathways were more critical to generation of RIBE in cells containing normally functioning mitochondria; while in mitochondrial DNA depleted cells, COX-2 mediated bystander processes were of less consequence in comparison to iNOS mediated RIBE (97). Therefore overall, the mitochondria of direct and indirectly affected cells may also present important targets in mediating the processes of RIBE (97) (98).

Taking the data relating to RIBE into consideration, it is more likely they are responsible for the late side effects and progressive worsening of radiotherapy injury than a large-scale cell death induced by direct lethal DNA damage (91) (99) (100). While the targeted cells may spread injury, the characteristic genetic alterations in directly irradiated cells differ from those cells that are not directly hit, as indicated by the differences in number of chromatid breaks seen in each group (95). To date, studies provide some mechanistic information and potential targets for combatting RIBE, but are limited by the use of α-particles (high LET), and be difficult to directly

extrapolate to injury caused by low LET X or gamma-ray treatments. Therefore, defining the molecular mechanisms or transmissible secreted factors that drive RIBE in individual cell types is integral to gaining an understanding and target reversal of chronic effects of radiotherapy injury (Figure 3).

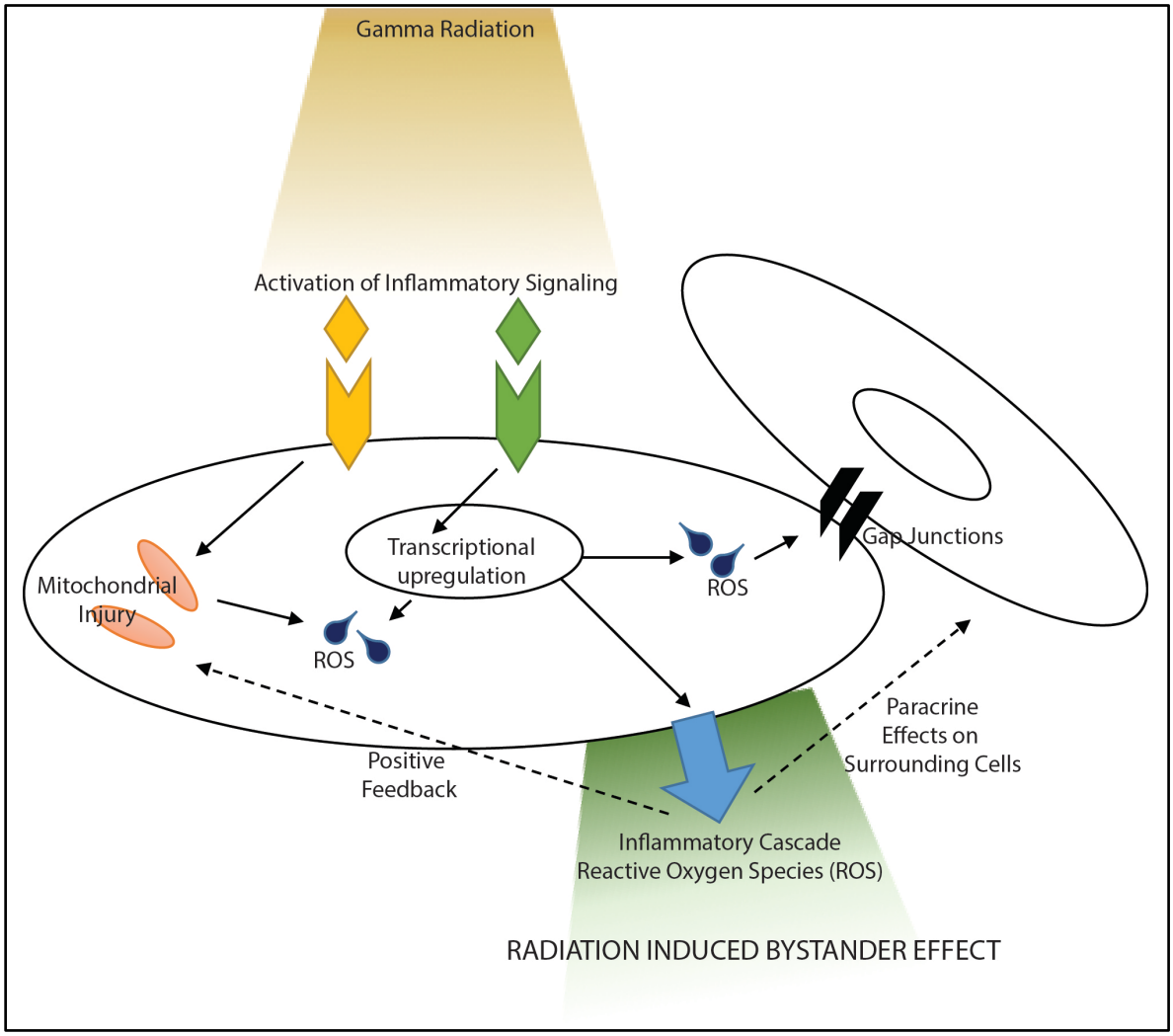

Figure 3

Figure 3 Mechanisms of radiation induced bystander effects

Schematic diagram detailing the mechanisms that lead to the development of radiation induced bystander effects. The direct action of gamma-radiation on targeted cells leads to the activation of several inflammatory cytokine cascades. Intracellular transcriptional alterations as well as significant mitochondrial damage lead to the development of reactive oxygen species and further inflammatory cytokines and growth factors. All of these processes are propagated to neighbouring cells via either direct cell-cell communication through gap junctions or indirectly by the paracrine secretome of the injured cells. In the zone of inflammation, these processes all generate positive feedback which prolongs the response and resultant damage. The exact molecular mechanisms that regulate this process as a result of radiotherapy injury to skin and subcutaneous soft tissue injury remain to be clearly elucidated.

1.5.6 Differences in responses of normal cells and tumour cells

A key difference between normal and tumour cells are mutations in cell cycle checkpoints. Activation of these checkpoints in normal cells allows time for repair of reversible damage, whereas acceleration through these phases in cancer cells, allows for the accumulation of lethal DNA damage, which results in cell death within a few cycles (63).

Direct cell injury is usually due to DNA damage, with more energy required to produce permanent double stranded DNA (dSDNA) breakage, than single stranded (sSDNA) breaks (63). Brown et al. therefore concluded that actively replicating cells are relatively radiosensitive, a characteristic of cancer cells which are rapidly dividing (63). However, significant impairment in DNA repair mechanisms of malignant cells, hinders the ability to repair sub-lethal damage, thus exposure to subsequent fractions of radiotherapy treatment, furthers the damage and leads to cancer cell death (63).

1.6 Improvements in the field of radiotherapy

The field of radiotherapy has made significant advances since the days of Roentgen's discovery of X-rays in 1895 and Curie's discovery of radium and gamma rays in 1898

(101). Fractionation aims to capitalize on normal cell repair mechanisms being more robust than those of tumour cells, allowing normal cells to repair sublethal damage and replace lethally injured cells by migration and repopulation (9) (17) (28) (34). The caveat is that each fraction contributes to accumulating tumour and normal cell injury, thus maintaining the inflammatory response.

In clinical practice, there are a variety of fractionation regimes such as hyperfractionation, which utilizes two or more small fractions per day, separated by at least six hours (the postulated time required for sub-lethal damage repair), or hypo-fractionation, which uses larger doses spread a few days apart (24) (102). The concept of fractionated radiotherapy came from observations of reduced late side-effects and improved tumour control (103). An important relationship exists between fraction dose and overall treatment duration. It is postulated that late effects are more responsive to modulation of fraction size rather than overall treatment time, unlike early/acute responses (104) (105). Certain dose-rates may lead to the formation of the 'reverse dose effect', particularly in more rapidly proliferating cells. This fractionated dose rate corresponds to cell accrual in G2 radiosensitive phase of the cell cycle; and subsequent small doses result in an increased proportion of lethally injured cells (106). For more slowly proliferating tissues, repopulation occurs after an extended delay and failure to immediately regenerate is thought to account for compensatory fibrosis and loss of intrinsic functionality of normal tissues (9).

3D guided conformal radiotherapy plays a vital role in the initial planning as well as Computer Tomography (CT), Magnetic Resonance Imaging (MRI) or Positive Emission Tomography (PET)-guided 'sculpted' delivery of radiotherapy to the tumour site with multileaf collimators (107). These collimators are made of small gold leaves, allowing computerized beam shapes to 'wrap' the tumour (24) and enable targeted dose escalation, calculated with computerized algorithms, while avoiding excessive normal tissue side effects. This is particularly useful for treatment of prostate cancer as nearby sensitive rectal tissue has an incidence of up to 60% for wound breakdown after radiotherapy (108).

Optimization of delivery techniques in the early 2000s saw the advent of reverse or inverse planned Intensity Modulated Radiotherapy (IMRT), which allowed for

modulation of photon beam intensity during the delivery of each fraction, allowing for tumour boost doses to be delivered to areas of high tumour burden while lowering intensity in areas of microscopic disease or normal tissue (109). Its utility has been demonstrated on concave surfaces such as in head and neck cancers, allowing for reduction in normal tissue doses therefore facilitating, for example, parotid preservation and reduction of the incidence of severe xerostomia (110). However, IMRT necessitates 2-3 times more monitor units, which results in increased total body dose due to increased radiation "leakage" (24) (111). Improvements to IMRT include adaptations such as tomotherapy, which utilizes a modified CT scanner to image and concurrently delivery radiotherapy in a dynamic 'live' format, yielding higher targeted doses to the tumour without increasing the treatment time (25).

Stereotactic radiotherapy was first utilized for intra-cranial lesions in conjunction with surgical devices such as the gamma-knife. This increased accuracy allowed for hypofractionation of a single fraction, with highly targeted delivery of Cobalt60 beams to treat small tumour volumes in a single day setting (112). Advances with this technique have allowed for the development of stereotactic body radiotherapy (SBRT), with particular utility in extra cranial tumours that are mobile in nature such as primary or metastatic hepatic or lung cancers, with 3 fractions of 20Gy successfully treating lung or liver lesions (113) (114) (115). This technique has been reported to provide strong ablative outcomes in early lung cancers (116) as well as significant symptomatic improvement for patients with widespread metastatic disease (117).

Stereotactic radio-surgery, multi-model image-guided radiotherapy and various fractionation regimes, have attempted to increasingly achieve the goals of maximizing irradiation of tumour cells while limiting normal tissue exposure. Other technical advancements include mouse models demonstrating the utility of radio-immunotherapy, combining β-radiation-emitting radionucleotides specifically targeting a range of cancer cells (118) (119). Nevertheless, toxicity of radiotherapy has not been completely circumvented, especially as normal tissue constraints are offset by dose escalation, individual radiosensitivity or concurrent chemotherapy (67).

1.7 Postulated effects of radiotherapy injury on each component of skin and subcutaneous tissue

The different patterns of intrinsic radiosensitivity among cells and tissues were first demonstrated by Bergonié and Tribondeau in 1906, who found cells in a state of active division or undifferentiation were more prone to radiotherapy injury. Over the years it has been noted that each tissue type yields a different response to irradiation, likely due to; cell type, rate of proliferation and available repair mechanisms (9). At an organ level, arrangement in functional units with potential reserves, allows for significant irradiation without large scale clinically detectable side effects, whereas organs with small alternative reserves (arranged in series such as the spinal cord), have very low tolerance to irradiation injury. Below is a comprehensive review of the literature aiming to summarise the effects of radiotherapy injury on cells that constitute the skin and subcutaneous tissue.

1.7.1 Fibroblasts

Fibrosis is a recognized rate-limiting complication of radiotherapy and is defined as the accumulation of excess ECM which interferes with normal tissue functioning (14). As tissues are damaged, fibrosis is initiated as part of the healing response (61). Fibroblasts are the key cell type mediating the deposition of ECM, but the mechanisms underlying the regulation of fibroblast death and abnormal collagen production in this context are yet to be elucidated (14). Several studies have attempted to characterise the biological and molecular basis of radiation induced fibrosis (RIF). Iwahira et al. examined histological differences between specimens obtained from irradiated and non-irradiated breast skin with hematoxylin and eosin staining. Results demonstrated that the irradiated epidermis was thickened and that the dermal papillary layer was relatively flattened with atrophy of the dermal appendages. On examination of the collagen with azan blue staining the authors found dense, unidirectionally aligned collagen fibres with marked hypocellularity of the dermis (120). In a sample set of 20 patients they concluded that these alterations remained for up to 14 years post-radiotherapy and were likely to contribute significantly to complications in the breast such as capsular contracture, implant extrusion and limited expansion of irradiated skin in patients undergoing breast reconstruction surgery (120). Morphologically, irradiated fibroblasts display a myofibroblastic or post-mitotic fibroblast phenotype and functionally have reduced proliferative potential (106) (121).

Moreover, the acquisition of a myofibroblast phenotype can result from the influence of injured keratinocytes (215). These myofibroblasts and/or radiation induced post-mitotic fibrocytes are thought be biochemically active despite having undergone clonogenic death and demonstrate permanent DNA damage with a 45% reduction in life span (122) (123). They produce ECM components in excess; with a 5-8 fold increase in production of collagens I, III and IV, which are altered in quality, proportion and quantity (121), while unable to proliferate normally in response to trauma or wounding; likely contributing to the characteristic clinical picture of fibrosis with poor wound healing capacity (17) (122) (124) (125). 70-80% of normal skin is composed of collagen I and the remainder mostly constituted by collagen III (126), with the balance in synthesis being tightly co-regulated (127). Autio et al. used skin blister fluid to demonstrate that collagen markers such as type I procollagen and type III procollagen concentrations were almost twice as high in irradiated compared to unirradiated breast skin (128). Porcine studies using irradiated skin fibroblasts in a 6-20 month chronic radiation injury model, demonstrated increased attachment and proliferation, as well as a prolonged population doubling compared to normal counterparts (129). Therefore, understanding fibroblast mediated collagen metabolism in irradiation may suggest further novel targets for ameliorating radiotherapy induced fibrosis.

In other models of pathological fibrosis, such as systemic sclerosis, a multicellular inflammatory response has been seen to significantly drive the development of fibrosis (125) (130). It has also been postulated that modulating early gene expression changes and cell-cell interactions through the generation of cytokines such as TNFα and IL-1 in macrophages or endothelial cells, may be able to alter the composition, actions and subsequent reactions of the fibroblast system (125). Using a model of radiation-induced lung fibrosis, Rubin et al. determined that alveolar macrophages increased TNFα, IL-1, PDGF and TGF-β secretion in response to irradiation, which in turn increased ECM secretion in neighboring fibroblasts (131). An important change in the paradigm of radiation injury has been the recognition that immediate changes due to irradiation "sets the stage" for numerous downstream reactions within the tissues that result in the clinical manifestation of chronic radiotherapy injury months to years later. Therefore, in order to ameliorate the progression of the injury, the early inflammatory response may be a vital target (see cytokine section 1.9.7 below).

Previously TGF-β has formed the cornerstone of the understanding of RIF, underpinning the many molecular mechanisms accountable for fibrotic processes (see 1.9.2). Reducing fibrosis to improve the function of cells comprising the irradiated tissues is a key pathway to ameliorate injury. Researchers have shown that although this post-mitotic differentiation of the fibroblast/fibrocyte system may be irreversible, factors such as persistent cytokine production, hypoxia and matrix degradation pathways (see section 1.9.4), can be explored to reduce this effect (132). Fibrosis has also been linked to the formation of lymphoedema after irradiation (see sections 1.7.4 and 1.8.6.3). It is postulated that fibrosis significantly impairs lymphatic tissue regeneration (133). Fibrosis also elicits a mechanical compressive effect as it distorts normal vessel architecture, interferes with lymphatic vessel vasodilation thus impairing flow, contributing to lymphatic fluid stasis and impairment of immuno-surveillance of the affected area (133). See sections 1.7.4 and 1.8.6.3 for further details.

1.7.2 Keratinocytes

Keratinocytes, especially those in the actively dividing basal layer of the epidermis are rapidly injured by irradiation due to inflammation causing an acute erythematous response. The degree of injury and the formation of dry or wet desquamation depends largely on the amount of residual basal cells capable of repopulation and differentiation to reconstitute the spinosum and corneum layers of skin. Cell death may reflect a loss of reproductive ability, whilst the retaining ability for terminal differentiation (134). The process of wound repair is highly dependent on cell migration from the basal layer to cover a wound, usually taking place on a scaffold of extracellular matrix secreted by mesenchymal cells, therefore reinstating the barrier function of skin (135). On complete coverage of the wound, cell-cell contact initiates differentiation from the basal subtype to form the stratified squamous keratinizing epithelium (136) (137). Radiotherapy with various dose rates may cause more severe acute damage with destruction of the basement membrane zone, which significantly slows re-epithelialisation (137). This significant compromise of the barrier function of the skin allows for continued inflammation and exposure of injured dermal structures to the external environment. Such an injury precedes the formation of ulcers (17)

(135). Gaining an understanding of the exact mechanisms of radiotherapy injury to keratinocyte function may help target therapies to improve wound healing and maintain the integrity of the epidermis. Goessler et al. showed that radiation reduced the proliferative ability of keratinocytes and altered the cytokeratin profile. Cytokeratins are epithelial associated proteins that determine both the epithelial architecture and sub-type, including the terms of mitotic activity and keratinocyte differentiation (138). For example, irradiated skin keratinocytes demonstrated change from high molecular weight keratins 1 and 10 to low molecular weight keratins 5 and 14, the latter often being found in fetal cells and possibly indicating irradiated keratinocytes regress into a less differentiated state (139). Furthermore, the Keratin 14 promotor regulates epidermal expression of activin B_A, which may become overexpressed in irradiated skin. Histologically, these changes correlate with a hyper-proliferative dermis, reduced adipose tissue, which is largely replaced with a dense, fibrotic dermis (140).

Epithelial cells, such as keratinocytes, are also sensitive to changes in the composition of underlying ECM. Therefore, if radiotherapy induces alterations in matricellular proteins such as SPARC (secreted protein acidic and rich in cysteine), thrombospondin, tenascin or osteopontin, this not only effects keratinocyte-matrix interactions, but also modulates integrin related intracellular signaling, which can significantly contribute to changes in cell migration. (141) (see section 1.9.3).

Within the five layers of the epidermis, the basal layer houses the population of stem cells (1.9%) and progenitor cells (14%), which have been characterised by integrin α-6 and CD71 staining and responsible for skin regeneration every 4 weeks (142). Interestingly, irradiation induced cell death is substantially greater in the progenitor cell population, while greater than 80% of the true stem cell population survived insult at the 2-week time point, as detected with clonogenic assays (143). This may support the hypothesis that damaged progenitors are rapidly removed from the site of injury with large scale cell death accounting for the acute erythematous response to irradiation. Therefore, the stem cell response to stress may involve the activation of mechanisms that repress apoptotic pathways and promote cell survival; all the while leaving cells vulnerable to incomplete DNA damage repair and in turn leading to the latent development of fibrosis or secondary carcinoma (142).

1.7.2.1 Epithelial to Mesenchymal Transformation (EMT)

The epidermal layer sustains communication via gap junctional complexes and it remains separated from adjacent tissues by the basement membrane structure. Epithelial tissues either function as a barrier externally or for absorption internally. Alternatively, mesenchymal cells are loosely arranged in a three-dimensional ECM and comprise the connective tissues adjoining epithelia. The transformation of epithelial cells to mesenchymal cells is essential during embryonic development and involves a multitude of phenotypic alterations including; loss of cell-cell adhesion, cell polarity, and gaining of migratory and invasive characteristics. In fibrotic tissues, myofibroblast accumulation is held responsible for secretion and deposition of excessive and altered collagens, compromising organ function. While myofibroblasts can originate from transformed fibroblasts, elegant cell tracing studies show that a significant portion of myofibroblasts arise from conversion of epithelial cells through an EMT process (144), thus further contributing to fibrosis, scarring and contracture of radiotherapy injured soft tissues.

The cascade of events in wound healing has been extensively studied and is regarded as a process that transitions from inflammation to proliferation; then to granulation and remodeling (137). In radiotherapy, the inflammatory stage is protracted and normal repair mechanisms are disrupted, leading to the progression of the acute side effects to the consequential and/or late side effects. The remodeling phases of wound healing are driven by complex epithelial-mesenchymal interactions between keratinocytes and fibroblasts. This association not only regulates wound healing, but also processes such as invasion involved in tumour progression (144) (145). On a functional level, Walter et al. showed that un-injured fibroblasts migrate faster than keratinocytes to bridge the ‘wound’ in a scratch assay under serum-containing and serum free conditions, and that this closure was accelerated in the presence of mesenchymal stem cell conditioned media (MSC^{CM}) (135). Multiple other groups have similarly shown that keratinocytes, under the influence of IL-1 and/or TGF-β activation, instruct fibroblasts in co-culture models to synthesize and secrete vital growth factors, which in turn stimulate keratinocyte proliferation in a paracrine fashion (146) (147). ECM production can therefore be regulated by mechanical

tension influencing de novo collagen synthesis, which in turn changes cellular interactions and functions (215).

The TGF-β family of cytokines and growth factors plays an extensive role in wound healing, inflammatory responses, production of collagen and irradiation-induced fibroblast senescence, as well as exerting effects on multiple cell types (61) (148) (149). Radiation is reported to potently activate TGFβ signaling, with studies indicating small 0.1Gy doses can trigger signaling within an hour (148).

Levine et al. demonstrated TGFβ2 and 3 subtypes were upregulated early in suprabasal keratinocytes in wound models, followed by a delayed increase in TGFβ1 in granulation tissue and hyperproliferative epithelial cells. This second peak also coincided with myofibroblast detection (150). Several groups have also demonstrated that injection of TGFβ1 and -2 neutralizing antibodies may reduce scarring in adult wounds, but neutralising all three subtypes does not yield the same outcomes, leading to the hypothesis that TGFβ3 neutralization may be detrimental to some critical aspects of physiological wound healing (61) (151). Furthermore, TGFβ signaling downstream to cytoplasmic mediators such as Smad3, has been implicated in radiation induced fibrosis and synthesis of ECM proteins. Smad-3 null mice or Smad 3 signal blockade showed improved healing of irradiated cutaneous wounds, decreased epithelial to mesenchymal transition and attenuated fibrotic responses (152) (for more see section 1.9.2).

Inhibition of TGFβ signaling in keratinocytes can result in increased keratinocyte proliferation and accelerated epidermal wound closure. Interestingly, similar fibroblast blockade results in reduced wound tensile strength, increased numbers of suprabasal keratinocytes but no effect on epidermal wound closure (153). This may illustrate the fact that the TGFβ family exerts varying effects on epidermal and mesenchymal cells, changing significantly during phases of the wound healing process. Therefore, generalized blockade of TGFβ may not achieve desirable gains in wound healing.

1.7.3 Blood Endothelial Cells

Developing evidence suggests that radiotherapy significantly influences neo-angiogenesis and alters existing vasculature, likely forcing endothelial cells into premature senescence and preventing effective revascularisation of RTX-damaged tissues (17). Immature vasculature is usually susceptible in both stability and response to further trauma (154) (155). Radiotherapy provokes production of free radicals, leading to increased vascular permeability, damaged endothelial cells, thrombosis and reduced intimal proliferation that results in a histological picture of obilterative fibrosis, predominantly affecting arterial rather than venous structures (1) (119) (156). The histological pattern of irradiation injury varies across the vessel spectrum and may be attributed to different mechanisms (Table 1). Fajardo et al. have shown that months to years after irradiation, capillary vascular histology is adversely altered with endothelial cell detachment from the basal lamina layer, thrombosis and loss of capillary segments (157) (158). Conversely, arterioles are characterised by hyalinisation of the media combined with sub-endothelial and adventitial layer fibrosis. Medium-large sized vessels show varying degrees of luminal narrowing most commonly attributed to intimal fibrosis (1) (159). Stewart et al. went on to examine plaques and lesions in irradiated arteries and found a predominance of granulocytic infiltration, macrophage-rich plaques susceptible to disruption and haemorrhage (160) (see section 1.8.6.2). In addition to this, Martin et al. conducted tissue lysis and PCR analysis of irradiated and matched un-irradiated vessels from patients undergoing delayed head and neck reconstruction and found persistent elevation of factors such as NFKB up to 8 years post-radiotherapy (161). This is significant, in that initial inflammatory responses to radiotherapy seem to persist and form the basis of chronic injury, thereby presenting potential therapeutic targets. Li et al. examined the vascular reactivity in irradiated pig coronary arteries and found decreased relaxation responses to substance P and sodium nitroprusside; suggesting direct endothelial cell damage and altered smooth muscle cells, which may have implications to adjusting vessel caliber and moderating tissue perfusion (162).

Vessel Subtype	Histological Change	Morphological Change	Sensitivity to RTX
Capillary Sinusoids	• Detachment of endothelial cells from basal lamina • Cell pyknosis (DNA condensation) • Capillary wall rupture • Thrombosis	• Dilation of vessel • Asymmetrical walls • Enlarged ECs • Loss of vasculature	+++++
Small Arteries 100 μm	• Fibrinoid Necrosis • Subendothelial or adventitial fibrosis • Hyalinisation of media • Lipid laden macrophage accumulation in intima*	• Thrombosis • Necrosis	+++
Medium Arteries 100-500 μm	• Intimal fibrosis with fibroblast to myofibroblast transformation. • Lipid laden macrophages + foam cell plaques* • Lymphocytic vasculitis.	• Narrowing or complete obstruction • Thrombosis • Vasculitic scarring	+++
Large Arteries >500 μm	• Myointimal proliferation • Lipid Deposits	• Occlusive or mural thrombus • Aneurysm – Rupture	++
Venous Structures	• Small- intimal/medial fibrosis • Large – fibrosis which may be due to previous tumour invasion.		++ + Organ specific changes e.g. liver = increased sensitivity.

Table 1 Histopathology of radiotherapy induced changes in the vascular tree

*Foam cells and plaques are less commonly seen in small-medium sized arteries as a result of spontaneous atherosclerosis, therefore these findings are quite suggestive of radiotherapy injury. ECs; endothelial cells. Sensitivity to radiotherapy graded from least (+) to most (+++++) as reported in the literature (17) (157) (158) (163).

Radiotherapy induced injury results in a phenotypic transition of endothelial cells to a prothrombotic, pro-coagulant and pro-inflammatory predisposition (164) In a general setting, the induction of apoptosis of endothelial cells has been shown to contribute to platelet/fibrin-rich thrombus formation and endothelial denudation (165). Irradiation can lead to up-regulation or alteration of cytokines and growth factors, cellular adhesion molecules (CAMs), vWF, ACE and prostacyclins (166) (167) on both endothelial and leukocyte surfaces. It has been shown that RTX induces up-regulation of adhesion molecules; modulating platelet adherence and forming luminal protrusions consisting of hyperproliferative endothelial cells. These effects cumulatively result in leukocytic influx, thrombosis and aberrant endothelial cell proliferation (13). A pro-coagulant endothelial surface, more stimulating for platelet aggregation and neutrophil adhesion, is also created by a decrease in plasminogen activator (PA) and thrombomodulin. ROS may also scavenge nitric oxide (NO), which impairs the ability of the vasculature to oppose vasoconstricting forces thus perpetuating pre-existing ischemia (162). Radiotherapy insults also increase production of thrombin, which increases endothelial and smooth muscle cell proliferation, migration, permeability and collagen production (17) (168). The mechanism is thought to be mediated by production of uPAR at the site of vascular injury and the hyper-proliferative state of dysfunctional cells may be responsible for accelerated plaque formation and vascular stenosis (168). Thrombin inhibition can hinder such processes and may be an important target to consider in amelioration of radiation injury to endothelial and surrounding smooth muscle cells (169) (170).

Irradiated endothelial cells have also been found to significantly influence the behavior of vascular smooth muscle cells (VSMCs) by promoting proliferation, migration and induction of a fibrogenic phenotype with overexpression of fibrillar collagens. On a molecular level, radiotherapy can induce TGFβ1/ALK5- dependent signaling and blockade of ALK5 is able to rescue sprouting but not proliferative function of endothelial cells (155). TGFβ1 is a paracrine factor which, via the Smad 3 pathway, is responsible for instigating inflammatory fibrotic vascular changes (164) and is upregulated in the phenomenon of endothelial-mesenchymal transition along with Notch and Wnt pathways (171), of which a defining characteristic is the acquisition of endothelial cell αSMA expression (171). But as discussed in a review by Shukla et al., blockade of a TGF-β (with such widespread multi-system influence),

will not have enough specificity to mitigate RTX injury without affecting key biological processes (54). Therefore, further investigations starting at the RNA and protein level are required to determine up or downstream targets amenable to be targeted with greater specificity.

1.7.4 Lymphatic Endothelial Cells

The lymphatic system, a one-way drainage system responsible for transporting excess interstitial fluid from tissue space to the blood circulation and directing lymphocytes and antigen-presenting cells from the lymphatic vessels to the lymph nodes for immunological surveillance. The capillaries are characterised by thin walls and a discontinuous basement allowing for passage of immune cells while also lacking pericyte or support cell coverage (172). As drainage in the lymphatic system progresses proximally, capillary channels empty into pre-collector and collector channels and smooth muscle cell coverage increases (172). Different lymphatic endothelial cell (LEC) subtypes express different markers which are likely to reflect customized responses to various stimuli, with dermal lymphatics predominantly expressing LYVE-1, EphB4, VEGFR-3, Prox-1 and Podoplanin, pre-collectors expressing similar profile with reduced LYVE-1 to collectors predominantly expressing podoplanin and VEGFR-3 (51).

Lymphangiogenesis is the formation of new lymphatic vessels during embryonic growth which is regulated by transcription factors SOX18 and Prox1 which initiate differentiation from the anterior cardinal vein (172). In an adult, processes of embryonic lymphangiogenesis are recapitulated when required to adapt to an increase in interstitial fluid or when faced with pathological insult such as chronic inflammation, trauma, lymphatic injury, secondary lymphoedema or obliteration of vessel flow due to tumor metastasis (173). Tumours can invade the lymphatic system through impairment of lymphatic structure and function characterised by increased permeability and intercellular openings, abnormal lymphangiogenic cues and overexpression of immunoreactive agents to promote cancer metastasis. The resulting immune response alteration and accumulation of interstitial fluid and proteins, is clinically known as lymphoedema (see section 1.8.6.3) (174).

The formation of a three-dimensional dermal lymphatic cell network requires a coordinated sprouting response to the release of several growth factors and receptors particularly VEGF-C which acts through VEGFR-3, angiopoetins (and their cognate Tie receptors), ECM signals and some B1 integrin signaling (172). In the setting of radiotherapy injury and subsequent insult in the form of surgery it is important to evaluate the processes involved in secondary lymphangiogenesis in the background of a previously injured 'pathological' tissue bed. The processes involved may not be the same as in the embryonic state of primary lymphatic development from the cardinal vein and may be governed by different micro-environmental and molecular cues (175).

Detry et al. modelled the process of lymphangiogenesis secondary to thermal cauterization in murine cornea and found LECs to migrate and elongate, forming interdigitating cord-like structures devoid of basement membrane but anchored to collagen fibrils via anchoring filaments. Observations of the abundance of lysosomes, intracellular vacuoles and matrix degradation products (within cell vesicles, intercellular spaces and in tubular luminal structures), suggested that ECM degradation and remodeling plays an important role in lymphangiogenesis, preparing the space for cords to migrate, or 'tunnel' into or connect together to form lymphatic vessel lumens (176). Similar processes were demonstrated in an *in-vitro* model utilizing thoracic duct sprouting in collagen I, demonstrating maximal sprouting of LYVE-1 positive cells at 11 days (176).

There is a paucity in the literature regarding the effects of radiotherapy on the lymphatic system. A more commonly described phenomenon is of TGF-β-mediated radiation fibrosis (see section 1.9.2), which may be linked to the development of lymphoedema. Therefore, the following section reviews pertinent studies in mechanisms understood to drive radiotherapy injury of lymphatic endothelial cells and vessels. James et al. examined the dorsal embryo skin of TGF-β receptor 1 and receptor 2 deficient mice and found altered LEC morphology and reduced lymphatic branching networks that were characterised by dysmorphic lymphatic vessels and diminished branching of LECs (177). These authors further demonstrated in human LEC *in-vitro* studies that TGF-β signaling disruption resulted in increased proliferation and up-regulation of VEGFR-3 and NRP2 expression at an mRNA level,

resulting in a hyperplastic lymphatic vasculature phenotype (177). Therefore, the role of TGF-β on lymphangiogenesis in embryonic ages may differ from pathological conditions such as trauma or irradiation injury.

Avraham et al. conducted an immunohistochemical analysis of matched tissue samples from limbs of patient's with lymphoedema and demonstrated increased TGF-β1 staining compared to normal leg skin punch biopsies specimen (83). Then, utilizing a surgical lymphoedema model in a mouse tail, the authors ligated superficial and deep lymphatic channels and administered TGF-β monoclonal antibody intraperitoneally to block systemic TGF-β signaling *in vivo*, aiming to substantiate if reduction in TGF-β mediated fibrosis would influence the lymphoedematous state. Systemic TGF-β blockade resulted in a 50-60% reduction of tail lymphoedema at 6 weeks, improved functional lymphatic flow assessed with microlymphangiography across the wound site as well as a twofold reduction in fibrosis assessed with Sirius red staining (83). Further studies have sought to clarify the relationship between fibrosis and impaired lymphatic regeneration, which may explain their co-existence and contribution to soft tissue edema in irradiated tissues. In another study, Avraham and colleagues demonstrated that fibrosis is associated with lymphatic vessels phenotypic abnormality; becoming dilated and ectatic in nature (133) (178). It is postulated that the significant alteration in tissue compliance as a result of fibrosis leads to lymphatic vessel obliteration and lymph fluid stasis. This stasis drives cytokine expression that furthers the development of fibrosis and continues to inhibit effective lymphangiogenesis. In lymphoedematous or fibrotic states, Clavin et al. demonstrated that up-regulation of TGF-β1 in murine tail tissues may also directly inhibit LEC proliferation, reduce LEC tube formation on a matrigel matrix *in vitro* and promote formation of lymphatic fibrosis (178); however TGF-β1 treatment of LECS did not alter VEGF-C and D secretion detected by ELISA (178). TGF-β1 inhibition in a mouse tail irradiation model demonstrated similar results to the surgical lymphoedema model; chiefly reduced fibrosis and improved lymphoedema (although transport defects were still detectable months after irradiation). Additionally, TGF-β1 inhibition did not provide protection from radiotherapy-related LEC depletion or cell death (179), suggesting the molecular mechanisms for LEC injury may result from alternative pathway changes. The observation of smooth muscle actin staining in

capillary lymphatics represents a pathological finding (180) in fibrotic or lymphoedematous tissues and may result from LEC transdifferentiation to fibroblastic or myofibroblastic cells (133).

Very few studies have specifically looked at cellular effects of radiotherapy injury on the lymphatic system, while there is a relative abundance of studies that link radiotherapy to the problematic development of lymphoedema (see section 1.8.6.3). As detailed above, mechanisms of injury are extrapolated from models of fibrosis postulating that this fibrosis may form a vicious cycle leading to lymphoedema (133). The status of lymphatic vessel density is reported inconsistently in the literature with some reporting reduced density in irradiated tissues (179) (181) (182), while others report increased lymphatic vessel density or diameter (predominantly in the acute/subacute phases after treatment) (183) (184) (185). However, it is important to note that these studies report static analyses of the state of lymphatic vasculature *in vivo*, and investigation pertaining to the effects of radiotherapy on dynamic LEC function and the molecular cues that govern these alterations is required.

Avraham et al. examined effects of irradiation on apoptosis and senescence of human dermal LECs *in vitro*, using TUNEL staining and FACS and demonstrated 15Gy irradiation did not significantly increase apoptosis, but larger doses of 30Gy increased apoptotic rates from 6.6% to 20.4% at 10 h (83). Assessment of LEC senescence with β-galactosidase staining after 4, 8, 12Gy irradiation showed a dose dependent increase in senescence from <40% in 0Gy, to up to 70% in 12Gy cells. These results suggest that rather than large scale apoptosis, radiotherapy injury may result in LEC senescence (83). A review by Azzam et al. postulated that the responses of certain cell types to injury (such as low dose (cGy) irradiation) may lead to an ‘adaptive response’ to the stress, resulting in activation of cellular repair mechanisms, in particular increases in antioxidant enzymes MnSOD, catalase and glutathione peroxidase (186). While these responses may protect cells from progressing to irreversible cell death, such defensive mechanisms may ‘over-compensate’ for injury, leading to prolonged cell survival of damaged cells for extended periods after stress (65). Mortimer et al. irradiated the flanks of pigs with a single dose of 18Gy and examined the effect of radiotherapy on lymphatic flow utilizing 99Tcm-colloid to calculate dermal clearance. They demonstrated two separate phases of impaired lymphatic fluid clearance in the

irradiated flanks; firstly, during 6-12 weeks, which they correlated with oedema and ischemia of the tissues; and secondly, at 1 year, where there was concurrent histological evidence of dermal and subcutaneous atrophy (187). Baker et al. attempted to gain better understanding of the effects of radiotherapy on the lymphatic system by systematically assessing the effects of popliteal nodal irradiation compared to surgical nodal-excision and a combination of both therapies in New Zealand white rabbits. They demonstrated, using a FITC-Dextran lymphatic infusion, that lymph fluid transport to the vascular system was decreased in the radiotherapy group to about a third of the control group. Immunohistochemical analysis of irradiated lymph nodes with Masson's trichrome demonstrated increased collagen deposition in the capsule and internal trabeculae. The patterns of lymphatic regeneration were evaluated using Evan's blue dye and showed that radiotherapy led to increased sprouting proximal to the lymph node, whereas combined radiotherapy and surgery lead to lymphatico-venous anastomoses (LVA), which could represent an endogenous attempt to find alternative pathways for lymphatic drainage (183). A similar finding in a human study by Edwards et al. which dates back to 1969, reported a 2.3% incidence of LVA in a series of 700 patients with lymphoedema as a result of surgical clearance secondary to malignancy (188). While this rate of LVA formation is relatively low, it may serve as a key regenerative mechanism whereby some patients escape developing incapacitating lymphoedema, making the molecular mechanisms of this process a highly relevant area requiring further investigation (188). Cui et al. investigated the effects of radiotherapy on lung lymphatic vessels and found LYVE-1 co-staining with TUNEL or 8-oxo-dG showed significantly increased rates of LEC apoptosis and oxidative stress, which was evident up to 16 weeks after irradiation and preceded the development of lung fibrosis which became apparent after this time point (182). Aebischer et al. extensively reviewed the responses of LECs to inflammatory stimulus and concluded that various mediators such as VEGF-A and NO increased permeability of UV radiation-damaged LECs while others such as TNFα, IL-1, histamine and VEGF-C were accountable for altered LEC barrier function and vessel pumping action (189).

Therefore, impaired lymphatic function results in abnormal permeability, inadequate transport of fluid, macromolecules, or cells from the interstitium and contributes to radiotherapy-induced soft tissue injury; which clinically manifests as oedema, fibrosis

and impaired immunosurveillance. The defects may be found in LECs and/or the surrounding matrix, both of which significantly influence each other and result in changes to interstitial pressure and derangement of lymphatic regenerative responses. Although the alterations of LECs are regarded to be causative to the detrimental effect of disorders such as lymphoedema, the mechanisms whereby LECs are involved in the whole pathological process are still uncertain (174). Additionally, effects of radiotherapy on the lymph node basins must also be considered, as their role is not just limited to immunological surveillance but also important in the concentration of lymphatic fluid as it traverses the node (due to increased oncotic pressure in the nodal capillaries) (183), which then effectively separates the afferent higher pressure system from the efferent lower pressure system, both of which are individually subjected to the effects of radiation induced fibrosis (183).

1.8 Clinical manifestations of radiotherapy injury – burden of disease and reconstructive challenges

1.8.1 Early side effects of radiotherapy

Radiation-induced soft tissue injury is commonly classified as acute (early within 10-14 days after starting treatment) or chronic (late, months to years after treatment). Acute radiation damage is most prominent in rapidly proliferating cells, such as the epidermis of skin, mucosa of intestines and bone marrow components (103). It is proposed that acute symptoms develop due to a large inflammatory response with subsequent loss/death of functional cells either through apoptosis, mitotic/clonogenic death or differentiation and senescence (9). There is said to be a dose-dependent death of these mature or post-mitotic cells on initial injury, then followed by an ‘avalanche effect’ during subsequent compensatory proliferation of cells already harbouring irradiation injury (190) (191). Overall, due to the shorter life span of cells in the skin and gut, the compensatory proliferation within the defined stem cell compartment (which is more tolerant to radiation than other types of cells), offsets injury by replacing functional cells. The lower rate of delivery in fractionated regimes, further allows recovery of the acute irradiation damage to the tissue between doses (192) (193).

1.8.2 Late side effects of radiotherapy

Described initially as “F” type functional tissues by Michalowski et al., complex tissues comprised of endothelial, mesenchymal and parenchymal cells have a much slower proliferative profile. They exist as functionally mature cells, as opposed to post-mitotic cells, which are able to undergo a limited number of further divisions to help replace depleted cells (9,194). A slowed self-renewal rate in such cell types does not allow for timely regeneration that is anticipated between fractionated doses and the time taken to display the effects of RTX-injury is delayed. For these reasons, these mature cells are now thought to harbor injury and maybe responsible for the late effects of radiotherapy injury (192) (193).

The late effects of radiation are classed as residual damage expressed months to years after radiation exposure and manifests in two ways - 1) as late effects on normal tissues (LENT); and 2) radiation-induced second malignancies (RISM) (195). Recently, late effects have been alternatively categorised as two pathological subtypes – 1) consequential late effects (CLE) and 2) generic late effects (GLE) (9) (103) (196). CLE are influenced by the severity of the acute radiation damage. Even with clinical healing after the acute response, the latent asymptomatic phase transitions into late symptomatic side effects such as skin and mucosal surface ulceration, thought to be significantly influenced by the overall treatment time. In contrast, GLE are those, which are independent of the acute reactions and are a secondary phenomenon (197) (198) (199). GLE display marked sensitivity to dose fractionation and are minimally effected by the overall treatment time (196). Therefore, modulation of acute effects will exclusively influence the consequential component of the late response (196). Moreover, quantitative functional markers of acute reactions will be predictive for CLE rather than for GLE.

Processes of erythema followed by dry then wet desquamation ensue in the weeks post radiation as a result of large-scale depletion of 10-20 layers of epithelial cells and their clonogenic potential. Dermal necrosis and atrophy constitute later effects as a result of dermal vascular insufficiency and fibroblast damage leading to tissue contracture (56,194). This predisposes to forming non-healing wounds or ulcers, with increased propensity for secondary infections that may be life or limb threatening (191). Histologically, irradiated skin and mucosa are characterised initially by

hyperemia, vascular congestion and plasma exudate. Later effects including hyperpigmentation, atrophy, lymphoedema and fibrosis-related contraction of tissues, largely due to vascular, mesenchymal and parenchymal tissue damage (69). Lastly, atypical dilation of superficial dermal capillaries causes telangiectasia and leads to friable and hyper-permeable vessels (56). As injured tissues attempt to regenerate and restore functionality, subsequent fractionated insults continue to perpetuate the inflammatory response. This is thought to cause slow parenchymal and endothelial cell depletion that may induces fibrogenesis in an attempt to restore structural integrity of tissues (17) (61).

1.8.3 Factors that influence severity of radiotherapy induced soft tissue injury

There are many factors that must be considered to account for the heterogeneity of individual responses and severity of reactions to radiotherapy (9). Firstly, the therapy related-factors such as fraction size, mode, and duration of treatment with or without concomitant chemotherapy, surgery and radiation modifiers, all influence the development of acute and late side effects, as detailed above (103) (200). Additionally, a variety of factors have been identified that increase the entrance dose at the skin, including positioning, length of exposure, angle of beams, high intensity modalities and concurrent fluoroscopy usage (63) (see section 1.5). Further, various tissue types such as rapidly proliferating cells of skin, gut mucosa and bone marrow display increased radio-sensitivity, with outcomes also depending upon pre-radiotherapy conditions (200). In particular, skin of the face, anterior neck, chest, abdomen and flexor creases of extremities are thought to display higher radiosensitivity in comparison to other areas of the body (63). Finally, patient factors can be divided into comorbidity-related and genetic predispositions. Factors that usually portend poor wound healing ability such as old age, obesity, diabetes and smoking also increase the risk and severity of radiotherapy injury. Specific conditions such as Gorlin syndrome, various connective tissue disorders (such as Lupus) and Gardner syndrome carry higher risk; as do patients predisposed with DNA repair disorders such as xeroderma pigmentosa and Fanconi anaemia, all of which are also implicated in increased risk of radiation injury (63) (191). Genetic predisposition to radiosensitivity is an area under heavy investigation and a connection has been established between the autosomal recessive disorder Ataxic Telangiectasia and

increased susceptibility to severe radiation cutaneous reactions (79,201).

1.8.4 Radiotherapy induced secondary malignancies

Patients treated for particular cancers such as lymphomas, leukaemias or anatomical areas such as the breast and genitals tend to display a higher risk of developing RISM due to an increased inherent radiosensitivity of these tissues and their surrounding counterparts. Mohanti et al. reported the overall risk of RISM between 2-10% for patients that survive greater than 5 years after treatment (195). RISM can be subdivided in to hematological malignancies, which arise within 3 years of treatment, or solid tumors which have a more latent presentation usually >10 years (202). Risk factors such as childhood irradiation and combination with other adjuvant treatments, such as chemotherapy, significantly increase the risk of RISM and resulting in a reduced latency period before presentation (195) (203). A murine example of mantle radiation, exposing large volumes of lung and chest wall tissue to irradiation to treat childhood Hodgkin lymphoma, resulting in a 30% risk of developing breast cancer by the age of 50 years (204). Common RISMs are listed in the Table 2 (adapted from Mohanti et al. (195)) and must be considered as a significant risk associated with radiotherapy in light of an increasing population of cancer survivors.

Primary Condition treated with Radiotherapy	**Radiation-Induced Secondary Malignancy**
Hodgkin's Disease	Thyroid Breast Lung Stomach
Breast Cancer	Leukemia Lung Contralateral Breast
Testicular Cancer	Leukemia Lymphoma Pelvic Malignancy Bone/Soft Tissue Sarcoma
Cervical Cancer	Bladder Rectal Leukemia Sarcoma
Paediatric Cancers	Thyroid Breast Leukemia Sarcoma

Table 2 Common Radiation Induced Secondary Malignancies

1.8.5 Assessment of radiotherapy injury (scales/grades)

Due to the large variation in responses to radiotherapy injury (as detailed in section 1.8.3), it has been difficult to produce a standardised scale or predictive model for the acute or late side effects of irradiation on normal tissues. An early attempt to characterise the clinical complications of radiotherapy was comprised by Rubin and Casarett with anecdotal reports of responses to radiotherapy in various organs, as well as a hierarchical stratification of cell radio-sensitivity (205). Even in such early publications it was recognized that the extent of radiotherapy injury was dependent on the inherent radiosensitivity of the cell-type, as well as the replicative state in which it existed, which varied significantly between organs (205). Features of irradiated skin, for example, were divided into clinical and subclinical manifestations across acute, subacute and late periods (56). In some patients, features of injury would manifest early as acute erythema, as their tissues were unable to tolerate the dose, while in others subclinical to clinical transition occurred after injurious insults such as trauma, infection or subsequent surgery. Such injury could also manifest as a result of chronic and progressive deterioration of tissues secondary to radiotherapy injury, hypothesized to be due to degeneration of parenchymal support, vascularity and ability to withstand any pathological stress resulting in hyperpigmentation, atrophy or a chronic non-healing necrotic ulcer (Figure 4) (205).

The seminal publication by Emami et al. in 1991 “tolerance of normal tissue to therapeutic irradiation” presented the collation of an extensive literature review and expert opinion as an elaboration of the concept of tolerance doses (TD) (31) (206). The minimal tolerance dose (TD5/5) and the maximum tolerance dose (TD 50/5) refer to severe life-threatening complications of 5% and 50%, respectively, occurring within 5 years of therapeutic irradiation – for skin this dose was determined as 55Gy and 70Gy respectively, using telangiectasia and necrosis as an end-point (31). Despite being one of the most commonly referenced papers guiding the field of normal tissue tolerance to radiotherapy its applicability is limited by a relative paucity in literature, the use of only 1-2 clinical endpoints and the fact that it pre-dated the era of image guided or intensity modulated radiotherapy (31) (200). Quantitative analyses of normal tissue effects in the clinic (QUANTEC) has since then attempted to gather and synthesize data available from CT guided and planned therapy regimes delivered in a 3D multi-beam format (207).

Several grading systems have been proposed to evaluate the effects of radiotherapy on normal tissues; the Radiation Therapy Oncology Group/European Organization for Research and Treatment of Cancer RTOG/EORTOC and the late effects on normal tissues (LENT) subjective, objective, management and analytic (SOMA) scale (208) (16) both utilize anatomical descriptors of injury graded from 1-4, increasing in severity from mild-moderate to severe and life threatening. More recently, The National Cancer Institute's common terminology criteria for adverse events (CTCAE v3.0) (209) has been 'SOMAtized' (16) (207) or combined with the LENT-SOMA scale, allowing for a more comprehensive and accurate assessment of irradiation injury – a system that will likely unify current and future outcome assessments (16). This scale holistically evaluates the continuum of acute and chronic side effects which includes patient symptoms, physical examination findings or pathophysiological syndromes, impact on quality of life and functional activities of daily living - along with necessary medical/surgical intervention. Ongoing efforts are directed towards integration of investigatory analytical parameters to aid in grading of injury (16) (195) (209) (Figure 4).

The skin is a large organ and one frequently affected by radiation injury with adverse events such as photosensitivity, rash/desquamation, ulceration, skin or wound breakdown which can be graded by the CTCAE v3.0. For example, if a wound complication is encountered it would be graded as follows: a grade of 1+ represents a minor wound (<25% incisional separation) with minimal symptoms requiring no further intervention; grade 2+ represents a wound with >25% incisional separation, still confined to the suprafascial compartment, with moderate symptomatology likely managed conservatively with dressings; grade 3+ represents a large wound with fascial disruption accompanied with severe symptoms requiring hospitalization and operative intervention such as debridement and closure; and lastly grade 4+ represents a major wound breakdown as a result of irreversible damage to tissues, with potentially life threatening complications that necessitate major surgical reconstruction such as free tissue transfer or therapeutic amputation for management (209). Systems of further interest include the immune, cardiac and lymphatic systems which are discussed as clinical syndromes resulting from radiotherapy injury in subsequent sections.

ACUTE
days - weeks
SUB-ACUTE
months
CHRONIC
months-years
LATE
years
Clinical Manifestation of Damage
Clinical Threshold
Sub-Clinical Damage
Wet/Dry Desquamation 14-18Gy
Erythema 2-6Gy
Dermal Necrosis + Ulceration 14-18Gy
Dermal Atrophy 14-18Gy
Lymphedema + Recurrent Infection 10-12Gy
Induration + Fibrosis 10-12Gy
Trauma
Infection
Recurrent Trauma
RISM
MILD
MODERATE
SEVERE
LIFE THREATENING
S
Asymptomatic
Intermittent Symptoms
Persistent Symptoms
Refractory Symptoms
O
Functions Intact
Functions Altered
Functions Impaired
Functions Collapsed
M
No Interventions or Intermittent Medical Treatment
Non-Invasive or Continuous Medial Interventions
Radiological or Surgical Intervention
Radical Intervention, Critical Care
A
Normal Lab Tests
Abnormal but Correctable Lab Tests
Abnormal & Difficult to Correct Lab Tests
Failing & Potentially Lethal Lab Tests

Figure 4

Figure 4 The clinicopathological course of radiotherapy induced soft tissue injury and the scale correlating grades of common adverse events:

A schematic diagram depicting the evolution of acute, subacute and chronic effects of radiotherapy injury to the skin and subcutaneous tissues (adapted from Rubin et al. (205)). The acute phase of injury is characterised by a sharp rise and fall in radiotherapy injury during delivery of fractionated radiotherapy commonly resulting in erythema, dry and wet desquamation after exposure to the indicated doses. After cessation of therapy, the progressive nature of radiotherapy injury and its clinical manifestations are further depicted by the graduated incline and green boxes highlighting the common adverse effects and the doses of exposure leading to their development (adapted from Koenig et al. (210)). At every phase of injury there are two components: clinical and subclinical damage, the latter which may not manifest until the patient is subjected to subsequent injury in the form of trauma, surgery or infection. The injurious stimulus or pathological state then demands the damaged tissue to undertake regeneration and failure to do so leads to the clinical manifestations of radiotherapy soft tissue injury. The chronic and late side effects ultimately result from degeneration of all components of the skin and soft tissue; poor vascularity, lymphatic fluid stasis, compromised immunosurveillance and fibrosis, likely correlating with severe to life threatening side effects necessitating radical intervention and complex surgical procedures. The SOMAtized version of The National Cancer Institute's common terminology criteria for adverse events (CTCAE v3.0) is listed in the table outlining the grading of radiotherapy soft tissue injury based on the symptomology, objective effects on the patient and their activities of daily living, the degree of medical intervention required and lastly the analytical quantification using laboratory test results as a surrogate for severity (adapted from Rubin et al. (16)).

1.8.6 Radiotherapy, free tissue transfer and clinical reconstructive challenges

Complications of radiotherapy soft tissue injury are frequently encountered by reconstructive surgeons, who are often involved with management of patients after oncological clearance. Options for reconstruction of the defects in either a primary or secondary setting are challenging as is reflected in a reduction in success of vascularized tissue transfers from 90% to 84% in a study by Schlutze-Mosgau et al. (211). Multivariate analyses of predictors of complications following head and neck cancer surgery showed pre-operative radiotherapy carried up to a four-fold increased risk for free flap complications (212) (213). The sections below address the common manifestations of radiotherapy-induced soft tissue injury such as fibrosis, poor wound healing, macrovascular disease, lymphoedema and infection. Subsequent sections attempt to highlight the reconstructive challenges radiotherapy poses for plastic surgeons in the specific management of breast, head and neck cancer and sarcoma patients.

1.8.6.1 Fibrosis, wound healing and microvascular complications

Severe or chronic tissue injury results in damage to both parenchymal cells and supporting stromal/ECM network. In general, the response to injurious stimuli is fibroproliferative (122), with repair initiated by deposition of ECM products, which simply 'patches' rather than regenerates the original tissue (214). This leads to a spectrum of clinical manifestations such as scarring, contracture or deficiency in healing in the form of ulceration and exposure of underlying structures resulting from impaired synthetic cellular functioning. Tissue healing is also dependent on; the proliferative capacity of the cells, integrity of ECM and resolution of injury/inflammation – processes which are all markedly deranged in radiotherapy soft tissue injury (98) (103) (214) (215) (216). Therefore, chronic injury results in an area of tissue with decreased resilience; demonstrating poor reparative capacity when faced with ongoing or subsequent damage (clinical effects see section 1.8.6.5, cellular and molecular mechanisms see 1.7.1, 1.9.2 and 1.9.4). Denham et al. reviewed the mechanisms of radiation fibrosis and suggested myofibroblastic transformation, premature terminal differentiation, excessive matrix deposition (type I and III collagen (128)) with unregulated negative feedback and inflammatory stimuli,

forming the foundations for persistent cellular dysfunction and evolving fibrotic change (17).

The effect of ionizing radiation on endothelial cells, microvasculature and larger vessels has profound effects on surgical outcomes for patients, particularly following reconstructive surgery in a pre-irradiated area. Free flap reconstruction successes have been shown to reduce from 94% without radiation down to 84% in irradiated head and neck cancer patients (217). Well-documented side effects of telangiectasia, blood vessel friability, microvascular thrombosis, poor wound healing and higher infection rates have been attributed to radiotherapy induced vascular dysfunction (154). Microvascular damage was traditionally thought to result in reduction in perfusion of irradiated tissues leading to ischemia and necrosis. However, recent studies have demonstrated that while perfusion is reduced, oxygenation of these tissues is maintained within normal ranges on hyperspectral imaging (218). Chin et al. proposed that alterations in the cellular and molecular activity of irradiated cells may reflect a state of senescence (see section 1.5.4), requiring less energy, thus avoiding epidermal hypoxia (218). However, on subsequent wounding of irradiated skin, tissue repair and regeneration then necessitates cellular proliferation, increased energy and oxygenation demands which challenge the hypoperfused tissues and result in impaired wound healing. A similar situation is faced when less aggressive malignancies are treated with irradiation alone, with substantial issues arising in the case of recurrence or failure of radiotherapy, then requiring surgical intervention. Operations in pre-irradiated tissue beds carry higher complication rates and pose increased difficulty, with normal surgical planes obscured in the presence of fibrosis (219). General consensus suggests radiotherapy either a few months before or even years after, compromises wound healing, leading to the need for further surgeries such as debridement and vacuum assisted closure or the need for more complex reconstructive procedures (220). Non-healing ulcers are a significant cause of morbidity for patients resulting in pain, recurrent infections and repeated hospital admissions. In the case of failed conservative management, simple reconstructive options such as excision and direct closure, skin grafting or local flaps are less viable options in the fibrotic and poorly vascularized tissue (119).

1.8.6.2 Macrovascular complications - radiation induced vasculopathies

Radiation arteritis and accelerated atherosclerosis (more commonly characterised by intimal foam cell accumulation rather than cholesterol related plaques) (163) carries an increased risk of carotid artery stenosis in supraclavicular irradiation, coronary artery disease in breast, chest wall and internal mammary artery (IMA) irradiation (221); leading to 1.5-4.0 fold risk of cerebrovascular and cardiovascular adverse events (222-226). Jurado et al. also report increasing incidence of peripheral vascular disease in vessels surrounding the field of irradiation and advocated for percutaneous intervention to prevent re-operation in an area of developed fibrosis and poor wound healing capacity (227). Stewart et al. modelled the phenotype of radiotherapy induced plaques using carotid arteries of hypercholesterolaemic $APOE^{-/-}$ mice and found a plaque composition of erythrocyte containing macrophages (65%), granulocytes (10%), as well as atypical endothelial cell morphology in comparison to non-irradiated controls. Such features were thought to predispose the lesions to instability in the form of intra-plaque hemorrhage (160). These characteristics deviate from features of atherosclerotic plaques found in age related atherosclerosis, thus provide evidence that radiotherapy injury to vascular system is an independent risk factor associated with the development of macrovascular complications (160). Pentraxin 3 (PTX3) is a relatively new marker for adverse cardiovascular outcomes and a study comparing irradiated head and neck vessels with controls from the same patient demonstrated up-regulation of PTX3 in majority of irradiated veins and increased TNFα and IL-1β in irradiated arteries. These markers may be key to explore further in the pathogenesis of radiotherapy-induced atherogenesis (228).

RTX's integral role in the treatment of malignancies such as breast cancer has been extensively evaluated, demonstrating a significant 66.6% reduction in local recurrence, improving cancer control and survivorship (229,230). This favourable reduction in cancer related mortality is, however, offset by an increase in non-cancer related morbidity/mortality. Becoming prominent 2 years to 3 decades after the completion of radiotherapy, the irradiated group displays up to 20-30% increase in mortality, attributable to an excess of vascular related deaths (230) (231). Furthermore, left sided breast irradiation is correlated with a 2.2x relative risk of fatal cardiovascular events, likely due to an increased cardiac field exposure when

compared to right sided breast radiotherapy (230). The risk of silent coronary events is higher in patients that have undergone mediastinal/chest-wall radiotherapy compared to with the general population (226). This may be due to damaged nerve endings that allow sentinel clinical events to go un-noticed, preventing early intervention and management. Patient's undergoing chest wall irradiation for Hodgkin's disease demonstrate a marked 6.3-fold increase risk of cardiovascular disease, and on subgroup analysis done by Aleman et al., showed a 13.6-fold risk if irradiation was given under the age of 21 years old (232). Overall this portends a 7.2 fold increase in cardiac-related deaths compared to a healthy population (226). Such studies, highlight the need to address the diseases of survivorship post radiotherapy, as these patients are at a substantially higher risk of non-cancer related morbidity and mortality as a consequence of their previous treatments.

1.8.6.3 Lymphoedema

Lymphoedema is defined as a condition, in which there is swelling of an area of the body that results from accumulation of proteinaceous fluid when drainage is impaired, relative to lymphatic fluid circulation (233). It may be further categorized as primary (mostly congenital) or secondary which is largely acquired as a side effect of treatments such as surgery or radiotherapy for cancer eradication or in the setting of trauma (234).

Primary Cancer	Annual Incidence (per annum) [a]	Incidence of Lymphoedema	
Breast	14680	SLNBx or ND ND + RTX	6-15% [b] 20-30% [c]
Melanoma	12510	UL ND + RTX LL ND + RTX	20% [d] 40% [d]
Prostate	18560	ND ND + RTX	25-30% [d] 66% [e]
Gynaecological	3680	ND + RTX	25-30% [d]

Table 3 Incidence of common cancers and Lymphoedema in Australia

Table 3 [a]Australian Institute of Health and Welfare 2012 report of incidence of common cancers per annum (11). Estimates of secondary lymphoedema incidence from studies or systematic reviews [b] Rebega et al. (235), [c] Warren et al. (236), [d] Hayes et al. (233) [e] A review from the Department of Health and Aging in 2004 (237).

Estimates are further subdivided relating to incidence with sentinel lymph-node biopsy (SLNBx), upper limb (UL) / lower limb (LL) node dissection (ND) and radiotherapy (RTX).

According to the latest CTCAE guidelines, radiotherapy injury to the lymphatic system results in adverse events such as dermal, limb or truncal lymphoedema or lymphoedema related fibrosis. Grade 1 lymphoedema results in a 5-10% limb circumference or volume discrepancy which increases to grade 3 involving a >30% difference and lastly grade 4 progressing to malignancies such as lymphangiosarcomas (reported at rates of 0.45% in lymphoedematous arms after breast cancer treatment (234)), where amputation is often indicated (209). Other commonly used diagnostic criteria for lymphoedema include i) 2cm circumferential alteration, ii) limb volume change >10%, iii) limb volume change >200ml and lastly iv) signs or patient reported symptoms (238). Armer et al. attempted to quantify which measurement was most reliable for detecting lymphoedema and found that at 60-month follow-up, >2cm change in limb circumference was the most common definition of lymphoedema, whereas limb volume alterations, signs and symptoms represented more conservative correlation with clinically diagnosed lymphoedema (238).

Secondary lymphoedema represents an area of great importance as cancer survivorship (especially breast cancer) increases, the incidence of lymphoedema and the problematic symptomology for patients becomes a great burden on quality of life, with 70-80% of patients presenting 1-2 years after initial diagnosis or surgery (233) (238) (239) see Table 3. Lymphoedema has a wide ranging impact on the patient, comprising of limitation of large movements such as walking, fine movements such as writing, as well as symptoms such as fatigue, aching and rigidity of limbs (233). A systematic review of unilateral arm lymphoedema after breast cancer conducted by DiSipio et al. concluded that one in five survivors of breast cancer are likely to develop lymphoedema (239), making it the most common cause of secondary lymphoedema in Australian patients (233). Hayes et al. provided a comprehensive overview for the management of secondary lymphoedema in Australia and similarly predicted around 20% of patients undergoing treatment for breast, uro-gynaecological, head and neck and melanoma skin cancers in Australia would suffer

from lymphoedema, totaling to 8000 new cases per annum (233). This places significant pressure on the health system and defines the need for clinicians and scientists to make earlier diagnoses and source methods of prevention and/or treatment for lymphoedema.

When attempting to identify the contribution of radiotherapy injury to lymphoedema, it is first noted that radiotherapy is commonly prescribed for patients with node positive disease. For example, in breast cancer, areas such as the chest wall, internal mammary lymph node network, supraclavicular fossa and/or axilla are targeted with therapeutic irradiation while aiming to minimize exposure to cardiac and respiratory structures. Patients undergoing lymph-node clearance with radiotherapy demonstrate significant rates of lymphoedema with radiation identified as a significant risk factor for the variable onset of incapacitating limb swelling. Rates of lymphoedema in literature vary between 6-9% with sentinel biopsy and radiotherapy increasing to 9-44% with the combination of axillary clearance and radiotherapy (235). Tsai et al. conducted a meta-analysis of risk factors contributing to the development of arm lymphoedema in survivors of breast cancers and were able to identify that axillary dissection conferred a 3.47 relative risk (RR) compared to no dissection or 3.07 RR compared to sentinel lymph node biopsy. Radiotherapy to any area related to the breast cancer lead to 1.92-fold increase in lymphoedema but targeted analysis demonstrated axillary irradiation increased this RR to 3.06 in studies that defined lymphoedema with known diagnostic criteria such as circumference or volumetric measurements. Therefore, breast cancer patients who are node positive (usually classed as >3 positive nodes) carried an overall higher risk of lymphoedema, as this patient subset proceed to have lymph node dissection and radiotherapy (240). Warren et al. reported a 6.8% incidence of lymphoedema in a series of 1501 patients who underwent treatment for breast malignancy, of which 73% required radiotherapy. On subgroup analysis, patients that required supraclavicular or axillary irradiation demonstrated over 21.9% and 21.1% incidence of lymphoedema respectively, with a hazard ratio of 1.7 when compared to breast or chest wall radiotherapy alone (236). Tran et al. reviewed the impact of irradiation in a cohort of 175 patients, followed for a median of 355 days and demonstrated a 15.6% incidence of arm lymphoedema in the radiotherapy group compared to 5.4% in control patients; while Rebegea et al.'s series of 305 patients reported 28.57% incidence in chest wall/mammary gland

irradiation, increasing significantly to 77.78% when lymphatic regions were also targeted (235) (241). Hayes et al. also reported that lower limb lymphoedema is just as common as upper limb lymphoedema, further supported by a recent randomized control trial in melanoma patients receiving radiotherapy or observation of groin lymph nodes, with the group receiving irradiation demonstrating a 20% incidence of grade 3-4 lymphoedema and 15% increase in limb volumes (233) (242). Cormier et al. reviewed over 7000 patients in 47 studies and concluded radiotherapy was associated with a 31% incidence of lymphoedema (243). Supporting these figures, a review by the Department of Health and Aging in 2004 reported rates of 25-30% lower limb lymphoedema following node biopsy and radiotherapy for prostate cancer, increasing to 66% following pelvic lymphadenectomy and radiotherapy (237). Therefore, it is evident from the literature, that radiotherapy increases the risk of lymphoedema, which is further increased if it specifically targets lymph node basins and is conducted in conjunction with surgical lymph node dissection. While the incidence can vary according to anatomical site, radiotherapy dosing regimens and risk factors such as increased BMI; secondary lymphoedema represents a significant problem in a population of increasing cancer survivors, living with the after effects of their cancer treatments.

Chang et al. demonstrated that in patients suffering from lymphoedema post-mastectomy, a 23.7% rate of improvement was found after delayed free tissue transfer, suggesting the interposition of healthy un-irradiated tissue may have the ability to mitigate lymphoedema (244). Alternative therapies such as fat grafting have also been reported to have beneficial and regenerative effects on lymphatic system damaged by radiotherapy, suggesting further investigation is needed to identify therapies that target this specific mode of injury (see section 1.11.3.2).

1.8.6.4 Infection

Separate to the acute inflammatory response of tissues to radiotherapy injury, irradiated tissues clinically exhibit a lower tolerance to infection, which further complicates healing in an already compromised site. Cummings et al. demonstrated that irradiated skin had fewer epidermal Langerhans cells and dermal dendritic cells (201) (245), and with the presence of lymphoedema and/or lymph node clearance, will set the stage for immunocompetence in irradiated tissues (246). In the presence of

lymphoedema the static fluid acts as a culture medium by facilitating bacterial growth which results in worsening LEC damage and further aggravation of lymphoedema (234). Common offending organisms in secondary lymphoedema-related infections (reported with rates as high as 41% (247)) include streptococcus, staphylococcus and polymicrobial etiologies, with enterococcal, cryptococcal and micrococcal species also reported in the literature (234).

1.8.6.5 Breast Cancer

The challenges posed by radiotherapy in the setting of breast reconstruction are numerous, with the methods and timing of reconstruction varying from one clinical center to the next. Kronowitz et al. reviewed the literature and concluded that implant based reconstruction in irradiated breast fields can be associated with a 47.5% increase in complications such as capsular contracture, 15% risk of extrusion, with up to 33% of patients requiring re-operation for replacement of implant with either a new implant or autologous tissue for reconstruction (248) (249). The complications are attributed to factors such as poor overlying skin flap vascularity with impaired tissue compliance on attempted expansion (119). Systematic review conducted by Mohmoh et al. suggested that pre or post-operative irradiation did not confer differences in complication rates, however, radiotherapy itself was a significant contributor to increased failure rates when compared to un-irradiated breast implant reconstructions (250) (251). This was further supported by findings in a review by Kronowitz et al. demonstrating 20% reduction in adverse events in patients undergoing autologous vs. implant reconstruction after radiotherapy; following the theory of importation of vascularized tissue may improve tissue quality and reduce complications in an irradiated tissue bed (249). The latissimus dorsi muscle may be used as a pedicled flap to support implant based reconstructions, although earlier published papers did not show a significant reduction in complications and capsular contractures (250) (252) (253) (254). However, in a more recent meta-analysis Fischer et al. concluded that subpectoral vs. latissimus dorsi covered implant placement conferred a 4.33 odds ratio of implant loss, suggesting additional muscle coverage was successful in reducing loss, infection and rates of re-operation in a pre-irradiated field (255) (256).

With a body of evidence suggesting significant complications rates associated with

radiotherapy and prosthetic reconstruction, autologous reconstruction is thought to be a safer option in patients requiring post-mastectomy radiotherapy (248). When a patient is a candidate for autologous free flap reconstruction the timing, (immediate vs. delayed surgery), in the setting of radiotherapy has been highly deliberated. Patients experience a higher incidence of revision surgery due to complications such as fat necrosis (with an odds ratio of 3.13 (257)) and flap contracture in the setting of immediate reconstruction and radiotherapy (258). Post-mastectomy and post-reconstruction radiotherapy were found to be the greatest risk factors with complications 5.40 times higher (CI 29.5-9.92) (258), compared to post-mastectomy-radiotherapy and delayed free flap reconstruction which reportedly drops overall late complication rates significantly from 87.5% to 8.6% (259) (260) (261). Furthermore, immediate reconstruction with either alloplastic or autologous methods have been associated with difficulties in delivering targeted therapeutic irradiation to chest wall and internal mammary lymph node tissue, without increasing exposure of non-targeted organs such as the lungs and heart (248) (262). Clinically, delayed reconstruction necessitates re-operating in a pre-irradiated surgical field, which presents challenges with fibrotic, scarred and less pliable tissue requiring substantial skin excision. Fosnot et al. reported that pre-operative radiotherapy carried an independent risk in increasing intra-operative vascular complications, suggesting irradiated vessels present an additional technical challenge during microvascular anastomoses (263). Current recommendations are for delayed-immediate autologous reconstruction in the setting of post-mastectomy radiotherapy, however there is a need for more standardised prospective outcome analysis. This algorithm allows for skin sparing mastectomy, if appropriate, with immediate tissue expander reconstruction followed by delayed autologous reconstruction on completion of adjuvant therapies such as radiotherapy (248) (257) (264).

1.8.6.6 Head and Neck Cancer

Radiotherapy is an important adjunct in the management of primary or recurrent head and neck cancers. Normal tissues susceptible to damage during irradiation of the oropharynx include the salivary glands, mandible, oesophagus and sensorineural apparatus of the internal ear (111). Chronic radiotherapy side effects to these areas can pose significant problems (especially with doses exceeding 60Gy) with an

incidence of: 60-90% of severe xerostomia (265), 15-30% dysphagia (265), 15% risk of osteoradionecrosis (266) and 40-50% risk of otological toxicity resulting in sensorineural hearing loss (267). The vascular morbidity associated with head and neck vessel irradiation as discussed in section 1.8.6.2 also significantly contributes to morbidity and mortality with an increase in cerebrovascular events (222) (268).

For the cohort of patients receiving radiotherapy for cancers involving the mandible; osteoradionecrosis (ORN) is an incapacitating side effect which can present with pain, orocutaneous fistula, exposure of bone/metal plates or pathological fracture (119). Conservative management with intravenous antibiotics and hyperbaric therapy may prevent ORN progression (266), however resolution requires re-operation in a pre-irradiated field with limited local reconstructive options necessitating complex vascularised bone transfers from the iliac crest or fibula bone (119). Cunha et al. irradiated murine femurs and demonstrated a significant reduction in bone density, increased adiposity and reduced osteoblastic activity rather than increased osteoclastic activity (269), suggesting impairment of the remodeling process.

Schultze-Mosgau et al. reviewed a series of 217 free microvascular tissue reconstructions in head and neck cancer patients by stratifying surgical success in groups receiving no radiotherapy as 94%, 40-50Gy as 90% with reduction to 84% in patients receiving 60-70Gy (211). The cohort of patients receiving high dose radiotherapy demonstrated irregular capillary architecture, fibrosis and a reduced density of microvascular $CD34^{+}$ staining on histology. These findings suggest vascularity of irradiated tissue may contribute to the 7% partial and 9% total failure rates (211). Similarly multivariate regression analysis by various groups correlated radiotherapy to be associated with a significant increase (odds ratio of >4) in free flap reconstructive complications (212) (213). A recent meta-analysis of pre-operative radiation and head and neck free flap outcomes by Herle et al. clearly demonstrated a statistically significant increase in free flap failure (relative risk 1.48) with necessary re-operation and incidence of fistula formation representing relative risks >2 (270).

1.8.6.7 Sarcoma

Neo-adjuvant or adjuvant radiotherapy has successfully been able to raise the local control rates of soft tissue sarcoma in combination with surgical excision, so that 90%

of patients can be managed without limb amputation (271). However, Bujiko et al. reported in a case series of 202 patients pre-operative radiotherapy conferred a 37% risk of wound break down comprised of 24% wound dehiscence, 6% wound infection, 3.5% seroma, 3% skin graft breakdown, and 0.5% risk of hematoma (272). Davis et al. randomized patients to pre vs. post-operative radiotherapy and measured outcomes such as fibrosis, lymphoedema and joint stiffness, concluding higher rates of complications in the post-operative setting at the two year mark (273). Akudugu et al. reported a 29% incidence of wound healing complications in their series of pre-operatively treated sarcoma patients and suggested that fibroblasts from patients with wound healing complications showed increased initial proliferative phenotype assessed with binary index, suggesting that the mechanism of radiotherapy damage may not necessarily involve suppression of fibroblastic activity (274).

1.9 Molecular markers of radiotherapy injury

After exposure to radiotherapy, each cell subtype initiates a signal transduction cascade as well as alteration in transcription factors, which then ultimately regulate expression of downstream genes that elicit a molecular response to radiotherapy injury. Signal transduction pathways include MAPK - EKR1/2, JNK, p38 and ATM, while transcription factors such as NFKB, AP1, GADD153 and p53 (64) (275) also appear to be heavily involved in mediating survival, apoptosis and secretory responses of injured cells. Below, the literature is reviewed for the most consistently reported molecular markers of radiotherapy injury in normal tissue cells, with some correlations made to studies that investigate the response of malignant cells to irradiation also.

1.9.1 Genetic markers of radiotherapy exposure

Various groups have attempted to determine the most effective bio-dosimeters for exposure to radiotherapy, not only to determine the severity of each individual's response but also for the potential use in prioritization and management of nuclear accidents or deliberate threats (276). Marchetti et al. extensively reviewed bioassays utilizing immunological, biochemical, or hematological measurements to determine an estimate for radiation exposure, but due to complexities, the length of time

required for most tests and individual baseline variation, no single test satisfactorily provided this assessment (276). With the advent of newer technologies allowing high throughput analysis of genome wide transcriptional and proteomic level changes, it was found that genes; ATM (ataxia telangiectasia mutated), H2AX (histone 2AX), CDKN1A (cyclin-dependent kinase inhibitor 1A) and TP53 (tumour protein 53) were altered as a result of a variety of radiation exposures (276).

1.9.2 TGFβ and SMAD pathways

TGFβ primarily exists in the extracellular space in a latent form and is part of a family of proteins consisting of TGF-β1 (a pleotropic cytokine most commonly produced), TGF-β2 and TGF-β3 isoforms (277). Once activated by an inciting event such as injury, ROS, proteases, integrins or thrombospondin1, it dissociates from the latency associated peptide (LAP) and forms active TGFβ capable of binding to both TGFBR1 and TGFBR2 trans-membrane serine/threonine kinase receptors to initiate intracellular signaling cascades. It is important to note that without active binding to both receptors, the ligand activated receptor complex is not formed and therefore a lack of Smad transcriptional complex formation means intracellular signaling does not proceed (148). TGFBR2 forms a phosphorylated complex with TGFBR1 to initiate intracellular signaling either through Smad dependent or Smad independent pathways. There are 8 individual Smad proteins; 5 receptor regulated Smad (R-Smad 1,2,3,5 and 8), one Co-mediator Smad (Co-Smad 4) activated by TGFBR1 and forms complexes with R-Smads and lastly two inhibitory Smad (I-Smad 6 and 7), which negatively regulate the actions of TGF-β. Smad independent pathways include Rho GTPases, protein phosphatase 2A and MAP kinase (14) (57) (148). Of late, more evidence suggests that chronic radiotherapy-induced fibrosis may be more attributed to Smad-independent pathways (278) (279). Grose et al. showed in Smad-3 null mice, the application of exogenous TGF-β1 to full thickness wounds stimulated ECM, suggesting that TGF-β1 matrix deposition may be occurring independently to Smad-3 signaling (280).

Dysfunction in the TGF-β system has implications across many cell types and disease processes and plays a vital role in normal and abnormal wound healing. It is found in fibroblasts, endothelial cells, lymphocytes, macrophages, and platelets, and some of

its many important functions include the initiation of tissue matrix production and stimulation of chemotactic migration of fibroblasts and monocytes (152) (220) (277). Up-regulation of the TGF-β signaling is a mechanism common to numerous conditions of pathological fibrosis (57) (103) (281), including following cancer treatments such as radiotherapy or chemotherapy (14) (57) (61) (119) (195) (220). Table 4 aims to summarise the TGF-β mediated effects on wound healing and radiotherapy related injury.

Brush et al. suggest that the impairment of normal healing results in compensatory hyper-activation of fibrotic pathways, in order to maintain tissue structure and integrity (61) (69) (212). Work by Lee et al. demonstrated persistent TGF-β1 over-expression in irradiated tissues, even after six months (212) (282); alterations that may in turn influence the function of fibroblasts, endothelial cells, lymphocytes, macrophages, and platelets (14) (57) (280). Tibbs at al. characterised the key cellular functions of TGF-β, including initiation of tissue matrix production and stimulation of chemotactic migration of fibroblasts and monocytes (220) (283). In contrast, Randall et al. showed oscillating TGF-β1 expression - decreased in the first 3 hours after RTX (normalizing by 2-7 days), then steadily increasing to up to 200% above normal levels more chronically (270) (282). Grose and Werner verified a role for TGF-β in RTX-induced fibrosis and investigated the modulation of downstream mediators such as Smad-3 (9) (280) (284). They demonstrated accelerated re-epithelialisation and decreased inflammation in Smad-$3^{-/-}$ mice compared with control animals (125) (280). Despite this evidence, however, attributing specific cellular effects of RTX-induced fibrosis to such a broad regulator as TGF-β has its limitations. The TGF-β super-family has multiple effects on numerous tissues and therefore therapeutic approaches that target this molecule may have insufficient specificity to ameliorate RTX damage, without jeopardizing other biological processes to which fibrosis is integral. Therefore, more targeted approaches directed at a specific area of signaling downstream may be more effective, rather than targeting upstream TGF-β or the receptors alone.

Promotes	Inhibits
Promotes invasion and metastases of breast cancer cells (57) (285)	Inhibits Endothelial cell proliferation (14)
Promotes terminal differentiation of proliferating fibroblasts to post-mitotic fibroblasts (124)	Inhibits basal keratinocyte proliferation (150)
Promotes fibroblast to myofibroblast differentiation (106)	Inhibits the functions of T/B and NK cells leading to immunosuppression (17) (280)
Promotes mesenchymal cell proliferation and collagen production (286)	Inhibits ECM breakdown (286)
Chemotactic factor for mast cells which may play a significant role in the development of radiation induced fibrosis (17)	Inhibits keratinocyte migration (153) (280)
Promotes fibrosis - as loss of SMAD 3 was shown to block EMT and reduce fibrosis. (152)	Impairs lymphangiogenesis as blockade of TGF-β1 results in improved lymphangiogenesis (83) (287)
Potent stimulator of expression of ECM proteins and integrins (280)	Reduces adipogenic differentiation through activation of Smad3 and is linked to CD105 expression on ADSC (288)

Table 4 Literature review of the effects of TGF-β on cellular processes

1.9.3 Integrins

Integrins consist of a group of receptors of around 20-25 transmembrane heterodimer receptors that play a crucial role in 1) detection of changes in the extracellular environment, 2) altering the transmission of signals based on the condition of the ECM to modulate intracellular signaling and vice versa (289). It is known that this signaling relationship is vital for key processes such as cell migration, proliferation and apoptosis, with radiotherapy causing a substantial change in the physical and chemical properties of the extracellular environment. Dysfunction of these interactions can be implicated in changing these processes which are fundamental to wound healing and are even implicated progression of cancer (290). The integrins undergo an internalization from the plasma membrane, exert effects intracellularly and are re-cycled to the cell surface. This process can happen through short (Rab4) or long loop (Rab11) processes; therefore, small changes in the extracellular

environment can be quickly detected and integrin trafficking signals changed accordingly. This speed of re-cycling has been shown to regulate cell migratory functions, with downstream integrin mediated activation of Rho/Rho Kinase (ROCK) GTPases (290). It is suggested that αvβ3 integrins are quickly recycled through the short loop and replaced on the cell surface, organized spatially on the polarized side of the cell. This rapid cycling is likely responsible for uni-directional cell (fibroblast) migration required in wound healing. This persistent stream of αvβ3 downstream signaling is sufficient in inhibiting α5β1 signaling which usually results in random cell migration via the ROCK-cofilin pathway (290).

Investigation regarding β1 integrin inhibition predominantly revolves around radiosensitising tumour cells as well as abolishing the pro-survival advantages of radiotherapy induced β1 integrin up-regulation (291). Studies show that inhibition of β1 integrin recycling, for example by tetanus toxins impairs cell migration (292), achieving a therapeutic effect for malignant cells, but may result in physiological impairment of normal cells. Raftopoulou et al. demonstrated that α5β1 integrins have been shown to activate ROCK via small GTPase. Cdc42 and Rac1 are proteins responsible for promoting migration by enhancing protrusion, polarization and generating lamellipodia in cells. RhoA, which acts in a biphasic manner, can then further contribute by promoting the contractility and traction required for migration (293). Alterations in the ECM (such as in radiotherapy induced fibrosis) disturbs this ideal migratory signaling, in particular high fibronectin concentrations in the extracellular environment induce a ‘stop’ signal for cell migration via inhibition of Cdc42 and Rac1 while further increasing RhoA, clinically correlating to poor wound healing and contracture formation. Integrin α4β1 interacts strongly with VCAM-1 and promotes pericyte and endothelial cell survival during processes of angiogenesis, and VEGF-C/D mediated lymphangiogenesis with antagonists resulting in cell death (294). Zhang et al. also demonstrated that integrin α5β1, a key receptor for fibronectin, increased the proliferation and reduced apoptosis of LECs via VEGF-C mediated transactivation of VEGFR-3 (295). They found that fibronectin was able to amplify this VEGF-C signaling cascade with increased VEGFR-3 phosphorylation associated with α5β1 signaling shown on co-immunoprecipitation studies, with downstream PI3K/AKT targets (295). α9β1 integrins on microvascular endothelial

cells demonstrated solid phase binding to VEGF-C and D, with the resulting migratory stimulus abrogated with the addition of anti-α9β1 antibody, indicating α9β1 may be a target to modulate lymphangiogenic responses to inflammatory stimuli (296). Therefore, blockade of β1 integrin up-regulation in normal tissues, may worsen radiotherapy-induced injury by impairing survival and ordered cell migration, essential for wound healing, angiogenesis and lymphangiogenesis (297) (298).

1.9.4 Matrix Metalloproteases and Tissue-Inhibitors of Metallo-Proteinases

Matrix mellaoproteases (MMPs) and their endogenous inhibitors tissue-inhibitors of metallo-proteinases (TIMPs) are proteins that play a significant role in the connective tissue remodeling phase of wound healing. MMPs are responsible for the degradation of ECM proteins, in order to maintain composition and equilibrium between synthesis and breakdown (299). They are largely produced by fibroblasts, macrophages and neutrophils in response to PDGF, FGF, IL-1 and TNF, while being inhibited by TGF-β and steroids (300). MMPs are further divided into subtypes such as interstitial collagenases (MMPs 1,2,3) which cleave fibrillar collagens I, II and III. Collagen I is the most abundant form and significantly contributes to tensile strength of the wound. During RTX MMP alterations demonstrated an early phase decrease in MMP-1, with later epidermal expression normalizing or increasing to slightly higher levels compared with controls, contributing to compromised wound strength and integrity (119) (213) (216). Other MMP subtypes include gelatinases (MMPs 2 and 9), which degrade amorphous collagens and fibronectin, stromelysins (MMPs 3,10,11) which in turn act on a variety of ECM components including proteoglycans, laminin, fibronectin, amorphous collagens and membrane bound MMPs (ADAMs). MMPs also play a role in the modulation of processes of migration and angiogenesis (301). Degradation of vessel basement membranes, stimulating the release of VEGF and FGF, supports neo-angiogenesis and matrix composition is also thought to guide migration of endothelial cells. Therefore, any alteration in this balance has profound effects on wound healing (119) (213). Lee et al. showed an imbalance of MMP-2 and TIMP-2 leads to excessive degradation of collagen IV contributing to radiotherapy induced injury to the blood brain barrier (215). Similarly in RTX-induced lung fibrosis, MMP-2 and MMP-9 were significantly increased, degrading type IV

collagen and affecting the structural integrity of lung tissues (302) as a result of the inflammatory cytokine reaction to RTX (see 1.9.7.2). Goessler et al. demonstrated increased levels of MMP-2,-12,-13 at the RNA and protein level in both keratinocytes and fibroblasts extracted from patients with chronic non-healing irradiation ulcers (139). Expression of these proteins in irradiated tissues shows that ECM remodeling is a dynamic process, and that irradiated, fibrotic tissue is constantly subjected to change, potentially allowing therapeutic intervention at both an early and later stage. While ECM degradation and proteolysis are vital to physiological processes such as angiogenesis, unregulated tissue destruction by irradiation induced MMPs may contribute to poor wound healing.

The activity of MMP-9 in wound healing was investigated by Ebrahimian et al., with elevated levels of MMP-9 in plasminogen activator inhibitor 1 PAI-$1^{-/-}$ mice demonstrating superior wound healing to PAI-1/MMP-$9^{-/-}$ mice and controls (303). Alternatively, Rutkowski et al. found that MMP-9 null mice developed more severe lymphoedema in comparison to wild types, which may in part be attributed to a lower baseline matrix density, allowing for increased expansion and fluid accumulation, along with insufficient remodeling of the matrix in response to the fluid stasis (304). An alternative hypothesis suggests any changes in the composition of ECM, e.g. in fibrosis may physically impair lymphatic fluid drainage while diminishing the effectiveness of lymphangiogenesis (246).

1.9.5 Adhesion Molecules

P-selectin and intracellular adhesion molecule-1 (ICAM-1) expression has been shown to be increased as a result of high dose radiation more so than lower doses, where E-Selectin has been implicated in causing increased neutrophil adhesion as a result of RTX (17).

Up-regulation of endothelial cell adhesion molecules E-Selectin, ICAM-1 and VCAM-1 may be a mechanism by which radiation induced inflammatory response results in vascular injury - changes postulated to have links with the development of CAD and CVD (13). Hallahan et al. and others have demonstrated increased levels of E-Selectin and ICAM mRNA after RTX of human umbilical vein endothelial cells or

human dermal endothelial cells *in vitro* (305-308). Up-regulation of E-selectin was shown to be short-lived (<20 h) while ICAM-1 persisted beyond 48 hours and was thought to be independent of cytokine induction or denovo protein synthesis in response to an injurious stimulus mediated through NFKB pathways (305). Cellular adhesion molecules are responsible for functional alterations such as increased arrest, adhesion and rolling of neutrophils or macrophages on the altered endothelial surface, facilitating increased inflammatory cell infiltration, sequestration, LDL peroxidation, thrombosis and atherosclerosis (309) (310). Furthermore, Balbay et al. found elevated serum concentrations of IL-1β, TNFα and soluble ICAM-1 in patients who had experienced acute myocardial infarction or stable angina highlighting the link between RTX injury, molecular pathological alteration of endothelial cells and the clinical correlation with CAD (310).

In vitro experiments in ICAM-1 knock-out mice demonstrate abrogation of RTX-induced inflammatory cell infiltrate in the lungs of irradiated mice, while others demonstrated reduced leukocyte emigration in irradiated mesenteric vessels pre-treated with anti-ICAM-1 monoclonal antibodies (311) (312) (313). Chang et al. showed that a Glycyrrhetinic acid (GA) inhibited TNF-α-stimulated ICAM-1 expression, leading to a decreased monocyte adhesion to HUVECs. This inhibition is attributed to GA interruption of both JNK/c-Jun and IκB/NFKB signaling pathways, which decrease activator protein-1 (AP-1) and NF-κB mediated ICAM-1 expression. The results suggested that GA may provide a beneficial effect in treating vascular diseases associated with inflammation, such as atherosclerosis (314).

1.9.6 Vascular Endothelial Growth Factors C and D:

VEGF-C and VEGF-D comprise the part of the VEGF family of growth factors that are primarily lymphangiogenic, with other members including VEGF-A, Placenta growth factor (PIGF) and VEGF-B (315) (316). These growth factors are secreted glycoproteins, characterised by a common VEGF-homology domain with VEGF-A and PIGF sharing 42% of their amino acid sequences and along with VEGF-B activated receptor tyrosine kinase VEGFR-1 (alternatively known as Flt-1) (317) (318). Homodimers of VEGF-A and heterodimers in combination with PIGF have also been found to activate VEGFR-2 (Flk-1/KDR) (319) (320). VEGF-C and D are

unique as they are secreted in an immature prepropeptide form, which undergoes sequential proteolytic cleaving by 'pro-protein convertases' to produce the mature form of the proteins, which exhibit increased affinity for their associated receptors VEGFR-2 and VEGFR-3 (Flt-4) (315) (321) (322). In adult tissues VEGFR-2 is situated on vascular endothelium while VEGFR-3 is found on lymphatic endothelium. While VEGF-C and D are able to activate VEGFR-3 in both partially or fully cleaved forms, VEGFR-2 activation necessitates complete proteolytically processed ligands, therefore mature forms of VEGF-C and D can mediate both processes of angiogenesis and lymphangiogenesis with high receptor affinity (321) (323) (324). So, in the instance where injury such as radiotherapy requires regeneration of both blood and lymphatic vessels (during different phases of repair), specific growth factors and receptors may be targeted to aid in a more directed approach to regeneration.

In surgical removal of lymph nodes or irradiation, there is either a physical or biochemically-induced injury to the lymphatic system, but the molecular mechanisms that drive the development of secondary lymphangiogenesis remain somewhat unclear (see section 1.7.4). It has been postulated that delivery of pro-lymphangiogenic factors such as VEGF-C and D may be able to promote regeneration of injured LECs, via activation of VEGFR-2/3 and therefore, reduce the burden of the resultant clinical lymphoedema (185) (325). However, elevated levels of VEGF-C can also lead to increased vessel permeability and lymphangiogenesis of dormant tumours, therefore requiring more thorough investigation before being employed for the treatment of secondary lymphoedema in the setting of cancer (325) (326). In mouse models of tail skin regeneration, Goldman et al. showed that an abundance of VEGF-C generated by VEGF-C overexpressing tumour cells, did not lead to increased LEC functionality or migration. The wound which was surgically created and bridged with a collagen matrix scaffold demonstrated that VEGF-C led to early hyperplasia of vessels, but once the stimulus was removed, lymphatic vessel density did not differ to controls (327). Furthermore, while LEC migration in a boyden chamber model was induced by VEGF-C chemoattraction, the addition of a fibrin matrix under the cells resulted in no increase in VEGF-C-mediated chemo-invasion (possibly due to inadequate availability of proteolytic factors or MMPs) (246) (326) (327). Examining this further, Rutkowski et al. demonstrated that surgically-induced mouse tail lymphoedema lead to a significant up-regulation of VEGF-C assessed by immunohistochemical staining,

increased lipid deposition and lymphatic vessel hyperplasia. These changes were attributed to the presence of static lymphatic fluid, with maximal swelling post wounding peaking at day 7, phenotypically characterised by dilated and ectatic vessels unable to functionally drain lymphatic fluid, further contributing to ongoing lymphoedema (304). Zampbell et al. found elevated levels of VEGF-C, VEGF-A and HGF in surgical lymphoedematous mouse tails distal to the site of vessel ligation, however this up-regulation did not appear to contribute to lymphangiogenesis or resolution of lymphoedema (328). Therefore, the exact method by which VEGF-C – VEGFR-3 pathway may reduce secondary lymphoedema remains unclear, as application of VEGF-C has been reported to increase LEC proliferation with ultimate failure to regenerate functional lymphatic vessels (329).

Jackowski et al. attempted to characterise the processes which drive lymphangiogenesis in the setting of RTX-injury by examining irradiated breast skin biopsy samples with contralateral skin controls. Immunofluorescent staining demonstrated increased macrophage infiltration ($CD68^+$) in irradiated samples (which persisted in samples taken > 8 weeks after therapy), along with a significant increase in VEGF-C^+ cells, 82% of which co-expressed $CD68^+$. These results suggest macrophages may be the major source of VEGF-C in irradiated tissues, attempting to drive regeneration of lymphatic vessels in response to RTX injury (184). Of note, there was no detected up-regulation of VEGF-D (184). In another model of fibrosis and tissue injury, examination of lung specimens with diffuse alveolar damage showed $CD68^+$ IHC staining in peri-lymphatic locations with some $CD68^+$ cells co-localizing with D240 and expressing VEGF-C. Separate to VEGF-C-mediated effects, the lymphangiogenic potential of these macrophages was also postulated to be linked to an alternative cytokine pathway; CCL19 (a ligand for CCR7), found to be expressed on proliferating lymphatic vasculature ($Ki67^+$) suggesting that lymphangiogenesis in inflammatory or fibrotic conditions may be driven by CCL19, increasing migration and lymphatic differentiation of $CCR7^+$ macrophages at the site of injury (330). A review by Ran et al. elaborated on the concept of macrophage mediated lymphangiogenesis via down-regulation of myeloid cell markers and transdifferentiation to LEC progenitor cells by increasing expression of markers such as VEGFR-3, podoplanin, LYVE1 and Prox1 (331). Alternatively other mesenchymal sources such as adipose derived stem cells (ADSC) are also able to demonstrate

increased lymphangiogenic marker expression with stimulation by factors such as VEGF-C, representing yet another source of progenitor cells to aid in post-radiotherapy lymphangiogenesis (287).

Therefore, the role of VEGF-C in RTX-injury, its source, the availability of proteolytic cleavage and receptor activation, along with other lymphangiogenic factors such as VEGF-D, Ang1 and adrenomedullin still require further interrogation, as candidates for the modulation of irradiation injury.

1.9.7 Cytokines, Chemokines and Receptors

Cytokines are soluble proteins which can be produced by a variety of different cells, and are important in immunological reactions (277). Cytokines are thought to be intricately involved in radiotherapy soft tissue injury, with each individual cytokine exerting a pleotropic (varying effect) on individual cell types through autocrine, paracrine or endocrine mechanisms to interact with specific surface receptors to then generate intracellular signaling and alteration of gene transcription (277). Their actions may be radio-sensitizing or radio-protective making them important candidates for manipulation to mitigate the harmful effects of radiotherapy. However, such approaches are complex as some cytokines act synergistically, while others may have some redundancy or in turn regulate the production of other cytokines (277). Classically described cytokine responses to irradiation include TNFα, IL-1, TGFβ, as well as more recently recognized chemotactic factors such as SDF-1α and IL-8 (98) (332) (333) which may play a significant role in recruitment of cells from distant, un-injured sites for regenerative purposes.

1.9.7.1 Tumour Necrosis Factorα

Tumour necrosis factorα (TNFα) plays an important role in majority of inflammatory responses and is secreted by a variety of immunological, endothelial and parenchymal cells. Potent stimulators of TNFα include lipopolysaccharides, interferons and irradiation (277). TNFα precursor is converted to active TNFα by TNFα-conversion enzyme, which can then interact with two different TNF receptors I and II, resulting in a wide variety of responses including inflammatory cell recruitment, parenchymal

cell proliferation and MMP synthesis (277). Radiotherapy related TNFα up-regulation has been shown at the RNA level and also receptor level in keratinocytes (334) as well as in several tumour cell lines such as sarcomas. TNFα is thought to act synergistically with IL-1, not only by increasing ROS and MMP expression (see below) but also recruiting other inflammatory cytokines such as IL-6 (277). There are numerous TNFα-inhibitors that are currently employed in the treatment of diseases of chronic inflammation such as rheumatoid arthritis and Crohn's disease (98), yet the use in amelioration of radiotherapy injury are unexplored. Major challenges include timing of injury and subsequent effects of immunosuppression in a patient with malignancy.

1.9.7.2 Interleukin-1

IL-1 exists in an α and β form and is commonly part of an acute-phase inflammatory reaction exerting a pro-inflammatory effect, largely produced by macrophages and endothelial cells. Irradiation also causes up-regulation of IL-1 in human keratinocytes (335) as demonstrated in a study by Koike et al. using 5Gy doses and RNA analysis at 5 hours (334). IL-1 exerts multiple effects by stimulating proliferation of keratinocytes and fibroblasts while also inducing MMP and collagen synthesis (277) (335). Yoo et al. determined that IL-1β stimulation of murine macrophages resulted in activation of NFKB, production of ROS (H_2O_2) and dose-dependent up-regulation of MMP-9 promoter activity. Pretreatment with N-acetyl cysteine (NAC), an antioxidant, abrogated these IL-1 mediated changes (302). The mechanisms behind IL-1β cytokine mediated production of ROS are thought to be driven by phospholipase A2, COX-2 mediated conversion of arachidonic acid to prostaglandins and subsequent NADPH oxidase, as well as through activation of various enzymes resulting in mitochondrial ROS generation (302) (336). Longer term assessment of radio-dermatitis and fibrosis also demonstrated decreased severity in IL-1 or IL-1-receptor deficient mice, which highlights that immediate RTX-induced cytokines may be key targets to mitigate long term clinical sequelae of radiotherapy injury (337).

1.9.7.3 Interleukin-6

IL-6 is primarily secreted by mononuclear phagocytic cells and has both pro and anti-inflammatory activities. It is able to recruit immune cells in an acute phase inflammatory reaction (277), while also acting as a contributor to fibrosis (130) and down-regulating IL-1 and TNFα expression (277). IL-6 signaling involves two major pathways. The first is via IL-6 receptor (expressed constitutively on hepatocytes and some lymphocytes) which initiates JAK1 and JAK2 kinase activation, phosphorylation and transduction of STAT 1/3, Src homology region 2 domain containing phosphatase and ERK (130). Alternatively, the majority of cells in the body express the gp130 subunit (which is able to bind to a variety of ligands and receptors) and allows for IL-6 signal transduction via soluble IL-6 receptor (sIL-6R), once liberated in response to an inflammatory stimuli such as IL-1, TNFα, IL-8 or CRP (130). Unlike traditional receptor cleavage, which acts as an antagonist and negatively regulate further cytokine secretion, sIL-6R is an agonist and therefore broadens the range of IL-6-mediated effects via trans-signaling (130). IL-6 is upregulated in endothelial cells after radiotherapy, as Meeren et al. demonstrated using 2Gy irradiation of HUVEC cells. This resulted in biologically active IL-6, detectable in cell supernatants up to 6 days after insult (333). RTX-induced IL-6 production was also found in other soft tissue constituents; keratinocytes and fibroblasts at both RNA and protein level. Additionally, the IL-6 promoter region also houses sites for NFkB, Activator protein 1 and cAMP responsive element binding protein (CREB) binding, which themselves have been found to be up-regulated as a result of radiotherapy (161) (277) (338). Siva et al. measured serum cytokine levels and found IL-6 levels to be significantly different in patients undergoing radiotherapy in comparison with chemo-radiotherapy which correlated with the risk of lung toxicity, as assessed by the CTCAE v2.0 (339). Therefore, IL-6 appears to constitute an integral part of the inflammatory response to radiotherapy both locally and systemically, therefore represents a potentially vital target for reducing irradiation injury.

1.9.7.4 Interleukin-8

IL-8 (CXCL8), part of the CXC chemokines, is a cytokine with strong chemotactic properties and is largely secreted by immune cells, but also by cells such as

keratinocytes, fibroblasts, endothelial cells and pigmented melanocytes (277). IL-8 is produced from a precursor which is converted by proteases such as cathepsin L, making a mature form in response to inflammatory stimuli such as TNFα, LPS, IL-1, viruses and irradiation (277). Its actions primarily lead to neutrophil degranulation but has also been shown to increase adhesion and angiogenic properties of endothelial cells by inducing up-regulation of VEGF-A and autocrine up-regulation of its receptor VEGFR-2 via NFkB pathway activation (306) (336) (340). Like IL-6, its promoter region houses sites for NFkB and AP1 binding, and together result in a large up-regulation of IL-8 in response to radiotherapy in a wide variety of cells (277). Additionally, Choi et al. conducted a series of *in vitro* and *in vivo* studies demonstrating the lymphangiogenic effects of IL-8 on LEC, largely mediated through CXCR2 signaling while also being independent of VEGF-C (341). Therefore, these early results suggest IL-8 up-regulation in response to inflammation and irradiation may prove to be a valuable target to assist in lymphangiogenesis post-radiotherapy injury.

1.9.7.5 Stromal derived factor 1 (SDF-1):

Traditionally, the chemokine SDF-1 known also as CXCL12 is involved in the regulation of many key developmental processes such as cardiac and neuronal development, neovascularization and tumorigenesis. Of increasing importance is its role in stem homing and recruitment, B cell lymphopoesis and leukocyte migration (342). SDF-1 itself, exists in both monomeric and dimeric configurations in a complex equilibrium. Its active form is largely monomeric, a configuration which is able to bind to both CXCR4 and CXCR7 with high affinity, while dimeric SDF-1 preferentially binds to CXCR4 (343) (344). SDF-1 is expressed predominantly by stromal cells in bone marrow and endothelial cell populations, although expression can be demonstrated in nearly all organs of the body, increased at times of injury. SDF-1 is thought to play a role in homing of local/distant stem or progenitor cells, which may mediate processes of tissue repair or regeneration (343) (345). Therefore, SDF-1 may play a vital role in diseases or conditions that induce a large or chronic inflammatory responses (342) in a biphasic modality, through pro-inflammatory actions of immune cell recruitment as well as anti-inflammatory actions such as suppression of T cell responses through reduced functionality of dendritic cell antigen

presentation (343). Ponomaryov et al. showed that sublethal doses of irradiation with concomitant treatment with 5-flurouracil enhanced the mRNA and protein levels of SDF-1 in the bone marrow and spleen in SCID/NOD mice (346). It is postulated that this increase in SDF-1 is a component of the host's immunological defense, which attempts to clear apoptotic cells through recruitment of macrophages to the site of injury or inflammation (346).

1.9.8 CXCR7

CXCR7 was initially cloned from dog thyroid cDNA, followed by isolation from human and mouse RDC1 homologues demonstrating >90% identity of both nucleotide and protein sequences, indicating high evolutionary conservation. (342,347). It is located on chromosome 2 (2q37.3) in humans, along with CXCR1, CXCR2 and CXCR4 (343) (345) (348). This receptor has been shown to be elevated in "transformed" cancer cells lines, activated endothelium and also on fetal liver cells and placenta. Along with CXCR4, it is thought to have a significant role in processes such as stem cell homing, tumor metastases, immune responses and angiogenesis, an area of active investigation in current literature (345).

This receptor is a 7-transmembrane receptor also known as RDC1 (342). The CXCR7 transfected breast cancer cell line (MDA MB 435s) demonstrated increased binding affinity of SDF-1, which could be blocked in the presence of CXCR7 antagonist CCX451 but not by CXCR4 antagonist AMD3100, demonstrating a clear distinction in receptor activity (342). This group's initial data also demonstrated that transformed cell or mouse tissues (e.g. tumour cell lines MCF-7, HeLa or BCL1), expressed CXCR7 abundantly, at times co-expressed with CXCR4 or even in the absence of CXCR4. Additionally, normal "non-transformed" tissues did not express surface CXCR7, but some CXCR7 mRNA could be detected. The overall conclusions drawn from this suggested that CXCR7 transmembrane protein is commonly present on "transformed" cells, not normal cells, although may be subject to post-translational modification given the presence of mRNA in some normal tissues (342).

CXCR7 is also found to be transiently expressed during embryogenesis, demonstrated by SDF-1 binding to fetal liver cells from CXCR4$^{-/-}$ mice (342). It has also been

implicated with importance in phases of rapid growth, vascularization and neural crest development. (343). Transcriptional regulation of CXCR7 is likely mediated by NFKB and HIF1α, similar to CXCR4 and SDF-1. It is thought that the interaction between CXCR7 and SDF-1results in internalization of the receptor, but fate of this receptor remains unclear. Some reviews state it is recycled to the cell surface, while others suggest overexpression above endogenous levels will lead to saturation and inability to recycle the receptor (343). This mechanism in effect would lead to an increase in extracellular SDF-1, therefore upregulating CXCR4 receptors, which would lead to CXCR4 endocytosis and degradation. Overall, these findings propose that CXCR7 plays a key regulatory role in the CXCR4/ SDF-1 signaling axis (349). It has also been linked to other cytokines e.g. IL-8 (350).

Burns et al. amongst other groups have demonstrated that increased CXCR7 leads to a survival advantage in comparison to wild type controls of breast cancer cell lines, with a 40% apoptotic rate in control cells, compared to almost negligible rates in CXCR7 transfected groups (342). As further proof of principle, CXCR7 antagonist CCX754 was able to diminish this CXCR7 induced protection in a dose-related manner (345).

More recently, the literature has begun to focus on CXCR7 and its functions as a decoy receptor (351) (348), a mechanism which may have significant implications in stem cell mediated repair of radiotherapy induced soft tissue injury. A decoy receptor is able to bind and internalize a growth factor/chemokine without resulting in the downstream mediation of further cellular responses (348). It is postulated that CXCR7 may act as a scavenger which sequesters SDF-1 (352) (353), act in concert with CXCR4 as a co-receptor potentially enhancing SDF-1 mediated signaling in the scenario where CXCR4/CXCR7 is heterodimeric in the presence of overexpression of both receptors in transfected cells (345). This has resulted in the need to re-visit the perhaps oversimplified concept of SDF-1 and its monogamous signaling through CXCR4.

A recent review by Puchert et al. states CXCR7 has 3 potential functions in varying cell populations; 1) it fails to activate G protein mediated signaling and results in no

calcium mobilization, 2) it functions as a decoy receptor to scavenge extracellular CXCL12/11, thereby inhibiting or reducing the potency of CXCR4/SDF-1 mediated intracellular signaling. 3) CXCR4/CXCR7 heterodimers increase SDF-1 mediated signaling in comparison to CXCR4 alone, suggesting CXCR7 may act as an enhancer of signaling – (switching from G protein to β arrestin dependent signaling).

1.9.9 MicroRNA (miRNAs) and Exosomes

MicroRNAs are a group of small sections of RNA not responsible for coding, but play a role in suppression of protein synthesis and causing targeted mRNA degradation, therefore they regulate post-transcriptional protein expression (354). MicroRNA molecular analysis conducted on irradiated human endothelial cells found 11 miRNAs to be significantly altered, corresponding with either up or down regulation of functions such as clonogenic division or proliferation. miR-125a, miR-189, miR-126a, miR-525-3p were found to be radioprotective while miR-127, miR-628-5p and let-7g made in human endothelial cells more radiotherapy sensitive (355) (354).

Global suppression of miRNAs induced by Argonaut e2 (AGO2) or DICER proteins resulted in increased radiotherapy related death reflected by cell cycle checkpoint activation and increased apoptosis, which overall may suggest miRNAs as a group carry pro-survival functions in radiotherapy induced endothelial injury (354). These findings represent an evolving field as miRNAs act as localized targets for interventions and when manipulated more accurately, may correspond with tight regulation of the responses of a variety of cells to ionizing radiation.

miRNAs along with secreted proteins can be released from a cell using the classical endoplasmic-reticulum-Golgi secretory apparatus, however recently, a less conventional pathway for secretion named exosomes is also gaining rapid interest. Exosomes are nanometer sized vesicles released from a cell and are capable of carrying miRNA, RNA or proteins (356). Exosome formation generally omits processing in the endoplasmic-reticulum and they are generated as multi-vesicular bodies which, as a result of direct membrane fusion, are released *in vivo* into bodily fluids or *in vitro* into culture medium as protein coated vesicles (357). Exosomes, therefore may be exploited as they carry the ability to facilitate cell-cell communication with transfer of therapeutic products (proteins and genetic material) to

injured cells (distant from their cell of origin) to aid in the regeneration of damaged cells (358). At the same time, spread of radiotherapy injury to locoregional cells may be propagated by exosomes and contribute to worsening of RIBE (100). Therefore, determining the effect of radiotherapy on the exosome profile of cells constituting subcutaneous tissues will also aid in the identification of pathological genetic and protein level alterations that lead to the clinical manifestation of radiotherapy soft tissue injury.

1.10 Current experimental techniques and strategies to combat radiotherapy soft tissue injury

Hyperbaric oxygen therapy (HBOT) has been used to treat radiotherapy induced soft tissue injury for decades and represents a key modality by which late radiation injury may be symptomatically managed (359). Animal models demonstrated that episodic application of hyperbaric oxygen to irradiated rabbit mandibular tissue was able to increase surrounding soft tissue blood vessel density, further confirmed with increased transcutaneous oximetry in human tissues of patients receiving such treatment for osteoradionecrosis (ORN) of the mandible (360). Bennett et al. conducted a comprehensive systematic review which concluded that HBOT can aid with healing of irradiated head and neck, anus and rectal tissue, while also reducing the incidence of ORN after dental extraction (359). Such studies were limited by unstandardised scales measuring tissue quality improvement and the review also highlighted issues surrounding the use of HBOT in previous cancerous beds which can be a relative contraindication (359).

A multitude of pharmacological agents are currently being developed as well as trialed, falling into the categories of radio-protective or radio-mitigative agents. Mitigators that aim to combat the prolonged oxidative stress resulting from chronic radiotherapy injury include anti-oxidants such as superoxide dismutase (SOD), Cu-Zn SOD (SOD1), pentoxifylline and vitamin E (275). The combination of the latter two has demonstrated efficacy in reduction of ORN and skin fibrosis in early clinical trials with small patient cohorts (361), while animal studies and human trials are also

beginning with SODs which are thought to confer protection via reduction in inflammatory cell infiltration and TGFβ up-regulation (275).

Off label usage of common medications such as anti-inflammatories, anti-coagulants, lipid lowering agents, antibiotics and inhibitors of the renin angiotensin system have each anecdotally or in early clinical trials demonstrated some benefit in reducing aspects of radiotherapy soft tissue injury (67). These medications are all relatively non-toxic and are commonly used to treat hypertension and hyperlipidaemia thereby lending themselves as good candidates for clinical trials, with early promising results, in particular for radiation pneumonitis, intestinal and renal toxicity (67) (103) (275).

Currently, cellular and molecular based therapies are based on manipulation of well-established yet ubiquitous drivers of fibrosis such as TGF-β, Rho/ROCK/CTGF pathways (67) (79). Such molecular targets, with broad involvement in a multitude of both physiological and pathological processes such as DNA replication, repair and apoptosis, present as poor targets for mitigation of specific radiotherapy induced injurious responses. Bourgier et al. proposed a 'bottom up' approach where specific molecular alterations in response to radiotherapy soft tissue injury should be investigated using genetic screening platforms *in-vitro* and *in-vivo*. Establishing such molecular platforms as well as an ideal and standardised imaging modality will allow clinical detection of injury and enable candidate therapy efficacy to be validated in clinical samples (67).

Lastly, an area gaining rapid interest is the utility of loco-regionally recruited or systemically delivered adult stem cells, which are shown to localise to injured tissue (including irradiated tissue) and reduce the severity of injury. The recruitment of these multipotent cells is thought to exert regenerative effects of vascular regeneration and tissue restoration via paracrine secretion of cytokines and growth factors (67) (362) (363). In particular ADSCs have gained popularity in plastic and reconstructive literature in the last decade and the potential mechanisms of action in mitigation of radiotherapy injury are reviewed in section 1.11.

1.11 Fat Grafting

Adipose tissue is heterogeneously distributed around the body and variable between individuals. Fat is mainly composed of lobules of mature adipocytes and has mechanical and aesthetic functions as well as roles in metabolism - a highly specialized type of connective tissue responsible for insulation, protection and energy regulation (9) (364) (365). The bulk of the non-adipocyte component, the cells within the stromal vascular fraction (SVF) are from mesodermal or mesenchymal origin and include pre-adipocytes, fibroblasts, endothelial cells, vascular smooth muscle cells, immune cells and ADSCs (Figure 5B) (365-370).

Plastic surgeons use fat in vascularised tissue flaps, non-vascularised composite grafts or stand-alone grafts in fat transfer (371) (367). The relative abundance of adipose tissue in most patients and ease of obtaining fat by lipoaspiration/liposuction with minimal donor morbidity has expanded the range of clinical indications for fat grafting; such as correcting cosmetic or contour defects, contractures and lymphoedema (300) (367) (372).

Initially in clinical observation (373) (374) then in animal models (69) (375); fat grafting was reported to improve the characteristics of overlying skin and soft-tissue in RTX-injury (300) (374) (375) (367). Subsequent clinical analysis verified softening of wrinkles or fibrotic tissue and resolution of pigment changes (54) (373) (375) (376). Clinical reports suggested that fat grafting may also reduce peri-prosthetic capsule contracture, vocal cord damage and chronic ulceration; and that it may rejuvenate aging skin (365) (369) (368) (371) (373-378). These clinical benefits were attributed to the regenerative properties of undifferentiated multi-potent ADSCs within the SVF of lipoaspirate (373) (379). ADSCs are thought to play a supportive role in adipogenesis and angiogenesis, while also modulating inflammation and immunity (54) (380) (381). Therefore, a role for ADSCs/fat graft ameliorating RTX-injury would be of interest to those working in tissue engineering, regenerative medicine and clinical plastic surgery.

However, despite promising clinical potential, a detailed understanding of the putative molecular mechanisms for ADSC-mediated reversal of RTX-injury remains elusive

(382) (383). Additionally, concerns have been raised that fat grafting following cancer treatment may enhance tumourigenesis in a former cancer bed (384) (385) (386). If fat grafting is to become a useful and validated clinical tool, these issues must be addressed. A thorough understanding of the molecular interactions and the functional and sub-cellular alterations caused by RTX-injury to ADSCs themselves is also needed. Without such insights, guidelines pertaining to the safety of fat grafting in these contexts cannot be developed (386) (387) (388).

1.11.1 Enhancing Fat Graft take using ADSCs and other growth factors

Due to the clinical origins of the field, the majority of mechanistic information regarding ADSC-mediated cellular effects has been derived from research investigating the enhancement of fat grafts. Therefore, in understanding what pathways may become activated in ADSC-mediated reversal of RTX soft-tissue injury, it is critical to first review this more well-established body of data.

An autologous tissue graft is defined as tissue transferred to a distant site, without its original blood supply. A fat graft therefore, must acquire a blood supply and nutrients from the tissue bed into which it is introduced, with early re-vascularisation to prevent graft necrosis that leads to volume depletion (389) (390). Unfortunately, fat grafts may resorb up to 70-100% of the initial injected tissue volume (391); a result attributed to poor graft neo-vascularisation, apoptosis and/or chronic fat necrosis (368-370) (386-391) (393). Whilst the many technical modifications to enhance fat graft have been described, ADSCs have emerged as a key focus of graft enhancement, and more recently as a critical component in reversing soft-tissue injury (394). ADSCs, first isolated by Zuk et al. over a decade ago (371), were postulated by Eto et al. to be more robust than mature adipocytes in resisting mechanical trauma during fat transfer (382) (393) (395) and to have lower metabolic demands (369) (371) (376) (377) (389) (396) (397) (398). Others demonstrated improved graft survival through increased angiogenesis, incorporating either imported endothelial progenitors or ADSCs into blood vessels (378) (379) 399). In contrast, Butala et al. suggested that introduced ADSCs may recruit further stem cells, particularly from bone marrow (379) (380) (399). To enhance the relative ADSCs abundance within fat grafts (382) (384) (399) (400), Yoshimura et al. proposed ‘cell-assisted lipotransfer enrichment’

(Figure 5C), by supplementing lipoaspirate with additional SVF (142) (386-389) (391) (401). The SVF (comprised of 10% ADSCs (372) (375) (392)), is obtained from a component of lipoaspirate, surplus to the volume anticipated to be required to fill a known defect (367). This surplus lipoaspirate is separated into components by centrifugation Figure 5A. Following collagenase digestion, further spinning produces a pellet, referred to as SVF. Finally, the SVF is re-introduced to the remaining lipoaspirate, in preparation for injecting the ADSC (369) (371) (389) (393) (395) (402-404). Later, Piccinno et al. explored graft enrichment using *in-vitro* purified and expanded ADSC populations (396) (405), while Lu et al. and Shoshani et al. performed co-injection of pro-angiogenic factors IL-8 and VEGF-A (397) (398) (400). These studies collectively suggested that such enrichment may further increase graft viability, neo-vascularisation and volume retention, while reducing necrosis/apoptosis rates (396) (398) (406). Building on this work, Kolle et al. conducted a randomized control trial to assess lipoaspirate-enrichment with ADSCs concentrations up to 2000 times above physiological levels (407). ADSC-enriched groups demonstrated higher volumes of graft retention on MRI and were associated with reduced apoptosis (399) (400). Overall, these findings further suggested that addition of ADSCs may improve graft take by enhancing adipogenesis, supporting angiogenesis and reducing cellular apoptosis (379) (381) (399) (408).

1.11.2 ADSCs; characteristics and isolation in lipoaspirate

Adult stem cells are uniquely capable of differentiating into more specialized cell types to: 1) replenish damaged cells, 2) maintain tissue integrity and 3) maintain cellular homeostasis during growth or wound healing (400) (407). Such properties make mesenchymal stem cells (MSCs) prime candidates for use in tissue regeneration (142) (386) (409-412) (287). The clinical use of autologous MSCs for tissue regeneration confers several advantages - chiefly, the ability to avoid host-immune responses. The benefits of ADSCs, are that the yield of stem cells from adipose tissue exceed that from bone marrow by about 500-fold (401) ($5x10^5$ ADSCs may be isolated from 400-600g of adipose tissue (332) (392)), along with superior ease of harvest and minimal donor site morbidity.

Similar to bone marrow derived stem cells (BMSCs), ADSCs are capable of differentiation into a diverse variety of mature tissues – skin, fat, cartilage, bone, muscle, endothelial and neurogenic cells when cultured with specific induction factors (369) (371) (402) (412).

Apart from this versatile trans-differentiation potential, ADSCs also exhibit an extensive secretory profile consisting of pro- and anti-inflammatory cytokines, chemokines and growth factors (288) (400) (403-405) (413-415). Whereas it was previously thought that ADSCs themselves differentiated to replace injured cells ("host replacement" or "building block" repair theories (367) (406) (407) (416) (417)); the secreted paracrine mediators are now thought to perform key active roles in ameliorating RTX and other injuries (381) by orchestrating autocrine or trophic paracrine effects on surrounding tissues (400). The unique secretory profile of ADSCs indicates that they specifically influence the molecular and biological pathways of tissue regeneration (407-409) (418) (419), angiogenesis (410) (411) (420) (421) and lymph-angiogenesis (284) (287); while suppressing local immune/inflammatory responses (288) (332) (373) (401) (422) and reducing fibrogenesis (369), see Table 5.

Since their initial description, the cell surface molecular marker profile of the ADSC has remained controversial (69) (423), predominantly due to differences between post-extraction purification protocols, culture conditions and variations in the use of whole or sub-total SVF (288) (370) (373) (389) (413) (414) . The International Society for Cellular Therapy defines ADSCs as cells that demonstrate plastic adherence in standard tissue culture conditions (415) (424), express a surface marker profile of $CD34^+$, $CD31^-$ and $CD45^-$ (9) (11) (51) (134) (284) (416-419) (421) (425) and demonstrate multi-potent 'tri-lineage' differentiation capabilities – i.e. differentiation into bone, cartilage and fat (366).

	Proposed Functional or Molecular Mechanism & model used.	Ref
1) ADSC Adipogenic differentiation results in restoration of tissue contour and volume.	Clinical studies demonstrate newly formed adipose tissue at the site of fat injection via either; a) direct differentiation of injected ADSC to adipocytes; or b) paracrine stimulation by injected ADSCs influence local stem cell to differentiation into adipocytes.	(371) (373) (402) (407) (412) (422) (423) (426-428)
2) ADSC injection increases perfusion of injured tissues or graft take to enhance viability by: **i) paracrine promotion of angiogenesis** **ii) supporting existing vascular structures**	a) Fat grafted sites in murine models of ischemic injury demonstrate GFP or DiI-labeled ADSCs differentiating to CD31+ endothelial cells *in-vivo*. b) Increased blood vessel density and co-localisation of fluorescently labeled ADSC within/ near capillaries. c) ADSCs form capillary networks on Matrigel matrix and stained positive for vWF. d) Release of angiogenic factors by ADSCs promotes revascularization and wound healing including: VEGF-A, VEGF-C, VEGF-D, IGF, PDGF-bb, FGF, TGF-β, HGF, IL-6, IL-8, MMP inhibitor 1 precursor, MCP-1, ANG and SDF-1.	(332) (356) (394) (402-404) (407) (409) (411) (412) (419) (426-436)
3) ADSCs reverse tissue injury by exerting anti-oxidant effects.	a) Anti-oxidant action provides protection against hypoxia, ischemia reperfusion and ROS induced damage. b) Factors such as: Hepatocyte growth factor (HGF), G-CSF, GM-CSF, IGFBPs, IL-12, PDGF-AA, Pigmented epithelial derived growth factor, Superoxide dismutase may mediate these effects.	(407) (433) (435) (437) (438)
4) Specific ADSC induced cytokines modulate immune and inflammatory responses.	a) BMSCs & ADSCs suppress T- & B-cell proliferation via NFKB mediated mechanisms. b) Cytokine & Adipokine secretion of IL-6 & IL-8 are chemoattractants for monocytes and macrophages.	(332) (356) (394) (409) (434-435) (437) (439-442)

	Recruitment promotes wound healing processes.	
5) ADSCs modulate granulation tissue formation, fibrosis & improve epithelialization and wound healing	*In-vitro* ADSC-induced alteration to fibroblast ECM remodeling gene expression via; a) Alteration of collagen type I & III production by fibroblasts co-cultured with $ADSC^{CM}$, mediated by down regulation of genes such as Col3a1, b) Up-regulation of type I procollagen a1 mRNA. c) Effective migration of keratinocyte and fibroblasts treated with $ADSC^{CM}$ leading to improved re-epithelialization	(362) (435) (438-450)
6) ADSCs secrete lymphangiogenic factors that aid in lymphangiogenesis, improving or reversing lymphoedema in damaged tissues.	a) Lymphatic fluid stasis results in increased TGF-β1, exerting a further anti-lymphangiogenic effect. Blockade of TGF-β1 along with VEGF-C ADSC stimulation resulted in elevated ADSC expression of lymphangiogenic factors; VEGF-C and lymphatic endothelial cell markers podoplanin and Prox-1 and increased ADSC survival *in-vitro*. b) Baseline ADSC production of IL-8, IGF-1, VEGF-D all promote lymphangiogenesis	(83) (173) (287) (373) (422) (423)
7) Recruitment of endogenous stem cells via a homing chemokine gradient.	a) Murine models have MSC homing to site of injury. Systemic injected human MSCs migrated and engrafted at the site of ischemic or necrotic injury. b) Stromal derived factor 1α secreted by ADSCs is the main chemo-attractant of systemic stem cells to the area of injury.	(37) (362) (376) (382) (438) (444-448) (451)

Table 5 The postulated regenerative mechanisms of ADSCs in clinical and pre-clinical models of tissue injury.

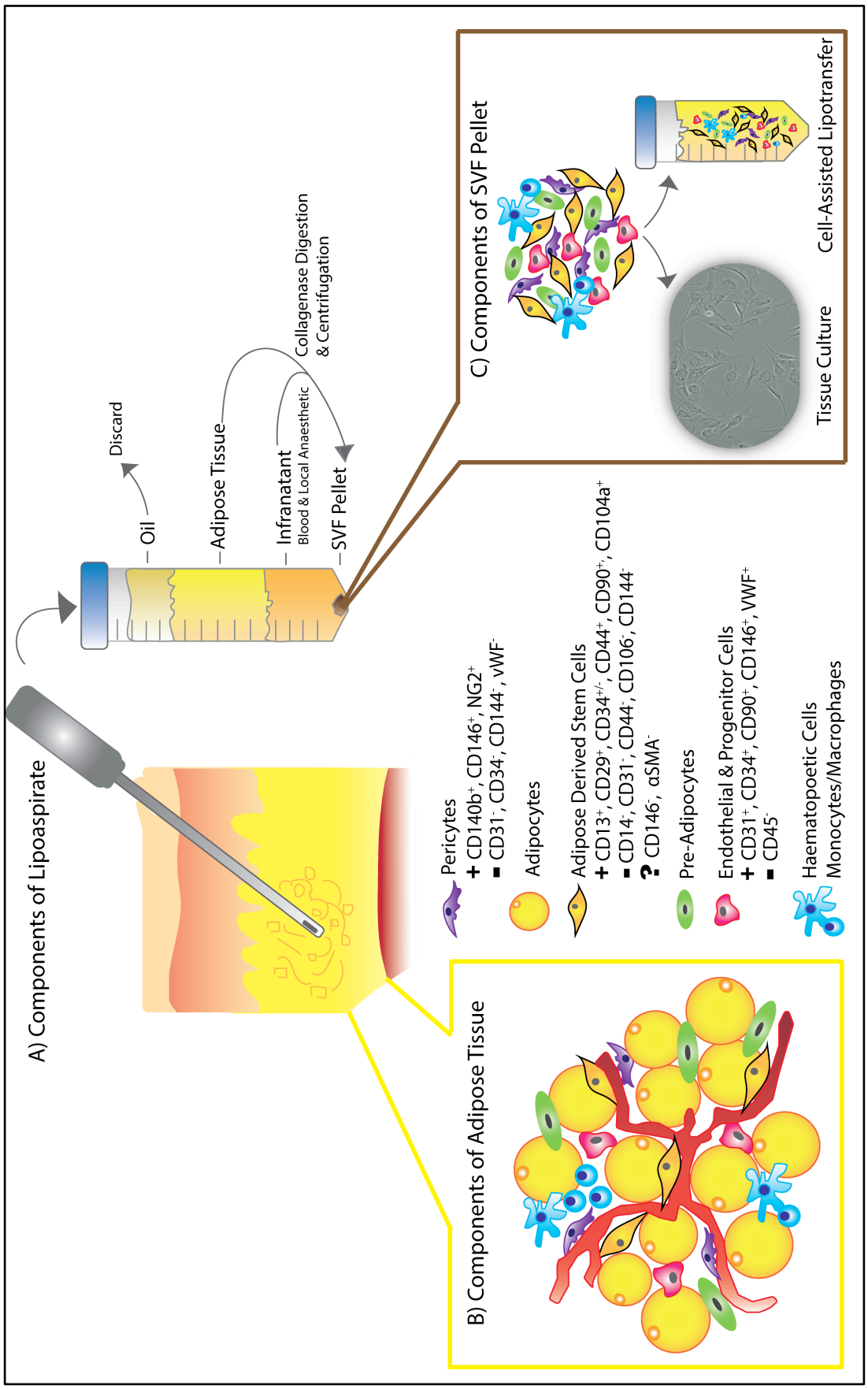
A) Components of Lipoaspirate
Discard
Oil
Adipose Tissue
Infranatant
Blood & Local Anaesthetic
Collagenase Digestion
& Centrifugation
SVF Pellet
C) Components of SVF Pellet
Tissue Culture
Cell-Assisted Lipotransfer
B) Components of Adipose Tissue
Pericytes
+ CD140b+, CD146+, NG2+
▪ CD31-, CD34-, CD144-, vWF-
Adipocytes
Adipose Derived Stem Cells
+ CD13+, CD29+, CD34+/-, CD44+, CD90+, CD104a+
▪ CD14-, CD31-, CD44-, CD106-, CD144-
? CD146-, αSMA-
Pre-Adipocytes
Endothelial & Progenitor Cells
+ CD31+, CD34+, CD90+, CD146+, VWF+
▪ CD45-
Haematopoetic Cells
Monocytes/Macrophages

Figure 5

Figure 5 Components of Adipose Tissue

(**A**) Schematic diagram depicting liposuction procedure – lipoaspiration of subcutaneous fat is performed, as previously described (30), followed by separation into layers of oil (discarded), aspirated adipose tissue and infranatant (composed of blood, plasma and local anaesthetic). **(B)** The components of adipose tissue and the key constituents of the SVF pellet are all present in en-bloc *in-vivo* adipose tissue as shown. Following collagenase digestion, incubation in control medium and centrifugation, the residual pellet is the so-called stromal vascular fraction (SVF). **(C)** SVF can be plated for tissue culture or added to unprocessed lipoaspirate as in the process of "cell-assisted lipotransfer" (60). The key surface markers of ADSCs, Pericytes, Endothelial and Progenitor Cells are shown, demonstrating the unique surface antigen profile of each cell type that allows their differentiation from ADSCs (smooth muscle cells and fibroblasts not shown).

1.11.3 ADSCs and Radiotherapy-induced soft tissue injury

When considering ADSC in the setting of RTX soft-tissue injury, two broad questions are raised: 1) What are the effects of injury on ADSCs? 2) How do ADSCs specifically modulate RTX-Injury? The sections below summarise the current literature pertaining to above questions.

1.11.3.1 Radiotherapy injury, Adipocytes and the SVF:

Injury induced by RTX has previously been explained by rapid, extensive necrotic or apoptotic cell death in the stem cell and progenitor populations (142). However, as neither of these mechanisms fully account for the chronic, progressive and evolving nature of RTX-injury in soft-tissues (17) (61), "sub-lethal" changes such as premature senescence, terminal differentiation or reproductive cell death have been implicated (142) (376) (452). More recent findings suggest that ADSCs display radio-resistance compared with other components of SVF such as adipocytes (452). This may be explained by a greater ability of MSCs to retain their proliferative capacity due to superior DNA damage repair mechanisms compared with those found in terminally differentiated cells (452). Bill et al. suggest that terminal differentiation of cells may correlate with increased G1-cell cycle arrest and reduced ability to repair RTX-induced double-stranded DNA breaks (453). Additionally, reduced metabolic

demands of steady-state ADSCs may protect them from hypoxia and subsequent apoptosis, enabling their preservation in order to perform regenerative functions (369) (454).

As ADSCs share many regenerative properties with BMSC, much of our understanding of mechanisms by which ADSCs modulate RTX-injury has been extrapolated from BMSC (381) (455). Ponomaryov et al. demonstrated that sublethal RTX-injury to BMSCs resulted in an increase in SDF-1 (also the main chemotactic factor for ADSCs) at both mRNA and protein level (346). This increased SDF-1 expression in-turn mediates homing of $CXCR4^{+}$ uninjured stem cells via a chemokine gradient (346). This gradient is integral to homing and importing uninjured ADSCs, as surviving ADSCs originating within the injured area may be significantly functionally impaired

Poglio et al. characterised the effects of RTX on murine adipose tissue primarily as decreasing adipocyte size and number, increasing ROS and impairing SVF proliferation and adipogenic differentiation (364). Whilst the overall composition of the SVF was unaltered by irradiation, the authors concluded that changes to the capacity of cells within the SVF to proliferate or differentiate could impair the regenerative properties of fat graft (364), as demonstrated by Li et al. in irradiated BMSCs which displayed suppression of proliferation, osteogenesis and adipogenesis (456). A further mechanism of action of ADSCs maybe a similar recruitment of and differentiation toward a fibroblastic phenotype seen in irradiated BMSCs (457) (332).

Functional cellular analysis performed by Schonmyer et al. suggested that irradiated murine BMSCs underwent low-level spontaneous osteoblastic differentiation, in preference to adipogenic or chondrogenic lineages (457). Furthermore, attenuation of the response of irradiated BMSCs to stimulation with lineage specific differentiation media was decreased in irradiated cells and was associated with down-regulation of bone-specific markers (ALP and osteocalcin) and adipose-specific markers (lipoprotein lipase, C/EBPb and leptin) (457). These findings further highlight the altered capacity of stem cells to respond to cues in their microenvironment to replenish damaged cells, following RTX (457). Mechanistically, alterations to paracrine signaling via Wnt10b and Sirtuin-1 (a subset of a family of proteins that

regulate stem cell differentiation) were also seen to mediate altered adipogenesis and osteogenic differentiation characteristics in BMSC (458). Meanwhile, another subset of the same protein family Wnt3a and Wnt5a, were found to be up-regulated in radiation injury and may additional induced senescence in irradiated BMSCs (367).

1.11.3.2 How ADSCs specifically modulate RTX-Injury

The original 'building block' theory that stem cells migrate to an area of injury to differentiate and replace the injured cell has been superseded, as only a small number of grafted cells - of which ADSCs make up an even smaller proportion (382) (459) - survive the fat transplant injection (393) (403). More recently, paracrine mechanisms such as immune-modulation and the generation of protein growth factors secreted by surviving grafted ADSCs, have gained favour (381) (428) (449) (460) (461). Walter et al. demonstrated modulation of keratinocyte and fibroblast migration in response to BMSC-conditioned media, and their study of the BMSC paracrine secretory profile presented detectable levels of IL-6, IL-8, MCP-1 and to a lesser degree RANTES (135) (402). The key differences in the protein growth factor profiles of the two types of MSCs as shown on cytokine array studies were IL8, IGF-1 and VEGF-D, which were secreted by ADSCs but not BMSCs (403). Given that the mechanisms underlying the overall profile of RTX-injury appear to involve poor vascularity, hypoxia and lymphoedema, and that these three growth factors are implicated in each - it seems intuitive that ADSCs could play critical role in reversing these micro-environmental changes. This protein secretion profile indicates that ADSCs may facilitate angiogenesis and lymphangiogenesis, in addition to simple anti-fibrotic effects with which they have been previously associated (246) (373) (436). However, further detailed systematic analysis of the secretory expression profiles of ADSCs is required to identify which specific growth factors are released, under which conditions, and how they may modulate the wound healing, angiogenesis and lymphangiogenesis (407) (429). Such an effect was typified by the down-regulation in VEGF-A production by ADSCs in response to irradiation, as shown by Ebrahimian et al. (412).

1.11.3.3 ADSCs and angiogenesis in hypoxia

RTX, particularly associated with subsequent surgery, creates tissue hypoxia by up-regulating expression of inducible transcription factor HIF1α, either through

generating ROS, Nitric Oxide, or inducing macrophage recruitment or release of stress granules (37). *In-vitro*, the constituent components of adipose tissue each responded differently to hypoxic stress stimuli as demonstrated by Haubner et al., who found that adipocytes, and to a lesser degree, endothelial cells, underwent apoptosis in hypoxic conditions, while ADSCs displayed superior cell viability (382); a finding verified by Frazier et al. in an ADSC cell viability study (451), Other authors further suggested that the superior survival capacity of ADSCs facilitates their contribution to active repair of adipose tissue, (376) (382) (411) (462), and that stem cells are maintained in a baseline state of relative hypoxia enabling them to derive protection from cyto- or genotoxic stressor by utilizing anaerobic metabolism (37,428). Alternative hypoxic pre-conditioning models such as mechanical thermal stress or nutrient deprivation have also shown superior stem cells survival, in addition to a modified paracrine secretory profile (9) (154) (407) (410) (411) (428) (430) (451) (459) (462) (463). Unsurprisingly, much of this hypoxia-induced growth factor expression profile is pro-angiogenic. Examples include HIF-1α and SDF-1a production (410) (451), which in turn increased secretion of pro-angiogenic and anti-apoptotic cytokines VEGF, HGF, bFGF, by up to 5-fold in spheroid models (154) (407) (430) (433) (462) (464). Frazier et al. found that $ADSC^{CM}$ from cells grown in hypoxic conditions demonstrated altered protein levels of Fibronectin 1, TGFβ1-induced protein, Osteonectin and Collagens (Type 1a1 and 1a2), potentially also facilitating angiogenic sprouts through ECM (433) (451). Despite this compelling pre-clinical work, increased proliferation, migration or sprouting may not necessarily correlate with the formation of functional vasculature or enhanced tissue perfusion *in vivo*, without the vessels first acquiring adequate vessel stability (426) (464). A study investigating the role of ADSCs in stabilizing endothelial networks attributed them with properties akin to those of pericytes, which act synergistically with endothelial cells to contribute to neo-angiogenesis. These ADSCs were specifically shown to establish neo-vessel connections with the pre-existing local vasculature and conducted blood flow as a stable network (465). In addition to these effects, hypoxia and ischemia have been independently observed to induce trans-differentiation of ADSCs into $CD31^{+}/VWF^{+}$ endothelial cells that may also contribute to the establishment of neo-vasculature (426) (427) (429) (435). Overall, ADSCs may contribute to angiogenesis by promoting paracrine effects that stabilise neo-vasculature, by supporting existing RTX-damaged blood vessels, or finally, by differentiation into

HMECs that integrate into forming vessels (429) (466). Local or systemic injection of labeled-ADSCs following body wall RTX treatment were associated with increased angiogenesis consisting of perivascular aggregation of $CD31^+$ ADSCs, which was interpreted as trans-differentiation of ADSCs to HMECs (412) (438) (466).

In addition to pro-angiogenic effects, ADSCs were also shown to display protective effects on non-vascular cells in hypoxic conditions. Lee et al. demonstrated anti-apoptotic effects in dermal fibroblasts, which developed enhanced resistance to oxidative stress when treated with $ADSC^{CM}$ (402) (433). Similarly, antioxidants superoxide dismutase and glutathione activity was enhanced in cell cycle analyses of fibroblasts cultured in $ADSC^{CM}$ (433). In a pre-clinical model of ischemia reperfusion injury, Uysal et al. injected ADSCs into axial flaps, subsequently clamping then finally unclamping the vascular pedicle to allow reperfusion. They showed enhanced flap viability and up-regulated expression of VEGF-A, TGF-β and FGF proteins detected immuno-histochemically (426). Collectively, these findings suggest that ADSCs produce growth factors that may ameliorate ischemic insults and can exert a protective effect against reperfusion injury (402) (426).

1.11.4 Mechanisms of ADSC-mediated reversal of RTX induced soft-tissue injury

In addition to anti-hypoxic effects ADSCs have also been shown to mediate alternative paracrine responses to RTX-injury including anti-inflammatory and anti-apoptotic effects as summarized in Figure 6.

In an investigation of the effects of irradiation on blood endothelial cells, Haubner et al. demonstrated up-regulated expression of inflammatory cytokines IL6, FGF, ICAM-1 and VCAM1. Co-culture with ADSCs in this model demonstrated reversed expression of all the detected inflammatory cytokines (394). Similarly, Chang et al. used a model of intra-peritoneal ADSC injection following abdominal irradiation to demonstrated a significant reduction in inflammation in ADSC-treated animals, with enhanced intestinal re-epithelialisation and improved survival rates. ADSC injection was associated with increased serum levels IL10, VEGFA, bFGF and EGF as well as enhanced SDF-1 mediated recruitment of hematopoietic stem cells to the site of injury

(438). Also, in the upper gastrointestinal tract, Lim et al. and Kojima et al. demonstrated protective and anti-apoptotic effects of ADSC injection in a model of RTX-induced salivary gland injury (467) (468).

Finally, the dermal and subcutaneous responses to ADSC injection in animal models of both in chronic RTX-wound healing and intact irradiated skin, manifested as increased dermal thickness quantified by reduction in fibrotic marker Smad-3 and a collagen-based scar index measurement (466) (469). An equivalent large animal model of ADSC-enriched fat graft injections following localized RTX demonstrated integration of q-dot-labeled ADSCs into the dermis, with associated favorable wound healing, enhanced epithelialization, increased subcutaneous adipose tissue and reduced apoptosis; along with recruitment and activation of lymphoid cells (409) (470).

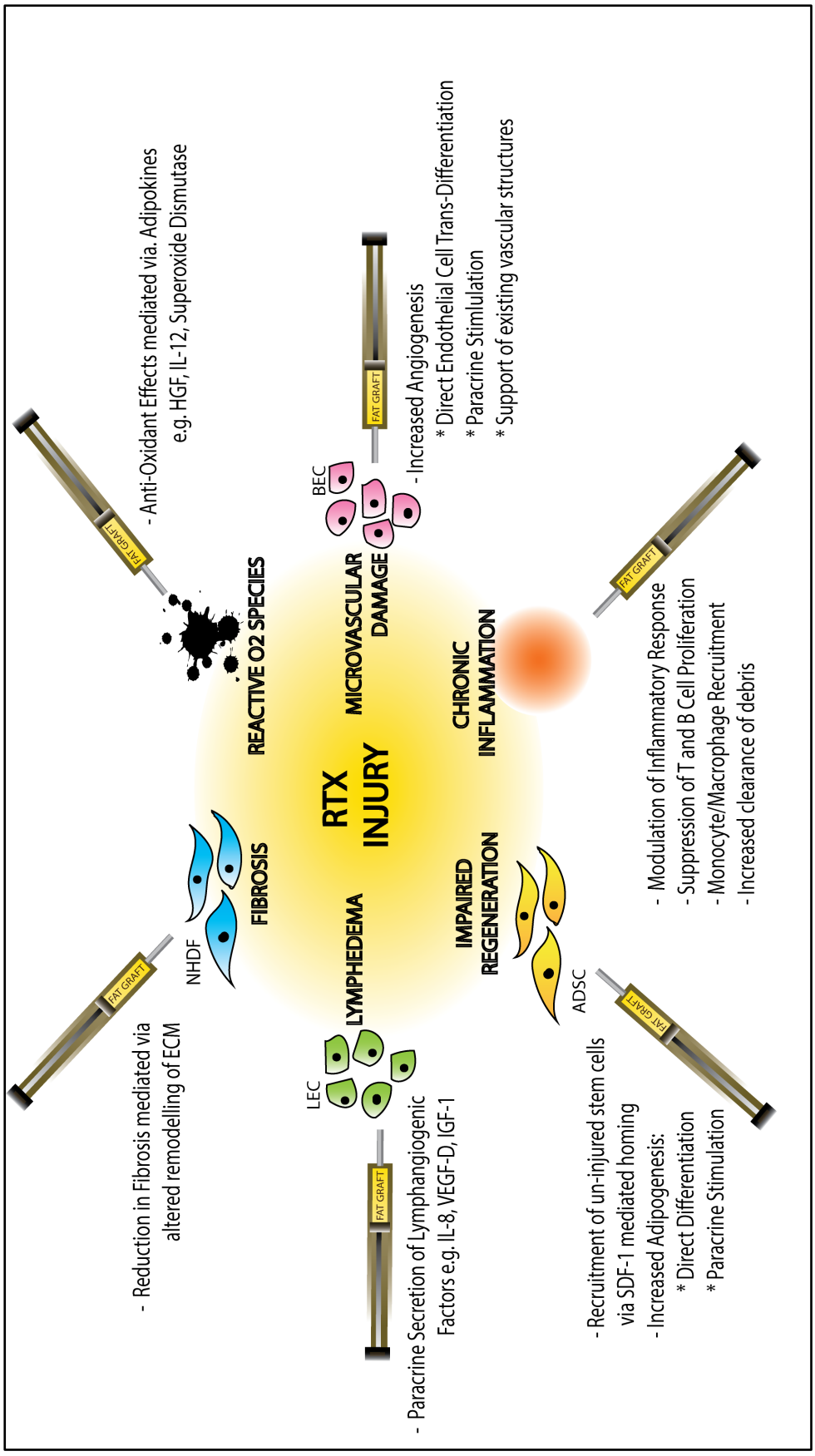
RTX INJURY
REACTIVE O2 SPECIES
MICROVASCULAR DAMAGE
CHRONIC INFLAMMATION
IMPAIRED REGENERATION
LYMPHEDEMA
FIBROSIS
- Anti-Oxidant Effects mediated via. Adipokines e.g. HGF, IL-12, Superoxide Dismutase
- Increased Angiogenesis
* Direct Endothelial Cell Trans-Differentiation
* Paracrine Stimulation
* Support of existing vascular structures
- Modulation of Inflammatory Response
- Suppression of T and B Cell Proliferation
- Monocyte/Macrophage Recruitment
- Increased clearance of debris
- Recruitment of un-injured stem cells via SDF-1 mediated homing
- Increased Adipogenesis:
* Direct Differentiation
* Paracrine Stimulation
- Paracrine Secretion of Lymphangiogenic Factors e.g. IL-8, VEGF-D, IGF-1
- Reduction in Fibrosis mediated via altered remodelling of ECM
BEC
LEC
NHDF
ADSC
FAT GRAFT

Figure 6

Figure 6 The proposed mechanisms of radiotherapy injury reversal by fat grafting and ADSC

Schematic diagram demonstrating the effects of Radiotherapy (RTX)-Injury on individual cellular components, the resulting clinical manifestations of injury and the mechanisms by which fat graft may ameliorate this soft-tissue injury. NHDF (Normal Human Dermal Fibroblasts), ECM (Extracellular Matrix), HGF (Hepatocyte Growth Factor), IL-12 (Interleukin-12), BEC (Blood endothelial cell), ADSC (Adipose derived stem cell), SDF-1 (Stromal Derived Factor-1), LEC (Lymphatic endothelial cell), IL-8 (Interleukin-8), VEGF-D (Vascular Derived Growth Factor –D), IGF-1 (Insulin-like Growth Factor 1).

1.11.5 Fat grafting and Oncological safety

Questions regarding oncological safety of fat grafting following cancer clearance have been raised (373,471). While long-term tissue changes following fat grafting may impede radiological surveillance for cancer recurrence (389) (472); Delay et al. state that experienced breast radiologists should be able to differentiate 'post-graft' from malignant calcifications (422). The major oncological concerns relate to the beneficial properties of ADSCs in RTX-injury potentially also promoting tumour growth in areas previously treated for cancer (129) (134) (144) (149) (385) (386) (424) (425). Molecular adaptations that promote engraftment and survival of fat include secreting protein growth factors such as VEGF-A or VEGF-D in response to hypoxia (see below) - both of which induce angiogenesis and lymphangiogenesis (51) (246) (430) (431) (436) stimulating breast cancer growth and metastases (9) (17) (26) (51) (58-61) (101-104) (106-111) (116-121) (129) (134) (144) (149) (154) (164) (218) (346) (385) (386) (424) (425) (471-477). Rumbek et al. found that while ADSCs may not necessarily trigger transformation of quiescent tumour cells to active growth, they could promote proliferation of residual cells after cancer resection and/or adjuvant therapy (386). In contrast, proponents of fat grafting argue that *in-vitro* models may not be representative of human tumours (475) (476). In light of evidence so far, Claro et al. and Zimmerlan et al. called for postponement of 'stem-cell enhanced' fat grafting for breast reconstruction until longer-term follow-up data is available (476) (478) (382) (386) (393) (424). Gutowski et al. proposed screening to exclude high-risk patients (such as those with BRACA1/2 mutation) from eligibility for fat grafting

(477). Nevertheless, fat grafting for breast reconstruction has been reported in over 3,000 patients in published trials (479) or case-reports (480). Whilst systematic reviews of current practice examined clinical efficacy, the lack of randomized controlled trials examining oncologic safety and insufficient follow-up of smaller studies mean that no clear conclusions have been reached (332) (381) (431) (435) (476) (478). Overall, a more detailed understanding of mechanisms by which fat graft may reverse RTX-injury - and how these pathways may cross-talk with the regulation of tumour growth are required.

1.11.6 Future Directions for Fat Grafting and Radiotherapy Injury:

While *in vitro* and *in vivo* models demonstrate the benefits of fat grafting, more comprehensive cellular and molecular analyses using genome-screening platforms are needed to elucidate the true mechanism behind ADSC-mediated reversal of RTX-injury. A detailed understanding of the reaction of individual cell types in response to RTX injury is required in order to treat pathological processes such as fibrosis, lymphoedema and hypoxia - which contribute to the formation of RTX induced soft-tissue injury. ADSCs may possess these characteristics, however a targeted molecular therapy that harnesses the beneficial effects of ADSCs, without raising the potential of enhanced tumour growth, activation or metastases is required.

2 CHAPTER 2: MATERIALS AND METHODS

2.1 Cell culture reagents, chemicals and general procedures

2.1.1 Cell culture and Passaging

Cell cultures of Normal Human Dermal Fibroblasts (NHDF), Normal Human Keratinocytes (NHEK), Human Placental Pericytes (hPC-PL), Human Dermal Lymphatic Endothelial Cells (HLEC) and Human Dermal Microvascular Endothelial Cells (HMEC) were established from cryopreserved commercially available vials or fresh tissue isolation and incubated in 37ºC, 5% CO_2 conditions (Table 6) in tissue culture treated flasks (CELLSTAR®, Germany). Cell-specific media (PromoCell, Germany or Lonza, Switzerland) was changed every 3 days (Table 7). Cells were passaged at 80-90% confluence with three consecutive washes with Phosphate Buffered Saline (PBS) (Lonza, Switzerland) and detached using Trypsin/EDTA 0.025%/0.01% (PromoCell, Germany) for 5 minutes and neutralized with Trypsin Neutralizing Solution (PromoCell Germany). Detached cells and media were aspirated and centrifuged for 5 minutes at 1500 rpm to obtain the cell pellet for resuspension, passaging or seeding for experiments.

Cell Type	Source/Company
Adipose Derived Stem Cells Adult (ADSC)	Derived from human tissues samples (see section 2.1.3)
Human Dermal Lymphatic Endothelial Cells Adult (LEC)	C-12217 PromoCell (Germany) Cryopreserved cells
Human Dermal Microvascular Endothelial Cells Adult (HMEC)	CC-2543 Lonza (Switzerland) Cryopreserved cells
Normal Human Dermal Fibroblasts Adult (NHDF)	C -12302 PromoCell (Germany) Cryopreserved cells
Normal Human Keratinocytes Adult (NHEK)	C-12003 PromoCell (Germany) Cryopreserved cells
Human Pericytes Placenta (hPL-PC)	C-12980 PromoCell (Germany) Cryopreserved cells
Human Aortic Endothelial Cells Adult (HAEC)	CC2535 Lonza (Switzerland) Cryopreserved cells
Coronary artery endothelial cells Adult (CAE)	CC2585 Lonza (Switzerland) Cryopreserved cells

Table 6 Proliferating cells used to establish *in-vitro* cell cultures

2.1.2 Growth medium and additives

Table 7 details the different media solutions used for cell culture, with variations in composition for different experimental designs and cell types.

Component	Volume	[Conc]	Company
Complete DMEM *ADSC, NHDF*			
DMEM 4.5 g/L Glucose with Ultraglutamine	500 ml	-	Lonza (Switzerland)
Fetal Calf Serum (10%) (Heat Inactivated 56°C for 30 minutes to destroy complement)	50 ml	-	SAFC Biosciences (USA)
Penicillin/Streptomycin	5 ml	-	Gibco (USA)
Sodium Pyruvate	5 ml	-	Gibco (USA)
Starvation DMEM *ADSC, NHDF*			
DMEM 4.5 g/L Glucose with Ultraglutamine	500 ml	-	Lonza (Switzerland)
Complete EGMV2 *HLEC*			
Endothelial Cell Basal Medium MV2	500 ml		PromoCell (Germany)
Fetal Calf Serum (5%)	25 ml		PromoCell (Germany)
Epidermal Growth Factor (human)	-	5 ng/ml	PromoCell (Germany)
Basic Fibroblast Growth Factor (human)	-	10 ng/ml	PromoCell (Germany)
Insulin-like Growth Factor (LongR^3 IGF-1)	-	20 ng/ml	PromoCell (Germany)
Vascular Endothelial Growth Factor 165	-	0.5 ng/ml	PromoCell (Germany)
Ascorbic Acid	-	1 µg/ml	PromoCell (Germany)
Hydrocortisone	-	0.2 µg/ml	PromoCell (Germany)
Basal EGMV2 *ADSC, HLEC*			

Endothelial Basal Medium MV2	500 ml	-	PromoCell (Germany)
Fetal Calf Serum (5%)	25 ml	-	PromoCell (Germany)
Starvation EGMV2 *HLEC*			
Endothelial Basal Medium MV2	500 ml	-	PromoCell (Germany)
Fetal Calf Serum (2%)	10 ml	-	PromoCell (Germany)
EBM2 *HMEC*			
Endothelial Cell Basal Medium 2	500 ml	-	Lonza (Switzerland)
Fetal Calf Serum	25 ml	-	Lonza (Switzerland)
Human epidermal growth factor	0.5 ml	-	Lonza (Switzerland)
Hydrocortisone	0.2 ml	-	Lonza (Switzerland)
GA (Gentamicin/Ampicillin)-	0.5 ml	-	Lonza (Switzerland)
Vascular endothelial growth factor	0.5 ml	-	Lonza (Switzerland)
Human Fibroblast Growth Factor B	2 ml	-	Lonza (Switzerland)
EGM-2MV *HAEC and CAE*			
Endothelial Cell Basal Medium 2	500 ml	-	Lonza (Switzerland)
Fetal Calf Serum	10 ml	-	Lonza (Switzerland)
Human epidermal growth factor	0.5 ml	-	Lonza (Switzerland)
Hydrocortisone	0.2 ml	-	Lonza (Switzerland)
GA (Gentamicin/Ampicillin)	0.5 ml	-	Lonza (Switzerland)
Vascular endothelial growth factor	0.5 ml	-	Lonza (Switzerland)
Human Fibroblast Growth Factor B	2 ml	-	Lonza (Switzerland)
Insulin-like Growth Factor (LongR^3 IGF-1)	0.5 ml		Lonza (Switzerland)
Ascorbic Acid	0.5 ml		Lonza (Switzerland)
Heparin	0.5 ml		Lonza (Switzerland)
NHEK Media *NHEK*			
Keratinocyte Basal Growth	500 ml	-	PromoCell (Germany)

Medium			
Bovine Pituitary Extract	-	0.004 ml/ml	PromoCell (Germany)
Epidermal Growth Factor (recombinant human)	-	0.125 ng/ml	PromoCell (Germany)
Insulin (recombinant human)	-	5 µg/ml	PromoCell (Germany)
Hydrocortisone	-	0.33 µg/ml	PromoCell (Germany)
Epinephrine	-	0.39 µg/ml	PromoCell (Germany)
Transferrin, holo (human)	-	10 µg/ml	PromoCell (Germany)
$CaCl_2$	-	0.06 mM	PromoCell (Germany)
Pericyte Media *hPL-PC*			
Pericyte Basal Growth Medium	500 ml	-	PromoCell (Germany)
Supplement Mix	25 ml	-	PromoCell (Germany)
Adipogenic Media *ADSC*			
DMEM 4.5 g/L Glucose with Ultraglutamine	500 ml		Lonza (Switzerland)
Fetal Calf Serum	50 ml		Lonza (Switzerland)
GA (Gentamicin/Ampicillin)	0.5 ml		Lonza (Switzerland)
Isobutyl-methylxanthine (IBMX),		0.5 mM	Lonza (Switzerland)
Dexamethasone		1 mM	Lonza (Switzerland)
Insulin		10 mM	Lonza (Switzerland)
Indomethacin		200 mM	Lonza (Switzerland)
Osteogenic Media *ADSC*			
DMEM 4.5 g/L Glucose with Ultraglutamine	500 ml		Lonza (Switzerland)
Fetal Calf Serum	50 ml		Lonza (Switzerland)
GA (Gentamicin/Ampicillin)	0.5 ml	-	Lonza (Switzerland)
Dexamethasone		0.1 mM	Lonza (Switzerland)
Ascorbate-2-phosphate		50 mM	Lonza (Switzerland)
ß-glycerophosphate		10 mM	Lonza (Switzerland)

Table 7 Cell Culture Growth Medium, Additives and Variations of Media

2.1.3 Isolation of ADSC from human samples

Patients undergoing elective reconstructive surgery at St. Vincent's Public Hospital or St. Vincent's Private hospitals (Fitzroy and East Melbourne, Victoria, Australia) were consented for collection of excess fresh adipose tissue or lipoaspirate (HREC 52/03). ADSC were isolated from tissues using the protocol described by Zuk et al. (371). Briefly, adipose tissue was washed in PBS (Lonza, Switzerland) then in complete DMEM (refer to Table 7). Tissue was finely diced and digested with Collagenase I (Life Technologies, USA) 1 mg/ml in PBS (Lonza, Switzerland) for 45-60 min at 37^{o}C in a shaking water bath. Digestion of ECM was neutralized by addition of equal amounts of complete DMEM followed by centrifugation at 1500 rpm for 6 min. The resultant cell pellet was washed in PBS and filtered through a 100 μm nylon mesh (BD Falcon, USA) to remove cellular debris. The pellet was then re-suspended in complete DMEM, seeded and incubated overnight. Media was changed after incubation and these cells washed with PBS (Lonza, Switzerland), to remove non-adherent cells e.g. red blood cells. Cells were passaged once 80-90% confluence was achieved to use to expand further or use for experimentation.

2.1.4 Generation of ADSC-Conditioned Media

ADSC cells were grown in T75 tissue culture treated flasks (CELLSTAR®, Greiner Bio-One, Germany) to 80-90% confluence in complete DMEM. This media was then aspirated; cells washed using PBS and were then cultured in a fresh complete DMEM for 72 h. Complete DMEM was used for ADSC conditioning, producing DMEM-ADSC^{CM} (ADSC-conditioned media), compatible for use with NHDF and ADSC. Basal EGMV2 (see Table 7) was used for ADSC conditioning producing EGMV2-ADSC^{CM}, compatible for use with LEC.

At 72 h, conditioned media was aspirated, centrifuged at 1800 rpm for 7 min to remove cell debris, filtered using a 0.22 μm Millex-GV Syringe Filter Unit (EMD Millipore, Germany) then frozen and stored at -80^{o}C if not used immediately for experimentation.

RTX- ADSC^{CM} and RTX-EGMV2-ASC-CM was generated by placing fresh media, on 80-90% confluent ADSC 48 h after 10Gy irradiation treatment. Media was then collected 72 h after incubation with irradiated ADSC and processed.

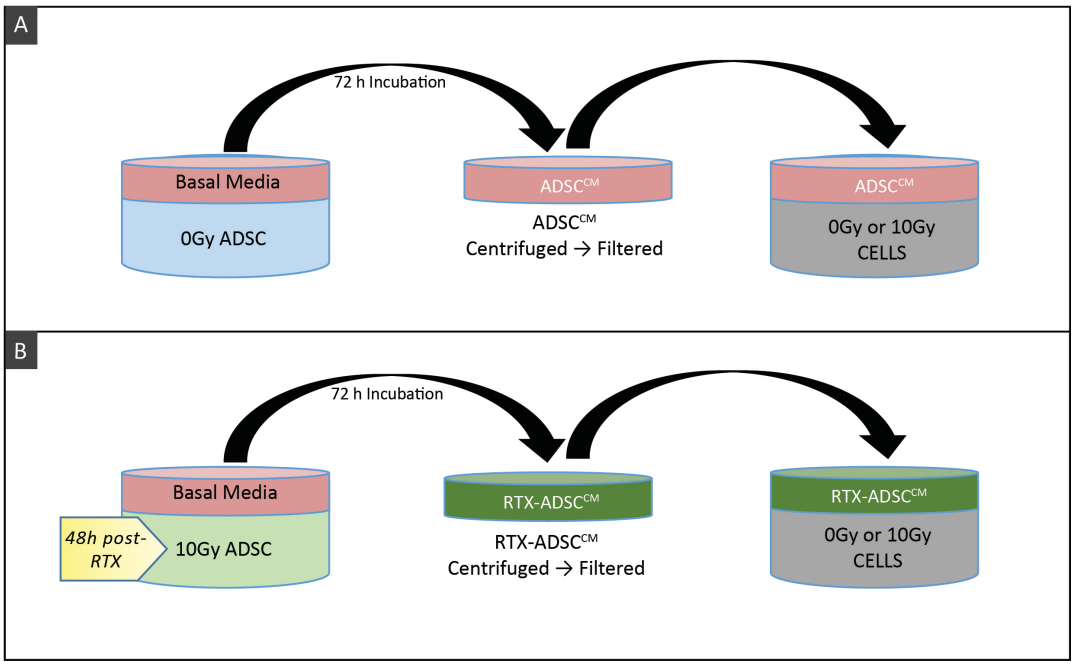

Figure 7

Figure 7 An *in-vitro* model of fat grafting – generation of adipose derived stem cell conditioned media

A schematic diagram describing the *in-vitro* model of fat grafting designed to interrogate the regenerative potential of the ADSC paracrine secretome. The methodology for the formation of (A) adipose derived stem cell conditioned media (ADSC^{CM}) after culture of 80-90% confluent 0Gy ADSC in the appropriate basal culture media (DMEM or EGMV2) for 72 h, followed by subsequent centrifugation to and filtration to remove cellular debris and application to alternative functional assays. (B) irradiated adipose derived stem cell conditioned media (RTX- ADSC^{CM}) was similarly produced by the same methodology described above with the exception of the use of 80-90% confluent 10Gy ADSC (48 h post-irradiation) for conditioning of basal media. This model was specifically designed to interrogate the effects that the irradiated ADSC secretome may have on surrounding healthy or injured cells, to validate the mode of injury termed radiation induced bystander effects (RIBE).

2.1.5 Cell irradiation and dosing regimes

Cells were irradiated at the Bio-resources Centre (Victoria, Australia) using a Gammacell® 40 Irradiator (Best® Theratronics, Canada). This machine delivered 0.9967584 Gy/Min with the chosen gamma irradiation dose evenly delivered across the irradiation drawer. Dose Uniformity (typical) was ±7% over a 260 mm diameter and 100 mm height chamber. Cells were irradiated using a single dose of 10Gy with control cells receiving 0Gy (no radiotherapy); while cells in fractionated groups received 2Gy in five separate doses over 48 h.

2.1.6 Growth factors and proteins

Growth factor / Protein	Reconstituted Concentration	Company
Interleukin 8 (IL-8)	0.1-0.3 ng/ml	Abcam (UK)
Recombinant Human Vascular Endothelial Growth Factor C (VEGF-C)	200-500 ng/ml	Vegenics Pty Ltd (Australia)
Recombinant Human Vascular Endothelial Growth Factor D (VEGF-D)	200-500 ng/ml	Vegenics Pty Ltd (Australia)
C-X-C chemokine receptor type 7 (CXCR7) full length protein	50-100 ng/ml	Abcam (UK)
Stromal Derived Factor-1α (SDF-1α) - full length active protein	50-100 ng/ml	Abcam (UK)
VGX-100 (Anti-VEGF-C)	10 µg/ml	Opthea Pty Ltd (Australia)
VGX-300 (Anti-VEGFR-3)	10 µg/ml	Opthea Pty Ltd (Australia)
A2-Macroglobulin		R&D (USA)
Inter-α-H2		Origene (USA)
Periostin (Osteoblast specific factor 2)		BioVendor (Czech Republic)
Recombinant Human Gremlin	200 µg/mL	R&D (USA)
Lactoferrin		Sigma Aldrich

		(Australia)
Recombinant Human NOV (CCN3)	250 µg/mL	R&D (USA)
Serpin		R&D (USA)
Recombinant Human SPARC (Osteonectin)	100 µg/mL	R&D (USA)
Vitamin D Binding Protein		Abcam (UK)

Table 8 Growth factors/proteins and titrated concentrations

2.2 *In-vitro* functional assay methods

2.2.1 Cell survival fraction

Cells were plated on 24 well tissue culture plates (BD Falcon, USA) at 50,000 cells/well in 1ml of the appropriate media solution. After overnight incubation, attached cells received either 10Gy (treatment) or 0Gy (control) irradiation. 48 h after treatment, cells were trypsinised, re-suspended and viable cells were counted using a hemocytometer and Trypan Blue (Gibco, USA). Plating efficiency (PE) was then calculated for 10Gy and 0Gy groups using the following formula:

$$PE = \frac{viable\ cell\ count(48hr)}{viable\ cell\ count(0hr)} \times 100$$

Plating efficiency was then utilized to calculate the survival fraction (SF) using the following formula:

$$SF = \frac{PE_{10gy}}{PE_{0gy}} \times 100$$

The 10Gy survival fraction assumes that as the control, 0Gy PE represents 100% survival. Utilizing plating efficiency to calculate survival fraction accounts for 'normal' cell losses that occur without the influence of radiation.

2.2.2 Proliferation and Apoptosis

Cells were plated in 200 µl of media in white walled 96 well plates (Nunc, Thermo Scientific, UK). After overnight incubation attached cells received 10Gy (treatment) or 0Gy (control) irradiation. 48 h after treatment, luminescence based assays were used to assess cell proliferation with CellTiter-Glo Cell Viability Assay (Promega, USA) and apoptosis with Caspase-Glo 3/7 Assay (Promega, USA) according to manufacturer's instructions. At 48 hours, 96 well plates were equilibrated to room temperature, 100 µl of media was aspirated from each well and topped up with 100 µl of the appropriate luminescence reagent, resulting in a 50:50 ratio of media:reagent. Each plate was shaken for 1 min in the FLUOstar OPTIMA Cell Plate Reader (Offenburg, Germany) and left to equilibrate, protected from light. The luminescence setting was used to measure readings from the underside of plates; 10 min post shake for proliferation and 60 min post shake for apoptosis. Each well was read in triplicate at a gain value of 1900.

2.2.3 Scratch migration

Scratch migration assays were conducted in 48 well or 96 well clear tissue culture plates (BD Falcon, USA), precoated with 10 µg/mL Human Fibronectin (Sigma Aldrich, Australia). Cells were plated at a density that would achieve 85-90% confluence overnight e.g. in a 96 well plate, 20,000 cells/well were plated for endothelial cell populations, while larger cells such as ADSC or NHDF were plated at 15,000 cells/well in 200 µl media/per well. After overnight incubation, attached cells received either 10Gy (treatment) or 0Gy (control) irradiation. 36 h post plating; cells were serum starved in the appropriate serum-free media for 12 h before the scratch wound was created at the 48 h time point. Scratch wounds were created using the 96-pin wound maker (Essen BioScience, USA) or a 1250 µl pipette tip. After wounding, cells were washed gently with PBS and replaced with fresh control or experimental media. Images of the 0 h and 48 h scratch wounds were taken using bright field microscopy at x4 objective on the Olympus IX71 Inverted Microscope (USA). Figure 8 summarises the methodology. The scratch area was calculated on ImageJ (National Institute of Health, USA) and mapped using the following formula:

$$Percentage\ Gap\ closure\ (\%) = \frac{Area(0hr)/Area(48hr)}{Area\ (0hr)} \times 100$$

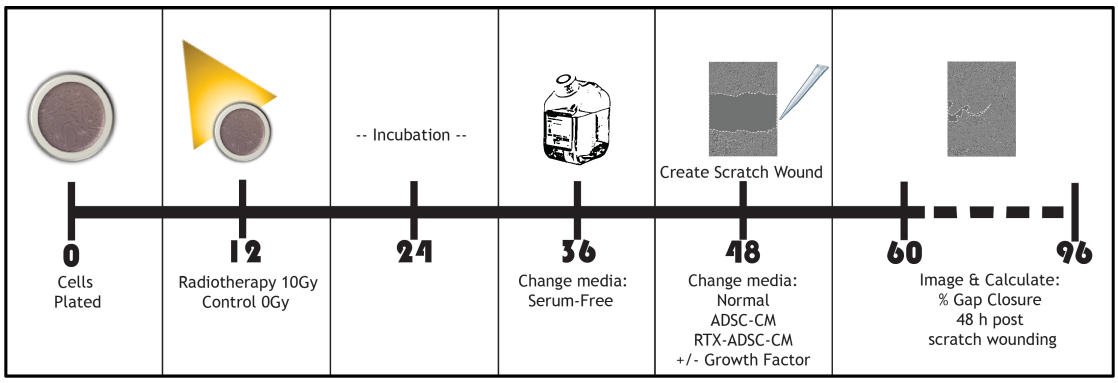

Figure 8

Figure 8 Scratch Assay Methodology and Timeline

The figure above details the timeline and methodology designed for the scratch wound assay used to assess the effect of radiotherapy injury and various media conditions on the migratory capacity of *in-vitro* cell cultures. 0 h: cells were seeded on a fibronectin coated cell culture well, left to incubate overnight and at 12 h received either a 10Gy radiotherapy dose or 0Gy control dose. Cells were incubated for another 24 h prior to a media change at 36 h to serum starved media to halt proliferation of cells prior to scratch wounding. At 48 h a scratch wound was created using a sterile 1250 µl pipette tip, well were washed and media for the appropriate experimental condition was replaced. Cells were photographed using brightfield microscopy at x 4 or x 10 objective at 0 h, then 6 hrly for initial experiments and a final image at 48 h was used to calculate the % gap closure compared to 0 h controls.

2.2.4 Endothelial cell assays

2.2.4.1 Tube formation

48 or 24 clear well plates (BD Falcon, USA) were pre-coated with a thick layer of Growth Factor Reduced Matrigel (BD Biosciences, USA) and allowed to solidify at 37ºC in a humidified atmosphere of 5% CO_2. Endothelial cells, LEC and HMEC, were seeded in control or experimental media followed by 10Gy irradiation

(treatment) or 0Gy (control) irradiation. Tube formation was assessed at 24 and 48 h using bright field microscopy at x2 to x10 objectives on the Olympus IX71 Inverted Microscope (USA), taking 5 photographs per well. Photographs were then quantified using the Lymphatic Vessel Analysis Protocol (LVAP) plug-in (481) for ImageJ (National Institute of Health (NIH), USA) using the following parameters; loops and branches as in Figure 9.

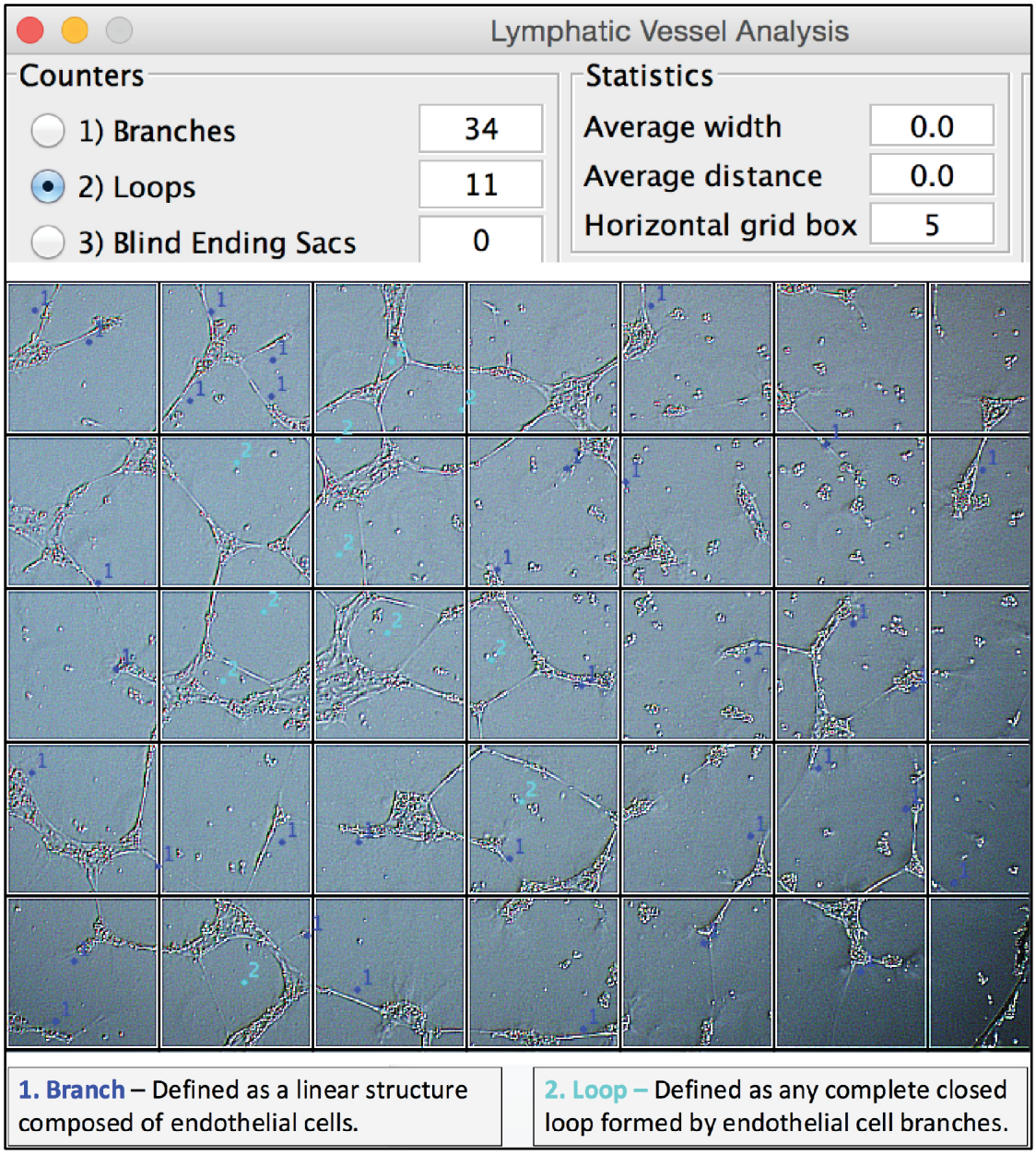

Figure 9

Figure 9 Lymphatic Vessel Analysis Platform – application for quantification of 2D tube formation assays in endothelial cell *in-vitro* assays

The image above displays LEC plated and photographed at 48 h using x10 objective bright field imaging. Each photograph was quantified after the application of 'GridNoOffset' function on ImageJ (NIH, USA) and initialization of the LVAP plug-in (481). Parameters quantified were (1) Branches – defined as a linear structure composed of endothelial cells or (2) Loops/Tubes – defined as a complete closed loop formed by endothelial cells. Counts were conducted working systematically from left to right along the grid boxes. 5 images per well were taken in standardised positions 12'oclock, 3'oclock, 6'oclock, 9'oclock and centrally, totals were tallied and averaged for further statistical analysis.

2.2.4.2 Spheroid sprouting

Cells were used to form 3D spheroids using a medium consisting of 20% methylcellulose solution with 80% appropriate complete growth media. 5000-20,000 cells/spheroid were used for baseline formation experiments. 5000 cells/spheroid were used for *in-vitro* sprouting experiments. Spheroids were formed with 5 µl volumes pipetted into non-adherent U-bottom 96 well plates (BD Falcon, USA). Spheroids were left to form over 3-4 h and then supplemented with 150 µl of 20% methylcellulose/80% media solution for incubation overnight. Spheroid plates then received 10Gy irradiation treatment or 0Gy control irradiation. Spheroids were aspirated using cut 300 µl pipette tips and seeded in a 48 well plate (BD Falcon, USA) in between 2 layers of 150 µl of fibrin from human plasma (Sigma Aldrich, Australia) and 15 µl of thrombin from human plasma (Sigma Aldrich, Australia). Spheroids were photographed at 0, 24 and 48 h time points with sprouting metric analysis conducted using ImageJ (NIH, USA) and the LVAP Plugin (481) using parameters sprout number, total length (µm) and average length (µm) .

2.2.5 ADSC Differentiation

30,000 ADSCs/well were plated in a 24-well plate and left to attach overnight. Plates then received 10Gy irradiation treatment or 0Gy control irradiation after overnight incubation. The differentiation media (see Table 7) was added 48 h post irradiation to

stimulate differentiation and media was changed with media changes conducted every 3 days for a 14 day incubation.

Adipogenic differentiation was assessed using Oil-Red-O staining (Sigma Aldrich, Australia), which indicates intracellular lipid accumulation visualized as red droplets. Osteogenic staining was confirmed with Alazarin Red staining (Sigma Aldrich, Australia) which is based on detection of calcium deposits in osteogenic culture. On day 14, cell media was aspirated and wells were washed 2-3 times with PBS. Cells were fixed with 4% paraformaldehyde (PFA) for 45 minutes, washed with PBS and stained with either filtered Oil Red O for 5 min or Alazarin Red for 45 min. After further washing with PBS or distilled water the cells were counterstained with hematoxylin for 5 min and 5 photographs per well were taken at x4 objective.

Quantification of differentiation was conducted using Adipo-Red and Osteo-Image Mineralisation Systems (Lonza, Switzerland) as per manufacturer's instructions. The fluorescent plate reader FLUOstar OPTIMA (Offenburg, Germany) was employed to obtain Adipo-Red output readings at 572 nm, and Osteo-Image readings at excitation/emission settings of 492/520 nm .

2.2.6 Spheroid Invasion Assay

The Cultrex® 96 well 3D Spheroid BME Cell Invasion Assay (Trevigen Inc, USA) was used to interrogate NHDF invasion according to manufacturer's instructions. Briefly, 0Gy and 10Gy NHDF cells suspended in spheroid formation ECM mixture, 50 µl aliquots containing 500 cells were added to a 96 well spheroid forming plate and left to form for 72 h. Invasion matrix was added along with control (complete DMEM) or experimental ($ADSC^{CM}$) media. Cell invasion was monitored with daily imaging at x4 objective for 11 days. Images were qualitatively analysed for invasion patterns, described as: ordered with uni-directional radial spread or disordered with haphazard radial spread and significant cell overlap. Quantitative analysis was conducted using ImageJ (NIH, USA), with image thresholding techniques used to measure the area of NHDF invasion in $pixels^2$.

2.2.7 Adhesion

96 well plates were coated with collagen I (Sigma Aldrich, Australia) solutions in concentrations of 0, 0.05, 0.125, 0.25, 0.5, 1.0, 2.5, 5 ng/ml diluted in 0.1% Bovine Serum Albumin (BSA) (Sigma Aldrich, Australia) in PBS. Each well was coated and incubated for 60 min in triplicate for each concentration. After collagen coating, the wells were blocked with 3% BSA in complete media and incubated for 30 min. Cells were trypsinised 48 h after treatment with irradiation (10Gy) or controls (0Gy) and re-suspended in normal media containing 0.1% BSA for 30 min to allow for recovery. Cells were then centrifuged and re-suspended in normal media for plating. 10,000 cells in 200 µl of media were plated per well for a 1 h incubation after which, wells were gently washed with PBS to remove non-adherent cells, fixed with ice cold methanol and stained with crystal violet ($C_{25}N_3H_{30}Cl$) for 10 min. Wells were washed with dH_2O and left to dry overnight. The following day 0.1 M sodium citrate solution was added to each well and adhesion was quantified by dye extraction and measurement at 540 nm absorbance using a microplate spectrophotometer (Benchmark Plus, Bio Rad, USA).

2.2.8 Collagen Contraction

24 well clear walled plates (BD Falcon, USA) were used to seed both 0Gy and 10Gy NHDF (48 h after irradiation or control treatment) at a density of 500,000 cells/well. Cells were suspended in a 200 µl collagen-1 (Sigma Aldrich, Australia) gel, with 1 ml of gel constituted by 700 µl Collagen-1, 100 µl 10xPBS (Lonza, Switzerland) and 200 µl of $NaHCO_3$ (11.76 mg/ml) (Sigma Aldrich, Australia). The gel was allowed to solidify with incubation for 30-40 min before the addition of 500 µl complete DMEM media to each well. 48 h after incubation the gels were circumferentially released from their attachments to the walls of the well and allowed to float freely in cell culture media for a further 24 h. Standardised photographs were taken from a mounted camera, with additional photographs taken at x2 objective using brightfield microscopy. Images were taken at 24 h post release and quantified using ImageJ (NIH, USA) by tracing and calculating the area of the collagen gel. The differences were represented as a fold change of 10Gy vs 0Gy to demonstrate the differences in contractility of irradiated versus control NHDF.

2.2.9 Chemotaxis Boyden chambers

FluoroBlok 96 well system with 8.0 µm Pore High density PET membrane (BD Falcon, USA) plates were used for chemotaxis assays. 150 µl media containing growth factors (refer to 2.1.6: Growth factors and proteins) at titrated concentrations were added to the basal chamber through the feeding port. 4000-5000 cells/well in 75 µl of the appropriate starvation media were seeded in the apical membrane and incubated for 24 h. Growth factor media was removed from the basal chamber and replaced with PBS to wash the basal surface of the PET membrane, where migrated cells were attached. The basal surface of the membrane was fixed with 4% paraformaldehyde solution for 30 min, washed with PBS twice and stained with 4',6-diamidino-2-phenylindole (DAPI) (Thermo Fischer Scientific, USA) for 20 min, washed again and stored in PBS at 4ºC. The basal surface of the membrane was imaged using an upright BX61 microscope (Olympus, Tokyo) using fluorescent settings at x4 objective, imaging the entire membrane. ImageJ (NIH, USA) was used to quantify the number of DAPI stained nuclei representing chemotactic cell migration. Briefly, the image was colour threshold adjusted to a set level, circular shaped particles were analyzed and counted, which represented the number of cells that had transmigrated from the apical to the basal side of the PET membrane. Control conditions/media were used as the baseline values from which fold changes in migration were calculated.

2.2.10 *In-vitro* model of fat grafting

The *in-vitro* model of fat grafting was designed based on the postulated regenerative potential of the ADSC paracrine secretome. $ADSC^{CM}$ or EGMV2- $ADSC^{CM}$ was produced as described in section 2.1.4 and depicted in Figure 7. $ADSC^{CM}$ or RTX-$ADSC^{CM}$ were used to treat control or irradiated cells for 48 h prior to *in-vitro* functional assay testing. Using this method the potential of salvaging or worsening of radiotherapy injury was determined in comparison to basal media controls.

2.3 RNA methods

2.3.1 RNA extraction and purification

RNA was extracted from tissue culture flasks at a set time after irradiation or control treatment using Qiazol® (QIAGEN, Germany) and purified with DNase and QIAGEN, Germany® RNEasy Plus Universal Kit Samples as per manufacturer's instructions. Samples were then stored at -80ºC or used immediately for cDNA synthesis (see section 2.3.2).

2.3.2 cDNA synthesis

After column extraction and purification, RNA sample concentration and purity was determined using a Nanodrop™ Spectrophotometer (Thermo Fischer Scientific, USA). Samples were appropriately diluted with nucleic acid free H_2O (QIAGEN, Germany) (if the initial concentration was greater than 100 ng/ml) and then reconstituted to give a 100 ng/ml concentration in 5 µl volume. High Capacity cDNA reverse transcription kit (Applied Biosystems, USA) was used to prepare a 5 µl reaction volume of: 1 µl RT Buffer, 1 µl 10X Random Primers, 0.4 µl dNTP Mix, 2.1 µl nucleic acid free water, 0.5 µl Multiscribe Reverse Transcriptase, which was then added to each sample tube. cDNA synthesis was conducted using Veriti 96 well thermal cycler (Applied Biosystems, USA) with settings for high capacity reverse transcription using 10 µl sample volumes as follows:

Step 1: 25ºC for 10 min

Step 2: 37ºC for 120 min

Step 3: 85ºC for 5 min

Step 4: 4ºC hold

Upon completion, reactions were maintained at 4ºC prior to reverse transcriptase polymerase chain reaction.

2.3.3 Reverse Transcriptase - Polymerase chain reaction (RT-PCR)

10 µl cDNA samples were removed from 4ºC storage on the thermal cycler and 90 µl of nucleic acid free H_2O was added to bring the cDNA to a concentration of 1 µg/ml. A RT-PCR template was used for planning of the 96 well plate and 10 µl reaction volumes consisting of: 2.5 µl nucleic acid free H_2O (QIAGEN, Germany), 5 µl

TaqMAN 2X Universal Master Mix (Applied BioSystems, USA), 0.5 µl RNA primer and 2 µl of cDNA were prepared as required. Sample mixtures were placed in a pre-heated GeneAmp 9700 thermal cycler (Applied Biosystems, USA) and reactions were carried out as follows:

Step 1: 50ºC for 2 min
Step 2: 95ºC for 20 sec
Step 3: 95ºC for 1 sec ⎫
Step 4: 60ºC for 20 sec ⎭ 40 Cycles

Upon completion of the reactions, data was analyzed for fold changes of expression compared to control groups.

2.3.3.1 Single primer analysis

Primers:

All purchased from Applied Biosystems (Thermo Fischer Scientific, USA)

Primer	***Assay Identification Code***
huVEGFR-2	Hs00911700_m1
huVEGFR-3	HS01047677_m1
huCXCR7	Hs00664172_s1
huIL-8	Hs00174193_m1
huPPARy	Hs01115513_m1
huLPL	Hs00173425_m1
huCEBPA	Hs00269972_s1
huFABP4	Hs1086177_m1
hu18S	Hs03003631_g1

2.3.3.2 PCR Pathway Analysis

384-well custom RT^2 Profiler PCR Arrays (QIAGEN, Germany) were used to interrogate RNA changes in signaling as part of pathway specific analyses. RNA was extracted as per methods detailed in (2.3.1), cDNA synthesized using RT^2 First Strand Kit (QIAGEN, Germany) and reverse transcribed using RT^2 SYBR Green Mastermix (QIAGEN, Germany) as per manufacturer's instructions and plated according to the pre-set 384 well layouts.

Gene expression levels in NHDF RNA extracted 4 h after 10Gy treatment were compared to 0Gy samples using the Notch Signaling pathway array (QIAGEN, Germany). Similarly, gene expression levels in NHDF RNA extracted 48 h after 10Gy treatment were compared to 0Gy samples using the Human Extracellular Matrix and Adhesion Molecule array (QIAGEN, Germany).

2.3.4 Next generation sequencing

RNA samples were extracted in duplicate for each cell type and treatment condition as per methods described in sections (2.3.1 and 2.3.2), 4 h after completion of treatment with a single dose of 10Gy, 5 doses of 2Gy delivered over 48 h along with matched 0Gy controls. The following samples were sent for next generation sequencing analysis:

NHDF	0Gy vs. 10Gy
NHEK	0Gy vs. 10Gy
hPL-PC	0Gy vs. 10Gy
HMEC	0Gy vs. 10Gy
HLEC	0Gy vs. 10Gy
HLEC	0Gy vs. 2Gy x 5
ADSC	0Gy vs. 10Gy
ADSC	0Gy vs. 2Gy x 5

Each sample underwent RNA sequencing (100 base pair single end) in the Illumina HiSeq machine at the Australian Genome Research Facility (AGRF, Melbourne, Australia). Reads from each sample were mapped to the hg19 genome using the Rsubread (482), edgeR (483) and limma (484) programs. The featureCounts function was used to tally the reads for each transcript, with transcripts less than 0.5 counts per million in at least two samples being removed from further analysis as they did not reach minimal expression levels. A multi-dimensional scaling plot was generated and demonstrated a clear separation between different cell types and radiotherapy treatment. A random effect model was implemented for differences between the days replicates were produced (485). Gene set analysis was carried out using c2 (curated gene sets from other profiling studies and sets from pathway databases) and c5 (Gene

Ontology) collections from Subramanian et al. (486). The genes were matched using their Gene Symbols and various testing methods such as Camera and Roast, which account for correlation between genes in each set, giving final result comparisons between treatment and control groups with stringent p-values (487) (488).

2.3.5 Analysis of next generation sequencing data

Various sequencing platforms were used for analysis of these RNA-seq data sets producing statistical tables, heat-maps and pathway plots. The Ensemble of Gene Set Enrichment Analyses (EGSEA) included h Hallmark signatures, c1 Positional Gene Sets, c2 Curated Gene Sets, c3 Motif Gene Sets, c5 GO Gene Sets, c6 Oncogenic signatures, c7 Immunologic signatures and KEGG Pathways.

2.4 Protein methods

2.4.1 General reagents, primary and secondary antibodies

Tris Buffered Saline (TBS): 50 mM Tris, 150 mM NaCl in MilliQ H_2O

Tris Buffered Saline-Tween (TBS-T): TBS with 0.05% Tween

Western Running Buffer: 100 ml 20X running buffer concentrate NuPAGE® MES SDS Running Buffer (*In-vitro*gen, USA)

Western Transfer Buffer: 100 ml 20X NuPAGE® transfer buffer concentrate (*In-vitro*gen, USA), 200 ml Methanol, 1ml Antioxidant NuPAGE® (*In-vitro*gen, USA), 1700 ml MilliQ H_2O

Loading Buffer: NuPAGE® LDS Sample Buffer (*In-vitro*gen, USA)

Reducing and Denaturing Solution: 1:10 dilution 1 M Dithiothreitol (DTT), 1:4 dilution of NuPAGE® LDS Sample Buffer (*In-vitro*gen, USA)

Elution Buffer: NuPAGE® LDS Sample Buffer and NuPAGE® Sample reducing agent (*In-vitro*gen, USA)

Size Marker: Chameleon Duo Pre-stained protein ladder (LI-COR Biosciences, Nebraska, USA)

Transfer Membrane: Immobilon-FL PVDF membrane (Merck Millipore Ltd, Darmstadt, Germany)

Blocking Buffer: Odyssey Blocking Buffer (LI-COR, USA)

Gel: NuPAGE® 4-12% Bis-Tris precast gels (*In-vitro*gen, USA)

Conjugation buffer: 20 mM Sodium Phosphate, 0.15 M NaCl (pH 7-9)

Quenching Buffer: 1 M Tris HCl (pH 7.5)

Crosslinker: BS^3 Crosslinker (Thermo Fischer Scientific, USA) prepared by dilution to 5 mM with conjugation buffer.

Antibodies:

Antibody	Dilution Used for IP or WB	Company
Anti-human CXCR7 (goat polyclonal)	WB 1:200	Santa Cruz Biotechnologies (USA)
Anti-human NOTCH-1 (rabbit polyclonal)	WB 1 µg/ml	Abcam (UK)
VEGFR-2 Antibody (rabbit monoclonal)	IP 1:100 WB 1:1000	Cell Signaling Technology (USA)
VEGFR-3 Antibody (rabbit polyclonal)	IP 1 µg/sample WB 1:200	Santa Cruz Biotechnologies (USA)
Phosphotyrosine Antibody (mouse monoclonal)	WB 1:1000	Upstate Technologies (USA)
Beta-Actin (mouse monoclonal)	WB 1:200	Santa Cruz Biotechnologies (USA)
Infra-red labelled reagents – 800 and 680 IRDye® conjugated polyclonal IgG antibodies		LI-COR Biosciences (USA)

Table 9 Antibody reagents used for immunoprecipitation and western blot experiments

2.4.2 Cell lysates

Cells were cultured to 80-90% confluence. At a set time-point after radiotherapy treatment cell lysates were generated with the addition of 1 ml of RIPA Buffer (Sigma Aldrich, Australia) and 10 µl of Protease Inhibitors (Sigma Aldrich, Australia) to each

flask. After a 10 min incubation at 4ºC, lysates were removed using cell scrapers and stored in -80ºC.

2.4.3 Immunoprecipitation

Dynabeads® Protein G (Life Technologies, AS, Norway), were used for immunoprecipitation of protein in specified samples prior to western blotting. 50 µl suspensions of Dynabeads® were prepared per sample according to manufacturer's instructions in a 1.5 ml eppendorf tubes (Eppendorf). Beads were incubated with 200 µl of PBS-Tween (PBS-T) containing antibody (at the appropriate dilution) at room temperature for 10 minutes with rotation. Dynabeads® were then placed on the supplied magnet to separate beads from supernatant. Supernatant was then aspirated and the Dynabeads® were washed with 200 µl of conjugation buffer (see section 2.4.1). The antibody was then crosslinked to the Dynabeads® with the addition of 250 µl of 5 mM BS^3 Crosslinker (Thermo Fischer Scientific, USA) and incubated at room temperature for 30 min with rotation. The crosslinker was quenched with the addition of 12.5 µl of Quenching Buffer and incubated for a further 15 min at room temperature with rotation. The antibody crosslinked Dynabeads® were then washed three times with PBS-T solution. 1 ml of sample was added and immunoprecipitated at 4ºC for 1 h with rotation. Immunoprecipitates were washed three times with PBS-T and eluted with the addition of 20 µl of Elution Buffer and 10 µl of Loading Buffer per sample, followed by 10 min of heating at 70ºC (see section 2.4.1). Tubes were placed on the magnet, beads discarded and immunoprecipitate supernatants of interest collected. Samples were then reduced with a denaturing solution (1:10 dilution of 1 M DTT), heated for a further 10 min at 70ºC before proceeding to SDS-Page and Western Blotting (see below sections 2.4.4, 2.4.5).

2.4.4 SDS-PAGE

Protein samples of cell lysates or conditioned media from both irradiated (10Gy) or control (0Gy) groups for analysis under reducing and denaturing conditions were combined with reducing and denaturing solution (see section 2.4.1) and heated at 70ºC for 10 min. Reduced or immunoprecipitated supernatant samples were then loaded on NuPAGE® 4-12% Bis-Tris precast gels (*In-vitro*gen) along with a lane containing Chameleon Duo Pre-stained protein ladder (LI-COR Biosciences). The gel

was run at 10-150 V until the size marker and/or sample-loading buffer had separated or run the length of the gel using an XCell SureLock™ and XCell II™ Blot Module System (*In-vitro*gen, USA).

2.4.5 Western blotting

Proteins were transferred to Immobilon-FL PVDF membrane (Merck Millipore Ltd, Darmstadt, Germany) using the XCell SureLock™ and XCell II™ Blot Module System (*In-vitro*gen, USA) according to manufacturer's instructions at 30 V for 1-1.5 h. Transfer membranes were then placed in a 50 ml Falcon™ Tube (Thermo Fischer Scientific, USA) and blocked with Odyssey Blocking Buffer (LI-COR Biosciences, USA) on a roller for 1-2 h at room temperature or overnight at 4ºC. The membrane was then incubated in primary antibody, diluted to the appropriate concentration in blocking buffer, for 1-2 h at room temperature or overnight at 4ºC on a roller. Membranes were then washed in TBS-T for five minutes three times and incubated with the appropriate secondary antibody conjugated to 800 IR dye® for 1 h at room temperature. Western blot membranes were imaged using the Odyssey Infrared Imaging System (LI-COR Biosciences, USA) to visualize proteins.

2.4.6 VEGFR-3 Activation

Established proliferating LEC cultures were treated with growth factors VEGF-C and VEGF-D as well as $ADSC^{CM}$ and RTX- $ADSC^{CM}$ for 10 min at which point cells were lysed for 15 min in an ice cold buffer consisting of: 1% Nonidet P-40, 20 mM Tris-HCl, pH 8.0, 137 mM NaCl, 10% glycerol, 2 mM EDTA, 1 mM activated sodium orthovanadate, 10 μg/ml aprotinin, and 10 μg/ml leupeptin as described by Harris et al. (489). VEGFR-2 was immunoprecipitated and targeted in Western blots using human VEGFR-2 (Cell Signaling Technologies, USA), and VEGFR-3 using human VEGFR-3 (Santa Cruz Biotechnology, USA). Phosphotyrosine residues were targeted with a monoclonal antibody against Phosphotyramine (Upstate Technologies, USA) to detect receptor activation induced by the growth factor or conditioned media treatments. For detection, secondary antibodies 800 IRDye®-conjugated IgG (LI-COR Biosciences, USA) were used. Proteins were imaged and visualized, on an Odyssey Infrared Imaging System (LI-COR Biosciences, USA) and relative band intensities were measured compared to controls.

2.4.7 BioAssays for Binding and Cross-linking of VEGFR-2 or VEGFR-3

Ba/F3 cell lines rely on the presence of interleukin-3 (IL-3) for proliferation and survival, therefore withdrawal of this factor results in cell death within 24 h. These cell line characteristics were manipulated to develop an assay to detect ligands able to crosslink and activate vascular endothelial growth factor receptor-2 (VEGFR-2) and -3 (VEGFR-3), which are key in promoting processes of angiogenesis and lymphangiogenesis. Methods described by Stacker et al. (490) are summarized below. Briefly, a chimeric receptor is generated where the extracellular region of the VEGFR-2 or 3 receptor is fused to the transmembrane and intracellular component of the erythropoietin receptor (EpoR). This merged protein is then expressed in Ba/F3 - cell line. Ba/F3 cells were exposed to 0Gy and 10Gy LEC conditioned media and if a ligand successfully crosslinked the VEGFR-2 or -3 receptor, the fused protein transduced an intracellular signal, activating the effector region in the cytoplasm and via Janus kinases (JAKs), thus promoting proliferation and viability of the cell. To quantify this crosslinking, the processes of DNA synthesis or proliferation of cells was monitored using a ViaLight Plus kit (Lonza, Switzerland), or Presto BlueTM cell viability reagent (*In-vitro*gen, USA) according to the manufacturers' protocols.

2.4.8 ELISA

ELISA was performed on ADSC and LEC conditioned media samples collected from cells at various time points after radiotherapy treatment. Human Quantikine Assays for IL-8, VEGF-C, VEGF-D and SDF-1α (R&D Systems, Minneapolis, USA) were used as per manufacturer's instructions to obtain protein concentrations in pg/ml compared to a standard curve generated from each kit.

2.5 Flow cytometry methods

2.5.1 Cell cycle analysis

FlowCellect™ Bivariate Cell Cycle Kit for G2/M Analysis (Merck Millipore) was used for examination of the effects of irradiation on cell cycle as well as alterations in the presence of $ADSC^{CM}$ and RTX- $ADSC^{CM}$ as per manufacturer's instructions. Flow cytometry was conducted using BD FACStar Plus Flow Cytometer (BD Biosciences, New Jersey, USA).

2.5.2 Cell labeling and time course experiments

0Gy and 10Gy LECs 4 h post radiotherapy treatment were trypsinised and washed with 0.5% FACS buffer (1% FCS in PBS), centrifuged and washed a second time. The cell pellet was re-suspended in FACS buffer at a concentration of $5x10^6$ cells in 100 µl and stained with anti-CXCR7 primary antibody (R&D Systems, USA) followed by incubation with goat anti-human Alexa Fluor 488 secondary antibody (Thermo Fischer, USA). Stained cells were centrifuged to remove supernatant and re-suspended in FACS buffer for repeat wash steps. After the third and final wash the cells were suspended in 100 µl of FACS fixative (1% Formaldehyde, 2% Glucose, 0.1% NaN_3 in PBS). Samples were transferred into appropriately labelled FACs tubes (BD Falcon, USA) and loaded on BD FACStar Plus Flow Cytometer (BD Biosciences, New Jersey, USA). Data was analysed using cytometry data analysis software FlowJo LLC (USA).

2.6 Immunocytochemistry and immunohistochemistry

2.6.1 General reagents, antibodies and wash buffers

PBS: 1x at pH 7.4

Sodium Azide Quench Solution: 0.1% Sodium Azide, 0.3% H_2O_2 in PBS

TritonX-100: 10% aqueous solution Triton X-100 (octyl phenol ethoxylate) (Union Carbide Corporation, The Dow Chemical Company (Dow Pacific), Altona, VIC, Australia) was diluted in PBS solution to make PBS-Tr (1X; 0.3% Triton X-100)

Antigen Retrieval Buffer: 10 mM citrate buffer pH 6.0 for antigen retrieval was made using 36 ml 0.1 M citric acid in 164 ml 0.1 M sodium citrate in dH_2O.

Primary Antibodies:

Antibody	Dilutions Used for ICC or IHC	Company
NOTCH-1 *rabbit α human*	IHC 1:200	Abcam (UK)
α-SMA *mouse α human*	IHC 1:300	Dako (Denmark)
CXCR7 *Clone 1168*	IHC 1:100	R&D Systems
SDF-1α *mouse α human*	IHC 1:80	R&D Systems
Podoplanin/D2-40 *mouse α human*	ICC 1:50 IHC 1:100	Dako (Denmark)
PECAM-1/CD31 *rabbit α human*	ICC 1:20 IHC 1:20	Thermo Fischer Scientific (USA)
LYVE-1 *rabbit α human*	ICC 1:100	Abcam (UK)
ICAM-1 *Rabbit monoclonal antibody reactive with human tissues*	IHC 1:400	Lifespan Biosciences (USA)
CD68 *mouse α human*	IHC 1:100	Dako (Denmark)
MitoTracker® Red Probes	100nM	*In-vitro*gen (USA)

Secondary Antibodies:

Antibody	Dilutions Used for ICC or IHC	Company
SAD4549 *goat α rabbit - biotin*	LYVE-1 ICC 1:800 *diluted in PBS*	Vector Laboratories (USA)
AF488 *goat α mouse*	D2-40 ICC 1:100 *diluted in DAKO diluent*	Vector Laboratories (USA)

CY3 *goat α rabbit*	CD31 ICC 1:200 *diluted in DAKO diluent*	Vector Laboratories (USA)
Anti-mouse or Anti-rabbit IgG Peroxidase - Dako Liquid DAB+ Substrate Chromogen System	As per manufacturer's instructions	Dako (Denmark)

2.6.2 Human tissue collection and ethics

Human tissue samples were collected from patients undergoing delayed reconstruction for cancer treatment at St. Vincent's Public Hospital (Fitzroy), St. Vincent's Private Hospital (Fitzroy, East Melbourne). Patients were appropriately consented prior to tissue collection in accordance with ethics protocol HREC No. 52/03.

2.6.3 Sample processing and slide preparation

Samples were collected and placed in formalin or 4% paraformaldehyde solution for a period of 24-48 h depending on tissue thickness, for fixation. Tissues were then cut to an appropriate size and placed inside biopsy cassettes containing PBS at 4ºC until processed. Samples were then processed using the Shandon Excelsior ES® automated tissue processor (Thermo Fischer Scientific, USA) set for an overnight 13 h run for arterial and venous samples and a long 22 h run for skin and subcutaneous tissue samples. Briefly, during the runs the tissues were dehydrated with increasing concentrations of ethanol, cleared of ethanol with histolene washes and infiltrated with paraffin wax at 60ºC with a vacuum setting. Samples were then transferred to hot paraffin in a mold, where they were orientated and embedded appropriately. The sample was then placed on a coldplate for 30 min of cooling, during which the wax solidified and was able to be extracted from the mold. The processed blocks of tissue were then cut using a microtome into 5-10 µm sections and mounted onto either Polysine (poly-l-lysine coated) or 3-APES (3-AMINOPROPYLTRIETHOXYSILANE coated) (Sigma Aldrich) histology slides for immunohistochemical staining.

2.6.4 Immunocytochemistry

Cells were cultured in 8-well Millicell® EZ Slides (Merck Millipore, Germany) to 60-70% confluence. At set time points cell media was aspirated, cells washed with PBS and fixed with 4% PFA for 30 min at room temperature. Slides were stored at 4°C in PBS. For immunocytochemical staining, the well holders were removed and each well was washed with PBS for 5 min twice. If required, cells were permeabilised with 1X 0.3% Triton X-100 at this stage. 60 µl sodium azide quench solution was added to each well for 20 min and PBS washes were repeated. A Dako Delimiting Pen (Dako, Denmark) was used to encircle each individual well to prevent antibody cross-contamination. Dako protein block (Dako, Denmark) was applied to each well for 15 min and then blotted off gently. Wells were incubated with 60 µl of appropriately diluted primary antibody (see section 2.6.1) for 60 min at room temperature. Wells were washed twice with PBS for 5 min. The appropriate secondary antibody (see section 2.6.1) was added to each well and incubated for 60 min protected from light. Wells were washed with PBS for 5 min followed by dH2O for 5 min. A single drop of Prolong® Gold Antifade Mountant (Thermo Fischer Scientific, USA) with DAPI was placed in each well, the slide was covered with a coverslip and left to dry overnight, protected from light, before viewing.

2.6.5 Immunohistochemistry of tissue sections

Hematoxylin and eosin staining was performed on human skin and arterial samples for basic tissue structural analysis. Human skin samples (irradiated and patient-matched normal tissues) were immunostained for D-240, CXCR7, SDF-1α, CD68, CD31, NOTCH-1 and α-SMA. Human arterial samples (irradiated and patient-matched normal tissue) were stained for CD31, ICAM-1 and CD68. Antigen retrieval was used for immunostaining; 10 mM citrate buffer pH 6.0 was used to fill a glass slide container above the level of the slides and maintained at a temperature of 95-100°C in a water bath for 10 minutes. The container was removed from the water bath and allowed to cool at room temperature, leaving the slides immersed in the citrate buffer solution. Slides were then washed for 5 min with PBS-T three times, and then with 3% H_2O_2 for 20 min for quenching of endogenous peroxidase activity, followed by three more PBS-T washes. A Dako Delimiting Pen (Dako, Denmark) was used to encircle tissue samples on the slides and a Dako protein block (Dako, Denmark) was

applied to each sample for 15 min and then blotted off gently. Primary antibody incubations (see section 2.6.1) were performed for 1 h at room temperature, followed by three PBS-T washes. Detection was performed using species appropriate biotin-conjugated secondary antibody (see section 2.6.1). Positive staining was detected using DAB Peroxidase (HRP) substrate Kit (Vector Laboratories, USA) or Dako Liquid DAB+ Substrate Chromogen System (Dako, Denmark). Controls were comprised of primary or secondary antibody alone or isotype matched IgG controls (R&D Systems, USA).

2.6.6 Imaging and photography techniques

Cell culture microscopy imaging was conducted using Olympus IX71 Inverted Microscope (USA). ICC and IHC photographs were imaged on Olympus BX61 upright microscope, using a DP71 digital camera (Olympus, Japan), using fluorescence if required.

In-vitro endothelial cell assays were quantified using the LVAP plugin on Image J (NIH, USA) using the parameters described in section 2.2.4. D2-40 quantification of lymphatic vessel density was undertaken using the LVAP plugin (481) on Image J (NIH, USA) using parameters; 1) Density, 2) Total Width and 3) Intervessel distance. Samples of human tissue with CXCR7+ve lymphatic vessels stained with D2-40 on serial sections quantified and graded with an intensity scale from 0-2. In all cases, quantifiers were blinded from the irradiation status of the *in-vitro* or tissue samples.

2.7 Proteomics methods

2.7.1 Ion exchange chromatography

Conditioned media was collected as described in (2.1.4) and fractionated using ion exchange chromatography for further mass spectrometry proteomic analysis. The following columns and buffers were used for anion and cation exchange:

	Anion (-)	Cation (+)
Column	HiTrap™ Q-Sepharose Fast Flow 1ml columns (GE Healthcare Bio-Sciences AB, Uppsala, Sweden).	HiTrap™ SP Sepharose Fast Flow 1ml columns (GE Healthcare Bio-Sciences AB).
Low Salt Buffer	20 mM Tris 50 mM NaCl pH 8.0	50 mM HEPES pH 7.0
High Salt Buffer	1 M NaCl pH 8.0	1 M NaCl pH 7.0

The circuit tubing and ion-exchange column were connected to the BioLogic™ LP Chromatography System with Fraction Collector (BIO-RAD, USA) and linked to the BioLogic™ Chromatography systems LP Data View Software for analysis of chromatograms during the elution of bound proteins.

The system was set to flow at 1 ml/min, line A was placed in the low salt buffer and line B in the high salt buffer. The columns were primed with 5 column volumes of low salt buffer followed by 10 column volumes of high salt buffer and finally washed with a further 5 column volumes of low salt buffer. 50 ml of conditioned media was then passed through the column and the waste collected in a tube labeled 'flow through'. After the conditioned media run was completed, the column was washed with 5 column volumes of low salt and waste collected in a tube labeled 'wash'.

The fraction collector was engaged to collect 1 ml fractions of column bound proteins using an increasing salt gradient for elution from 100-1000 mM. Fractions were numerically labeled and collection continued until the chromatogram plateaued. The column was then regenerated with 10 column volumes high salt and then by 20% ethanol and stored.

2.7.2 Sample preparation, precipitation and protein assay

Collected fractions were then washed, buffer exchanged, de-salted and concentrated to give a final volume of 250-500 µl using PBS washes and Amicon® Ultra-4 10K

Centrifugal Filter Devices (Merck Millipore Ltd, Darmstadt, Germany). Samples were then placed in 2 ml Eppendorf tubes (Eppendorf, Hamburg, Germany) and five times the sample volume of ice-cold Acetone (Sigma Aldrich, Australia) was added and placed in the -20ºC freezer for protein precipitation overnight. Precipitated proteins were centrifuged and the pellet reconstituted using 100 µl of 8 M Urea, 50 mM triethylammonium bicarbonate (TEAB) and 10 mM Tris(2-carboxyethyl)phosphine hydrochloride (TCEP) reducing solution. The samples were vortexed and sonicated to ensure the pellet is completely dissolved. A protein assay was conducted using Pierce® Microplate BCA Protein Assay Kit – Reducing Agent Compatible (Thermo Fischer Scientific, USA) according to the manufacturer's instructions to determine the concentration of protein in each reduced fraction collected.

2.7.3 Sample cleanup, trypsinisation and alkylation

Reduced fraction samples were centrifuged for 10 min at 14,000 g, the appropriate volume was aspirated to give a total of 100 µg of protein and supplemented to give a final volume of 200 µl. Samples were placed on a shaker for 30 min at 37ºC. 55 mM of Iodoacetamide (Sigma Aldrich, Australia) was added to each sample and left to incubate for 30 min covered from light. Each sample was diluted with 25 mM TEAB to a final concentration of 1 M urea. Each sample was then digested overnight with Pierce Trypsin Protease – MS Grade (Thermo Fischer Scientific, USA) on a shaker at 37ºC. Samples were removed from the shaker acidified with the addition 8 µl of 100% Formic Acid. Oasis HLB 3 cc Extraction Cartridges (Waters, Massachusetts, USA) were used for Solid Phase Extraction clean up. Cartridges were primed with 1 ml of 80% acetonitrile (ACN), 0.1% Trifluoracetic Acid (TFA) followed by 1 ml of 0.1% TFA. Samples were then loaded, cartridges washed with 1.5 ml 0.1% TFA and bound sample eluted with 800 µl of 80% ACN, 0.1% TFA solution. Samples were dehydrated to a 400 µl volume using a SpeedVAC™ (Thermo Fischer Scientific, USA) and then placed in a freeze dryer overnight.

2.7.4 Dimethyl labeling and reconstitution for mass spectrometry

Samples were removed from the freeze dryer, reconstituted with 100 mM TEAB and sonicated to ensure thorough mixing. One set of samples was labeled with 4 µl of 4% formaldehyde – CH_2O representing a normal light label, the second set labeled with

CD_2O representing an intermediate heavy label. The paired samples were then mixed and placed in mass spectrometry tubes (Sigma Aldrich, Australia) in 4°C.

Samples that were to run unlabeled were reconstituted using 97% of 0.1% Formic Acid, 3% ACN in a 100-200 µl volume. Samples were thoroughly vortexed and sonicated, spun at 18000 g for 10 min and 30 µl of the supernatant was placed in mass spectrometry tubes in 4°C prior to loading on the Orbitrap LC-MS machine (Thermo Fischer Scientific, USA).

2.7.5 Mass spectrometry peptide sequence analysis

The data was analyzed with the Mass Spectrometry Informatics Laboratory Environment 2.0 (MSILE2) software program (Bio21 and University of Melbourne, Australia). The peptide sequences search was conducted using the online MASCOT (Matrix Science) search engine utilizing UniProt/SwissProt databases. The data search was processed using the following parameters: Taxonomy: Homo Sapien; Enzyme: Trypsin; Missed Cleavages: up to 2 allowed for identity; Variable Modifications: methionine oxidation; Fixed Modifications: carbamidomethyl C; Mass Values: monoisotopic; Protein Mass: unrestricted; Peptide mass tolerance: ±20 ppm; Fragment Mass Tolerance: ± 0.6 Da. Proteins were successfully identified on the basis of two or more unique peptides, whose individual ion scores were >29 (the identity score threshold), with a $p < 0.05$.

2.7.6 Pathway enrichment analysis

Selected and verified proteins were entered into a proteomics analysis platform: functional enrichment analysis tool (FunRich) to evaluate common networks that link genes or proteins of interest.

2.8 Metabolomics methods

2.8.1 Extraction and derivatisation of media samples

1 ml samples of conditioned media samples were generated as detailed in section 2.1.4. 50 µl of media was mixed with 150 µl of Methanol and 50 µl Chloroform (a 1:3:1 ratio solution). Samples were centrifuged for 5 min at $0^{O}C$. The supernatant was transferred to 1.5 ml eppendorf tubes containing 100 µl of milliQ H_2O, producing a biphasic solution. Samples were vortexed and centrifuged for a further 5 min at $0^{o}C$. 30 µl of the top layer of the biphasic solution is taken and derivatised using 20 µl of methoxyamine hydrochloride and 20 µl of N, O-Bistrifluoroacetamide (BSTFA) with 1% Trimethylsilyl chloride (TMCS).

2.8.2 Metabolic arrest and extraction of cell lysates

6 well cell culture plates were removed from the incubator; media was aspirated and stored in labeled eppendorf tubes. MilliQ H_2O was placed in each well, gently rocked and aspirated. Cell culture plates were placed on a tray of ice and liquid nitrogen was poured in each well, metabolically arresting cells as it evaporated. Extraction was conducted with the addition of 600 µl of 90% 9:1 Methanol:Chloroform solution to each well. Cells were detached using a cell scraper and cell lysates were collected, spun at 16,000 g at $4^{o}C$ for 3 min. The supernatant was aspirated, 10 µl of internal standard was added to each sample and labeled tubes were taken to Metabolomics Australia (Bio21, Parkville, Australia) on dry ice. Samples were then dried, reconstituted with 50-100 µl of ACN and injected for analysis on either gas-liquid partition chromatography (GLPC) or fast liquid chromatography quadrupole time-of-flight mass spectrometry (LC- QToF-MS).

2.8.3 Threonine supplementation

Threonine supplementation to DMEM (Lonza), Adipogenic and Osteogenic differentiation media (Lonza) was based on the standard threonine concentration of 95.2 mg/L contained in complete DMEM. L-Threonine (Sigma Aldrich) was added to the respective media solutions at the appropriate concentrations and filtered to produce media containing 2-5x the basal threonine concentration.

2.8.4 Threonine labeling and time course

13Carbon stable isotope labeled threonine (Sigma Aldrich) was added to DMEM to achieve x3 concentration of basal levels for threonine. ADSC were cultured in threonine labeled media and cell lysates were produced as described in section 2.8.2. Time course labeling experiments were conducted with labeling time points of 1,5,10 and 30 min as well as 1 h and 24 h time points.

2.8.5 Gas and liquid chromatography analysis

Data was collected and interpreted in collaboration with Metabolomics Australia (Bio 21). Briefly, data was pre-treated with analysis with a raw data matrix. Log transformation was undertaken to account for uneven dispersion, common to metabolomics results. Internal standard and median normalization was undertaken to account for sample-to-sample variation. Statistical analysis was completed utilizing Metabolomics Australia® Package including multi-variate, hierarchal cluster and principal component analysis along with relative log abundance and uni-variate analysis of media only, $ADSC^{CM}$ and RTX- $ADSC^{CM}$ groups.

2.8.6 Metabolic pathway analysis

Significantly altered metabolites were analysed for Kegg Pathway enrichment using platforms such as integrated molecular pathway level analysis (IMPaLA) (491).

2.9 Mouse ear irradiation model

2.9.1 Ethics

All experiments were performed on animals in accordance with the guidelines set by the Animal Ethics Committee (AEC) of St. Vincent's Hospital, Melbourne and the National Health and Medical Research Council of Australia AEC No. 015-15r5.

2.9.2 Strains

All experiments were performed using 6-24 week old male and female PROX-1 Green fluorescent protein (GFP) bacterial artificial chromosome (BAC) transgenic

mice, strain; Tg(Prox-1EGFP) KY221Gsat/Mmcd (IMB Animal Facility, University of Queensland, Australia).

2.9.3 Anesthesia and analgesia

Ketamine 100 mg/ml / Xylazine 20 mg/ml was prepared as 1 ml in each 8 ml of 0.9% normal saline. Mice were weighed prior to irradiation treatment and anaesthetized for ear irradiation (10Gy) or control irradiation (0Gy) using ketamine (44 mg/kg) and xylazine (8 mg/kg), delivered using a 27 gauge diabetic needle intra-peritoneally. Mice were anesthetized for ear wounding (see below) using inhaled anesthetic (isoflurane, (2-chloro-2-(difluoromethoxy)-1,1,1-trifluoro-ethane)) administered in a 15 x 15 x 30 cm custom-made Perspex chamber with rebreathing apparatus, attached to an anesthetic apparatus. A mixture of 4% isoflurane in 3.0 L/min oxygen was administered for 1 minute, and then adjusted to 3% isoflurane in 0.2 L/min oxygen for maintenance.

2.9.4 Irradiation protocol, dosing and positioning

Mice were transported to Peter MacCallum Cancer Centre and anesthetized as described in 2.9.3. Anaesthetized mice were placed, right side lateral, on a custom-made mouse ear irradiation plate (Dr. Jim Hagekyriakou, Department of Physical Sciences, Peter MacCallum Cancer Centre, Australia). The plate ensured isolated single ear irradiation, with a lead shield utilized to protect the remainder of the mouse from gamma ray exposure (Figure 10). Mice received 10Gy irradiation or 0Gy irradiation for controls.

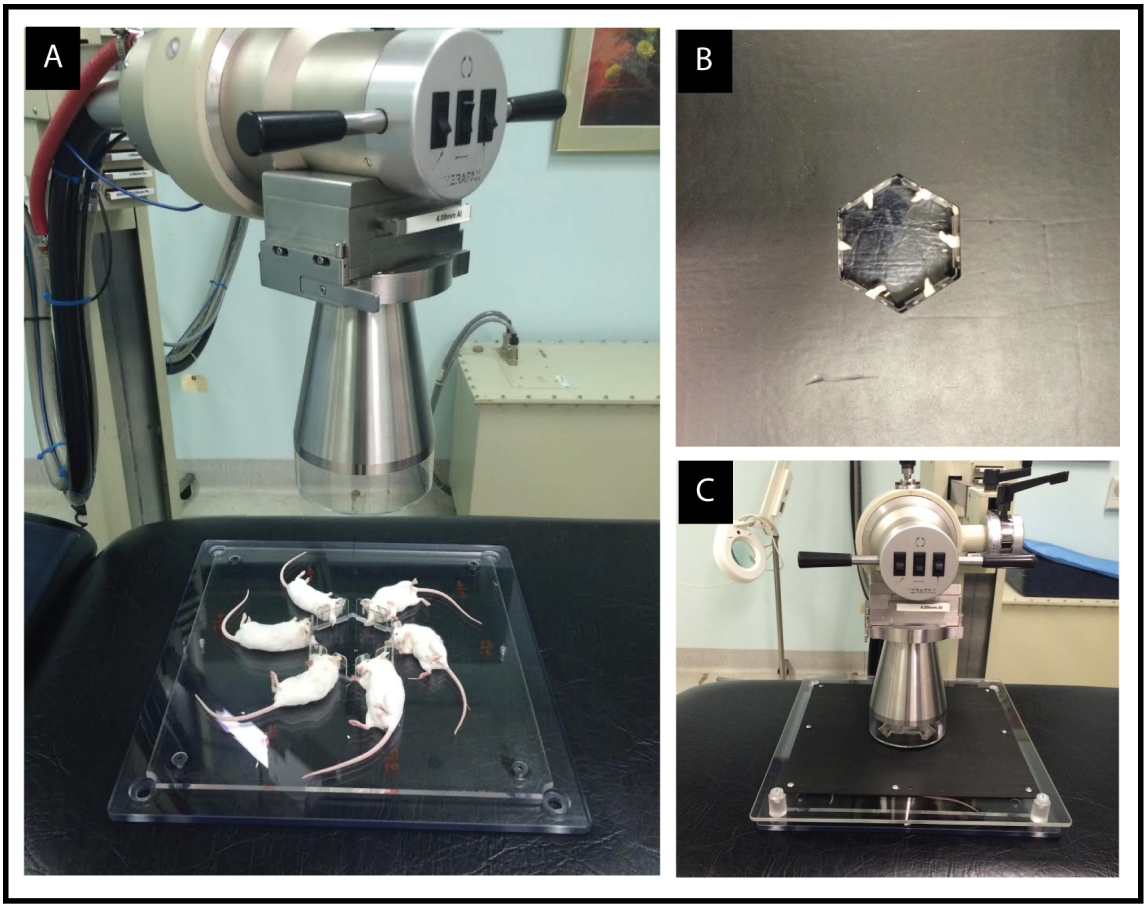

Figure 10

Figure 10 Mouse Ear Irradiation Protocol

(A) Anaesthetised mice were placed in a right side lateral position on the custom-made ear irradiation plate. (B) A lead cover was placed on top, shielding the remainder of the mouse from direct exposure to gamma rays. (C) The external beam radiotherapy device was lowered over the exposed ears, which then received 10Gy of irradiation.

2.9.5 Ear wounding

Both irradiated (right) and control ears (left) of PROX1-GFP mice (IMB, Queensland, Australia) were wounded with a standard 2 mm ear numbering punch. Wounding was conducted 1-3 weeks after irradiation and mice were sacrificed for ear harvest 1-3 weeks after wounding.

2.9.6 Euthanasia

Euthanasia was performed by cervical dislocation by experienced animal facility technicians in accordance with animal ethics guidelines. The staff, in accordance with current regulations and protocols, disposed of carcasses.

2.9.7 Harvest, fixation and preparation of ears for whole-mounting

Ears from deceased mice were harvested using a transverse incision across the base of the ear. Excessive hair was trimmed with scissors. Ears were fixed by immersion in 4% PFA/PBS for 24 h in 4°C in at least five times the volume of the specimen in fluid. Following fixation the ears were changed to a PBS immersion, the cartilage layer was peeled and removed under microscopic vision, leaving the volar epidermal and dermal layers intact for further whole mount analysis (see section 2.9.8).

2.9.8 Imaging and lymphatic vessel quantification

2.9.8.1 Confocal microscopy

Wounded ears were harvested, mounted in 90% Glycerol (Sigma Aldrich, Australia) using a coverwell (Grace Biolabs, USA) and imaged with a Nikon A1R confocal microscope (USA). Images were created by utilizing a Maximum Intensity Projection of the Z stack using ImageJ (NIH, USA). These images were further segmented into a binary skeleton for analysis of vessel morphology parameters including vessel sprouts and branches with the "Analyse Skeleton" plugin as per the protocol described by Arganda-Carreras et al. (492).

2.9.8.2 Quantification of lymphatic vessels

Lymphatic vessel analysis was conducted utilizing ImageJ macro described by Arganda-Carreras et al. (492). Using this method, a skeleton of the lymphatic vasculature was created for quantification from the confocal images. Sprouts were defined as blind ending linear structures (termed end-points in the macro) while branches were defined as vessel segments between branch points (or junctions) of lymphatic vessels. The quantification of Branches/mm^2 was therefore determined to

be indicative of neo-lymphatic sprouting and the formation of a stable lymphatic network.

2.10 Statistical analysis

Statistical analysis of differences between experimental groups and controls were conducted utilizing a Student's *t*-test or one-way ANOVA, with or without multiple group comparisons, where indicated. A p-value <0.05 was considered statistically significant (GraphPad Prism 6.0, California, USA).

3 CHAPTER 3: Characterizing the effects of radiotherapy injury on stromal cells and the mechanisms driving fibrosis and impaired wound healing

3.1 Introduction

The side-effects of radiotherapy are segregated into acute and chronic processes. Firstly, erythema, dry followed by wet desquamation in the initial weeks are the result of large-scale depletion of 10-20 layers of epidermal epithelial cells and their proliferative potential. Dermal necrosis and atrophy occur later and are thought to result from a combination of dermal vascular insufficiency and fibroblast injury, in turn, leading to fibrosis and tissue contracture (56) (194). As in most organs, the skin heals from physical and chemical trauma such as exposure to ionizing radiation through a process of fibrosis, which compensates for tissue regeneration due to a failure of the host defense system to completely eliminate the effects of the injurious agent (493). While the immune system plays a crucial role in the development of fibrosis (9), an understanding of primary effector cells (keratinocytes and dermal fibroblasts), which constitute components of the epidermis and dermis, is also required to investigate the alterations that culminate in the development of radiotherapy-induced fibrosis.

On a molecular level, the cellular response to radiotherapy has generally been characterised as fibroproliferative in nature (122), with repair being initiated by deposition of collagen and other ECM products, which form a patch rather than restoring or regenerating the original tissue (214). This in-effective ‘filling of space’ leads to the eventual manifestation of a spectrum of clinical issues (Figure 11) ranging from scarring, capsular contracture around breast prosthesis (254), limitation of range of joint motion, deficient skin healing manifested as chronic ulceration, poor healing and wound breakdown that may lead to exposure of underlying structures (98). Such chronic ulcerated wounds, require specialised dressing regimes, rigorous antimicrobial therapy and if conservative treatment fails, progress to surgical management. Prior to any reconstruction, debridement and resection of the extensively damaged tissue is required (Figure 11 B,D,G,H), substantially increasing the size of the defect requiring reconstruction. These open wounds necessitate more

complex salvage reconstruction and due to the lack of locoregional options requires recruitment of un-irradiated vascular tissue from a distant site.

In order to characterize the effects of radiotherapy injury on individual cell functions, a set of *in-vitro* experiments was designed to interrogate the effect of gamma irradiation on normal human epidermal keratinocytes (NHEK) and normal human dermal fibroblasts (NHDF) cell proliferation, apoptosis and migration along with NHDF specific functions of adhesion, invasion and contraction. TGFβ has been described as the main molecular mediator of the fibrotic processes (57), as discussed in section 1.9.2. However, the TGFβ super-family is known to have multiple effects on numerous tissues and therefore therapeutic approaches to target this molecule may have insufficient specificity to ameliorate RTX damage (152), without jeopardizing other biological processes to which fibrosis is integral. Therefore, reducing fibrosis to aid in the improvement of the functional integrity of irradiated tissues remains a key focus. More targeted approaches directed at specific downstream signaling may be more effective, rather than pursuing upstream pleiotropic targets (where one gene can influence multiple effects), such as TGFβ alone. Alternatively, investigating molecular dysregulation resulting from radiotherapy injury using Next Generation sequencing platforms, will facilitate the identification of novel candidates offering targeted approaches to ameliorate the fibrotic and debilitating effects of radiotherapy (Figure 11).

3.2 Results - Normal Human Epidermal Keratinocytes (NHEK)

NHEK cultures were established from proliferating cells and cultured in medium containing essential growth factors (see 2.1.1 and 2.1.2). Cells were passaged on reaching 80-90% confluence and utilized for *in-vitro* functional assays between passage 2-6.

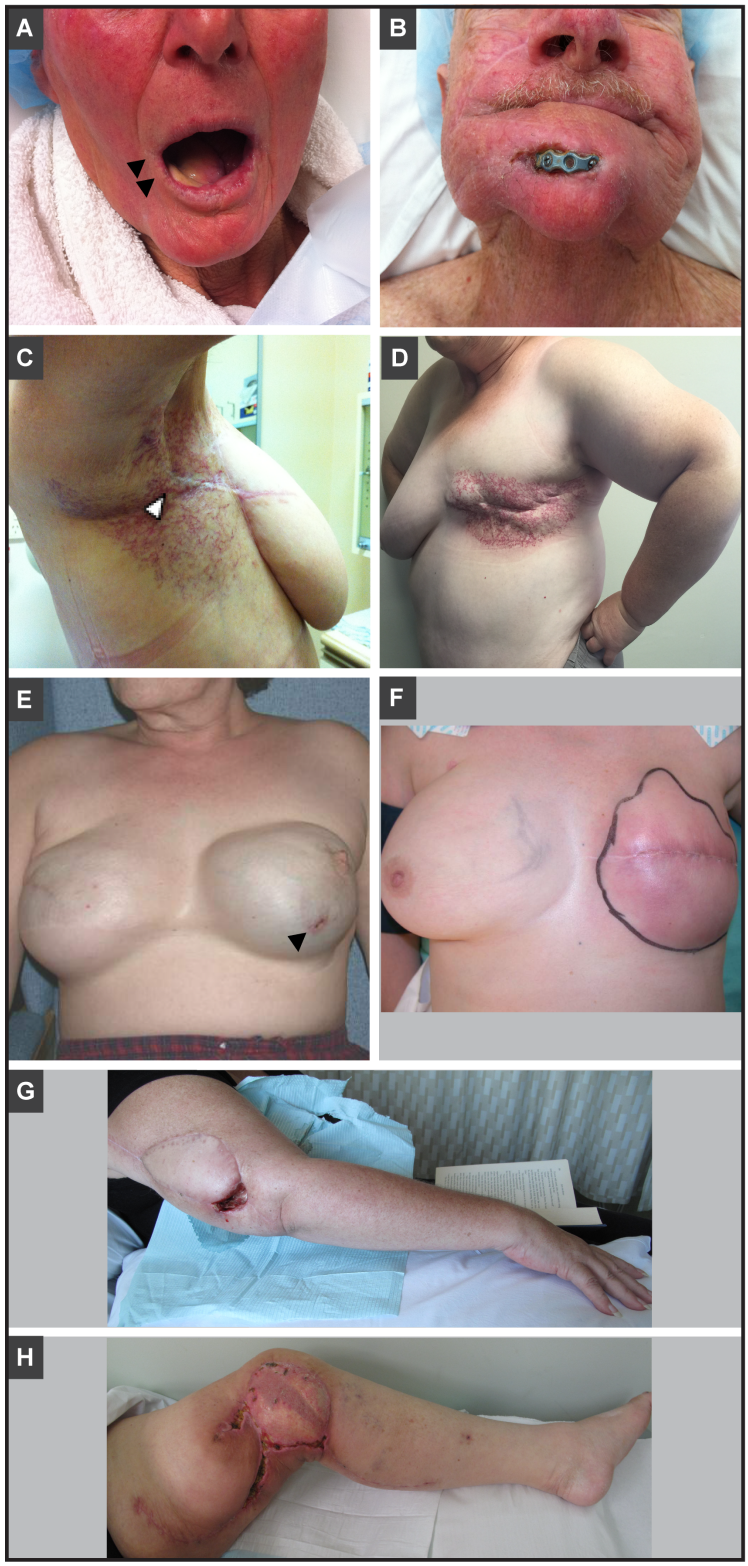

Figure 11

Figure 11 Clinical manifestations of radiotherapy induced soft tissue injury

Clinical photographs demonstrating the spectrum of complications resulting from radiotherapy-induced soft tissue injury to normal tissues. (A) The erythematous reaction seen in tissues, secondary to intraoral tumour radiotherapy, showing the development of scarring and contracture (▲ ▲) of the right lower lip, distorting the oral aperture and leading to oral incompetence. (B) The integrity and compliance of irradiated tissues is compromised, resulting in wound break down and exposure of underlying structures such as bone or metal reconstruction plates. (C) Adjuvant radiotherapy for control of lymph node involvement of cancers from the breast or chest wall resulting in severe scarring, telangiectasia skin change and fibrosis, which can significantly impair the mobility of the upper limb due to axillary contractures (△). (D) Severe desquamation and erythematous reactions to radiotherapy can lead to the formation of significant chest wall scarring, distortion and soft tissue deformity. (E) Radiotherapy of the chest wall causes capsular contractures and pressure necrosis (▲) in an implant-based breast reconstruction. (F) Irradiated tissues demonstrate reduced compliance and tolerance to increased pressure, exemplified by the attempts to expand this skin envelope with a tissue expander. The rigid tissues can then become compromised with superimposed cellulitis. (G) and (H) demonstrate significant issues with wound healing, even in situations where healthy, un-irradiated tissue has been transferred from a distant site of the body to the irradiated field.

3.2.1 Cell survival Dynamics

The effect of radiotherapy on NHEK cell survival was first determined utilizing a survival fraction calculation (see 2.2.1). A set number of cells were seeded in a 24 well plate, left to attach overnight and received irradiation (10Gy) or control treatment (0Gy). 48 h after treatment, viability was determined by cell counting, based on exclusion of trypan blue dye uptake in viable cells with intact cell membranes. Calculation of 0Gy and 10Gy plating efficiency preceded determination of 10Gy NHEK survival fraction, accounting for a degree normal cell loss (for more calculation descriptions see 2.2.1).

Irradiation of NHEK results in a survival fraction of 56%, compared to normal (0Gy) cells, therefore representing a 44% reduction in cell survival of 10Gy NHEK (Figure 12 A,B). To further examine which processes may contribute to this significant reduction in NHEK cell survival, proliferation and apoptosis experiments were conducted (see 2.2.2). To replicate the clinical scenario in which patients receive smaller doses over a protracted period of time, a fractionated experimental group was assigned to receive five 2Gy doses delivered over a 48 h interval, a single dose group was assigned to receive one 10Gy dose and the control group received 0Gy. Briefly, cells were seeded in a white walled 96-well plate, left to attach overnight, with irradiation treatment commencing the following day. CellTitre Glo® (Promega) or Caspase3/7® (Promega) luminescent reagents were added to the wells 48 h post-radiotherapy to determine cell proliferation and apoptotic activity respectively, by obtaining values using a luminometer plate reader (see 2.2.2 for more detailed methodology and settings). NHEK display a significant 29.2 ± 9.4% reduction in proliferation after 2Gy x 5 and a 27.6 ± 7.6% reduction in proliferation after 10Gy irradiation compared with 0Gy controls (Figure 12 C). While the two irradiated regimes significantly reduced NHEK proliferation compared to 0Gy controls, there was no significant difference in the proliferative activity detected between 2Gy x 5 and 10Gy NHEK ($p>0.05$). NHEK apoptotic activity mediated by Caspase 3/7 activation was not significantly altered by fractionated or single dose radiotherapy when compared to control cells at the 48 h time point (Figure 12 D). Therefore, since both groups of irradiation decreased NHEK proliferation and there was no significant difference between the irradiated groups, subsequent experiments were performed with a single dose of 10Gy.

3.2.2 Migration

NHEK migration constitutes an integral part of the wound healing response, allowing for epidermal coverage, reconstituting the skin-surface barrier. The acute erythematous "sunburn-like" effects of radiotherapy in a clinical setting are in part attributed to significant damage to NHEK, resulting in dry/wet desquamation which usually resolves in the 6-8 weeks post-cessation of treatment (119). However, a subsequent insult to a pre-irradiated area, either via minor trauma or re-operation, often leads to the development of a chronic non-healing ulcer resulting from the poor wound healing capacity of the injured tissues (Figure 11) (196). To investigate the effects of irradiation on NHEK migration a two-dimensional scratch wound model was utilized. Cells were seeded on fibronectin coated plates, left to attach overnight before receiving either a single 10Gy dose or control 0Gy. Cells were serum starved 12 h prior to creating the 'wound' (see 2.2.3 for timelines and detailed methodology). Once the wound was created at 0 h (Figure 13 A,D), wells were photographed using standardised bright-field microscopy, and images were quantified on ImageJ to map % gap closure at 6 h intervals over 48 h. The percentage gap closure was calculated relative to the 0 h scratch at all time points and plotted graphically (Figure 13 C). In this assay 10Gy NHEK demonstrated significant impairment in migratory function, uniformly lagging behind 0Gy controls from 6 h timepoint onwards. At 48 h; 0Gy NHEK achieve 90 ± 4.8% gap closure (Figure 13 B), while 10Gy NHEK only achieve 41 ± 6.4% gap closure (Figure 13 E), representing a significant 49 ± 8.0% difference (Figure 13 F).

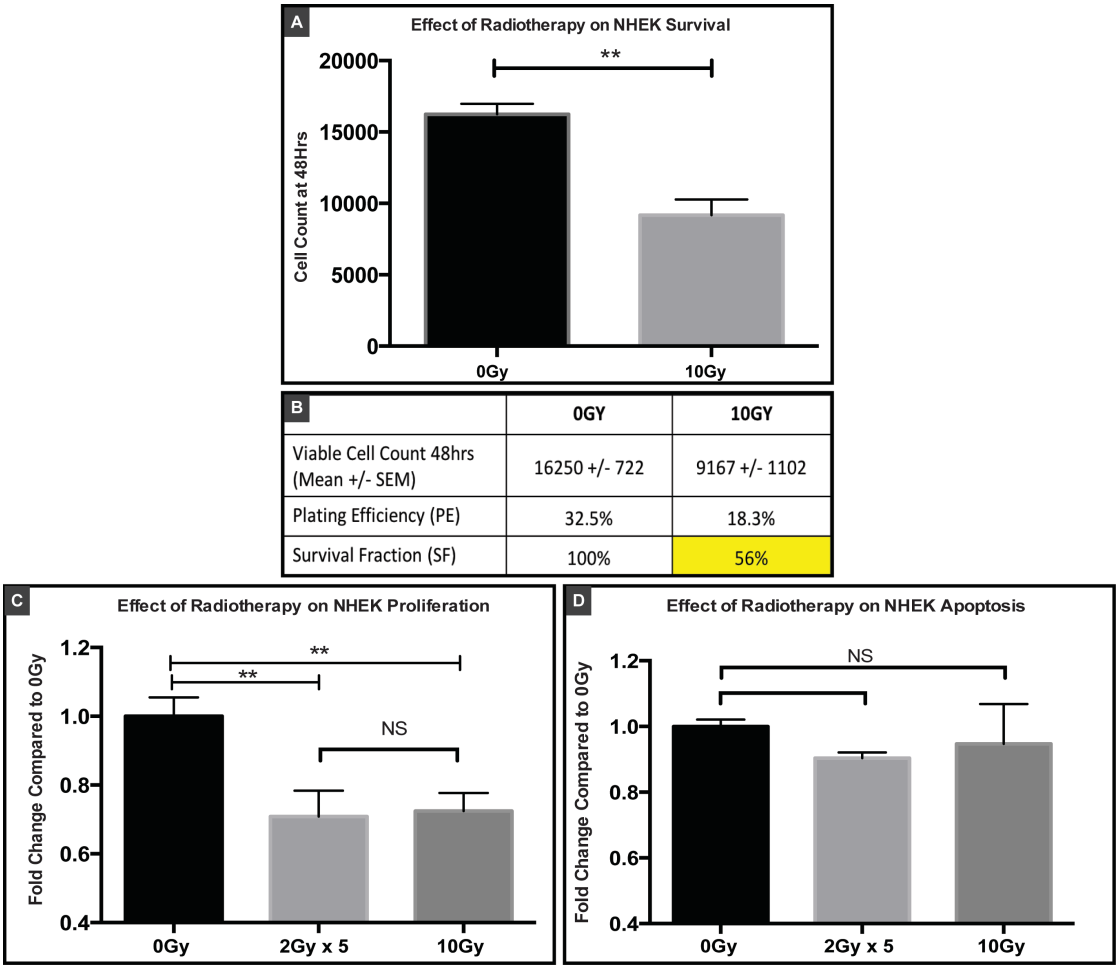

Figure 12

Figure 12 Radiotherapy decreases NHEK cell survival and proliferation without affecting apoptosis

(A) Effect of radiotherapy on NHEK survival represented by viable cell numbers 48 h after irradiation (10Gy) or control (0Gy) treatment. (B) Quantification of 0Gy and 10Gy viable cell counts showed plating efficiency and the survival fraction of 10Gy NHEK was reduced in comparison to 0Gy controls (assuming 100% survival of 0Gy control group cells). The effects of 2Gy x 5 and 10Gy irradiation doses (C) decreased NHEK proliferation without (D) significant alteration in NHEK apoptosis, represented as fold changes compared to 0Gy control groups. Asterisks above bar-graph indicate statistical significance (** = $p<0.01$, NS = not significant), error bars represent (SEM), with $n\geq3$.

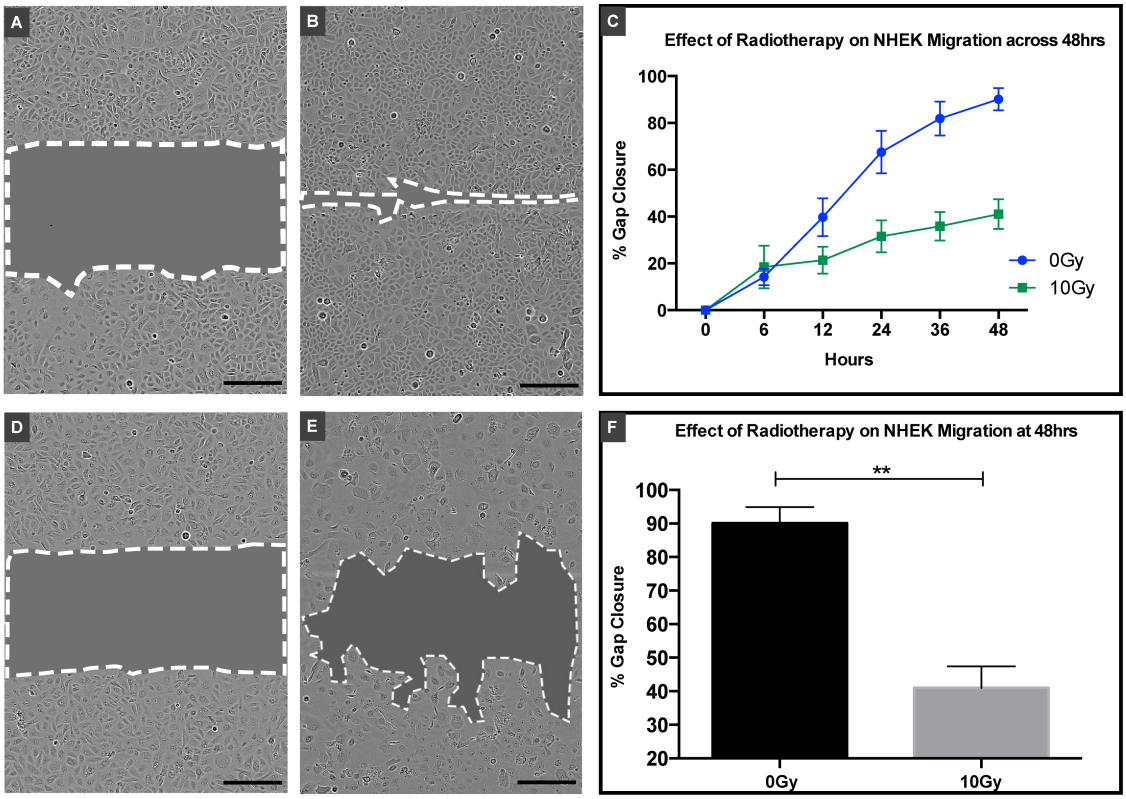

Figure 13

Figure 13 Radiotherapy significantly impairs NHEK migration across 48 h

Bright field imaging (x10 objective) of NHEK every 6 h post creation of a scratch in a two dimensional wound assay on a confluent mono-layer of proliferating cells was conducted. Representative images of 0Gy NHEK at (A) 0 h then (B) 48 h and 10Gy NHEK at (D) 0 h then (E) 48 h were quantified (C) by calculating the % gap closure compared to 0 h controls at 6 h intervals and demonstrated the significantly impaired migratory capacity of 10Gy NHEK. (F) analysis of differences in % gap closure between 0Gy and 10Gy NHEK scratch wound areas at the 48 h end-point graphically displays the severe reduction in 10Gy NHEK migration function. In (A),(B),(D),(E); Scale Bar 300µm, dotted line represents periphery of scratch wound and grey shaded area represents scratch wound area. Asterisks above bar-graph indicate statistical significance (** = $p<0.01$, NS = not significant), error bars represent SEM, with $n\geq3$.

3.3 Results - Normal Human Dermal Fibroblasts (NHDF)

Fibroblasts are key cells involved in both physiological and pathological wound healing responses, with impaired activity leading to poor tensile wound strength and recurrent breakdowns (286), whereas over-activation and excessive extracellular matrix deposition is thought to lead to fibrosis, contracture and scarring (122). In the setting of radiotherapy injury, both these issues are encountered in a pre-irradiated field, therefore the following functional assays were designed to further delineate the effects of radiotherapy injury on dynamic functions on NHDF.

3.3.1 Cell Survival Dynamics

With the same methodology as described for NHEK, the effect of radiotherapy on NHDF cell survival was first determined utilizing a survival fraction calculation (see 2.2.1). A set number of cells were seeded in a 24 well plate, left to attach overnight, received irradiation (10Gy) or control treatment (0Gy) and left in standard culture conditions for 48 h, after which viability was determined by cell counting based on exclusion of trypan blue dye uptake in viable cells with intact cell membranes. Calculation of 0Gy and 10Gy plating efficiency preceded determination of 10Gy NHDF survival fraction, accounting for a degree normal cell loss (for more calculation descriptions see 2.2.1).

Irradiation of NHDF results in a survival fraction of 59% compared to normal (0Gy) cells, therefore representing a 41% reduction in cell survival of 10Gy NHDF (Figure 14 A,B). To further examine which processes may contribute to this significant reduction in NHDF cell survival, proliferation and apoptosis experiments were conducted (see 2.2.2). To replicate the clinical scenario in which patients receive smaller doses over a protracted period of time, a fractionated experimental group was assigned to receive five 2Gy doses delivered over a 48hr interval, a single dose group was assigned to receive one 10Gy dose and the control group received 0Gy. Briefly, cells were seeded in a white walled 96-well plate, left to attach overnight, with irradiation treatment commencing the following day. CellTitre Glo® (Promega) or Caspase3/7® (Promega) luminescent reagents were added to the wells 48 h post-radiotherapy to determine cell proliferation and apoptotic activity respectively, by obtaining values using a luminometer plate reader (see 2.2.2 for more detailed

methodology and settings). NHDF display a significant 16.6 ± 5.1% reduction in proliferation after 2Gy x 5 and a 13.6 ± 3.7% reduction in proliferation after 10Gy irradiation compared with 0Gy controls (Figure 14 C). While the two irradiated regimes significantly reduced NHDF proliferation compared to 0Gy controls, there was no significant difference in the proliferative activity detected between 2Gy x 5 and 10Gy NHDF. NHDF apoptotic activity mediated by Caspase 3/7 activation demonstrated trends of increase that did not reach statistical significance in either fractionated or single dose radiotherapy groups (Figure 14 D). Therefore, since both groups of irradiation decreased NHDF proliferation, with no significant difference between the irradiated groups, subsequent NHDF functional assays were performed with a single experimental dose of 10Gy. This was additionally relevant as 10Gy resulted in sublethal injury in both NHDF and all other cellular components of skin and soft tissue.

3.3.2 Change in cellular morphology

In the process of normal cell culture protocols, a morphological difference was noted between 0Gy and 10Gy NHDF; with irradiated cells displaying an elongated and enlarged phenotype. To quantify this morphological difference, three-dimensional spheroids were formed in 20% methylcellulose and complete DMEM media using non-adherent U-bottom cell culture plates (see 2.2.4.2). Spheroid area was measured 12 h after formation, using standard bright field microscopy and ImageJ software (NIH). The effect of both radiotherapy and number of cells/spheroid on spheroid area was determined by formation of several spheroid variations (Figure 15 A-F). Quantification and statistical analyses using a two-way ANOVA determined that both radiotherapy and cells/spheroid were significant factors in contributing to differences in spheroid area ($p<0.05$). As expected, as cells/spheroid were increased from 5000 to 20,000 cells/spheroid, the area of 0Gy (Figure 15 G) and 10Gy (Figure 15 H) spheroids also significantly increased. However, on comparing 0Gy vs. 10Gy spheroids formed with the same number of cells, 10Gy NHDF spheroids displayed significantly increased area compared to 0Gy controls across all variations of cells/spheroid (Figure 15 I), with a 1.49 ± 0.21 fold increase in area of 10Gy 5000 cells/spheroid, 1.27 ± 0.19 fold increase in area of 10Gy 10,000 cells/spheroid and 1.74 ± 0.17 fold increase in area of 10Gy 20,000 cells/spheroid. Therefore, this

experiment illustrates that irradiation of NHDF results in an increase in cell size, validating the morphological alterations observed in routine cell culture.

3.3.3 Migration

NHDF migration constitutes an integral part of the wound healing response, providing a scaffold, through secretion of various ECM components allowing for the processes of epidermal/dermal wound healing and angiogenic processes to take place (293). To investigate the effects of irradiation on NHDF migration a two-dimensional scratch wound model was utilized, to determine if such functional impairment may contribute to a dysfunctional wound healing response. Cells were seeded on fibronectin coated wells, left to attach overnight before receiving either a single 10Gy dose or control 0Gy. Cells were serum starved 12 h prior to creating the 'wound' (see 2.2.3 for timelines and detailed methodology). Once the wound was created at 0 h (Figure 16 A,D), wells were photographed using standardised bright field microscopy, and images were quantified on ImageJ to map % gap closure at 6 h intervals over 48 h. The percentage gap closure was calculated relative to the 0 h scratch at all time points and plotted (Figure 16 C); with 10Gy NHDF demonstrating an unexpected, significant increase in migratory function, accelerated compared with 0Gy controls from the 0 h onwards. At 48 h; 0Gy NHDF achieve 71 ± 2.8% gap closure (Figure 16B), while 10Gy NHDF achieve 79 ± 3.8% gap closure (Figure 16 E), representing an 8 ± 2.9% difference ($p<0.05$) between the two groups (Figure 16 F).

3.3.4 Invasion

Invasion studies are usually conducted in the context of studying metastases in carcinogenic cell lines. Once a cancer cell acquires metastatic potential, it is able to invade through the basement membrane (the junction between the epithelial structures and meso/endothelial structures), thereby spreading beyond a confined area (494).

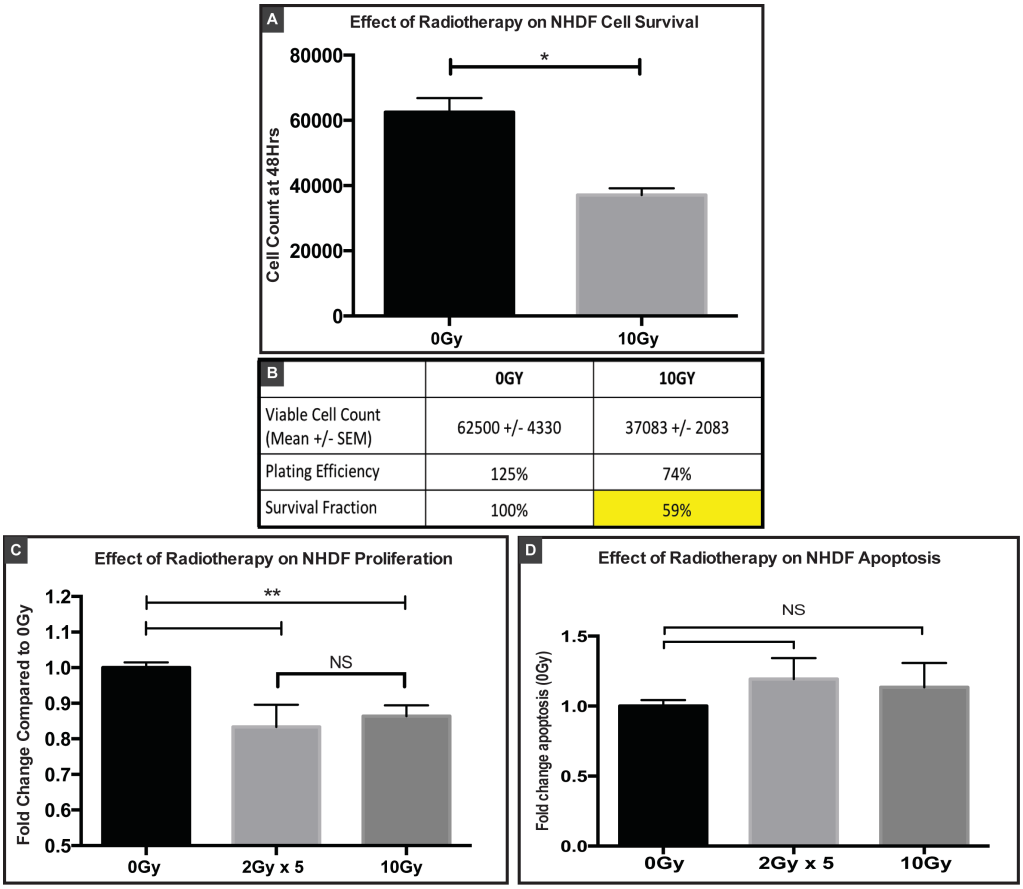

Figure 14

Figure 14 Radiotherapy decreases NHDF cell survival and proliferation without affecting apoptosis

(A) Effect of radiotherapy on NHDF survival represented by viable cell numbers 48 h after irradiation (10Gy) or control (0Gy) treatment. (B) Quantification of 0Gy and 10Gy viable cell counts showed plating efficiency and the survival fraction of 10Gy NHDF was reduced in comparison to 0Gy controls (assuming 100% survival of 0Gy control group cells). The effects of 2Gy x 5 and 10Gy irradiation doses (C) decreased NHDF proliferation without (D) significant alteration in NHDF apoptosis, represented as fold changes compared to 0Gy control groups. Asterisks above bar-graph indicate statistical significance (** = $p<0.01$, NS = not significant), error bars represent SEM, with $n\geq3$.

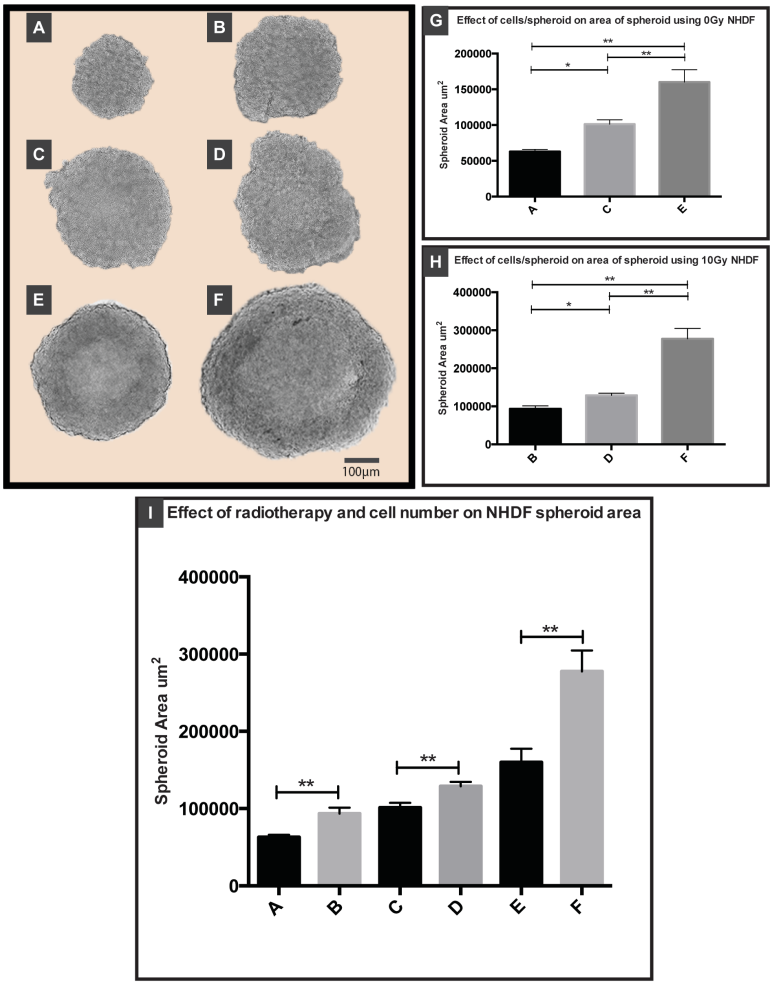

Figure 15

Figure 15 Radiotherapy results in altered cell morphology and increased NHDF cell size in a spheroid model

NHDF spheroids imaged using bright-field microscopy (x10 objective) in the following variations: (A) 0Gy 5000 cells/spheroid, (B) 10Gy 5000 cells/spheroid, (C) 0Gy 10,000 cells/spheroid, (D) 10Gy 10,000 cells/spheroid, (E) 0Gy 20,000 cells/spheroid, (F) 10Gy 20,000 cells/spheroid. (G) Quantification of 0Gy spheroids and the incremental increase in spheroid area as cells/spheroid were increased. (H) Quantification of 10Gy spheroids and the incremental increase in spheroid area as cells/spheroid were increased. (I) Quantification of differences in spheroid areas between 0Gy and 10Gy groups across all cells/spheroid compositions, validating the morphological increase in 10Gy NHDF size with the demonstrable increase in 10Gy spheroids size compared to the relevant 0Gy cells/spheroid control. Scale bar in (A-F) 100 µm, asterisks above bar-graph indicate statistical significance (* = $p<0.05$, ** = $p<0.01$, NS = not significant), error bars represent SEM, with $n\geq3$.

The composition of the extracellular matrix is largely regulated by stromal cell populations such as fibroblasts (494), which have the capacity to govern the microenvironment to make it favorable for processes such as proliferation, differentiation, adhesion and migration in both physiological and pathological settings (495). Shelton et al. demonstrated that in a senescent state, fibroblasts have a comparative RNA profile to a state of inflammation, with up-regulation of factors such as IL-1, IL-15, MCP-1, Gro-α, perhaps contributing to an impaired wound healing response if such stimulation persists (495)., Papadopoulou et al. further demonstrated the interaction of irradiation-induced senescent fibroblasts with lung cancer cell lines in SCID mice accelerated tumour growth through alterations in the ECM composition, particularly with up-regulation of MMPs 1, 2 and 3 (496). Tsai et al. demonstrated a similar phenomenon in the setting of breast cancer cells with up-regulation of MMPs 3, 7, 9, 10 and 12, with concurrent increased collagenolysis activity (497). In contrast, other studies have shown no significant impact on the growth of breast cancer cells when co-cultured with irradiated fibroblasts (498). Together these findings suggest that the interaction between irradiated stromal and cancer cells may have variable responses dependent on body site or may be a dynamic system in flux when investigated at different time points. As detailed in sections 3.2, 3.3.1 and 3.3.3, radiotherapy significantly alters NHDF morphology (with an elongation and increase in cell size) as well as increasing their migration capacity in a two dimensional setting, therefore, further investigation of cell migration in relation to an ECM interface was sought to interrogate characteristics of migration and/or invasion.

Cultrex® 3D Spheroid BME cell invasion assay was utilized according to manufacturer's directions to investigate the effects of radiotherapy on NHDF outgrowth and invasion. The spheroid and subsequent cellular outgrowths were captured using bright-field microscopy at and followed for a period of 11 days post-seeding. Morphological comparisons between 0 and 10Gy cell outgrowths were observed and recorded by a blinded observer, as well as quantification of cell outgrowth area using a thresholding technique in ImageJ (NIH) (see section 2.2.6 for further methodology).

0Gy NHDF demonstrated cell outgrowth at day 1, progressing symmetrically from the central cell mass, peaking at day 9 and then slowly regressing (Figure 17 A,B). 10Gy NHDF demonstrated cell outgrowth from day 1, more noticeable from day 2 onwards from a denser central cell mass with disordered outgrowth patterns displaying asymmetry and increased fragmentation (Figure 17 A,C). On quantification of spheroid outgrowth areas, 0Gy NHDF demonstrate a significantly greater area of outgrowth across 11 days when compared to 10Gy NHDF (Figure 17 D).

3.3.5 Adhesion

Collagen-I is a major structural component of human skin, constituting around 80% of the collagen constituents and provides necessary tensile strength (127). Therefore, due to its abundance in normal tissues, a human collagen-I ECM was used to coat 96 well plates at varying concentrations from 0 ng/ml (control) to 5 ng/ml to assess the effects of radiotherapy on the adhesive properties of NHDF 48 h after 10Gy irradiation and 0Gy control treatment. Adhesion of 10Gy NHDF at all concentrations of collagen-I was increased compared to 0Gy NHDF controls (Figure 18 A), demonstrated with crystal violet staining of adherent cells (for detailed methodology see section 2.2.7). The magnitude of change was quantified with spectrophotometer readings at 540nm after solubilisation of the crystal violet stain with sodium hydrogen carbonate (Figure 18 B) across all concentrations. 10Gy NHDF demonstrated a significant 49 ± 15% increased adherence when compared to 0Gy controls one hour after of seeding onto a 5 ng/ml Collagen-I matrix (Figure 18 C).

3.3.6 Contraction and alpha-smooth muscle actin expression (αSMA)

After demonstrating that radiotherapy is able to increase NHDF 2D migration, create disordered patterns of cell outgrowth in a 3D matrix and increase adherence to a collagen-I matrix, the effect on the contractility of NHDF was investigated. Clinical manifestations of radiotherapy injury such as capsular contracture (254) in the breast suggest there is a physical traction that cumulatively leads to such mechanical distortion of tissue (see Figure 11 A-E). An *in-vitro* model was designed to interrogate the processes of NHDF mediated contraction.

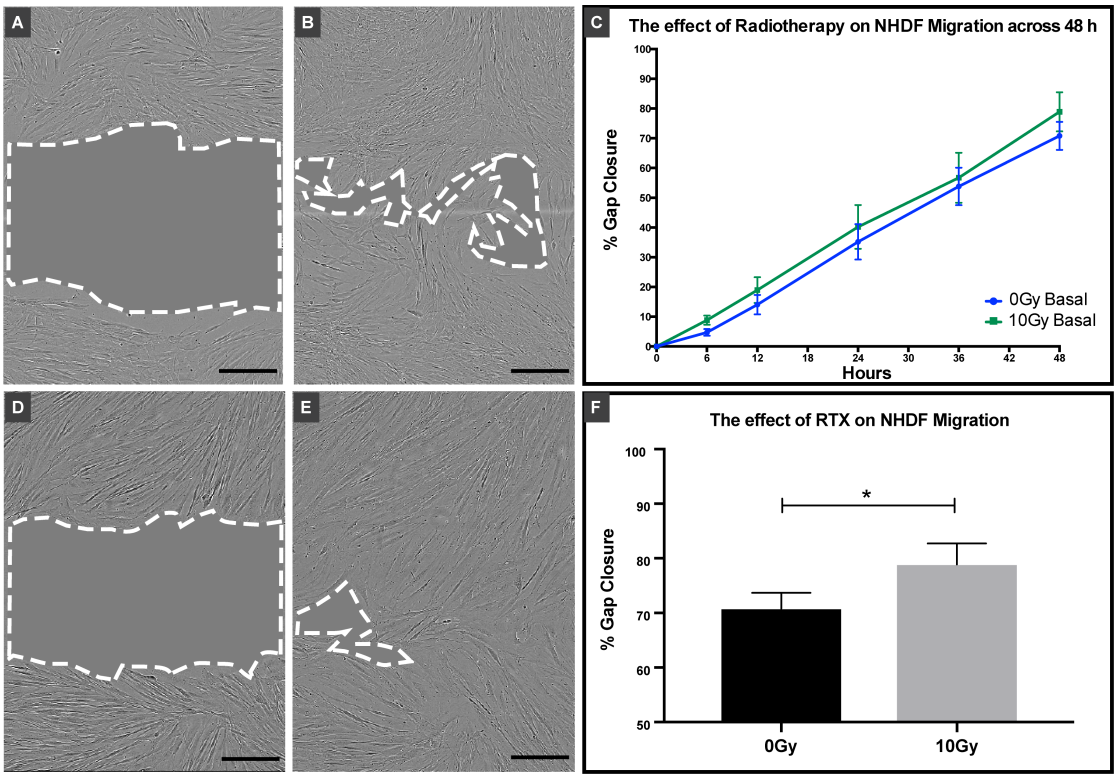

Figure 16

Figure 16 Radiotherapy significantly increases the migratory capacity of NHDF across 48 h

Bright field imaging (x10 objective) of NHDF every 6 h post creation of a scratch in a two dimensional wound assay on a confluent mono-layer of proliferating cells was conducted. Representative images of 0Gy NHDF at (A) 0 h then (B) 48 h and 10Gy NHDF at (D) 0 h then (E) 48 h were quantified (C) by calculating the % gap closure compared to 0 h controls at 6 h intervals and demonstrated the increased migratory capacity of 10Gy NHDF across all time-points. (F) analysis of differences in % gap closure between 0Gy and 10Gy NHDF scratch wound areas at the 48 h end-point graphically demonstrates the unexpected increase in migration of 10Gy NHDF. In (A),(B),(D),(E); Scale Bar 300µm, dotted line represents periphery of scratch wound and grey shaded area represents scratch wound area. Asterisks above bar-graph indicate statistical significance (* = $p<0.05$), error bars represent SEM, with $n\geq3$.

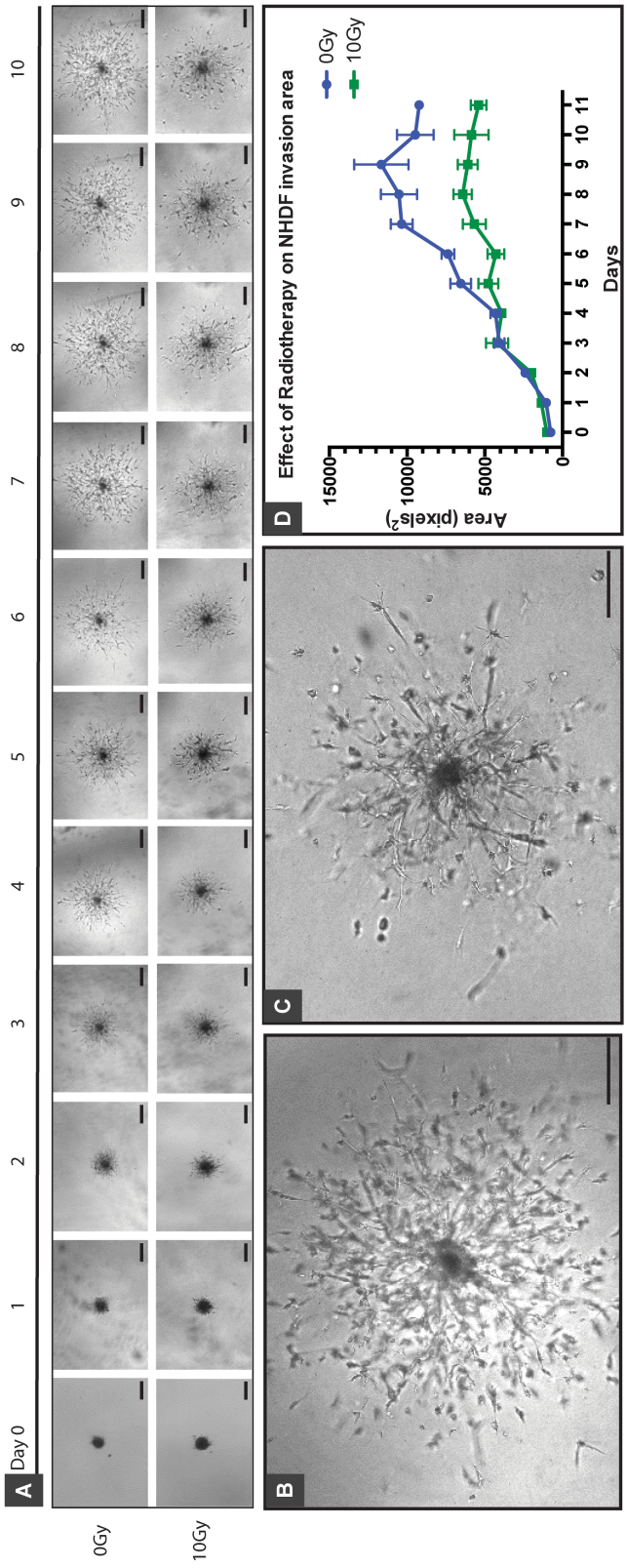
A
Day 0
1
2
3
4
5
6
7
8
9
10
0Gy
10Gy
B
C
D
Effect of Radiotherapy on NHDF invasion area
0Gy
10Gy
Area (pixels²)
15000
10000
5000
0
0 1 2 3 4 5 6 7 8 9 10 11
Days

Figure 17

Figure 17 Radiotherapy results in disordered NHDF outgrowth patterns in a 3D invasion model

(A) Representative images of 0Gy and 10Gy NHDF spheroid cell outgrowth morphology photographed at x4 objective using bright field microscopy across 10 days. (B) 0Gy NHDF cell outgrowth captured at Day 11 demonstrating a symmetrical pattern of invasion migrating from a central core of cells. (C) 10Gy NHDF cell outgrowth captured at Day 11 demonstrating asymmetrical and disordered sprouting from a denser central core of cells. (D) Quantification of cell outgrowth areas across 11 days, with day 11 results demonstrating 0Gy NHDF outgrowths measured as 6485 ± 1117 $pixel^2$ compared to 4260 ± 539 $pixel^2$ area in 10Gy NHDF ($p<0.05$, Student's T-Test). A two-way ANOVA demonstrated that day number and radiotherapy respectively contributed to 68% and 11% of the variation in spheroid outgrowth area ($p<0.01$). Scale Bar (A-C) 200 μm. Error bars represent SEM, with $n\geq3$.

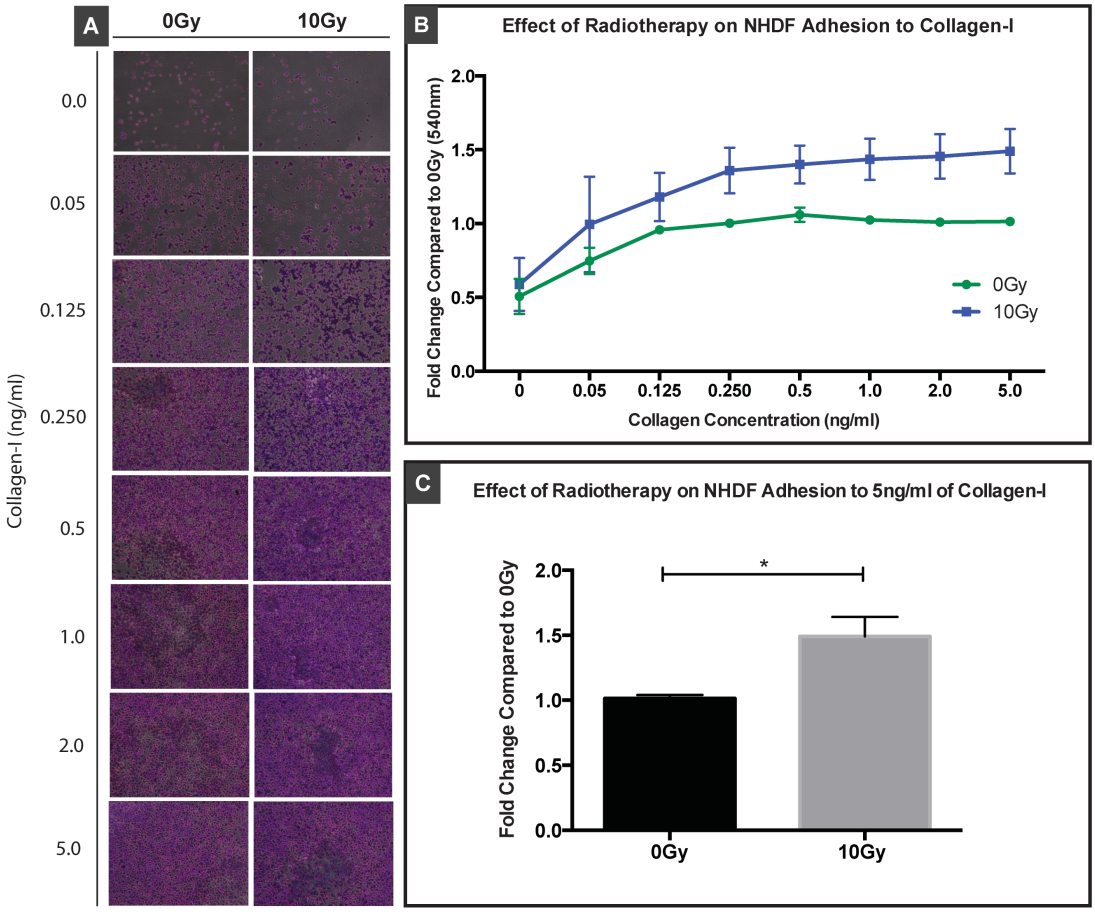

Figure 18

Figure 18 Radiotherapy results in increased NHDF adhesion to a collagen-I matrix

(A) Representative images of crystal violet staining of 0Gy and 10Gy NHDF plated on varying collagen-I matrix concentrations ranging from 0 to 5 ng/ml. The staining demonstrates a global increase in the number of adherent 10Gy NHDF cells at all collagen-I concentrations compared to 0Gy controls with (B) quantification of adherent cells by solubilisation of crystal violet and spectrophotometric analysis at 540nm. (C) At the highest concentration of 5 ng/ml collagen-I tested, 10Gy NHDF demonstrate significantly increased adhesion compared to 0Gy controls. Asterisks above bar-graph indicate statistical significance (* = $p<0.05$), error bars represent SEM, with $n\geq3$.

0Gy and 10Gy NHDF (48 h after irradiation) were seeded at a 500,000 cell/well density in 24 well plates, pre-mixed with 200µl of collagen-I matrix (see section 2.2.8 for more details). The gel was allowed to set before the addition of cell culture media and then cultured at 37ºC for 48 hours. The gel was then gently released from the circumference of the well and allowed to free float in cell culture media for a period of 24 hours. Standardised photographs were taken from a mounted camera, with additional photographs taken at x2 objective using brightfield microscopy. The area of the collagen gel was traced and represented as a 10Gy vs 0Gy fold change. 10Gy NHDF collagen-I gels, (Figure 19 B), demonstrated a 16.9% increased contraction in comparison to 0Gy NHDF Collagen-I gel controls (Figure 19 A,C). This suggests that irradiation does play a role in increasing contractility of NHDF, but the molecular mechanisms that govern this process require further investigation.

The finding of increased fibroblast contractility resulting from radiotherapy injury may be linked to the hypothesis of fibroblast to myofibroblast transformation, characterised as a prominent feature in many fibro-proliferative pathologies (493). Resident fibroblasts found in un-injured tissues are thought to produce small amounts of ECM, but once challenged by inflammatory or injurious stimuli, become 'activated' or transform into myofibroblasts (499). In doing so they acquire the expression of αSMA which imparts a robust contractile ability along with altered ECM regulation (500). Myofibroblasts are thought to play a crucial role in the latter processes of normal wound healing, providing timely contraction of the wound followed by apoptotic clearance (119).

Nevertheless, in pathological conditions such as radiotherapy injury, a chronically inflamed microenvironment allows the actions of myofibroblasts to persist leading to an excessive ECM deposition and contraction of the injured tissues (493,499). Alternatively, irradiated fibroblasts may differentiate into post-mitotic fibroblasts, exhibiting low proliferative capacity and altered ECM metabolism (106,499), which may represent another cell sub-type implicated in the chronic and progressive development of tissue fibrosis.

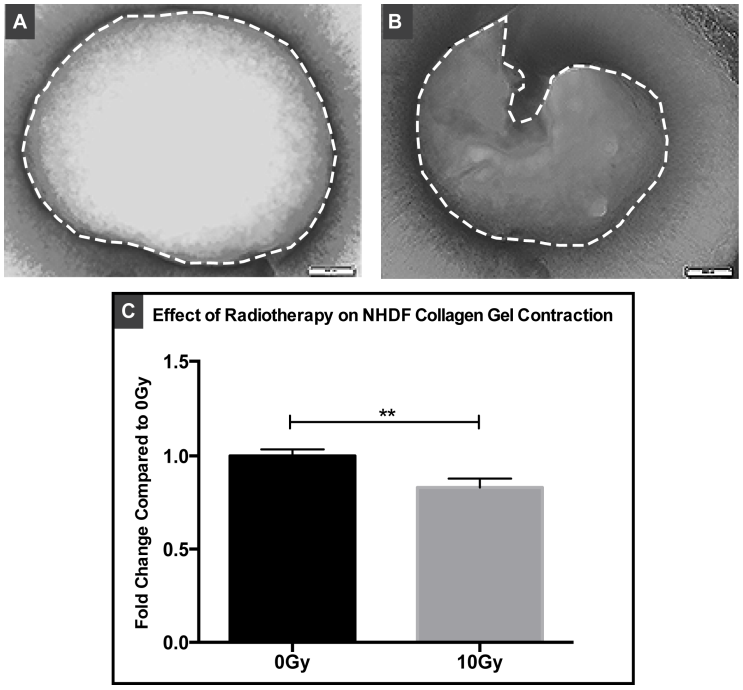

Figure 19

Figure 19 Radiotherapy increases the contractility of NHDF

Fixed collagen-I gels were released circumferentially from well edges 48 h after seeding with (A) 0Gy NHDF and (B) 10Gy NHDF, allowed to float in media and contract over 24 h. (C) Quantification of gel areas demonstrated a significant 16.9% reduction in 10Gy NHDF collagen-I gel area, which was deemed representative of an increased contractile ability compared to 0Gy NHDF gels. Scale bar (A, B) 500 μm. Asterisks above bar-graph indicate statistical significance (** = $p<0.01$), error bars represent SEM, with $n\geq3$.

In order to examine expression of αSMA as a result of radiotherapy injury to NHDF, cells were plated on cell culture slides, allowed to attach overnight and subsequently treated with either 10Gy or 0Gy (control) doses of radiotherapy. Cells were fixed with 4% PFA 48 h after injury and stained with anti-αSMA antibody (see section 2.6.4 for more details). ICC staining of 0Gy NHDF demonstrated little αSMA staining, when present, located at the periphery of the cytoplasm (Figure 20 A,C). 10Gy NHDF demonstrated moderate expression of αSMA which uniformly spanned the cytoplasm of cells expressing this protein (Figure 20 B,D). Both 0Gy and 10Gy NHDF exhibited

heterogeneous expression of αSMA, which appeared more prominent in the irradiated cells, however this difference was not quantified. To examine if the expression of αSMA was altered in irradiated vs. normal skin tissue samples from patients' undergoing delayed reconstructive after radiotherapy treatment; IHC αSMA staining of 10 matched skin samples was undertaken (as described in section 2.6). Normal tissues demonstrated αSMA staining of epidermal and dermal structures with moderate staining of perivascular structures (Figure 20 E,G). Such staining is likely accounted for by the baseline expression in vascular smooth muscle cells or pericytes known to express αSMA (501). Irradiated skin samples however, demonstrated moderate staining of epidermal and dermal structures (increased relative to their matched normal controls), with strong αSMA staining of perivascular structures Figure 20 F,H). Although IHC findings were not specifically quantified, they were discussed through personal correspondence with a pathologist. IHC of the tissue samples did not demonstrate a large increase in dermal αSMA expression in irradiated specimens, therefore a marker more specific to NHDF radiotherapy-injury rather than αSMA (involved in numerous pathological models of fibrosis) is required. (499). The observed increased perivascular staining in irradiated tissues, is however, in line with findings by Milliat et al., who demonstrated *in vitro* that co-culture of irradiated endothelial cells with irradiated vascular smooth muscle cells lead to RNA and protein level increases in αSMA expression (164), perhaps contributing to a component of vascular injury resulting from radiotherapy.

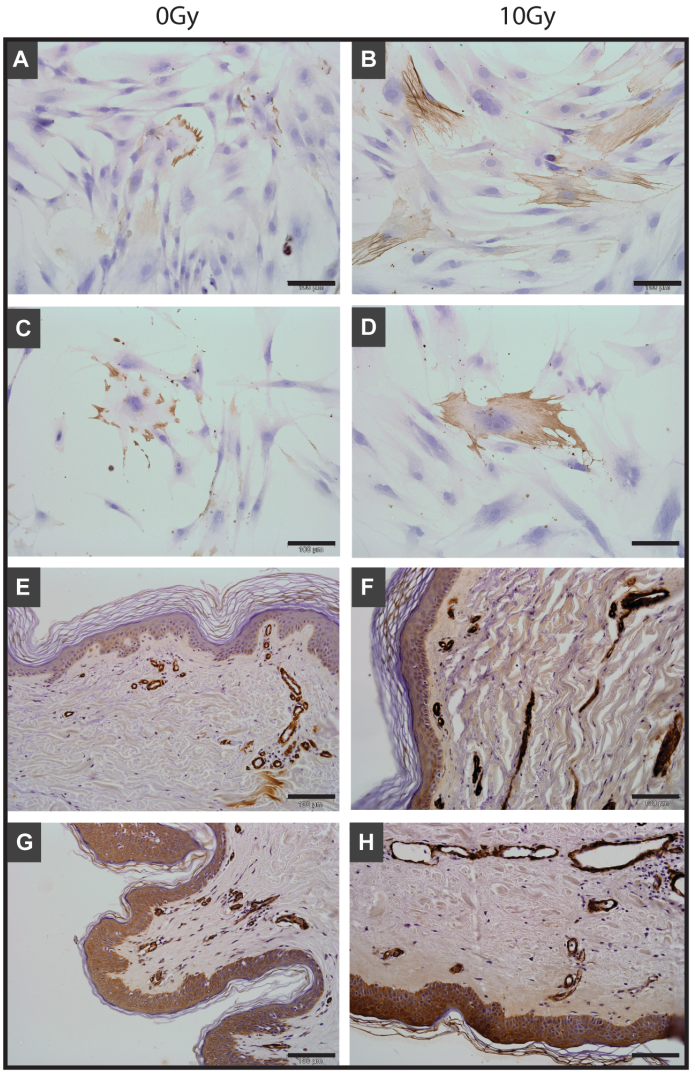

Figure 20

Figure 20 Radiotherapy alters the distribution of αSMA expression in NHDF *in-vitro* and increases the perivascular expression in irradiated tissue samples

Images of immunocytochemical staining of tissue culture slides at x20 objective with 0Gy NHDF (A,C) and 10Gy NHDF (B,D) with anti-αSMA antibody demonstrate the expression and distribution of αSMA changes in NHDF 48 h after 0Gy or 10Gy irradiation. 10Gy NHDF (B,D) display more uniform expression of αSMA. Images of immunohistochemical staining (x20 objective) of sections from normal human skin (E,G) with patient-matched irradiated skin samples (F, H) with anti-αSMA antibody, demonstrating a slight increase in dermal and moderate increase in perivascular αSMA staining (not quantified). Scale bars (A-D) 50 μm, (E-H) 100 μm, with n≥3.

3.4 Results - The molecular effects radiotherapy injury on NHEK and NHDF

3.4.1 Next Generation Sequencing

Next Generation Sequencing RNA analysis was conducted on both NHEK and NHDF to interrogate the changes that occur at a molecular level after radiotherapy induced injury. This technique served as a robust tool to examine the underlying pathways that may drive tissue fibrosis and impaired wound healing in the setting of irradiation, with aims to identify a distinct set of alterations in gene expression that distinguish irradiated cells from normal cells.

Standardised numbers of NHEK and NHDF were plated in cell culture flasks and irradiated once 80-90% confluence was achieved, to mimic intact skin. RNA extraction was undertaken at 4 h using the QIAGEN, Germany® RNEasy Plus Universal Kit as per manufacturer's instructions. Samples were then tested for purity and quality control using the Nanodrop^{TM} Spectrophotometer (Thermo Fischer Scientific, USA) and stored at -80^{o}C, till further processing. The 4 h time point of extraction was chosen to capture early RNA signaling changes in response to radiotherapy injury, which in the setting of chronic radiotherapy injury are thought to persist or propagate via downstream signaling cascades (54), further supported by findings from Dickey et al. who demonstrated the clusters of molecular alterations at 30 minutes, 48 h and 7 days post-radiotherapy in airway epithelial cells did not display markedly different profiles (502). Each sample underwent RNA sequencing (100 base pair single end) in the Illumina HiSeq machine at the Australian Genome Research Facility (AGRF) and results were presented in a series of spreadsheets and heat maps along with a comprehensive pathway analysis platform (see 2.3.4, 2.3.5 for detailed methodology). Next generation sequencing demonstrated several significant differences between the expression profiles of 10Gy NHEK and NHDF in comparison to their un-injured 0Gy controls (see Table 10 and Table 11). 10Gy NHEK significantly altered the expression of 24 genes at 4 hours, while 10Gy NHDF demonstrated alteration in 86 genes at 4 hours, with adjusted p-values <0.05.

Gene ID	Symbols	Gene Name	Chr	logFC
29950	SERTAD1	SERTA domain containing 1	19	0.681680153
55294	FBXW7	F-box and WD repeat domain containing 7, E3 ubiquitin protein ligase	4	0.654743835
7748	ZNF195	zinc finger protein 195	11	0.673408439
4851	NOTCH1	notch 1	9	0.849687712
54149	C21orf91	chromosome 21 open reading frame 91	21	0.911456154
168002	DACT2	dapper, antagonist of beta-catenin, homolog 2 (Xenopus laevis)	6	-1.103338917
29965	CDIP1	cell death-inducing p53 target 1	16	0.55328094
1026	CDKN1A	cyclin-dependent kinase inhibitor 1A (p21, Cip1)	6	1.030192809
23072	HECW1	HECT, C2 and WW domain containing E3 ubiquitin protein ligase 1	7	2.605199697
94241	TP53INP1	tumor protein p53 inducible nuclear protein 1	8	0.947398613

Table 10 Top ten NHEK Next Generation Sequencing Candidates

Top ten gene candidates from next generation sequencing analysis demonstrating the molecular alterations between 10Gy NHEK in comparison to 0Gy controls, 4 hours after radiotherapy injury (adjusted p values <0.01). Chr = chromosome, logFC = log fold change.

Gene ID	Symbols	Gene Name	Chr	logFC
1026	CDKN1A	cyclin-dependent kinase inhibitor 1A (p21, Cip1)	6	2.408406671
57103	C12orf5	chromosome 12 open reading frame 5	12	1.240482462
1647	GADD45A	growth arrest and DNA-damage-inducible, alpha	1	1.1753191
9518	GDF15	growth differentiation factor 15	19	2.17051098
29950	SERTAD1	SERTA domain containing 1	19	0.916230849
8793	TNFRSF10D	tumor necrosis factor receptor superfamily, member 10d, decoy with truncated death domain	8	1.095429396
94241	TP53INP1	tumor protein p53 inducible nuclear protein 1	8	1.413796463
4193	MDM2	Mdm2, p53 E3 ubiquitin protein ligase homolog (mouse)	12	1.922298682
8493	PPM1D	protein phosphatase, Mg2+/Mn2+ dependent, 1D	17	1.394962714

Table 11 Top ten NHDF Next Generation Sequencing Candidates

Top ten gene candidates from next generation sequencing analysis demonstrating the molecular alterations between 10Gy NHDF in comparison to 0Gy controls, 4 hours after radiotherapy injury (adjusted p values <0.01).

Amongst the top ten altered RNA candidates found in 10Gy NHEK, NHDF or both, genes of interest included CDKN1A, GADD45A, TP53INP1, SESN1, MDM2 which all play a role in cell cycle regulation/arrest, DNA damage response and repair by exerting anti-oxidant, anti-proliferative and pro-apoptotic effects (503). Pathview analysis demonstrated that NHEK (Figure 21 A) and NHDF (Figure 21 B) display significant enrichment of genes in the p53 signaling pathway, which may be primarily accountable for the functional alterations of significantly reduced cell survival fractions and cell proliferation as demonstrated in sections 3.2.1 and 3.3.1. Additionally, with experimental findings that radiotherapy did not significantly result in caspase 3/7 mediated apoptosis, up-regulated candidates such as CDKN1A (aka. p21) and GADD45, which feed into pathways of cell cycle arrest, may provide an explanation of cellular senescence without large scale cell death.

3.4.2 Notch-1

The highly conserved NOTCH-1 signaling system regulates cell-fate determination (504) and was found to be significantly up regulated in both NHEK and NHDF after irradiation. NOTCH-1 mediated signaling takes place with binding of Jagged or Delta-family ligands leading to proteolytic cleavage and release of Notch intracellular domain (NICD) with translocation to the nucleus for transcriptional regulation (505). Its more traditional roles include multi-system organ development with abilities to induce differentiation or maintain a state of un-differentiation as required (505). Several studies have demonstrated that NOTCH-1 plays a crucial role in facilitating EMT (506) and myofibroblastic transformation of fibroblasts, with inhibition of NOTCH-1 signaling leading to improvement in fibro-proliferative conditions such idiopathic pulmonary fibrosis, scleroderma and systemic sclerosis (507) (508). Therefore, to further interrogate NOTCH-1 upstream and downstream signaling in NHDF, a customized PCR array plate for the NOTCH pathway signaling (QIAGEN, Germany) was used. Four matched NHDF samples underwent RNA extraction 4 h post 10Gy or 0Gy (control) treatment using the QIAGEN, Germany® RNEasy Plus Universal Kit as per manufacturer's instructions. Samples were then tested for purity and quality control using the Nanodrop^{TM} Spectrophotometer (Thermo Fischer Scientific, USA) and stored at -80^{o}C, till further processing. Samples were added to the 384-well pre-primed NOTCH-1 PCR plate (see section 2.3.3.2 for more details).

The Notch pathway plate analysis was able to validate genes found to be altered on next generation sequencing such as CDKN1A, demonstrating a large 4.72 fold increase in expression after irradiation of NHDF in comparison to 0Gy controls. Other candidates significantly up-regulated such as c-Fos induced growth factor (FIGF, also known as VEGF-D), glycogen synthase kinase 3 beta (GSK3B), Nicastrin (NCSTN) and sel-1 suppressor of lin-12 like (SEL1L) represented candidates not found to be significantly altered on the initial next generation screening platform. Interestingly, Notch-1 demonstrated a 1.56 fold increase in expression, but did not reach statistical significance in RNA samples used in the NOTCH pathway analysis plates.

3.4.3 Extracellular Matrix Proteins

To further investigate altered irradiated NHDF functions and the molecular processes which may drive these changes, four matched NHDF underwent RNA extraction 48 h after 10Gy or 0Gy (control) irradiation, to correlate with functional assay end-points. The QIAGEN, Germany® RNEasy Plus Universal Kit as per manufacturer's instructions for RNA extraction and purification, with samples then tested for purity and quality control using the Nanodrop™ Spectrophotometer (Thermo Fischer Scientific, USA) and stored at -80°C, till further processing. 10Gy NHDF RNA samples with matched 0Gy controls were added to the 384-well pre-primed ECM PCR plate (see section 2.3.3.2 for more details), designed specifically to test for selected genes involved in ECM regulation.

Six ECM genes were found to be significantly up-regulated in 10Gy NHDF in comparison to their 0Gy controls 48 h after irradiation (Figure 23 B). Collagens 4A2, 7A1 and 8A1 demonstrated a 1.41, 1.51 and 2.14-fold increase in irradiated NHDF compared to controls, respectively. Laminin C1 demonstrated a 1.64-fold increase while members of the MMP family subtypes 2 and 11 showed a 2.07 and 2.31-fold increase, respectively, as a result of irradiation of NHDF. While numerous studies have hypothesized that radiotherapy induced fibrosis results from increased ECM deposition and decreased degradation (301), few studies have specifically looked at the exact changes in composition. The alterations in ECM composition responsible for the clinical effects of radiation fibrosis, most commonly described in IHC studies

include increased Collagen I and III, MMP-2 and MMP-9, TIMP 1 and 2 (see section 1.9.4) (509) (215) (121) while connective tissue growth factor is thought to contribute to intestinal radiotherapy injury (499). These specific alterations in NHDF ECM gene expression resulting from radiotherapy (Figure 23 A,B) provide a clearer mechanistic understanding of the molecular mechanisms that may drive the functional cellular alterations in irradiated NHDF leading to disordered migration and invasion along-with increased adhesion and contraction, discussed in detail below (see 3.5).

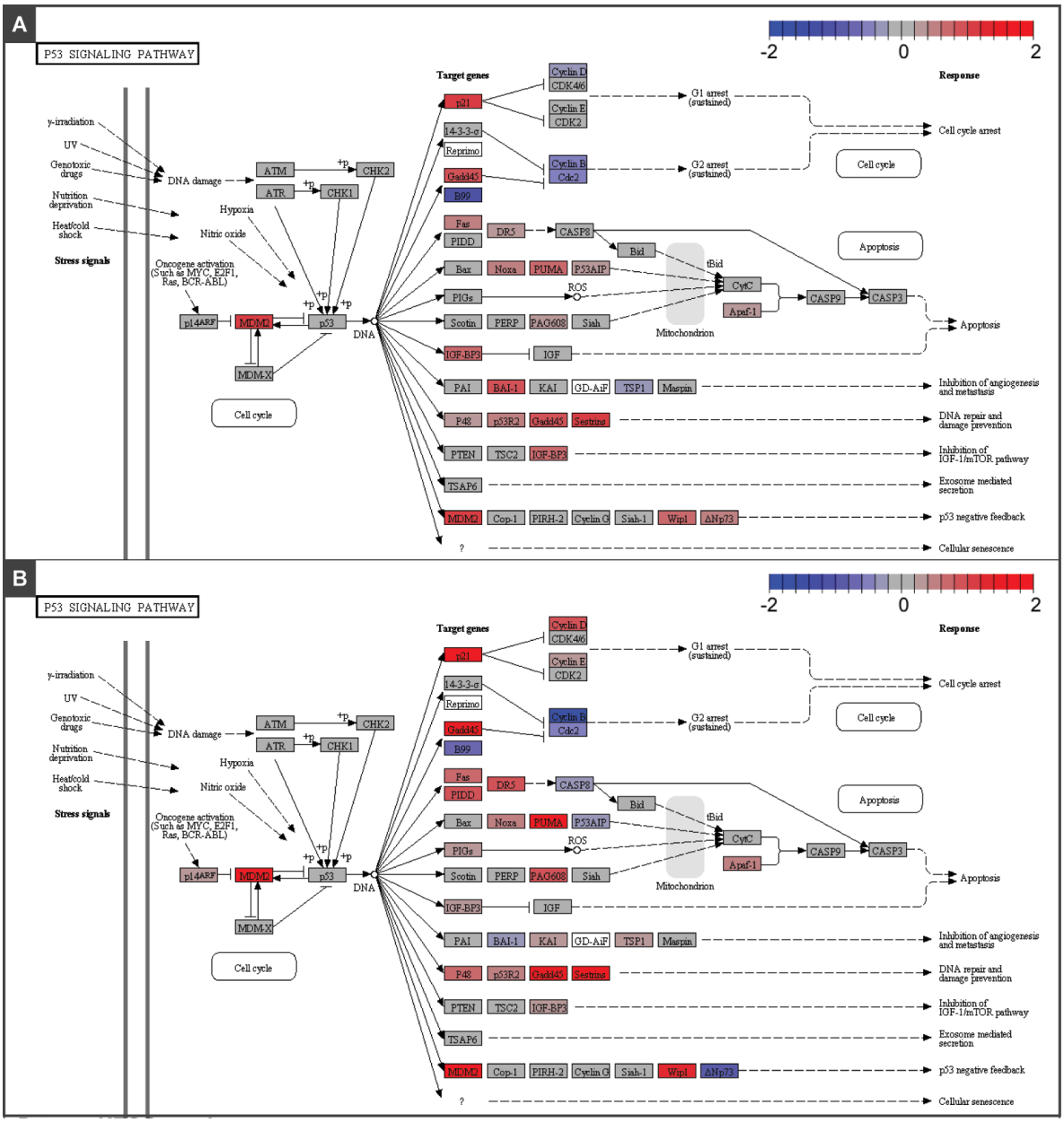

Figure 21

Figure 21 Radiotherapy injury to NHEK and NHDF results in significant enrichment of p53 signaling pathway gene expression

Ensemble of Gene Set Enrichment Analyses (EGSEA) was utilized for gene enrichment and pathway analysis. KEGG pathways allowed for mapping of specific molecular pathway signatures altered in response to radiotherapy injury, with a gradient scale of blue: representing down-regulation, grey: no significant fold change and red: up-regulation in comparison to 0Gy controls. (A) 10Gy NHEK display modest enrichment of genes involved in p53 signaling, while (B) 10Gy NHDF display significant enrichment of genes involved in p53 signaling 4 hours after irradiation in comparison to 0Gy controls.

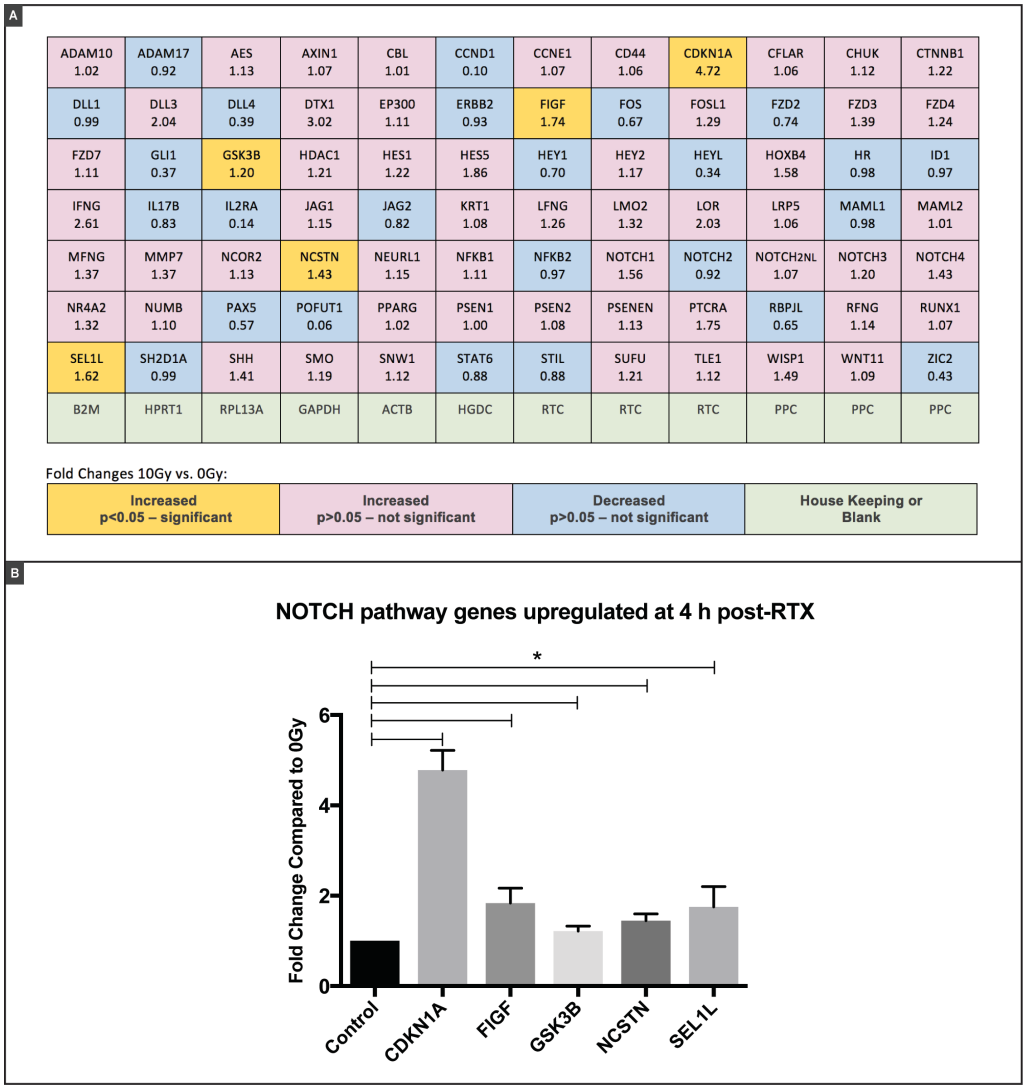

Figure 22

Figure 22 Radiotherapy injury in NHDF results in alterations of gene expression in the NOTCH signaling pathway

(A) A plate map of gene candidates involved in NOTCH signaling pathways with differences in RNA expression of 10Gy NHDF (4 h after irradiation) vs. 0Gy NHDF controls represented as a fold change. Genes up-regulated with statistical significance are represented in yellow boxes, expression up-regulated without statistical significance p>0.05 represented in pink boxes, expression down-regulated without statistical significance p>0.05 represented in blue boxes, and lastly, housekeeping genes and blank wells represented by green boxes. (B) A graph depicting the statistically significant genes up-regulated by radiotherapy injury of NHDF at the 4 h time point. Asterisks above bar-graph indicate statistical significance (* = $p<0.05$), error bars represent SEM, with $n\geq3$.

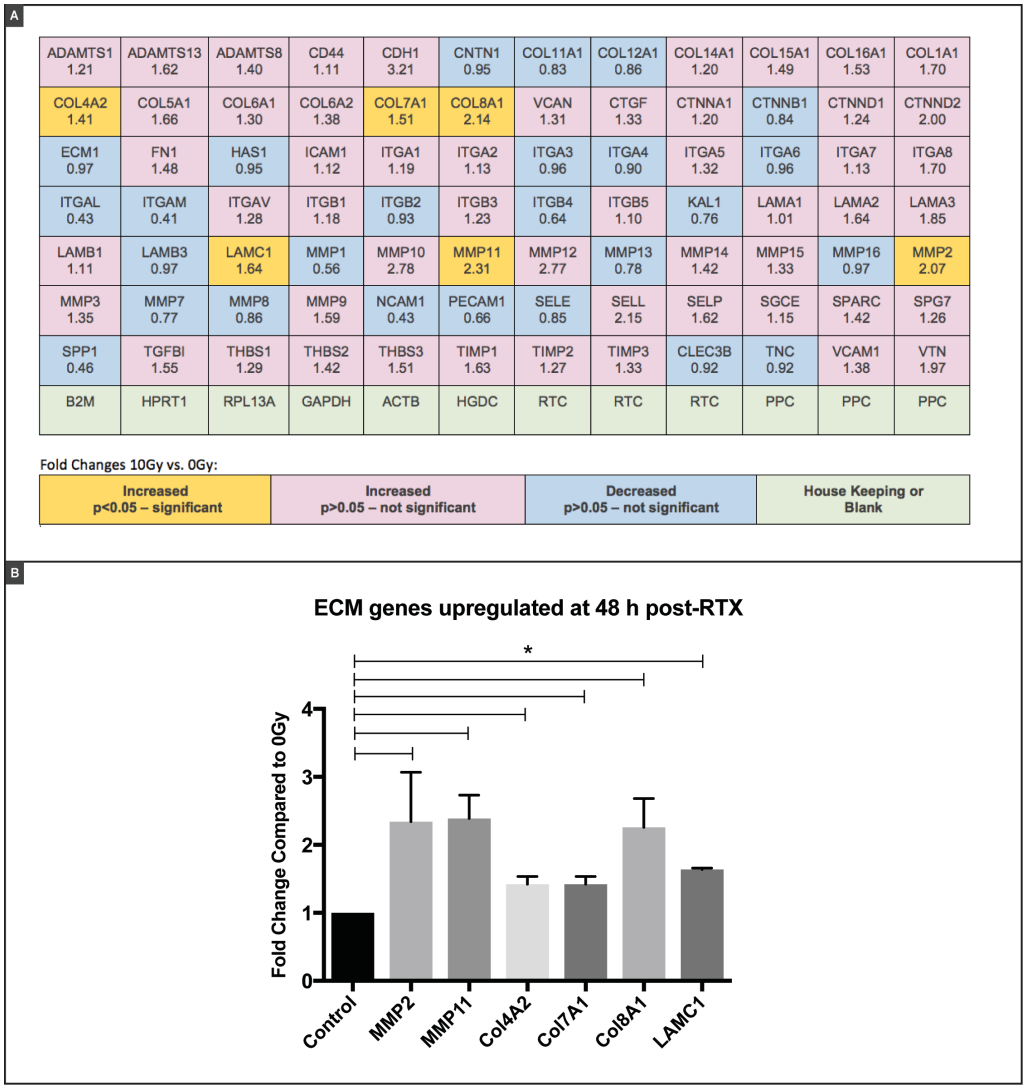

Figure 23

Figure 23 Radiotherapy injury in NHDF results in altered expression of ECM signaling pathways

(A) A plate map of gene candidates involved in ECM signaling pathways with differences in RNA expression of 10Gy NHDF (48 h after irradiation) vs. 0Gy NHDF controls represented as a fold change. Genes up-regulated with statistical significance are represented in yellow boxes, expression up-regulated without statistical significance p>0.05 represented in pink boxes, expression down regulated without statistical significance p>0.05 represented in blue boxes, and lastly, housekeeping genes and blank wells represented by green boxes. (B) A graph depicting the statistically significant genes up-regulated by radiotherapy injury of NHDF at the 48 hour time point. Asterisks above bar-graph indicate statistical significance (* = $p<0.05$), error bars represent SEM, with $n\geq3$.

3.5 Discussion

Radiotherapy injury of NHEK and NHDF result in significant cellular dysfunction and alteration of various molecular signaling pathways. The results in this chapter, therefore, contribute specific mechanistic information as to how irradiation of normal tissues can lead to clinical manifestations of poor wound healing and tissue fibrosis.

From the perspective of cell survival dynamics, the reduction in survival fraction of NHEK and NHDF is likely the result of a marked reduction in proliferative capacity rather than increased apoptosis. These dynamic processes are likely bridged by cellular senescence, induced by radiotherapy, whereby cells are forced into a post-mitotic phase, halted in progressing through the cell cycle or terminally differentiated and unable to functionally contribute to any regenerative wound healing processes (121) (125). Senescence leads to shortening of telomeres and activation of p53-dependent DNA damage response pathways that facilitate cell cycle arrest (510). The presented findings demonstrate significant radiotherapy induced transcriptional alterations with RNA up-regulation of genes CDKN1A, GADD45A, TP53INP1, SESN1, MDM2 providing the molecular cues driving the suppression of proliferation in irradiated NHEK and NHDF, which are likely in a phase of cell cycle arrest (503). On further analysis, NHDF and NHEK irradiation also resulted in a significant enrichment of genes responsive to p53 signaling, in particular CDKN1A (also known as p21), further validated with repeat PCR analysis. CDKN1A is known to be overexpressed in senescent cells leading to prolonged G1 phase arrest (510). Other p53 mediated pathways are also responsible for activation of apoptosis, however, the current *in-vitro* study doses were designed to focus on sub-lethal effects of radiotherapy injury. Additionally, large scale apoptosis which may result from high dose gamma-irradiation, is also not clinically representative of radiotherapy soft tissue injury in the setting of oncological treatment. Seluanov et al. demonstrated that senescent ‘old’ fibroblasts do not proceed through p53-dependent apoptotic pathways but rather divert to necrosis when faced with subsequent insult such as trauma or genotoxic stress (510). Such mechanisms may be paralleled by the sub-lethally irradiated 10Gy NHDF or NHEK in the present study, which initially survive the insult and on subsequent stimulation with e.g. wounding, display a dysfunctional response.

The observed morphological increase in size of irradiated fibroblasts was quantified with larger spheroid area measurements in 10Gy vs. 0Gy spheroids constructed with the same number of cells. This further supports the hypotheses that irradiation of NHDF results in cellular senescence; as findings in this chapter demonstrate cellular swelling, flattening and reduced proliferative potential, thought to be defining features of senescent cells (82) (87). The phenotypic elongation in many fibrotic conditions has long been attributed to a 'myofibroblastic transformation' of the fibroblasts, demonstrating an altered secretory profile and the acquisition of a more uniform αSMA expression as shown in ICC staining of 10Gy NHDF. While the IHC of irradiated patient tissue samples, did not display a global increase in dermal αSMA staining, perivascular staining intensity was more pronounced. Coppe et al. demonstrated fetal lung fibroblasts, made senescent with low serum and hypoxic conditioning, resulted in up-regulation of VEGF at both RNA and protein level, thus stimulating angiogenesis (87). Similarly in the present study, 10Gy NHDF resulted in up-regulation of FIGF (aka VEGF-D) a potent inducer of lymphangiogenesis (315). Altogether, past and current studies suggest irradiated NHDF are likely to take part in influencing other microenvironmental processes which suffer secondary to perivascular and dermal fibrosis (133), namely angio- and lymphangiogenesis, clinically manifesting as impaired tissue perfusion, wound healing capacity and lymphoedema.

Cell migration is considered to be an essential cellular activity in maintenance of homeostasis in processes of cell growth, differentiation, wound healing and angiogenesis (121) (214). When a scratch wound is created, the cell monolayer responds to the disruption of cell-cell contact and an increased concentration of growth factors at the wound margin, allowing wound healing through a combination of proliferation and migration (461). Irradiated NHEK demonstrated significant impairment in migratory function, likely to account for early clinical reactions of dry and wet desquamation leading to delayed re-epithelialisation. This process is likely to be further impacted by suppression of proliferation, slowing the regeneration and differentiation process from the basal (stem cell) layer of keratinocytes (137). However, NHDF migration counterintuitively increased as a result of radiotherapy injury. This finding may contribute to the understanding of a novel mechanism that

drives RIBE, with the hypermigratory profile of irradiated NHDF contributing to the spread of damage beyond the targeted field. Increased migration may be interpreted as advantageous, as in previous wound healing studies that suggest fibroblast migration precedes NHEK migration providing a scaffold for re-epithelialisation (135). However, when interpreted in the context of a 'gain in function' in sub-lethally injured cells, the manner and pattern of migration, must also be considered. Uniform cell migration necessitates formation of attachments at the leading cell front (lamellipodium), contraction of the cell body and detachment posteriorly (293). Furthermore, functional and directed cell migration involves sequential assembly, breakdown and re-organization of cytoskeletal proteins along with ordered deposition of extracellular matrix proteins which act as the cell scaffold (293). Observation and analysis of the migratory patterns of irradiated NHDF outgrowth from a 3D construct of cells demonstrated significantly disordered propagation from a dense core of adherent cells, with a haphazard arrangement, often migrating with a lack of direction and significant overlap. Linking these observations to additional findings in this chapter, it appears that sub-lethal radiotherapy injury to NHDF results in a hypo-proliferative state and dysregulation of normal apoptotic pathways, which counter-intuitively gives rise to hyperactivity in other constitutional functions of migration, adhesion and contractility. This may represent a transition to an 'invasive' phenotype which is able to spread damage in a chaotic manner beyond margins of directly targeted tissue, contributing to chronic and progressive tissue fibrosis.

The most significantly altered molecular candidates in both NHEK and NHDF, as discussed above, are likely to contribute to the anti-proliferative, pro-senescent effects of radiotherapy injury. However, other detected changes in gene expression may be vital up-stream candidates that govern cellular processes altered by irradiation in normal cells. NOTCH-1 represents a candidate of particular interest, upregulated as a result of radiotherapy in both NHEK and NHDF. As mentioned in 3.4.2, many studies have suggested that NOTCH-1 plays a crucial role in facilitating EMT (506) and myofibroblastic transformation of fibroblasts, with inhibition of signaling leading to improvement in fibro-proliferative conditions such idiopathic pulmonary fibrosis, scleroderma and systemic sclerosis (507) (508). Liu et al. demonstrated that Notch activity is relatively high in quiescent fibroblasts, inducing cell cycle arrest in mouse embryonic fibroblasts and reducing proliferation in NHDF without an increase in

apoptosis (511). Alternatively in TNF-α activated rheumatoid synovial fibroblasts, NOTCH-1 up-regulation was attributed to the acquisition of a de-differentiated and invasive phenotype, with downstream stimulation of MMP3, 11 and 17 (512). Syed et al. also demonstrated up-regulation of NOTCH-1 in keloid fibroblasts, another model of a fibroproliferative disease, and were able to demonstrate abrogation of this 'invasive phenotype' by NOTCH-1 and ligand Jag-1 siRNA knockdown resulting in impaired cell spreading attachment and proliferation of keloid derived fibroblasts (513). Additionally, treatment with Jag-1 further enhanced migration of fibroblasts, a noteworthy finding as results detailed in Chapter 6 demonstrate Jag-1 up-regulation in irradiated ADSC. Baseline NOTCH-1 expression is also responsible for keratinocyte differentiation and maintaining epithelial layers, however overexpression and activation of NOTCH-1, can result in induction of CDKN1A (p21), significant growth arrest (514) and derangement in processes required to maintain an intact epithelial layer. Considering the results of the present studies as well as the role of NOTCH-1 signaling in the literature, the increased RNA expression of NOTCH-1 in irradiated NHDF may be held accountable for hypoproliferation and senescence resulting in an increased adhesive, contractile and migratory profile with evidence of perturbed ECM matrix remodeling.

Perturbations in ECM remodeling is characteristic of many fibro-proliferative disorders and is likely a significant driving force for the development of radiotherapy induced tissue fibrosis. ECM is a dynamic structure, which provides structural support and through alterations in its biochemical composition can regulate individual cell behavior (515). Up-regulation of collagens leading to ECM stiffness has been shown to mechanically result in activation of focal adhesion kinases (FAK) which can impact migration, cell-cell communication and impair luminal structure formation (515). Current literature reviews postulate that radiotherapy injury leads to defective collagen deposition, increased wound breakdown and decreased tensile strength, which progressively transitions to a state of excessive deposition and widespread tissue fibrosis (119). While collagenous deposition is described as a major problem, most papers fail to specify the collagen subtypes involved. Results in this chapter show NHDF mediated alterations in the ECM turnover as a result of radiotherapy injury lead to a significant RNA up-regulation collagen subtypes 4A2, 7A1, 8A1 and Laminin1C, which are novel in comparison to the classically reported up-regulation of

collagens I and III (128) (509) (516). Laminin and Collagen IV constitute an integral part of the basement-membrane zone (BMZ), which is likely to be significantly impacted by radiotherapy injury of NHEK and NHDF. In recent years the BMZ has been recognized as more than just a structural component of skin, and rather a key regulator of cell behavior (517). Up-regulation of matrix gene expression of collagen IV and laminin can be interpreted to have two main effects; firstly, hypertrophy of the BMZ compartment of skin and vascular structures which may negatively impact tissue compliance - reducing the capacity and physical space for processes such as angiogenesis and lymphangiogenesis. Secondly, BMZ thickening may provide some of the anti-tumorigenic benefits of radiotherapy, increasing the substrate through which remnant or recurrent cancer cells would have to invade, resulting in loculation of invasive and metastatic cancer cells. Collagen VII is a network forming collagen (518) and is known to interact closely with laminin and collagen IV while also forming connections with dermal collagen I, thereby providing a key connection between epidermal and dermal compartments (519). The resulting effects of excess collagen VII are not well described in the literature, while deficiencies in collagen VII are linked to dystrophic epidermolysis bullosa (519). In present studies up-regulation of Col VIIA2 could account for the increased anchoring or adhesive nature of irradiated fibroblasts when plated on various concentrations of collagen I matrix, thus further facilitating the hyper-migratory functions acquired after injury.

As ECM remodeling constitutes a dynamic process, current studies also demonstrate a significant radiotherapy induced up-regulation of proteolytic gene expression driven by MMP 2 and 11 in NHDF. As reviewed in 1.9.4, MMP 2 (gelatinase A) is primarily responsible for degradation of amorphous collagens and fibronectin, while also playing a role in the final steps of fibrillar collagen (I, II III) degradation (509). MMP 2 up-regulation may account for the increase in irradiated NDHF migration detected in the 2D wounding model (see section 3.3.3), as MMP 2 mediated degradation of fibronectin may facilitate hypermigratory behaviour. In hypoxic states (which may draw parallels with radiotherapy injury), Miyazaki et al. demonstrated that collagen-I arrangement is unstructured due to excessive MMP 2 driven proteolytic activity, thought to aid in angiogenic processes to overcome hypoxia (520). While proteolysis of ECM may facilitate the creation of space for endothelial cell migration and sprouting, it is likely to destabilize the structural integrity of the dermal layers,

especially when challenged with trauma or re-operation in the irradiated field (139). A similar process may be occurring in irradiated tissues, as MMP 2 attempts to facilitate NHDF migration, which then provides a scaffold for NHEK migration allowing for epidermal and dermal healing. Several groups have also shown that MMP 2 is responsible for degradation of collagen IV in the BMZ of lung (302), brain (215) and skin (139) post-irradiation. Therefore, key regulatory pathways controlling the balance of radiotherapy related collagen IV and MMP 2 up-regulation require further investigation. Thewes et al. demonstrated MMP 11 expression with IHC staining of peri-tumoural fibroblasts as well as in dermatofibromas (521). MMP 11 also known as stromelysin 3, is able to degrade a variety of extracellular matrix components including proteoglycans, laminin, fibronectin, amorphous collagens and membrane bound MMPs (ADAMs). Radiotherapy injury to NHDF results in increased expression of MMP 11, which may also facilitate proteolysis of laminin and fibronectin, resulting in an attempt to balance the radiotherapy related up-regulation of laminin, while facilitating processes of disorganized invasion and hypermigration of injured cells.

Lastly, during molecular interrogation of the effects of radiotherapy on NHDF there was no detection of early RNA up-regulation of TGF-β or downstream signaling molecules on next generation sequencing screening – a finding somewhat contrary to the longstanding dogma implicating this signaling cascade in radiation induced fibrosis. While some studies report that a small number of TGF-β-mediated responses may be activated independent of Smad3, it is generally accepted that Smad3 activation is essential for majority of TGF-β mediated signaling (522) while alternative components contribute to modulation of the extent of the response (152). The absence of any RNA alterations in TGF-β/Smad3 expression suggest that TGF-β is an unlikely candidate responsible for the *in-vitro* irradiation induced alterations in NHDF cell behavior detailed in this chapter.

3.6 Conclusion:

Overall, the data presented indicates that radiotherapy injury to NHEK and NHDF results in significant molecular alterations, which may manifest as dysfunction in key homeostatic functions of viability, proliferation, migration, adhesion, contraction and invasion.

The study results propose that radiotherapy injury in NHEK and NHDF leads to RNA up-regulation of Notch-1, p53 mediated signaling and several cell cycle arrest genes, in the absence of traditionally described TGF-β signaling activation. These senescent cells demonstrate altered morphology, reduced cell proliferation without increased apoptosis and continue to exist as 'biologically active' cells, altered in their basic homeostatic capabilities and responses to injury. Counter-intuitively the 'senescent' NHDF demonstrate a transition into a more invasive phenotype by demonstrating increased migration, disordered invasion, increased adhesion and contractility which may explain the clinical manifestations of extensive, debilitating radiotherapy induced tissue fibrosis. It is important to note, that while these differences emerge in the context of exogenous 10Gy irradiation, additional signaling pathways from ECM, cytokines, chemokines and growth factors may contribute significantly in driving cellular dysfunction and a state of chronic inflammation. The discussed gene candidates require further protein level analysis along with knock-down studies demonstrating the potential mitigation of NHDF contractility and development of tissue fibrosis, thereby improving the overall capacity of irradiated tissues to functionally heal a wound. Mapping of radiotherapy-induced injury and the associated molecular signatures in individual patients utilizing sequencing and IHC of serial skin biopsies may allow for longitudinal assessment and validation of key gene candidates found in the present studies. These techniques of validation may then allow for the development of targeted treatments to reduce radiotherapy induced fibrosis.

4 CHAPTER 4: Characterizing the effects of radiotherapy injury on the micro and macrovascular systems

4.1 Introduction

Radiotherapy is used as an adjuvant for cancer treatment in over half of all solid malignancies (281). As detailed in section 1.6, while substantial improvements have been made to specifically target tumours, a degree of radiation exposure and therefore injury to normal tissues is an inevitable consequence. Australia boasts one of the highest rates of head and neck cancer and breast cancer with 1/49 people and 1/8 females being diagnosed before the age of 85 respectively (281). Head and neck, breast and sarcomatous cancers requiring radiotherapy treatment result in significant exposure of macrovascular structures leading to: widespread damage, accelerated atherosclerosis and manifestations of coronary, cerebral- or peripheral arterial occlusive disease (9). At a microvascular level, damage precipitates the development of chronic radiotherapy soft tissue injury: tissue hypoxia, poor angiogenic capability, impaired wound healing and parenchymal changes of tissue fibrosis (523).

With the advent of national breast screening and improvement in surgical and adjuvant treatments, breast cancer mortality has dramatically decreased by 37% between 1991 and 2010 (281). The Australian Institute of Health and Welfare reported 5-year relative survival from breast cancer during 2007-2011 as >90%, with over 168,000 people surviving after cancer diagnosis in the past 28 years, a figure that is estimated to increase to 250,000 by the year 2020 (281). The clinical guidelines for the management of early breast cancers advocate for breast conservative surgery in combination with adjuvant radiotherapy, resulting in a significant 66.6% reduction in local recurrence (524). Level I evidence suggests equivocal rates of survival and distant metastases when compared to total mastectomy alone, along with added psychological benefits of improved body image (524). Collectively these statistics highlight an important issue; a large population of patients live as breast cancer survivors after breast and chest wall irradiation. Radiotherapy injury to this region include local breast tissue deformity, osteitis of ribs, acute radiation pneumonitis, brachial plexopathy, secondary malignancy, and most importantly vascular and cardiac damage (524). The burden of non-cancer related morbidity and mortality requires immediate attention in this growing population of cancer survivors.

In terms of major macrovascular complications of radiotherapy; the links between coronary artery disease (CAD) and cardiac-related mortality following breast cancer and radiotherapy have been well documented (525) (526). The effects of 'older style', less targeted radiotherapy carried increased risks of myocardial infarction (hazard ratio 2.55, $p<0.001$) documented in the 1970-80s (223) (527). However, more recent literature reviews continue to provide evidence of cardiac and vascular related morbidity and mortality even with improvements in radiotherapy delivery techniques. A review from the Early Breast Cancer Trialists' Collaborative Group (EBCTGs), demonstrated increased mortality rates in women receiving radiotherapy, chiefly attributed to a 30% increase in cardiovascular-related deaths more than 2 years after irradiation (230). The risk of silent coronary events is also higher in patients that have undergone mediastinal/chest-wall radiotherapy compared to the general population, perhaps due to neural tissue damage (226). This damage may impair detection of smaller sentinel events, allowing disease progression without early intervention and management of radiation-associated cardiovascular disease.

A review by Stewart et al. suggested that irradiation of the left side of the breast results in the delivery of 3-17Gy, with internal mammary chain irradiation further increasing doses to the left anterior descending (LAD) coronary artery (528). Several studies have segregated patients receiving left sided versus right sided breast or chest wall radiotherapy and have demonstrated left side radiotherapy results in increased cardiac volume irradiation, increased incidence of CAD (529) (530), along with a 17-20% increase in risk of fatal myocardial infarctions (230) (531) when compared to right sided breast/chest irradiation.

Improvement in modern radiotherapy regimes have attempted to limit excessive radiation exposure to cardiac structures. Nevertheless, exposure dose still remains in the range of 1-5Gy, increasing up to 3-17Gy in left sided or internal mammary node irradiation (532) (533). Taylor et al. also noted that even when the heart is not in the direct field of radiation, it may still receive a scatter dose of 1-2Gy (534). Additionally, groups specifically analysing coronary artery exposure determined the LAD coronary artery (CA) may be exposed to levels as high as 7.6Gy, even when total cardiac exposure is only 2.3Gy (535) (534). Therefore, in all cases, cardiac and CA exposure is still sufficient to precipitate development of CAD, despite the advent

of improved radiotherapy delivery techniques (225). An increasing number of recent publications have focused on re-evaluating the epidemiology of post-radiotherapy CAD with more modern radiotherapy regimes. Boero et al. evaluated 29,102 patients diagnosed with breast cancer between 2000-2009 and determined that people with left sided radiotherapy doses were at higher risk of requiring percutaneous coronary intervention at 10 years post therapy however, laterality did not influence overall cardiac mortality (536). In another study, by far the largest cohort to date, Henson et al. prospectively analysed 300,000 women in the US Surveillance Epidemiology and End Results (SEER) cancer registries. In a specific comparison of mortality between left vs. right-sided tumours and radiotherapy it was observed that cardiac mortality was higher in left side irradiation by a ratio of 1.19 <10 years post-diagnoses, increasing significantly to 1.9 times > 20 years after diagnosis (537). Therefore, the larger studies with longer followup suggest timeframes of >10-20 years before CAD and its complications may become clinically apparent (230).

Despite this evidence of the damaging effects of radiotherapy on CAs, the mechanisms underlying radiation induced macrovascular disease are not well known. It is believed that radiation arteritis and accelerated atherosclerosis (more commonly characterised by intimal foam cell accumulation rather than cholesterol related plaques) (163) result from changes such as obliterative fibrosis of the smaller vessels of the organ, and a macroangiopathy of the larger arteries (Table 1) (222-225).

For decades the clinical side effects of radiotherapy such as telangiectasia, blood vessel friability, microvascular thrombosis and poor wound healing have illustrated that radiotherapy results in significant microvascular dysfunction (154). Radiotherapy induced injury is thought to result in a phenotypic transition of endothelial cells to a prothrombotic, pro-coagulant and pro-inflammatory predisposition (164). Inflammatory stimulus such as irradiation can lead to dysregulation of cellular adhesion molecules (CAMs), von Willebrand factor (vWF), angiotensin converting enzyme (ACE) and prostacyclins (166) (167) on both endothelial and leukocyte surfaces. Such alterations are hypothesized to result in leukocytic influx, thrombosis and aberrant endothelial cell proliferation (13).

While treating less aggressive malignancies with irradiation alone may be a preferred

option, substantial problems arise in the case of recurrence or failure of treatment. Operations in pre-irradiated tissue beds carry higher complication rates and morbidity, posed by increased difficulty with normal surgical planes obscured in the presence of fibrosis (219) (270). Simple wound closure techniques such as grafts are usually inadequate due to the poor vascularity of the tissue, necessitating transfer of vascularized un-irradiated tissue from a distant site of the body to reconstruct the defect (119). Free microvascular tissue reconstruction successes have been shown to vary; in one particular study from 94% without radiation down to 84% in irradiated head and neck cancer patients (217), while a meta-analysis by Herle et al. yielded statistically significant risk ratios for flap failure (RR 1.48) complications (RR 1.84), reoperation (RR 2.06) and fistula formation (RR 2.05) (270).

In order to investigate the effects of radiotherapy injury on the vascular system this chapter focuses on histological analysis of irradiated and normal vessels collected from patients undergoing delayed cancer reconstruction post-radiotherapy. Following our histopathological observations, functional experiments interrogating cellular changes resulting from radiotherapy injury in human dermal blood microvascular endothelial cells (HMECs) and pericyte support cells were conducted in conjunction with next generation sequencing, in order to analyse molecular level alterations concurrently. Key candidate protein expression levels were then validated using patient arterial samples.

4.2 Results – Human Microvascular Endothelial Cells (HMEC)

4.2.1 Histological analysis of radiotherapy induced injury to arterial structures

To examine the histological effects of radiotherapy injury in arterial structures, samples of irradiated internal mammary arteries (IMA) and patient matched un-irradiated deep inferior epigastric arteries (DIEA) were collected from 10 female patients undergoing delayed reconstruction following mastectomy and radiotherapy for breast cancer (HREC 52/03). The mean patient age was 54.4 ± 2.81 years and the mean time since radiotherapy was 3.81 ± 0.87 years (Table 13). The IMA was chosen as a surrogate for the CA due to the significant safety and ethical issues relating to harvesting a portion of the coronary arteries themselves. The irradiated IMAs form an excellent representative model of CAs due to their similar caliber, position in field of

radiotherapy and their routine use as replacements for CA in CA bypass grafting (CABG) procedures.

The arterial samples were fixed in paraformaldehyde and embedded in paraffin, before being cut into 5 μm sections and stained with hematoxylin and eosin (H and E), mounted on slides and light microscopy photographs, taken on an Olympus BX61 microscope. Slides were then presented to a pathologist blinded to the irradiation status and observations regarding histological differences were recorded (Table 13), (Figure 24). The most consistent abnormality noted in the irradiated vessels was evident in the media layer, with 8/10 irradiated arteries displaying evidence of smooth muscle cell atrophy and separation of muscular cell layers by myxoid stromal matrix deposition (mucin and glycoproteins) (Figure 24), findings not present in any normal arteries. These features may contribute to decreased tensile strength and increased vessel fragility (personal communication with A/Professor Slavin, Department of Pathology, St. Vincent's Hospital, Melbourne, Australia). Other changes observed included intimal thickening in 3/10 normal and 4/10 irradiated arteries, which may also be part of an age-related change. Focal calcification (arteriosclerosis) was noted in 1/10 normal and 1/10 irradiated arteries and visible dissection in 1/10 irradiated arteries (Figure 24).

Age (years)	Years since RTX	Intimal Thickening		Medial Myxoid Δ		ICAM-1+ Endothelial Surface		CD68+ Macrophage Location	
		N	RTX	N	RTX	N	RTX	N	RTX
59	2		+		+		+	A	M / A
60	3		+		+		+		
42	9	+					+	A	A
68	7	+			+		+	A	I / M / A
57	5	+							A
51	5				+		+	M / A	I / M / A
57	2				+		+	M / A	I / M / A
39	0.12		+		+			A	M / A
61	4							M / A	M / A
50	1				+		+		A
Average:		**Total:**							
54.4 +/- 2.81	**3.81 +/- 0.87**	**3/10**	**3/10**	**0/10**	**8/10**	**0/10**	**7/10**	**I 0/10 M 3/10 A 7/10**	**I 3/10 M 6/10 A 9/10**

Table 12 Patient demographics, clinical characteristics and IHC analyses of matched unirradiated DIEA and irradiated IMA tissue samples.

Table 12 Data collected included the age of patient in years and time since radiotherapy treatment as part of their adjuvant cancer treatment. IHC analysis parameters include the presence of intimal thickening, medial myxoid change (Δ), ICAM-1 positive endothelial staining and CD68 positive macrophage staining. (N) designates normal control arterial samples (DIEA), (RTX) represents irradiated matched arterial samples (IMA). (+) represents a positive finding in the arterial sample, (I) intima, (M) media, (A) adventitia, blank fields represent no relevant findings.

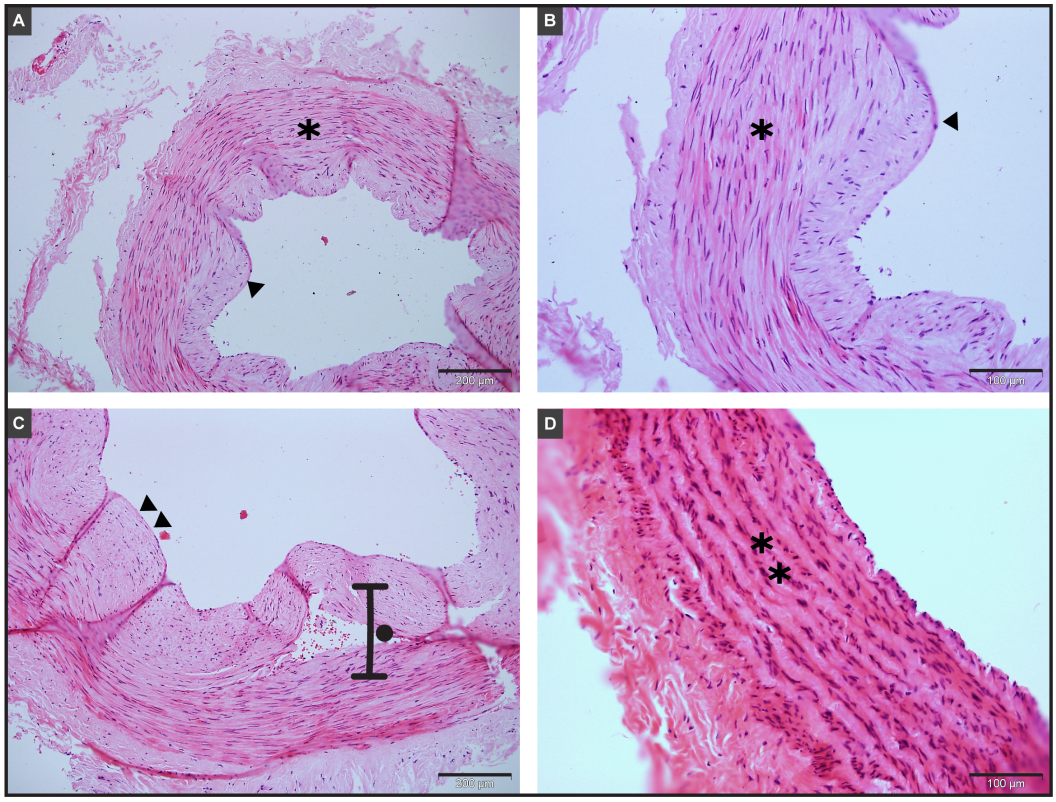

Figure 24

Figure 24 Adjuvant radiotherapy treatment result in morphological alterations of blood vessels

Sections of normal un-irradiated DIEA (A, B) and irradiated IMA (C, D) were cut into 5 µm sections and stained with hematoxylin and eosin for histopathological analysis. (A) x10 objective light microscopy of normal human DIEA, demonstrates a concentrically arranged intima and media layer structure (*), with the presence of segmental intimal hyperplasia, commonly an age-related process (▲). (B) x20 objective image of a normal human DIEA, shows symmetrical arrangement of smooth muscle cells in the media layer (*). (C) In contrast to the segmental age-related processes, x 10 objective image of an irradiated IMA demonstrated the global presence of intimal hyperplasia (▲▲) and dissection separating the intima and media layers (●). (D) image that illustrates at x20 objective the characteristics of a medial myxoid change (**) in 8/10 irradiated IMA specimens; separation of atrophied smooth muscle cells with increased ECM deposition is seen, resulting in a widening of space between cell layers. Scale bars (A and C) 200 µm, (B and D) 100 µm, n=10.

4.2.2 HMEC Cell Survival Dynamics

In order to further characterize radiotherapy-induced changes at an endothelial cell level, functional bio-assays were performed according to the key fundamental processes collectively to contribute to neo-angiogenesis. HMEC cultures were established from proliferating cells and cultured in medium containing essential growth factors (see 2.1.1 and 2.1.2). Cells were passaged on reaching 80-90% confluence and utilized for *in-vitro* functional assays between passage 2-6.

The effect of radiotherapy on HMEC cell survival was first determined utilizing a survival fraction calculation (see 2.2.1). A set number of cells were seeded in a 24 well plate, left to attach overnight, received irradiation (10Gy) or control treatment (0Gy) and left in standard culture conditions for 48 h, after which viability was determined by cell counting based on exclusion of trypan blue dye uptake in viable cells with intact cell membranes. Calculation of 0Gy and 10Gy plating efficiency preceded a determination of 10Gy HMEC survival fraction and accounted for a degree normal cell loss in the plating process (for more calculation descriptions see 2.2.1). Irradiation of HMEC resulted in a survival fraction of 46% compared to normal (0Gy) cells (assumed to have a 100% survival fraction), therefore representing a 54% reduction in cell survival of 10Gy HMEC (Figure 25 A,B). To further examine the processes that may contribute to a reduction in HMEC cell survival, proliferation and apoptosis experiments were conducted (see 2.2.2). To replicate the clinical scenario where patients receive smaller doses over a protracted period of time, a fractionated experimental group was assigned to receive five 2Gy doses delivered over a 48 h interval, a single dose group was assigned to receive one 10Gy dose and the control group received 0Gy. Briefly, cells were seeded in a white-walled 96 well plate, left to attach overnight, with irradiation treatment commencing the following day. CellTitre Glo® (Promega) or Caspase3/7® (Promega) luminescent reagents were added to the wells 48 h post-radiotherapy to determine cell proliferation and apoptotic activity respectively, by obtaining values using a luminometer plate reader (see 2.2.2 for more detailed methodology and settings). HMEC display a 4.5 ± 4.5% trend in reduction in proliferation after 2Gy x 5 and an 11.3 ± 3.4% reduction in proliferation after 10Gy irradiation, compared with 0Gy controls at equivalent timepoints (Figure 25 C). HMEC apoptotic activity mediated by Caspase 3/7 activation was interestingly decreased by 11.0 ± 0.1% after 2Gy x 5 and 21.2 ± 2.9% after 10Gy irradiation

(Figure 25 D). Therefore, since both groups of irradiation decreased HMEC apoptosis, subsequent experiments were performed with a single dose of 10Gy for efficiency of experimental design.

4.2.3 HMEC Migration

To investigate the effects of irradiation on HMEC migration, a two-dimensional scratch wound model was utilized, to determine if such functional impairment may contribute to poor wound healing. Cells were seeded on fibronectin coated plates, left to attach overnight before receiving either a single 10Gy dose or control 0Gy. Cells were serum starved 12 h prior to creating the 'wound' (see 2.2.3 for timelines and detailed methodology). Once the wound was created at 0 h (Figure 26 A,D), wells were photographed using standardised bright-field microscopy, and images were quantified on ImageJ to map % gap closure at 6 h intervals over 48 hours. The percentage gap closure was calculated relative to the 0 h scratch at all time points and plotted (Figure 26 C), with no significant difference in migration between the two groups. At 48 h; 0Gy HMEC achieve 98.9 ± 5.7% gap closure (Figure 26 B) and 10Gy HMEC achieve 98.8 ± 4.3% gap closure (Figure 26 E), representing no significant difference between the two groups at the 48 h (Figure 26 F).

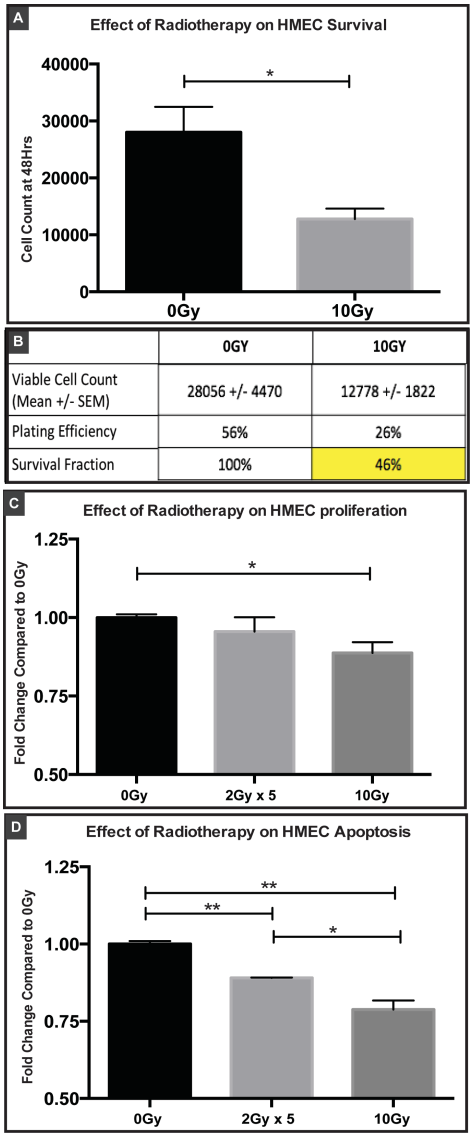

Figure 25

Figure 25 Radiotherapy decreases HMEC cell survival, proliferation and apoptosis

(A) Effect of radiotherapy on HMEC survival represented by viable cell numbers 48 h after irradiation (10Gy) or control (0Gy) treatment. (B) Quantification of 0Gy and 10Gy viable cell counts showed plating efficiency and the survival fraction of 10Gy HMEC was reduced in comparison to 0Gy controls (assuming 100% survival of 0Gy control group cells). The effects of 2Gy x 5 and 10Gy irradiation doses (C) decreased HMEC proliferation and (D) significantly decreased HMEC apoptosis, represented as fold changes compared to 0Gy control groups. Asterisks above bar-graph indicate statistical significance (* = $p<0.05$, ** = $p<0.01$), error bars represent SEM, with $n\geq3$.

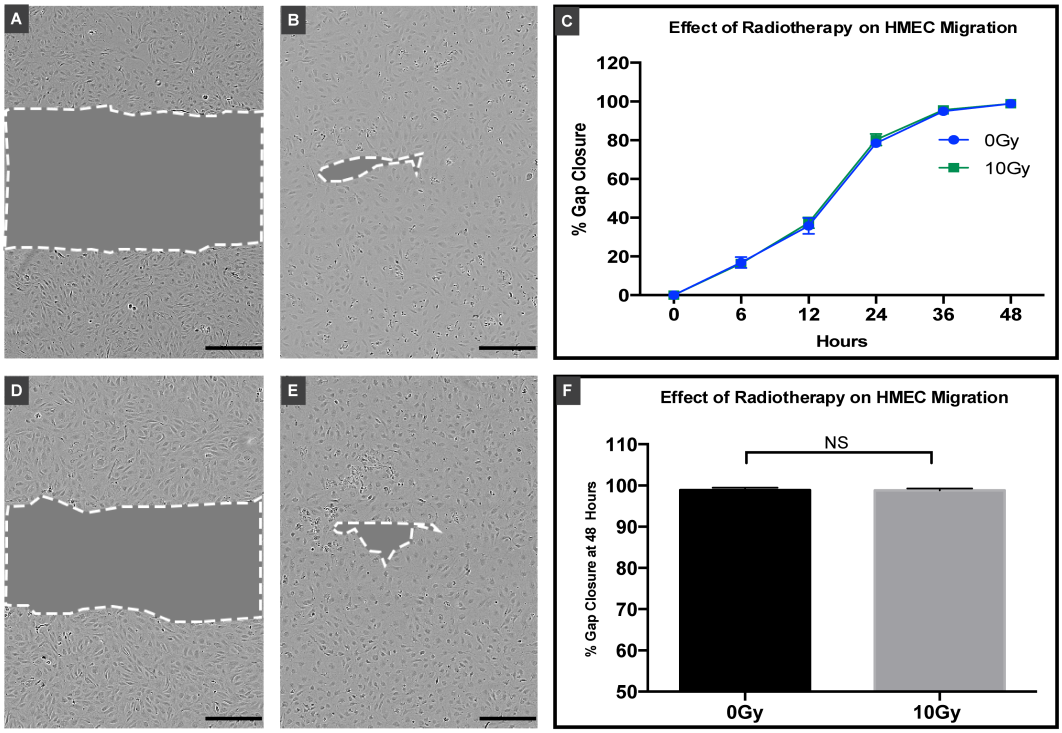

Figure 26

Figure 26 Radiotherapy does not significantly impair HMEC migration across 48 h

Bright field imaging (x10 objective) of HMEC every 6 h post creation of a scratch in a two dimensional wound assay on a confluent mono-layer of proliferating cells was conducted. Representative images of 0Gy HMEC at (A) 0 h then (B) 48 h and 10Gy HMEC at (D) 0 h then (E) 48 h were quantified (C) by calculating the % gap closure compared to 0 h controls at 6 h intervals and demonstrated no significant impairment in the migratory capacity of 10Gy HMEC. In (F) analysis of % gap closure between 0Gy and 10Gy HMEC scratch wound areas at the 48 h end-point is graphically displayed demonstrating no significant difference as a result of HEMC irradiation. In (A),(B),(D),(E); Scale Bar 300µm, dotted line represents periphery of scratch wound and grey shaded area represents scratch wound area. NS = not significant, error bars represent SEM, with n≥3.

4.2.4 HMEC Tube formation

Two dimensional tube formation assays were conducted to evaluate the effects of radiotherapy on angiogenic abilities of HMEC. Briefly, HMEC were seeded in 24 well plates on a pre-set coating of Growth factor reduced (GFR) Matrigel and immediately received either a single 10Gy dose or control 0Gy dose. Standard brightfield microscopy was used, 5 photographs per well at x10 objective were acquired at 24 and 48 h post-radiotherapy. This two-dimensional assay was performed to assess attachment, migration and the ability of endothelial cells to form tube-like structures. Photographs were quantified by counting branches and loops using ImageJ (NIH) with the Lymphatic Vessel Analysis Plug-in (LVAP), see section 2.2.4.1 for detailed methodology (481). Irradiated HMEC displayed reduced ability to form 2D tubes forming 3.64 ± 0.76 complete tubes per x10 field at 48 h compared to 8.51 ± 0.85 tubes per x10 field in 0Gy HMEC controls (Figure 27 A-C) ($p<0.05$). The number of branches from branch points was, however, not significantly altered (Figure 27 D).

4.2.5 HMEC Spheroid sprouting

To analyze the effects of radiotherapy on HMEC angiogenic processes in more detail, a 3D spheroid sprouting experiment was utilized. Briefly, HMEC spheroids were constructed using non-adherent u-bottom 96 well plates and left to form overnight in 10% methylcellulose and Endothelial Growth Medium (538), which received either 10Gy irradiation or a 0Gy control dose after 12 h incubation. Spheroids were transferred and seeded in 48 well plate in a 3D gel utilizing 150 µl sandwich of human fibrin (90%) and thrombin (10%). Spheroids were photographed at x10 objective using bright field microscopy at 24 h and 48 h time points (Figure 28 A,B) and sprouting metric analysis was conducted using ImageJ (NIH) and LVAP Plug-in quantifying parameters of: 1) number of sprouts, 2) branch points, 3) average and 4) total sprout lengths. Irradiation of HMEC spheroids resulted in significant attenuation of 3D sprouting. A reduction in the number of sprouts was seen in 10Gy HMEC (0.77 ± 0.46 sprouts/spheroid) compared with 0Gy HMEC controls (9.0 0 ± 2.17 sprouts/spheroid) (Figure 28 A-C). Branch points were reduced in 10Gy HMEC spheroids (0.22 ± 1.47 branch points/spheroid) vs. 0Gy HMEC controls (3.50 ± 1.24 branch points/spheroid) (Figure 28 D). Total sprout length was also significantly

altered in 0Gy HMEC spheroids (437.7 ± 92.2 µm) vs 10Gy spheroids (44.7 ± 22.6 µm) (Figure 28 F). However, average sprout length was not found to be different between the two groups (Figure 28 E).

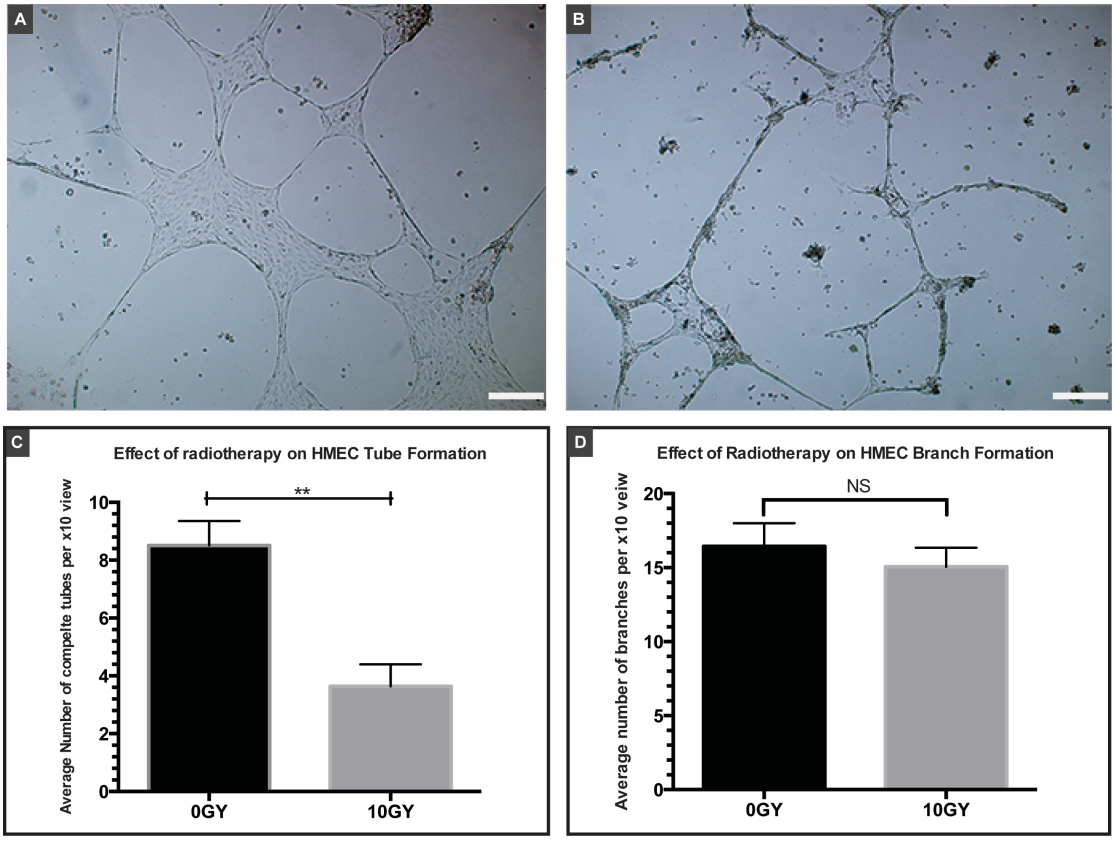

Figure 27

Figure 27 Radiotherapy results in reduced HMEC tube formation

x10 objective bright field imaging of HMEC seeded on GFR Matrigel photographed at 48 h after radiotherapy, with (A) 0Gy control HMEC displaying ordered and well-formed tubes, while (B) 10Gy HMECs display a reduced tube formation with disorganized structure. (C) Quantification of number of tubes formed per x10 field demonstrated a significant reduction as a result of radiotherapy at 48 h. (D) Analyses of differences in number of branches at 48 h demonstrated no difference between 0Gy and 10Gy HMECs. Scale Bar 100 µm. Asterisks above bar-graph indicate statistical significance (** = $p<0.01$, NS = not significant), error bars represent SEM, with $n\geq3$.

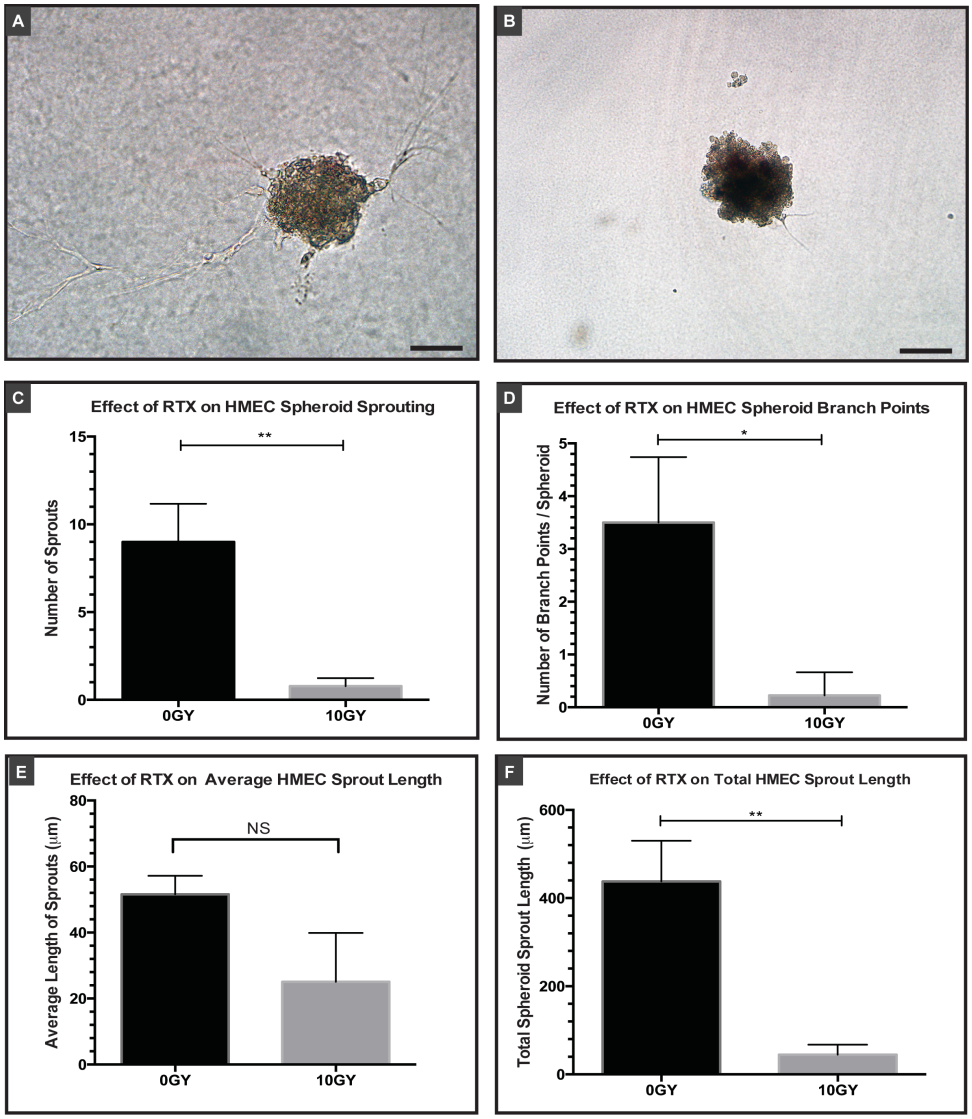

Figure 28

Figure 28 Radiotherapy decreases HMEC spheroid sprouting parameters

x10 objective bright field microscopy was used to capture images of spheroids 48 h after seeding in a fibrin/thrombin gel and irradiation with (A) 0Gy and (B) 10Gy doses. Sprouting metric quantification was undertaken with ImageJ LVAP plug in determining sprouting parameters at 48 h in 10Gy vs 0Gy HMEC spheroids and demonstrated: (C) a significant reduction in number of sprouts per spheroid and (D) spheroid branch points identified as the point where >2 sprouts originated, (E) a trending reduction in average sprout length and (F) a significant reduction in total sprout length per spheroid in µm. Scale Bar in (A-B) 100 µm. Asterisks above bar-graph indicate statistical significance (* = $p<0.05$, ** = $p<0.01$, NS = not significant), error bars represent SEM, with $n\geq3$.

4.2.6 HMEC Next Generation Sequencing

Having determined that radiotherapy injury to HMEC results in functional alterations of reduced proliferation, apoptosis and angiogenic capacity without changing their migratory capacity, the next phase involved experiments to determine the molecular changes that govern these processes.

Next Generation Sequencing RNA analysis was conducted on HMEC to interrogate the changes that occur at a molecular level after radiotherapy induced injury. As described in 2.3.4, this technique is able to offer an in depth analysis of the underlying pathways that may drive the impairment in angiogenic processes resulting from irradiation. These analyses aimed to identify a distinct set of alterations in gene expression that distinguish irradiated HMEC from normal HMEC.

Standardised numbers of HMEC were plated in cell culture flasks and irradiated once 80-90% confluence was achieved. RNA extraction was undertaken at 4 h using the QIAGEN, Germany® RNEasy Plus Universal Kit as per manufacturer's instructions. Samples were then tested for purity and quality control using the Nanodrop^{TM} Spectrophotometer (Thermo Fischer Scientific, USA) and stored at -80^{o}C, till further processing. Each sample underwent RNA sequencing (100 base pair single end) in the Illumina HiSeq machine at the Australian Genome Research Facility (AGRF) and results were presented in a series of spreadsheets and heat maps along with a comprehensive pathway analysis platform (see 2.3.4, 2.3.5 for detailed methodology).

Next generation sequencing demonstrated several significant differences between the expression profile of 10Gy HMEC in comparison to un-injured 0Gy controls. 10Gy HMEC significantly altered the expression of 679 genes at 4 h with adjusted p-values <0.05. The top ten candidates altered as a result of radiotherapy injury are listed in Table 12, with significant enrichment of the p53 mediated signaling pathways, similar to NHDF and NHEK (see 3.4.1) profiles. Sequencing data also demonstrated significant up-regulation of cell adhesion molecules; ICAM-1 with a 1.69 log fold increase in irradiated HMEC compared to controls and a large 5.16 log fold change increase in E-selectin expression. On further pathway analysis, cell adhesion molecule signaling between endothelial cells and leukocytes demonstrated significant alterations as a result of radiotherapy injury (Figure 29). The literature suggests that

ICAM-1, in particular, is implicated in atherothrombotic pathology (539) and other groups such as Haubner et al. have similarly demonstrated its up-regulation in response to radiotherapy injury *in-vitro* in endothelial populations (394), therefore it was selected for further validation as detailed in section 4.2.8.

Gene ID	Symbols	Gene Name	Chr	logFC
355	FAS	Fas (TNF receptor superfamily, member 6)	10	1.910790107
467	ATF3	activating transcription factor 3	1	3.674744809
55294	FBXW7	F-box and WD repeat domain containing 7, E3 ubiquitin protein ligase	4	1.082983488
64393	ZMAT3	zinc finger, matrin-type 3	3	1.413005349
1026	CDKN1A	cyclin-dependent kinase inhibitor 1A (p21, Cip1)	6	1.935914483
81788	NUAK2	NUAK family, SNF1-like kinase, 2	1	2.066240159
57103	C12orf5	chromosome 12 open reading frame 5	12	1.139372918
4193	MDM2	Mdm2, p53 E3 ubiquitin protein ligase homolog (mouse)	12	2.178855747
80149	ZC3H12A	zinc finger CCCH-type containing 12A	1	1.249013239
6401	SELE	E-selectin	1	5.162841783
3383	ICAM-1	intercellular adhesion molecule 1	19	1.69356192

Table 13 Notable HMEC Next Generation Sequencing Candidates

Top ten gene candidates (blue/white) from next generation sequencing analysis demonstrating the molecular alterations between 10Gy HMEC in comparison to 0Gy controls, 4 h after radiotherapy injury (adjusted p values <0.01). Adhesion molecules of interest that were significantly up-regulated after irradiation (orange). Chr = chromosome, logFC = log fold change.

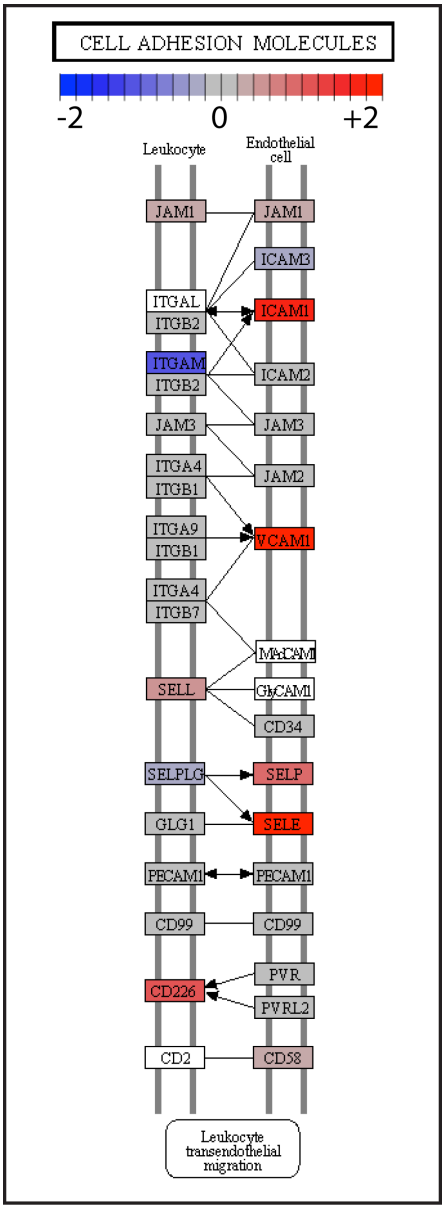

Figure 29

Figure 29 Ensemble of Gene Set Enrichment Analyses (EGSEA) was utilized for gene enrichment and pathway analysis. KEGG pathways allowed for mapping of specific signaling pathways that were altered in response to radiotherapy injury, with a gradient scale of blue representing down-regulation, grey: no significant fold change and red: up-regulation in comparison to 0Gy controls. Enrichment of cell adhesion molecule signaling pathways in 10Gy irradiated HMEC compared to 0Gy controls, demonstrates a significant up-regulation of endothelial cell adhesion molecules such as ICAM-1 ($p<0.05$), SEL-E ($p<0.05$), and VCAM-1 (which did not reach statistical significance), 4 h after irradiation.

4.2.7 Effects of radiotherapy on human aortic and coronary endothelial cells

As discussed in section 4.1, the micro and macrovascular damage resulting from radiotherapy injury is not limited to just dermal endothelial cell populations, but in the case of chest wall or head and neck irradiation can also affect medium to large size vessels such as coronary and carotid arteries. Radiotherapy may result in different patterns of injury in various subgroups of endothelial cells, which may be clinically relevant in the pathogenesis of cerebro- or cardiovascular injury. Basic functional assays of proliferation, apoptosis and migration were conducted on human aortic endothelial cells (HAEC) and coronary artery endothelial cells (CAE) to ascertain the effect of radiotherapy injury in these endothelial cell (EC) populations which line the large sized vessels such as the aorta and medium sized vessels such as coronary arteries respectively (see 2.1.1 for details).

In these assays, 10Gy HAEC were demonstrated to undergo a significant reduction in proliferation at 48h when compared to 0Gy controls (17.6 ± 0.77 % reduction Figure 30 A). As was seen in HMEC, there was a significant reduction in the rate of apoptosis of 10Gy HAEC of compared to 0Gy controls (22 ± 0.39% reduction Figure 30B). Unlike the migration of HMEC, which was not significantly altered by radiotherapy injury, HAEC migration was significantly reduced from 81.4 ± 2.73% gap closure at 48 h in HAEC, to 61.2 ± 3.4% in the irradiated counterparts (Figure 30 C), suggesting radiotherapy injury to large vessel EC may lead to impaired processes of neo-intimalisation and intimal remodeling after injury, processes which may in turn contribute to thrombosis and atherosclerosis (540).

CAE from human coronary vessels were interrogated next and proliferation assays demonstrated a significant reduction in proliferation at 48 h after irradiation when compared with 0Gy CAE (11.2 ± 2.8% reduction Figure 30 D). As seen in both HMEC and HAEC, there was a significant reduction in the rate of apoptosis of after radiotherapy compared to 0Gy CAE (14.1 ± 6.5% reduction Figure 30 E). CAE migration, similar to results seen in HMEC, demonstrated no significant change in migratory capacity after radiotherapy (Figure 30 F).

Next generation sequencing determined ICAM-1 to be a key molecular marker of radiotherapy injury in EC populations and was selected as a candidate as it was found to be significantly upregulated (see section 4.2.6). Validation of ICAM-1 was performed in HMEC initially using reverse transcription PCR and found to be significantly altered with 10Gy HMEC boasting a 1.46 ± 0.06 fold change compared to 0Gy HMEC controls (Figure 30 G) at 48 h. Irradiation of HAEC led to a significant 1.76 ± 0.26 fold change in ICAM-1 expression compared to un-irradiated controls (Figure 30 H) at 48 h. However, while irradiated CAE demonstrated a trend of increased expression of ICAM-1, this did not reach statistical significance (Figure 30 I). E-selectin, another candidate from the next generation sequencing panel was shown to be significantly increased after irradiation, however PCR validation at 48 h in all irradiated populations of HMEC, HAEC and CAE failed to reach statistical significance (Figure 30 J-L). This finding however, may be a result of a transient rise in E-selectin levels (with next generation RNA extraction conducted at 4 h, while validation was performed with samples extracted 48 h post-radiotherapy to better match assay end-points). The validation of ICAM-1 at transcriptional level in three distinct endothelial cell populations, requires further interrogation and substantiation at a protein level.

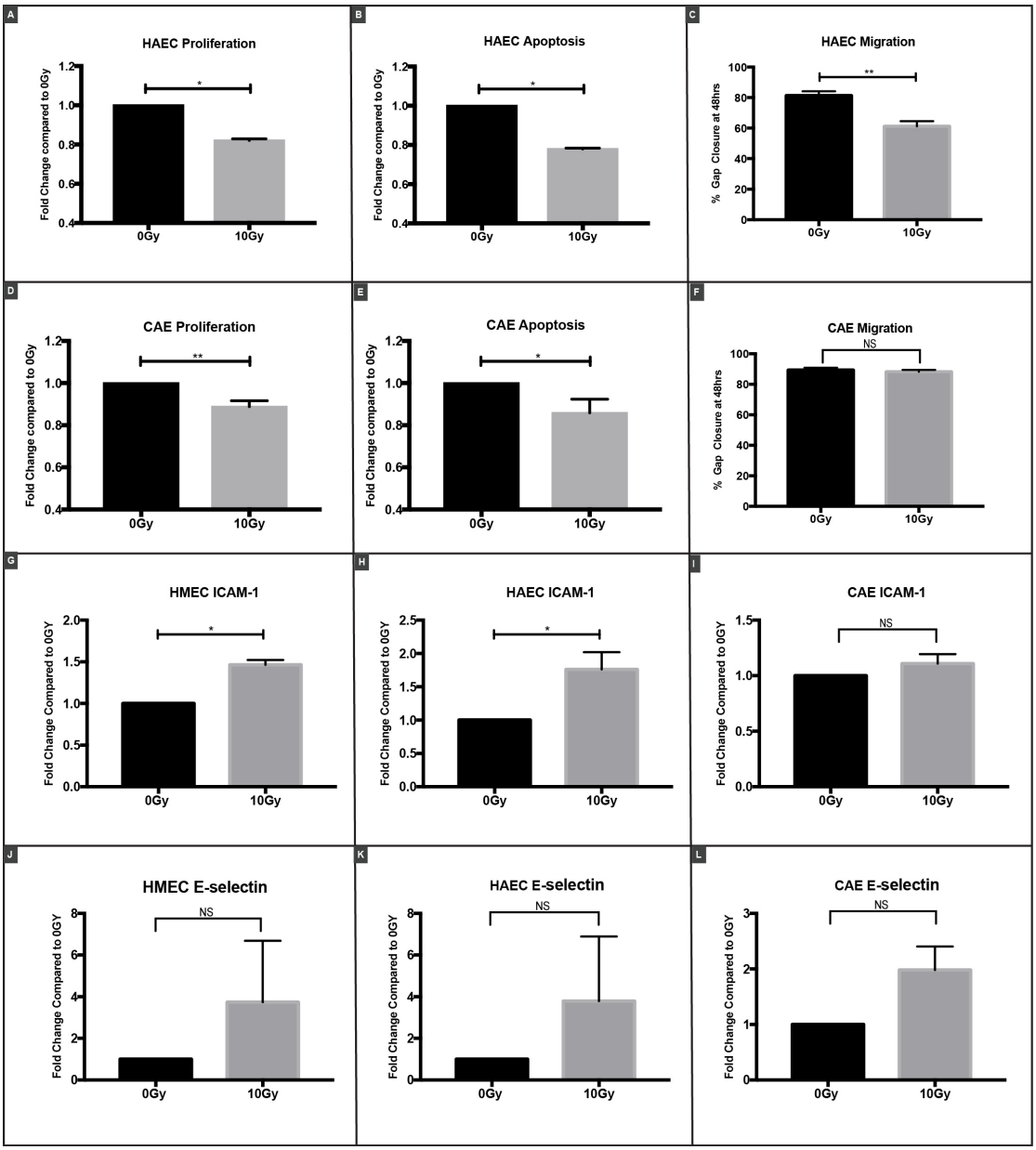
A
HAEC Proliferation
Fold Change compared to 0Gy
1.2
1.0
0.8
0.6
0.4
*
0Gy
10Gy
B
HAEC Apoptosis
Fold Change compared to 0Gy
1.2
1.0
0.8
0.6
0.4
*
0Gy
10Gy
C
HAEC Migration
% Gap Closure at 48hrs
100
80
60
40
20
0
**
0Gy
10Gy
D
CAE Proliferation
Fold Change compared to 0Gy
1.2
1.0
0.8
0.6
0.4
**
0Gy
10Gy
E
CAE Apoptosis
Fold Change compared to 0Gy
1.2
1.0
0.8
0.6
0.4
*
0Gy
10Gy
F
CAE Migration
% Gap Closure at 48hrs
100
80
60
40
20
0
NS
0Gy
10Gy
G
HMEC ICAM-1
Fold Change Compared to 0GY
2.0
1.5
1.0
0.5
0.0
*
0Gy
10Gy
H
HAEC ICAM-1
Fold Change Compared to 0GY
2.5
2.0
1.5
1.0
0.5
0.0
*
0Gy
10Gy
I
CAE ICAM-1
Fold Change Compared to 0GY
1.5
1.0
0.5
0.0
NS
0Gy
10Gy
J
HMEC E-selectin
Fold Change Compared to 0GY
8
6
4
2
0
NS
0Gy
10Gy
K
HAEC E-selectin
Fold Change Compared to 0GY
8
6
4
2
0
NS
0Gy
10Gy
L
CAE E-selectin
Fold Change Compared to 0GY
3
2
1
0
NS
0Gy
10Gy

Figure 30

Figure 30 The effects of radiotherapy injury on HAEC and CAE with validation of ICAM-1 transcriptional up-regulation with PCR

Analyses of the effects of 10Gy irradiation doses on alternative endothelial cell populations (A) HAEC proliferation, (B) HAEC apoptosis, (D) CAE proliferation and (E) CAE apoptosis represented as fold changes compared to 0Gy control groups based on luminescence readings. Quantification of the differences in % Gap closure between 0Gy and 10Gy (C) HAEC migration and (F) CAE migration 48 h post wounding compared to 0 h controls. PCR validation of candidates significantly upregulated on next generation sequencing showing significant increases in gene expression of ICAM-1 48 h post-radiotherapy in (G) 10Gy HMEC and (H) 10Gy HAEC compared to 0Gy controls, while (I) 10Gy CAE only demonstrate a trending increase in ICAM-1 expression compared to 0Gy controls. E-selectin expression demonstrated trends of increase at 48 h in (J) 10Gy HMEC, (K) 10Gy HAEC and (L) 10Gy CAE compared to 0Gy controls, however did not reach statistical significance. Asterisks above bar-graph indicate statistical significance (* = $p<0.05$, ** = $p<0.01$, NS = not significant), error bars represent SEM, with $n\geq3$.

4.2.8 Immunohistochemistry of irradiated and normal human arterial samples

Using the same patient samples as described in 4.2.1, serial sections underwent antigen retrieval using citrate buffer heated to 90ºC for 2 min, then quenched for peroxidase using 3% H_2O_2 for 5 min and protein blocked for a further 5 min. Anti-ICAM-1 primary antibody was applied for 1 h followed by a goat-anti-rabbit biotin secondary antibody for 30 min. Detection colour was developed using DAB-plus (DAKO, Denmark) for 5 min and counterstained with H and E prior to mounting. On analyses with x20 objective light microscopy, 0/10 normal arterial samples demonstrated ICAM-1 staining on the endothelial surface (Figure 31 A,B). In contrast, 7/10 arterial samples collected from the zone of irradiation displayed ICAM-1 positive staining on the endothelial surface (Figure 31 C,D), confirming the findings of ICAM-1 RNA up-regulation as a result of radiotherapy injury in EC populations, present and persisting at a protein level in arterial samples months to years after irradiation (see Table 13 for patient characteristics and a summary of the IHC findings). Negatively stained IgG isotype controls (data not shown), were used to confirm that ICAM-1 specific staining did not result from non-specific interactions within the tissue sample.

Similarly, further serial sections of the same arterial samples were stained with anti-CD68 antibody to detect the spatial location of any macrophages present in these vessels. Radiotherapy injury and the resultant inflammatory response is thought to recruit macrophages to the site of injury (541), which continue to persist after cessation of the injurious stimulus, and may be accountable for secretion of various growth factors and cytokines contributing to the maintenance of inflammation, RIBE and the development of atherosclerotic plaques in vascular structures (160). Of the ten matched patient samples stained, a significant difference in the distribution of CD68 +ve macrophages was observed when irradiated and normal artery samples were compared by a blinded observer. In normal vessels CD68 +ve macrophages were predominantly located in the adventitia in 7/10 arteries and in the media layer in 3/10 arteries (Figure 32 A,B). However, in irradiated arteries there was a global increase in CD68 +ve macrophages not only in the adventitial tissue but also in the intimal-medial layers (Figure 32 C,D), observations not quantified. Macrophages were located in the adventitial layer in 9/10, medial layer in 6/10 and intimal layer in 3/10 irradiated arteries (summarized in Table 13). The increased abundance and the

peripheral to central shift in location of macrophages in chronically irradiated patient arterial samples suggests that these immune/inflammatory cells and their secreted proteins may play a significant role in radiotherapy related arterial and endothelial injury.

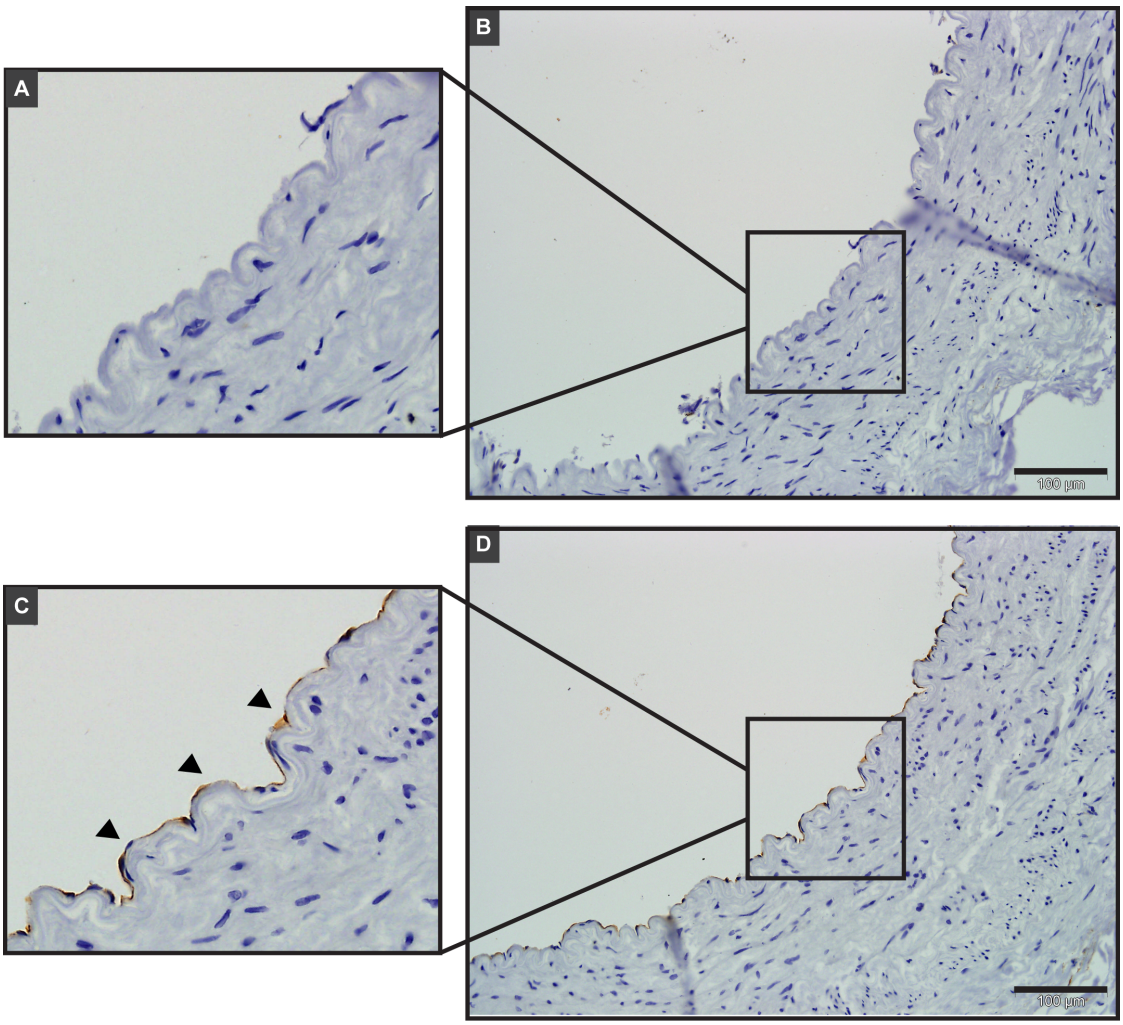

Figure 31

Figure 31 Radiotherapy results in up-regulation of ICAM-1 in the endothelium of internal mammary arteries

Sections of normal un-irradiated DIEA (A, B) and irradiated IMA (C, D) were cut into 5 µm sections and stained with anti-ICAM-1 antibody and photographed at x20 objective using light microscopy. Representative images magnified further demonstrate no endothelial ICAM-1 positive staining in normal arterial samples (A,B), while 7/10 irradiated samples (C,D) demonstrated endothelial ICAM-1 positive staining (▲). Scale bars (B,D) 100 µm, n=10.

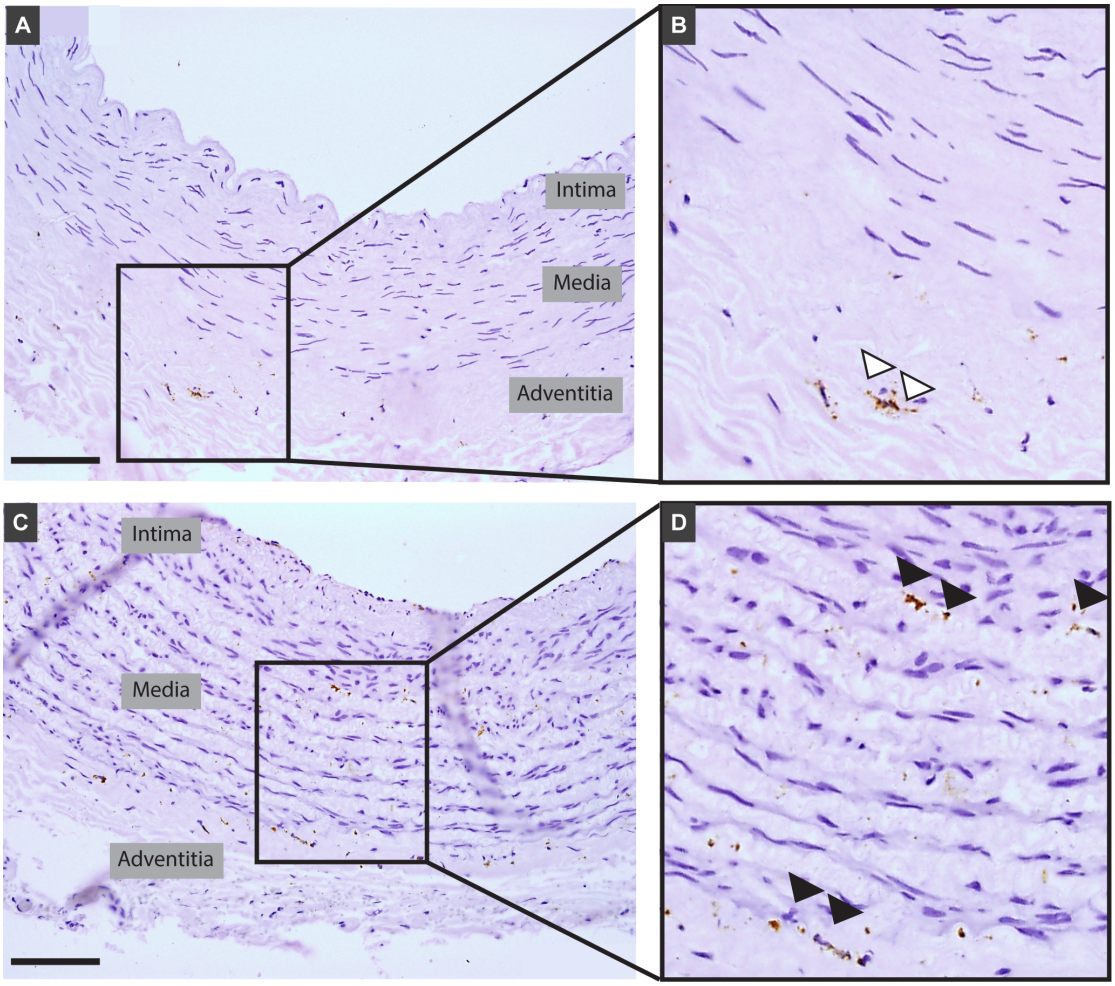

Figure 32

Figure 32 Radiotherapy alters macrophage recruitment and distribution in arterial tissue samples

Sections of normal un-irradiated DIEA (A, B) and patient matched irradiated IMA (C, D) were stained with anti-CD68 antibody and photographed at x20 objective using light microscopy. (A) unirradiated DIEA magnified in (B) demonstrate a predominantly adventitial location of CD68 +ve macrophages (△) compared with (C) irradiated IMA, magnified in (D) which display an increase in medial and intimal distribution of CD68 +ve macrophages (▲). Scale bars (A,C) 100 μm, n=10.

4.2.9 Pericyte Cell Survival Dynamics

Pericytes are a subtype of cells that are fibroblastic in morphology and mostly arise from the mesoderm. They are commonly located on the outer surface of vascular structures (501) (542). Pericytes are thought to play a significant role in embryological processes of blood vessel formation but also in regulation and maintenance of formed vessels. Specific functions include the regulation of tissue perfusion by control of factors such as blood pressure and flow through contractile actions of αSMA expressing pericytes on the underlying vasculature (542). In the context of wounding, when damaged blood vessels are required to undergo angiogenesis for regeneration, pre-existing pericytes are thought to detach, the injured basement membrane is degraded allowing for surrounding EC proliferation and migration. Once immature vessel structures have been formed, there is an EC driven recruitment of pericytes which inhibits further endothelial cell proliferation, promotes differentiation and leads to neo-vessel stability (542). More recent literature has reported that pericytes also possess a multi-potent differentiation capacity, similar to mesenchymal stem cells (501) with a molecular profile of adhesion molecule $CD146^{+}$, proteoglycan $NG2^{+}$, $CD34^{-}$ and CD 31^{-}, distinct from endothelial progenitor and ADSC profiles (54).

After characterization of the functional and molecular responses of the inner-most layer of a vascular structure (EC) to radiotherapy injury, pericytes – a vascular support cell, underwent similar interrogation. Human pericyte cell cultures were established from proliferating cells extracted from human placenta tissue (PromoCell, Germany) and cultured in medium containing essential growth factors (see 2.1.1 and 2.1.2). Cells were passaged on reaching 80-90% confluence and utilized for *in-vitro* functional assays between passage 2-6.

The effect of radiotherapy on pericyte cell survival was first determined utilizing a survival fraction calculation (see 2.2.1). A set number of cells were seeded in a 24 well plate, left to attach overnight, received irradiation (10Gy) or control treatment (0Gy) and left in standard culture conditions for 48 h, after which viability was determined by cell counting based on exclusion of trypan blue dye uptake in viable

cells with intact cell membranes. Calculation of 0Gy and 10Gy plating efficiency preceded the determination of 10Gy pericyte survival fraction in order to quantify a degree normal cell loss (for more calculation descriptions see 2.2.1). Irradiation of pericytes resulted in a survival fraction of 65% compared to 0Gy cells (which were assumed to have a 100% survival rate), however this did not reach statistical significance (Figure 33 A, B). To further examine the processes that may contribute to the trending reduction in pericyte cell survival, proliferation and apoptosis experiments were also conducted (see 2.2.2). To replicate the clinical scenario in which patients receive smaller doses over a more protracted duration, a fractionated experimental group was assigned to receive five 2Gy doses delivered over a 48 h interval, a single dose group was assigned to receive one 10Gy dose and the control group received 0Gy. Briefly, cells were seeded in a white-walled 96 well plate, left to attach overnight, with irradiation treatment commencing the following day. CellTitre Glo® (Promega) or Caspase3/7® (Promega) luminescent reagents were added to the wells 48 h post-radiotherapy to determine cell proliferation and apoptotic activity respectively, by obtaining values using a luminometer plate reader (see 2.2.2 for more detailed methodology and settings). Pericytes displayed an 18.1 ± 5.5% reduction in proliferation after 2Gy x 5 and a 17.7 ± 4.0% reduction in proliferation after 10Gy irradiation compared with 0Gy controls $p<0.05$ (Figure 33 C). Interestingly, pericyte apoptotic activity mediated by Caspase 3/7 activation was not significantly altered with both 2Gy x 5 and 10Gy experimental groups as shown in (Figure 33 D). Therefore, since both groups of irradiation decreased pericyte proliferation, with no significant difference between the two experimental groups, subsequent experiments were performed with a single dose of 10Gy for efficiency of experimental design.

4.2.10 Pericyte Migration

To investigate the effects of irradiation on pericyte migration a 2D scratch wound model was utilized as previously described in section 4.2.2 (see 2.2.3 for timelines and detailed methodology). At 48 h, 0Gy pericytes achieved 96.7 ± 0.78% gap closure (Figure 34 B) and 10Gy pericytes achieved 99.1 ± 0.40% gap closure (Figure 34 E), representing a small but significant difference of 2.33 ± 0.88% between the two groups (Figure 34 F).

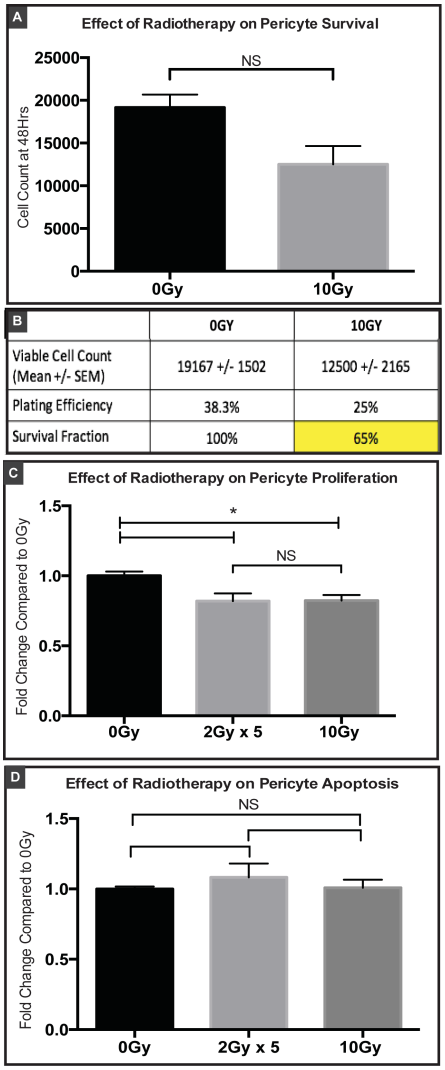

Figure 33

Figure 33 Radiotherapy reduces pericyte cell survival and proliferation without significantly altering apoptosis

(A) Effect of radiotherapy on pericyte survival represented by viable cell numbers 48 h after irradiation (10Gy) or control (0Gy) treatment. (B) Quantification of 0Gy and 10Gy viable cell counts showed plating efficiency and the survival fraction of 10Gy pericytes was reduced in comparison to 0Gy controls (assuming 100% survival of 0Gy control group cells) $p>0.05$. The effects of 2Gy x 5 and 10Gy irradiation doses (C) significantly decreased pericyte proliferation without (D) significant alteration in pericyte apoptosis, represented as fold changes compared to 0Gy control groups. Asterisks above bar-graph indicate statistical significance (* = $p<0.05$, NS = not significant), error bars represent SEM, with $n\geq3$.

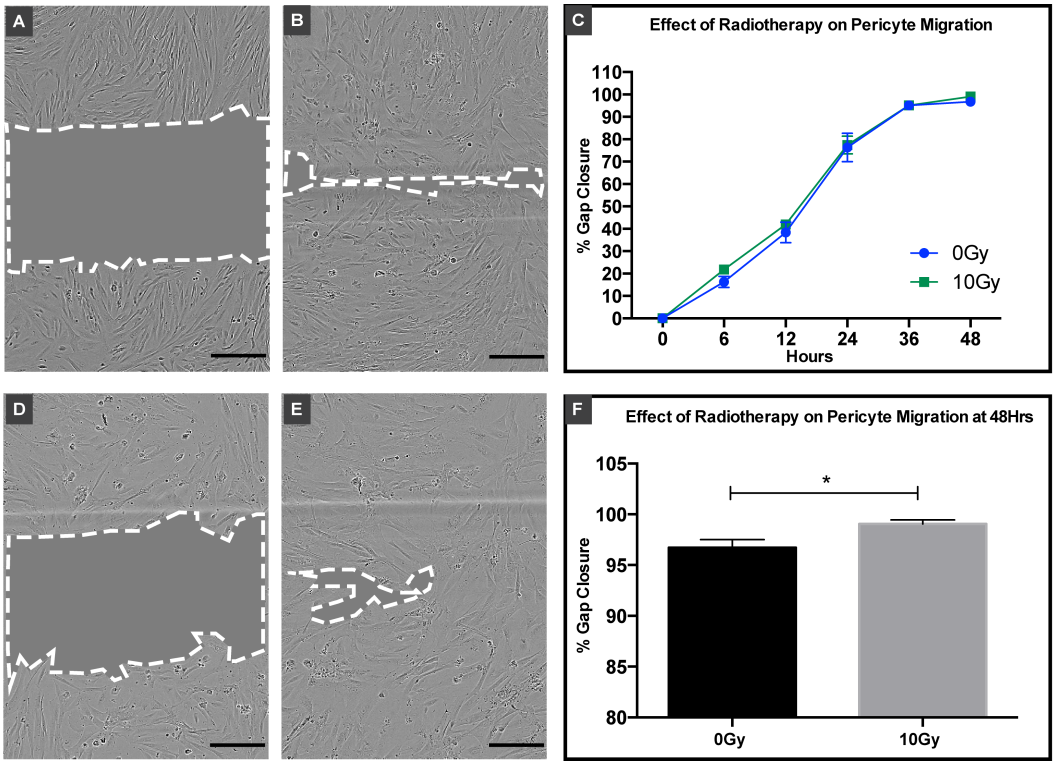

Figure 34

Figure 34 Radiotherapy significantly increases migration of pericytes across 48 h

Bright field imaging (x10 objective) of pericytes every 6 h post creation of a scratch in a two dimensional wound assay on a confluent mono-layer of proliferating cells was conducted. Representative images of 0Gy pericytes at (A) 0 h then (B) 48 h and 10Gy NHDF at (D) 0 h then (E) 48 h were quantified (C) by calculating the % gap closure compared to 0 h controls at 6 h intervals and demonstrated the increased migratory capacity of 10Gy pericytes across all time-points. (F) analysis of differences in % gap closure between 0Gy and 10Gy pericyte scratch wound areas at the 48 h end-point graphically demonstrates the unexpected increase in migration of 10Gy pericytes. In (A),(B),(D),(E); Scale Bar 300µm, dotted line represents periphery of scratch wound and grey shaded area represents scratch wound area. Asterisks above bar-graph indicate statistical significance (* = $p<0.05$), error bars represent SEM, with $n\geq3$.

4.3 Discussion

The results presented in this chapter demonstrate that radiotherapy injury to components of the vasculature such as HMEC, HAEC, CAE and pericytes can result in significant cellular dysfunction and reveals mechanistic information as to how irradiation may lead to poor wound healing, accelerated athero-thrombosis and the associated clinical sequelae. The findings of the above experiments collectively propose that irradiation may lead to atherogenic vascular disease by causing histological changes in the vasculature and altering expression of adhesion molecules, which may prompt accelerated development of CAD. Radiation in addition, significantly altered the ability of HMEC to undergo functional sprouting angiogenesis, which could render the vascular supply downstream of the arterial injury less able to adapt to ischemia, further compounded by the lack of appropriate pericyte support responses to facilitate neo-vessel stabilisation. Overall, such a proposed mechanism contradicts the traditional dogma related to end-arteritis obliterans and hypoperfusion underpinning the clinical manifestations of radiotherapy soft tissue injury (158) (543).

The most consistent abnormality noted on blinded assessment of irradiated IMAs vs. normal DIEAs was a change in the composition and structure of the media. Medium sized arteries such as the IMA typically have 5-6 layers of smooth muscle cells, compactly arranged in a concentric pattern (268). Radiotherapy resulted in a myxoid change in the media of these arteries characterised by smooth muscle cell atrophy, reduced cytoplasmic content, increased separation of layers by deposition of mucinous extracellular matrix composed of glycoproteins, rendering these arteries as fragile and damaged (personal communication with A/Professor John Slavin – Senior Pathologist, St. Vincent's Hospital, Melbourne). This pathological alteration, termed 'medial myxoid change' may remodel over time or persist and progress, undergoing fibrotic change with excess collagen deposition, thus impairing arterial compliance (162). The latter is more likely given the progressive nature of radiotherapy injury. This observed histopathological change draws parallels with cystic medial degeneration (CMD) or cystic medial necrosis seen in the media of large vessels e.g. the aorta in patients suffering from Marfan syndrome and other connective tissue disorders; significantly increasing the risk of dissection and/or aneurysm formation (544). Such changes in medium-sized or coronary vasculature are less well described

in the literature. A case report by Hake et al. implicated CMD changes as a cause for multiple sub-intimal thromboses rendering the patient's IMA unsuitable for CA bypass grafting (545). In the presence of multiple small infarcts in examined myocardial tissues as well as absence of significant atheromatous plaque, Segal et al. suggested a role for CMD in vasospasm (546). Another case report described CMD in coronary arteries of a patient who underwent fatal vasospasm while being weaned from coronary bypass. Kay et al. evaluated histological changes after intracoronary radiation for atheromectomy in four patients and found radiolucency in the artery which correlated with an area of increased myxoid matrix deposition; high in proteoglycans and low in mature collagens and elastin (547). This overall picture is comparable with the histological alterations of irradiated IMA specimen presented in this chapter, linking arterial media changes with radiotherapy injury. Histopathological findings of CMD-like changes in irradiated IMAs could therefore demonstrate a structural change responsible for the prothrombotic, pro-atherosclerotic nature of irradiated vessels, thereby increasing the risk for coronary artery disease morbidity and mortality either through athero-thrombosis formation, dissection or episodes of severe vasospasm. Such alterations also carry significant implications for free flap reconstructions using irradiated recipient vessels, with spasm and prothrombotic propensity potentially contributing to the pathogenesis of anastomotic complications necessitating return to theatre or subsequent flap failure (270) (548). The parallels to CAD that are made by using IMA data in this chapter, are drawn based on the anatomical location of these vessels lying in the zone of breast, chest wall and mediastinal irradiation as well as similar functional alterations in *in vitro* assays using HAEC and CAE in comparison to HMEC. Additionally, IMAs are inherently less prone to form atheromatous plaques (549) (550), therefore results presented may in fact underestimate the effect of radiotherapy induced atherosclerosis on the CA.

Telangiectasia in chronically irradiated tissues falsely projects a state of visible hypervascularity in superficial layers of irradiated skin, yet this does not reflect the hypoperfused state of underlying tissues in the zone of radiotherapy injury. The progressive and persistent state of hypoperfusion, results in chronic nutritional deprivation, with ischemia driving parenchymal atrophy and fibrosis (543). An early study by Aitasalo et al. demonstrated a transient decrease in the partial pressure of

oxygen detected in subcutaneous tissues utilizing a rabbit hind leg irradiation model, which did not persist in a chronic setting (551). In the 1990s Rudolph et al. challenged the notion of radiotherapy induced ischemia and compared transcutaneous measurements of the partial pressure of oxygen in irradiated vs. normal patient skin (463). Findings demonstrated the oxygenation of irradiated skin was not significantly different to normal tissues, measured during inspiration in room air and with oxygen supplementation (463), therefore concluding that ischemia alone is unlikely to be the sole precipitant for the clinical manifestations of radiotherapy injury. In more recent literature the topic of perfusion and oxygenation of irradiated tissues has been re-examined with more sophisticated testing methodology. Chin et al. utilized hyperspectral imaging techniques to measure the perfusion and oxygenation of irradiated murine flank tissue and demonstrated a significant 21% reduction in perfusion of tissues with no difference in oxygenation of tissues compared to un-irradiated areas (218). Several groups have attempted to analyse the changes in density of vasculature result from radiotherapy injury, with some reporting a decrease (218) (306), while others report no significant alteration blood vessel density post radiotherapy treatment with <60Gy (211) (552). Clinical manifestations of microvascular injury such as poor wound healing, ungraftable tissue beds and chronic ulceration remain poorly defined mechanistically and continue to contribute to significant patient morbidity. While gross morphological changes in tissue vasculature may lead to impaired perfusion, post-radiotherapy alterations in vascular density and the effects on the maintenance of oxygenation in 'metabolically impaired irradiated tissue' (218), also remain poorly elucidated.

On a cellular and functional level, the data presented in this chapter demonstrate that radiotherapy injury to HMEC results in significant reduction in the survival fraction of the cells, which is due to a combination of a reduction in proliferation rather than an increased rate of apoptosis after injury (Figure 25). It may be postulated from these results that irradiated HMEC undergo apoptosis only if actively dividing at the time of injury, while the remaining population become senescent and display a significant reduction in proliferative and angiogenic capabilities. This concept is in keeping with Kleibeuker et al's observations that immature vessels are more radiosensitive in comparison to their mature counterparts (154) responding to molecular up-regulation of cell cycle arrest mediators, such as CDKN1A and MDM2, also identified in the

next generation sequencing data. Such a reduction in proliferation combined with a senescent morphological change has also been linked to the development of atherothrombotic disease (553). Irradiated HMEC, HAEC and CAE all demonstrated a significant reduction in apoptosis compared to their 0Gy controls. This is a counterintuitive finding and may reflect a protective endothelial response to radiotherapy injury, allowing for persistence of sublethally damaged cells carrying maladaptive alterations in their homeostatic capabilities. Therefore, radioprotective strategies proposed in a review by Korpela et al. to reduce apoptosis (553) may not necessarily resolve the injury. Irradiated HMEC and CAE demonstrated no significant impairment in migratory function in two dimensional wounding, however HMEC tube formation and three dimensional sprouting, branching and total sprout length parameters were all significantly reduced. This selective impairment of processes may be interpreted in the context of two described modalities of angiogenesis; intussusceptive (vessel splitting) versus true sprouting neo-angiogenesis (154). Radiotherapy appears to significantly impair parameters of sprouting angiogenesis shown in the 3D spheroid model while the processes required for intussusceptive angiogenesis such as two dimensional branching and migration of HMEC, remain relatively spared. This may represent an attempt to reorganize the existing vasculature in irradiated tissue (154) (155). Such adaptions to restore adequate vascularization and perfusion of irradiated tissues may further be impaired by damage to the support cells which stabilize immature vessels, namely the pericytes. The results presented in this chapter suggest that irradiation demonstrates a trend in reducing the survival fraction of 10Gy pericytes compared to the 0Gy controls, similarly resulting from a reduced proliferative potential rather than increased rates of apoptosis. However, radiotherapy appears to result in a small, but significant, increase in the migratory abilities of pericytes, similar to the response of NHDF presented in section 3.3.3. Pericytes possess a fibroblastic morphology (542) and this accelerated and disordered migratory capacity may affect angiogenesis in two ways. Firstly, this may result in a thickening of perivascular tissues, reducing compliance and causing spasm or constriction of damaged vessels. This may also create a fibrous barrier, preventing effective neo-angiogenesis, which necessitates creation of space for endothelial cell tip sprouting and migration (554). The increased intensity of αSMA in a perivascular location presented in (Figure 20) in irradiated tissues, requires further interrogation with co-

staining of fibroblast, smooth muscle cell or pericyte markers to isolate the source. Secondly, any angiogenesis that does take place in an irradiated bed is likely to be inadequately supported by the injured hypoproliferative pericytes, leading to failure of stabilisation of neo-vasculature, resulting in leaky vessels unable to sufficiently perfuse and oxygenate tissues.

Once the cellular functional alterations resulting from irradiation of HMEC and pericytes were established, the molecular cues driving these changes were interrogated utilizing next generation sequencing. There was significant enrichment of pathways involving adhesion molecules after irradiation of HMEC, namely ICAM-1 which was validated using PCR in HMEC and HAEC endothelial populations. These findings were in line with other groups who have described *in vitro* HMEC mRNA up-regulation of ICAM-1 in response to radiotherapy injury (305) (307) (308) (394), while others have demonstrated increased IHC or flow cytometry detected presence of ICAM-1 in irradiated tissue specimens such as oral mucosa (306), heart, lung and intestinal tissue (539) (555). Up-regulation of cellular adhesion molecules are implicated in the development of functional alterations such as increased rolling, adhesion and arrest of neutrophils or monocytes on the altered endothelial surface, facilitating increased inflammatory cell infiltration, sequestration, LDL peroxidation, thrombosis, inflammatory mediators and atherosclerosis (307) (309) (310) (556) (557). Furthermore, inflammation in atherosclerotic lesions leads to plaque remodeling and an increased susceptibility to rupture and thrombosis (540). The results presented, further demonstrate positive ICAM-1 endothelial staining of 7/10 irradiated IMA samples compared to 0/10 un-irradiated patient matched DIEA, which validates protein level expression of the RNA up-regulation of ICAM-1 found *in vitro*. To our knowledge these results demonstrate for the first time the persistent and chronic up-regulation of ICAM-1 as a result of radiotherapy injury in an *in-vivo* human artery model. These results strongly suggest the potential role of ICAM-1 in post-radiotherapy CAD and other vascular complications, additionally supported by the detection of increased intimal and medial presence of $CD68^{+}$ macrophages in irradiated vessels compared to un-irradiated controls (see Table 13). As mentioned in the above, IMA appear to display a relative resistance to the development of atherosclerotic plaques, even when transplanted in CABG procedures and removed from patients suffering coronary events. Otsuka et al. suggested that the endothelial

cell population lining IMA express increased levels of endothelial nitric oxide synthase and heparin sulfate, resulting in protection from athero-thrombotic events (549). In spite of these protective properties in IMA, radiotherapy is still able to result in a significant up-regulation of ICAM-1 on the endothelial surface of these arteries, persisting months to years after cessation of treatment, suggesting that irradiation is able to induce significant damage, even in more robust arterial structures. Reinforced by the findings in this chapter, the risks of radiotherapy-induced CAD should be seriously considered and discussed in patient consultation for breast cancer treatment. Breast conserving surgery such as lumpectomy inevitably subjects the patient to irradiation, however mastectomy alone may avoid radiotherapy in early stage disease thus removing the risk of radiotherapy related CAD.

Adhesive molecules are important in endothelial-leucocyte interaction and leucocyte recruitment into subendothelial tissues, which represent the initial stages of the development of atherosclerotic lesions (558). The interaction between circulating monocytes and endothelial cells acts as a potent source of cytokines and growth factors which affect smooth muscle cell kinetics, can reduce the fibrinolytic potential of endothelial cells via PAI-1 up-regulation and in atherosclerotic lesions lead to plaque rupture and thrombosis (559) (560). Other studies have also demonstrated that circulating levels of ICAM-1, VCAM-1 and E-selectin can serve as molecular markers for atherosclerosis and CAD indirectly implying their role in both atherogenesis and thrombogenesis (559). Ikeda et al. also suggest that monocyte – endothelial cell interaction through adhesion molecules may upgrade production of MMP-1 and MMP-2 which weakens any pre-existing atherosclerotic plaques and predisposes patients to acute coronary syndromes (559).

If ICAM-1 is implicated in radiation induced vascular injury, therapy against ICAM-1 and VCAM-1, or selectins may represent potential avenues by which post radiation acute coronary syndromes and microvascular complications can be reduced. Therapies that were postulated to result in mitigation of ICAM-1 expression such as treatment with antioxidants or pravastatin, counterintuitively have been shown to increase ICAM-1 expression (311) (561), while demonstrating anti-inflammatory effects mediated via TNFα mediated suppression. However, specific ICAM-1

inhibition utilizing knockout murine models have demonstrated abrogation of leukocytic infiltration in a model of thoracic irradiation (312), pretreatment with anti-ICAM-1 antibodies targeting irradiated gastrointestinal tissues, mesenteric vasculature or *in vitro* cultures of human umbilical vein cells demonstrated reduced adherence of leukocytes and endothelial cell permeability (13) (305) (313). These findings suggest that ICAM-1 is an important therapeutic target for ameliorating radiation-induced leukocyte– endothelial cell interactions. Inhibiting the ligand binding capability of endothelial cell surface ICAM-1, with leukocyte ligands in the irradiated tissues may lead to a significant reduction in leukocyte influx, macrophage homing, the magnitude and duration of inflammation. These changes could culminate in a reduction in athero-thrombotic events and improvement in angiogenesis in irradiated tissues (562) (563). Figure 35 below summarises the findings of this chapter detailing the various effects of radiotherapy on the vascular system.

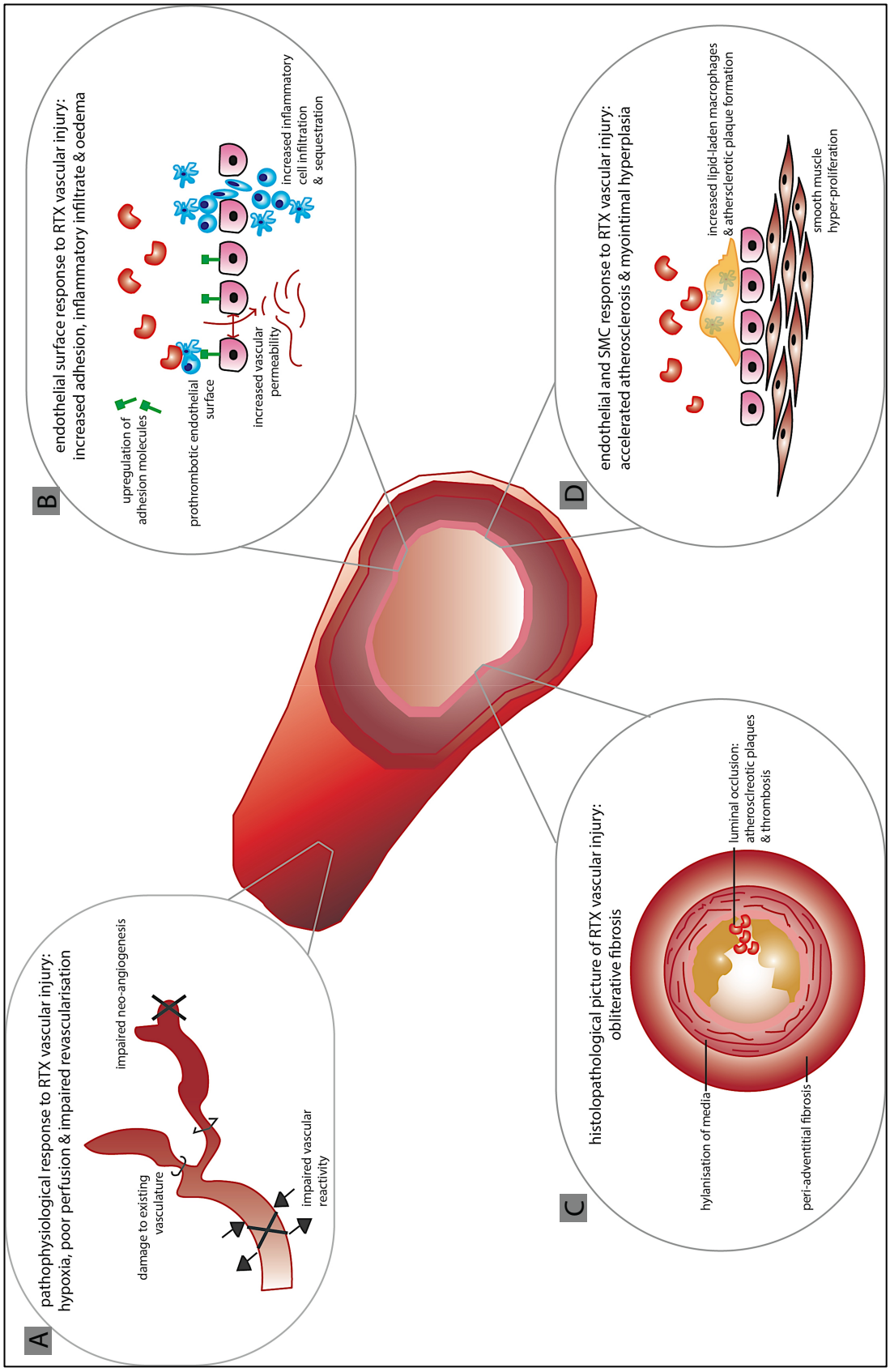
A
pathophysiological response to RTX vascular injury:
hypoxia, poor perfusion & impaired revascularisation
impaired neo-angiogenesis
damage to existing vasculature
impaired vascular reactivity
B
endothelial surface response to RTX vascular injury:
increased adhesion, inflammatory infiltrate & oedema
upregulation of adhesion molecules
prothrombotic endothelial surface
increased vascular permeability
increased inflammatory cell infiltration & sequestration
C
histolopathological picture of RTX vascular injury:
obliterative fibrosis
luminal occlusion: atherosclreotic plaques & thrombosis
hylanisation of media
peri-adventitial fibrosis
D
endothelial and SMC response to RTX vascular injury:
accelerated atherosclerosis & myointimal hyperplasia
increased lipid-laden macrophages & atherscleroric plaque formation
smooth muscle hyper-proliferation

Figure 35

Figure 35 The multi-faceted effect of radiotherapy injury on micro and microvasculature: structural, functional and molecular alterations

This figure summarises the multi-faceted impairment resulting from radiotherapy injury to the micro and macrovascular systems. (A) On a pathophysiological level, damaged vasculature displays impaired reactivity as a result of structural and molecular level alterations. Existing vasculature, namely the endothelial cells are significantly damaged and display poor capability for functional neoangiogenesis. (B) the up-regulation of adhesion molecules such as ICAM-1, shown to persist for months – years post-cessation of treatment; lead to deleterious effects such as increased vascular permeability and inflammatory cell infiltration as well as a prothrombotic endothelial surface. (C) Histopathological changes of concentric intimal thickening and medial myxoid change may contribute to increased atherosclerosis, vessel fragility, dissection and aneurysm formation. Lastly, (D) demonstrates endothelial and smooth muscle cell responses which lead to the development of accelerated atherosclerosis and myointimal hyperplasia resulting in the clinical manifestations of impaired perfusion as well as cardiovascular and cerebrovascular disease.

4.4 Conclusion

Irradiated tissues display several changes in its vasculature representing potential triggers for radiotherapy-associated clinical complications. Such alterations include morphological changes, as well as up-regulation in the expression of adhesion molecules namely ICAM-1 and E-selectin. These functional and molecular changes may contribute directly to impaired neo-angiogenesis and arterial occlusion by rendering the microvascular environment more susceptible to insult from leukocytic/macrophage infiltration, vasospasm and athero-thrombosis. These changes are likely to result in the impaired perfusion of irradiated tissues along with poor capacity to respond to subsequent trauma, surgery and infection with functional angiogenesis. The results presented in this chapter effectively validate the molecular up-regulation of ICAM-1 in irradiated endothelial cells *in vitro* using immunohistochemistry in a human tissue model, demonstrating the utility in further exploring mitigation of ICAM-1 in order to reverse radiation injury to both micro and macrovascular systems.

5 CHAPTER 5: Characterizing the effects of radiotherapy injury on the lymphatic system

5.1 Introduction

The lymphatic system is intricately implicated in cancer treatment as lymphogenous metastases is an important method by which the primary tumour spreads to become disseminated around the body – ultimately representing a life-limiting event. Therefore, treatment of the lymph node basin draining a tumour is a key component of cancer therapy, which may then result in lymphoedema (see section 1.8.6.3)

This chapter focuses on the effect of radiotherapy injury to the lymphatic system. As the lymphatic vasculature and lymph nodes are often the target of anti-tumourigenic therapies; where pathological recapitulation of the process of lymphangiogenesis takes place to enhance the routes of potential tumour cell metastasis by creating greater numbers of 'on-ramps' to the lymphatic system (initial lymphatics) or by 'widening the free-ways' at the level of collecting lymphatics (564) (565). However, damage to normal tissue lymphatics can lead to significant morbidity and mortality associated with lymphatic fluid stasis, clinical lymphedema and impaired immunosurveillance (183).

The lymphatic system, forms a hierarchical one-directional vascular network responsible for transporting excess interstitial fluid to the blood circulation and directing lymphocytes and antigen-presenting cells from the lymphatic vessels to the lymph nodes for immunological surveillance (51). The initial capillaries are blind ending absorptive sacs characterised by thin walls and discontinuous basement membrane allowing for passage of immune cells while also lacking pericyte or support cell coverage (172). This facilitates an influx of interstitial fluid through a combination of mechanical ECM-related and cytoskeletal alterations, utilization of specialized cellular junction proteins and pinocytosis (51). As drainage in the lymphatic system progresses proximally, capillary channels empty into pre-collector and collector channels, smooth muscle cell coverage increases and the lymphatics become more structurally robust containing a series of uni-directional valves. Intrinsic rhythmic pulsations traffic the lymph and its infiltrate (cellular and non-cellular

matter) towards the filtering lymph nodes, which are critical in generating both anti-tumoural and immune responses (172). Lymphangiogenesis: the formation of new lymphatic vessels, is spontaneous in nature during embryonic growth phases and follows the initial trajectory of blood vessel formation. Processes of lymphangiogenesis in adults are primarily needed when faced with pathological insult, such as chronic inflammation, trauma, secondary lymphoedema and tumor metastasis (173). The impairment of lymphatic structure and function is characterised by increased permeability and intercellular openings leading to poor interstitial fluid clearance, reflux leading to subcutaneous tissue swelling. Abnormal lymphangiogenic cues can result in dysfunctional lymphangiogenesis (327), immune response alteration and further accumulation of interstitial fluid and proteins, clinically manifesting as truncal or limb lymphoedema (see section 1.8.6.3) (174).

Lymphoedema (Figure 36 A-B) is defined as a condition in which swelling occurs in an area of the body which results from accumulation of proteinaceous fluid when drainage is impaired relative to lymphatic fluid circulation (233). Lymphoedema may be categorized as primary (congenital) or secondary, which is acquired most commonly as a side effect of treatments such as surgery or radiotherapy for cancer eradication or in the setting of significant trauma (234). As detailed in section 1.8.6.3, it is estimated that 20% of patients undergoing treatment for malignancies such as breast, head and neck, uro-gynaecological and skin cancers develop lymphoedema, contributing to more than 8000 new cases of lymphoedema per annum in Australia alone (233). Secondary lymphoedema often manifests within two years of cancer diagnosis, surgery and/or radiotherapy to the affected lymph node basins (238) (239), with troublesome symptomology and functional deficits resulting in great physical and psychological burden on patients. Numerous studies have suggested that radiotherapy is a significant and independent risk factor contributing to the incidence of secondary lymphoedema (243). Sentinel lymph node biopsy or lymph node dissection procedures alone carry a risk of up to 20% for development of secondary lymphoedema (243). In the presence of radiation, the risk increases to up to 40% in the upper limb and greater than 60% in the lower limb (see Table 3) (233) (235) (240-244).

In addition to lymphoedema, irradiated tissues demonstrate impaired immunosurveillance (234) as described in section 1.8.6.4. It is likely the cumulative effects of fluid stasis along with damage to the components of the immune system, such as dendritic and Langerhans cells, allow for superimposed infection contributing to ongoing wound healing issues (201) (245).

Current treatments offered for lymphoedema aim to achieve symptomatic relief with manual massage and compression garments but are difficult to tolerate and therefore compliance is poor. Invasive surgical therapies, such as liposuction, surgical tissue excision and lymphatico-venous-anastomoses not possible for every patient. Additionally, anecdotal reports of methods using fat grafting or the recruitment of free vascularised tissue demonstrate promising results in alleviating the effects of lymphoedema (244) (287). However the mechanisms of action require further scientific investigation.

Several studies have attempted to identify the effects of radiotherapy injury on LEC and implicate TGF-β-mediated fibrosis as a key contributor to the damage inflicted on the lymphatic system (83) (177). These studies suggest that abnormal *in-vitro* LEC morphology and lymphangiogenic functioning, peri-lymphatic fibrosis and impaired tissue compliance lead to the development of lymphoedema in murine models under the influence of TGF-β. They further attempt to abrogate local or systemic TGF-β via antibody blockade and claimed reduction in development and severity of lymphoedema (83) (133) (177) (178). In an alternative animal model of radiotherapy injury, irradiation of pig flanks demonstrated a "biphasic" impairment of lymphatic drainage. The authors suggest the lymphoedema is initially linked to inflammation and oedema but that later lymphoedema results from dermal and subcutaneous fibrosis (187). Fluid transport studies using FITC-Dextran lymphatic infusion in the lower limbs of New Zealand white rabbits receiving popliteal node irradiation demonstrated nearly 60% flow reduction associated with lymph node capsule fibrosis (183). Baker et al. claimed that they observed the formation of natural lymphatico-venous anastomoses (LVA), as a compensatory response, which they hypothesized might improve lymphatic fluid clearance (183). A similar finding was reported in a human study conducted in the late 1960s. The authors detected a 2.3% incidence of

LVA in patients with secondary lymphoedema as qualified with x-ray imaging after injection with Ultrafluid Lipiodol and the characteristic globular appearance of oil contrast material in blood vessels (188), see section 1.7.4 for more detail.

In order to investigate the effects of radiotherapy injury on the lymphatic system this chapter focuses on the histological analysis of irradiated and normal tissues collected from patients undergoing delayed cancer reconstruction post-radiotherapy. Following our histopathological observations, functional experiments interrogating cellular changes resulting from radiotherapy injury in LEC were conducted. Next, next generation sequencing was employed to analyse molecular level alterations resulting from radiotherapy injury. Exploration of key RNA candidates, identified in the gene sequencing, were validated at protein level using patient tissue samples and various other molecular techniques. Subsequent experiments explored the effects of treating LECs with novel protein candidates as well as traditional lymphangiogenic factors, as avenues of treatment of the clinical manifestation of radiotherapy induced LEC injury and lymphoedema.

5.2 Results – Lymphatic Endothelial Cells (LEC)

5.2.1 Cellular/functional effects of radiotherapy on LEC

5.2.1.1 Lymphatic staining in human tissues (D240)

Previous authors have studied the effects of RTX on dermal lymphatics in an animal models (83), determining that the density of lymphatic vessels was diminished in irradiated tail skin. Therefore, initial experiments sought to elucidate whether the same pattern of diminished lymphatic vessel density held in human tissues (Figure 36 C, D). In order to perform a controlled comparison, irradiated skin from the chest wall of patients treated with radiotherapy (Figure 36 D) was compared to unirradiated skin from the same patient (Figure 36 C). Samples from a total of ten patients who were undergoing delayed cancer reconstruction surgery were collected. These groups were comprised of surplus tissues that were harvested simultaneously and treated identically thereafter. Briefly, the tissues were placed in labeled formalin-containing pots before transportation of the fixed samples to the histology laboratory for

subsequent transfer to paraffin blocks prior to cutting and staining. IHC was performed using a validated monoclonal antibody D2-40 against human podoplanin (Figure 36 C,D) (a well-established marker of LECs) (51). Quantification was performed using the LVAP plugin and protocol for Image J, as previously described (481). D2-40 immuno-staining of control and irradiated tissues demonstrated clear staining of lymphatic vessels in both groups (Figure 36 C,D) compared with negative controls (data not shown). Quantification of the lymphatic vessel density (LVD) demonstrated that irradiated tissues did not have a significantly different LVD or lymphatic vessel number compared with control samples from non-irradiated areas in the same patient (LVD 1.61 ± 0.77 0Gy vs. LVD 1.05 ± 0.10 10Gy (Figure 36 E)). Quantification of D2-40 positive lymphatic vessels determined that 0Gy samples had an average of 8.04 ± 3 .83 vessels per x10 objective and 10Gy samples had 5.17 ± 0.51 vessels per x10 objective, the difference showing a trending decrease in irradiated samples, however did not reach statistical significance (Figure 36 F). Similarly, quantification of lymphatic vessel width determined 180.1 ± 16.2 μm average vessel width and 842.9 ± 50.6 μm total vessel width in 0Gy; and 199.3 ± 12.1 μm average vessel width and 1028 ± 89.2 μm. total vessel width in 10Gy. The irradiated samples demonstrated a trend of increased width compared to control samples from non-irradiated areas in the same patient, however these results did not reach statistical significance (Figure 36 G,H).

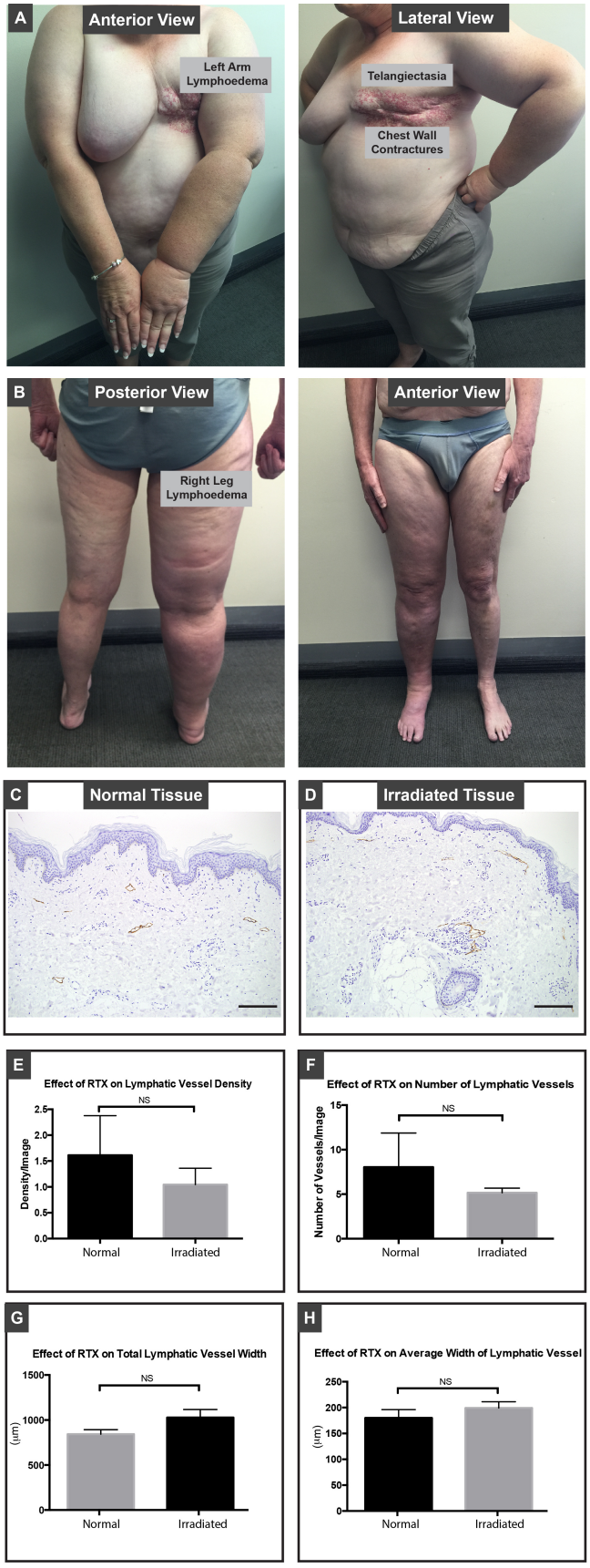
A
Anterior View
Left Arm Lymphoedema
Lateral View
Telangiectasia
Chest Wall Contractures
B
Posterior View
Right Leg Lymphoedema
Anterior View
C
Normal Tissue
D
Irradiated Tissue
E
Effect of RTX on Lymphatic Vessel Density
NS
Density/Image
2.5
2.0
1.5
1.0
0.5
0.0
Normal
Irradiated
F
Effect of RTX on Number of Lymphatic Vessels
NS
Number of Vessels/Image
15
10
5
0
Normal
Irradiated
G
Effect of RTX on Total Lymphatic Vessel Width
NS
(µm)
1500
1000
500
0
Normal
Irradiated
H
Effect of RTX on Average Width of Lymphatic Vessel
NS
(µm)
250
200
150
100
50
0
Normal
Irradiated

Figure 36

Figure 36 Clinical examples of Radiotherapy induced Lymphoedema and histological analysis of lymphatic vessel characterstics in normal and irradiated patient samples.

Clinical examples of radiotherapy-induced lymphoedema in two separate patients: (A) anterior and lateral views of extensive chest wall telangiectasia, fibrosis and scarring along with left arm lymphoedema in the setting of mastectomy and radiotherapy for breast cancer; (B) Posterior and anterior view of lower limb lymphoedema in the setting of a right lower limb melanoma, groin dissection and radiotherapy to the inguinal lymph nodes. Light microscopy images taken at x10 objective of D2-40 monoclonal antibody staining of (C) normal skin samples and compared with simultaneously harvested patient matched irradiated skin samples (D). Stained skin samples were quantified for various parameters using the LVAP protocol (481); (E) Lymphatic vessel density (LVD) and (F) number of lymphatic vessels which demonstrated a trending decrease in irradiated samples compared to normal tissue controls (statistically not significant). Additional quantification of (G) lymphatic vessel width and (H) average lymphatic vessel width, demonstrated a trend of increased width in irradiated samples, which again did not reach statistical significance. Scale Bar in (C) and (D) 200 μm. NS = not significant, error bars represent SEM, with n=10.

5.2.1.2 Cell Survival Dynamics

In order to further characterize radiotherapy-induced changes at a LEC level, a panel of functional bio-assays were performed based on fundamental processes that together contribute to lymphangiogenesis. LEC cultures were established from proliferating cells and cultured in medium containing essential growth factors (see 2.1.1 and 2.1.2). Cells were passaged on reaching 80-90% confluence and utilized for *in-vitro* functional assays between passage 2-6.

The effect of radiotherapy on LEC survival was first determined utilizing a survival fraction calculation (see 2.2.1). A set number of cells were seeded in a 24 well plate, left to attach overnight, then were either irradiated (10Gy) or underwent sham treatment (0Gy). They were left in standard culture conditions for 48 h, after which viability was determined by cell counting based on exclusion of trypan blue dye uptake in viable cells with intact cell membranes. Calculation of 0Gy and 10Gy plating efficiency preceded determination of 10Gy LEC survival fraction. This calculation accounted for a degree of normal cell loss (for more calculation descriptions see 2.2.1). As demonstrated in (Figure 37 A,B), irradiation of LECs results in a survival fraction of 72% compared to normal (0Gy) cells, therefore representing a 28% reduction in cell survival in 10Gy LEC. To further examine the processes that may contribute to the reduction in LEC cell survival, proliferation and apoptosis assays were conducted (see 2.2.2). To replicate the clinical scenario in which patients receive smaller doses over a protracted period of time, a fractionated experimental group was assigned to receive five 2Gy doses delivered over a 48 h interval and compared with a single dose group was assigned to receive one 10Gy dose and the control group received 0Gy. Briefly, cells were seeded into a white walled 96 well plate, left to attach overnight, with irradiation treatment commencing the following day. CellTitre Glo® (Promega) or Caspase3/7® (Promega) luminescent reagents were added to the wells 48 h post-radiotherapy to determine cell proliferation and apoptotic activity respectively, by obtaining values using a luminometer plate reader (see 2.2.2 for more detailed methodology and settings). In these studies, LECs displayed a 12.4 ± 8.5% trend of reduction in proliferation after 2Gy x 5 and a significant 27.0 ± 4.2% reduction in proliferation after 10Gy irradiation compared with 0Gy controls (Figure 37 C). LEC apoptotic activity mediated by Caspase 3/7

activation was decreased by 31.5 ± 6.6% after 2Gy x 5 and a 33.7 ± 3.0% after 10Gy irradiation compared with 0Gy controls (Figure 37 D). Therefore, as the effects of RTX on LEC demonstrated similarities in direction of effect between fractionated and single dose treatments, subsequent experiments were performed with a single dose of 10Gy for ease of experimental design.

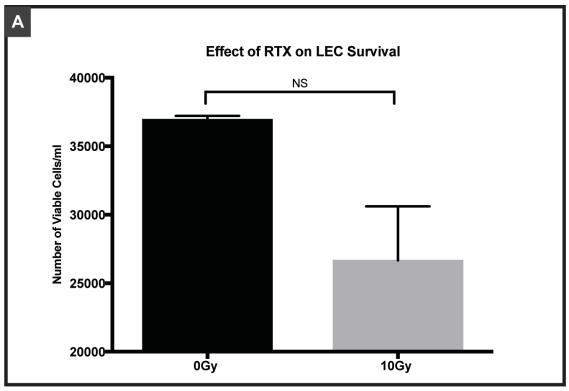

B

	0Gy	10Gy
Viable Cell Count (Mean +/- SEM)	36944 ± 278	26667 ± 3938
Plating Efficiency	74%	53%
Survival Fraction	100%	**72%**

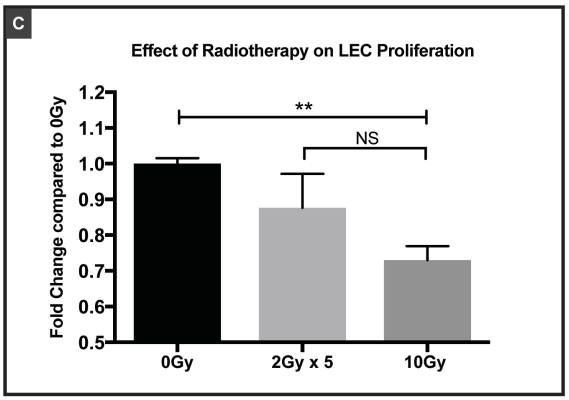

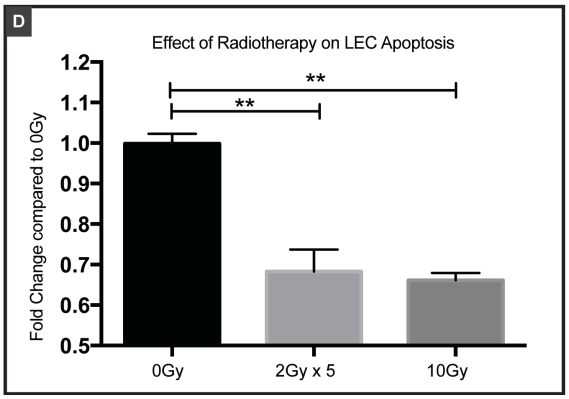

Figure 37

Figure 37 Radiotherapy decreases LEC proliferation and apoptosis

(A) Effect of radiotherapy on LEC survival represented by viable cell numbers 48 h after irradiation (10Gy) or control (0Gy) treatment. (B) Quantification of 0Gy and 10Gy viable cell counts showed plating efficiency and the survival fraction of 10Gy LEC demonstrated trends of reduction in comparison to 0Gy controls (assuming 100% survival of 0Gy control group cells). The effects of 2Gy x 5 and 10Gy irradiation doses decreased LEC proliferation (C) and decreased LEC apoptosis (D), represented as fold changes compared to 0Gy control groups. Asterisks above bar-graph indicate statistical significance (** = $p<0.01$, NS = not significant), error bars represent SEM, with $n\geq3$.

5.2.1.3 Cell morphological and molecular characterization of normal and irradiated LEC

As LECs were cultured and passaged for *in-vitro* functional assays, a reduction in cell density and increase in irradiated cell size was observed with bright field microscopy (Figure 38 A,B). To determine if the basic molecular expression of LECs was altered by radiotherapy, IHC was performed on 0Gy and 10Gy LECs 48 h after radiotherapy for key endothelial and lymphatic cell markers (PECAM/CD31 and D2-40/Podoplanin) (see section 2.6 for detailed methodology). Staining demonstrated that both 0Gy (Figure 38 C,E) and 10Gy (Figure 38 D,F) LEC stained positive for both CD31 and D2-40. These findings confirmed that irradiated LECs still retain the basic molecular characterization inherent to that of LEC. The observed increase in size of irradiated LECs was quantified in an assay where 3D spheroids were formed in variations of 5000, 10,000 and 20,000 cells/spheroids from 0Gy and 10Gy LECs (see 2.2.4.2 for more detailed methodology for spheroid formation). Images of the formed spheroids were captured using bright field microscopy and their size in μm^2 was quantified using ImageJ software (National Institute of Health, USA). A two way ANNOVA test determined that 81.2% of the variation in spheroid size resulted from the difference in cell size, however 5.05% was as a result of radiotherapy of LEC ($p<0.01$). On closer examination, 10,000 cells/spheroids constructed from 10Gy cells (Figure 38 J) demonstrated a significant 43.7 ± 10.1% increase in size (μm^2), compared with 0Gy controls (Figure 38 I). Meanwhile 20,000 cells/spheroid, formed

from 10Gy cells (Figure 38 L) demonstrated a significant 17.2 ± 5.4% increase in size (μm^2) compared with 0Gy controls (Figure 38 K). Additionally, it was observed that spheroids formed from 10Gy cells demonstrated reduced cell-to-cell adhesion, discernible in (Figure 38 H,J,L) compared to their (Figure 38 G,I,K) 0Gy controls.

5.2.1.4 *In-vitro* lymphangiogenic functional assays

In-vitro assays were designed and conducted to establish the effect of radiation on the "homeostatic" functional profile of LECs i.e. the major functions required to carry out the key process that enable lymphatic regeneration and lymphangiogenesis. The functions that were interrogated included proliferation, apoptosis, migration, tube formation, vessel branching and spheroid formation. This panel of functional assays demonstrated that radiotherapy significantly altered key homeostatic functions in LECs, with some results demonstrating changes contrary to conventional dogma. 10Gy radiotherapy resulted in a 27 ± 4.2% reduction in LEC proliferation (Figure 39 A), however also resulted in a 33.7 ± 3.0% reduction in apoptosis (Figure 39 B), suggesting that sub-lethal radiotherapy-induced injury does not proceed to cause large-scale cell death and may indicate a state of induced LEC senescence. In order to then interrogate the other functions integral to regeneration of lymphatic vessels, LEC migration, tube formation and branching were next analyzed in both 2D and 3D assays (see sections 2.2.3 and 2.2.4 for detailed methodology). Irradiation significantly reduced the 2D migration capabilities of LEC by 28.7% at 48 h (Figure 39 C) compared with 0Gy cells which achieved 99.7 ± 0.27% gap closure (Figure 39 E) while 10Gy cells achieved 71.0 ± 4.04% gap closure (Figure 39 H) in normal media conditions at 48 h.

2D tube formation assays conducted using growth-factor reduced matrigel demonstrated that 0Gy LECs formed 40.4 ± 2.31 branches and 1.22 ± 0.22 tubes per x10 field imaged (Figure 39 K), while 10Gy LECs formed a significantly reduced number of both branches (13.1 ± 1.20) and tubes (0.26 ± 0.08) (Figure 39 N) in normal media conditions (Figure 39 F,I). 3D spheroid-sprouting assays were performed and parameters including number of sprouts, average length of sprouts and total length of sprouts were determined on spheroid photographs (bright field microscopy at x10 objective) using ImageJ and the LVAP plugin (481). As shown in

Figure 38 E, irradiated LECs demonstrated reduced cell-cell adhesion when forming spheroids and it was subsequently noted that spheroids formed from pre-irradiated LECs failed to retain a spherical formation when seeded for sprouting assays in the 3D fibrin/thrombin gel (data not shown). Therefore, spheroids were constructed from 0Gy LECs, left to optimally form overnight, then irradiated and placed in the 3D gel to analyze sprouting parameters. 0Gy LEC spheroids (Figure 39 P) demonstrated an average of 3.4 ± 0.43 sprouts/spheroid, average spheroid sprout length of 32.17 ± 3.24 μm and total sprout length/spheroid of 111.9 ± 20.46 μm. 10Gy LEC spheroids (Figure 39 Q) demonstrated an average of 2.33 ± 0.45 sprouts/spheroid, average spheroid sprout length of 23.03 ± 3.36 μm and a total sprout length/spheroid of 66.98 ± 21.13 μm. The irradiated spheroids demonstrated a trend of reduction in number of sprouts/spheroid (Figure 39 L) and average spheroid sprout length (Figure 39 O) however, the total sprout length per spheroid was significantly reduced as a result of radiotherapy (Figure 39 R).

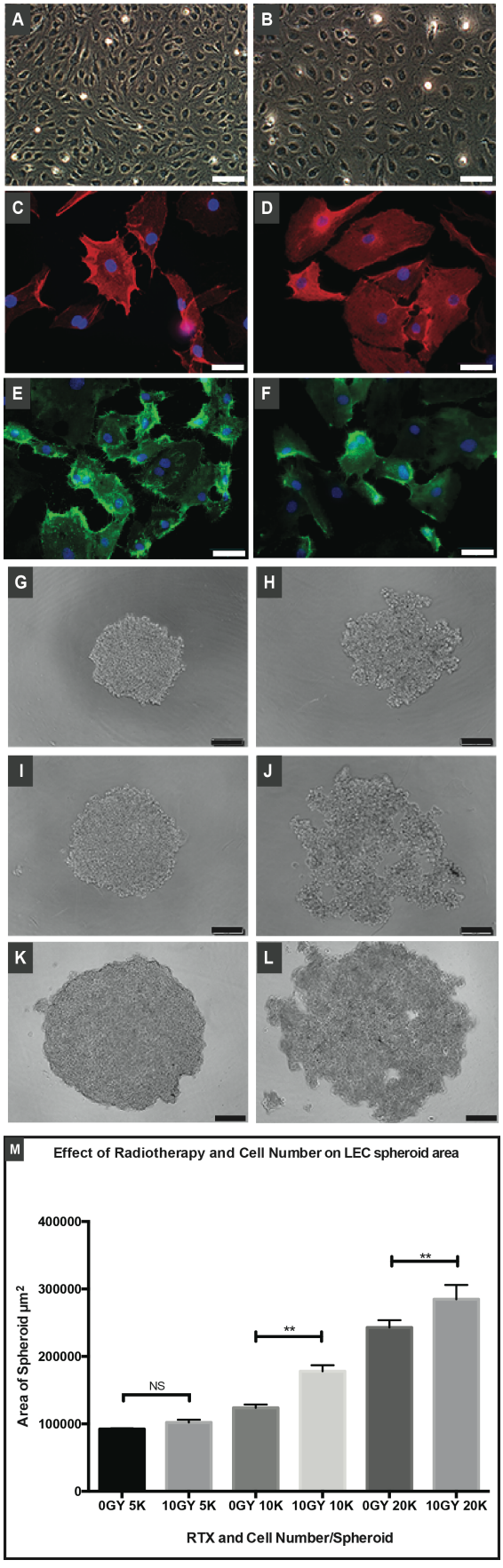
A
B
C
D
E
F
G
H
I
J
K
L
M
Effect of Radiotherapy and Cell Number on LEC spheroid area
Area of Spheroid µm²
400000
300000
200000
100000
0
NS
**
**
0GY 5K
10GY 5K
0GY 10K
10GY 10K
0GY 20K
10GY 20K
RTX and Cell Number/Spheroid

Figure 38

Figure 38 Morphological Alterations and Lymphatic Marker Characterization of normal and irradiated LECs

(A) x10 objective bright field microscopy imaging of confluent 0Gy LECs in normal culture conditions, demonstrating cobblestone-like appearance. (B) x10 objective bright field microscopy of confluent 10Gy LECs, 48 h after irradiation, in normal culture conditions, demonstrating a similar cobblestone appearance with a visually apparent increase in cell size (not quantified). (C) and (D) Immunohistochemistry at x20 objective of 0Gy and 10Gy LEC respectively stained with anti-CD31 (PECAM) rabbit anti human primary antibody, red fluorescent goat anti rabbit secondary antibody and DAPI. (E) and (F) Immunocytochemistry at x20 objective of 0Gy and 10Gy LEC stained with anti-D2-40 (Podoplanin) mouse anti human primary antibody, green fluorescent goat anti mouse secondary antibody and DAPI. Spheroids formed at 24 h post-seeding, imaged at x10 objective bright field microscopy (G) 5000 cell 0Gy LEC spheroid, (H) 5000 cell 10Gy LEC spheroid, (I) 10000 cell 0Gy LEC spheroid, (J) 10000 cell 10Gy LEC spheroid, (K) 20000 cell 0Gy LEC spheroid, (L) 20000 cell 10Gy LEC spheroid. (M) Quantification determining effects of irradiation and number of cells per spheroid on spheroid area. Scale bar (A), (B) and (G-L) 100 μm, (C) and (D) 50 μm. Asterisks above bar-graph indicate statistical significance (** = $p<0.01$, NS = not significant), error bars represent SEM, with $n\geq3$.

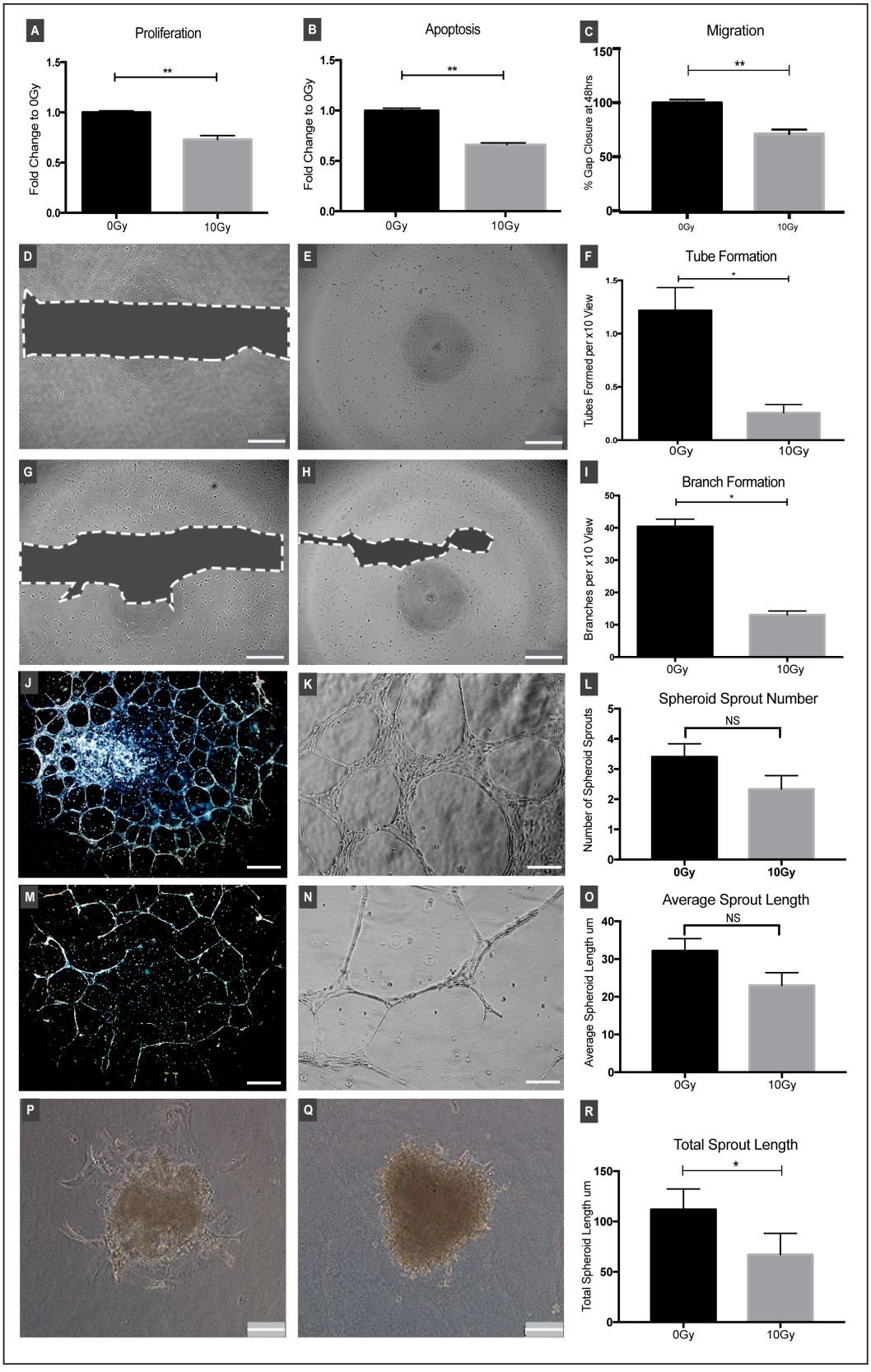
A
Proliferation
Fold Change to 0Gy
1.5
1.0
0.5
0.0
**
0Gy
10Gy
B
Apoptosis
Fold Change to 0Gy
1.5
1.0
0.5
0.0
**
0Gy
10Gy
C
Migration
% Gap Closure at 48hrs
150
100
50
0
**
0Gy
10Gy
D
E
F
Tube Formation
Tubes Formed per x10 View
1.5
1.0
0.5
0.0
*
0Gy
10Gy
G
H
I
Branch Formation
Branches per x10 View
50
40
30
20
10
0
*
0Gy
10Gy
J
K
L
Spheroid Sprout Number
Number of Spheroid Sprouts
5
4
3
2
1
0
NS
0Gy
10Gy
M
N
O
Average Sprout Length
Average Spheroid Length um
40
30
20
10
0
NS
0Gy
10Gy
P
Q
R
Total Sprout Length
Total Spheroid Length um
150
100
50
0
*
0Gy
10Gy

Figure 39

Figure 39 The *in-vitro* effects of radiotherapy on LEC lymphangiogenic functions
The effect of radiotherapy on LEC survival 48 h after irradiation (10Gy) or control (0Gy) treatment. (A) Proliferation and (B) Apoptosis represented as fold changes compared to 0Gy control groups. x4 objective bright field imaging of LEC were taken post the creation of a scratch wound on a confluent mono-layer of proliferating cells. (D) 0Gy LEC scratch wound area at 0 h, (E) 0Gy LEC scratch wound area at 48 h, (G) 10Gy LEC scratch wound area at 0 h, (H) 10Gy LEC scratch wound area at 48 h. (C) Quantification of the % gap closure at 48 h compared to 0hr controls demonstrate the effects of radiotherapy on LEC migration. Bright field imaging of LEC seeded on GFR Matrigel photographed at 24 and 48 h after radiotherapy, with (J) 0Gy control LEC at 24 h x2 objective and (K) 0Gy control LEC at 48 h x10 objective demonstrating organized and well-formed tubes, while (M) 10Gy irradiated cells at 24 h x2 objective and (N) 10Gy irradiated cells at 48 h x10 objective displaying reduced tube formation with disorganized structure. (F) Quantification of number of tubes formed per x10 view as determined with the LVAP plug-in using ImageJ (NIH), demonstrating a significant reduction as a result of radiotherapy at 48 h. (I) Analyses of differences in number of LEC branch points formed at 48 h also demonstrated a signification reduction as a result of radiotherapy. X20 objective bright field microscopy was used to capture images of spheroids 48 hours after seeding in a fibrin/thrombin gel and irradiation with (P) 0Gy and (Q) 10Gy doses. In (D), (E), (G), (H); Scale Bar 200μm, dotted line represents periphery of scratch wound and grey shaded area represents scratch wound area. In (J), (M); Scale bar 400μm, (K), (N); Scale bar 100μm and (P), (Q); Scale Bar 50 μm. Asterisks above bar-graphs indicate statistical significance (* = $p<0.05$, ** = $p<0.01$, NS = not significant), error bars represent SEM, with $n\geq3$.

5.2.1.5 Prox-1 GFP mouse ear wounding model

Validation of the functional effects of radiotherapy on LECs *in-vitro* was conducted using an *in-vivo* ear wounding model in Prox-1 GFP mice. Briefly, mice underwent anaesthetic sedation, 10Gy irradiation of their right ears while their shielded left ear served as a control receiving 0Gy. A surgical wound was created one week after irradiation and mice were culled at the 1, 2 and 3 week post-wounding time points. Ear tissue was dissected, fixed and wholemounted for imaging with confocal microscopy. The GFP expressing lymphatic vessels were quantified using Image J (NIH) and a macro by Arganda-Carreras et al. (492). Ear lymphatics were analysed for sprouting (blind ending sacs) and branch points. Irradiated ears demonstrated a trend in reduction of branching and sprouts at 1 week and significant reduction in both parameters at the 2 and 3 week timepoints compared to un-irradiated controls (Figure 40 A, F, G). These findings represent reduced lymphatic vessel density (not quantified) and significant impairment in neo-lymphangiogenesis in irradiated ears post-wounding (Figure 40 C,E) compared to un-irradiated ear controls (Figure 40 B,D).

5.2.2 The molecular effects of radiotherapy on LEC

5.2.2.1 Next generation sequencing

Having determined functional alterations in the panel of bioassays, next generation sequencing RNA analysis was conducted on LECs to interrogate the changes that occur at a molecular level after radiotherapy induced injury. As described in 2.3.4, it is able to offer an in-depth analysis of the underlying pathways that may drive the impairment in lymphangiogenic processes resulting from irradiation. These analyses aimed to identify a distinct set of alterations in gene expression that distinguish irradiated cells from normal cells.

Standardised numbers of LECs were plated in cell culture flasks and once 80-90% confluence was achieved they were irradiated with two regimes; one group received a single dose of 10Gy with the second group received five 2Gy fractions across 48 h with 0Gy control groups for each.

RNA extraction was undertaken at 4 h after the 10Gy dose or after the final 2Gy fractionated dose using the QIAGEN, Germany® RNEasy Plus Universal Kit as per manufacturer's instructions. Samples were then tested for purity and quality control using the Nanodrop^{TM} Spectrophotometer (Thermo Fischer Scientific, USA) and stored at -80^{o}C, till further processing. Each sample underwent RNA sequencing (100 base pair single end) in the Illumina HiSeq machine at the Australian Genome Research Facility (AGRF) and results were presented in a series of spreadsheets and heat maps along with a comprehensive pathway analysis platform (see 2.3.4, 2.3.5 for detailed methodology).

Next generation sequencing demonstrated several significant differences between the expression profile of 10Gy Single Dose and five 2Gy fractionated doses in comparison to un-injured 0Gy controls. 10Gy LEC significantly altered the expression of 607 genes at 4 hours with adjusted p-values <0.05, while 2Gy x 5 LECs demonstrated 827 altered genes at 4 hours. The top ten candidates that were changed in response to radiotherapy injury along with known lymphangiogenic factors, lymphangiogenic markers and key chemokines for each irradiation regime are listed in Table 14 and Table 15.

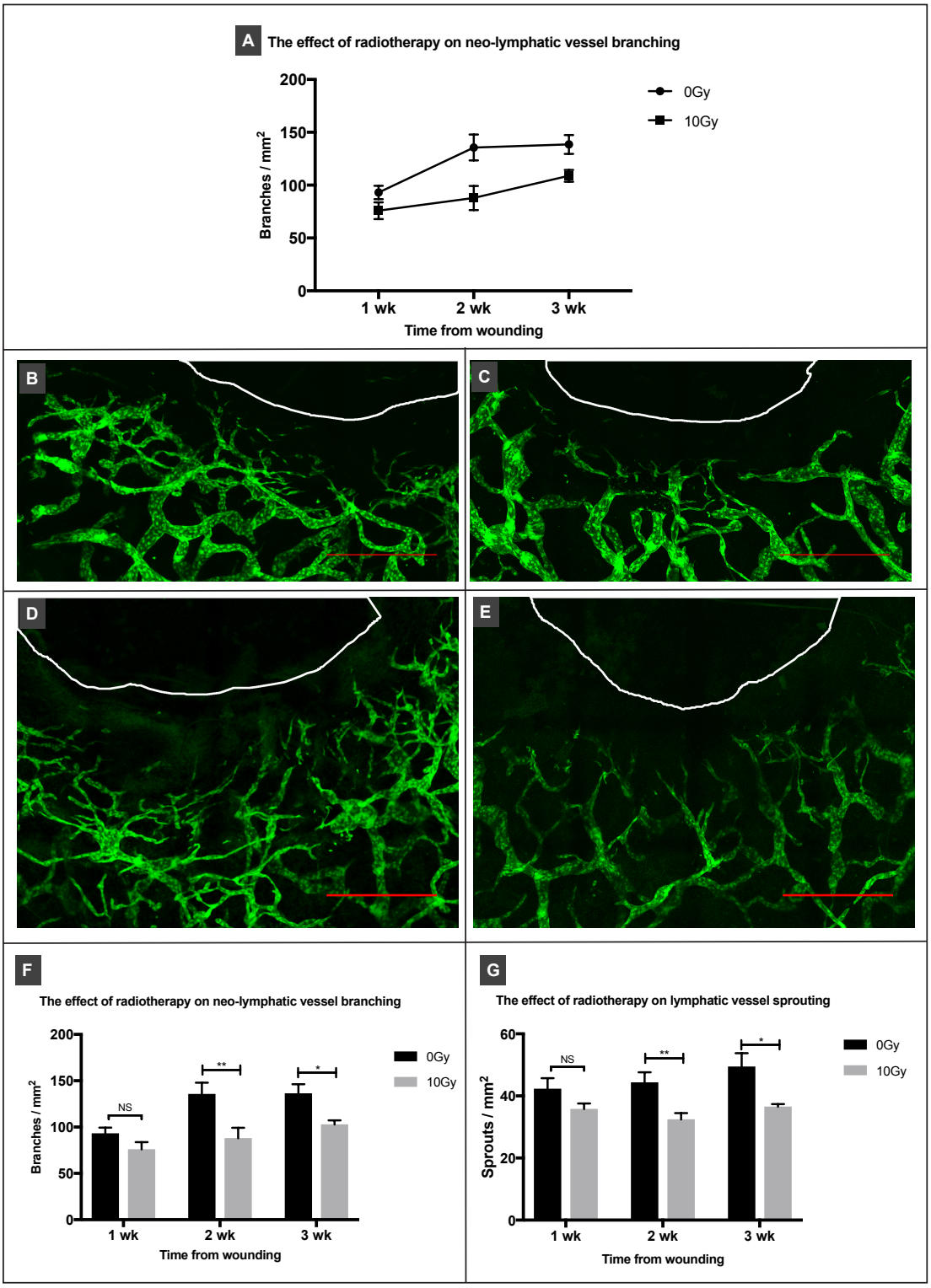
A
The effect of radiotherapy on neo-lymphatic vessel branching
Branches / mm2
200
150
100
50
0
1 wk
2 wk
3 wk
Time from wounding
0Gy
10Gy
B
C
D
E
F
The effect of radiotherapy on neo-lymphatic vessel branching
Branches / mm2
NS
**
*
1 wk
2 wk
3 wk
Time from wounding
0Gy
10Gy
G
The effect of radiotherapy on lymphatic vessel sprouting
Sprouts / mm2
60
40
20
0
NS
**
*
1 wk
2 wk
3 wk
Time from wounding
0Gy
10Gy

Figure 40

Figure 40 Radiotherapy results in impaired lymphangiogenesis post wounding in a PROX-1 GFP mouse ear model

(A) A graph depicting quantification of 0Gy and 10Gy lymphatic vessel branch points (branches/mm^2) at 1, 2 and 3 weeks after wounding demonstrating a reduction in the irradiated group across all time points. Confocal microscopy images representative of GFP lymphatic vessels in (B) 0Gy ear wound at 1 week, (C) 10Gy ear wound at 1 week, (D) 0Gy ear wound at 3 weeks and (E) 10Gy ear wound at 3 weeks representing a significant impairment in neo-lymphangiogenesis after wounding and radiotherapy. Quantification of the branches/mm^2 (F) and sprouting (G) in both 0Gy and 10Gy ears across 1, 2 and 3 week timepoints post wounding Asterisks above bar-graphs indicate statistical significance (* = $p<0.05$, ** = $p<0.01$, NS = not significant), error bars represent SEM, with $n\geq3$.

GeneID	Symbols	GeneName	Chr	logFC	adj.P.Val
Top 10 Candidates and Lymphangiogenic Factors					
3576	IL-8	interleukin 8	4	3.16	2.69E-09
1026	CDKN1A	cyclin-dependent kinase inhibitor 1A (p21, Cip1)	6	2.06	3.13E-06
355	FAS	Fas (TNF receptor superfamily, member 6)	10	2.11	3.13E-06
2643	GCH1	GTP cyclohydrolase 1	14	1.28	3.13E-06
6364	CCL20	chemokine (C-C motif) ligand 20	2	2.39	3.64E-06
55294	FBXW7	F-box and WD repeat domain containing 7, E3 ubiquitin protein ligase	4	1.08	4.89E-06
467	ATF3	Activating Transcription Factor 3	1	2.89	7.77E-06
7538	ZFP36	ZFP36 ring finger protein	19	1.85	8.87E-06
10769	PLK2	polo-like kinase 2	5	1.22	8.87E-06
1052	CEBPD	CCAAT/enhancer binding protein (C/EBP), delta	8	1.81	8.87E-06
3569	IL-6	interleukin 6 (interferon, beta 2)	7	2.46	0.065
7424	VEGF-C	vascular endothelial growth factor C	4	0.13	0.760
2277	VEGFD	Vascular endothelial growth factor D		0.21	0.88
Chemokine Family					
57007	CXCR7	chemokine (C-X-C motif) receptor 7	2	2.30	0.003
7852	CXCR4	chemokine (C-X-C motif) receptor 4	2	-0.13	0.927
6387	CXCL12	chemokine (C-X-C motif) ligand 12	10	-0.31	0.571
3577	CXCR1	chemokine (C-X-C motif) receptor 1	2	0.43	0.539
3579	CXCR2	Chemokine (C-X-C motif) receptor 2	2	0.43	0.813
2919	CXCL1	chemokine (C-X-C motif) ligand 1	4	2.50	1.53E-05
2920	CXCL2	chemokine (C-X-C motif) ligand 2	4	3.04	6.62E-05
2921	CXCL3	chemokine (C-X-C motif) ligand 3	4	3.89	0.0021
6364	CCL20	chemokine (C-C motif) ligand 20	2	2.39	3.64E-06
6366	CCL21	chemokine (C-C motif) ligand 21	9	-1.26	0.0046
6347	CCL2	chemokine (C-C motif) ligand 2	17	2.01	0.009
6355	CCL8	chemokine (C-C motif) ligand 8	17	2.55	0.037
Lymphatic Markers					
10894	LYVE1	lymphatic vessel endothelial hyaluronan receptor 1	11	-0.37	0.576
2050	EPHB4	EPH receptor B4	7	-0.41	0.030
2324	FLT4	fms-related tyrosine kinase 4	5	-0.20	0.675
10630	PDPN	podoplanin	1	0.11	0.806
5629	PROX1	prospero homeobox 1	1	-0.63	0.135

5175	PECAM1	platelet/endothelial cell adhesion molecule 1	17	-0.10	0.843
1948	EFNB2	ephrin-B2	13	-0.13	0.834

Table 14 - Gene expression alterations of 10Gy LEC in comparison to 0Gy LEC controls

Table 14 Key Candidates from the next generation sequencing data comparing 10Gy single dose irradiated LECs to 0Gy controls. The table details the top ten gene candidates, known key lymphangiogenic factors, lymphangiogenic markers as well as chemokines and the differential gene expression resulting from radiotherapy injury (blue boxes indicate gene expression changes that reach statistical significance $p<0.05$). Chr = chromosome, logFC = log fold change.

GeneID	Symbols	GeneName	Chr	logFC	adj.P.Val
Top 10 Candidates and Lymphangiogenic Factors					
355	FAS	Fas (TNF receptor superfamily, member 6)	4	3.16	3E-05
7292	TNFSF4	tumor necrosis factor (ligand) superfamily, member 4	6	2.06	3E-05
3990	LIPC	lipase, hepatic	10	2.11	4E-05
8531	CSDA	cold shock domain protein A	14	1.28	4E-05
2982	GUCY1A3	guanylate cyclase 1, soluble, alpha 3	2	2.39	4E-05
2701	GJA4	gap junction protein, alpha 4, 37kDa	4	1.08	6E-05
50484	RRM2B	ribonucleotide reductase M2 B (TP53 inducible)	1	2.89	6E-05
1026	CDKN1A	cyclin-dependent kinase inhibitor 1A (p21, Cip1)	19	1.85	8E-05
132671	SPATA18	spermatogenesis associated 18	5	1.22	2E-04
57535	KIAA1324	KIAA1324	8	1.81	3E-04
3576	IL-8	interleukin 8	4	0.803	0.01
3569	IL-6	interleukin 6 (interferon, beta 2)	7	0.884	0.065
7424	VEGF-C	vascular endothelial growth factor C	4	-0.641	0.052
2277	VEGFD	Vascular endothelial growth factor D		0.941	0.336
Chemokine Family					
57007	CXCR7	chemokine (C-X-C motif) receptor 7	2	0.421	0.660
7852	CXCR4	chemokine (C-X-C motif) receptor 4	2	0.725	0.418
6387	CXCL12	chemokine (C-X-C motif) ligand 12	10	-0.134	0.802
6364	CCL20	chemokine (C-C motif) ligand 20	2	-0.425	0.355
6366	CCL21	chemokine (C-C motif) ligand 21	9	-1.11	0.01
3577	CXCR1	chemokine (C-X-C motif) receptor 1	2	0.371	0.562
3579	CXCR2	Chemokine (C-X-C motif) receptor 2	2	0.371	0.815
Lymphatic Markers					
10894	LYVE1	lymphatic vessel endothelial hyaluronan receptor 1	11	-0.083	0.896
2050	EPHB4	EPH receptor B4	7	-0.344	0.0597
2324	FLT4	fms-related tyrosine kinase 4	5	-0.210	0.591
10630	PDPN	podoplanin	1	0.303	0.356
5629	PROX1	prospero homeobox 1	1	-0.475	0.249
5175	PECAM1	platelet/endothelial cell adhesion molecule 1	17	-0.156	0.715
1948	EFNB2	ephrin-B2	13	-1.158	0.010

Table 15 - Gene expression alterations of 2Gy x 5 LEC in comparison to 0Gy LEC controls

Table 15 Key Candidates from the next generation sequencing data comparing five 2Gy fractionated dose irradiated LECs to 0Gy controls. The table details the top ten gene candidates, known key lymphangiogenic factors, lymphangiogenic markers as well as chemokines and the differential gene expression resulting from radiotherapy injury (blue boxes indicate gene expression changes that reach statistical significance $p<0.05$). Chr = chromosome, logFC = log fold change.

5.2.2.2 IL-8 Validation

IL-8 is a cytokine produced by a variety of cells in response to inflammation leading to neutrophil degranulation, increased adhesion and angiogenesis (277) (340). IL-8 demonstrated a 3.16 log fold change up-regulation in response to a single dose of 10Gy and a 0.803 log fold change in response to a five fractionated 2Gy doses and was the candidate most significantly altered by irradiation of LEC. To validate the next generation findings at an RNA level RT-PCR was performed. To then ascertain if these changes were translated to a protein level ELISA testing was performed on media isolated from 10Gy LECs 48 h post radiotherapy and compared to media isolated from 0Gy LECs. Findings demonstrated that LEC RNA tested for IL-8 gene expression 4 h post radiotherapy demonstrated a statistically significant fold change of 6.94 compared to 0Gy controls (Figure 41 A). On further interrogation, it was found that these changes were correlated at protein level with 10Gy LEC media samples demonstrating a fold change of 1.46 compared to 0Gy controls with ELISA detection of IL-8 protein (Figure 41 B). An average of 4 individual paired experiments demonstrated that 0Gy LEC media contained 383 pg/ml of IL-8 while 10Gy media contained 1723 pg/ml of IL-8 protein.

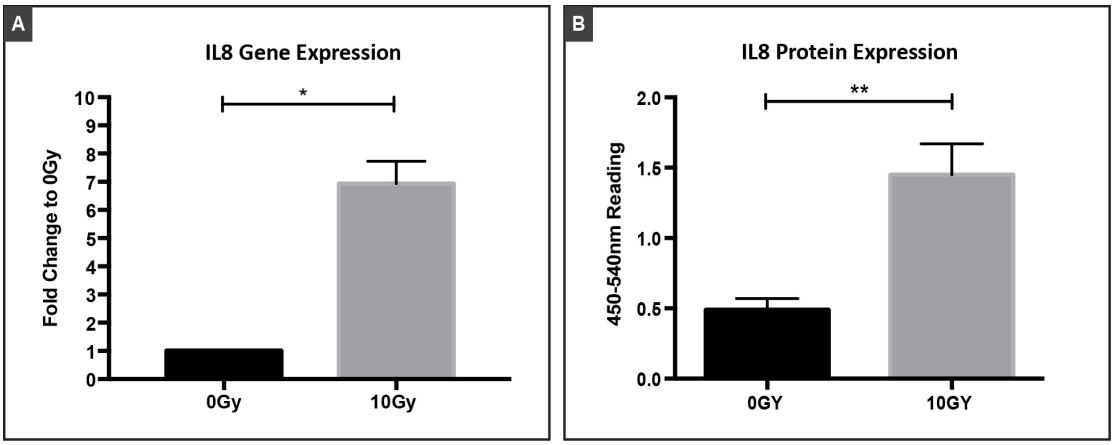

Figure 41

Figure 41 Radiotherapy results in increased IL-8 RNA and protein expression in LECs

Validation of increased (A) IL-8 gene expression using RT-PCR quantification and (B) IL-8 protein expression using ELISA in irradiated LECs or irradiated LEC media compared to their un-irradiated counterparts respectively. Asterisks above bar-graph indicate statistical significance (* = $p<0.05$, ** = $p<0.01$), error bars represent SEM, with $n\geq3$.

5.2.2.3 CXCR7 Validation

CXCR7 is a transmembrane receptor which plays a key role in regulating CXCR4/CXCL12 mediated stem cell homing, acts as a decoy receptor and may play a role in secondary lymphangiogenesis (349) (566). CXCR7 demonstrated a 2.30 log fold change up-regulation in response to a single dose of 10Gy and was therefore chosen as a candidate for validation in radiotherapy induced LEC injury. CXCR7 also demonstrated a 0.41 log fold change in response to five fractionated 2Gy doses, however this did not reach statistical significance, which may demonstrate the cyclical nature of CXCR7 expression in irradiated LECs. To validate the next generation findings at an RNA level, RT-PCR was performed. Findings demonstrated that LEC RNA tested for CXCR7 gene expression 4 h post radiotherapy demonstrated a statistically significant fold change of 5.09 compared to 0Gy controls (Figure 42 A).

To then ascertain if these changes were translated to protein level, flow cytometry and western blotting was performed and cells or cell lysates isolated from 0Gy and 10Gy LECs. Additionally, IHC staining of matched normal and irradiated human skin samples was conducted using serial sections, to determine the expression of CXCR7 on serially stained D2-40 positive lymphatic vessels (Figure 42 D,F**)**. Briefly, LECs were washed with 0.5% FACS buffer/PBS and stained with anti-CXCR7 antibody (R&D Systems 11G8 antibody) followed by goat anti-human Alexa Fluor 488 (FITC). Staining quantified on BD FACStar Plus Flow Cytometer (BD Biosciences, New Jersey, USA) using the FITC-A channel. Samples were processed 4 h post radiotherapy to match next generation sequencing time points. 0Gy cells demonstrated a median fluorescence intensity (MFI) of 236 whilst 10Gy LEC demonstrated an increased MFI of 2604 demonstrating increased expression of CXCR7 (Figure 42 B). Immunoprecipitation western blot analyses of 0Gy and 10Gy LEC cell lysates were conducted by pre-clearance with protein G beads then immunoprecipitation with anti-CXCR7 antibody (R&D Systems 11G8 antibody) cross-linking to protein G beads, followed by Western blot with an anti-CXCR7 antibody incubation (Santa Cruz antibody). Proteins were visualised with 800IR labelled secondary antibodies (Odyssey) and imaged using an Odyssey Scanner. 10Gy samples visually demonstrate a more prominent band at the level 50 kb, in keeping with increased CXCR7 expression at protein level in comparison to the band on 0Gy LECs (Figure 42 C). Blinded quantification of ten matched normal (Figure 42 E) and irradiated (Figure 42 G) human skin samples, collected from patients undergoing microvascular free tissue transfer reconstruction months to years after radiotherapy treatment, was undertaken. A grading scale of 0-2 was employed in determining strength of CXCR7 expression in a serial section where D2-40 positive lymphatics were identified first, then represented as a mean vessel score. Normal tissues demonstrated a mean vessel score of 0.26 ± 0.08 while irradiated tissues demonstrated a score of 0.73 ± 0.13 which illustrated a statistically significant increase in lymphatic vessel CXCR7 staining intensity in irradiated tissue (Figure 42 H,I). These above changes validate the next generation sequencing findings illustrating that CXCR7 is upregulated in lymphatic endothelial cells at both RNA and protein level in both settings of acute (hours) and chronic (months) after radiotherapy.

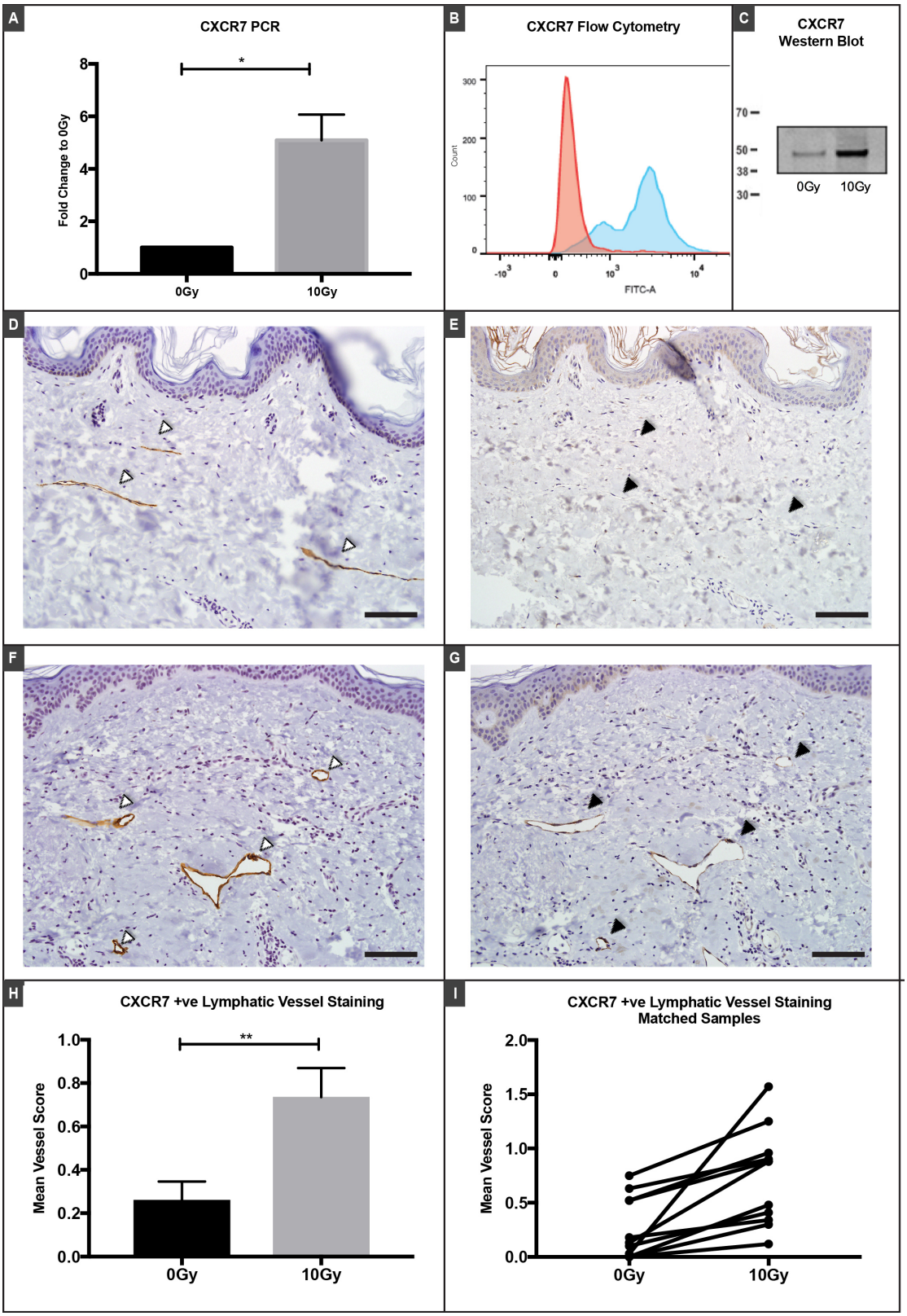
A
CXCR7 PCR
Fold Change to 0Gy
0Gy
10Gy
B
CXCR7 Flow Cytometry
Count
FITC-A
C
CXCR7
Western Blot
0Gy
10Gy
D
E
F
G
H
CXCR7 +ve Lymphatic Vessel Staining
Mean Vessel Score
0Gy
10Gy
I
CXCR7 +ve Lymphatic Vessel Staining
Matched Samples
Mean Vessel Score
0Gy
10Gy

Figure 42

Figure 42 Radiotherapy results in increased CXCR7 RNA and protein expression in LECs

(A) CXCR7 gene expression validation using RT-PCR quantification demonstrates a significant increase in the 10Gy LEC. (B) Flow Analysis Cytometry of 0Gy (red) and 10Gy (blue) LEC stained with CXCR7 demonstrating an increased number of events and median fluorescence intensity in 10Gy LEC. (C) Immunoprecipitation for CXCR7 and western blot analysis illustrates a prominent band in 10Gy LEC in comparison to 0Gy at the level of 50 kb, consistent with increased protein level expression of CXCR7. (D) Normal skin IHC stained identifying D2-40 +ve lymphatic vessels (△) with x20 objective imaging, with serial imaging of (E) normal control human tissue stained with anti-CXCR7 antibody demonstrating little or no expression of CXCR7 protein on lymphatic vessels (▲). While matched (F) irradiated skin human skin samples (from the same patient) were similarly stained to identify D2-40 +ve lymphatic vessels (△) with x20 objective imaging, (G) irradiated skin samples clearly demonstrate stronger CXCR7+ve stained lymphatic vessels (▲), identified as D2-40 +ve on serial sections. (H) Quantification of the mean strength of CXCR7 staining on D2-40 positive lymphatic vessels demonstrated a statistically significant increase in staining of irradiated tissues. (I) A graph illustrating that in all ten patient matched normal and irradiated tissue samples, the mean vessel score of CXCR7 +ve staining was increased in irradiated tissue when compared to normal tissue controls. (D-G) Scale bar 100 μm. Asterisks above bar-graph indicate statistical significance (* = $p<0.05$, ** = $p<0.01$), error bars represent SEM, with $n\geq3$.

5.2.3 Functional response of LEC to IL-8, CXCR7

Both IL-8 and CXCR7 were highlighted as key RNA candidates upregulated in LECs as a result of radiotherapy injury, and further translated to protein level up-regulation as detailed in sections 5.2.2.2 and 5.2.2.3 above. The up-regulation of these candidates in response to radiotherapy injury may represent an attempt at driving lymphangiogenesis in sublethally damaged LECs. Recent studies have demonstrated that IL-8 may have a lymphangiogenic stimulus on LEC, stimulating pathways outside of the VEGF family (341), while other groups have shown it to increase angiogenic signaling through up-regulation of VEGFR-2 signaling (336) (340). Additionally, Singh et al. determined that IL-8 expression in human prostate cancer cells resulted in up-regulation of CXCR7, the second key candidate selected for validation (350), however its effect on secondary lymphangiogenesis is not clearly established in the current literature. Therefore, to ascertain the functional effects of IL-8 and CXCR7, key functional assays of proliferation, migration and boyden chamber chemotaxis were conducted to establish whether these proteins demonstrated lymphangiogenic potential in normal LECs or mitigated the injury in irradiated LECs.

0Gy LECs demonstrated statistically significant increases in cell proliferation with the addition of IL-8 (with the average luminescence readings of control and treated cells 909.1 ± 25.9 and 1075 ± 7.9 respectively) representing a fold change of 1.18. Similarly, treatment of 0Gy LEC with CXCR7 demonstrated a statistically significant increase in proliferation with average luminescence readings of control and treated cells 909.1 ± 25.9 and 995.3 ± 27.7 respectively (Figure 43A) representing a fold change of 1.09. 10Gy, radiation-injured LECs however did not demonstrate a significant increase in proliferation with IL-8 or CXCR7 treatment (with average luminescence rates of 862.8 ± 27.2, 852.7 ± 31.8 and 805.5 ± 34.9 for 10Gy controls, IL-8-treated 10Gy LECs and CXCR7-treated 10Gy LECs respectively (Figure 43B). While the addition of these growth factors demonstrated a lymphangiogenic effect on normal LEC proliferation without improving this function in irradiated LEC, the contrary was demonstrated with cell migration in a 2D scratch model. 0Gy LECs in control media demonstrated an 83.0 ± 4.0% gap closure at 48 h, which did not significantly differ after addition of IL-8 or CXCR7 with 83.1 ± 2.3% and 86.3 ± 3.1% gap closures respectively (Figure 43 C). Alternatively, 10Gy LECs in control media demonstrated a 10.2 ± 5.2% gap closure at 48 h, which was significantly

increased with addition of IL-8 to 27.7 ± 4.9%. CXCR7 increased gap closure to 27.8 ± 3.3% (Figure 43 D). Chemotaxis of LECs was interrogated using boyden chamber assays, where a set number of cells in control media were seeded in the top chamber, followed by placing control or growth factor-containing media in the bottom chamber which is separated by a thin membrane. Chambers were incubated for 24 h and 0Gy and 10Gy LEC chemotaxis was quantified as a fold change in comparison to control media by fixation, staining and quantification of DAPI +ve cells on the undersurface of membrane. This cell count represented cells that have migrated in response to the growth factor-mediated chemotactic gradient. 0Gy LECs did not demonstrate a significantly altered rate of chemotaxis with the addition of IL-8 (a fold change of 1.04 ± 0.04) or CXCR7 (a fold change of 1.07 ± 0.04) when compared to 0Gy un-supplemented control media (Figure 43 E). Similarly, 10Gy LEC did not demonstrate a significantly increased rate of chemotaxis with IL-8 (1.05 ± 0.04) or CXCR7 (1.03 ± 0.04) represented as a fold change compared to 10Gy control media (Figure 43 F).

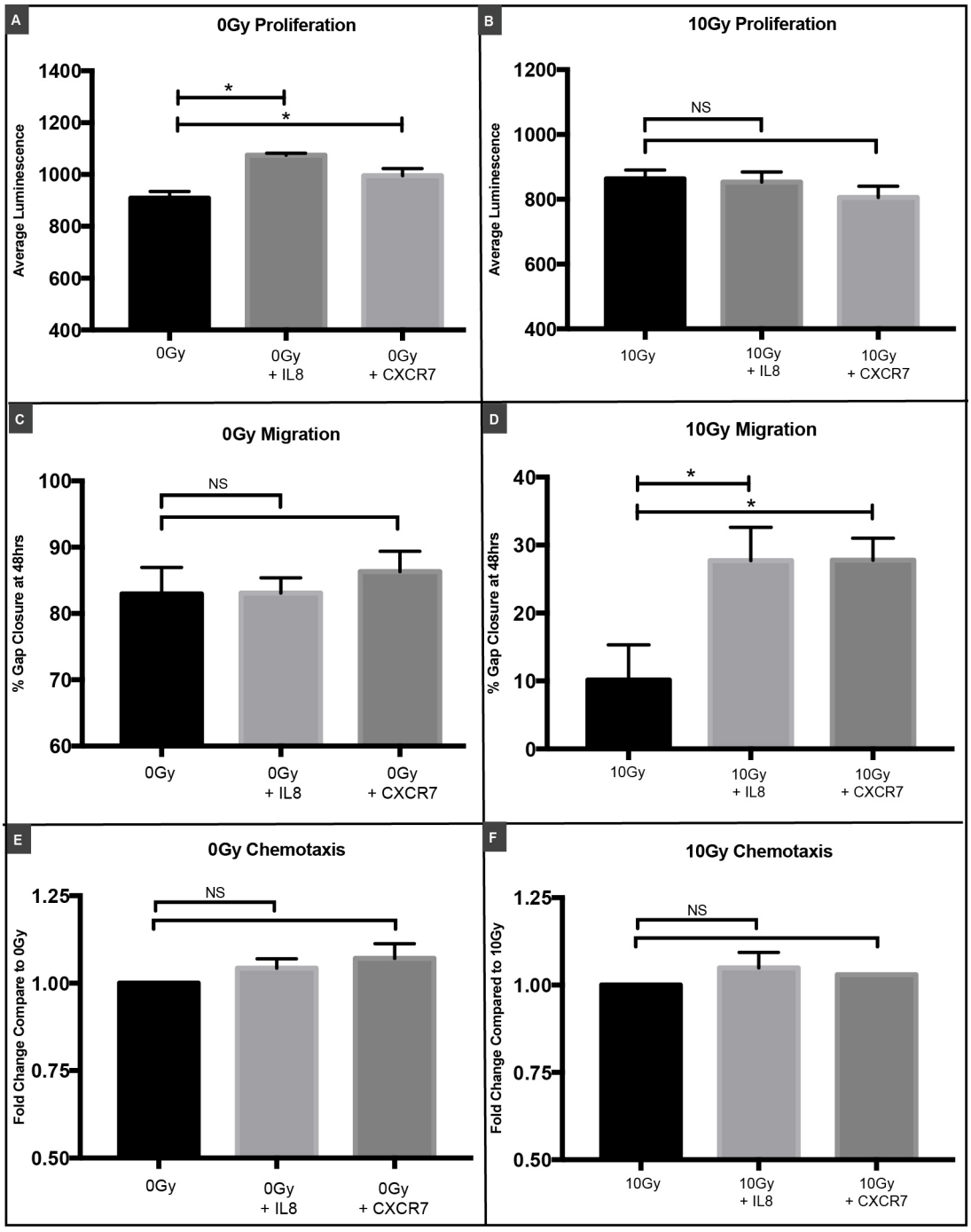
A
0Gy Proliferation
Average Luminescence
1400
1200
1000
800
600
400
*
*
0Gy
0Gy + IL8
0Gy + CXCR7
B
10Gy Proliferation
Average Luminescence
1200
1000
800
600
400
NS
10Gy
10Gy + IL8
10Gy + CXCR7
C
0Gy Migration
% Gap Closure at 48hrs
100
90
80
70
60
NS
0Gy
0Gy + IL8
0Gy + CXCR7
D
10Gy Migration
% Gap Closure at 48hrs
40
30
20
10
0
*
*
10Gy
10Gy + IL8
10Gy + CXCR7
E
0Gy Chemotaxis
Fold Change Compare to 0Gy
1.25
1.00
0.75
0.50
NS
0Gy
0Gy + IL8
0Gy + CXCR7
F
10Gy Chemotaxis
Fold Change Compared to 10Gy
1.25
1.00
0.75
0.50
NS
10Gy
10Gy + IL8
10Gy + CXCR7

Figure 43

Figure 43 IL-8 and CXCR7 stimulation results in selective lymphangiogenic effect on 0Gy and 10Gy LECs

The effect of the addition of IL-8 and CXCR7 on the proliferation of (A) 0Gy LEC and (B) 10Gy LECs quantified by the average luminescence readings corresponding to the amount of ATP produced by proliferating cells. The effect on (C) 0Gy and (D) 10Gy LEC migration with the addition of IL-8 and CXCR7 quantified as the % gap closure at 48 h, compared to the 0 h timepoint. The effect of IL-8 and CXCR7 on the chemotaxis of (E) 0Gy and (F) 10Gy LECs, quantified by a fold-change in the number of DAPI +ve cells on the underside of the boyden chamber membrane. Asterisks above bar-graph indicate statistical significance (* = $p<0.05$, NS = not significant), error bars represent SEM, with $n\geq3$.

5.2.4 Functional response of LEC to VEGF-C and -D

The best-studied lymphangiogenic growth factors are VEGF-C and VEGF-D and their receptor VEGFR-3 (565,567). VEGF-C delivery in a number of forms, including recombinant protein, viral vector or naked plasmid, can reverse surgically induced lymphoedema in a number of animal lymphoedema models (see (565)). However, there are problems associated with VEGF-C therapy as it may initially increase LEC proliferation and lymphatic vessel growth, without adequately improving LEC migration or functionality (327). Goldman et al. concluded - VEGF-C alone could not permanently improve lymphatic size, density, or organization in regenerating adult skin (327). It has been postulated by many groups that delivery of pro-lymphangiogenic factors such as VEGF-C and VEGF-D may be able to promote regeneration of injured LECs, via activation of VEGF-R2/3 and therefore reduce the burden of the resultant clinical lymphoedema (185) (325). However, increased levels of VEGF-C have also been correlated with increased vessel permeability and therefore increase local interstitial fluid as well as lymphangiogenesis of any potential dormant tumours. Therefore the use of VEGF-C requires more thorough investigation before being used for treatment of secondary lymphoedema in an oncological setting (325) (326).

VEGF-C and D were not found to be significantly altered in our next generation sequencing data as a result of radiotherapy injury to LECs. However due to the enhancement of expression of alternative non-VEGFR3 pathways, experiments were designed to determine the effects of these potent and traditional lymphangiogenic factors on the baseline functions of 0Gy and 10Gy LEC.

The addition of VEGF-C and VEGF-D increased proliferation with average luminescence readings of 0Gy controls 900.1 ± 25.9, 0Gy with VEGF-C 1167 ± 43.1 and 0Gy with VEGF-D 1067 ± 21.2 representing a significant fold change of 1.3 and 1.19 respectively (Figure 44 A). Similarly, 10Gy proliferation was increased by the addition of VEGF-C with average luminescence readings of 10Gy controls 862.8 ± 27.19 and 10Gy with VEGF-C 980.8 ± 22.95 representing a significant fold change of 1.14, while the addition of VEGF-D resulted in an average luminescence reading 912 ± 27.06, representing a 1.06 fold change which did not reach statistical significance (Figure 44 B). 0Gy LEC migration was not significantly improved with the addition of VEGF-C or VEGF-D demonstrated by % gap closures of 82.95 ±4 .01 (controls), 89.04 ± 7.96 (VEGF-C) and 73.54 ± 12.36 (VEGF-D) at 48 h, likely due to the fact that normal LEC have unimpaired migratory potential and achieve relative confluence and gap closure at the 48 h timepoint (Figure 44 C). 10Gy LEC migration, which is significantly decreased with radiotherapy injury in comparison to 0Gy controls, demonstrated a large and significant “boost” to migratory potential with the addition of VEGF-C and VEGF-D (% gap closures of 10.15 ± 5.15 (controls) increasing to 70.06 ± 6.836 (VEGF-C) and 41.53 ± 6.912 (VEGFD) at 48 h (Figure 44 D)). When tested for their chemotactic potential, both VEGF-C and D demonstrated a significant increase in chemotaxis; demonstrated with the addition of VEGF-C to 0Gy LEC resulting in a 1.47 ± 0.12 fold increase in chemotaxis and a 1.26 ± 0.04 fold increase in response to VEGF-D compared to 0Gy controls (Figure 44 E). Similarly, addition of VEGF-C to 10Gy LEC lead to a 1.45 ± 0.05 fold increase in chemotaxis and VEGF-D lead to a 1.35 ± 0.05 fold increase compared to 10Gy controls (Figure 44 F).

As is evident from the results above, VEGF-C and D demonstrate lymphangiogenic potential in both 0Gy and 10Gy LECs, however the functional effects and magnitude of lymphangiogenic stimulation differs in each situation. Globally VEGF-C

stimulation increased proliferation and chemotaxis in both 0Gy and 10Gy LECs, however the effect was more pronounced in 0Gy LECs in comparison with 10Gy LECs. Alternatively, 10Gy LEC migration was markedly improved with VEGF-C treatment, while 0Gy LEC did not demonstrate similar significant improvements. VEGF-D followed similar trends to those described for VEGF-C. Specific experiments were designed to further interrogate the VEGF-C/VEGF-D signaling pathways in normal and irradiated LECs and determine the strength and capability of each of these growth factors to activate VEGFR-3 (see section 7.2.5.2).

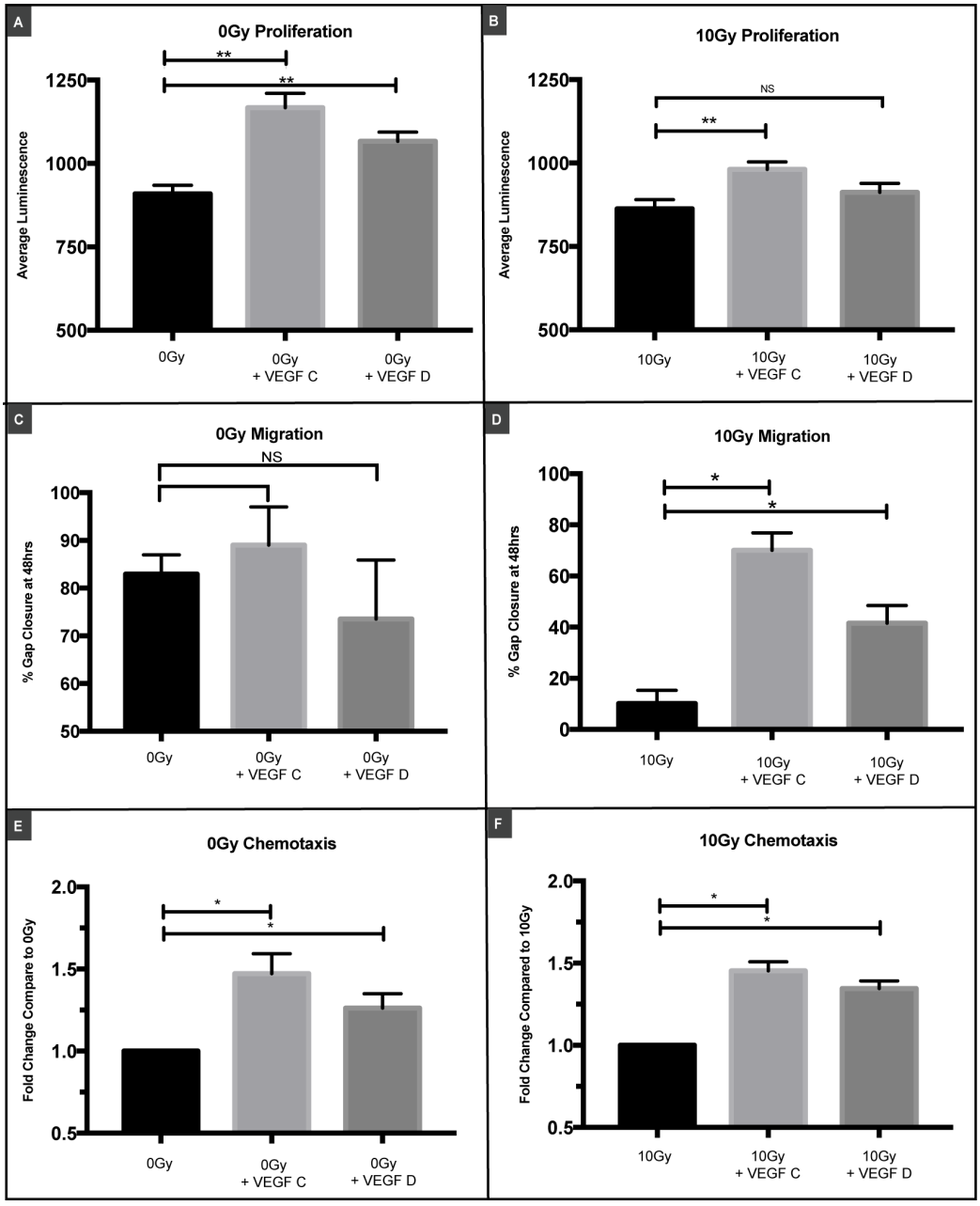

Figure 44

Figure 44 - The effect of VEGF-C and D on the function of 0Gy and 10Gy LECs
The effect of the addition of VEGF-C and VEGF-D on the proliferation of (A) 0Gy LEC and (B) 10Gy LEC quantified by the average luminescence readings corresponding to the amount of ATP produced by proliferating cells. The effect on (C) 0Gy and (D) 10Gy LEC migration with the addition of VEGF-C and VEGF-D quantified as the percentage gap closure at 48 h compared to the 0 h timepoint. The effect of VEGF-C and VEGF-D on the chemotaxis of (E) 0Gy and (F) 10Gy LECs quantified by a fold change in the number of DAPI positive cells on the underside of the boyden chamber membrane representing transmigrated cells in comparison to their respective control media groups. Asterisks above bar-graphs indicate statistical significance (* = $p<0.05$, ** = $p<0.01$, NS = not significant), error bars represent SEM, with $n\geq3$.

5.3 Discussion

The results presented in this chapter demonstrate that radiotherapy injury to the lymphatic system results in significant cellular dysfunction and further advances our understanding of the mechanisms that drive the development of clinical manifestations of lymphoedema and impaired immunosurveillance in irradiated tissue.

Radiotherapy delivered in regimes of a single 10Gy dose or five sequential 2Gy doses, reflect exposure of normal tissue during clinical irradiation for cancer treatment and both demonstrated a reduction in LEC proliferation, but also a reduction in rates of apoptosis when compared to un-irradiated 0Gy groups. These alterations in survival dynamics challenge more traditional hypotheses that propose large scale cell death is accountable for the deficits in LEC function after radiotherapy injury.

Unlike apoptotic cells, which are removed from tissues via a regulated and contained process of cell death, irradiation of LEC results in substantial sub-lethal injury. Consequently, LECs undergo a process of accelerated senescence and become dysfunctional in their homeostatic abilities and responses to physiological lymphangiogenic stimuli or subsequent injury. The results also demonstrate that radiotherapy-injured LECs display morphological changes of cellular swelling and

reduced cell-to-cell adhesion, in keeping with findings by Day et al. who studied irradiated human pulmonary aortic endothelial cell populations (568). Chen et al. postulated that such a change may be reversible in models of metabolic syndromes such as hyperglycemia (569). This manifestation of cellular swelling is also known as hydropic change or vacuolar degeneration, and is usually representative of a non-lethal injury to cells which results in alterations of plasma membrane integrity, cellular adhesive properties, endoplasmic reticulum and mitochondrial structure (570). The finding that irradiated LECs demonstrated decreased rates of apoptosis has not been described and may provide a mechanism as to why sublethally injured LECs display aberrant homeostatic functioning. Further, these findings support the concept of RIBE (100) in which irradiated LECs are not cleared in a controlled manner from injured tissues and the quiescent, senescent or abnormal cells persist and continue to contribute to the spread of damage to surrounding tissues as a "delayed release" of the injury (571).

Sublethally injured LECs exhibited several forms of cellular dysfunction 48 h after irradiation, resulting in a significantly diminished capacity to perform key lymphangiogenic processes such as cell migration, tube formation and spheroid sprouting when compared to healthy cell controls. These dynamic cellular functional assays correlated with the static histological analysis done by Avraham et al. on irradiated murine tissue which demonstrated ectatic and phenotypically abnormal lymphatic vasculature (133).

The molecular alterations driving these functional changes were established using the next generation sequencing techniques described above. Numerous pro-inflammatory cytokines and proteins were shown to be altered in response to radiotherapy injury, while key lymphatic markers were largely unchanged demonstrating preservation of LEC identity. The top candidate, most significantly altered by radiotherapy in LEC was IL-8, Interleukin 8 (CXCL8), a member of the CXC chemokines. It is a cytokine with strong chemotactic properties and is largely secreted by immune cells, but also by keratinocytes, fibroblasts, endothelial cells and pigmented melanocytes (277). Up-regulation at RNA level was confirmed at the protein level with increased IL-8 present in ELISA testing of conditioned media from irradiated LEC, associated with a significant fold change of 4.5 times compared to unirradiated LEC media controls. IL-

8 is produced from a precursor which is converted by proteases such as cathepsin L, making a mature form in response to inflammatory stimuli such as TNFα, LPS, IL-1, viruses and irradiation (277). It has been reported that up-regulation of IL-8 primarily leads to neutrophil degranulation but can also increase adhesion and angiogenic properties of endothelial cells by inducing VEGF expression and autocrine up-regulation of its receptor VEGFR-2 via NFKB pathway activation (306) (336) (340). The IL-8 promoter region houses sites for NFKB and AP1 binding, and together result in a large up-regulation of IL-8 in response to radiotherapy in a wide variety of cells (277). In relation to its action on LEC, IL-8 has been shown to downregulate $P57^{kip2}$ which is a cell cycle inhibitor in neonatal foreskin derived LECs which requires the suppression of PROX1. However, in the presence of excess PROX1 expression, IL-8 cannot mediate negative regulation of cell cycle inhibition, suggesting a reciprocal relationship between PROX1 and IL-8 (341). The levels of PROX1 expression were not significantly altered in the next generation screening as a result of LEC radiotherapy, therefore the potent up-regulation of IL-8 may represent an attempt at promoting the progression of LECs through the cell cycle, providing lymphangiogenic stimulus to the sublethally damaged LECs. However, Li et al. explored methods to mitigate the inflammatory effects of IL-8 after radiotherapy via a subarachnoid infusion of IL-8 monoclonal antibody, using a cranial irradiation injury model in rabbits (572). They were able to demonstrate a significant reduction in IL-8 in cerebrospinal fluid, reduced glial fibrillary acidic protein and bacterial NOS +ve staining on IHC of sampled cranial tissue. These findings are representative of a reduction in tissue injury and correlate with less cerebral oedema compared to normal saline controls (572).

To separate the inflammatory and potential lymphangiogenic effects of IL-8, Choi et al. demonstrated the therapeutic benefits of IL-8 treatment in a series of *in-vitro* LEC and *in-vivo* murine studies (341). *In-vitro* studies determined that the IL-8 receptor CXCR2 was highly expressed on LECs, whereas, an inflammatory stimulus such as TNFα was required to increase expression of CXCR1 from low basal levels (341). IL-8 treatment of LECs favourably promoted *in-vitro* LEC functioning (independent of VEGF-C), which was abrogated in presence of a CXCR2 inhibitor (341). IL-8 containing matrigel plug models along with tail lymphedema models in transgenic

mice overexpressing IL-8 also demonstrated increased LYVE-1+ lymphatic vessels linked to the lymphangiogenic effects of IL-8 (341). They also demonstrated that in response to inflammatory (TNFα) and lymphangiogenic (9-cis-retinoic acid) stimulation respectively, LEC IL-8 mRNA and protein secretion was significantly increased, from basal levels of ~500 pg/ml (341) (573). These studies correlate with findings of an increase in IL-8 protein expression from 383 pg/ml in 0Gy LEC to 1723 pg/ml in irradiated LEC presented in this chapter. However, the next generation sequencing data did not demonstrate changes in expression of CXCR1 and CXCR2, suggesting that radiotherapy induced up-regulation of IL-8 in LEC may result from pathways separate from TNFα mediated inflammatory effects. The clinical implications of these findings are that radiotherapy injury to LEC may represent a separate entity to a generalized inflammatory response

It must be remembered that IL-8 secretion as a result of inflammatory or injurious stimulus may not result in release of functional protein used in assays above demonstrating IL-8 mediated lymphangiogenic effects in healthy LECs, which may not be reflective of responses of damaged LECs in the field of tissue injury. Nonetheless, IL-8 up-regulation in response to inflammation and irradiation may prove to be a valuable pathway to target for the mitigation of radiotherapy injury to enhance lymphangiogenesis. Therefore, subsequent experiments designed to further supplement both 0Gy and 10Gy LEC with IL-8 and determine the effects this had on cellular function demonstrated lymphangiogenic capabilities by increasing 0Gy LEC proliferation and also significantly increasing the migratory capacity of 10Gy LEC. From this data, it can be concluded that the increase in IL-8 levels after irradiation of LECs may represent a response by the LECs themselves to increase lymphangiogenesis in injured LEC populations.

Furthermore, extrapolating from studies on tumour cell lines Singh et al. showed IL-8 expression in human prostate cancer cell to result in up-regulation of CXCR7 at both RNA and protein level, a change that is thought to promote cell proliferation, which in tumour cells may facilitate in metastases but in normal cell populations may represent an attempt to regenerate damage as a result of inflammatory or injurious stimuli such as radiotherapy (350). This phenomenon was pertinent to explore further, as the next

generation sequencing data also demonstrated radiotherapy induced up-regulation of CXCR7 in LECs. This was validated at the RNA level using RT-PCR as well as multiple assays to verify this change was translated to protein level with FACS demonstrating up-regulation at 4 h post radiotherapy, western blotting at 48 h and IHC demonstrating this change persisted in lymphatic endothelial cells months-years post radiotherapy treatment.

CXCR7 may function as a decoy receptor and play a significant role in stem cell homing mechanisms involving CXCR4 and SDF-1 (see 1.9.8) and is investigated and discussed in detail in 6.2.5. However, the next generation sequencing data did not demonstrate significant changes in CXCR4 expression, therefore the large and significant increase in transcriptional and translational up-regulation of CXCR7 may be the commanding mechanism of signaling in irradiated tissues. The effects of CXCR7 on lymphangiogenesis are scantly reported in the literature, with few groups suggesting its key in normal developmental processes such as neurogenesis, angiogenesis, chemotaxis and cellular proliferation (574). $CXCR7^{-/-}$ mice displayed hyperproliferative LEC phenotypes leading to dysfunctional vessels with increased diameter and reduced branching complexity (574). Additionally Neusser et al. demonstrated up-regulation of CXCR7 on lymphatic endothelium in samples of tissue with renal allograft rejection, again demonstrating increased expression with inflammation and may serve to regulate several chemokine gradients which directly affect LEC functions, attempts at secondary lymphangiogenesis and also dendritic cell trafficking (566).

To interrogate the effect that CXCR7 has on 0Gy and 10Gy LEC, each group was treated with CXCR7 protein and key functional assays were examined. CXCR7 was able to significantly increase the proliferation of 0Gy LECs without having the same effect on irradiated LECs (Figure 43 A), while exhibiting a notable lymphangiogenic effect on 10Gy LEC migration (Figure 43 D). This data allows us to conclude the CXCR7 has the potential to exert selective lymphangiogenic stimulus on both normal and irradiated LEC, which is important to note, given our experiments suggest that CXCR7 up-regulation persists beyond the acute phase of injury and is present in human dermal lymphatic samples months to years after treatment (Figure 42).

Other candidates of interest from the next generation sequencing data that correlated with the severely diminished functional capacity of LEC post irradiation include the downregulation of a key signaling system; EphB4 and ephrinb2. The Eph family of receptors and the ephrin ligands demonstrate bidirectional signaling where ephrins initiate forward signaling but also have an ephrin dependent reverse signaling in cells that express ephrins (575). Zhang et al. demonstrated that selective inhibition of EphB4 resulted in defective lymphatic valve development (576). While Wang et al. showed that *in-vitro* knock out of ephrinB2 reduced the ability of LEC tube formation, migration as well as VEGF-C induced VEGFR-3 tyrosine phosphorylation (575). These papers, together with early findings from the next generation sequencing data suggest that radiotherapy mediated downregulation of this signaling system in LEC may play a role in the resultant cellular dysfunction and requires further validation.

Next generation sequencing also demonstrated a downregulation of CCL21 which interacts with a G protein coupled chemokine receptor expressed by mature dendritic cells (577). In recent studies, CCL21 has been linked to the ability of inflamed or injured LECS to recruit CCR7+ inflammatory cells (173) (577), with CCR7 knockout mice displaying abolished DC migration to dermal lymphatics. Thus, induced inflammatory states in autoimmune disease, physical or chemical injury are likely to increase LEC expression of CCL21, recruiting CCR7+ cells such as macrophages to aid in repair and regeneration of tissues. However these findings suggest such a process may be impaired with radiotherapy injury in LEC. Abrogation of the CCL21-CCR7 pathway and its deleterious effect on DC trafficking is likely to significantly impair the body's first line of defense against infection (577).

VEGF-C and D are well studied and potent lymphangiogenic factors, therefore when 0Gy and 10Gy LEC were treated with VEGF-C and D the cells demonstrated lymphangiogenic effects with increases in proliferation, migration and chemotaxis in both groups. However, 10Gy LEC response to stimulation with VEGF-C and D led to a slightly dampened response in comparison to 0Gy LEC counterparts. This suggested that while VEGF-C and D are powerful lymphangiogenic factors, irradiated and injured LEC responses to VEGF-C and D treatment may be diminished and suboptimal. Up-regulation of more novel candidates such as IL-8 and CXCR7 in

response to irradiation, may represent alternative pathways attempting to stimulate lymphangiogenesis specifically in response to radiotherapy injury of LECs.

These putative alterations of lymphangiogenic mechanisms that are independent of the "traditional" lymphangiogenic factors VEGF-C and VEGF-D, may represent an "emergency contingency" route of lymphangiogenesis in certain injury contexts. It may further offer novel avenues by which to enhance lymphangiogenesis to repair lymphatic injury and ameliorate RTX-induced lymphoedema.

5.4 Conclusion

The results in this chapter demonstrate the globally suppressive effect of radiotherapy injury on LECs. LEC morphology was substantially altered displaying hydropic change and reduced cell-to-cell adhesion indicative of a senescent phenotype. The cumulative effects of these acquired changes in LEC post radiation along with a reduction in apoptosis allow for these abnormal cells to continue to propagate cellular dysfunction and damage to surrounding tissues. Irradiated LEC displayed significant impairment in key functions such as migration, tube formation and sprouting - all essential to carry out functional lymphangiogenesis.

Radiation did not result in changes of expression of key lymphangiogenic markers, however did lead to up-regulation of the novel candidates IL-8 and CXCR7. This transcriptional up-regulation was validated at a protein level and both candidates demonstrated the capacity to exert selective lymphangiogenic effects on both normal and irradiated LEC. The responses of irradiated LECs to traditional VEGF-C and VEGF-D stimulation via the VEGFR3 pathway appeared dampened in comparison to un-irradiated LECs. Therefore IL-8 and CXCR7 may serve as therapeutic candidates to mitigate the effects of radiotherapy-induced LEC injury. However, as mentioned in the discussion above, the role of CXCR7 as a decoy receptor and its potential interaction with stem cell populations is pertinent to note and is further investigated and discussed in Chapter 6. Other candidates that may be of therapeutic benefit include the EphB4 and ephrinb2 as well as the possibility of CCL21 mediated immunosuppression of irradiated tissues, all which warrant further investigation.

6 CHAPTER 6: Characterizing the effects of radiotherapy injury on adipose derived stem cells

6.1 Introduction

Adult mesenchymal stem cells (MSCs) are thought to have the unique capability to aid in regeneration in injured tissues by differentiating into specialized cell types and restoring wound integrity (400) (407). Such properties make MSCs prime candidates for use in tissue regeneration (142) (287) (386) (409) (410) (411). The ability to use autologous MSCs for the purposes of tissue regeneration boasts multiple advantages - particularly the avoidance of a host immune response. Additionally, the yield of stem cell extraction from adipose tissue is about 500-fold higher than that from bone marrow, along with the ease of harvest and reduced donor site morbidity (332) (392).

MSCs have been isolated from multiple sources in humans including placenta, umbilical cord, skin, adipose tissue, muscle, kidney, blood vessels and bone marrow, which have been most abundantly studied in the literature (578) (579). Adipose derived stem cells (ADSC) are a subtype of MSCs, first characterised by Zuk et al., demonstrating adherence to a plastic surface, fibroblast-like morphology and an ability for adipogenic, osteogenic and chondrogenic differentiation (366). The interest in the therapeutic potential of this abundant source of adult MSCs has rapidly escalated in the last decade, particularly with benefits demonstrated in reconstructive and cosmetic surgical applications such as fat grafting for lipofilling, contouring or correction of scarring and fibrosis post radiation therapy (54). While numerous groups have attempted to characterise the molecular markers that identify ADSC, there is a lack of consistency in the literature as the Zuk protocol of extraction results in a heterogeneous cell mixture also known as the stromal vascular fraction (SVF). This SVF is composed of ADSC, endothelial cell progenitors, monocytes/macrophages, pericytes and pre-adipocytes (54). A comprehensive comparative review of the known and accepted markers for ADSC determined that the most commonly described cell marker profile for ADSC was $CD90^{+}$, $CD\ 45^{-}$, $CD31^{-}$ and $CD34^{+/-}$, however there is some overlap amongst the cell types listed above (54).

Apart from their wide-ranging differentiation potential, ADSCs also exhibit an extensive secretory profile consisting of pro- and anti-inflammatory cytokines,

chemokines and growth factors, thought to be responsible for the regenerative properties attributed to ADSC (288) (400) (403-405) (413-415 . Major mechanisms of stem cell-mediated tissue repair (identified from research in BMSCs), are attributed to their ability to home to a site of injury or inflammation, differentiate into cell lineages to replace damaged cells and secrete growth factors and cytokines that lead to anti-inflammatory, anti-fibrotic, angiogenic and lymphangiogenic effects (54) (383) (578). However, in order to discern the mechanisms by which ADSC are thought to modulate RTX induced injury in other cell subtypes, the effects of radiotherapy injury on ADSC themselves need to be investigated first.

RTX soft tissue injury has been thought to be responsible for significant necrosis and apoptosis in stem cell and progenitor cell populations, which in turn are thought to be highly sensitive to the effects of ionizing radiation (142). However, as large-scale cell death does not account for the chronic, progressive and evolving nature of RTX-injury in soft-tissues (17) (61), "sub-lethal" alterations such as premature senescence, reproductive cell death or terminal differentiation may also be implicated (142) (376) (452). Knowledge regarding the effects of radiotherapy injury on MSCs are largely derived from experiments on BMSCs, with fewer studies on ADSC in the current literature. Ponomaryov et al. demonstrated increased expression of SDF-1 at both the RNA and protein level in response to sublethal RTX-injury in BMSCs (346). SDF-1, in-turn, mediated homing of $CXCR4^{+}$ uninjured BMSCs via a chemokine gradient (346), which may also be central to importing uninjured ADSCs to the site of injury, as surviving ADSCs originating within the affected area could be significantly functionally impaired (135) (287) (332) (402). Poglio et al. characterised the effects of RTX on murine adipose tissue and whilst the overall composition of the SVF was unchanged by irradiation, the authors concluded that alterations to the proliferative and differentiation capacity of cells within the SVF could impair the regenerative properties of fat graft (364). Li et al. also demonstrated suppressed proliferation, osteogenesis and adipogenesis in irradiated BMSCs further supporting the mechanism above (456). Additionally, changes in the microenvironment may influence ADSC paracrine signaling as well as encourage differentiation toward a fibroblastic phenotype, a change characteristic in irradiated tissues (457) (458).

To gain a better understanding as to the effects of radiotherapy on components of adipose tissue, a model of hypoxia may be utilized as a surrogate as the combination of radiotherapy injury and surgery leads to the up-regulation of HIF1α in response to tissue hypoxia via ROS, Nitric Oxide, or inducing macrophage recruitment or release of stress granules (37). Haubner et al. demonstrated that the individual components of adipose tissue each responded differently to hypoxic stress stimuli; and that ADSC display superior cell viability in comparison to adipocytes and endothelial cells (382) - a finding verified by Frazier et al. in a viability study (451). Some authors suggest that stem cells are maintained in a relative state of hypoxia by utilizing anaerobic metabolism (376) (382) (411) (462), a protective mechanism which may also facilitate more effective and active regeneration in the face of injurious stimuli (37) (428). Additionally, hypoxic pre-conditioning models demonstrate a modified paracrine secretory profile in stem cells with a significant increase in expression of pro-angiogenic and anti-apoptotic growth factors which will have a significant impact on the responses of other cells types in the irradiated microenvironment (9) (154) (407) (410) (411) (428) (430) (451) (459) (462) (463).

This chapter focuses on determining the effects of radiotherapy-induced injury on ADSCs; first by interrogating key homeostatic functions of proliferation, apoptosis, migration, differentiation and response to chemotactic stimuli. The latter half of the chapter interrogates molecular alterations resulting from single and fractionated doses of radiotherapy. The last portion of the chapter attempts to characterize the changes in ADSC secretome using metabolomic, proteomic and exosome discovery platforms (the results of the latter are discussed in Chapter 7).

6.2 Results – Adipose Derived Stem Cells (ADSC)

Adipose Derived Stem cells (ADSC) were isolated from fresh human subcutaneous abdominal adipose tissue according to ethics approval (HREC 52/03). Briefly, tissue was digested with collagenase, cells were selected based on plastic adherence and tested for ability to differentiate in response to adipogenic and osteogenic culture medium (for more details see section 2.1.3). Proliferating cells were used for functional and molecular assays between passage 1 to 4 and cultured in complete DMEM (see 2.1.2) for expansion and passaged on reaching 80-90% confluence.

6.2.1 Cell Survival Dynamics

The effect of radiotherapy on ADSC cell survival was first determined utilizing a survival fraction calculation (see 2.2.1). A set number of cells were seeded in a 24 well plate, left to attach overnight, received irradiation (10Gy) or control treatment (0Gy) and left in standard culture conditions for 48 h, after which viability was determined by cell counting based on exclusion of trypan blue dye uptake in viable cells with intact cell membranes. Calculation of 0Gy and 10Gy plating efficiency preceded determination of 10Gy ADSC survival fraction, accounting for a degree normal cell loss (for more calculation descriptions see 2.2.1). As demonstrated in (Figure 45 A,B), irradiation of ADSCs results in a survival fraction of 81% compared to normal (0Gy) cells, therefore representing a 19% reduction in cell survival of 10Gy ADSCs (however this did not reach statistical significance). To further examine the processes that may contribute to the trending reduction in ADSC cell survival, proliferation and apoptosis experiments were conducted (see 2.2.2). To replicate the clinical scenario where patients receive smaller doses over a protracted period of time, a fractionated experimental group was assigned to receive five 2Gy doses delivered over a 48 h interval, a single dose group was assigned to receive one 10Gy dose and the control group received 0Gy. Briefly, cells were seeded in a white walled 96 well plate, left to attach overnight, with irradiation treatment commencing the following day. CellTitre Glo® (Promega) or Caspase3/7® (Promega) luminescent reagents were added to the wells 48 h post-radiotherapy to determine cell proliferation and apoptotic activity respectively, by obtaining values using a luminometer plate reader (see 2.2.2 for more detailed methodology and settings). ADSCs display a 5.86 ± 1.10% trend increase in proliferation after 2Gy x 5 and a 10.67 ± 4.65% reduction in proliferation after 10Gy irradiation compared with 0Gy controls ($p<0.05$) (Figure 45 C). ADSC apoptotic activity, mediated by Caspase 3/7 activation, was in fact decreased as a result of radiotherapy with 2Gy x 5 and 10Gy experimental groups as shown in (Figure 45 D), with a 6.41 ± 0.93% trending reduction in apoptosis after 2Gy x 5 and a significant 10.16 ± 2.54% reduction after 10Gy ($p<0.01$). Subsequent experiments were performed with a single dose of 10Gy for ease of experimental design.

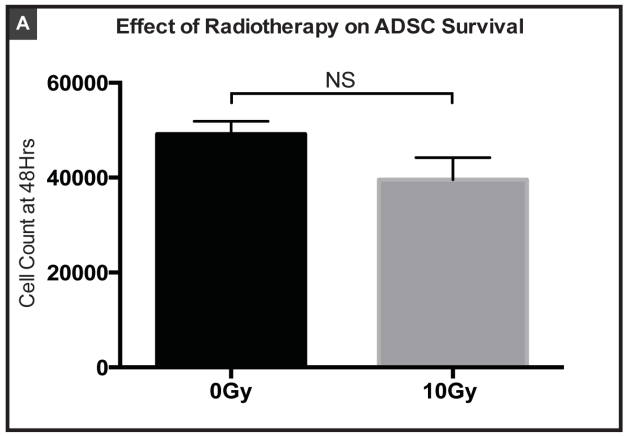

B	0GY	10GY
Viable Cell Count (Mean +/- SEM)	49167 +/- 2732	39583 +/- 4640
Plating Efficiency	98%	79%
Survival Fraction	100%	81%

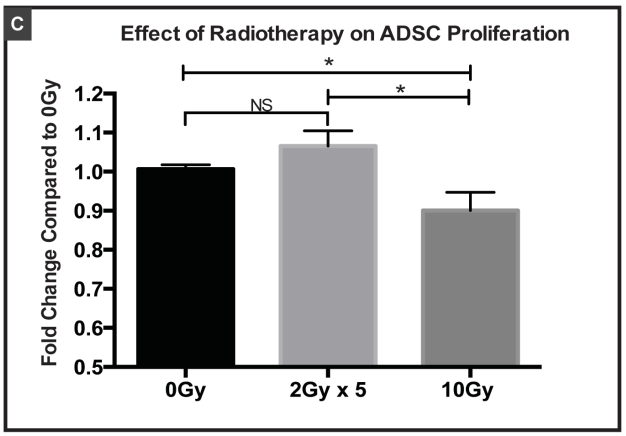

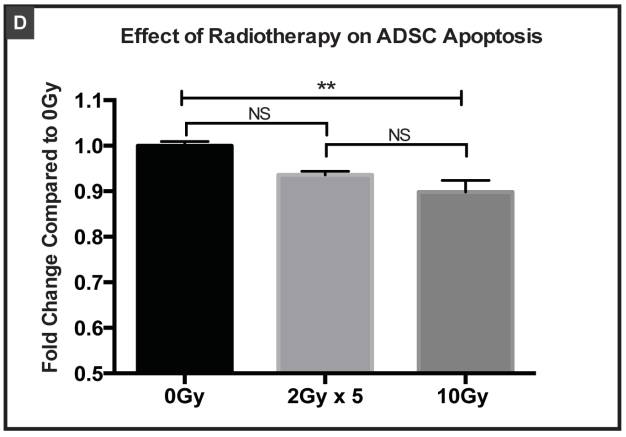

Figure 45

Figure 45 RTX alters the survival dynamics of ADSC with reduced proliferation and apoptosis

(A) Effect of radiotherapy on ADSC survival represented by viable cell numbers 48 hours after irradiation (10Gy) or control (0Gy) treatment. (B) Quantification of results demonstrating 0Gy and 10Gy viable cell counts, plating efficiencies and the survival fraction of 10Gy ADSC, assuming 100% survival of 0Gy control group cells. Analyses of the effects of 2Gy x 5 and 10Gy irradiation doses on ADSC (C) Proliferation and (D) Apoptosis represented as fold changes compared to 0Gy control groups. Asterisks above bar-graphs indicate statistical significance (* = $p<0.05$, ** = $p<0.01$, NS = not significant), error bars represent SEM, with $n\geq3$.

6.2.2 Migration

To investigate the effects of irradiation on ADSC migration a 2D scratch wound model was utilized, to determine if such functional impairment may contribute to poor wound healing and recruitment of stem cells. Cells were seeded on fibronectin coated plates, left to attach overnight before receiving either a single 10Gy dose or control 0Gy. Cells were serum starved 12 h prior to creating the 'wound' (see 2.2.3 for timelines and detailed methodology). Once the wound was created at 0 h (Figure 46 A,D), wells were photographed using standardised bright-field microscopy, and images were quantified on ImageJ to map % gap closure at 6 h intervals over 48 h. The percentage gap closure was calculated relative to the 0 h scratch at all time points and plotted (Figure 46 C), with a significant difference in migration between the two groups. At 48 h; 0Gy ADSC achieved 93.9 ± 0.1.76% gap closure (Figure 46 B) and 10Gy ADSC achieved 85.2 ± 2.71% gap closure (Figure 46 E), representing a significant difference of 8.62 ± 3.24% between the two groups at the 48 h ($p<0.05$) (Figure 46 F).

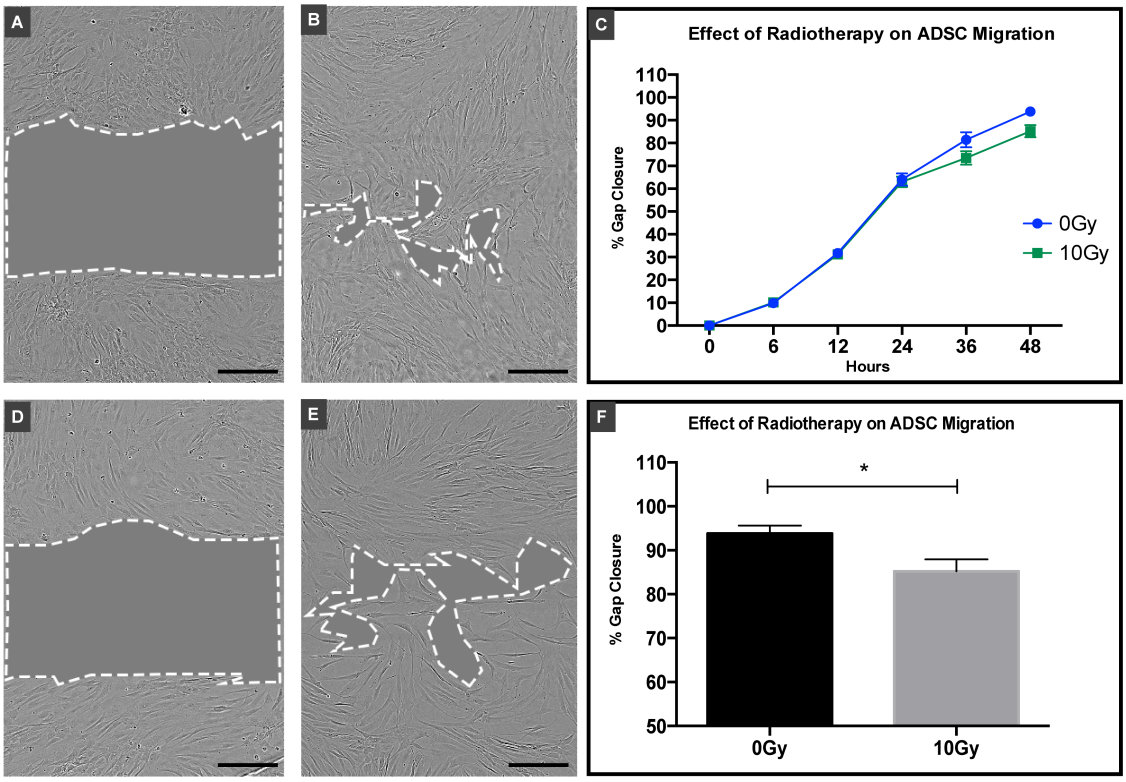

Figure 46

Figure 46 RTX reduces the migratory capacity of ADSC

x10 objective bright field imaging of ADSC, taken every 6 h post creation of the scratch wound on a confluent mono-layer of proliferating cells. (A) 0Gy ADSC scratch wound area at 0 h, (B) 0Gy ADSC scratch wound area at 48 h, (D) 10Gy ADSC scratch wound area at 0 h, (E) 10Gy ADSC scratch wound area at 48 h. (E) Quantification of the % Gap closure compared to 0 h controls calculated at 6 h intervals to demonstrate the effects of radiotherapy on ADSC migration. (F) Analyses of differences in % gap closure between 0Gy and 10Gy ADSC scratch wound areas at 48 h post wounding. In (A), (B), (D), (E); Scale Bar 300 µm, dotted line represents periphery of scratch wound and grey shaded area represents scratch wound area. Asterisks above bar graphs indicate statistical significance. Asterisks above bar-graph indicate statistical significance (* = $p<0.05$), error bars represent SEM, with $n\geq3$.

6.2.3 Adipogenic Differentiation

ADSCs possess the capability of differentiating into mature adipocytes under the influence of adipogenic factors (416) (see adipogenic medium contents section 2.2.5). Irradiated tissues often display a degree of atrophy, with fibrosis and scarring leading to poor quality, non-pliable and thin tissue. It was postulated that atrophy of adipose tissue in the zone of irradiation may result from two processes; death of adipocytes or the inability of local ADSCs to differentiate and replenish adipose tissue. Furthermore, with the advent of fat grafting and the clinical anecdotal evidence of tissue softening after injection in an irradiated tissue bed (373), an experiment was designed to investigate the effects of radiotherapy on the adipogenic potential of ADSCs. Briefly, ADSCs were plated in cell culture wells at a set density in complete DMEM (see section 2.1.2), left to attach overnight before receiving either a single 10Gy dose or control 0Gy. 48 h after irradiation the complete DMEM was aspirated, cells gently washed with PBS and replaced with adipogenic differentiation media. Differentiation media was then changed every 3-4 days for a duration of 14 days. On day 14 cells were either fixed and stained with Oil-Red-O, Adipo-red (Lonza, Switzerland) assay reagents or lysed for RNA extraction (Qiagen, Germany) as per methods detailed in sections 2.2.5 and 2.3.1 respectively. Quantification of adipogenic differentiation was conducted by solubilisation of Adipo-Red staining and standardised fluorescent plate reading, with results expressed as a fold change compared with 0Gy Controls.

Initial experiments with Oil-Red-O staining demonstrated a visible decrease in the amount of adipogenic differentiation present in irradiated 10Gy cell groups when imaged with x10 objective bright field microscopy (Figure 47 B,C). Quantification was performed using the Adipo-Red (Lonza, Switzerland) reagents. A 44.09 ± 3.78% reduction in adipogenic differentiation between 10Gy and 0Gy ADSCs was demonstrated to have been induced with adipogenic medium for 14 days ($p<0.05$) (Figure 47 A). To further investigate this deleterious effect of radiotherapy, RNA was isolated from 0Gy and 10Gy ADSCs 14 days after adipogenic differentiation and PCR conducted to determine the expression of adipogenic transcription factors FABP4, CEBPb, LPL, PPARγ and Leptin. Expression of FABP4 demonstrated a significant

1.51 fold decrease in 10Gy ADSCs compared to 0Gy controls ($p<0.05$) (Figure 47 D). CEBPb and LPL expression was also decreased in 10Gy ADSC compared with 0Gy controls by a fold change of 1.61 and 1.45 respectively ($p<0.05$) (Figure 47 E,F). Transcription factor PPARγ demonstrated a trend of decreased expression in 10Gy ADSC, while Leptin expression demonstrated a trend of increased expression in 10Gy ADSC compared to 0Gy controls, but neither reached statistical significance (Figure 47 G,H).

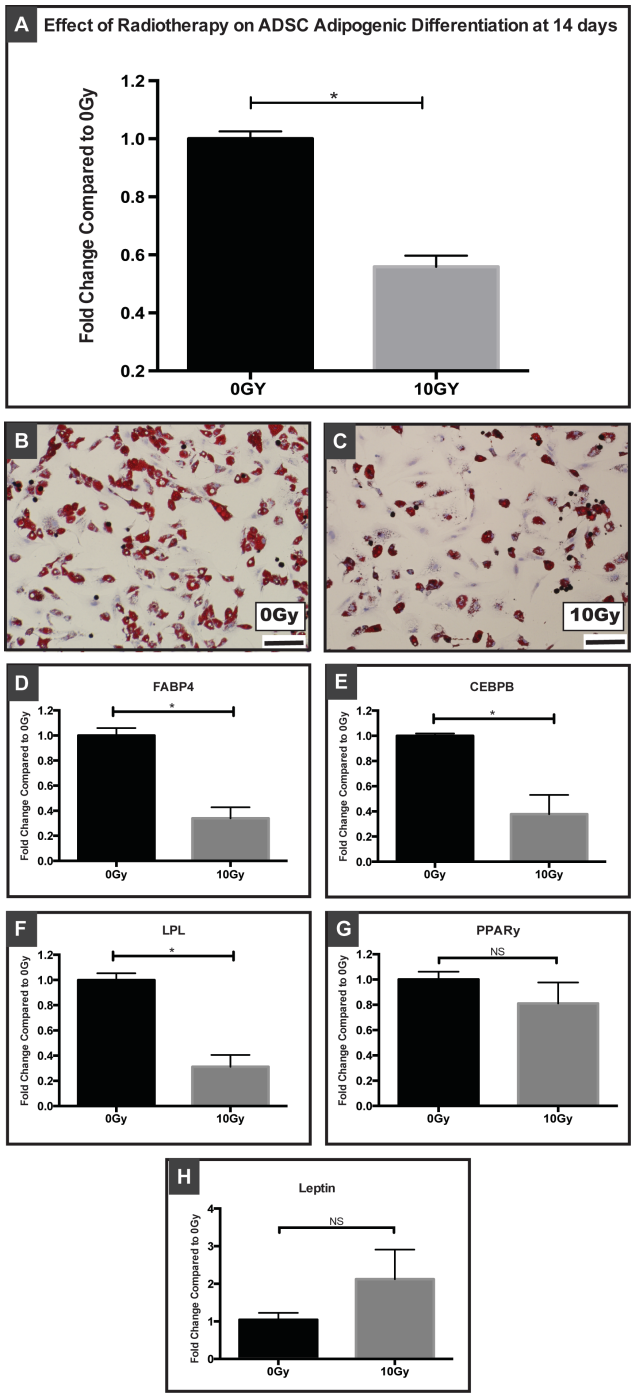

Figure 47

Figure 47 RTX reduces the adipogenic differentiation of ADSCs

(A) Fluorescent plate reader quantification of solubilized Adipo-Red staining demonstrating a significant decrease in adipogenic differentiation of 10Gy ADSCs compared to 0Gy controls at day 14. x 10 objective bright field photography of oil-red-o staining with red lipid droplets representing adipogenic differentiation of 0Gy ADSCs (B) and 10Gy ADSCs (C), counterstained with hematoxylin. The expression of key adipogenic transcription factors was investigated with PCR analysis of ADSC RNA collected after 14 days of adipogenic differentiation induction, represented as a fold change of 10Gy ADSC compared to 0Gy controls. 10Gy ADSC demonstrated a significant decrease in expression of FABP4 (C), CEBPb (D) and LPL (E). Scale bar (B,C) 100 μm. Asterisks above bar graphs indicate statistical significance. Asterisks above bar-graph indicate statistical significance (* = $p<0.05$, NS = not significant), error bars represent SEM, with $n\geq3$.

6.2.4 Osteogenic Differentiation

In addition to adipogenesis, the multi-potent differentiation potential of ADSCs also includes cartilaginous and osteogenic differentiation (366). However, as discussed in section 1.11.3, the effects of irradiation on this population of stem cells is poorly described. The BMSC responses characterised by Schonmeyr et al. in a murine model of irradiation demonstrated a significant degree of attenuation in adipogenic differentiation, and enhanced 'spontaneous' osteogenic differentiation (457). In the context of fat grafting for breast reconstruction, a key issue identified is the difficulty presented in differentiation of malignant breast calcification from calcified fat necrosis following fat grafting (386). This may impair the clinicians' ongoing ability to conduct long term radiological screening tests. Current guidelines reported by Gutowski et al. and the American Society of Plastic Surgeons (ASPS) suggest that augmentation of fat graft with stem cells requires further scientific investigation to ensure safety and that long term radiological surveillance programs will enhance education and training in distinguishing between benign and malignant calcifications (477). Experiments were designed to further investigate the effects of radiotherapy on ADSC osteogenic differentiation (a potential factor that may contribute to observable calcification and suspicious changes in irradiated breast tissues). The assay was

conducted with ADSCs in cell culture wells at a set density in complete DMEM, left to attach overnight before exposure to either a single 10Gy dose or control 0Gy. 48 h after irradiation the complete DMEM was aspirated, then the cells gently washed with PBS and replaced with osteogenic differentiation media. Differentiation media was changed every 3-4 days for a duration of 14 days. On day 14 cells were fixed and stained with either Alazarin Red or Osteo-Image (Lonza, Switzerland) assay reagents as per methods detailed in section 2.2.5. Quantification of osteogenic differentiation was conducted by performing solubilisation of Osteo-Image staining and standardised fluorescent plate reading, with results expressed as a fold change compared against 0Gy Controls.

Initial experiments were performed with Alazarin Red staining (Figure 48 B,D) and Osteo-Image staining reagents (Figure 48 A,C), which identify calcification representative of osteogenic differentiation. These assays demonstrated a visible increase in the amount of osteogenic differentiation present in irradiated 10Gy cell groups as imaged with x10 objective bright field microscopy, comparison with 0Gy ADSCs. This difference was then quantified using the Osteo-Image (Lonza) reagents which found a small but significant increase in osteogenic differentiation when comparing 10Gy to 0Gy ADSC ($6.30 \pm 1.78\%$, $p<0.05$) induced with osteogenic medium for 14 days (Figure 48E).

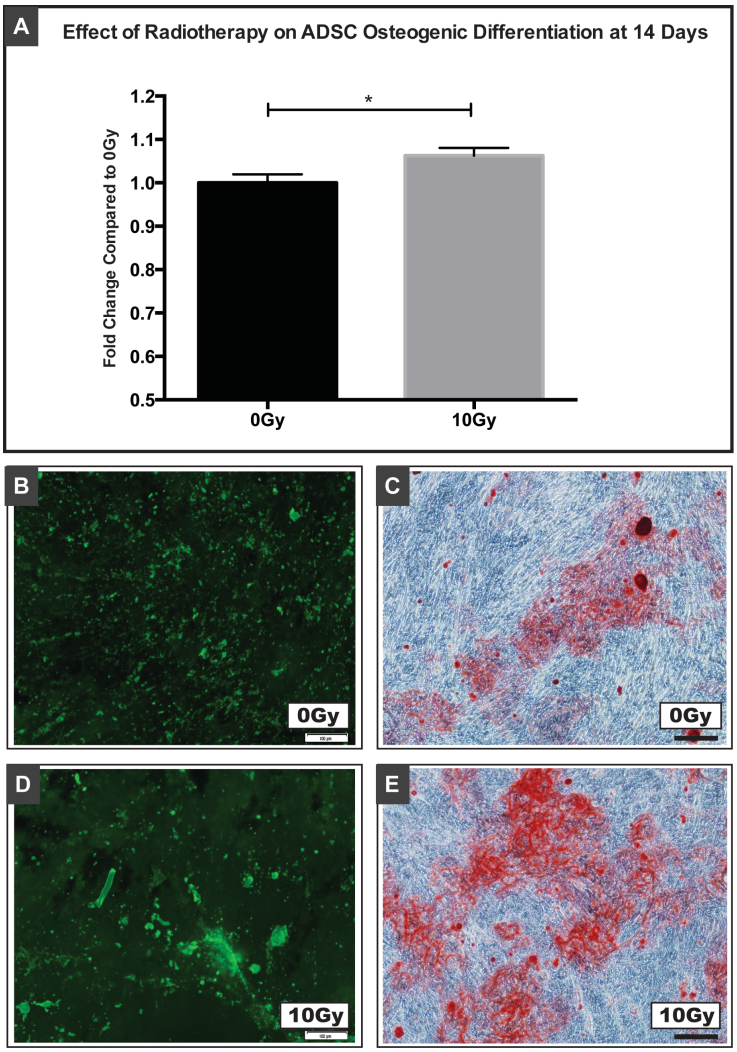

Figure 48

Figure 48 The effect of radiotherapy of ADSC Osteogenic Differentiation

x 10 objective bright field photography of Osteo-Image and Alazarin Red immunocytochemistry demonstrating staining of areas of calcification representing osteogenic differentiation of 0Gy ADSC (A,B) and 10Gy ADSC (C,D) respectively. (E) Fluorescent plate reader quantification of solubilized Osteo-Image staining demonstrating a significant increase in osteogenic differentiation of 10Gy ADSC compared to 0Gy controls at day 14. Scale bar (A-D) 100 μm. Asterisks above bar graphs indicate statistical significance. Asterisks above bar-graph indicate statistical significance (* = $p<0.05$), error bars represent SEM, with $n\geq3$.

6.2.5 Chemotactic Migration

6.2.5.1 The effect of radiotherapy on ADSC Chemotaxis and response to SDF-1α

The regenerative capacity of ADSC is not only dependent on their multipotent differentiation potential and their ability to secrete cytokines and growth factors, but also their important capacity to migrate and "home" to the site of inflammation or injury in order to exert these regenerative effects (580) (581). Boyden chambers were used to characterize the effects of radiotherapy on the chemotactic migration of ADSC in response to complete media containing 10% fetal calf serum. In particular, their responsiveness to SDF-1α, a chemokine which plays a vital role in the recruitment, migration and differentiation of stem cells was of great mechanistic interest (582). For detailed methods; see section 2.2.9. Results for Boyden chamber assays were expressed as fold changes in comparison to basal media controls to account for any differences in the chemotaxis of 0Gy and 10Gy ADSC in response to basal media, however no significant difference was determined (Figure 49 A,B,G). One-way ANOVA test with multiple comparisons was used to determine the statistical significance between 0Gy, 10Gy and media variations. 0Gy ADSCs demonstrated a significant 4.36 ± 0.24 fold increase in migration with a gradient in complete media conditions (Figure 49 C) and a 1.53 ± 0.11 fold increase in migration with 100 ng/ml of SDF-1α ($p<0.05$) (Figure 49 E) above 0Gy basal media controls (Figure 49 A). However, in comparison to their 0Gy counterparts 10Gy ADSC demonstrated a dampened chemotactic response to complete media with a 3.14 ± 0.37 fold increase in migration above 10Gy basal media controls ($p<0.05$) (Figure 49 D). Also, stimulation of 10Gy ADSC with a 100 ng/ml SDF-1α gradient failed to increase chemotaxis (Figure 49 F) when compared to 10Gy basal media controls (Figure 49 B).

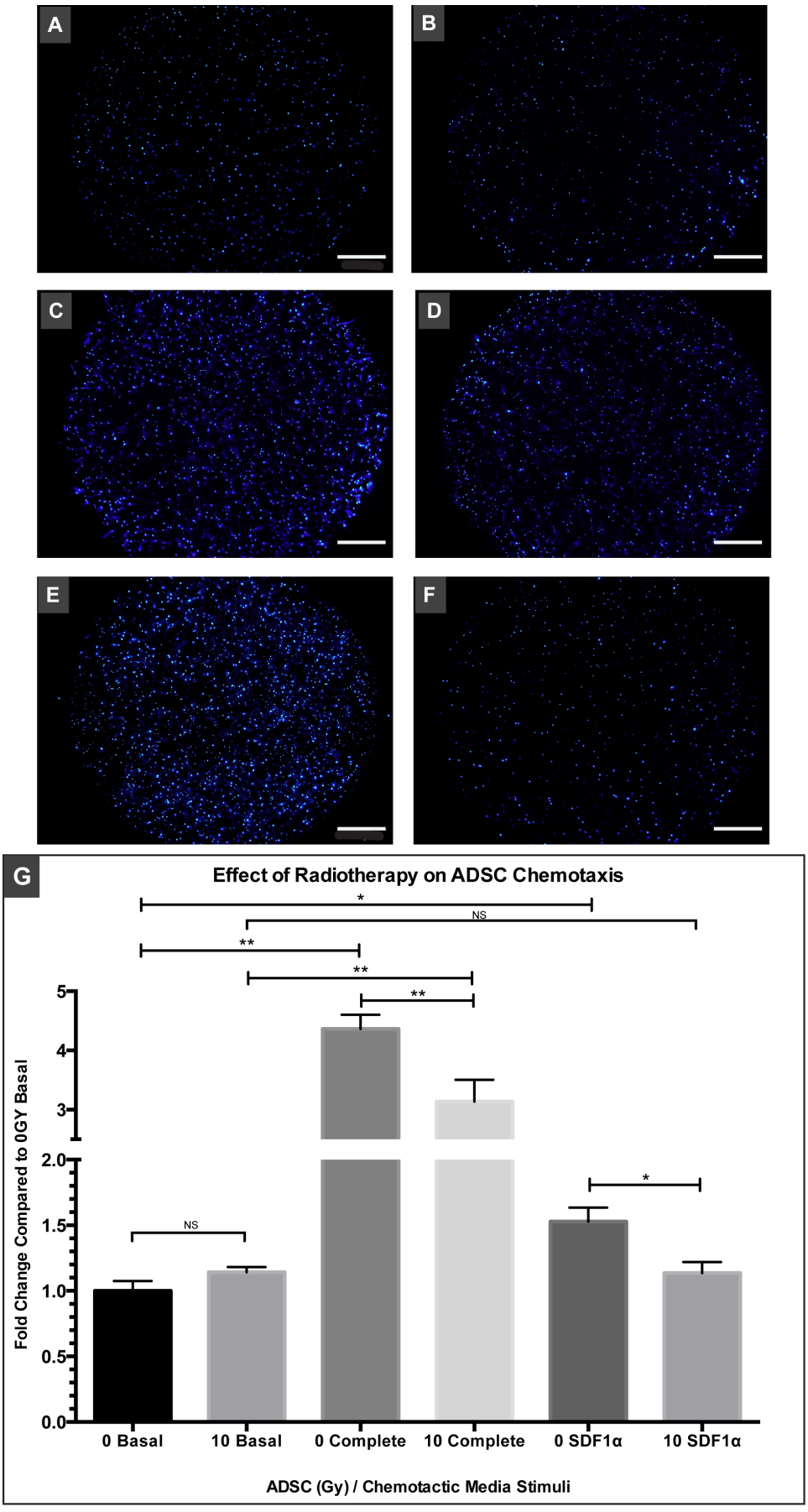
A
B
C
D
E
F
G
Effect of Radiotherapy on ADSC Chemotaxis
*
NS
**
**
**
5
4
3
2.0
1.5
1.0
0.5
0.0
NS
*
Fold Change Compared to 0GY Basal
0 Basal
10 Basal
0 Complete
10 Complete
0 SDF1α
10 SDF1α
ADSC (Gy) / Chemotactic Media Stimuli

Figure 49

Figure 49 RTX reduces the migratory capacity of ADSC to chemotactic stimulation with complete media and SDF-1α

DAPI stained cells photographed on the underside of the boyden chamber membrane (representing ADSC migrated in response to the set chemotactic gradient) were imaged with fluorescence microscopy and quantified with ImageJ (NIH). A representative image of DAPI staining at x4 objective of (A) 0Gy ADSC chemotaxis in response to basal media, (B) 10Gy ADSC chemotaxis in response to basal media, (C) 0Gy ADSC chemotaxis in response to complete DMEM, (D) 10Gy ADSC chemotaxis in response to complete DMEM, (E) 0Gy ADSC chemotaxis in response to 100 ng/ml SDF-1α and (F) 10Gy ADSC chemotaxis in response to 100 ng/ml SDF-1α. (G) A graph representing the quantification of the DAPI staining using 0Gy ADSC basal media as a control and experimental media conditions expressed as a fold change compared to the control. Scale bar (A-F) 200μm. Asterisks above bar-graph indicate statistical significance (* = $p<0.05$, ** = $p<0.01$, NS = not significant), error bars represent SEM, with $n\geq3$.

6.2.5.2 The CXCR7 Sink

As discussed in Section 5.2.2.3, CXCR7 is a chemokine that was up-regulated at an mRNA level in irradiated LECs and protein expression in LEC lysates was confirmed by western blot, flow cytometry and immunohistochemical staining of skin samples from patients who had previously undergone radiotherapy. There is a paucity of evidence determining the effects of CXCR7 in lymphangiogenesis, however experimental models pertaining to developmental growth and cell injury have ascertained its role as a 'decoy' receptor in the CXCR4/7 and SDF-1α signaling pathway (343) (351) (574). A decoy receptor is a specific receptor that is able to bind and internalize a growth factor or chemokine without resulting in the same downstream signaling due to a lack of G protein linked signal transduction, GTP hydrolysis and calcium mobilization (348) (351). Instead, it is postulated that its actions as a scavenger may either sequester SDF-1α (352) (353) or act in concert with CXCR4 as a co-receptor to potentially enhance SDF-1α mediated signaling in the

scenario where CXCR4/CXCR7 heterodimerize when both receptors are overexpressed in transfected cells (345). These findings have prompted scientists to re-visit the concept of SDF-1α and its monogamous signaling through CXCR4. The presence of increased CXCR7, secreted by irradiated LECs, may act as a decoy and block the biological pathways of stem cell recruitment and homing, a pathway that may be important in regenerating tissue after an insult such as radiotherapy. While these pathways are well established in BMSCs, these mechanisms have not been extensively explored in ADSC. Therefore, it was sought to interrogate the effect of CXCR7 on the chemotaxis of ADSC using an SDF-1α gradient.

It was found that 0Gy ADSCs demonstrated increased chemotaxis driven by 100 ng/ml of SDF-1α (a fold change of 1.7 ± 0.1) (Figure 50B) compared to 0Gy Basal media controls (Figure 50A), measured by the fluorescent staining intensity of DAPI positive cells on the underside of the boyden chamber membrane ($p<0.05$) (Figure 50 D). With the addition of an equivalent quantity of 100 ng/ml of CXCR7 to the SDF-1α, the chemotactic migration of healthy ADSCs was significantly reduced (fold change of 1.1 ± 0.15 (Figure 50C) compared to 0Gy controls, $p<0.05$ (Figure 50 D)). The results above indicate that the addition of CXCR7 to SDF-1α abolished the SDF-1α-mediated chemotaxis of 0Gy ADSCs and confirmed its action as a potential 'scavenger'; creating a chemotactic sink.

In contrast to the findings in 0Gy ADSC, SDF-1α, did not generate the same chemotactic gradient in 10Gy ADSC. No significant increase was seen in the fold change of 10Gy ADSC migration in cells subjected to either the addition of SDF-1α (1.0 ± 0.07) (Figure 50 F), or the addition of SDF-1α and CXCR7 (0.88 +/-± 0.07) (Figure 50 G) when compared to 10Gy basal media controls (Figure 50 E). These findings represent an impaired response of injured irradiated ADSCs to a physiological SDF-1α chemotactic signal and may account for reduced loco-regional stem cell recruitment to the irradiated area. Therefore, in 10Gy ADSC, the effect of CXCR7 in moderating the SDF-1α chemotactic gradient (Figure 50 E) is not as pertinent as in 0Gy ADSC chemotaxis.

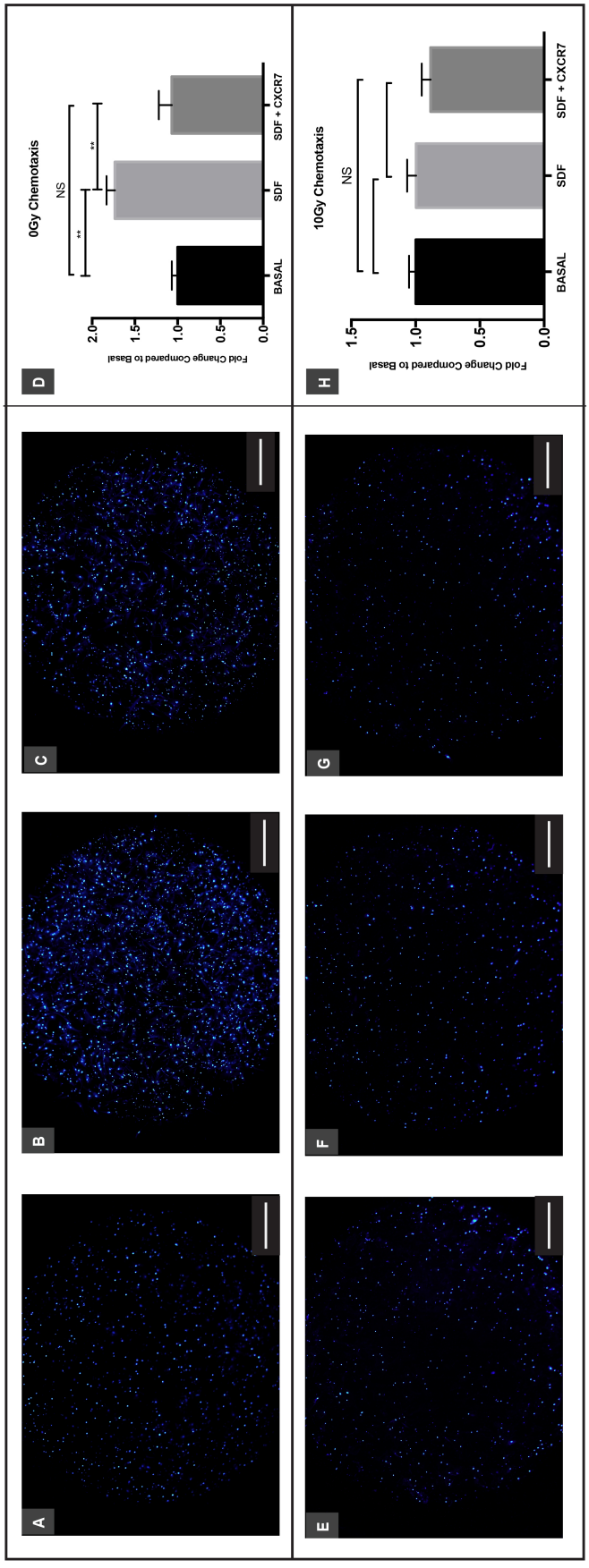
A
B
C
D
0Gy Chemotaxis
NS
**
**
Fold Change Compared to Basal
2.0
1.5
1.0
0.5
0.0
BASAL
SDF
SDF + CXCR7
E
F
G
H
10Gy Chemotaxis
NS
Fold Change Compared to Basal
1.5
1.0
0.5
0.0
BASAL
SDF
SDF + CXCR7

Figure 50

Figure 50 CXCR7 ablates SDF-1α mediated chemotaxis of 0Gy ADSC without altering 10Gy ADSC chemotaxis

DAPI fluorescence quantification of cells on the underside of the boyden chamber representing ADSC which have migrated in response to a chemotactic gradient. A representative image of DAPI staining at x4 objective of (A) 0Gy ADSC chemotaxis in response to basal media, (B) 0Gy ADSC chemotaxis in response to 100 ng/ml SDF-1α, (C) 0Gy ADSC chemotaxis in response to 100 ng/ml SDF-1α with 100 ng/ml CXCR7. (D) Graph representation of the quantification of the DAPI staining using 0Gy ADSC basal media as a control and experimental media conditions expressed as a fold change compared to the control. A representative image of DAPI staining at x4 objective of (E) 10Gy ADSC chemotaxis in response to basal media, (F) 10Gy ADSC chemotaxis in response to 100 ng/ml SDF-1α, (G) 10Gy ADSC chemotaxis in response to 100 ng/ml SDF-1α with 100 ng/ml CXCR7. (H) A graph representation of the quantification of DAPI staining using 10Gy ADSC basal media as a control and experimental media conditions expressed as a fold change compared to the control. Scale bar (A-C and E-G) 200μm. Asterisks above bar-graphs indicate statistical significance (** = $p<0.01$, NS = not significant), error bars represent SEM, with $n\geq3$.

6.2.6 Next Generation Sequencing

Next Generation Sequencing RNA analysis was conducted on ADSC to interrogate the changes that occur at a molecular level after radiotherapy induced injury. As described in 2.3.4, it is able to offer an in-depth analysis of the underlying pathways that may drive the impairment in differentiation potential and stem cell recruitment resulting from irradiation. These analyses aim to identify a distinct set of alterations in gene expression that distinguish irradiated cells from normal cells.

Standardised numbers of ADSC were plated in cell culture flasks and once 80-90% confluence was achieved they were irradiated with two regimes; one group received a single dose of 10Gy and the second group received five 2Gy fractions across 48 h with 0Gy control groups for each. RNA extraction was undertaken at 4 h after the 10Gy dose or after the final 2Gy fractionated dose using the QIAGEN, Germany® RNEasy Plus Universal Kit as per manufacturer's instructions. Samples were then tested for purity and quality control using the Nanodrop™ Spectrophotometer (Thermo Fischer Scientific, USA) and stored at -80ºC, till further processing. Each sample underwent RNA sequencing (100 base pair single end) in the Illumina HiSeq machine at the Australian Genome Research Facility (AGRF) and results were presented in a series of spreadsheets and heat maps along with a comprehensive pathway analysis platform (see 2.3.4, 2.3.5 for detailed methodology).

Next generation sequencing demonstrated several significant differences between the expression profile of 10Gy Single Dose and five 2Gy fractionated doses in comparison to un-injured 0Gy controls. 10Gy ADSC significantly altered the expression of 95 genes at 4 h with adjusted p-values <0.05, while 2Gy x 5 LECs demonstrated 345 altered genes at 4 h. The top ten candidates changed in response to radiotherapy injury are listed in Table 16 and Table 17.

Gene ID	Symbols	Gene Name	Chr	logFC
10140	TOB1	transducer of ERBB2, 1	17	1.038837795
1647	GADD45A	growth arrest and DNA-damage-inducible, alpha	1	1.29344262
10769	PLK2	polo-like kinase 2	5	1.35436875
1026	CDKN1A	cyclin-dependent kinase inhibitor 1A (p21, Cip1)	6	1.783012979
9518	GDF15	growth differentiation factor 15	19	2.099602749
57103	C12orf5	chromosome 12 open reading frame 5	12	1.119576761
8493	PPM1D	protein phosphatase, Mg2+/Mn2+ dependent, 1D	17	1.43228378
8793	TNFRSF10D	tumor necrosis factor receptor superfamily, member 10d, decoy with truncated death domain	8	1.008356642
7832	BTG2	BTG family, member 2	1	2.04694469
4193	MDM2	Mdm2, p53 E3 ubiquitin protein ligase homolog (mouse)	12	1.958040368

Table 16 Gene expression alterations of 10Gy ADSC in comparison to 0Gy ADSC controls

Table 16 Key Candidates from the next generation sequencing data comparing 10Gy single dose irradiated ADSC to 0Gy controls. The table details the top ten gene candidates demonstrating differential gene expression resulting from radiotherapy injury (blue boxes indicate gene expression changes that reach statistical significance $p<0.05$). Chr = chromosome, logFC = log fold change.

Gene ID	Symbols	Gene Name	Chr	logFC
1647	GADD45A	growth arrest and DNA-damage-inducible, alpha	1	1.596855902
9518	GDF15	growth differentiation factor 15	19	2.005393154
1026	CDKN1A	cyclin-dependent kinase inhibitor 1A (p21, Cip1)	6	1.621443832
50484	RRM2B	ribonucleotide reductase M2 B (TP53 inducible)	8	0.957057754
157638	FAM84B	family with sequence similarity 84, member B	8	1.966906938
23210	JMJD6	jumonji domain containing 6	17	-0.867038279
79094	CHAC1	ChaC, cation transport regulator homolog 1 (E. coli)	15	2.85871981
26031	OSBPL3	oxysterol binding protein-like 3	7	0.962395768
132671	SPATA18	spermatogenesis associated 18	4	1.237588275
8493	PPM1D	protein phosphatase, Mg2+/Mn2+ dependent, 1D	17	1.184087581

Table 17 Gene expression alterations of ADSC recieving 5 fractions of 2Gy in comparison to 0Gy ADSC controls

Table 17 Key Candidates from the next generation sequencing data comparing 5 fractionated doses of 2Gy irradiated ADSC to 0Gy controls. The table details the top ten gene candidates demonstrating differential gene expression resulting from radiotherapy injury (blue boxes indicate gene expression changes that reach statistical significance $p<0.05$). Chr = chromosome, logFC = log fold change.

6.2.7 Metabolomic alterations in irradiated ADSC

The metabolism of a cell is integral to the process of energy production as well as the formation of proteins consisting of key cellular building blocks such as amino acids, cholesterol, lipids and glucose (583). Mitochondria are the key organelles within a cell, which occupy up to 25% of a cell's volume, consume around 90% of the body's oxygen and are themselves, a rich source of reactive oxygen species (ROS) (65). The mitochondria act as the 'power houses' of the cell (97). In the setting of an insult to cells such as ionizing radiation, mitochondrial injury results in the generation of surplus ROS. Alterations in the mitochondrial metabolic activity, specifically dysfunction of oxidation-reduction reactions, may contribute to worsening the injury or perpetuating damage to the cell membrane (62). The oxidative damage is also thought to be detrimental to mitochondrial proteins; leading to deletions in the mitochondrial genome such as mitochondrial ATPase, NADH dehydrogenase complex I and cytochrome c oxidase (65).

In order to interrogate the effects of radiotherapy on ADSC metabolism, experiments were designed using 0Gy and 10Gy ADSC to generate conditioned media (CM) which was extracted after 72 h of incubation. Samples were processed and derivatised to undergo gas chromatography analysis using plain DMEM media as a control. Table 18 details the results below. The most significantly altered amino acid, Threonine, was found to be utilized by normal ADSC leading to a 3.61-fold change reduction in levels when compared to RTX-ADSC^{CM}. DMEM control media demonstrated detectable levels of threonine, levels which were decreased in ADSC^{CM}, yet still remained elevated in RTX- ADSC^{CM} as demonstrated in (Figure 51 A). To validate this finding, gas chromatography analysis was conducted on cell lysates of both 0Gy

and 10Gy ADSCs, which demonstrated a trend of 0.66 fold reduction in the presence of threonine within the irradiated ADSC lysate (Figure 51 B). These data demonstrate that threonine uptake pathways and/or subsequent utilization of this essential amino acid may be impaired as a result of radiotherapy injury of ADSC, the consequences of which are explored further in section 7.2.8.

Additional experiments were undertaken to determine the metabolic differences between normal and irradiated ADSC, utilizing gas chromatography analysis of cell lysates as well as liquid chromatography of conditioned media samples Table 18.

Metabolite	Fold change 10Gy vs 0Gy	t-statistic	BH Adjusted p-value	standard error
GC MEDIA ANALYSIS				
Threonine	3.607	103.244	0.001	0.035
Maltose	-0.650	-3.264	0.338	0.199
Galactose-6-phosphate	-0.549	-2.870	0.346	0.191
Pyruvic acid	0.352	2.870	0.352	0.123
Serine	0.763	2.363	0.355	0.323
Phenylalanine	0.399	2.468	0.355	0.162
Sucrose	-0.528	-2.603	0.355	0.203
Tryptophan	-1.038	-2.711	0.355	0.383
GC CELL LYSATE ANALYSIS				
Threonine	-0.667	-2.629	0.338	0.254
Lactic acid	-2.563	-4.829	0.140	0.531
Glycine	-0.250	-4.368	0.143	0.057
Serine	0.837	3.324	0.220	0.252
LC MEDIA ANALYSIS				
Creatinine	3.778	5.579	0.037	0.677
Tetrahydrofolate	2.213	5.761	0.037	0.384
Palmitoyl.CoA	0.411	4.484	0.037	0.092
Cytosine	-2.410	-4.897	0.037	0.492
Hexadecanoic.acid	-0.478	-4.222	0.054	0.113
Adenosine	-1.058	-4.271	0.057	0.248
Heptadecanoic.acid	-3.722	-3.839	0.066	0.969
Inosine	-0.928	-3.813	0.075	0.243
Erythrose.4.phosphate	-1.519	-3.471	0.075	0.438
Guanosine	-1.339	-3.423	0.103	0.391
D.Galacturonate	-2.180	-3.626	0.106	0.601

Isocitrate	0.804	3.689	0.110	0.218
Adenine	-1.705	-3.278	0.110	0.520
D.Glucuronate	-2.256	-3.467	0.110	0.651
Sedoheptulose.7.phosphate	-0.836	-3.026	0.128	0.276
N2.Acetyl.L.lysine	1.989	2.888	0.138	0.689
N.Acetylglutamine	0.302	2.969	0.138	0.102
D.Glucose	0.291	2.689	0.138	0.108
D.Fructose	0.287	2.679	0.138	0.107
Proline	-0.256	-2.842	0.138	0.090
Tetradecanoics.acid	-0.421	-2.939	0.138	0.143
Uracil	-0.594	-2.846	0.138	0.209
CoA	-1.248	-2.874	0.138	0.434
myo.Inositol.	0.289	2.633	0.139	0.110
PS.14.0.14.0..1.2.	-1.475	-2.819	0.143	0.523
Uridine	-0.723	-2.736	0.143	0.264
Glycylglycine	-0.733	-2.559	0.143	0.286
Orotate	-0.956	-2.627	0.146	0.364
Thymine	3.249	2.744	0.156	1.184
L.Cysteate	-0.251	-2.504	0.156	0.100
Dodecanoic.acid	-0.461	-2.480	0.156	0.186
Ala.Gly	-1.273	-2.587	0.156	0.492
IDP Phosphate	-1.309	-2.399	0.156	0.546
HEPES	-1.774	-2.553	0.156	0.695
Acetylcholine	-1.367	-2.338	0.177	0.585
Alanine	-0.396	-2.289	0.181	0.173
D.Galactarate	-0.907	-2.261	0.182	0.401
D.ribulose.5.phosphate	-0.910	-2.350	0.191	0.387
LC CELL LYSATE ANALYSIS				
Cytosine	-2.365	-6.417	0.013	0.368
Creatinine	3.615	5.595	0.031	0.646
Tetrahydrofolate	2.210	5.648	0.031	0.391
Palmitoyl-CoA	0.422	4.888	0.031	0.086
Hexadecanoic acid	-0.466	-4.200	0.047	0.111

Table 18 ADSC Metabolic Alterations

Table 18 Metabolomic alterations of 10Gy ADSC^{CM} and cell lysates in comparison to 0Gy ADSC controls using gas and liquid chromatography mass spectrometry

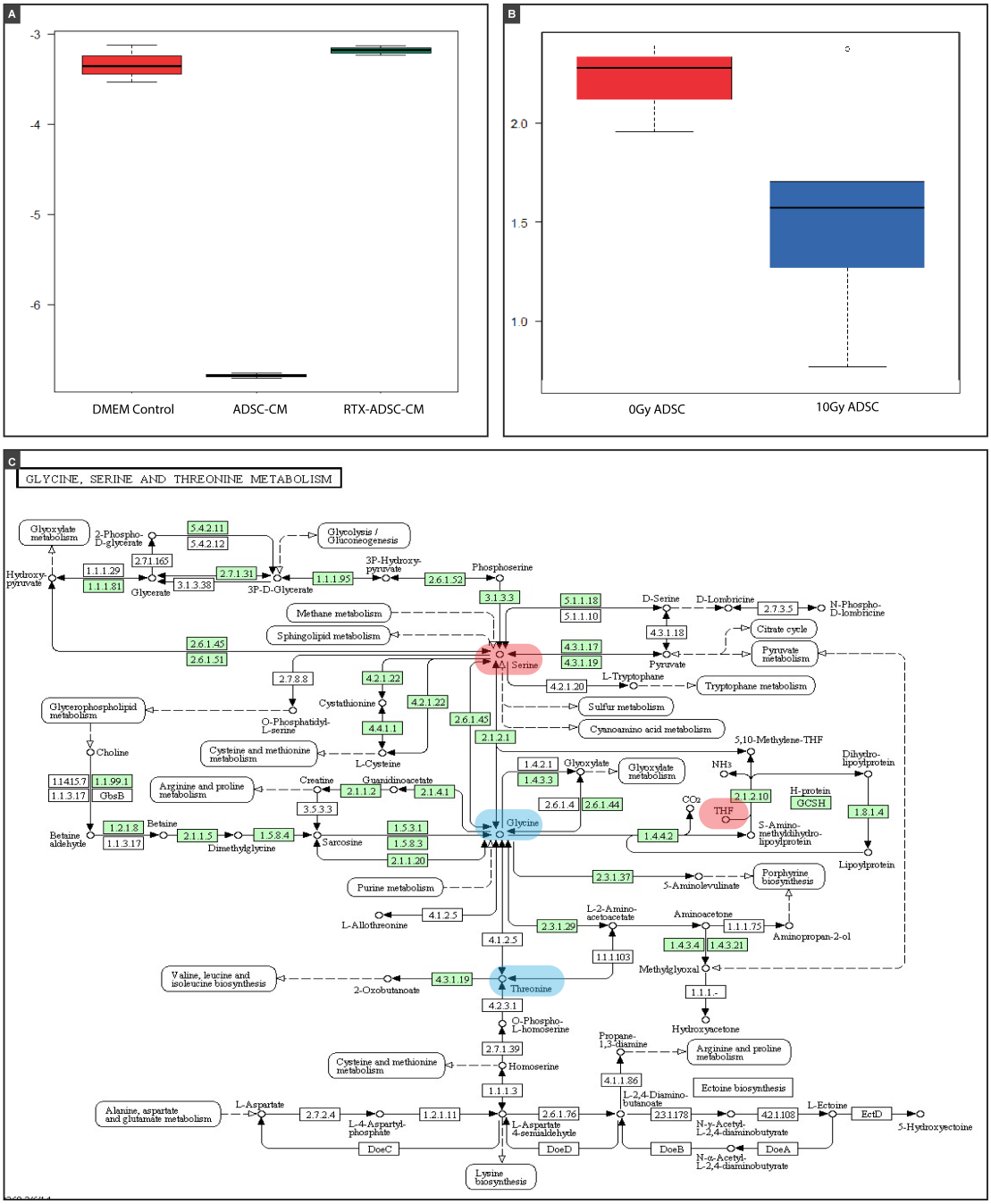
A
-3
-4
-5
-6
DMEM Control
ADSC-CM
RTX-ADSC-CM
B
2.0
1.5
1.0
0Gy ADSC
10Gy ADSC
C
GLYCINE, SERINE AND THREONINE METABOLISM
Glyoxylate metabolism
2-Phospho-D-glycerate
Glycolysis / Gluconeogenesis
Hydroxy-pyruvate
Glycerate
3P-Hydroxy-pyruvate
3P-D-Glycerate
Phosphoserine
Methane metabolism
Sphingolipid metabolism
Serine
D-Serine
D-Lombricine
N-Phospho-D-lombricine
Citrate cycle
Pyruvate metabolism
Pyruvate
L-Tryptophane
Tryptophane metabolism
Sulfur metabolism
Cyanoamino acid metabolism
Glycerophospholipid metabolism
O-Phosphatidyl-L-serine
Cystathionine
Choline
Cysteine and methionine metabolism
L-Cysteine
5,10-Methylene-THF
Dihydro-lipoylprotein
H-protein
GCSH
Lipoylprotein
Glyoxylate
Glyoxylate metabolism
NH3
CO2
THF
S-Amino-methyldihydro-lipoylprotein
Arginine and proline metabolism
Creatine
Guanidinoacetate
Betaine aldehyde
Betaine
Dimethylglycine
Sarcosine
Glycine
Purine metabolism
Porphyrine biosynthesis
5-Aminolevulinate
L-Allothreonine
L-2-Amino-acetoacetate
Aminoacetone
Aminopropan-2-ol
Methylglyoxal
Valine, leucine and isoleucine biosynthesis
2-Oxobutanoate
Threonine
Hydroxyacetone
O-Phospho-L-homoserine
Propane-1,3-diamine
Cysteine and methionine metabolism
Homoserine
Arginine and proline metabolism
Ectoine biosynthesis
L-2,4-Diamino-butanoate
Alanine, aspartate and glutamate metabolism
L-Aspartate
L-4-Aspartyl-phosphate
L-Aspartate 4-semialdehyde
N-γ-Acetyl-L-2,4-diaminobutyrate
N-γ-Acetyl-L-2,4-diaminobutyrate
L-Ectoine
EctD
5-Hydroxyectoine
DoeC
DoeD
DoeB
DoeA
Lysine biosynthesis

Figure 51

Figure 51 KEGG pathway – Glycine, Serine and Threonine Metabolism Pathway changes in 10Gy ADSC compared to 0Gy Controls

(A) Box plot of the gas chromatography detectable levels of L-threonine in DMEM (Controls), $ADSC^{CM}$ (0Gy CM) and RTX- $ADSC^{CM}$ (10Gy CM) which graphically demonstrates the reduction of threonine in $ADSC^{CM}$, in contrast to RTX- $ADSC^{CM}$. (B) Box plot of liquid chromatography detectable levels of L-threonine in 0Gy ADSC lysates and 10Gy ADSC lysates, graphically demonstrating more abundant detection of threonine in 0Gy ADSC lysates. (C) KEGG pathway Glycine- Serine-Threonine (adapted from Kanehisa et al. (584) (585)) highlighting in red candidates increased in 10Gy ADSC lysates, while candidates in blue are decreased in 10Gy ADSC lysates in comparison to 0Gy ADSC lysate controls. y-axis in (A) and (B) represents expression fold change of metabolite, error bars represent SEM, with $n \geq 3$.

6.3 Discussion

The results of this chapter demonstrate the insult of radiotherapy induced soft-tissue injury to ADSC significantly alters their cellular functioning and response to various homeostatic stimuli. Various groups have also demonstrated that supplementing fat graft with SVF leads to increased fat graft retention, reduced atrophy and increased vascularity in fat grafted tissues (387) (391). Therefore, for the purposes of replicating models of fat grafting and the cells used in the clinical setting, the SVF derived from fresh adipose tissue was not further purified to obtain a truer population of ADSC. Instead this heterogeneous cell fraction, the regenerative component which comprises of ADSCs, was used for experimentation to determine the effects radiotherapy had on their homeostatic and regenerative functions.

Key changes in the survival dynamics of ADSCs reflected findings similar to those in endothelial cell populations: reduced proliferation with concurrent reduction in apoptosis, however the survival fraction of irradiated ADSCs was relatively favourable at 81%, compared to other mesenchymal and endothelial cell populations (Figure 45 A,B). The limited literature pertaining to radiotherapy injury to ADSC also suggests that ADSC display a relative radio-resistance compared with other components of SVF such as adipocytes (569) (578), possibly attributable to superior

DNA damage repair mechanisms compared with those found in terminally differentiated cells (569). The decreased metabolic demands of resting ADSCs may result in protection from hypoxia and subsequent apoptosis (369) (454). While this characteristic may protect ADSC from radiotherapy-induced apoptosis, it is likely to lead to an increased presence of sub-lethally injured, sub optimally functioning stem cells in an area of radiotherapy injury, which continue to contribute to the chronic inflammatory state, carrying poor regenerative potential and propagating the spread of injury to surrounding tissues.

The next generation sequencing data, supports these functional changes demonstrated in the altered survival dynamics of irradiated ADSC with the significant up-regulation of cell cycle arrest proteins. The results presented a consistent up-regulation of genes resulting from both a single dose of 10Gy or five fractions of 2Gy; namely growth differentiation factor 15 (GDF15), growth arrest and DNA damage-inducible alpha (GADD45A), cyclin-dependent kinase inhibitor 1A (CDKN1A) and protein phosphatase dependent 1D (PPM1D). From these candidates GDF15 was of particular interest. Studies have demonstrated that radiotherapy results in the up-regulation of GDF15 from doses as low as 100mGy, a cytokine part of the TGF-β superfamily, which conferred resistance to radiotherapy-induced damage. Silencing of this gene in a line of immortalized human fibroblasts resulted in sensitization of these cells to radiotherapy, negated cell cycle arrest and, while it did not alter levels cell cycle mediators such as CDKN1A, it did increase expression of TGF-β and GADD45A (586). Uchiyama et al. also demonstrated that increased levels of GDF15 played a role in inducing osteogenic differentiation in BMSC, a finding in keeping with the increase in ADSC osteogenic differentiation in irradiated vs. normal ADSC (587) (see 6.2.4). In tumour cells increased expression of GDF15 also constituted an anti-apoptotic effect which was thought to be protective to the effects of radiotherapy (588). Additionally Koga et al. demonstrated a 6-fold increase in serum levels of GDF15 in patients with mitochondrial disorders (589), which may also play a role in the cellular dysfunction of ADSC injured by radiotherapy (see 6.2.7). Therefore, this up-regulation of GDF15 in response to radiotherapy injury of ADSC can account for the dysregulation of key homeostatic functions found in the *in vitro* studies detailed

above and may be a key factor to consider in mitigating the response of ADSC radiotherapy-induced injury.

The results in this chapter also demonstrated that radiotherapy significantly impairs the adipogenic potential of ADSCs, shown at both a qualitative level with staining and quantitative level with extraction of the Oil Red O staining. However, it was vital to consider that the reduced proliferative potential of irradiated ADSC would also contribute to the qualitative and quantitative reduction of adipogenesis. Molecular level interrogation using PCR confirmed significant down-regulation of key adipogenic genes FABP4, CEBPb and LPL. These *in-vitro* findings correlate with the clinical characteristics of irradiated tissues, which are often fibrotic, with an atrophied layer of subcutaneous fat leading to contractures and poor compliance of tissues. Furthermore, the reduction observed in response to adipogenic stimuli suggests that radiotherapy impairs the ability of local ADSCs to undergo adipogenic differentiation, highlighting the need to import healthy loco-regional or distant stem cells to the irradiated area in order to carry out functional adipogenesis. Nicolay et al. reported consistent genetic expression of BMP6 and RUNX2 as well as PPARγ after 10Gy irradiation of bone marrow cells, illustrating that irradiated BMSC are still able to undergo a level of adipogenic and osteogenic differentiation, however they provided no quantitative comparisons (578). In contrast, Marina et al. isolated ADSC from irradiated adipose tissue collected from head and neck cancer patients, demonstrating no significant differences in adipogenic and osteogenic differentiation with staining quantification compared to patient matched controls, albeit with a small patient sample of six. The study also mentions a failure to isolate ADSC from irradiated tissues in six out of the twelve patient samples (590), perhaps suggesting the degree of atrophy and attrition in adipogenic potential of ADSCs, a finding corroborating results presented in this chapter.

The results presented demonstrated that increased osteogenesis occurred in irradiated ADSCs when compared to normal controls. Various groups have attempted to determine the differentiation potential and fate of BMSC after irradiation to long bones with Li et al., amongst others, reporting a reduction in osteogenic potential (with down regulation of Wnt pathways) with varying reports of increased

adipogenesis (269) contributing to the development of osteoporotic bone (456) (579). There is a deficiency of studies in the literature pertaining to the effects of radiotherapy on ADSC osteogenic differentiation potential. However the preliminary results presented here suggest this increased predisposition for osteogenic differentiation may contribute to the clinical picture of fibrosis and calcification in irradiated soft tissue. Further interrogation of the molecular cues driving this differentiation process are required, however early conclusions can be drawn as this is an unfavourable characteristic in soft tissues and previous cancerous tissue beds, already lacking supple and pliable characteristics.

Recovery of tissues and organs from radiotherapy induced soft tissue injury is thought to be critically dependent on the repopulation of resident stem cells, defined as a subset of cells with capacity of both self-renewal and differentiation (362). Circulating trafficking of BMSC have been shown to be involved in repair of damage in multiple organs – brain, skin and spinal cord (362). Reduction in migration in 2-D models as well as in response to chemotactic stimuli with growth factor containing media also demonstrate a disruption in a vital homeostatic function of ADSCs. The ability to migrate or home to an area of inflammation, infection or injury is a prerequisite for these cells to be able to exert their therapeutic influence (either by secretion of cytokines or growth factors or by differentiation to replace damaged cells) and restore functionality to the injured tissues. The impaired responsiveness of irradiated ADSC to chemotactic stimuli suggests that the chronic inflammation and injurious state induced by radiotherapy may be further worsened by the inability of loco-regional ADSC recruitment and thus regenerative repair. The chemotactic sink created by the presence of CXCR7 (secreted by irradiated LEC) was validated by a reduction in SDF-1α mediated chemotaxis in healthy ADSC. This finding highlights a key feature of radiotherapy-induced soft tissue injury and the microenvironment that is created: injury to each cell subtype leads to further damaging stimuli resulting in interactions that can further impair regeneration or functioning of all cells in the zone of injury. The inability of SDF-1α to successfully recruit healthy ADSC with its chemotactic stimulus in the presence of CXCR7 in an irradiated microenvironment, further suggests that healthy un-irradiated ADSC introduced into an area of radiotherapy soft tissue injury e.g. by the means of mechanically fat grafting, may

compensate for the impaired ability of endogenous stem cell recruitment and the subsequent regenerative effects.

The metabolism of a cell powers the variety of processes required to perform homeostatic functions, in particular to stem cells. This adaptable flux of energy can regulate between states of quiescence to active proliferation (591). Metabolic processes are fueled by substrates such as glucose, amino acids and fatty acids which are handled by a delicate balancing of catabolic (breakdown and energy production) and anabolic (construction of macromolecules) processes (591). Depending on the individual cell type and its required specialized functioning, alternative metabolic pathways may be activated in order to meet these bioenergetic demands (591). In addition to the generation of energy, recent research has demonstrated that metabolic regulation may also contribute to genetic regulation of a cell's behavior through driving transcriptional alterations (592). With this in mind, the reduced ability of irradiated ADSC to uptake and utilize the essential amino acid threonine, may require further investigation as to its role in ADSC cell function and metabolism (see section 7.2.9).

The role of threonine, an essential amino acid, has been scarcely reported in the literature, however the findings above suggest there is a significant impairment in the ability of irradiated human ADSCs to uptake and utilize L-Threonine. There are two main described pathways for the processing of threonine; threonine dehydrogenase which metabolises threonine to form glycine and acetyl-CoA or threonine dehydratase which catabolizes threonine to ammonium ions and 2-ketobutyrate (593). Threonine dehydrogenase is an enzyme that is responsible for the processing of this amino acid in murine models and some groups have determined threonine to be vital to the proliferation and maintenance of pluripotency in murine embryonic stem cells (594-596). The literature pertaining to human adult stem cell populations and the role threonine plays in their metabolism is scant. The enzyme threonine dehydrogenase has not been well characterised in human cells, as Pencharz et al. demonstrated that this pathway may account for only 7-11% of threonine catabolism in humans (593), therefore the role of threonine and its degradative pathways in adult mesenchymal stem cells also requires further investigation.

6.4 Conclusion

The results in this chapter clearly demonstrate the adverse impact of radiotherapy injury to ADSCs. The reduction in proliferation as well as apoptosis again demonstrates that irradiated ADSC, like the endothelial populations, acquire a state of senescence and persist as cells unable to perform key homeostatic functions. The diminished capacity of 10Gy ADSC migration, response to chemotactic stimuli and adipogenic differentiation all represent significant impairment in the capabilities of these cells to carry out their regenerative and reparative functions. In addition to this, the validation of CXCR7 mediated blockade of chemotaxis and homing of healthy ADSC in response to SDF1α further establishes the complexity and severity of radiotherapy soft tissue injury. Not only does radiation impair loco-regional ADSC function, but may also block the recruitment of functional ADSCs, from sites distant to the injury. While mechanical introduction of healthy adipose tissue and ADSC by means of fat grafting may overcome the failure of recruitment mechanisms described above, manipulation of key molecular and metabolomic candidates may improve the microenvironment and attempt to mitigate radiotherapy injury to both targeted and grafted ADSC.

7 CHAPTER 7: Characterising the mechanisms of radiotherapy injury reversal using adipose derived stem cells

7.1 Introduction

Adipose tissue is composed of mature adipocytes and a stromal vascular fraction, and constitutes a type of connective tissue specialized to fulfill mechanical, aesthetic and metabolic functions (368-371) (393). In the past decade, the use of fat grafting as a surgical method to correct cosmetic contour defects as well as scarred and contracted tissue, has re-gained popularity in the field of plastic surgery (372) (382), especially in light of the abundance of adipose tissue, ease of harvest and minimal donor site morbidity (371). In particular, its novel application in the setting of radiotherapy soft-tissue injury has highlighted the need for more scientific evaluation into its mechanisms of action.

Clinical observations relating to the introduction of fat into irradiated soft tissues leading to improvement in tissue quality, degree of fibrosis and pigmentation (300) (373-375) were later validated in animal models (69) (375). In the clinical scenarios of breast and head and neck cancer, fat grafting resulted in observed improvements in radiotherapy-induced capsular contracture, chronic ulceration and vocal cord damage, further demonstrating the wide applicability of fat grafting in improving the 'diseases of cancer survivorship' (368) (369) (371) (373-378).

As detailed in Table 5, the clinical benefits of fat grafting have previously been attributed the regenerative properties of the undifferentiated multi-potent ADSCs within the SVF of lipoaspirate (373) (379). ADSCs are thought to exercise their regenerative potential through a combination of supporting adipogenesis, angiogenesis and lymphangiogenesis; by modulating inflammatory, immune and reactive oxygen species-mediated processes; and by recruiting un-injured stem cells (380) (381). However, despite promising clinical potential and the postulated mechanisms of regenerative action, a scientific understanding of the putative molecular drivers of ADSC-mediated reversal of RTX-injury remain unknown (382) (383). These reparative effects of uninjured ADSCs on other cell types may well become compromised when ADSCs are exposed to radiation injury. The functional

and molecular alterations caused by RTX-injury to ADSC are detailed in chapter 6, demonstrating the significant impairment in proliferative, migratory, chemotactic and differentiation capacities of ADSCs subjected to 10Gy radiation doses. It is postulated that these functional alterations significantly contribute to the development of chronic soft tissue injury. These findings further highlighted the need for recruitment of healthy ADSCs via stem cell homing, a process shown to be impaired as a result of the radiotherapy induced CXCR7 sink (see section 6.2.5), leaving the 'artificial' introduction of healthy ADSCs into the injured area via fat grafting as a method to abrogate of the cellular damage resulting from irradiation.

Autologous tissue transferred to a distant site without its original blood supply is defined as a tissue graft. Therefore, to prevent graft necrosis and loss, fat graft must acquire a blood supply and nutrients from the recipient tissue bed (389) (390). Unfortunately, reports suggest that fat grafts may resorb up to 70-100% of the initial injected tissue volume (391) due to poor graft neo-vascularisation, apoptosis and/or chronic fat necrosis – all effects that are more pronounced in an microenvironment of irradiated tissues (368-370) (386) (387) (390-393). To enhance the relative abundance of ADSC within fat grafts, Yoshimura et al. proposed 'cell-assisted lipotransfer enrichment' (Figure 5C), by supplementing lipoaspirate with additional SVF (387). Numerous studies also suggested that such enrichment may further enhance graft viability, neo-vascularisation and volume retention, while reducing ADSC necrosis/apoptosis rates (142) (386-389) (391) (401).

The 'building block' theory of stem cell differentiation to replace injured cells was once the prevailing wisdom (597). However, observations of higher fat graft resorption rates and the resulting small numbers of engrafted ADSCs lead to this understanding being superseded by theories relating to a paracrine mechanism of immune-modulation via secreted protein growth factors generated by ADSCs which survive the grafting process These proteins may secreted by conventional endoplasmic-reticulum-golgi apparatus mediated secretion or unconventional pathways such as exosomes which are classified as extracellular vesicles released upon fusion with a multivesicular body and the cell plasma membrane (598) (see section 1.9.9) (428) (449) (460). Extrapolated from studies performed using BMSCs,

the proteins secreted by these cells may mitigate fibrosis, hypoxia and inflammation, as well as the processes of angiogenesis and lymphangiogenesis (246) (373) (436).

Few studies, however, have specifically examined the therapeutic properties of ADSCs (see section 1.11.4). One of these is a study in which Haubner et al. demonstrated a mitigation of radiotherapy-induced up-regulation of inflammatory cytokines IL-6, FGF, ICAM-1 and VCAM1 in BECs, using a co-culture model with ADSCs (394). Similarly, Chang et al. used a model of abdominal irradiation followed by intra-peritoneal ADSC injection that resulted in improved intestinal re-epithelialisation and survival rates in ADSC-treated animals (438). Also in the upper gastrointestinal tract, Lim et al. and Kojima et al. used a RTX-induced salivary gland injury model to demonstrate protective and anti-apoptotic effects of ADSC injection (468) (467). Most relevant in the context of chronic radiotherapy soft tissue injury was work by Sultan et al. and Huang et al., in which animal models of fat grafting in irradiated skin and subcutaneous tissues demonstrated increased dermal thickness, quantified by a reduction in collagen-based scar index measurements and staining of Smad-3, a marker of fibrosis (466) (469).

The experiments in this chapter first sought to establish the validity of the regenerative effects of ADSC on irradiated cells such as NHDFs and LECs, after having established the effects of radiotherapy injury on each of these individual cells types in *in-vitro* models. Subsequent experiments were then designed to undertake a detailed systematic analysis of the secretory expression profiles of ADSCs, using multiple investigation platforms to investigate the specific mechanisms by which they reverse radiotherapy soft tissue injury.

7.2 Results

7.2.1 The effects of fat grafting on normal and irradiated NHDF – mitigation of a hyper-migratory state

A model of fat grafting, designed to utilise the paracrine secretome of the ADSC, was first applied to NHDF to interrogate the effects this might have on migratory function in a scratch wound assay. $ADSC^{CM}$ was generated by extraction of media from 80%

confluent ADSCs after a 72-hour period of conditioning with DMEM complete media (standard media solution for optimal ADSC growth). Media was aspirated, centrifuged to remove cell debris and filtered prior to addition to NHDFs in the *in-vitro* model of fat grafting (see section 2.1.4 for detailed methodology). As established in section 3.3.3, radiotherapy injury results in increased NHDF migratory capacity, (0Gy NHDF demonstrated a 70.8 ± 4.7% gap closure (Figure 52 B) at 48 h, vs. 78.9 ± 6.8% in 10Gy NHDF (Figure 52 E) $p<0.05$). This radiotherapy induced hypermigratory state, along with features of increased NHDF cell size, adhesion and contractile ability are collectively thought lead to the clinical manifestations of fibrosis. In particular, the increased migratory capacity of irradiated NHDF may also account for propagation of radiotherapy-induced damage to surrounding cells, thereby spreading the injury beyond the cells directly targeted by gamma rays. The addition of $ADSC^{CM}$ to 0Gy NHDF resulted in a 78.0 ± 7.0% gap closure at 48 h (Figure 52 C), which was not significantly different compared with basal media controls. However, the addition of $ADSC^{CM}$ to 10Gy NHDF resulted in a 61.4 ± 8.1% gap closure at 48 h (Figure 52 F), representing a 17.5% reduction in migration (Figure 52 G) ($p<0.01$). This effective reduction in migration with the treatment using $ADSC^{CM}$ demonstrated that putative factors in the ADSC paracrine secretome can mitigate the effects of radiotherapy-induced injury to NHDF. Introduction of fat graft in a pre-irradiated tissue bed may therefore contain or interfere with the spread of radiotherapy injury and the development of fibrosis. These novel results suggest a mechanistic explanation of the clinical observations of softening and reduction of fibrosis described in clinical fat grafting studies (373).

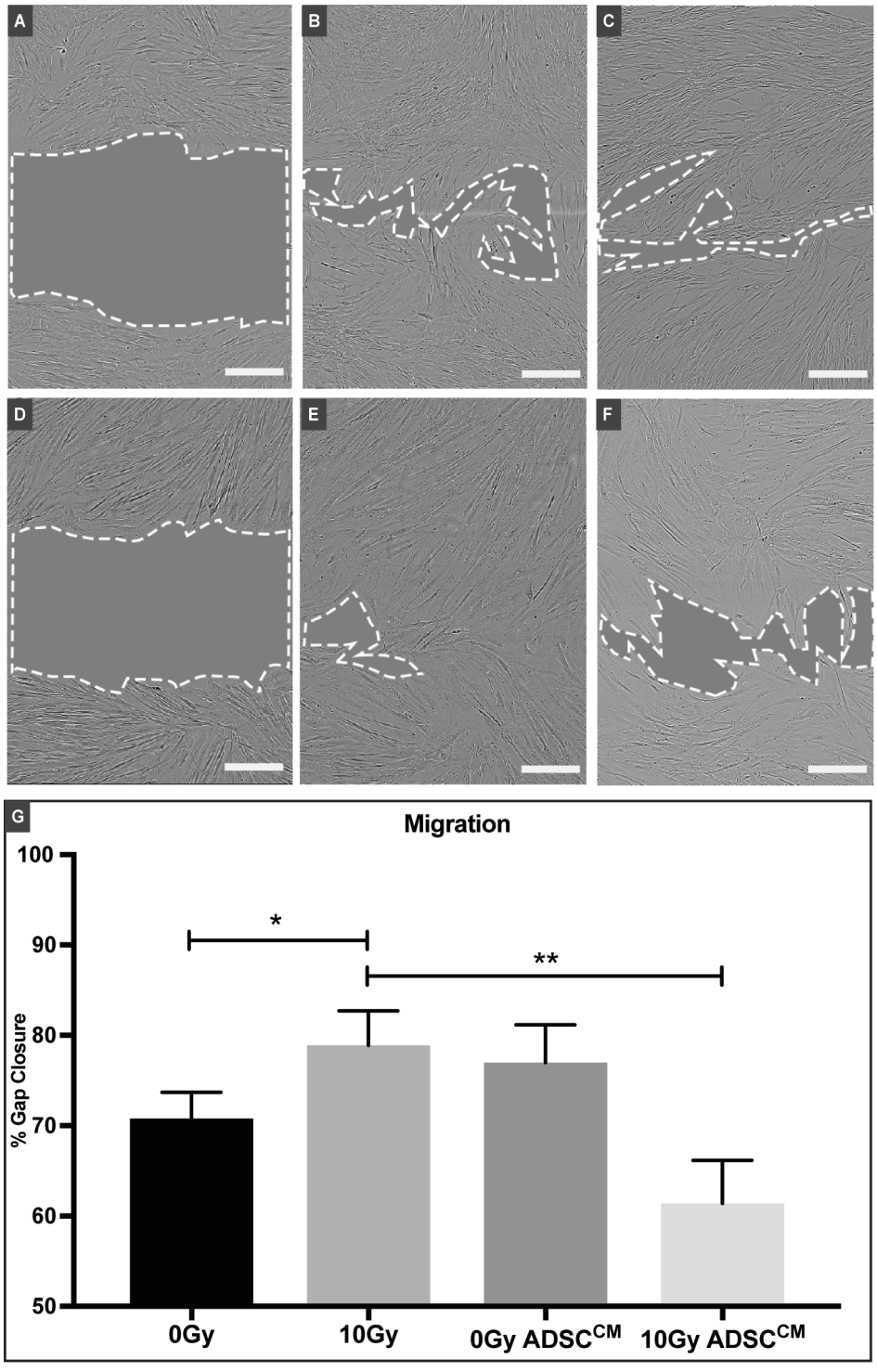
A
B
C
D
E
F
G
Migration
100
90
80
70
60
50
% Gap Closure
*
**
0Gy
10Gy
0Gy ADSC^CM
10Gy ADSC^CM

Figure 52

Figure 52 ADSC^{CM} reverses the hypermigratory state of irradiated NHDF

x10 objective bright field imaging of NHDF was taken at 0 and 48 h post creation of the scratch wound on a confluent mono-layer of proliferating cells. (A) 0Gy NHDF scratch wound area at 0 h, (B) 0Gy NHDF in basal media (complete DMEM) scratch wound area at 48 h, (C) 0Gy NHDF in ADSC^{CM} scratch wound area at 48 h, (D) 10Gy NHDF scratch wound area at 0 h, (E) 10Gy NHDF in basal media (complete DMEM) scratch wound area at 48 h, (F) 10Gy NHDF in ADSC^{CM} scratch wound area at 48 h. (G) Quantification and analyses of the % Gap closure at 48 h compared to 0 h controls demonstrating differences resulting from radiotherapy injury and treatment with ADSC^{CM} in a model of fat grafting. In (A-F); Scale Bar 300 μm, dotted white line represents periphery of scratch wound and grey shaded area represents scratch wound area. Asterisks above bar-graph indicate statistical significance (* = $p<0.05$, ** = $p<0.01$), error bars represent SEM, with $n\geq3$.

7.2.2 The effects of fat grafting on LEC

Validation of the therapeutic benefits of fat grafting (ADSC^{CM}) on irradiated NHDF, expanded the application of this model with the aims to explore the potential of salvaging the marked effect of radiotherapy injury on LECs.

7.2.2.1 Optimising ADSC^{CM} for use with LEC

ADSC^{CM} was generated by extraction of media from 80% confluent ADSCs after a 72-hour period of conditioning. Media was aspirated, centrifuged to remove cell debris and filtered prior to addition to other cell cultures in the application of the *in-vitro* model of fat grafting (see section 2.1.4 for detailed methodology). Standard media used for ADSC culture was determined to be complete DMEM, providing optimal cell growth conditions. However, to make this conditioned media compatible with other cell types, such as LECs, alternative media conditions were explored. Overall, it was found that LECs were optimally cultured in complete EGMV2, therefore ADSCs were cultured in a variety of media conditions to determine the effect the media composition had on baseline ADSC proliferation. The media conditions included: Complete DMEM, Serum Starved DMEM, Complete EGMV2 and Basal EGMV2 (devoid of additional lymphangiogenic growth factors) covering

the ideal compositions for ADSCs and LECs and their serum starved or growth factor reduced counterparts (see Table 7 for detailed media composition). ADSC proliferation in Complete DMEM, compared to Serum Starved DMEM, demonstrated a reduction of 42.9% (average luminescence values of 8310 ± 178.2 vs 4733 ± 88.22 respectively $p<0.01$), an effect likely due to the lack of 10% FCS in serum starved media. Complete EGMV2, on the other hand, increased ADSC proliferation (48.5% compared to Complete DMEM - average luminescence values of 11962 ± 379 vs 8310 ± 178.2 respectively $p<0.01$). This effect was attributable to the addition of lymphangiogenic growth factors, despite a lower FCS content. Lastly, Basal EGMV2 culture resulted in a 12.5% reduction in proliferation due to a 5% reduction in FCS content (average luminescence values were 7062 ± 194 vs, 8310 ± 178.2 respectively $p<0.01$ (Figure 53 A)). It was anticipated that the additional lymphangiogenic growth factors in Complete EGMV2 might alter the baseline function and paracrine secretome of ADSCs and therefore such an altered ADSC secretome may not be representative of the normal ADSCs from the fat used in the grafting model. In light of these experimental findings, Basal EGMV2 was selected to 'pre-condition' the ADSCs for the production of $ADSC^{CM}$ suitable for use with LECs in the fat grafting *in-vitro* assay panel. Basal EGMV2 was shown to exert minimal effects on ADSC proliferative rates in comparison with the ideal Complete DMEM culture medium.

To implement the model of fat grafting, baseline LEC functions in both Complete EGMV2 and Basal EGMV2 media conditions were established, the latter acting as the control group for fat grafting experiments. 0Gy LEC migration was reduced by from 78.1 ± 4.8 in Basal EGMV2 (Figure 53 Fiii) from 99.7 ± 0.27 % Complete EGMV2 (Figure 53 Fii) gap closure at 48 h (28.8% reduction, $p<0.01$). 10Gy LEC migration was reduced by 67% in Basal EGMV2 (Figure 53 Fvi) compared to Complete EGMV2 (Figure 53 Fv) (23.4 ± 5.13 vs 71.0 ± 4.0 % gap closure at 48 h respectively $p<0.01$). Irradiation of LECs resulted in a 22.8% reduction in migration compared to 0Gy controls in Complete EGMV2, however culture in Basal EGMV2 amplified this reduced migration to 70% $p<0.01$ (Figure 53 B). Additionally, to verify that LECs cultured in Basal EGMV2 continued to express key lymphatic molecular markers, ICC staining using D2-40 (Podoplanin) primary antibody and green fluorescent secondary antibody with DAPI nuclei staining was conducted as shown in Figure 53

Ei-iv. Using the tube formation assay, similar results to the alterations in migratory function were demonstrated in culture of 0Gy (Figure 53 Gii) and 10Gy (Figure 53 Giv) LECs in Basal EGMV2 compared to 0Gy (Figure 53 Gi) and 10Gy (Figure 53 Giii) LECs in Complete EGMV2 (see Figure 53 C, D). Basal EGMV2 culture in comparison to Complete EGMV2 culture resulted in a 39.1% reduction in branch formation of 0Gy LECs (24.6 ± 3.37 vs 40.4 ± 2.31 branches per x10 objective field at 48 h respectively $p<0.01$), 25.4% trend in reduction of branch formation of 10Gy LECs (13.1 ± 1.20 vs 9.75 ± 1.04 branches per x10 field at 48 h respectively), a 54% reduction of 0Gy LEC tube formation (1.22 ± 0.22 vs 0.56±0.17 tubes per x10 field at 48 h respectively $p<0.01$) and a 50% trend in reduction of 10Gy LEC tube formation (0.26 ± 0.08 vs 0.13 ± 0.05 tubes per x10 field at 48 h respectively).

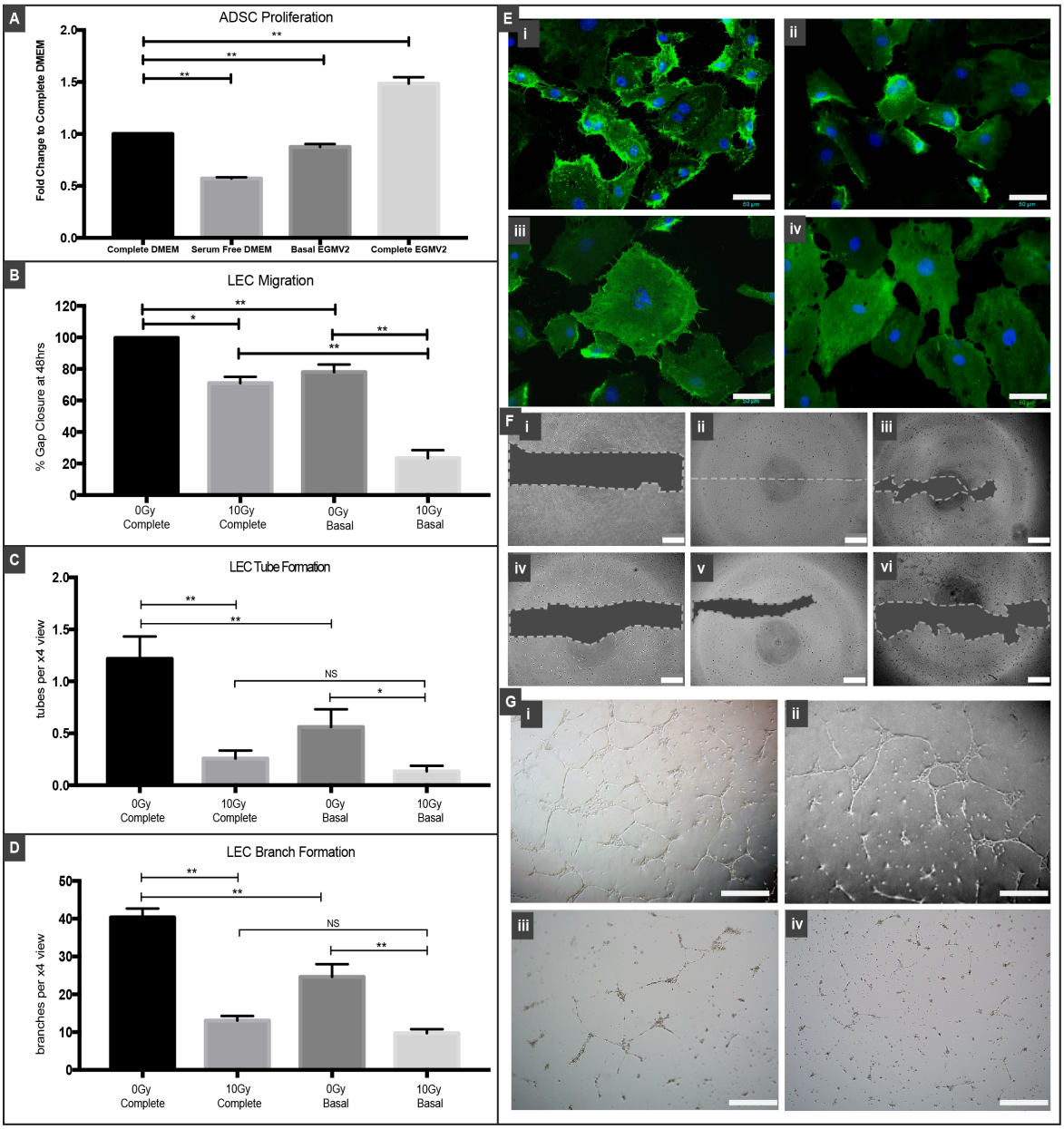
A
ADSC Proliferation
Fold Change to Complete DMEM
Complete DMEM
Serum Free DMEM
Basal EGMV2
Complete EGMV2
B
LEC Migration
% Gap Closure at 48hrs
0Gy Complete
10Gy Complete
0Gy Basal
10Gy Basal
C
LEC Tube Formation
tubes per x4 view
NS
D
LEC Branch Formation
branches per x4 view
E
F
G

Figure 53

Figure 53 Media optimization for LEC fat grafting experiments: The effect of differential media conditions on ADSCs and the effect of basal media on LECs

(A) Quantification of the effects of differential medial conditions on ADSC proliferation using CellTitre-Glo Luminescence (Promega, Germany) assay with results displayed as a fold change in relation to Complete DMEM media controls. Quantification of the effects of Complete EGMV2 media and Basal EGMV2 media on both 0Gy and 10Gy LEC functions of (B) Migration with % gap closure (C) Tube formation and (D) Branch formation at 48h. Immunocytochemistry at x20 objective of (Ei) 0Gy LECs in Complete EGMV2 (Eii) 0Gy LECs in Basal EGMV2, (Eiii) 10Gy LECs in Complete EGMV2, (Eiv) 10Gy LECs in Basal EGMV2 stained with D2-40 (Podoplanin) antibody, green fluorescent secondary antibody and DAPI. X4 objective bright field imaging of LECs were taken post the creation of a scratch wound on a confluent mono-layer of proliferating cells: (Fi) 0Gy LEC scratch wound area at 0 h, (Fii) 0Gy LECs scratch wound area at 48 h in complete EGMV2, (Fiii) 0Gy LEC scratch wound area of 48 h in basal EGMV2, (Fiv) 10Gy LECs scratch wound area at 0 h, (Fv) 10Gy LECs scratch wound area at 48 h in complete EGMV2, (Fvi) 10Gy LECs scratch wound area of 48 h in basal EGMV2. Bright field imaging of LECs seeded on GFR Matrigel photographed at x10 objective 48 h post-plating, with (Gi) 0Gy LECs in complete EGMV2 (Gii) 0Gy LECs in basal EGMV2 demonstrating a reduction in the latter group. (Giii) 10Gy LECs in complete EGMV2 (Giv) 10Gy LECs in basal EGMV2 displaying reduced tube formation in addition to an already disorganized structure compared to 0Gy counterparts. (Ei-iv); Scale Bar 50 μm, (Fi-vi) Scale Bar 200 μm, dotted line represents periphery of scratch wound and grey shaded area represents scratch wound area, (Gi-iv); Scale Bar 100 μm. Asterisks above bar-graphs indicate statistical significance (* = $p<0.05$, ** = $p<0.01$, NS = not significant), error bars represent SEM, with $n\geq3$.

7.2.3 Reversal of radiotherapy injury to LEC with ADSC conditioned media

Having established a baseline response of LECs subjected to radiotherapy injury and developed a model of fat grafting with media compatible to use with LECs, the established array of key LEC functional assays was repeated with the application of EGMV2-ADSC^{CM}. This fat grafting model used media extracted from ADSCs after 72 h of conditioning to produce EGMV2-ADSC^{CM} (see Table 7 for detailed composition). Hereafter, EGMV2-ADSC^{CM} will be referred to as ADSC^{CM}.

To ensure that both 0Gy and 10Gy LECs cultured in Basal EGMV2 and ADSC^{CM} continued to express key lymphatic molecular markers, immunocytochemistry staining using D2-40 (Podoplanin) primary antibody and green fluorescent secondary antibody with DAPI nuclei staining was conducted (Figure 54 A-C and F-H).

7.2.3.1 Proliferation

As established in section 5.2.1.2, radiotherapy injury results in diminished proliferative capacity of LECs, quantified using CellTiter-Glo (Promega, Germany) Luminescence assay. Specific to this experiment, where basal media conditions formed the control groups, irradiation of LECs resulted in a 27.8% reduction in proliferation, similar to complete media conditions (average luminescence results of 0Gy LECs 1112 ± 13.7 vs 10 Gy LECs 802.3 ± 39.69 $p<0.01$). Applying the model of fat grafting to both 0Gy and 10Gy LECs, the effects of ADSC^{CM} on LEC proliferation were further interrogated. Addition of ADSC^{CM} to healthy 0Gy LECs did not demonstrate a significant change in proliferative function with average luminescence values of 1112 ± 13.7 vs 1035 ± 8.177 respectively (Figure 54 D), likely a result of robust LEC proliferation in the setting of no radiotherapy injury. However, ADSC^{CM} did significantly increase the proliferation of 10Gy LECs by 10.3% $p<0.01$ (Figure 54 D), which partially restored the diminished proliferative potential of irradiated LECs, with average luminescence values of 802.3 ±3 9.69 vs 884.8 ± 14.4 respectively. This result demonstrates that ADSC^{CM} is able to exert a lymphangiogenic effect on irradiated LECs by partial salvage of their proliferative potential. However it is evident that this treatment alone is not able to fully restore proliferative capacity to that of 0Gy LECs.

7.2.3.2 Migration

It was established in section 5.2.1.4 that radiotherapy injury markedly reduces the migratory capacity of LECs in a two dimensional wound healing assay. The use of basal media conditions as the control group in the fat grafting experiments resulted in further reduction in migration of both 0Gy and 10Gy LECs when compared to complete media conditions (detailed in section 7.2.2.1), largely attributed to the lack of lymphangiogenic growth factors in basal growth medium. Radiotherapy of LECs resulted in reduced migration (Figure 54 G) with a difference of 54.7% in gap closure when compared to normal LEC controls (Figure 54 L) in basal media (23.4 ± 5.13% vs 78.1 ± 4.81% gap closure at 48 h $p<0.01$). The addition of $ADSC^{CM}$ demonstrated a pronounced lymphangiogenic stimulus on both 0Gy and 10Gy LEC migration (Figure 54 E). 0Gy LECs treated with $ADSC^{CM}$ (Figure 54 H) led to a 27.3% increase in percentage gap closure at 48 h compared to basal media controls (99.41 ± 0.39 vs 78.1 ± 4.81% respectively $p<0.01$). 10Gy LECs treated with $ADSC^{CM}$ (Figure 54 R) demonstrated a large increase in migratory capacity in the order of a 236.3% increase in comparison to the severely diminished migration of 10Gy LECs in basal media controls (78.69 ± 6.75 vs 23.4 ± 5.13% respectively $p<0.01$). The magnitude of increase in 10Gy LEC migration treated with $ADSC^{CM}$ restores the % gap closure to similar values to that of 0Gy basal controls. This is a key finding that highlights the potency of the lymphangiogenic stimulus of $ADSC^{CM}$ specifically targeting and salvaging the injurious effects of radiotherapy on LEC migration.

7.2.3.3 Tube Formation

As established in Section 5.2.1.4, radiotherapy significantly impairs the tube and branch forming capacity of LECs. The model of fat grafting was applied to the two dimensional tube formation assay to determine the potential for mitigating the injury, with aims to improve tube formation as a surrogate for functional lymphangiogenesis. Similar to the migration assay, $ADSC^{CM}$ demonstrated marked lymphangiogenic effect on both 0Gy and 10Gy tube (Figure 54 I) and branch formation (Figure 54 J) functions. 0Gy LEC tube formation at 48 h (Figure 54 M) was increased from 0.56 ± 0.17 tubes per x10 field in basal media to 1.53 ± 0.32 in $ADSC^{CM}$ $p<0.01$ (Figure 54 O). 0Gy LEC branch formation at 48 h was also increased from 24.6 ± 3.37 per x10 field in basal media to 42.0 ± 4.43 when treated with $ADSC^{CM}$ $p<0.01$. 10Gy LEC

tube formation at 48 h (Figure 54 S) was increased from 0.13 ± 0.05 tubes per x10 field in basal media to 0.93 ± 0.14 in $ADSC^{CM}$ $p<0.01$ (Figure 54 T). 10Gy LEC branch formation at 48 h was also increased from 9.75 ± 1.04 per x10 field in basal media to 15.2 ± 1.28 when treated with $ADSC^{CM}$ $p<0.01$. While the results above indicate the ability of $ADSC^{CM}$ to aid in lymphangiogenic processes in healthy normal LEC, the effects on 10Gy LEC additionally demonstrate a salvage of functions diminished by radiotherapy injury.

Collectively, the assays presented in this section demonstrate that $ADSC^{CM}$ has the capability to aid or restore the cellular functions of LECs that are critical to lymphangiogenesis and therefore tissue regeneration, even in nutritionally depleted LEC populations. In particular, irradiated LEC proliferation was enhanced and processes vital to lymphangiogenesis such as LEC migration, tube and branch formation were also salvaged from the damaged state inflicted by radiotherapy injury. This *in-vitro* data provides a proof of principle that $ADSC^{CM}$ is able to mitigate radiotherapy induced LEC injury, which requires correlation with *in-vivo* studies.

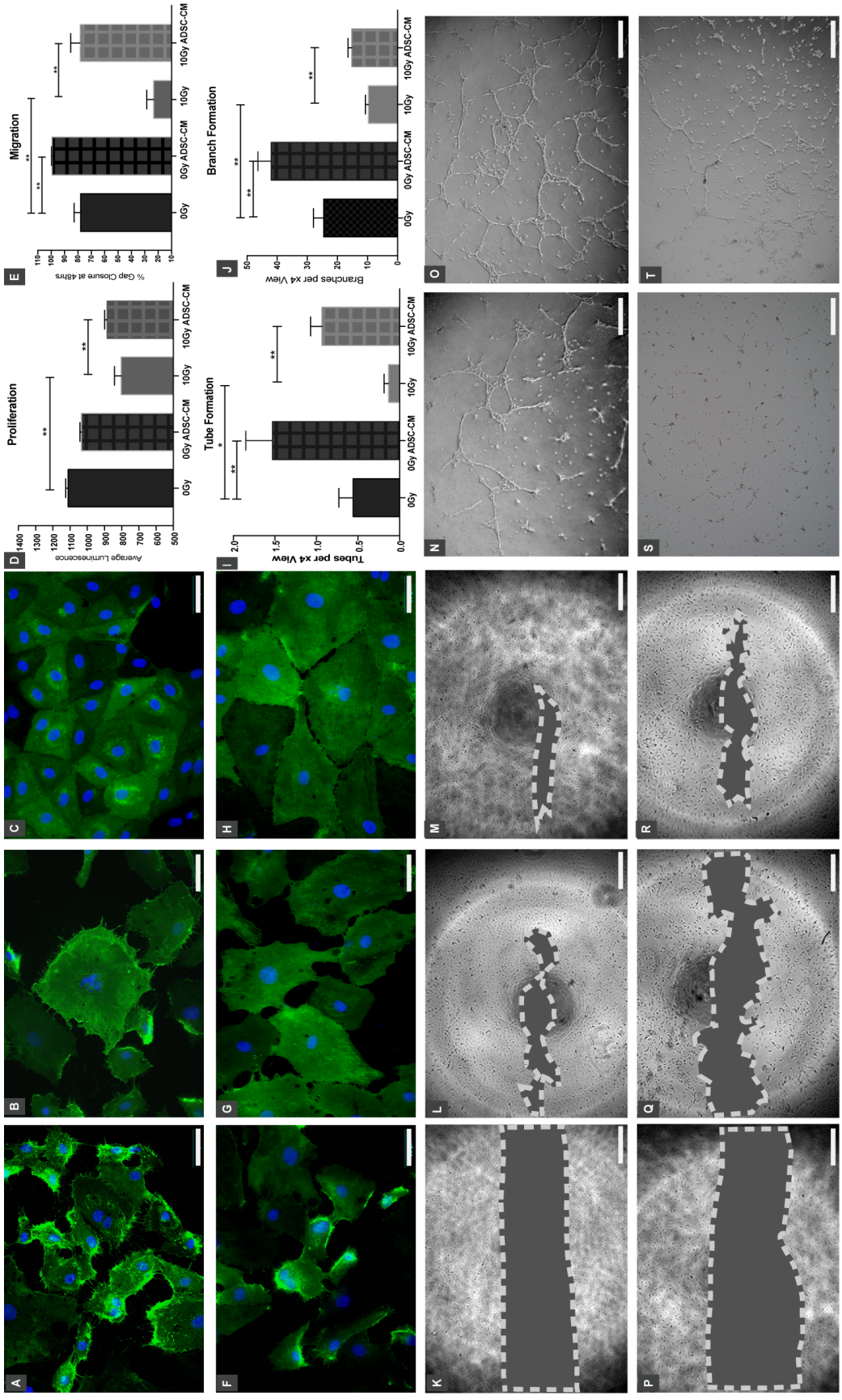
A
B
C
D
Proliferation
Average Luminescence
1400
1300
1200
1100
1000
900
800
700
600
500
0Gy
0Gy ADSC-CM
10Gy
10Gy ADSC-CM
**
**
E
Migration
% Gap Closure at 48hrs
110
100
90
80
70
60
50
40
30
20
10
0Gy
0Gy ADSC-CM
10Gy
10Gy ADSC-CM
**
**
**
F
G
H
I
Tube Formation
Tubes per x4 View
2.0
1.5
1.0
0.5
0.0
0Gy
0Gy ADSC-CM
10Gy
10Gy ADSC-CM
*
**
**
J
Branch Formation
Branches per x4 View
50
40
30
20
10
0
0Gy
0Gy ADSC-CM
10Gy
10Gy ADSC-CM
**
**
**
K
L
M
N
O
P
Q
R
S
T

Figure 54

Figure 54 ADSC^{CM} reverses the effects of radiotherapy induced injury to LECs
Immunocytochemistry at x20 objective of LEC stained with D2-40 (Podoplanin) antibody, green fluorescent secondary antibody and DAPI confirming that key expression of podoplanin is retained with both radiation and alteration of media conditions; (A) 0Gy LEC in complete EGMV2, (B) 0Gy LEC in basal EGMV2, (C) 0Gy LEC in ADSC^{CM}, (F) 10Gy LEC in complete EGMV2, (G) 10Gy LEC in basal EGMV2, (H) 10Gy LEC in ADSC^{CM}. (D) Treatment of 0Gy and 10Gy LEC with ADSC^{CM} demonstrated a small but significant increase in proliferation of 10Gy LEC quantified with CellTiter-Glo (Promega) Luminescence assays. (E) Similarly, quantification of the % gap closure at 48 h demonstrated that treatment of both 0Gy and 10Gy cells with ADSC^{CM} significantly increased migration of these cells, in 0Gy cells promoting lymphangiogenic activity of LEC while in 10Gy cells salvaging the impaired migration of irradiated LEC. X4 objective bright field imaging of LEC were taken post the creation of a scratch wound on a confluent mono-layer of proliferating cells. (K) 0Gy LEC scratch wound area at 0 h, (L) 0Gy LEC scratch wound area at 48 h in basal EGMV2, (M) 0Gy LEC scratch wound area of 48 h in ADSC^{CM}, (P) 10Gy LEC scratch wound area at 0 h, (Q) 10Gy LEC scratch wound area at 48 h in basal EGMV2, (R) 10Gy LEC scratch wound area of 48 h in ADSC^{CM}. Bright field imaging of LEC seeded on GFR Matrigel photographed at x10 magnification 48 h post-plating, with (N) 0Gy LEC in basal EGMV2 (O) 0Gy LEC in ADSC^{CM} demonstrating a lymphangiogenic effect with increased tube and branch formation quantified with LVAP analysis on Image J in (I) and (J) respectively. (S) 10Gy LEC in basal EGMV2 vs (T) 10Gy LEC in ADSC^{CM} displaying some salvage of tube and branch formation quantified with LVAP analysis on ImageJ in (I) and (J) respectively. (A-C and F-H); scale bar 50 μm, (K-M and P-R); scale bar 200 μm - dotted line represents periphery of scratch wound and grey shaded area represents scratch wound area, (N,O,S,T); scale bar 100 μm. Asterisks above bar-graphs indicate statistical significance (* = $p<0.05$, ** = $p<0.01$), error bars represent SEM, with $n\geq3$.

7.2.4 The double hit – effects of irradiated ADSC^{CM} on NHDF and LEC

Chapter 6 demonstrates the significant impact of radiotherapy-induced injury on the homeostatic functions of ADSC. These findings must also be taken into consideration when exploring the therapeutic benefits of ADSC^{CM}. Normal tissues that are inevitably targeted in the process of tumour irradiation result in injury to each individual cell type that constitutes the skin and underlying subcutaneous tissue. The above results of this thesis have demonstrated that this damage leads to a significant impact on cellular functions, the effects of which also extend to cell-to-cell interactions. ADSC^{CM} demonstrated the ability to ameliorate radiotherapy induced damage in both NHDF and LEC, therefore the same model was applied to these cell types, using conditioned media from irradiated ADSC to simulate the irradiated microenvironment and a 'double hit' model of injury.

RTX- ADSC^{CM} was generated by extraction of media from 80% confluent ADSC, 48 h post irradiation and a further 72 h period of conditioning. Complete DMEM media was used for conditioning and NHDF experiments while basal EGMV2 was used for conditioning for LEC experiments. Otherwise identical in the processes followed to produce ADSC^{CM}; media was aspirated, centrifuged to remove cell debris and filtered prior to addition to NHDF or LEC in the application of the *in-vitro* model of irradiated ADSC fat grafting (see section 2.1.4 for detailed methodology).

7.2.4.1 The effect of RTX-ADSC^{CM} on NHDF

As established in sections 3.3.3 and 7.2.1, radiotherapy injury resulted in an increase in the migratory capacity of NHDF, which was moderated in the presence of ADSC^{CM}. In chapter 6, it was also determined that increased levels of CXCR7 produced as a result of irradiation of LEC, led to a blockade in SDF-1α mediated chemotaxis of healthy ADSC to the area of injury. Therefore, in the microenvironment of radiotherapy injured soft tissues, the tissue bed must rely upon the regenerative effects of local ADSC. Local ADSC however, have also been subjected to the effects of radiotherapy, and therefore this model attempted to establish the interactions of the irradiated ADSC^{CM} secretome with NHDF.

The addition of RTX- ADSC^{CM} to 0Gy NHDF (Figure 55 C) resulted in a significant increase of 18.5% gap closure at 48 h compared to basal media controls $p<0.05$ (Figure 55 B) (89.3 ± 1.1% vs 70.8 ± 4.7%, respectively). In contrast, the addition of RTX- ADSC^{CM} to 10Gy NHDF (Figure 55 F) did not result in a significant difference in migration of 10Gy NHDF in basal media controls (Figure 55 E) (85.8 ± 5.4% vs 78.9 ± 6.8% respectively). These findings suggest that irradiated ADSCs may secrete factors that are able to trigger a radiotherapy injury response in un-irradiated healthy NHDFs (Figure 55 G), by increasing their migratory potential and demonstrating similar trends in the already hyper migratory irradiated NHDF (although these results did not reach statistical significance). Overall, the increased migratory capacity of 0Gy NHDF in the presence of RTX-ADSC^{CM} may demonstrate a significant contribution to the development of clinical fibrosis and ongoing cellular dysfunction resulting from irradiation and the subsequent pathological cell-cell interactions.

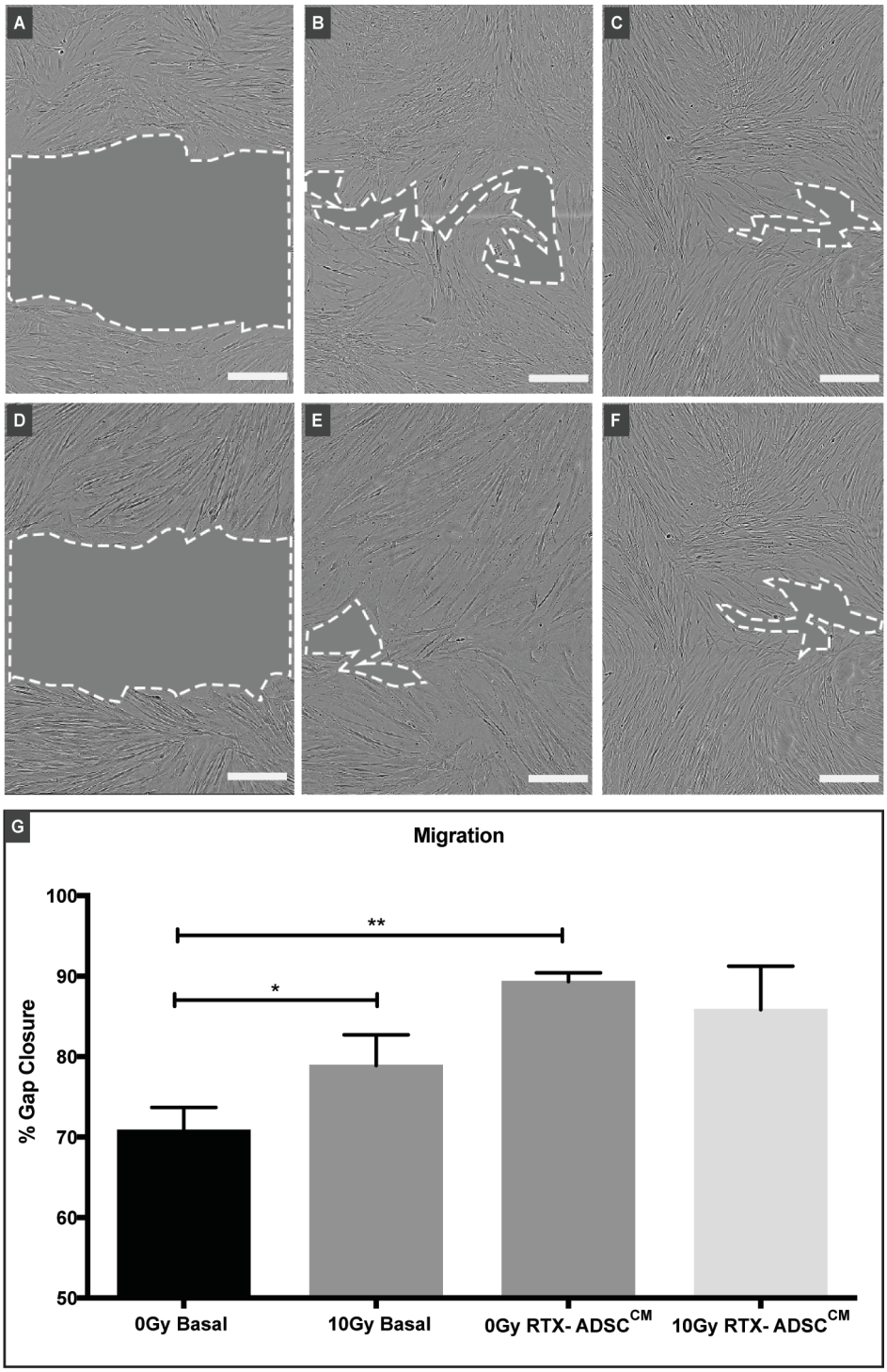
A
B
C
D
E
F
G
Migration
% Gap Closure
100
90
80
70
60
50
**
*
0Gy Basal
10Gy Basal
0Gy RTX- ADSC CM
10Gy RTX- ADSC CM

Figure 55

Figure 55 RTX-ADSC^{CM} induces a hypermigratory state in normal NHDF – the double hit injury

x 10 objective bright field imaging of NHDF taken at 0 and 48 h post creation of the scratch wound on a confluent mono-layer of proliferating cells. (A) 0Gy NHDF scratch wound area at 0 h, (B) 0Gy NHDF in basal media (complete DMEM) scratch wound area at 48 h, (C) 0Gy NHDF in RTX-ADSC^{CM} scratch wound area at 48 h, (D) 10Gy NHDF scratch wound area at 0 h, (E) 10Gy NHDF in basal media (complete DMEM) scratch wound area at 48 h, (F) 10Gy NHDF in RTX- ADSC^{CM} scratch wound area at 48 h. (G) Quantification and analyses of the % Gap closure at 48 h compared to 0 h controls demonstrating differences resulting from radiotherapy injury and treatment with RTX-ADSC^{CM} in a model representing fat grafting using irradiated ADSC. In (A-F); Scale Bar 300 μm, dotted white line represents periphery of scratch wound and grey shaded area represents scratch wound area. Asterisks above bar-graph indicate statistical significance (* = $p<0.05$, ** = $p<0.01$), error bars represent SEM, with $n\geq3$.

7.2.4.2 The effect of RTX-ADSC^{CM} on LEC

Having established a baseline response of LECs subjected to radiotherapy and the significant lymphangiogenic stimulus of ADSC^{CM}, it was sought to test the influence of irradiated ADSC^{CM} on LECs with treatment of conditioned media derived from RTX-ADSC. The established array of key LEC functional assays was repeated with the application of the irradiated fat grafting model using media extracted from RTX-ADSCs 48 h post irradiation, conditioned in basal EGMV2 for 72 h to produce RTX-EGMV2- ADSC^{CM} (see Table 7 for detailed composition). For the remainder of this chapter, RTX-EGMV2- ADSC^{CM} will be referred to as RTX- ADSC^{CM}.

To ensure that both 0Gy and 10Gy LEC cultured in Basal EGMV2 and RTX-ADSC^{CM} continued to express key lymphatic molecular markers, immunocytochemistry staining using D2-40 (Podoplanin) primary antibody and green fluorescent secondary antibody with DAPI nuclei staining was conducted to confirm this (Figure 56 A-C and F-H).

As established in section 5.2.1.2, radiotherapy injury results in diminished proliferative capacity of LEC, quantified using CellTiter-Glo (Promega, Germany) Luminescence assay. Specific to this experiment, where basal media conditions formed the control groups, treatment of 0Gy LEC with RTX- $ADSC^{CM}$ did not result in a significant change in the proliferation (Figure 56 D). However, addition of RTX-$ADSC^{CM}$ to 10Gy LEC resulted in a further 35.4% decrease in proliferation in comparison to 10Gy basal media controls, which represents proof of principle of the "double hit" hypothesis – worsening of radiotherapy induced injury with the addition of the RTX- $ADSC^{CM}$ secretome (average luminescence values of 517.8 ± 61.8 vs 802.3 ± 39.69 (Figure 56D) $p<0.01$).

Section 5.2.1.4 established that radiotherapy injury markedly reduces the migratory capacity of LECs in a two dimensional wound healing assay with significant lymphangiogenic stimulus exerted by the presence of $ADSC^{CM}$ when applied to both 0Gy and 10Gy LEC. The addition of RTX- $ADSC^{CM}$ demonstrated varying effects on both 0Gy and 10Gy LEC migration (Figure 56 E). 0Gy LEC treated with RTX-$ADSC^{CM}$ (Figure 56 M) led to a significant increase of 19.2% in percentage gap closure at 48 h compared to basal media controls (Figure 56 L) (97.29 ± 1.28 vs 78.1 ± 4.81% respectively $p<0.05$). 10Gy LEC treated with RTX- $ADSC^{CM}$ (Figure 56 R) demonstrated a further reduction in migratory capacity in the order of 98.2% compared to 10Gy LEC in basal media controls (Figure 56 Q) (0.41 ± 2.24 vs 23.4 ± 5.13% respectively $p<0.05$). The magnitude of the decrease in 10Gy LEC migration treated with RTX- $ADSC^{CM}$ demonstrates the potent effect of irradiated cell-cell interactions, further worsening the function of irradiated LEC in the presence of factors secreted by irradiated ADSC. This mechanism likely contributes to the poor lymphangiogenic potential of irradiated tissues and the resultant clinical lymphoedematous states.

Similar to the migratory functions of irradiated LEC, Section 5.2.1.4 determined that radiotherapy significantly impaired the tube and branch forming capacity of LEC while section 7.2.3.3 ascertained that $ADSC^{CM}$ was able to significantly salvage the injurious effects of radiotherapy on LEC tube and branch formation. The model of fat grafting with irradiated $ADSC^{CM}$ was applied to the two dimensional tube formation assay and demonstrated a trending anti-lymphangiogenic effect on 10Gy tube (Figure

56 I) and branch formation (Figure 56 J) functions. 0Gy LEC tube formation at 48 h was not significantly altered with the addition of RTX-ADSC^{CM} (Figure 56 N) compared to basal medial controls (Figure 56 O). 10Gy LEC tube formation demonstrated trends of decrease with the addition of RTX-ADSC^{CM} (Figure 56 T) compared to 10Gy basal media controls (Figure 56 S) (0.07 ± 0.04 vs 0.13 ± 0.05 tubes per x10 view at 48 h respectively), but did not reach statistical significance. 0Gy LEC branch formation with the addition of RTX-ADSC^{CM} was also not significantly altered. The parameters of branch formation with the addition of RTX-ADSC^{CM} again resulted in a trend of decreased branch formation compared to 10Gy basal media controls without reaching statistical significance (5.35 ± 2.24 vs 9.75 ± 1.04 branches per x10 view at 48 h respectively).

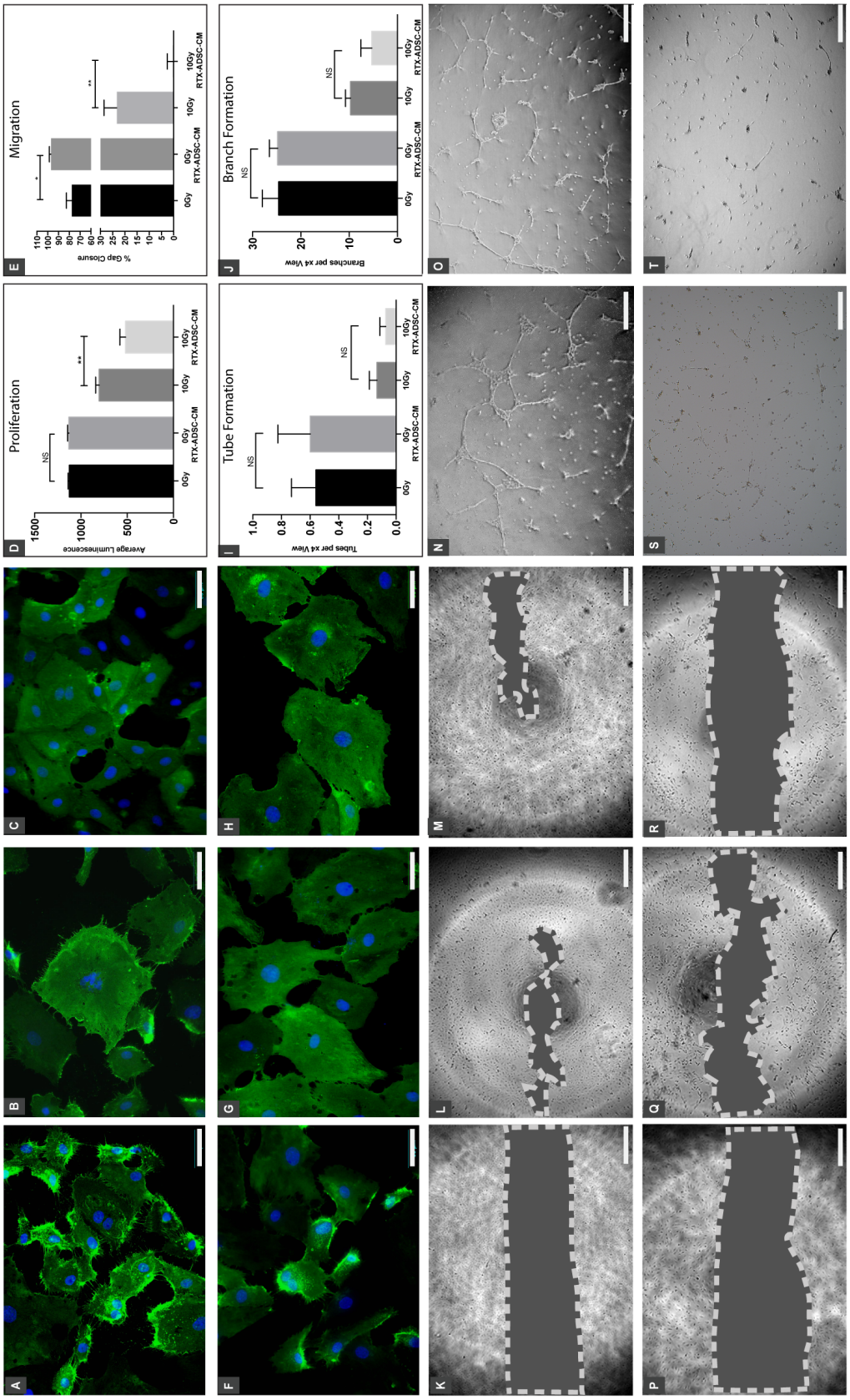
A
B
C
D
Proliferation
Average Luminescence
1500
1000
500
0
NS
**
0Gy
0Gy
RTX-ADSC-CM
10Gy
10Gy
RTX-ADSC-CM
E
Migration
% Gap Closure
110
100
90
80
70
60
30
25
20
15
10
5
0
*
**
0Gy
0Gy
RTX-ADSC-CM
10Gy
10Gy
RTX-ADSC-CM
F
G
H
I
Tube Formation
Tubes per x4 View
1.0
0.8
0.6
0.4
0.2
0.0
NS
NS
0Gy
0Gy
RTX-ADSC-CM
10Gy
10Gy
RTX-ADSC-CM
J
Branch Formation
Branches per x4 View
30
20
10
0
NS
NS
0Gy
0Gy
RTX-ADSC-CM
10Gy
10Gy
RTX-ADSC-CM
K
L
M
N
O
P
Q
R
S
T

Figure 56

Figure 56 RTX- ADSC^{CM} exacerbates the effects of radiotherapy in LECs – the double hit injury

Immunocytochemistry at x20 objective of LEC stained with D2-40 (Podoplanin) antibody, green fluorescent secondary antibody and DAPI confirming that key expression of podoplanin is retained with both radiation and alteration of media conditions; (A) 0Gy LEC in complete EGMV2, (B) 0Gy LEC in basal EGMV2, (C) 0Gy LEC in RTX-ADSC^{CM}, (F) 10Gy LEC in complete EGMV2, (G) 10Gy LEC in basal EGMV2, (H) 10Gy LEC in RTX-ADSC^{CM}. (D) Treatment of 0Gy and 10Gy LEC with RTX-ADSC^{CM} demonstrated a small but significant decrease in proliferation of 10Gy LEC quantified with CellTiter-Glo (Promega, Germany) Luminescence assays. (E) Similarly, quantification of the % gap closure at 48 h demonstrates that treatment of both 0Gy and 10Gy cells with RTX-ADSC^{CM} results in differential migration cells, increased in 0Gy LEC, while decreased with worsening injury of 10Gy LEC. x4 objective bright field imaging of LEC were taken post the creation of a scratch wound on a confluent mono-layer of proliferating cells. (K) 0Gy LEC scratch wound area at 0 h, (L) 0Gy LEC scratch wound area at 48 h in basal EGMV2, (M) 0Gy LEC scratch wound area of 48 h in RTX-ADSC^{CM}, (P) 10Gy LEC scratch wound area at 0 h, (Q) 10Gy LEC scratch wound area at 48 h in basal EGMV2, (R) 10Gy LEC scratch wound area of 48 h in RTX-ADSC^{CM}. Bright field imaging of LEC seeded on GFR Matrigel photographed at x10 objective 48 h post-plating, with (N) 0Gy LEC in basal EGMV2 vs (O) 0Gy LEC in RTX-ADSC^{CM} demonstrating no significant change in tube and branch formation quantified with LVAP analysis on ImageJ in (I) and (J) respectively. (S) 10Gy LEC in basal EGMV2 vs (T) 10Gy LEC in RTX-ADSC^{CM} display a trend of reduced tube and branch formation quantified with LVAP analysis on ImageJ in (I) and (J) respectively. (A-C and F-H); scale bar 50 μm, (K-M and P-R); scale bar 200 μm - dotted line represents periphery of scratch wound and grey shaded area represents scratch wound area, (N,O,S,T); scale bar 100 μm. Asterisks above bar-graphs indicate statistical significance (* = $p<0.05$, ** = $p<0.01$, NS = not significant), error bars represent SEM, with $n\geq3$.

7.2.5 ADSC^{CM} salvage of irradiated LEC - not primarily VEGFR-3 dependent

7.2.5.1 ADSC^{CM} ELISA for Lymphangiogenic factors

As determined in the assays in section 7.2.3, ADSC^{CM} was able to exert a strong lymphangiogenic effect on both 0Gy LEC and 10Gy LEC, with the latter resulting in partial reversal of irradiation injury. ADSC^{CM} was generated using the paracrine secretome of a heterogeneous group of cells that collectively constitute the stromal vascular fraction (see section 1.11.2), of which ADSC carry the regenerative potential. The model of fat grafting was designed based on the hypothesis that this complex array of secreted growth factors and cytokines would drive general and cell specific regeneration resulting from radiotherapy injury. With validation of this phenomenon in preceding sections, the subsequent investigations attempt to establish and characterize the components of ADSC^{CM}. Given the profound lymphangiogenic stimulus on LECs demonstrated using treatment with ADSC^{CM}, the initial experiments aimed to determine the presence and levels of traditional lymphangiogenic factors VEGF-C, VEGF-D and IL-8 protein, whilst simultaneously determining if these levels were altered as a result of irradiation of ADSC.

ADSC^{CM} and RTX- ADSC^{CM} were generated as described in section 2.1.4, after 72 h of conditioning in standard cell culture conditions. The media was extracted, processed and stored in -20^{o}C. Matched ADSC^{CM} and RTX-ADSC^{CM} samples were then tested for levels of VEGF-C, D and IL-8 using an ELISA assay, with quantities reported in pg/ml using a kit generated standard curve to extrapolate values based on absorbance spectrophotometry readings at 450-540 nm. ADSC^{CM} demonstrated an average of 2086 pg/ml of VEGF-C (0.46 ± 0.10 absorbance) compared to RTX-ADSC^{CM} where 775 pg/ml of VEGF-C was detected (0.23 ± 0.021 absorbance) (Figure 57 A). These findings demonstrated that while both media sets produced detectable levels of VEGF-C, the significantly reduced amount detected in RTX-ADSC^{CM} may reflect an impaired capacity of irradiated ADSC to provide lymphangiogenic stimulation to LEC in the surrounding tissue. VEGF-D in both ADSC^{CM} and RTX-ADSC^{CM} was detected at very nominal levels of 5.18 pg/ml (0.021 ± 0.002 absorbance) and 8.78 pg/ml (0.023 ± 0.002 absorbance) respectively

(Figure 57 B), with no statistically significant difference demonstrated between both groups. IL-8, a cytokine that has been demonstrated in LEC to be increased as a result of radiotherapy injury (see section 5.2.2.2) is also thought to possess some lymphangiogenic capabilities (340). However, IL-8 ELISA assays in both $ADSC^{CM}$ and $RTX\text{-}ADSC^{CM}$ demonstrated levels less than 40 pg/ml, not amenable to extrapolation on the standard curve due to the insignificant amounts with absorption spectrophotometry values of 0.11 ± 0.04 and 0.06 ± 0.004 respectively (Figure 57 C)

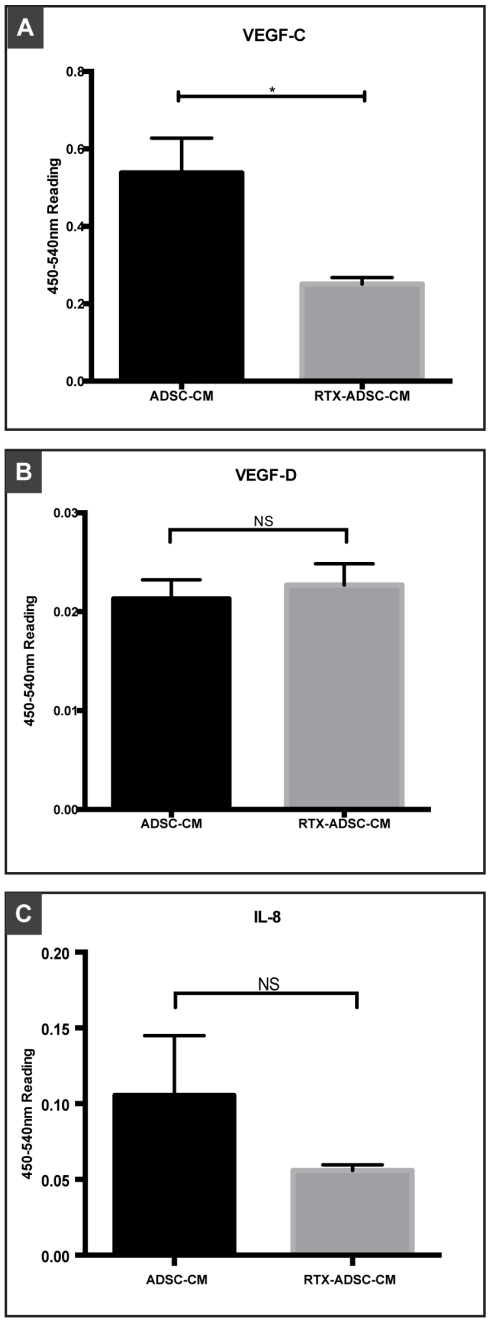

Figure 57

Figure 57 The lymphangiogenic secretome of ADSC and the effects of radiotherapy on production of VEGF-C, D and IL-8

ELISA assays testing for (A) VEGF-C, (B) VEGF-D and (C) IL-8 levels in $ADSC^{CM}$ and RTX-$ADSC^{CM}$. Results are represented as averages of absorbance photospectrometry readings at 450-540nm wavelength detection which were then extrapolated on the standard curve generated by protein standards to give a value in pg/ml if present at detectable levels. Asterisks above bar-graphs indicate statistical significance (* = $p<0.05$, NS = not significant), error bars represent SEM, with $n\geq3$.

7.2.5.2 VEGFR-3 activation

The ability of LECs to respond to VEGF-C or VEGF-D signaling pathways can be determined by the strength and capability of these growth factors to activate VEGFR-2 and VEGFR-3. Briefly, 48 h after radiotherapy treatment or control treatment, 0Gy and 10Gy LECs were stimulated for 10 min with control media, VEGF-C, VEGF-D, $ADSC^{CM}$ or RTX-$ADSC^{CM}$. Following stimulation, whole cell lysates were prepared and immunoprecipitated with VEGFR-2 and VEGFR-3 antibodies before SDS-PAGE and Western blotting. Blots were probed with antibodies to phosphotyrosine to compare the degree of phosphorylated (activated) VEGFR-2 or VEGFR-3 in both (Figure 58 A) 0Gy and (Figure 58 B) 10Gy LECs. These results demonstrated strong activation of VEGFR-2 in 0 Gy LECs in response to VEGF-C and VEGF-D stimulation with amelioration of activation in 10 Gy LECs. While, VEGFR-3 phosphorylation in 10 Gy LECs in response to VEGF-C and VEGF-D stimulation was detectable, it was significantly dampened in comparison to the activation induced in 0 Gy LECs. The intensities of VEGFR-2 and VEGFR-3 bands in 0 Gy and 10 Gy LECs in Western blots across titrations of 20 μg, 10 μg, 5 μg, 2.5 μg (Figure 58 C,D) were quantified by a ratio comparison to β-Actin loading controls by densitrometry analysis of bands on ImageJ (NIH) which demonstrated no significant differences between 0 Gy and 10 Gy LECs at each concentration. Similarly, RNA expression of VEGF Receptors (VEGFR2 and VEGFR3) on 0 Gy and 10 Gy LECs using a β-Actin housekeeping gene control did not demonstrate any significant differences in expression by PCR analysis (Figure 58 E). Lastly, $ADSC^{CM}$ and RTX-$ADSC^{CM}$ were tested using bio-assays to detect the ability of ligands in the conditioned media to bind, crosslink and activate the extracellular domains of VEGFR-2 and VEGFR-3. These assays were conducted using VEGFR-2/3-EpoR-Ba/F3 cell lines as per

methods described by Stacker et al. and Achen et al. (315) (490) and in section 2.4.7. Briefly, these bioassays used cell lines generated to express chimeric receptors composed of the human VEGFR-2 or VEGFR-3 extracellular domains along with mouse erythropoietin transmembrane and cytoplasmic domains (599). Ligand binding and cross-linking of these chimeric receptors facilitated survival and proliferation of these cells, which was quantified by the addition of ViaLight^{TM} cell viability reagent (Lonza, Switzerland) according to the manufacturers' protocols and read using a fluorescence plate reader. The results demonstrate weak but detectable levels of VEGFR-2 cross-linking in the presence of ADSC^{CM}, RTX-ADSC^{CM} and their diluted counterparts in comparison to the strong activation in response to VEGF-C and VEGF-D individually (Figure 58 F). Activation of VEGFR-3 (Figure 58 G) displayed similar results. Collectively these results strongly support the hypothesis that ADSC^{CM} mediated regenerative effects on LECs are not primarily driven by VEGF-C, VEGF-D, VEGFR-2 or -3 signaling.

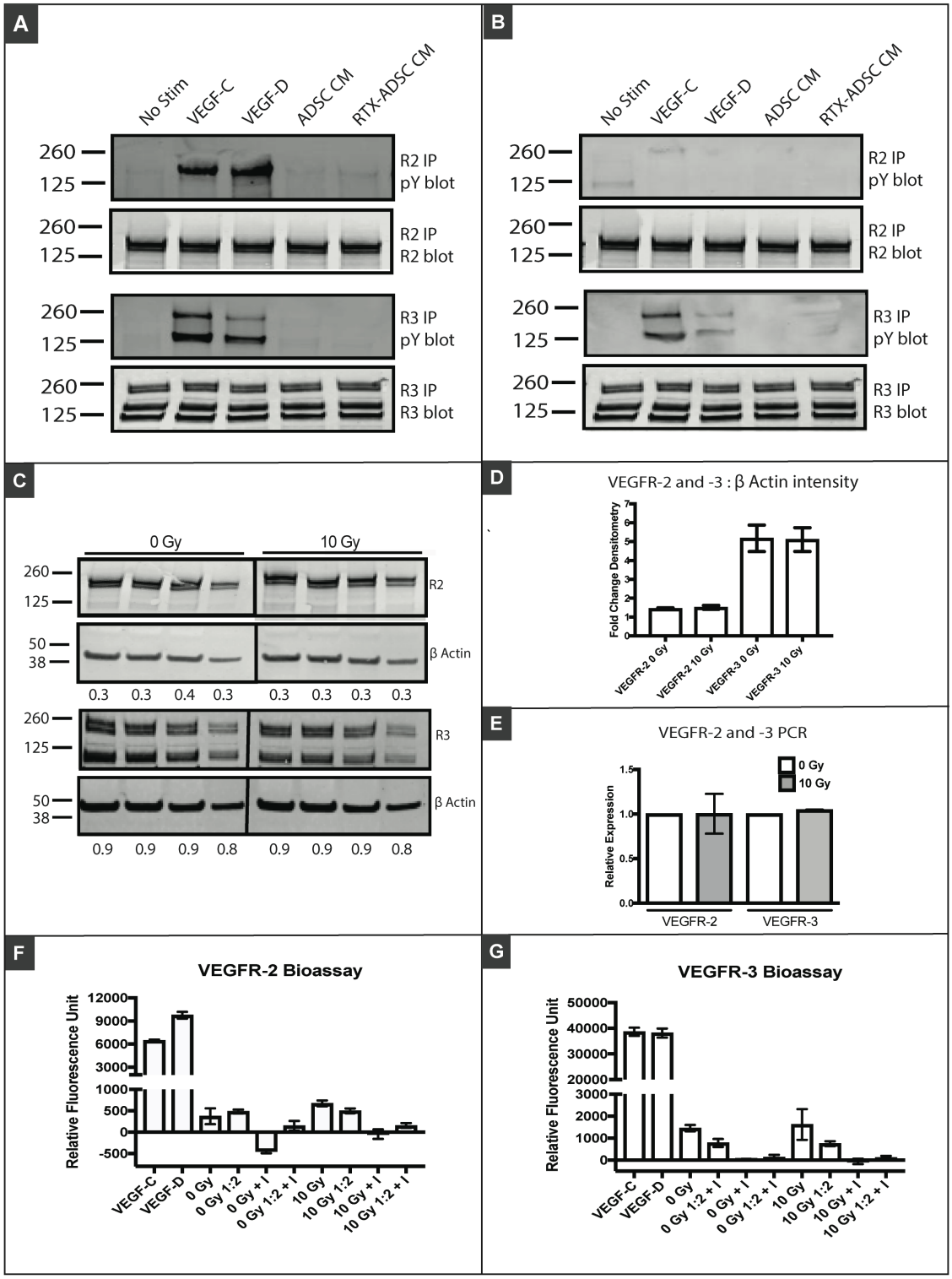
A
No Stim
VEGF-C
VEGF-D
ADSC CM
RTX-ADSC CM
260
125
R2 IP
pY blot
R2 IP
R2 blot
R3 IP
pY blot
R3 IP
R3 blot
B
C
0 Gy
10 Gy
R2
β Actin
50
38
0.3 0.3 0.4 0.3 0.3 0.3 0.3 0.3
R3
0.9 0.9 0.9 0.8 0.9 0.9 0.9 0.8
D
VEGFR-2 and -3 : β Actin intensity
Fold Change Densitometry
VEGFR-2 0 Gy
VEGFR-2 10 Gy
VEGFR-3 0 Gy
VEGFR-3 10 Gy
E
VEGFR-2 and -3 PCR
Relative Expression
VEGFR-2
VEGFR-3
F
VEGFR-2 Bioassay
Relative Fluorescence Unit
VEGF-C
VEGF-D
0 Gy
0 Gy 1:2
0 Gy + I
0 Gy 1:2 + I
10 Gy
10 Gy 1:2
10 Gy + I
10 Gy 1:2 + I
G
VEGFR-3 Bioassay

Figure 58

Figure 58 The effects of radiotherapy on LEC and ADSC^{CM}-mediated activation of VEGF-C/VEGF-D – VEGFR-2/VEGFR-3 signaling pathways

Activation of VEGFR-2 and VEGFR-3 on LEC by VEGF-C, VEGF-D, ADSC^{CM} and RTX-ADSC^{CM} with (A) depicting western blots from 0Gy LEC samples and (B) depicting blots from irradiated 10Gy LEC samples (molecular weights are depicted to the left of the blots). (C) Expression of VEGF Receptors (R2 and R3) on 0Gy and 10Gy LECs with β-Actin loading control. (D) Quantitation of bands determined by the ratio of total VEGFR-2 or VEGFR-3 band intensity : β-Actin loading control band intensity and is listed in text beneath the blots in (C). Molecular weights are depicted to the left of the blots. (E) Relative expression of VEGF receptors (R2 and R3) : β-Actin on 0Gy and 10Gy LEC as determined by qPCR. (F) VEGFR-2- EpoR-Ba/F3 and (G) VEGFR-3-EpoR-Ba/F3 bioassays showing cross-linking of VEGF receptors in response to VEGF-C, VEGF-D, ADSC^{CM} (0Gy) or RTX-ADSC^{CM} (10Gy). *I* indicates the presence of 1 g VGX300 inhibitor, *1:2* indicates a 1:2 dilution of conditioned media. *R2*: VEGFR-2, *R3*: VEGFR-3, *pY*: phosphotyrosine. Error bars represent SEM, with n≥3.

7.2.6 VEGF-C and VEGFR-3 trap – the effects on LEC

Due to the striking lymphangiogenic influence of ADSC^{CM} on both normal and irradiated LEC functions, we sought to uncover the mechanism by which the fat graft model exerted these effects. As demonstrated above, ADSC are able to produce functional levels of VEGF-C and to a lesser extent VEGF-D, detected in ADSC^{CM}. Additionally, both 0Gy and 10Gy LEC are able to express and activate VEGFR-3 mediated signaling in response to VEGF-C and VEGF-D stimulation, while stimulation with ADSC^{CM} and RTX-ADSC^{CM} did not lead to significant phosphorylation of VEGFR-3 mediated signaling. In addition to these findings it was deemed that 10Gy LEC (while responsive to VEGF-C and VEGF-D), demonstrate dampened activation of VEGFR-3. Subsequently, proof of principle experiments were designed to determine whether the lymphangiogenic stimulus of ADSC^{CM} was driven by VEGF-C/VEGF-D and the VEGFR-3 signaling pathway, by blocking components of this signaling axis with the use of monoclonal antibodies.

To determine if VEGF-C was the specific growth factor driving LEC regeneration mediated by $ADSC^{CM}$, VEGF-C neutralizing antibody; VGX100 (Circadian) was used. Subsequently the VEGFR-3-trap; VGX300 monoclonal antibody to VEGFR-3 (Circadian See section 2.4.1) was used to achieve universal blockade both of the major lymphangiogenic growth factors, VEGF-C and VEGF-D.

Previous sections demonstrated that 0Gy LEC proliferation in basal media was not significantly altered with treatment with $ADSC^{CM}$. In keeping with these findings, the addition of VGX100 and VGX300 did not significantly impact 0Gy LEC proliferation when compared to $ADSC^{CM}$ treated and control groups (Figure 59A). However, the lymphangiogenic effect of $ADSC^{CM}$ on 10Gy LEC demonstrated an increase in proliferation when compared to basal media controls (average luminescence values of 884.8 ± 14.4 vs 802.3 ± 39.7 respectively $p<0.05$). The addition of VGX100 and VGX300 to $ADSC^{CM}$ treated groups resulted in no significant difference in proliferative rates of 10Gy LEC when compared to the 10Gy-$ADSC^{CM}$ treated group (average luminescence values of 875.9 ± 28.3 and 847.3 ± 29.3 compared to 884.8 ± 14.4 respectively) (Figure 59 B). However, when comparing the proliferative rates of 10Gy LEC treated with VGX100 and VGX300 to 10Gy basal media controls, the groups demonstrated trends of increased proliferation that did not reach statistical significance. Collectively these findings demonstrate that 10Gy LEC proliferation is increased in the presence of $ADSC^{CM}$ and with anti-VEGF-C and anti-VEGFR-3 treatment in addition to $ADSC^{CM}$ treated LEC, the rates of proliferation were not significantly altered in comparison to the $ADSC^{CM}$ treatment alone.

The migratory function of both 0Gy and 10Gy LEC demonstrated a considerable lymphangiogenic response to treatment with $ADSC^{CM}$. To determine if VEGF-C or VEGFR-3 signaling played a role in the lymphangiogenic stimulus of $ADSC^{CM}$, VGX100 and VGX300 monoclonal antibody was added to the $ADSC^{CM}$ and migratory functions were mapped across 48 h using the established scratch wound model. 0Gy LEC migration was increased in the presence of $ADSC^{CM}$ and continued to demonstrate statistically significant increase in migratory rates with addition of VGX100 and VGX300 when compared to 0Gy basal media controls (% gap closure at 48 h of 0Gy LEC in basal media 69.7 ± 4.32, $ADSC^{CM}$ 93.7 ± 1.84, $ADSC^{CM}$ + VGX100 86.7 ± 5.5 and $ADSC^{CM}$ + VGX300 91.3 ± 2.01 $p<0.05$) as depicted in

Figure 59 C. 10Gy LEC migration assays interrogated with the same format as described above, demonstrated the same principles. Treatment of 10Gy LEC with $ADSC^{CM}$ results in an improvement in migration with a 38.5 ± 4.22 percentage gap closure at 48 h increased to 71.7 ± 5.93% $p<0.05$ (Figure 59 D). The addition of VGX100 and VGX300 to the $ADSC^{CM}$ treated groups resulted in a 66.0 ± 6.36% and 60.5 ± 7.03% gap closure at 48 h, which was not significantly different when compared to rates of 10Gy LEC treated with $ADSC^{CM}$ alone. Additionally, the regenerative benefit of improved 10Gy LEC migration rates in presence of $ADSC^{CM}$ were also not significantly changed as both VGX100 and VGX300 groups continued to demonstrate a beneficial increase in migration compared to 10Gy basal media controls (Figure 59 D). Taking these results into consideration, the addition of VGX100 and VGX300 did not significantly alter the lymphangiogenic effect on 0Gy and 10Gy LEC migration when compared to the $ADSC^{CM}$ treated groups, suggesting that VEGF-C and VEGFR-3 signaling are not the primary drivers of $ADSC^{CM}$'s lymphangiogenic effects.

The chemotactic effects of $ADSC^{CM}$ on both 0Gy and 10Gy LEC were established and demonstrated a 1.32 ± 0.10 and 1.56 ± 0.11 fold change when compared to basal media controls respectively (Figure 59 E,F**)**. As $ADSC^{CM}$ provided a strong chemotactic stimulus on both 0Gy and 10Gy LEC, the VEGF-C blockade using VGX100 and VEGFR-3 blockage using VGX300 was added to the bottom chamber of the boyden assay containing $ADSC^{CM}$. In 0Gy LEC the addition of VGX100 and VGX300 to $ADSC^{CM}$ resulted a 1.14 ± 0.06 and 1.16 ± 0.07 fold change compared to basal media controls. These results represented a trend of increased chemotaxis of 0Gy LEC compared to basal media controls, however the fold changes were also not significantly altered when compared to the $ADSC^{CM}$ treatment group alone (Figure 59 E). In 10Gy LEC the addition of VGX100 and VGX300 to $ADSC^{CM}$ resulted a 1.36 ± 0.06 and 1.40 ± 0.10 fold change compared to basal media controls. These results continued to represent an increased chemotaxis of 10Gy LEC compared to basal media controls $p<0.05$, while the fold change was not significantly altered in comparison to $ADSC^{CM}$ treatment group alone (Figure 59 F).

Therefore, these results demonstrate that treatment of 0Gy and 10Gy LECs with $ADSC^{CM}$/VGX100 (VEGF-C neutralizing antibody) and $ADSC^{CM}$/VGX300

(VEGFR-3-trap) did not significantly alter the functional responses of the two LEC populations to treatment with ADSC^{CM} alone.

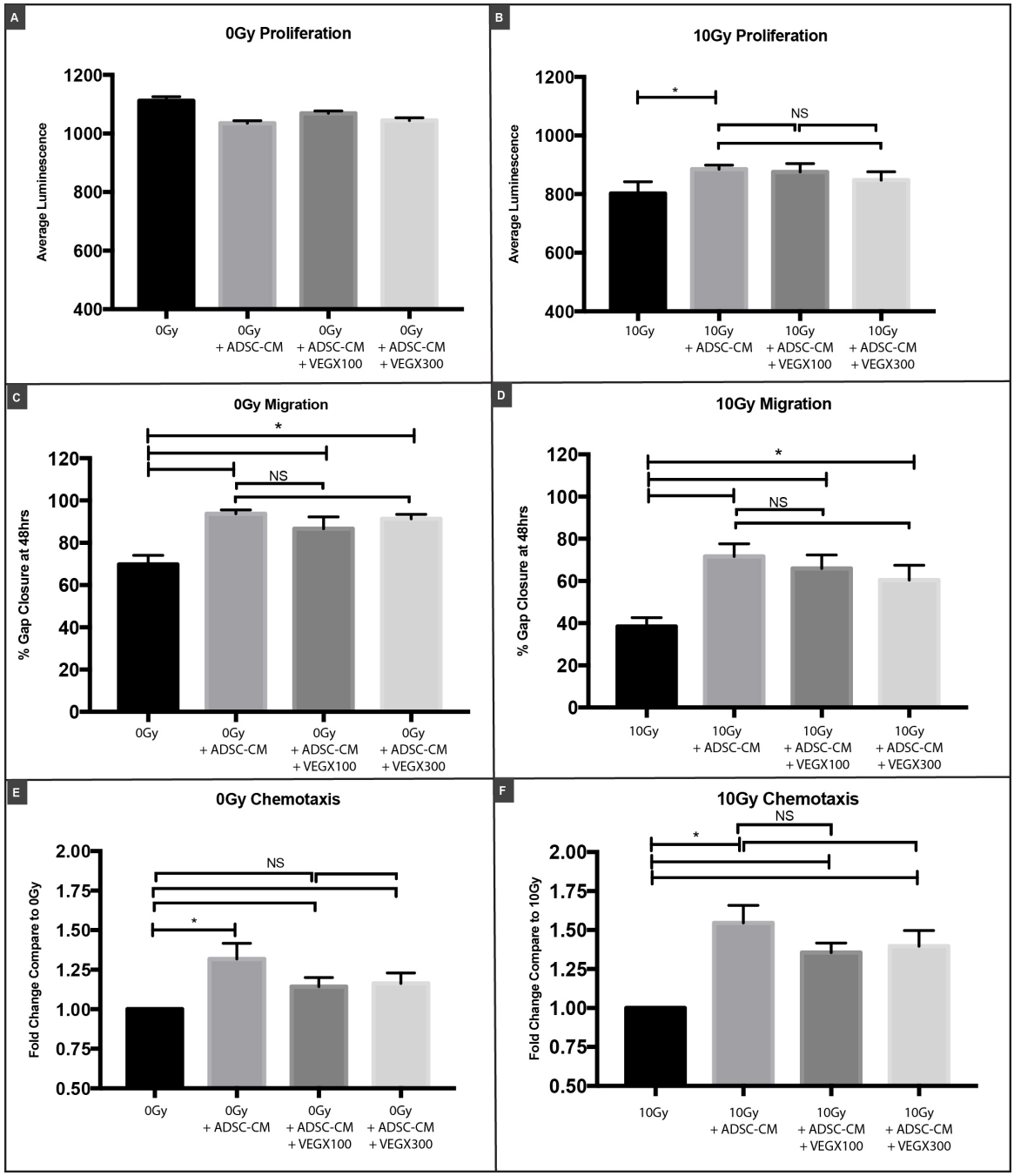

Figure 59

Figure 59 The application of a VEGFR-3 trap demonstrated the salvage effect of ADSC^{CM} is not primarily driven by VEGF-C/D mediated signaling.

Quantification of the effects of ADSC^{CM}, ADSC^{CM}/VGX100 and ADSC^{CM}/VGX300 on (A) 0Gy LEC proliferation and (B) 10Gy LEC proliferation tested utilizing the CellTiter-Glo (Promega, Germany) and average luminescence values. Migration assays were quantified by calculation of the % gap closure at 48 h in 0Gy (C) and 10Gy (D) LEC treated with ADSC^{CM}, ADSC^{CM}/VGX100 and ADSC^{CM}/VGX300 compared to basal media controls. Quantification of the chemotactic migration of 0Gy (E) and 10Gy (F) LEC in response to ADSC^{CM}, ADSC^{CM}/VGX100 and ADSC^{CM}/VGX300 gradients. Chemotaxis was quantified by fluorescence counts of DAPI positive cells on the underside of the boyden chamber membrane represented as fold changes compared to basal media controls. Asterisks above bar-graphs indicate statistical significance (* = $p<0.05$, NS = not significant), error bars represent SEM, with $n\geq3$.

7.2.7 Proteomic analysis of ADSC^{CM}-salvage of irradiated LEC

The results of this chapter have thus far determined that firstly, ADSC^{CM} is able exert a lymphangiogenic stimulus on 0Gy LEC functions while salvaging the homeostatic functions of 10Gy LEC compromised by radiotherapy injury. Secondly, ADSC^{CM} is able to produce functional VEGF-C and smaller amounts of VEGF-D, which are able to activate VEGFR-3 signaling when both 0Gy and 10Gy LEC are stimulated. Thirdly, the therapeutic effects of ADSC^{CM} on both 0Gy and 10Gy LEC are not primarily driven by VEGF-C or VEGFR-3 mediated signaling, as blockade of these pathways does not diminish the lymphangiogenic stimulus of ADSC^{CM}. Therefore, the mechanisms by which ADSC^{CM} exerts its potent therapeutic effects remains to be determined. To further investigate the composition of ADSC^{CM}, which is likely a heterogeneous mixture of cytokines and growth factors secreted by ADSC in physiological conditions, the proteomics platform was utilized.

While cells require a certain level of supplementation with fetal calf serum and/or growth factors to optimize *in-vitro* cell proliferation, the presence of these proteins is

likely to mask detection of cell secreted growth factors in the conditioned media generated at 72 h. Taking this into consideration a pilot study was run to determine the proteomic content of ADSC^{CM} (ADSC conditioned in DMEM + 10% FCS + 5% penicillin/streptomycin) and compared to the detection of the proteasome generated from serum free ADSC^{CM} (ADSC conditioned in DMEM + 5% penicillin/streptomycin). Clear differences were observed in the proliferation of the cells over the 72 h of conditioning (not quantified), with light microscopy also demonstrating signs of cellular stress in the serum starved group (cellular swelling, formation of vacuoles and fatty change). The pilot proteomic analysis of ADSC^{CM} demonstrated the top 10 hits were all bovine proteins, which constituted about 72% of all identified peptides, while bovine serum albumin alone made up 45% of all identified peptides. This finding led to the conclusion that any potential proteins of interest, secreted by the human ADSC would likely be masked by the highly abundant bovine proteins in the fetal calf serum component of the media. Alternatively, analysis of the serum-free and starved ADSC^{CM} demonstrated that bovine proteins still represented about 50% of all identified peptides (likely present from ADSC cell growth expansion prior to conditioned media generation), but also demonstrated some human growth factors in the top hits. Of note; connective tissue growth factor, transforming growth factor beta inducing proteins, latent transforming growth factor binding protein, pigment epithelium derived factor and insulin like growth factor binding protein (data not shown). However, given the obvious physiological stress of culture in serum-starved media, ADSC would likely produce proteins in response to stress, which would represent a significantly different profile to those produced in their physiological state and accountable for the regenerative effects of ADSC^{CM}.

To further determine the mechanisms by which ADSC^{CM} specifically exerts a lymphangiogenic effect on irradiated LECs, EGMV2-ADSC^{CM} version of ADSC^{CM} was fractionated using ion exchange chromatography techniques (see 2.7.1 for detailed methodology). Each fraction of ADSC^{CM} was then tested utilizing the migration assay as a screening tool, testing the effects on 0Gy and 10Gy LEC migration (Figure 60 A and B respectively). Complete ADSC^{CM} was used as a positive control, basal media as the control and starvation media as the negative control (see section 2.1.2 for detailed media compositions). Fractions that demonstrated a trend for lymphangiogenic migratory stimulus on 0Gy LEC (Figure

60 A) or salvage of 10Gy LEC migration (Figure 60 B) i.e. fractions that increased the % gap closure at 48 h compared to basal media controls, were selected. 17 fractions with the most effective lymphangiogenic migratory stimulus then underwent further processing and mass spectrometry analysis to determine the proteomic contents (Figure 60 C) (see 2.7 for further details).

After obtaining the data read out determining the detected peptide sequences in each of the 17 chosen fractions; peptide sequence analysis, homology and identity scoring was employed to process the data to obtain an accurate representation of the proteasome of each fraction (data not shown). It is important to note that while these 17 fractions demonstrated beneficial effects on LEC migration compared to basal media controls, none demonstrated as significant effect as complete $ADSC^{CM}$ did alone.

The proteins in the favourable fractions were listed and ranked according to frequency of detection across the chosen fractions. In conjunction, a literature search was conducted to determine if any of these listed proteins had demonstrated lymphangiogenic potential reported in other experimental models. This process however determined that many of the repeatedly detected proteins were likely novel proteins that had minimal reported lymphangiogenic effects in the literature. The top nine candidates were selected, with the tenth group representing a mixture of all nine candidates and their effect on LEC migration was further validated using the established 2-D scratch migration model.

The nine candidates chosen were alpha-2-macroglobulin (α2mac), inter-alpha-trypsin inhibitor heavy chain H2 (IAH2), Periostin, Gremlin, Lactoferrin, NOV, Serpin, SPARC (Osteonectin), Vitamin D binding protein (VitDBP), with the tenth group composed of a mixture of all nine candidates. Each protein candidate was tested using the scratch migration assay to determine its individual effect on 0Gy (Figure 60 D) and 10Gy (Figure 60 E) LEC migration, with basal media acting as a control and $ADSC^{CM}$ as the positive control. As hypothesized each single growth factor, and the mixture of all nine candidates was not significantly able to improve 0Gy or 10Gy LEC migration in comparison to basal media controls, while $ADSC^{CM}$ continued to significantly do so. Further investigation is likely required to optimize the

concentrations of these proteins and to repeat further assays to determine fully if they have any specific lymphangiogenic capacity. Alternatively, a single protein may not be able to salvage irradiated LEC function. Therefore, this finding may suggest that 'packaged' groups of protein products (exosomes) (see section 1.9.9) may be required to exert the total biological effects of the $ADSC^{CM}$. In order to analyse whether such factors were critical for ADSC restorative function, exosomes components of $ADSC^{CM}$ were investigated.

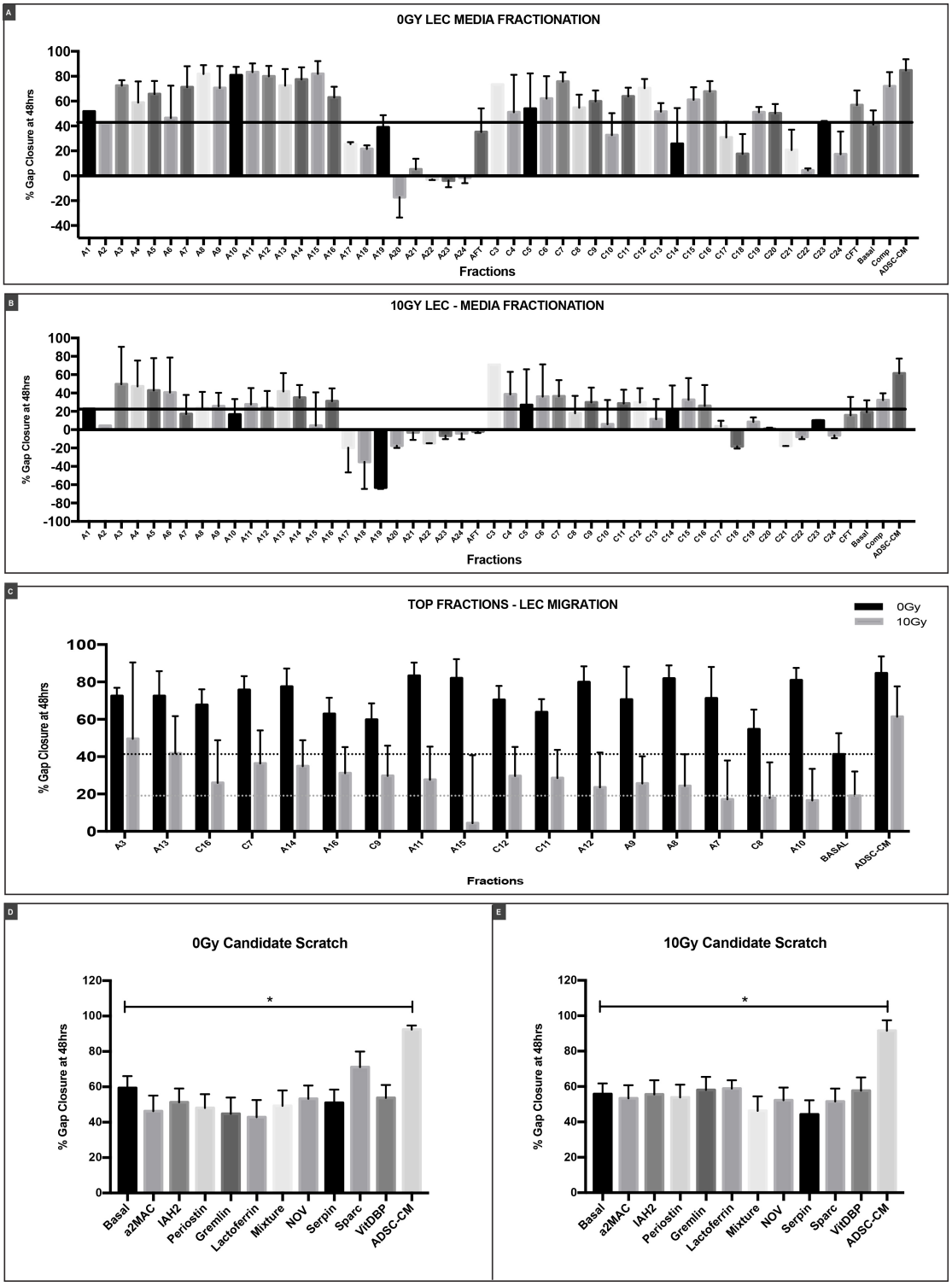
A
0GY LEC MEDIA FRACTIONATION
% Gap Closure at 48hrs
Fractions
B
10GY LEC - MEDIA FRACTIONATION
% Gap Closure at 48hrs
Fractions
C
TOP FRACTIONS - LEC MIGRATION
0Gy
10Gy
% Gap Closure at 48hrs
A3
A13
C16
C7
A14
A16
C9
A11
A15
C12
C11
A12
A9
A8
A7
C8
A10
BASAL
ADSC-CM
Fractions
D
0Gy Candidate Scratch
% Gap Closure at 48hrs
Basal
a2MAC
IAH2
Periostin
Gremlin
Lactoferrin
Mixture
NOV
Serpin
Sparc
VitDBP
ADSC-CM
E
10Gy Candidate Scratch
% Gap Closure at 48hrs
Basal
a2MAC
IAH2
Periostin
Gremlin
Lactoferrin
Mixture
NOV
Serpin
Sparc
VitDBP
ADSC-CM

Figure 60

Figure 60 ADSC^{CM} fractionation, protein candidate selection and the effects on LEC migration

Ion exchange fractionation techniques were employed to separate ADSC^{CM} using both "A" Anion and "C" Cation exchange chromatography with a graded salt buffer elution. (A) demonstrated the effect of each separate fraction on 0Gy LEC migration and (B) represented the same effects on 10Gy migration quantified as % gap closure at 48 h. The horizontal black line in (A) and (B) represents % gap closure of the basal media control. The most lymphangiogenic fractions across both 0Gy and 10Gy groups were selected to interrogate further with mass spectrometry and proteomic analysis (C), with the black and grey dotted line representing the % gap closure of basal media controls for 0Gy and 10Gy LEC respectively. Protein candidates of interest identified from the mass spectrometry data were then individually and in combination added to 0Gy (D) and 10Gy (E) LEC to determine their potential effects on migratory capacity. X- axis labels; A fractions = anion C fractions = cations, AFT = anion flow through, CFT = cation flow through, basal = 5% FCS + EMGV2, complete = growth factors + 5% FCS + EGMV2 and ADSC^{CM} = EGMV2 ADSC^{CM}. Asterisks above bar-graphs indicate statistical significance (* = $p<0.05$), error bars represent SEM, with $n\geq3$.

7.2.8 Exosome analysis of ADSC^{CM} and its effects on LEC

An alternative way to interrogate the therapeutic potential of ADSC^{CM} included utilizing further proteomics analysis in conjunction with exosome analysis. Samples of ADSC^{CM} and RTX-ADSC^{CM} preparations were generated for testing of the exosome component of these two variations of CM. Parallel experiments were designed to extract cell lysates from 0Gy LEC, 0Gy LEC treated with ADSC^{CM} and similarly 10Gy LEC and 10Gy LEC treated with ADSC^{CM} to determine the induction or repression of protein expression in each group. Preliminary data demonstrated key differences between the groups described above and generated early data to build a platform to further execute a thorough investigation of the exosomal component of ADSC^{CM} and its beneficial effects on LEC.

Briefly, exosome preparations of ADSC^{CM} and RTX-ADSC^{CM} were generated after standard production of these CM samples. Cell lysates were extracted from 0Gy and

10Gy LEC grown in basal media conditions as well as in the presence of $ADSC^{CM}$ treatment for 48 h. Samples underwent gel slice excision, processing; reduction, alkylation, trypsin digestion and peptide extraction after which they were analyzed using high performance liquid chromatography and mass spectrometry techniques. Label-free quantification (LFQ) was used for enrichment and annotation analysis and the detected peptide sequences were then searched using various databases for human proteins (Figure 61 A).

Analysis of the exosome contents of $ADSC^{CM}$ and RTX-$ADSC^{CM}$ identified 499 proteins in $ADSC^{CM}$ and 465 proteins in RTX-$ADSC^{CM}$, with a crossover of 380 proteins common to both media formulations (Figure 61 B). On further interrogation, 203 proteins were identified as unique, demonstrating a fold change greater than two that reached statistical significance ($p<0.05$). Of these 203 proteins 88 were shown to be upregulated in RTX-$ADSC^{CM}$ in comparison to $ADSC^{CM}$ and, when grouped using enrichment software analysis, pathways involving these proteins were represented by cell adhesion, response to organic substance, chromosome organisation, blood vessel development, extracellular matrix organisation, peptidase activity and kinase binding. The top 30 enriched proteins in RTX-$ADSC^{CM}$ are represented in Table 19. Conversely 115 proteins were significantly repressed in RTX-$ADSC^{CM}$ in comparison with $ADSC^{CM}$ i.e. are present in greater abundance in $ADSC^{CM}$ and may account for the therapeutic effects seen with LEC and NHDF treatment. The top 30 repressed proteins in RTX-$ADSC^{CM}$ are represented in Table 20 with enrichment of pathways such as calcium ion binding, RNA binding, carbohydrate binding, endopeptidase activity, enzyme inhibitor activity, antioxidant activity, peroxidase activity, regulation of cell death, response to organic substances, response to oxidative stress, cell redox homeostasis, membrane organisation and regulation of cellular protein metabolic processes.

Closer interrogation of LEC lysates, was conducted to determine the proteomic level alterations that result from radiotherapy injury and the salvage with addition of $ADSC^{CM}$. Mass spectrometry analysis demonstrated 63 proteins in 0Gy LEC, 200 proteins in 10Gy LEC were uniquely expressed with an additional 1503 proteins expressed in both 0Gy and 10Gy LEC (Figure 61 C). On further stringent analysis with pathway enrichment platforms, proteins that were significantly and differentially

expressed (with a fold change greater than 2) were analysed further. As depicted in Figure 61 F; 221 proteins were upregulated in 10Gy vs 0Gy LEC while 72 were significantly repressed. The figure also details the pathway analysis demonstrating clusters of functions associated with induced or repressed proteins, some which form interesting preliminary links that correlate with the functional data presented in previous chapters.

After establishing the baseline differences in between 10Gy and 0Gy LEC further analysis was done comparing 0Gy LEC + $ADSC^{CM}$ vs. 10Gy LEC + $ADSC^{CM}$ (Figure 61 D) and more importantly, to determine the therapeutics of $ADSC^{CM}$ in irradiated LEC was the analysis of 10Gy LEC + $ADSC^{CM}$ vs. 10Gy LEC (Figure 61 E). Initial analysis demonstrated 119 unique proteins expressed in 10Gy LEC, 303 in 10Gy LEC with $ADSC^{CM}$ treatment along with 1584 proteins common to both groups (Figure 61 E). With further detailed analysis it was determined that 139 proteins were induced in 10Gy LEC + $ADSC^{CM}$, while 351 were uniquely and significantly repressed in comparison to 10Gy LEC lysates (Figure 61 G) and as detailed within Figure 61 G the relevant functional pathways are also highlighted.

To answer the key question of how $ADSC^{CM}$ specifically reverses damage to 10Gy LEC, the data was sorted to identify proteins significantly upregulated in 10Gy LEC which were additionally significantly repressed with the addition of $ADSC^{CM}$. Concurrently the data was sorted to identify proteins significantly repressed in 10Gy LEC which were simultaneously induced with the addition of $ADSC^{CM}$. Table 21 clearly represents these results. This baseline information provides a solid foundation from which future experimentation should incorporate manipulation of the proteins listed in Table 21 while correlating these proteins with exosome analysis of proteins in $ADSC^{CM}$ (Table 19 and Table 20). Further *in-vitro* and *in-vivo* validation of selected proteins should be combined using bioinformatic analysis to tie together molecular, metabolomic and proteomic data established in this thesis to apply a holistic approach to determining the proven therapeutic mechanisms of $ADSC^{CM}$ on LEC.

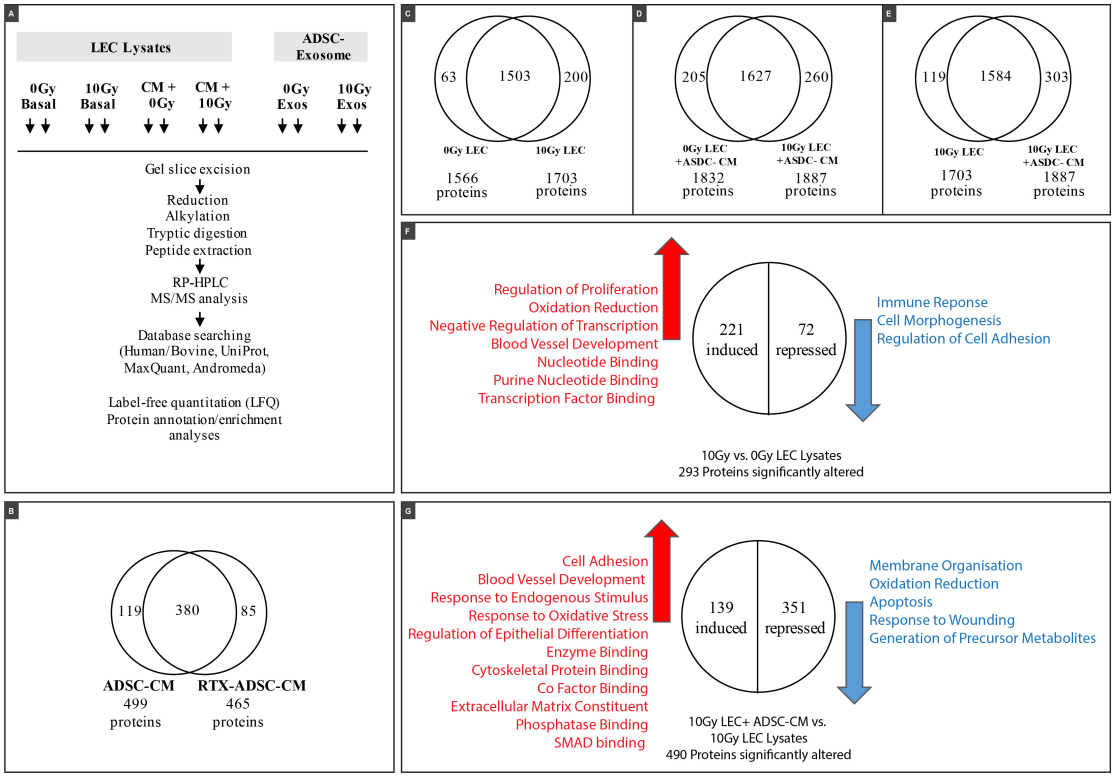

Figure 61

Figure 61 ADSC and LEC Exosome Analysis

Figure 61 (A) represents the work flow of sample processing to interrogate the exosome composition of ADSC^{CM} and RTX-ADSC^{CM} along with proteomic analysis of the effects of radiotherapy injury and ADSC^{CM} treatment on 0Gy and 10Gy LEC Lysates. Venn diagrams represent protein identification in the specified samples with unique proteins on the periphery and overlapped segments signifying proteins identified in both samples. In the case of (B) the Venn diagram identifies proteins detected in exosome extracts of ADSC^{CM} and RTX-ADSC^{CM}. Diagrams representing the number of proteins identified in (C) represent 0Gy LEC and 10Gy LEC lysates, (D) 0Gy LEC + ADSC^{CM} treatment and 10Gy LEC + ADSC^{CM} and (E) 10Gy LEC and 10Gy LEC + ADSC^{CM}. (F) and (G) represents a more rigorous analysis of proteins significantly enriched or suppressed (i.e. a fold change of >2 with a p value of <0.05). (F) represents 10Gy vs 0Gy LEC lysates determining the effects of radiotherapy injury on the proteasome of these cells, with enriched (red) or suppressed (blue) pathways generated from pathway analysis of the altered proteins. (G) demonstrates the potential therapeutic alterations resulting from ADSC^{CM} treatment of 10Gy LEC compared to 10Gy LEC lysates alone with enriched (red) or suppressed (blue) pathways generated from pathway analysis of the altered proteins.

Protein	Protein description	Gene name	Normalised LFQ Ratio[c]	
			10Gy / 0Gy	P-value
Q3T7B8	tRNA isopentenylpyrophosphate transferase isoform 5	TRIT1	5941000.5	3.79E-06
B4E3P2	cDNA FLJ60401, highly similar to PDZ domain-containing protein 2		1693400.5	1.83E-04
K7EK07	Histone H3 (Fragment)	H3F3B	1320550.5	6.65E-04
Q58EZ8	GEMIN5 protein (Fragment)	GEMIN5	1208750.5	1.24E-03
F8VZJ2	Nascent polypeptide-associated complex subunit alpha	NACA	1018580.0	2.10E-04
A4D110	Putative uncharacterised protein	LOC401309 tcag7.949	926235.0	4.44E-04
E1A689	Mutant Apo B 100		871650.5	5.54E-03
E9PSH3	Tetraspanin-4 (Fragment)	TSPAN4	736800.5	7.23E-03
B7Z478	Proteasome (Prosome, macropain) subunit, beta type, 2, isoform CRA_b (cDNA FLJ51890, highly similar to Proteasome subunit beta type 2 (EC 3.4.25.1))	PSMB2 hCG_1812781	695820.0	2.79E-03
P21964	Catechol O-methyltransferase (EC 2.1.1.6)	COMT	602250.0	3.88E-03
P02462	Collagen alpha-1(IV) chain [Cleaved into: Arresten]	COL4A1	470885.5	1.94E-02
V9HW29	Kinesin-like protein	HEL-S-61	466680.5	2.02E-02
P11233	Ras-related protein Ral-A	RALA RAL	454110.5	2.19E-02
G3V1B3	60S ribosomal protein L21 (Ribosomal protein L21, isoform CRA_f)	RPL21 hCG_2020044	446615.0	9.68E-03
X6R4N5	Erythroid membrane-associated protein	ERMAP	428470.5	2.49E-02
P17174	Aspartate aminotransferase, cytoplasmic (cAspAT) (EC 2.6.1.1) (EC 2.6.1.3) (Cysteine aminotransferase, cytoplasmic) (Cysteine transaminase, cytoplasmic) (cCAT) (Glutamate oxaloacetate transaminase 1) (Transaminase A)	GOT1	426265.5	2.53E-02
B5BUB1	RuvB-like 1 (Fragment)	RUVBL1	425020.0	1.19E-02
A0A0A1HAV9	H.sapiens ras-related Hrab4 protein		409660.5	2.45E-02
Q59EG0	Basement membrane-specific heparan sulfate proteoglycan core protein variant (Fragment)		401685.0	1.34E-02
Q6FIE9	TOLLIP protein (Toll interacting protein) (Toll interacting protein, isoform CRA_a) (cDNA, FLJ96670, Homo sapiens toll interacting protein (TOLLIP), mRNA)	TOLLIP hCG_40380	363230.0	1.41E-02
R4GNH3	26S protease regulatory subunit 6A	PSMC3	346265.5	2.86E-02
Q4LDE5	Sushi, von Willebrand factor type A, EGF and pentraxin domain-containing protein 1 (CCP module-containing protein 22) (Polydom) (Selectin-like osteoblast-derived protein) (SEL-OB) (Serologically defined breast cancer antigen NY-BR-38)	SVEP1 C9orf13 CCP22 SELOB	345315.0	1.47E-02
A4D275	Actin related protein 2/3 complex, subunit 1B, 41kDa (Actin related protein 2/3 complex, subunit 1B, 41kDa, isoform CRA_a) (cDNA, FLJ95695, Homo sapiens actin related protein 2/3 complex, subunit 1B, 41kDa(ARPC1B), mRNA)	ARPC1B hCG_19475 tcag7.662	344880.5	2.81E-02
B4E2L8	cDNA FLJ53487, highly similar to Coagulation factor XIII A chain (EC 2.3.2.13)		338020.5	2.86E-02
F5GYN4	Ubiquitin thioesterase OTUB1	OTUB1	337030.5	2.97E-02
Q5T7C4	High mobility group protein B1	HMGB1	332885.0	1.62E-02
Q9Y230	RuvB-like 2 (EC 3.6.4.12) (48 kDa TATA box-binding protein-interacting protein) (48 kDa TBP-interacting protein) (51 kDa erythrocyte	RUVBL2 INO80J TIP48	330415.5	3.02E-02

	cytosolic protein) (ECP-51) (INO80 complex subunit J) (Repressing pontin 52) (Reptin 52) (TIP49b) (TIP60-associated protein 54-beta) (TAP54-beta)	TIP49B CGI-46		
Q8N5I2	Arrestin domain-containing protein 1	ARRDC1	321140.5	3.17E-02
B4DLR3	cDNA FLJ54020, highly similar to Heterogeneous nuclear ribonucleoprotein U		317250.5	2.98E-02
A0A087X2D0	Serine/arginine-rich-splicing factor 3	SRSF3	311365.0	1.74E-02

Table 19 Top 30 proteins significantly upregulated in RTX-ADSC^{CM} in comparison to ADSC^{CM} exosomes

Protein	Protein description	Gene name	Normalised LFQ Ratio[c]	
			10Gy / 0Gy	P-value
A4D2G3	Olfactory receptor 2A25 (Olfactory receptor 2A27)	OR2A25 OR2A25P OR2A27	-15494500.5	5.74E-07
L0R5F6	Alternative protein TNS4	TNS4	-7255500.5	1.54E-06
Q6FGX3	RAB6A protein	RAB6A	-3477650.0	1.07E-11
L8E7D1	Alternative protein LY75	LY75	-2376400.5	1.06E-04
Q14432	cGMP-inhibited 3',5'-cyclic phosphodiesterase A (EC 3.1.4.17) (Cyclic GMP-inhibited phosphodiesterase A) (CGI-PDE A)	PDE3A	-2231300.5	9.64E-05
E7EVA0	Microtubule-associated protein	MAP4	-1696750.0	6.22E-07
P31151	Protein S100-A7 (Psoriasin) (S100 calcium-binding protein A7)	S100A7 PSOR1 S100A7C	-1193600.5	2.05E-03
P09382	Galectin-1 (Gal-1) (14 kDa laminin-binding protein) (HLBP14) (14 kDa lectin) (Beta-galactoside-binding lectin L-14-I) (Galaptin) (HBL) (HPL) (Lactose-binding lectin 1) (Lectin galactoside-binding soluble 1) (Putative MAPK-activating protein PM12) (S-Lac lectin 1)	LGALS1	-1042235.0	2.54E-04
H6VRG2	Keratin 1	KRT1	-1028100.5	3.63E-03
Q0QF37	Malate dehydrogenase (EC 1.1.1.37) (Fragment)	MDH2	-960030.0	6.43E-04
P04040	Catalase (EC 1.11.1.6)	CAT	-937685.0	6.85E-04
Q5HYG8	Serine hydroxymethyltransferase (EC 2.1.2.1)	DKFZp686P09201	-855460.0	1.24E-03
B4DWH0	cDNA FLJ55670, highly similar to EGF-containing fibulin-like extracellularmatrix protein 1		-834335.0	1.42E-03
P07384	Calpain-1 catalytic subunit (EC 3.4.22.52) (Calcium-activated neutral proteinase 1) (CANP 1) (Calpain mu-type) (Calpain-1 large subunit) (Cell proliferation-inducing gene 30 protein) (Micromolar-calpain) (muCANP)	CAPN1 CANPL1 PIG30	-800800.5	8.84E-03
X6RJP6	Transgelin-2 (Fragment)	TAGLN2	-782860.0	2.00E-03
V9HWG9	Epididymis secretory protein Li 21 (Glutathione S-transferase omega 1, isoform CRA_b)	HEL-S-21 GSTO1 hCG_21844	-747360.0	2.65E-03
F8VVM2	Phosphate carrier protein, mitochondrial	SLC25A3	-734630.0	2.81E-03
L8E983	Alternative protein LRP2	LRP2	-703000.5	1.11E-02
P46939	Utrophin (Dystrophin-related protein 1) (DRP-1)	UTRN DMDL DRP1	-657480.0	3.41E-03
Q6NUR7	Ezrin	EZR	-627150.5	1.34E-02
A0A024R3R5	Lamin B receptor, isoform CRA_a	LBR hCG_32785	-622600.5	1.13E-02

V9HW35	Epididymis secretory protein Li 55	HEL-S-55	-608400.5	1.40E-02
Q9H360	PRO1331 (cDNA, FLJ92443)		-595750.5	1.28E-02
B4DKB2	Endothelin-converting enzyme 1 (cDNA FLJ59212, highly similar to Endothelin-converting enzyme 1 (EC 3.4.24.71))	ECE1	-588400.5	1.60E-02
P28370	Probable global transcription activator SNF2L1 (EC 3.6.4.-) (ATP-dependent helicase SMARCA1) (Nucleosome-remodeling factor subunit SNF2L) (SWI/SNF-related matrix-associated actin-dependent regulator of chromatin subfamily A member 1)	SMARCA1 SNF2L SNF2L1	-586650.5	1.32E-02
E9PIR7	Thioredoxin reductase 1, cytoplasmic	TXNRD1	-582600.5	1.60E-02
A0A024R0V4	Vasodilator-stimulated phosphoprotein, isoform CRA_a	VASP hCG_20727	-540605.0	7.70E-03
J3KTA4	Probable ATP-dependent RNA helicase DDX5	DDX5	-521700.5	1.69E-02
Q9HDC9	Adipocyte plasma membrane-associated protein (Protein BSCv)	APMAP C20orf3 UNQ1869/ PRO4305	-508395.0	8.53E-03
Q5T1H1	Protein eyes shut homolog (Epidermal growth factor-like protein 10) (EGF-like protein 10) (Epidermal growth factor-like protein 11) (EGF-like protein 11) (Protein spacemaker homolog)	EYS C6orf178 C6orf179 C6orf180 EGFL10 EGFL11 SPAM UNQ9424/ PRO34591	-490995.5	2.35E-02

Table 20 Top 30 proteins significantly down regulated in RTX-ADSC^{CM} in comparison to ADSC^{CM} exosomes

Increased in 10Gy LEC and Decreased in 10Gy LEC + ADSC^{CM}		
Q96N83	Podocalyxin (Podocalyxin-like protein 1)	PODXL
F2Z2V0	Copine-1 (Fragment)	CPNE1
P98160	Basement membrane-specific heparan sulfate proteoglycan core protein	HSPG2
B4DLR8	NAD(P)H dehydrogenase [quinone] 1 (cDNA FLJ50573, highly similar to Homo sapiens NAD(P)H dehydrogenase, quinone 1 (NQO1), transcript variant 3, mRNA)	NQO1
E7EWC2	Ras GTPase-activating-like protein IQGAP2 (Fragment)	IQGAP2
B4DSV5	DNA helicase (EC 3.6.4.12)	
A6H592	MHC class I antigen (Fragment)	HLA-A
E1Y6U0	MHC class I antigen (Fragment)	HLA-B
A0A0D9SFI6	Four and a half LIM domains protein 1 (Fragment)	FHL1
G1ENK8	MHC class I antigen (Fragment)	HLA-B
V9HW21	Epididymis luminal protein 76	HEL-76
A0A024R407	Microtubule-associated protein	MAP2 hCG_1776452
W6CHX3	MHC class I antigen (Fragment)	
I4AY87	Macrophage migration inhibitory factor (Fragment)	MIF
B4DPC0	cDNA FLJ52713, moderately similar to Mus musculus leucine rich repeat (in FLII) interacting protein 1 (Lrrfip1), mRNA	
Q86W20	Protease serine 1 (EC 3.4.21.4) (Fragment)	PRSS1
Q6ZMY0	cDNA FLJ16598 fis, clone TESTI4006473, weakly similar to ATP-dependent RNA helicase A	
A8K132	cDNA FLJ75476, highly similar to Homo sapiens glutaminase (GLS), mRNA	

Q53FG5	Minichromosome maintenance deficient protein 5 variant (Fragment)	
R4QU15	MHC class I antigen (Fragment)	HLA-A
A0A024R5W4	HCG40688, isoform CRA_a	hCG_40688
H7C3D2	LIM and cysteine-rich domains protein 1	LMCD1
A6NML8	Diaphanous homolog 2 (Drosophila), isoform CRA_c (Protein diaphanous homolog 2)	DIAPH2 hCG_1811114
A8K7N0	cDNA FLJ75556, highly similar to Homo sapiens ribosomal protein L14, mRNA	
Q9NQC3	Reticulon-4 (Foocen) (Neurite outgrowth inhibitor) (Nogo protein) (Neuroendocrine-specific protein) (NSP) (Neuroendocrine-specific protein C homolog) (RTN-x) (Reticulon-5)	RTN4 KIAA0886 NOGO My043 SP1507
Q658Z6	Putative uncharacterised protein DKFZp451J085	DKFZp451J085
H0YLP6	60S ribosomal protein L28	RPL28
E9PP23	Lysosomal acid phosphatase (Fragment)	ACP2
A2A3R5	40S ribosomal protein S6	RPS6 hCG_1741512
A1L3A9	TBC1 domain family, member 9B (With GRAM domain)	TBC1D9B
K7EN45	Peptidyl-prolyl cis-trans isomerase NIMA-interacting 1 (Fragment)	PIN1
Q8TCU6	Phosphatidylinositol 3,4,5-trisphosphate-dependent Rac exchanger 1 protein (P-Rex1) (PtdIns(3,4,5)-dependent Rac exchanger 1)	PREX1 KIAA1415
L0R5C7	Alternative protein SCP2	SCP2
Q3B874	STRN protein (Fragment)	STRN
E5RJP2	Vinexin (Fragment)	SORBS3
O95864	Fatty acid desaturase 2 (EC 1.14.19.3) (Acyl-CoA 6-desaturase) (Delta(6) fatty acid desaturase) (D6D) (Delta(6) desaturase) (Delta-6 desaturase)	FADS2
B8ZZB8	CB1 cannabinoid receptor-interacting protein 1	CNRIP1
P08754	Guanine nucleotide-binding protein G(k) subunit alpha (G(i) alpha-3)	GNAI3
C9J0E4	Cystatin-A	CSTA
G5EA09	Syndecan binding protein (Syntenin), isoform CRA_a (Syntenin-1)	SDCBP hCG_1787561
Q05CM9	PSIP1 protein (Fragment)	PSIP1
Q9P266	Junctional protein associated with coronary artery disease (JCAD)	KIAA1462 JCAD
B4DMR3	cDNA FLJ51896, highly similar to Glia-derived nexin	
Q5U091	Neuroblastoma RAS viral (V-ras) oncogene homolog (Neuroblastoma RAS viral (V-ras) oncogene homolog, isoform CRA_a)	NRAS hCG_38454
B2RD40	cDNA, FLJ96442, highly similar to Homo sapiens copine II (CPNE2), mRNA	
Q8TCS8	Polyribonucleotide nucleotidyltransferase 1, mitochondrial (EC 2.7.7.8) (3'-5' RNA exonuclease OLD35) (PNPase old-35) (Polynucleotide phosphorylase 1) (PNPase 1) (Polynucleotide phosphorylase-like protein)	PNPT1 PNPASE
A8HT81	Glutathione S-transferase M2 (Muscle) (Fragment)	GSTM2
B4DZ22	cDNA FLJ54042, highly similar to ATP-binding cassette sub-family D member 3	
Q9NX14	NADH dehydrogenase [ubiquinone] 1 beta subcomplex subunit 11, mitochondrial (Complex I-ESSS) (CI-ESSS) (NADH-ubiquinone oxidoreductase ESSS subunit) (Neuronal protein 17.3) (Np17.3) (p17.3)	NDUFB11 UNQ111/PRO1064
G5E9E7	Tight junction protein 1 (Zona occludens 1), isoform CRA_e (Tight junction protein ZO-1)	TJP1 hCG_27621
H0YIQ2	YLP motif-containing protein 1 (Fragment)	YLPM1
A0A024R610	Neogenin homolog 1 (Chicken), isoform CRA_a	NEO1 hCG_2003750
A0A0E3DBZ6	MHC class I antigen (Fragment)	HLA-A
B4DNS2	cDNA FLJ51602, highly similar to Interferon-induced guanylate-binding protein 1	
B4DP97	cDNA FLJ52934, highly similar to Tyrosine-protein phosphatase non-receptortype substrate 1	

V9HWG1	Epididymis secretory sperm binding protein Li 134P	HEL-S-134P
C9JCX1	Muscleblind-like protein 1 (Fragment)	MBNL1
C9JAZ1	Metaxin-2 (Fragment)	MTX2
B3KWP7	cDNA FLJ43538 fis, clone PLACE7008431, highly similar to Homo sapiens phosphatidylinositol-4-phosphate 5-kinase, type II, gamma (PIP5K2C), mRNA	
A0A024RDA1	Exocyst complex component 1, isoform CRA_a	EXOC1 hCG_20601
F8VSC5	SCY1-like protein 2 (Fragment)	SCYL2
E7EVJ5	Cytoplasmic FMR1-interacting protein 2	CYFIP2
Q9P265	Disco-interacting protein 2 homolog B (DIP2 homolog B)	DIP2B KIAA1463
Q15645	Pachytene checkpoint protein 2 homolog (Human papillomavirus type 16 E1 protein-binding protein) (16E1-BP) (HPV16 E1 protein-binding protein) (Thyroid hormone receptor interactor 13) (Thyroid receptor-interacting protein 13) (TR-interacting protein 13) (TRIP-13)	TRIP13 PCH2
Q8WZ75	Roundabout homolog 4 (Magic roundabout)	ROBO4 UNQ421/PRO3674
H0Y764	Neurobeachin-like protein 2 (Fragment)	NBEAL2
H0YJW7	SRA stem-loop-interacting RNA-binding protein, mitochondrial (Fragment)	SLIRP
E3UPC4	MHC class I antigen	HLA-C
H7C048	SWI/SNF-related matrix-associated actin-dependent regulator of chromatin subfamily E member 1 (Fragment)	SMARCE1
A6NKT7	RanBP2-like and GRIP domain-containing protein 3	RGPD3 RGP3
J3KTG2	Pre-mRNA-splicing factor ATP-dependent RNA helicase PRP16 (Fragment)	DHX38
B4DFP5	cDNA FLJ57484, highly similar to Hepatocyte growth factor-regulated tyrosine kinase substrate	
Q53H87	Formyltetrahydrofolate dehydrogenase isoform a variant (Fragment)	
A8K2E3	cDNA FLJ77491, highly similar to Homo sapiens leptin receptor (LEPR), transcript variant 2, mRNA	
E7EWK3	ATP-dependent RNA helicase DHX36 (Fragment)	DHX36
P55795	Heterogeneous nuclear ribonucleoprotein H2 (hnRNP H2) (FTP-3) (Heterogeneous nuclear ribonucleoprotein H') (hnRNP H') [Cleaved into: Heterogeneous nuclear ribonucleoprotein H2, N-terminally processed]	HNRNPH2 FTP3 HNRPH2
Q96AB6	Protein N-terminal asparagine amidohydrolase (EC 3.5.1.-) (Protein NH2-terminal asparagine amidohydrolase) (PNAA) (Protein NH2-terminal asparagine deamidase) (PNAD) (Protein N-terminal Asn amidase) (Protein N-terminal asparagine amidase) (Protein NTN-amidase)	NTAN1
A6H8X9	Centrosomal protein 170kDa	CEP170
Q9UBV8	Peflin (PEF protein with a long N-terminal hydrophobic domain) (Penta-EF hand domain-containing protein 1)	PEF1 ABP32 UNQ1845/PRO3573
B4DHP4	cDNA FLJ59688, highly similar to Cob(I)yrinic acid a,c-diamideadenosyltransferase, mitochondrial (EC2.5.1.17)	
Q8WUT1	POLDIP3 protein (Polymerase delta-interacting protein 3)	POLDIP3
P80723	Brain acid soluble protein 1 (22 kDa neuronal tissue-enriched acidic protein) (Neuronal axonal membrane protein NAP-22)	BASP1 NAP22
Q02413	Desmoglein-1 (Cadherin family member 4) (Desmosomal glycoprotein 1) (DG1) (DGI) (Pemphigus foliaceus antigen)	DSG1 CDHF4
Q32MZ4	Leucine-rich repeat flightless-interacting protein 1 (LRR FLII-interacting protein 1) (GC-binding factor 2) (TAR RNA-interacting protein)	LRRFIP1 GCF2 TRIP
Q68DI5	Putative uncharacterised protein DKFZp781H1425	DKFZp781H1425
H3BUM8	Ubiquitin domain-containing protein UBFD1	UBFD1
K7ELA4	Chromobox protein homolog 1	CBX1
Q4LDX3	Tyrosine-protein kinase (EC 2.7.10.2)	JAK1
Q8TDW0	Volume-regulated anion channel subunit LRRC8C (Factor for adipocyte differentiation 158) (Leucine-rich repeat-containing protein 8C)	LRRC8C AD158 FAD158

Q6NUR1	Non-SMC condensin I complex, subunit G	NCAPG
F5H702	39S ribosomal protein L48, mitochondrial	MRPL48
H0Y6I0	Golgin subfamily A member 4 (Fragment)	GOLGA4
A0A024R3V8	Translin-associated factor X, isoform CRA_c	TSNAX hCG_14691
B3KS18	cDNA FLJ35285 fis, clone PROST2008079, highly similar to Golgi phosphoprotein 3	
B4DTK0	cDNA FLJ50669, highly similar to Squalene synthetase (EC 2.5.1.21)	
Decreased in 10Gy LEC and increased with 10Gy LEC + ADSC^{CM}		
B2RCE6	cDNA, FLJ96027, highly similar to Homo sapiens reversion-inducing-cysteine-rich protein with kazal motifs (RECK), mRNA	
V9H0D5	MSH2 protein	MSH2
B3KVN0	cDNA FLJ16785 fis, clone NT2RI2015342, highly similar to Solute carrier family 2, facilitated glucose transporter member 1	
B3KSG0	cDNA FLJ36142 fis, clone TESTI2025006, highly similar to Homo sapiens myo-inositol 1-phosphate synthase A1 (ISYNA1), mRNA	
B7Z2V7	cDNA FLJ54602, highly similar to Syntaxin-binding protein 1	
I3RW89	MHC class Ib antigen (Fragment)	HLA-E
P15289	Arylsulfatase A (ASA) (EC 3.1.6.8) (Cerebroside-sulfatase) [Cleaved into: Arylsulfatase A component B; Arylsulfatase A component C]	ARSA
Q59G69	Glia maturation factor, beta variant (Fragment)	
Q9H3K6	BolA-like protein 2	BOLA2 BOLA2A My016; BOLA2B
Q9UNS2	COP9 signalosome complex subunit 3 (SGN3) (Signalosome subunit 3) (JAB1-containing signalosome subunit 3)	COPS3 CSN3
O94915	Protein furry homolog-like (ALL1-fused gene from chromosome 4p12 protein)	FRYL AF4P12 KIAA0826
Q8NBL9	cDNA PSEC0119 fis, clone PLACE1002376, highly similar to GPI transamidase component PIG-S	
B5FX47	Liver F protein (Fragment)	
Q8IZ83	Aldehyde dehydrogenase family 16 member A1	ALDH16A1
A0A087WZ13	Ribonucleoprotein PTB-binding 1	RAVER1
A0A024R4T4	Ubiquitin-conjugating enzyme E2M (UBC12 homolog, yeast), isoform CRA_a	UBE2M hCG_2045958
P27658	Collagen alpha-1(VIII) chain (Endothelial collagen) [Cleaved into: Vastatin]	COL8A1 C3orf7
Q13442	28 kDa heat- and acid-stable phosphoprotein (PDGF-associated protein) (PAP) (PDGFA-associated protein 1) (PAP1)	PDAP1 HASPP28
A0A024RDM2	Crystallin, lambda 1, isoform CRA_a	CRYL1 hCG_20495
B3KNE8	cDNA FLJ14470 fis, clone MAMMA1001008, highly similar to Beta-secretase 2 (EC 3.4.23.45)	
E9PEP6	Neuropilin-1	NRP1
B3KWS6	cDNA FLJ43731 fis, clone TESTI1000391, highly similar to Breast cancer anti-estrogen resistance protein 1	
P10909	Clusterin (Aging-associated gene 4 protein) (Apolipoprotein J) (Apo-J) (Complement cytolysis inhibitor) (CLI) (Complement-associated protein SP-40,40) (Ku70-binding protein 1) (NA1/NA2) (Testosterone-repressed prostate message 2) (TRPM-2) [Cleaved into: Clusterin beta chain (ApoJalpha) (Complement cytolysis inhibitor a chain); Clusterin alpha chain (ApoJbeta) (Complement cytolysis inhibitor b chain)]	CLU APOJ CLI KUB1 AAG4
Q10588	ADP-ribosyl cyclase/cyclic ADP-ribose hydrolase 2 (EC 3.2.2.6) (ADP-ribosyl cyclase 2) (Bone marrow stromal antigen 1) (BST-1) (Cyclic ADP-ribose hydrolase 2) (cADPr hydrolase 2) (CD antigen CD157)	BST1
A0A075B738	Platelet endothelial cell adhesion molecule	PECAM1
B2DFW8	MHC class I antigen (Fragment)	HLA-A

Table 21 Proteomic Analysis of 0Gy LEC, 10Gy LEC in basal conditions and ADSC^{CM} treatment.

Table 21 Proteomic Analysis was used to determine the expression of proteins that were significantly and differentially upregulated or suppressed in 10Gy LEC compared to 0Gy LEC, whose expression was subsequently significantly reversed with the addition of $ADSC^{CM}$. All proteins listed demonstrated a fold change of at least 2 in label-free quantitation intensity compared to their respective controls, with p values <0.05.

7.2.9 Therapuetics of threonine supplementation of ADSC

As determined in section 6.2.7, the ability of irradiated ADSC to uptake and/or utilize the essential amino acid threonine is significantly impaired when compared to un-irradiated and healthy counterparts. Immunocytochemical staining of 0Gy and 10Gy ADSC using a mitotracker staining demonstrated that 0Gy ADSC retain elongated and regular mitochondrial structure (Figure 62 N), while 10Gy ADSC appear to have a more fragmented structure (Figure 62 O) which could represent structural damage accounting for the functional impairments found in irradiated ADSC. The role of threonine in stem cell metabolism is scantly reported in the literature and is thought to play a role in energy production and influencing the 'stemness' of the cells themselves (600). However, this data is predominantly drawn from murine studies and the human pathways of threonine metabolism still remain largely unknown (593). To this effect, with the aims of reducing the impact of radiotherapy induced injury to ADSC, key functional assays of proliferation and adipogenic differentiation (both significantly impaired by irradiation), were repeated to assess the effects of threonine supplementation.

The concentration of threonine in DMEM (Lonza) used for culture of ADSC in standard conditions was 95.2 mg/ml. For the purpose of supplementation experiments this concentration was doubled with the addition of L-Threonine (Sigma Aldrich), to both DMEM and adipogenic differentiation media and then filter sterilised to produce threonine supplemented (T+) media. The addition of T+ media resulted in a 5.9% increase in proliferation of 0Gy ADSC, represented by a 1.06 ± 0.01 fold change compared to normal media controls $p<0.01$ (Figure 62 A), while it did not change the proliferation of 10Gy ADSC significantly (Figure 62 B) at 48 h. Supplementation of threonine to adipogenic media and analysis of differentiation at the 14 day timepoint

demonstrated improvement in the adipogenic yield of 0Gy ADSC (Figure 62 C) with a 43.4% increase (fold change of 1.43 ± 0.07 compared to normal media controls $p<0.01$) and 10Gy ADSC (Figure 62 D) with a 14.5% increase (fold change of 1.15 ± 0.05 compared to normal media controls $p<0.05$). To further determine whether this beneficial increase in adipogenesis in both 0Gy and 10Gy ADSC was a result of transcriptional alteration of traditional adipogenic genes, RT-PCR was conducted on RNA samples collected from differentiated cells on day 14. All results were represented as a fold change in comparison to 0Gy normal media controls. While radiotherapy injury appeared to significantly impair transcription of LPL, FABP4, CEBPb (as shown in section 6.2.3) there were no significant alterations in expression of LPL (Figure 62 I), FABP4 (Figure 62 J), PPARy (Figure 62 K), CEBPB (Figure 62 L) or Leptin (Figure 62 M) when comparing their expression between 0Gy and 0Gy T+ groups or 10Gy and 10GyT+ groups. Expression of 0Gy normal media controls, 0Gy T+ media, 10Gy normal media controls and 10Gy T+ media for the following genes were as follows LPL; 1 ± 0.05, 0.82 ± 0.1, 0.31 ± 0.09, 0.46 ±0 .07 (Figure 62 I), FABP4; 1 ± 0.06, 0.91 ± 0.06, 0.34 ± 0.09, 0.57 ± 0.09 (Figure 62 J), PPARy; 1 ± 0.06, 1 ± 0.12, 0.81 ± 0.17, 0.87 ± 0.13 (Figure 62 K), CEBPb; 1 ± 0.02, 0.97 ± 0.03, 0.38 ± 0.15, 0.42 ± 0.63 (Figure 62 L) and lastly Leptin; 1 ± 0.19, 0.96 ± 0.33, 2.1 ± 0.79, 2.58 ± 0.93 (Figure 62 M). Collectively, threonine supplementation was able to achieve an increase in 0Gy ADSC proliferation along with an improvement in both 0Gy and 10GY ADSC adipogenesis, which seems to act independent of regulation of traditional adipogenic transcription factors.

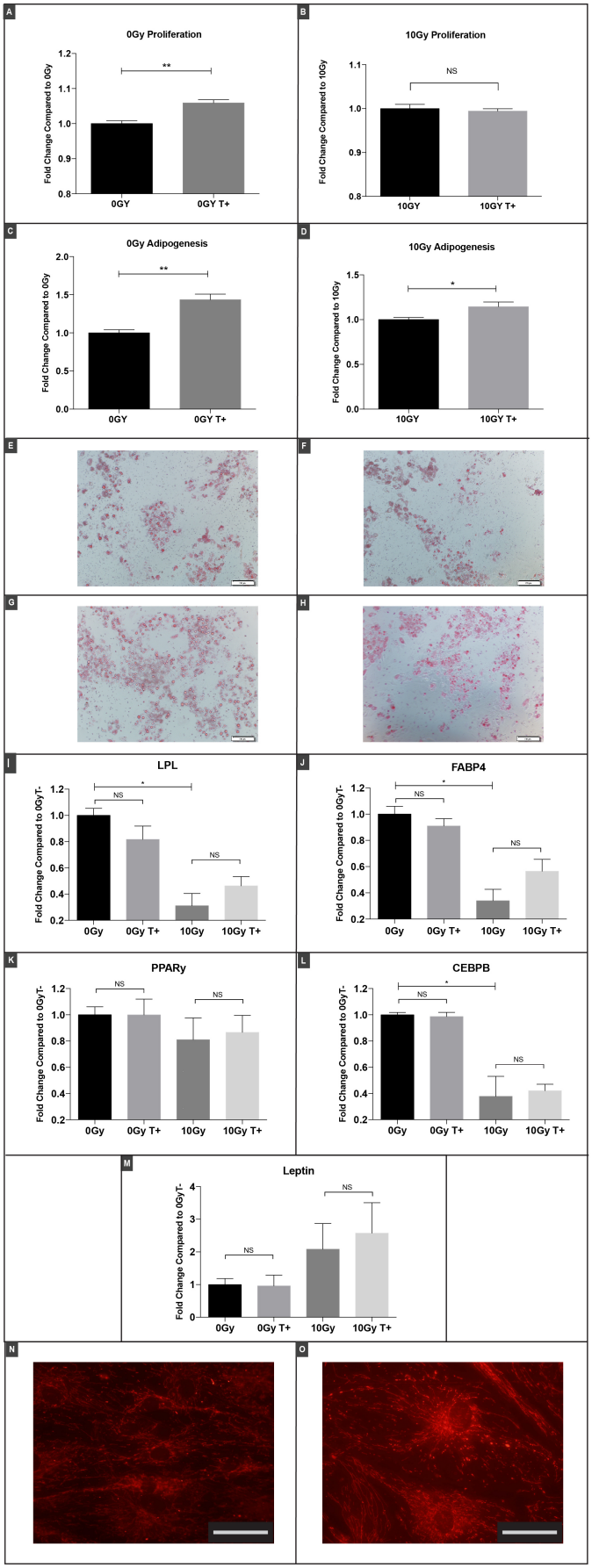
A
0Gy Proliferation
Fold Change Compared to 0Gy
**
0GY
0GY T+
B
10Gy Proliferation
Fold Change Compared to 10Gy
NS
10GY
10GY T+
C
0Gy Adipogenesis
Fold Change Compared to 0Gy
**
0GY
0GY T+
D
10Gy Adipogenesis
Fold Change Compared to 10Gy
*
10GY
10GY T+
E
F
G
H
I
LPL
Fold Change Compared to 0GyT-
NS
*
NS
0Gy
0Gy T+
10Gy
10Gy T+
J
FABP4
Fold Change Compared to 0GyT-
NS
*
NS
0Gy
0Gy T+
10Gy
10Gy T+
K
PPARγ
Fold Change Compared to 0GyT-
NS
NS
0Gy
0Gy T+
10Gy
10Gy T+
L
CEBPB
Fold Change Compared to 0GyT-
NS
*
NS
0Gy
0Gy T+
10Gy
10Gy T+
M
Leptin
Fold Change Compared to 0GyT-
NS
NS
0Gy
0Gy T+
10Gy
10Gy T+
N
O

Figure 62

Figure 62 The effect of threonine supplementation of 0Gy and 10Gy ADSC function

Quantification of (A) 0GY and (B) 10Gy ADSC proliferation at 48 h using CellTitre Glo (Promega, Germany) luminescence assay demonstrated a significant increase in 0Gy ADSC proliferation with threonine supplementation. Fluorescent plate reader quantification of solubilized Adipo-Red (Lonza, Switzerland) staining demonstrating a significant increase in adipogenic differentiation of 0Gy (C) and 10Gy (D) ADSC with threonine supplementation at day 14. x10 objective bright field photography of ADSC stained with Oil-Red-O which identifies lipid droplets in red, representing adipogenic differentiation while counterstained with hematoxylin for cell nuclei. (E) 0Gy ADSC in normal media, (F) 10Gy ADSC in normal media, (G) 0Gy ADSC with threonine supplementation and (H) 10Gy ADSC with threonine supplementation at day 14. The effect of threonine supplementation on the expression of key adipogenic transcription factors was investigated using PCR analysis of ADSC RNA collected 14 days after induction of adipogenic differentiation. The results were represented as a fold change compared with 0Gy normal media controls. Threonine supplementation did not seem to significantly alter the expression of these traditional adipogenic genes in either 0Gy or 10Gy ADSCs with PCR results quantified for the following genes: (I) LPL, (J) FABP4, (K) PPARy, (L) CEBPb and (M) Leptin. (N) 0Gy ADSC immunofluorescence staining using a mitotracker stain demonstrating normal mitochondrial morphology while (O) 10Gy ADSC demonstrates a state of 'fission' with fragmented mitochondrial structure. Scale bar (E-H) 100 μm. (N,O) 50 μm. Asterisks above bar-graphs indicate statistical significance (* = $p<0.05$, ** = $p<0.01$, NS = not significant), error bars represent SEM, with $n\geq3$.

7.2.10 Threonine labeling and tracking in ADSC

At physiological levels, irradiation of ADSCs was shown to result in reduced uptake of threonine from culture medium; whereas supplementation with threonine was able to enhance 0Gy proliferation and adipogenic differentiation in both 0Gy and 10Gy ADSCs. Labeling experiments were designed using 13Carbon stable isotope labeled threonine (Sigma Aldrich), which was added to DMEM to achieve x3 concentration of basal levels for threonine. 0Gy and 10Gy ADSCs were cultured in threonine-

labeled media and cell lysates were produced as described in section 2.8.2. Time course labeling experiments were then conducted with labeling time points of 1,5,10 and 30 minutes, as well as 1 h and 24 h time points, which attempted to determine the levels of intracellular threonine. Additionally, key metabolites in the serine/threonine and tri-carboxylic acid (TCA) pathways were also investigated. The introduction of labelled threonine with 13carbon (13C) resulted in 60% detection of the 13C label across at all timepoints across threonine metabolism pathways, in both 0Gy and 10Gy ADSCs (data not shown). Additionally, metabolites from the TCA pathway (serine, glycine and pyruvate), as well as those from threonine metabolism pathways (valine, leucine, isoleucine, alanine, aspartate and glutamate), which are commonly detectable by gas chromatography mass spectrometry (GC-MS), did not demonstrate any labeling. These data suggested that, despite reduced uptake of threonine by 10Gy ADSCs in normal media conditions, x3 concentration of labeled threonine did not demonstrate any differences in levels of uptake (and therefore detection of labeled metabolites), between 0Gy and 10Gy ADSCs. In these sets of experiments, therefore, the fate of this labeled threonine remained undetermined.

To elucidate whether threonine supplementation influenced proliferation through glucose trafficking in glycolysis or TCA pathways, 'dual labeling' experiments were employed. Firstly, 13C Threonine was added at low media concentrations (identical to normal media concentrations), along with 13C Glucose. Cell lysates were then prepared at 10 mins, 1 h and 24 h after addition of the labeled media, and processed for GC-MS. 30% 13C Glucose labeling was detected across all samples (metabolite labeling is shown in Table 22). There were no significant differences in 13C Glucose labeling levels detected between 0Gy and 10Gy ADSC groups. As determined by initial experiments, the introduction of supraphysiological levels of labelled threonine (3 times the concentration of normal media controls) was able to enhance the uptake of threonine into ADSCs that had been irradiated (10Gy). Therefore, the same experiments were repeated with dual-labeling using 13C Glucose and x3 13C Threonine media. Cell lysates were again extracted and processed at 10 mins, 1 h and 24 h after addition of media. 28% 13C Glucose labeling was detected across all samples with the metabolite labeling (Table 23), with no significant differences demonstrated between 0Gy and 10Gy ADSCs. The limited detection of 13C glucose with low or high threonine supplementation in metabolites of energy production in the

TCA pathways, suggested that threonine is unlikely to be involved in directly regulating energy production. Therefore, alternative pathways - including protein or fatty acid synthesis - require further interrogation to identify which mechanisms may be able to exert the beneficial effects of ADSC-treatment.

Metabolite	10 mins	1 h	24 h
Fructose-6-phosphate	100%	100%	100%
Glucose-6-phosphate	100%	100%	100%
Lactate	3%	3%	18%
Alanine	3%	3%	3%
Glycine	0%	0%	0%
TCA cycle	0%	0%	5-10%(?)
Cholesterol	0%	0%	0%

Table 22 Metabolic uptake studies tracking 0Gy and 10Gy ADSC labeled with 13C Glucose with low dose threonine

Metabolite	10 mins	1 h	24 h
Fructose-6-phosphate	90%	90%	90%
Glucose-6-phosphate	90%	90%	90%
Lactate	3%	3%	10%
Alanine	3%	3%	3%
Glycine	0%	0%	0%
TCA cycle	0%	0%	5-10%(?)
Cholesterol	0%	0%	0%

Table 23 Metabolic uptake studies tracking 0Gy and 10Gy ADSC labeled with 13C Glucose with high dose threonine supplementation

7.3 Discussion

$ADSC^{CM}$ was successfully able to mitigate the effects of radiotherapy injury on NHDF migration and LEC proliferation, migration, tube formation. Further, the application of $ADSC^{CM}$ to healthy LECs also demonstrated a significant lymphangiogenic effect on normal LEC populations. Hsiao et al. attempted to characterize the paracrine secretion profile of ADSCs, using mRNA mini-arrays designed to detect a specific growth factor-secretion profile based on suspected candidates derived from the literature. The mini-arrays were used to detect a profile distinct from other stem cell varieties, with particularly high expression levels of IL8, IGF-1 and VEGF-D proteins (403). These three growth factors, in particular, have each demonstrated lymphangiogenic activity, and taken together, suggest a privileged role for ADSCs in the process of lymphangiogenesis (54).

In the setting of disease, some benefits have been demonstrated from the use of ADSC introduced as a therapeutic intervention in animal models of surgical lymphoedema. Yan et al. found that transient short-term stimulation of ADSCs with VEGF-C resulted in further enhanced VEGF-A, VEGF-C and Prox-1 expression *in vitro,* and was associated with a marked pro-lymphangiogenic response following *in vivo* implantation in an animal model(287). These changes were taken as a readout of more fertile cell populations for use in fat grafting (287). These authors also reported that the stimulated ADSCs further exhibited increased cellular proliferation and survival capacity; and that this lymphangiogenic response was potentiated by TGF-β1 blockade (287). Shimizu et al. injected 2 million mouse ADSCs into a mouse tail lymphoedema model and assessed tail circumference for the next 29 days (601). The authors reported that lymphoedema was improved significantly by local injection of ADSCs and histological analysis indicated that lymphatic capillary density was greater in the ADSC-treated group than in the PBS control groups. They also attributed the lymphangiogenic effects of ADSCs to VEGF-C, demonstrated by co-localisation on IHC staining as well as increased VEGF-C RNA expression in tissues and plasma (601) - these results were confirmed in a study by Yoshida et al. (602). Hwang et al. used a hind-limb electrocautery-induced lymphoedema model in mice and implanted either human ADSCs alone, a VEGF-C-containing hydrogel, or a combination of both, then followed all groups of mice for 28 days (603). In this study, the combined treatment group showed a significantly decreased dermal oedema depth,

compared with the groups of mice that received only ADSC or VEGF-C-containing hydrogel treatments alone. IHC analysis demonstrated that the combined treatment group showed significantly greater lymphatic vessel regeneration than all the other groups and the authors commented on co-localized staining of ADSCs and LYVE-1, only in the combined ADSC/VEGF-C treatment group, postulating that ADSCs exhibit a lymphatic endothelial differentiation under VEGF-C stimulus (603).

In subsequent work, the long-term efficacy of the interventions described in the Hwang et al. study has been questioned, given the relatively short follow-up in these murine studies. Additionally, these and other studies mentioned above are representative only of surgical models of lymphoedema, and not models of radiotherapy injury, which is a distinct entity as established in this thesis thus far (54). In contrast, Zhou et al. used a surgical (ring-barking skin removal) and radiotherapy model to create lymphoedema in rabbit hind limbs. These lymphoedematous limbs were then injected with rabbit BMSCs and/or VEGF-C into the limbs at the site of skin removal and irradiation, at the 3-month mark following injury. The injured limbs were then followed for a total of 6 months (604). An increase in lymphatic vessel numbers was evident 28 days after treatment in *all* treatment groups, compared to control groups, and 6 months after surgery and/or radiotherapy there were significant decreases in limb volume (604), with the combination therapy representing maximal effect. In terms of clinical studies, two small human studies of MSC treatment for lymphoedema following axillary dissection for breast cancer have been published (605) (606). Both studies reported promising results with improved symptoms, reduction in swelling and more sustained limb volume reduction; these improved limbs were further not reliant on compliance with compressive therapies. However, in both studies, participant numbers were small and both studies have been criticized on methodological grounds (243), and larger clinical studies will be needed to assess the true effectiveness of ADSC therapy for surgical and radiotherapy induced lymphoedema.

Many of the studies described above compare the therapeutics of MSCs with or without concurrent VEGF-C therapy. Collectively, the lymphangiogenic potential appears to be linked to VEGF-C-mediated regeneration either of LECs or whole lymphatic vessels, with mechanisms suggesting that VEGF-C stimulates ADSC

differentiation into a lymphatic phenotype. The data in section 7.2.5.1 demonstrated that whilst there were detectable levels of VEGF-C protein produced by normal ADSCs, production was reduced following exposure to radiotherapy injury (Figure 57) . Overall, VEGF-C and VEGF-D and their receptor VEGFR-3 represent the best studied lymphangiogenic growth factor pathway (565). VEGF-C delivery in a number of forms including recombinant protein, viral vector or naked plasmid can reverse surgically-induced lymphoedema in a number of animal species, using different lymphoedema models (565). However, there are problems associated with VEGF-C therapy, as Goldman et al. demonstrated an initial increase LEC proliferation and lymphatic vessel growth, but minimal improvement in LEC migration or functionality (327). Therefore, it was concluded that VEGF-C alone could not permanently improve lymphatic size, density, or organization in regenerating adult skin (327). In mature adult tissues, VEGFR-2 is situated on vascular endothelium, while VEGFR-3 is found on lymphatic endothelium. While VEGF-C and VEGF-D are able to activate VEGFR-3 in both partial or fully cleaved forms, VEGFR-2 activation requires completely proteolytically processed ligands. Therefore, mature forms of VEGF-C and VEGF-D can mediate both processes of angiogenesis and lymphangiogenesis with high receptor affinity (321) (323) (324). Consequently, in the case in which an injury such as radiotherapy requires regeneration of both blood and lymphatic vessels (during different phases of repair), specific growth factors and receptors may be targeted to assist in a more temporally specific regeneration. However, the exact manner in which the VEGF-C/VEGF-D–VEGFR-3 pathway may be utilized to sustainably reduce secondary lymphoedema remains unclear. The application of VEGF-C to aid in lymphatic damage has been reported to increase LEC proliferation in shorter term follow-up, however, Nakamura et el. suggested this stimulation fails to regenerate functional lymphatic vessels in longer term followup (329).

As detailed in section 5.2.4, normal and irradiated LECs both respond favorably to treatment with traditional lymphangiogenic factors VEGF-C and VEGF-D, with demonstrable improvements in proliferation, migration and chemotactic functions, however the amplitude of response in 10Gy LECs was less pronounced. Stimulation of LECs with VEGF-C and VEGF-D demonstrated significant differences in the activation of VEGFR-2 and VEGFR-3 in 10Gy LECs compared to 0Gy controls, as

demonstrated using phosphotyrosine probed western blots (Figure 58 A, B). VEGF-C and VEGF-D stimulation of 10Gy LECs did not result in any detectable activation of VEGFR-2, along with a significantly reduced activation of VEGFR-3, suggesting a severe impairment in this signaling cascade subsequent to radiotherapy-induced damage to LECs (Figure 58 B). Further examination also demonstrated that detection of VEGFR-2/3 receptor normalized with a β-actin control is not altered by varying antibody concentrations, with no differences detected in VEGFR-2/3 immunoprecipitation on Western blots or RNA expression in both 0Gy and 10Gy LEC. Overall, there is no discernible difference at a transcriptional or translational level of VEGFR-2/3 in both 0Gy and 10Gy LECs, however there is ablation of VEGFR-2 and dampening of VEGFR-3 activation in 10 Gy LECs (Figure 58 C,D). The results in this chapter have clearly validated the powerful lymphangiogenic stimulus of $ADSC^{CM}$ on normal but also irradiated LECs by significantly improving key cellular functions, which are altered as a result of radiotherapy injury. The literature discussed above attributes ADSC-mediated lymphatic regeneration to the influence of VEGF-C. ELISA assays in this chapter also confirm the presence of both VEGF-C and to a smaller extent VEGF-D in $ADSC^{CM}$. Taken together these findings raise key questions which are addressed sequentially in this discussion: (i) does $ADSC^{CM}$ mediate its lymphangiogenic effects on LECs via VEGFR-2 and VEGFR-3 signaling? (ii) does $ADSC^{CM}$ produce biologically functional VEGF-C and D? (iii) if the VEGF-C/VEGF-D–VEGFR-3 signaling cascade is selectively blocked, does $ADSC^{CM}$ retain its lymphangiogenic potential? (iv) are there other lymphangiogenic growth factors in the paracrine secretome of $ADSC^{CM}$ that act independently of VEGFR-3 mediated signaling?

Immunoprecipitation western blots of VEGFR-2 and -3 with phosphotyrosine did not lead to any detectable activation in both 0Gy and 10Gy LEC stimulated with $ADSC^{CM}$ and $RTX\text{-}ADSC^{CM}$. This result suggests constituents of both conditioned media types, do not primarily mediate their lymphangiogenic effect through this signaling cascade. While ELISA assays demonstrated detectable levels of VEGF-C and VEGF-D in $ADSC^{CM}$, bioassays also confirmed these proteins are functional and able to activate VEGFR-2 and -3 in VEGFR2/3-EpoR-Ba/F3 cells. They also displayed appropriate alterations in bio-activity in response to dilution and VEGX300 inhibition, and expectedly significantly lower bioactivity in comparison to VEGF-C

and VEGF-D positive controls. The subsequent experiments then demonstrated that selective blockade of VEGF-C with VGX-100 and VEGFR-3 with VGX300, did not significantly impair the lymphangiogenic stimulus of $ADSC^{CM}$ on both 0Gy and 10Gy LEC. Taken together these results comprehensively indicate the restorative effect of $ADSC^{CM}$ on the functions of irradiated LECs are not primarily driven by the traditional VEGF-C/VEGFR-2/3 lymphangiogenic pathways.

On review of the literature, it is evident that little is known about VEGF-C/VEGFR-3 independent postnatal lymphangiogenesis (607). Haiko et al. showed that VEGF-$C^{-/-}$; VEGF-$D^{-/-}$ double knockout murine embryos and VEGF-$C^{-/-}$ deficient embryos failed to develop lymphatic vasculature, whereas VEGF-$D^{-/-}$ mice developed essentially normal lymphatics (608). Current knowledge suggests VEGF-C and VEGF-D are the only ligands known to activate VEGFR-3, however such stimulation may also occur with binding of co-receptors, namely Neuropilin-2 (Nrp2) (609). Nrp2 was initially described as a moderator of axonal regulation. Yuan et al. demonstrated homozygous Nrp2 mutants displayed a reduction in lymphatic vessel density, concluding it is a key factor in lymphangiogenic modulation (610). Xu et al. further demonstrated that antibody or genetic mediated blockade of Nrp2/VEGFR-3 led to selective disruption of VEGF-C mediated lymphatic vessel sprouting (609) On next generation gene sequencing both 10Gy and 2Gy x 5 LEC Nrp2 demonstrated a trending decrease in expression in LECs compared to 0 Gy controls, however did not reach statistical significance (-0.431 in 10Gy LEC and -0.0973 in 2Gy x 5 LEC). Deng et al. examined the molecular controls of lymphatic VEGFR-3 signaling and demonstrated that VEGF-C stimulation of LECs *in-vitro* could lead to the formation of VEGFR-3/VEGFR-2 complexes, unlike VEGF-A stimulation. Suppressing VEGFR-2 or its co-receptor neuropilin 1 (Nrp1) specifically eliminated VEGF-C–induced AKT but not ERK activation, whereas silencing of Nrp2 had minimal effect on either signaling pathway (611). Exosome proteomic analysis demonstrated a down regulation of Nrp1 in 10Gy LECs which was reprogrammed and subsequently increased with $ADSC^{CM}$ treatment and this signaling cascade therefore warrants further investigation. Overall, the VEGF-C/VEGFR-2 and 3 independent mechanism of $ADSC^{CM}$ salvage of 10Gy LEC function also necessitates further investigation to identify novel components and/or less conventional pathways responsible for the marked regenerative lymphangiogenic effects of $ADSC^{CM}$.

To approach this, ion exchange chromatography fractionation of ADSC^{CM} was utilized as a method to identify key components of ADSC^{CM} resulting in the potent lymphangiogenic stimulus on both 0Gy and 10Gy LEC migration. The results demonstrated the detection of several novel proteins, not routinely associated with lymphangiogenic pathways in current literature. While pilot screening of each individual candidate protein or a combination of all proteins, failed to significantly improve migration of 0Gy or 10Gy LEC in comparison to ADSC^{CM}, further optimization with dose titration curves and/or VEGFR-2/3 phosphotyrosine activation western blots would be beneficial to establish each protein's full lymphangiogenic potential.

The use of exosomal proteomic analysis also lays a solid foundation from which exploration of the novel therapeutics of ADSC^{CM} may be conducted as exosomes carry the unique capability to influence the bioactivity of neighbouring cells, shown to regulate several processes such as immune responses, tumour progression and neurodegenerative disorders (598). The results of this thesis strongly indicate that cell to cell communication and the paracrine secretome of ADSC play a key role in the spread of radiotherapy injury and its subsequent modulation, illustrating the utility of investigating exosomal contents and interactions between cell types. Early data clearly demonstrates dysregulation of several proteins either up or down regulated in 10Gy LECs as a result of radiotherapy injury along with concurrent re-programming or reversal of expression with ADSC^{CM} treatment. These processes require further interrogation, combined with information from molecular and metabolomics data to identify specific protein candidates that result in targeted regeneration of irradiated LECs.

Radiotherapy injury to ADSC themselves led to significant cellular dysfunction as detailed in Chapter 6, therefore it was postulated this would also lead to changes in their therapeutic paracrine secretome. RTX-ADSC^{CM} was able to induce injury in normal cells, while it also worsened the impact of radiotherapy injury on the functions of NHDFs and LECs. These assays demonstrate a key principle that is integral to the understanding of radiotherapy induced soft tissue injury; not only are the individual cell functions compromised as a result of irradiation, but these alterations also contribute significantly to the propagation and perpetuation of injury in the

surrounding microenvironment. These experiments provided data that supports the mechanism of radiotherapy induced bystander effect; leading to a pronounced deterioration of normal cellular functions (not initially targeted by radiotherapy) resulting from irradiated cell-cell communications. The proteomic analysis of RTX-ADSC^{CM} exosome contents demonstrated significant alterations of 85 unique proteins in comparison to ADSC^{CM}. As RTX-ADSC^{CM} appears to have a profound anti-lymphangiogenic effect, these proteins may also provide potential therapeutic avenues that could be exploited and explored in the field of tumour metastases.

Lastly, the differences in uptake and utilization of threonine, an essential amino acid, in 0Gy and 10Gy ADSC were investigated further with supplementation and tracking experiments. Threonine supplementation to 2-3 times the physiological level, overcame the inability of 10Gy ADSC uptake threonine as well demonstrating marked functional improvements in 0Gy ADSC proliferation, 0Gy and 10Gy ADSC adipogenesis, without alteration of traditional adipogenic gene expression. The tracking experiments conducted with 13C Glucose co-labelling did not demonstrate any significant differences in uptake of threonine or labeling of key metabolites in the threonine-serine-glycine or tri-cyclic acid cycle, suggesting the additional threonine is not shunted into pathways of glucose trafficking and glycolysis. Therefore, alternative protein synthesis and fatty acid synthesis pathways require further metabolomic investigation. However, supplementation of 0Gy ADSC with threonine clearly demonstrates potential to improve the quality and yield of fat grafting in physiological conditions and should be validated as a therapeutic adjunct in animal and human clinical studies.

8 Conclusions and Future Perspectives

It has long been appreciated that normal tissue tolerance to radiotherapy injury dictates and limits the doses used to achieve oncological effect on tumour cells. The clinical side effects of radiotherapy injury have been categorized as acute and chronic, resulting from substantial injury to each component that comprises the skin and subcutaneous tissue, however the effects on each cellular subtype have not been elucidated. As cancer diagnosis, surgical management and adjunct therapies have substantially improved, a growing population of cancer survivors continue to suffer from the chronic and debilitating effects of radiotherapy injury, clinically manifested as fibrosis, lymphedema, recurrent infection and poor wound healing. This thesis has aimed to uncover the cellular and molecular mechanisms of radiotherapy soft tissue injury in integral cell populations, while for the first time attempting to thoroughly investigate the therapeutic mechanisms of ADSC in fat graft, defining a novel therapy that can specifically target irradiation damage.

In order to investigate radiotherapy soft tissue injury, it was first necessary to establish and optimize an *in-vitro* model of injury that reflected clinical and sublethal damage to normal human tissue cells. A protocol of 10Gy single dose irradiation in comparison to 5 fractionated doses of 2Gy was used to interrogate cultures of proliferating NHEK, NHDF, Pericytes, HMEC, LEC and ADSC. A panel of assays was designed: cell viability, proliferation, apoptosis and migration and were devised to punitively analyse the effects of radiotherapy injury in each cell type. Screening proliferation and apoptosis assays of all cell types was conducted using 10Gy and 2Gy x 5 doses in comparison to 0Gy controls, which determined that the effect of radiotherapy injury was not significantly different between each experimental group, therefore subsequent analyses were conducted using a single 10Gy dose. Further dedicated assays, pertinent to the specialized function of each cell type were also developed to quantify the unique functional alterations resulting from radiotherapy injury. Such assays included cell adhesion, contraction and invasion in NHDFs, 2D and 3D models of tube formation and sprouting in endothelial cells, differentiation assays in ADSCs, as well as chemotaxis assays used to analyse the responses of cells to growth factor and cytokine gradients.

The traditional dogma of radiotherapy injury resulting in large scale irreversible cell death from double stranded DNA breaks (38), global suppression of all key cellular functions, affecting all cell types in the same fashion is substantially challenged by findings in this thesis. Each individual cell type demonstrated a unique injury profile in response to radiotherapy. Novel and notable findings included the hypermigratory response of irradiated NHDF and pericytes, the suppression of apoptosis in irradiated HMEC, LEC and ADSC populations as well as the significant alteration in differentiation capacities of ADSCs.

Next generation sequencing was able to provide an in-depth analysis of the molecular alterations resulting from radiotherapy injury to each individual cell type, which through pathway analysis could be mapped and aligned with key elements of cellular dysfunction exhibited in the functional bio-assays designed to model the key processes underpinning lymphangiogenesis. Overall, characterising the cellular and molecular level alterations in irradiated normal tissue cells established a baseline profile to which future therapeutic modalities could be applied. Such therapies could then be evaluated for their efficacy in reducing the burden and manifestations of radiotherapy soft tissue injury. Globally there was evident up-regulation of cell cycle arrest proteins in all cell populations, which may be linked to cellular senescence (84), however each individual cell type also demonstrated unique transcriptional alterations in response to radiotherapy. Notable changes in RNA expression included increased ICAM-1 in HMEC, IL-8 and CXCR7 in LEC and ECM component dysregulation in NHDFs. Interestingly, these findings again challenge the doctrine of TGF-β mediated radiotherapy injury, which did not feature as a major alteration across all cell types (125) (148).

While each individual cell type was interrogated in a stand-alone experiment, radiotherapy injury is defined by a complex inter-play of cell-cell interactions driven by molecular alterations and transmitted by mechanisms of indirect spread such as the release of reactive oxygen species, secreted paracrine factors and chemokines, and finally, possibly exosomes. These components of the injury likely all contribute to the continuum of events that disseminates damage to tissues surrounding the original irradiated tissues. Integrating the findings of this thesis, the overall picture of

radiotherapy injury can be summarized in relation to the following novel concepts: (i) radiotherapy injury to normal tissues is sublethal in nature, resulting in reduced proliferation but also reduced apoptosis of damaged cells; (ii) these damaged cells, likely in a state of senescence, continue to contribute to the cellular microenvironment displaying significant cellular dysfunction, altered paracrine secretome as well as abnormal responses to physiological stimuli; (iii) irradiated cells are able to influence the behavior of surrounding cells by paracrine mechanisms leading to worsening of radiotherapy injury or induction of damaging effects in cells not immediately in the zone of injury; (iv) the dampening or ablation of key signaling cascades in irradiated cells leads to up-regulation of alternative pathways to attempt regeneration.

To explain these concepts with mechanisms established in this thesis, the reduction in apoptosis of irradiated cell populations may serve as a logical starting point to explain the development of RIBE. These radiation-induced senescent cells are biochemically active despite having undergone clonogenic death (122) (123), producing an altered paracrine secretome, while unable to proliferate normally in response to subsequent trauma or wounding. It remains to be determined whether these changes are reversible, and if not, therapies that encourage apoptosis of these damaged cells may be beneficial in removing these cells from the irradiated tissues, thus minimising the severity of RIBE.

The hypermigratory, adhesive and invasive NHDF phenotype acquired as a result of irradiation is likely linked to the molecular up-regulation of collagens IV, VII, and VIII as well as MMPs 2 and 11. These pathological alterations may be beneficial from an oncological stand point as collagens IV, VII, and VIII are integral components of the basement membrane and these changes may confine residual or recurrent cancer cells. However, the disordered and hypermigratory patterns of 2-D and 3-D NHDF migration may lead to spread of damage beyond the immediate zone of injury, achieving wound closure by haphazard bridging of a gap, which then manifests progressive and clinically debilitating wound contracture. The increased expression of perivascular αSMA in irradiated human samples, irradiated NHDF in culture and the hypermigratory change common to both pericytes and NHDF may contribute to the compromised tissue and vessel compliance. The impairment of perivascular support

cells in combination with diminished HMEC angiogenic capabilities, an ICAM-1 mediated prothrombotic, atherogenic and 'leaky' intimal surface, sets the scene for dysfunctional neoangiogenesis, unable to support the vascularity of an irradiated tissue bed, particularly when subsequently further insulted . The damage to the media with myxoid change and persistent up-regulation of ICAM-1 in medium sized vessels such as the IMA in the field of radiation again provide a target to mitigate the development of atherothrombotic pathologies associated with radiotherapy injury.

Impaired tissue compliance, linked to radiotherapy-induced fibrosis has also been associated with compromised lymphangiogenesis and lymphatic fluid stasis (133). Radiotherapy demonstrates a globally suppressive effect on all LEC homeostatic functions along with molecular and protein level up-regulation of IL-8 and CXCR7. Stimulation of LECs with traditional lymphangiogenic factors VEGF-C and VEGF-D displayed diminished responsiveness in 10Gy LECs, with ablated activation of VEGFR-2 signaling and significantly dampened VEGFR-3 signaling. IL-8 and CXCR7, novel proteins upregulated in 10y LECs, each demonstrated selective lymphangiogenic effects in 0Gy and 10Gy LECs, therefore potentially representing an attempt by 10Gy LECs to stimulate lymphatic regeneration independent of VEGFC/D/VEGFR-3 signaling cascades. Recent studies in the literature also validate these findings in alternative models of injury where IL-8 was used in the treatment of a murine tail surgical lymphoedema model, demonstrating promotion of LEC proliferation, tube formation, and migration without activating VEGFR-3 signaling, nor inflammatory pathways normally associated with IL-8 activity (341). Additionally, Singh et al. linked the expression of IL-8 in prostate cancer cell lines to further increase the expression of CXCR7, which may conceivably represent a key interaction in irradiated LECs (350). The up-regulation of CXCR7 however, has implications in the homing of ADSCs and the CXCR4/SDF1α axis of signaling. The results in this thesis confirmed the recently described mechanism of CXCR7 as a decoy receptor, abolishing the chemotactic migration of uninjured ADSCs in response to SDF1α gradients. Applied to the setting of radiotherapy injury, these results suggest an inability of irradiated tissues to successfully recruit healthy loco-regional or distant ADSCs. Therefore, in the clinical setting, patients may rely only on the mechanical introduction via methods such as fat grafting to mediate regenerative

effects. Downregulation of CXCR7 in irradiated tissues may be able to restore homeostatic ADSC homing, but may also be implicated in worsening the damage to irradiated LECs, if the lymphangiogenic stimulus of CXCR7 were to be removed. The interplay of these mechanisms is illustrated in Figure 63.

Authors who have investigated the effects of injurious stimuli such as hypoxia and radiotherapy on ADSCs have demonstrated a superior ADSC survival capacity compared to other cellular components of fat grafts, through utilization of anaerobic metabolism, a finding validated in this thesis as ADSCs demonstrated the most minimal reduction in cell viability of all cell types. However, the sub-lethal radiotherapy-induced injury was found to damage the ADSCs' capacity for proliferation, adipogenesis, responsiveness to SDF1α chemotactic cues, threonine metabolism and significantly altered its paracrine secretory profile. Such functional alterations in injured ADSCs may account for the inability of local ADSCs to regenerate surrounding tissues following radiotherapy injury leading to a 'double hit' type injury, in which there is a worsening of the effects of radiotherapy injury in 10Gy LECs and damage inflicted on normal cells such as NHDFs, adjacent to the targeted zone.

The paracrine regenerative properties of ADSCs were utilized to develop a model of the clinical phenomenon of radiotherapy soft-tissue injury reversal, using fat grafting, with a particular focus on NHDFs and LECs, to explore therapeutic avenues to reduce fibrosis and lymphoedema. The validation of the potent lymphangiogenic effects of $ADSC^{CM}$ on both 0Gy and 10Gy LECs represented a key finding, novel due to its independence from traditional VEGF-C/VEGF-D–VEGFR-2/3-mediated signaling. The potential to identify a VEGF-C/VEGF-D independent means to reduce the morbidity of radiotherapy-induced lymphedema in cancer survivors (243) (244) is additionally advantageous as these growth factors are strongly implicated in tumour recurrence and metastases (51) (326). A comprehensive multi-platform approach was utilized to interrogate the therapeutics of $ADSC^{CM}$; employing next generation sequencing, metabolomics, proteomic and exosome mass spectrometry techniques. This data has presented several novel candidates requiring validation of their

lymphangiogenic potential. In addition, exosome analysis has provided credible information of $ADSC^{CM}$ proteins that lead to ‘re-programming’ of 10Gy LECs.

There are several interesting leads to follow in future work at the conclusion of this thesis. These include the validation of $ADSC^{CM}$-mediated reversal of NHDF injury by manipulation of ECM components; ICAM-1 knockdown models to improve micro- and macro-vascular damage; and the clinical validation of therapeutic threonine supplementation to optimize fat graft retention in a physiological setting. Further investigation of the VEGF-C/VEGF-D/VEGFR-3 independent mechanisms of $ADSC^{CM}$-mediated lymphangiogenesis will provide novel targeted therapeutic approaches by which to reduce radiotherapy-specific dysfunction in irradiated LECs. These approaches would carry the benefits from an oncological perspective of containing metastasis of recurrent disease, but also from the perspective of developing therapeutics for the treatment of lymphoedema and other diseases relating to the aftermath of radiotherapy treatment. Understanding of the cellular and molecular mechanisms of radiotherapy-induced soft-tissue injury and $ADSC^{CM}$-mediated reversal of the resulting dysfunction should facilitate the manipulation of these pathological alterations to reduce the burden of chronic debilitating side effects in cancer survivors.

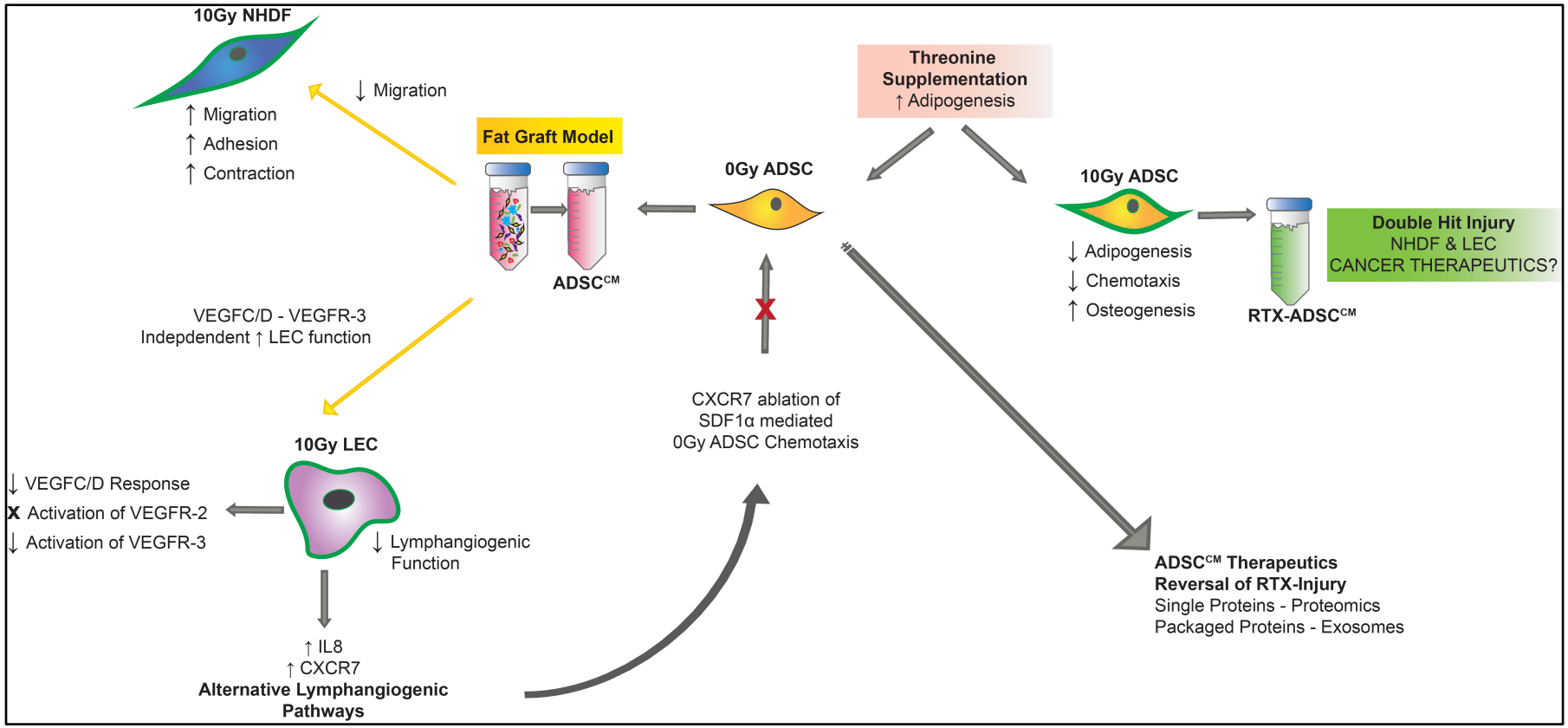

Figure 63

Figure 63 The effects of radiotherapy injury to NHDF, LEC and ADSC and the therapeutic salvage of this damage using ADSC^{CM} and Threonine

9 Bibliography

1. Sheaff M, Baithun S. Pathological effects of ionizing radiation. Current Diagnostic Pathology. Elsevier; 2013 Aug 13;4(2):106–15.

2. IAEA. Radiation Oncology Physics:. 2005 Jun 7;:1–696.

3. Khan FM. The Physics of Radiation Therapy. Lippincott Williams & Wilkins; 2012. 1 p.

4. McMillan TJ, Steel GG. DNA damage and cell killing. Arnold; 2002.

5. Lliakis G. The role of DNA double strand breaks in lonizing radiation-induced killing of eukaryotic cells. Bioessays. 1991 Dec;13(12):641–8.

6. Pereira GC, Traughber M, Muzic RF. The Role of Imaging in Radiation Therapy Planning: Past, Present, and Future. BioMed Research International. 2014;2014(5):1–9.

7. Wideröe R. Über ein neues Prinzip zur Herstellung hoher Spannungen. Archiv f Elektrotechnik. Springer-Verlag; 1928 Jul;21(4):387–406.

8. Greene D, Williams PC. Linear Accelerators for Radiation Therapy, Second Edition - David Greene, P.C Williams - Google Books. 1997.

9. Stewart FA, Akleyev AV, Hauer-Jensen M, Hendry JH, Kleiman NJ, MacVittie TJ, et al. ICRP PUBLICATION 118: ICRP Statement on Tissue Reactions and Early and Late Effects of Radiation in Normal Tissues and Organs â€“ Threshold Doses for Tissue Reactions in a Radiation Protection Context: A LONG ROAD. Annals of the ICRP. Elsevier Ltd; 2012 Apr 1;41(1-2):1–322.

10. Kry SF, Kry SF, Smith SA, Smith SA, Weathers R, Weathers R, et al. Skin dose during radiotherapy: a summary and general estimation technique. Journal of Applied Clinical Medical Physics. 2012;13(3).

11. AIHW, AIHW. Australian Institute of Health and Welfare & Australasian Association of Cancer Registries 2012. 70 ed. Canberra; 2012 Nov 13;:1–215.

12. Delaney G, Jacob S, Featherstone C, Barton M. The role of radiotherapy in cancer treatment. Cancer. 2005 Sep 15;104(6):1129–37.

13. Quarmby S, Quarmby S, Kumar P, Kumar P, Kumar S, Kumar S. Radiation-induced normal tissue injury: Role of adhesion molecules in leukocyte-endothelial cell interactions. Int J Cancer. 1999 Jul 30;82(3):385–95.

14. Bentzen SM. Preventing or reducing late side effects of radiation therapy: radiobiology meets molecular pathology. Nature Reviews Cancer. Nature Publishing Group; 2006 Sep;6(9):702–13.

15. Mullan F. Seasons of Survival: Reflections of a Physician with Cancer. N Engl J Med. 1985 Jul 25;313(4):270–3.

16. Rubin P, Constine LS, Marks LB, Okunieff P. CURED I - LENT Late Effects of Cancer Treatment on Normal Tissues. Springer Science & Business Media; 2007. 1 p.

17. Denham JW, Hauer-Jensen M. The radiotherapeutic injury – a complex "Wound." Radiother Oncol. Elsevier; 2002;63(2):129–45.

18. Roentgen Wc. [On A New Kind Of Ray (First Report)]. Munch Med Wochenschr. 1959 Jul 24;101:1237–9.

19. Becquerel J, Crowther Ja. Discovery Of Radioactivity. Nature. 1948.

20. Curie E. Marie And Pierre Curie And The Discovery Of Radium. Vol. 23, The British Journal Of Radiology. 1950. 4 P.

21. Chaoul H. [Short-Distance Roentgenotherapy (Contact Roentgenotherapy)]. J Radiol Electrol Arch Electr Medicale. 1950;31(5-6):290–8.

22. Mould RF. A Century of X-Rays and Radioactivity in Medicine: With Emphasis on ... - R.F Mould - Google Books. 1993.

23. Grubbé EH. Priority in the Therapeutic Use of X-rays. Radiology. 1933 Aug;21(2):156–62.

24. Connell PP, Hellman S. Advances in Radiotherapy and Implications for the Next Century: A Historical Perspective. Cancer Research. 2009 Jan 15;69(2):383–92.

25. Thariat J, Hannoun-Levi J-M, Myint AS, Vuong Te, Gérard J-P. PERSPECTIVES. Nature Reviews Clinical Oncology. Nature Publishing Group; 2012 Nov 27;10(1):52–60.

26. Taylor Ls. History Of The International Commission On Radiological Protection (IcRP). Health Phys. 1958 Sep;1(2):97–104.

27. BERGONIE J, TRIBONDEAU L. Interpretation Of Some Results Of Radiotherapy And An Attempt At Determining A Logical Technique Of Treatment. Radiation Research. 1959 Sep 30;11:587–8.

28. Coutard H. PRINCIPLES OF X RAY THERAPY OF MALIGNANT DISEASES. The Lancet. Elsevier; 1934 Jul;224(5784):1–8.

29. Kaplan HS. Historic Milestones In Radiobiology And Radiation Therapy. Semin Oncol. 1979 Dec;6(4):479–89.

30. FRY DW, R S HARVIE RB, MULLETT LB, WALKINSHAW W. A Travelling-Wave Linear Accelerator For 4-Mev. Electrons. Nature. 1948 Nov 27;162(4126):859–61.

31. Emami B, Emami B, Lyman J, Lyman J, Brown A, Brown A, et al. Tolerance of normal tissue to therapeutic irradiation. International Journal of Radiation Oncology*Biology*Physics. 1991 May;21(1):109–22.

32. Johns HE, Cunningham JR. Johns: The Physics of Radiology 4th edn (Springfield,... - Google Scholar. 1983.

33. Fletcher GH. The evolution of the basic concepts underlying the practice of radiotherapy from 1949 to 1977. Radiology. 1978 Apr;127(1):3–19.

34. Withers HR, Taylor JM, Maciejewski B. Treatment volume and tissue tolerance. Int J Radiat Oncol Biol Phys. 1988 Apr;14(4):751–9.

35. Gray LH, Conger AD, Ebert M, Hornsey S, Scott OCA. The Concentration of Oxygen Dissolved in Tissues at the Time of Irradiation as a Factor in Radiotherapy. Br J Radiol. 1953 Dec;26(312):638–48.

36. Mottram JC. A Factor of Importance in the Radio Sensitivity of Tumours. Br J Radiol. 1936 Sep;9(105):606–14.

37. Dewhirst MW, Cao Y, Moeller B. Cycling hypoxia and free radicals regulate angiogenesis and radiotherapy response. Nature Reviews Cancer. 2008 Jun;8(6):425–37.

38. Puck TT, Puck TT, Marcus PI, Marcus PI. Action of X-rays on mammalian cells. J Exp Med. Rockefeller Univ Press; 1956;103(5):653–66.

39. Strong EW. PREOPERATIVE RADIATION AND RADICAL NECK Dissection. Surg Clin N Amer, 49: 271-6(Apr 1969). 1969 Jan 1.

40. Schneider Jj, Fletcher Gh, H Thomas Barkley Jr. Control By Irradiation Alone Of Nonfixed Clinically Positive Lymph Nodes From Squamous Cell Carcinoma Of The Oral Cavity, Oropharynx, Supraglottic Larynx, And Hypopharynx. American Journal Of Roentgenology. American Roentgen Ray Society; 1975.

41. GH F. Indications for combination of irradiation and surgery. J Radiol Electrol Med Nucl. 1976 May 1;57(5):379–90.

42. C D Haagensen APS. Carcinoma of the Breast. III. Results of Treatment, 1935-1942. Annals of Surgery. Lippincott, Williams, and Wilkins; 1951 Aug 1;134(2):151.

43. Robbins GF, Lucas JC, Fracchia AA, Farrow JH, Chu FC. An evaluation of postoperative prophylactic radiation therapy in breast cancer. Surg Gynecol Obstet. 1966 May;122(5):979–82.

44. Paterson R, Russell MH. Clinical trials in malignant disease: Part III—Breast cancer: Evaluation of post-operative radiotherapy. Journal of the Faculty of Radiologists. 1959.

45. Bertozzi S, Londero AP. The sentinel lymph node biopsy for breast cancer over the years. Eur J Gynaecol Oncol. 2016;37(1):13–6.

46. Paquet-Fifield S, Levy SM, Sato T, Shayan R, Karnezis T, Davydova N, et al. Vascular endothelial growth factor-d modulates caliber and function of initial lymphatics in the dermis. J Invest Dermatol. 2013 Aug;133(8):2074–84.

47. Cochran AJ, Wen DR, Morton DL. Management of the regional lymph nodes in patients with cutaneous malignant melanoma. World journal of surgery. 1992.

48. Park C, Seid P, Morita E, Iwanaga K. Internal mammary sentinel lymph node mapping for invasive breast cancer: implications for staging and treatment. The Breast. 2005.

49. Thompson JF, Uren RF. Lymphatic mapping and sentinel node biopsy for melanoma. 2001.

50. Wood TF, Nora DT, Morton DL, Turner RR, Rangel D, Hutchinson W, et al. One hundred consecutive cases of sentinel lymph node mapping in early colorectal carcinoma: detection of missed micrometastases. J Gastrointest Surg. 2002 May;6(3):322–9–discussion229–30.

51. Shayan R. Lymphatic vessels in cancer metastasis: bridging the gaps. Carcinogenesis. 2006 Apr 5;27(9):1729–38.

52. Veronesi U, Saccozzi R, Del Vecchio M, Banfi A, Clemente C, De Lena M, et al. Comparing Radical Mastectomy with Quadrantectomy, Axillary Dissection, and Radiotherapy in Patients with Small Cancers of the Breast. N Engl J Med. 1981 Jul 2;305(1):6–11.

53. Veronesi U, Cascinelli N, Mariani L, Greco M, Saccozzi R, Luini A, et al. Twenty-Year Follow-up of a Randomized Study Comparing Breast-Conserving Surgery with Radical Mastectomy for Early Breast Cancer. N Engl J Med. 2002 Oct 17;347(16):1227–32.

54. Lipi Shukla WAMRS. Adipose-Derived Stem Cells in Radiotherapy Injury: A New Frontier. Frontiers in Surgery. Frontiers Media SA; 2015;2.

55. Dörr W. Radiobiology of tissue reactions. Annals of the ICRP. 2015 Jun;44(1 Suppl):58–68.

56. Hopewell JW. The skin: its structure and response to ionizing radiation. Int J Radiat Biol. Informa UK Ltd UK; 1990;57(4):751–73.

57. Anscher MS. Targeting the TGF- 1 Pathway to Prevent Normal Tissue Injury After Cancer Therapy. Oncologist. 2010 Apr 22;15(4):350–9.

58. Quach KY, Morales J, Butson MJ, Rosenfeld AB, Metcalfe PE. Measurement of radiotherapy x-ray skin dose on a chest wall phantom.

Med Phys. 2000 Jul;27(7):1676–80.

59. Kendal WS. The application of probability-generating functions to linear-quadratic radiation survival curves. Int J Radiat Biol. Informa UK Ltd UK; 2000;76(4):581–7.

60. Citrin D, Cotrim AP, Hyodo F, Baum BJ, Krishna MC, Mitchell JB. Radioprotectors and mitigators of radiation-induced normal tissue injury. Oncologist. 2010;15(4):360–71.

61. Brush J, Lipnick SL, Phillips T, Sitko J, McDonald JT, McBride WH. Molecular mechanisms of late normal tissue injury. Seminars in Radiation Oncology. 2007 Apr;17(2):121–30.

62. Leach JK, Van Tuyle G, Lin PS, Schmidt-Ullrich R, Mikkelsen RB. Ionizing radiation-induced, mitochondria-dependent generation of reactive oxygen/nitrogen. Cancer Research. 2001 May 15;61(10):3894–901.

63. Brown KR, Rzucidlo E. Acute and chronic radiation injury. YMVA. Elsevier Inc; 2011 Jan 1;53(S):15S–21S.

64. Spitz DR, Azzam EI, Li JJ, Gius D. Metabolic oxidation/reduction reactions and cellular responses to ionizing radiation: a unifying concept in stress response biology. Cancer Metastasis Rev. 2004 Aug;23(3-4):311–22.

65. Azzam EI, Jay-Gerin J-P, Pain D. Ionizing radiation-induced metabolic oxidative stress and prolonged cell injury. Cancer Letters. 2012 Dec;327(1-2):48–60.

66. Greenberger JS, Greenberger JS. Strategies for discovery of small molecule radiation protectors and radiation mitigators. 2012 Jan 12;:1–12.

67. Bourgier C, Levy A, Vozenin M-C, Deutsch E. Pharmacological strategies to spare normal tissues from radiation damage: useless or overlooked therapeutics? Cancer Metastasis Rev. 2012 Jun 16;31(3-4):699–712.

68. Epperly MW, Gretton JA, DeFilippi SJ, Sikora CA, Liggitt D, Koe G, et al. Modulation of Radiation-Induced Cytokine Elevation Associated with Esophagitis and Esophageal Stricture by Manganese Superoxide Dismutase-Plasmid/Liposome (SOD2-PL) Gene Therapy. Radiation …. 2001.

69. Coleman CN. Effects of radiation on normal tissue: consequences and mechanisms. Science. 2004 Apr 30;304(5671):693–4.

70. Hubenak JR, Zhang Q, Branch CD, Kronowitz SJ. Mechanisms of Injury to Normal Tissue after Radiotherapy. Plast Reconstr Surg. 2014 Jan;133(1):49e–56e.

71. Shrivastav M, De Haro LP, Nickoloff JA. Regulation of DNA double-strand break repair pathway choice. Cell Res. 2008 Jan;18(1):134–47.

72. Dörr W. Three A's of repopulation during fractionated irradiation of squamous epithelia: asymmetry loss, acceleration of stem-cell divisions and abortive divisions. Int J Radiat Biol. 1997.

73. Turesson Ragnhild Bernefors Majli I, Turesson Ragnhild Bernefors Majli I. Normal Tissue Response to Low Doses of Radiotherapy Assessed by Molecular Markers□A Study of Skin in Patients Treated for Prostate Cancer. Acta Oncol. 2001 Jan;40(8):941–51.

74. Dörr W, Weber-Frisch M. Effect of changing weekly dose on accelerated repopulation during fractionated irradiation of mouse tongue mucosa. Int J Radiat Biol. 1995 May;67(5):577–85.

75. Dörr W, Emmendörfer H, Weber-Frisch M. Tissue kinetics in mouse tongue mucosa during daily fractionated radiotherapy. Cell Prolif. 1996 Sep;29(9):495–504.

76. Zhou T, Chou J, Mullen TE, Elkon R, Zhou Y, Simpson DA, et al. Identification of primary transcriptional regulation of cell cycle-regulated genes upon DNA damage. Cell Cycle. Landes Bioscience; 2007;6(8):972–81.

77. Malumbres M, Barbacid M. Mammalian cyclin-dependent kinases. Trends in Biochemical Sciences. 2005 Nov;30(11):630–41.

78. Belyakov OV, Folkard M, Mothersill C, Prise KM, Michael BD. Bystander-induced differentiation: a major response to targeted irradiation of a urothelial explant model. Mutat Res. 2006 May 11;597(1-2):43–9.

79. Andreassen CN, Alsner J. Genetic variants and normal tissue toxicity after radiotherapy: a systematic review. Radiotherapy and Oncology. 2009.

80. Sokolov MV, Smilenov LB, Hall EJ, Panyutin IG, Bonner WM, Sedelnikova OA. Ionizing radiation induces DNA double-strand breaks in bystander primary human fibroblasts. Oncogene. 2005 Sep 19;24(49):7257–65.

81. Marples B, Wouters BG, Joiner MC. An association between the radiation-induced arrest of G2-phase cells and low-dose hyper-radiosensitivity: a plausible underlying mechanism? Radiation Research. 2003rd ed. 2007 Dec;160(1):38–45.

82. Rodier F, Campisi J. Four faces of cellular senescence. J Cell Biol. 2011 Feb 21;192(4):547–56.

83. Avraham T, Daluvoy S, Zampell J, Yan A, Haviv YS, Rockson SG, et al. Blockade of Transforming Growth Factor-β1 Accelerates Lymphatic

Regeneration during Wound Repair. Am J Pathol. American Society for Investigative Pathology; 2010 Dec 29;177(6):3202–14.

84. Oh CW, Bump EA, Kim JS, Janigro D, Mayberg MR. Induction of a senescence-like phenotype in bovine aortic endothelial cells by ionizing radiation. Radiation Research. 2001 Sep;156(3):232–40.

85. Igarashi K, Sakimoto I, Kataoka K, Ohta K, Miura M. Radiation-induced senescence-like phenotype in proliferating and plateau-phase vascular endothelial cells. Exp Cell Res. 2007 Sep 10;313(15):3326–36.

86. Zhang K-J, Zhu Y, Sun H-Y, Huang L-F, Fu J-R, Liu W-L. Mechanism of radiation induced premature senescence of bone marrow stromal cells: experiment with murine bone marrow stromal cells. Zhonghua Yi Xue Za Zhi. 2006 Dec 26;86(48):3431–4.

87. Coppé J-P, Kauser K, Campisi J, Beauséjour CM. Secretion of vascular endothelial growth factor by primary human fibroblasts at senescence. J Biol Chem. 2006 Oct 6;281(40):29568–74.

88. Chung HY, Cesari M, Anton S, Marzetti E, Giovannini S, Seo AY, et al. Molecular inflammation: underpinnings of aging and age-related diseases. Ageing Res Rev. 2009 Jan;8(1):18–30.

89. Nagasawa H, Little JB. Induction of Sister Chromatid Exchanges by Extremely Low Doses of α-Particles. Cancer Research. 1992.

90. Seymour CB, Mothersill C. Delayed expression of lethal mutations and genomic instability in the progeny of human epithelial cells that survived in a bystander-killing environment. Radiat Oncol Investig. 1997;5(3):106–10.

91. Rzeszowska-Wolny J, Herok R, Widel M, Hancock R. X-irradiation and bystander effects induce similar changes of transcript profiles in most functional pathways in human melanoma cells. DNA Repair. 2009 Jun;8(6):732–8.

92. Rzeszowska-Wolny J, Przybyszewski WM, Widel M. European Journal of Pharmacology. European Journal of Pharmacology. Elsevier B.V; 2009 Dec 25;625(1-3):156–64.

93. Hei TK, Zhou H, Ivanov VN, Hong M, Lieberman HB, Brenner DJ, et al. Mechanism of radiation-induced bystander effects: a unifying model. Journal of Pharmacy and Pharmacology. 2008 Aug;60(8):943–50.

94. Yang H, Asaad N, Held KD. Medium-mediated intercellular communication is involved in bystander responses of X-ray-irradiated normal human fibroblasts. Oncogene. 2005 Jan 31;24(12):2096–103.

95. Zhou H, Suzuki M, Randers-Pehrson G, Vannais D, Chen G, Trosko JE, et al. Radiation risk to low fluences of alpha particles may be greater than we thought. Proc Natl Acad Sci USA. 2001 Dec 4;98(25):14410–5.

96. Morgan WF. Is there a common mechanism underlying genomic instability, bystander effects and other nontargeted effects of exposure to ionizing radiation? Oncogene. 2003 Oct 13;22(45):7094–9.

97. Zhou H, Ivanov VN, Lien Y-C, Davidson M, Hei TK. Mitochondrial function and nuclear factor-kappaB-mediated signaling in radiation-induced bystander effects. Cancer Research. 2008 Apr 1;68(7):2233–40.

98. Kim JH, Jenrow KA, Brown SL. Mechanisms of radiation-induced normal tissue toxicity and implications for future clinical trials. Radiat Oncol J. 2014 Sep;32(3):103–15.

99. Wright EG. Manifestations and mechanisms of non-targeted effects of ionizing radiation. Mutation Research/Fundamental and Molecular Mechanisms of Mutagenesis. 2010 May;687(1-2):28–33.

100. Wideł M, Przybyszewski W, Rzeszowska-Wolny J. [Radiation-induced bystander effect: the important part of ionizing radiation response. Potential clinical implications]. Postepy Hig Med Dosw (Online). 2009;63:377–88.

101. Del Regato JA. One hundred years of radiation oncology. 1995. 1 p.

102. DeVita VT, Lawrence TS, Rosenberg SA. Cancer: Principles & Practice of Oncology. Lippincott Williams & Wilkins; 2012. 1 p.

103. Stone HB, Coleman CN, Anscher MS, McBride WH. Effects of radiation on normal tissue: consequences and mechanisms. The Lancet Oncology. 2003 Sep;4(9):529–36.

104. Thames HD, Withers HR, Peters LJ, Fletcher GH. Changes in early and late radiation responses with altered dose fractionation: implications for dose-survival relationships. Int J Radiat Oncol Biol Phys. 1982 Feb;8(2):219–26.

105. Fowler JF, Fowler JF. The first James Kirk memorial lecture. What next in fractionated radiotherapy? The British Journal of Cancer Supplement. Nature Publishing Group; 1984;6:285.

106. Delanian S, Delanian S, Martin M, Martin M, Bravard A, Bravard A, et al. Abnormal phenotype of cultured fibroblasts in human skin with chronic radiotherapy damage. Radiotherapy and Oncology. 1998 Jun;47(3):255–61.

107. Baskar R. Cancer and Radiation Therapy: Current Advances and Future Directions. Int J Med Sci. 2012 Jan 11;9(3):193–9.

108. Saleh DB, Saleh DB, Liddington MI, Liddington MI, Loughenbury P, Loughenbury P, et al. Reconstruction of the irradiated perineum following extended abdomino-perineal excision for cancer - An algorithmic approach. J Plast Reconstr Aesthet Surg. 2012 Jun 29.

109. Butler EB, Teh BS, Grant WH III, Uhl BM, Kuppersmith RB, Chiu JK, et al. Smart (simultaneous modulated accelerated radiation therapy) boost: a new accelerated fractionation schedule for the treatment of head and neck cancer with intensity modulated radiotherapy. International Journal of Radiation Oncology*Biology*Physics. Elsevier; 1999 Aug;45(1):21–32.

110. Trotti A, Trotti A, Bellm LA, Bellm LA, Epstein JB, Epstein JB, et al. Mucositis incidence, severity and associated outcomes in patients with head and neck cancer receiving radiotherapy with or without chemotherapy: a systematic literature review. Radiotherapy and Oncology. 2003 Mar;66(3):253–62.

111. Bhide SA, Bhide SA, Newbold KL, Newbold KL, Harrington KJ, Harrington KJ, et al. Clinical evaluation of intensity-modulated radiotherapy for head and neck cancers. Br J Radiol. 2012 May;85(1013):487–94.

112. Gérard JP, Aubert B, Buchheit I. [Recommendation of the working group commissioned by the French Nuclear Safety Authority on stereotactic radiation therapy]. … : journal de la Societe …. 2012.

113. Schefter TE, Kavanagh BD, Timmerman RD, Cardenes HR, Baron A, Gaspar LE. A phase I trial of stereotactic body radiation therapy (SBRT) for liver metastases. Int J Radiat Oncol Biol Phys. 2005 Aug 1;62(5):1371–8.

114. McGarry RC, Papiez L, Williams M, Whitford T, Timmerman RD. Stereotactic body radiation therapy of early-stage non-small-cell lung carcinoma: phase I study. Int J Radiat Oncol Biol Phys. 2005 Nov 15;63(4):1010–5.

115. Salama JK, Kirkpatrick JP, Yin F-F. Stereotactic body radiotherapy treatment of extracranial metastases. Nature Reviews Clinical Oncology. 2012 Nov;9(11):654–65.

116. Lagerwaard FJ, Verstegen NE, Haasbeek CJA, Slotman BJ, Paul MA, Smit EF, et al. Outcomes of stereotactic ablative radiotherapy in patients with potentially operable stage I non-small cell lung cancer. Int J Radiat Oncol Biol Phys. 2012 May 1;83(1):348–53.

117. Milano MT, Katz AW, Zhang H, Okunieff P. Oligometastases treated with stereotactic body radiotherapy: long-term follow-up of prospective study. Int J Radiat Oncol Biol Phys. 2012 Jul 1;83(3):878–86.

118. Vallabhajosula S, Smith-Jones PM, Navarro V, Goldsmith SJ, Bander NH. Radioimmunotherapy of prostate cancer in human xenografts using monoclonal antibodies specific to prostate specific membrane antigen (PSMA): studies in nude mice. Prostate. 2004 Feb 1;58(2):145–55.

119. Dormand E-L, Banwell PE, Goodacre TE. Radiotherapy and wound

healing. Int Wound Journal. 2005 Jun;2(2):112–27.

120. Iwahira Y, Iwahira Y, Nagase T, Nagase T, Nakagami G, Nakagami G, et al. Histopathological comparisons of irradiated and non-irradiated breast skin from the same individuals. British Journal of Plastic Surgery. Elsevier Ltd; 2012 Nov 1;65(11):1496–505.

121. Herskind C. Fibroblast differentiation in subcutaneous fibrosis after postmastectomy radiotherapy. Acta Oncol. Informa UK Ltd UK; 2000;39(3):383–8.

122. Rodemann HP, Bamberg M. Cellular basis of radiation-induced fibrosis. Radiotherapy and Oncology. Elsevier; 2003 Jan 30;35(2):83–90.

123. Hill RP, Kaspler P, Griffin AM, O'Sullivan B, Catton C, Alasti H, et al. Studies of the in vivo radiosensitivity of human skin fibroblasts. Radiother Oncol. 2007 Jul;84(1):75–83.

124. Rodemann HP, Rodemann HP, Peterson HP, Peterson HP, Schwenke K, Schwenke K, et al. Terminal differentiation of human fibroblasts is induced by radiation. Scanning Microsc. 1991 Dec 1;5(4):1135–42; discussion1142–3.

125. Rodemann HP, Blaese MA. Responses of Normal Cells to Ionizing Radiation. Seminars in Radiation Oncology. 2007 Apr;17(2):81–8.

126. BAUER EA, UITTO J. COLLAGEN IN CUTANEOUS DISEASES. Int J Dermatol. 1979 May;18(4):251–70.

127. Oikarinen A, Autio P, Kiistala U, Risteli L, Risteli J. A New Method to Measure Type I and III Collagen Synthesis in Human Skin In Vivo: Demonstration of Decreased Collagen Synthesis After Topical Glucocorticoid Treatment. J Investig Dermatol. 1992 Feb;98(2):220–5.

128. P Autio TSMTIEJRTL. Demonstration of increased collagen synthesis in irradiated human skin in vivo. British Journal of Cancer. Nature Publishing Group; 1998 Jun 1;77(12):2331.

129. Martin M, Remy J, Daburon F. Abnormal proliferation and aging of cultured fibroblasts from pigs with subcutaneous fibrosis induced by gamma irradiation. J Invest Dermatol. Nature Publishing Group; 1989;93(4):497–500.

130. O'Reilly S, Ciechomska M, Cant R, Hügle T, van Laar JM. Interleukin-6, its role in fibrosing conditions. Cytokine & Growth Factor Reviews. 2012 Jun;23(3):99–107.

131. Rubin P, Finkelstein J, Shapiro D. Molecular biology mechanisms in the radiation induction of pulmonary injury syndromes: Interrelationship between the alveolar macrophage and the septal fibroblast. International Journal of Radiation Oncology*Biology*Physics. 1992 Jan;24(1):93–101.

132. Anscher MS, Anscher MS. The Irreversibility of Radiation-Induced Fibrosis: Fact or Folklore? 2005.

133. Avraham T, Clavin NW, Daluvoy SV, Fernandez J, Soares MA, Cordeiro AP, et al. Fibrosis Is a Key Inhibitor of Lymphatic Regeneration. Plast Reconstr Surg. 2009 Aug;124(2):438–50.

134. Walter M, Liang S, Ghosh S, Hornsby PJ, Li R. Interleukin 6 secreted from adipose stromal cells promotes migration and invasion of breast cancer cells. Oncogene. 2009 Jul 30;28(30):2745–55.

135. Walter M, Wright KT, Fuller HR, MacNeil S, Johnson WEB. Mesenchymal stem cell-conditioned medium accelerates skin wound healing: An in vitro study of fibroblast and keratinocyte scratch assays. Exp Cell Res. Elsevier; 2010;316(7):1271–81.

136. Metcalfe AD, Ferguson MWJ. Tissue engineering of replacement skin: the crossroads of biomaterials, wound healing, embryonic development, stem cells and regeneration. J R Soc Interface. 2007 Jun 22;4(14):413–37.

137. Diegelmann RF, Diegelmann RF, Evans MC, Evans MC. Wound healing: an overview of acute, fibrotic and delayed healing. Front Biosci. 2004.

138. Bragulla HH, Homberger DG. Structure and functions of keratin proteins in simple, stratified, keratinized and cornified epithelia. J Anat. 2009 Apr;214(4):516–59.

139. Goessler UR, Goessler UR, Bugert P, Bugert P, Kassner S, Kassner S, et al. In vitro analysis of radiation-induced dermal wounds. YMHN [Internet]. Elsevier Inc; 2010 Jun 1;142(6):845–50. Available from: http://oto.sagepub.com/lookup/doi/10.1016/j.otohns.2010.01.033

140. Sivan V, Sivan V, Vozenin-Brotons M-C, Vozenin-Brotons M-C, Tricaud Y, Tricaud Y, et al. Altered proliferation and differentiation of human epidermis in cases of skin fibrosis after radiotherapy. Int J Radiat Oncol Biol Phys. 2002 Jun;53(2):385–93.

141. Goh YY, Pal M, Chong HC, Zhu P, Tan MJ, Punugu L, et al. Angiopoietin-Like 4 Interacts with Integrins. AJPA. American Society for Investigative Pathology; 2010 Dec 29;177(6):2791–803.

142. Harfouche G, le T Martin M. Response of normal stem cells to ionizing radiation: A balance between homeostasis and genomic stability. Mutation Research-Reviews in Mutation Research. Elsevier B.V; 2010 Mar 31;704(1-3):167–74.

143. Rachidi W, Harfourche G, Lemaitre G, Amiot F, Vaigot P, Martin MT. Sensing radiosensitivity of human epidermal stem cells. Radiother Oncol. 2007 Jun;83(3):267–76.

144. Thiery JP, Acloque H, Huang RYJ, Nieto MA. Epithelial-Mesenchymal Transitions in Development and Disease. Cell. 2009 Nov;139(5):871–90.

145. Martin P, Martin P, Parkhurst SM, Parkhurst SM. Parallels between tissue repair and embryo morphogenesis. Development. 2004 Jul;131(13):3021–34.

146. Waelti ER, Waelti ER, Inaebnit SP, Inaebnit SP, Rast HP, Rast HP, et al. Co-culture of human keratinocytes on post-mitotic human dermal fibroblast feeder cells: production of large amounts of interleukin 6. J Invest Dermatol. 1992 May;98(5):805–8.

147. Smola H, Smola H, Thiekötter G, Thiekötter G, Fusenig NE, Fusenig NE. Mutual induction of growth factor gene expression by epidermal-dermal cell interaction. J Cell Biol. 1993 Jul;122(2):417–29.

148. Shi Y, Massagué J. Mechanisms of TGF-β signaling from cell membrane to the nucleus. Cell. Elsevier; 2003;113(6):685–700.

149. Xu Q, Wang L, Li H, Han Q, Li J, Qu X, et al. Mesenchymal stem cells play a potential role in regulating the establishment and maintenance of epithelial-mesenchymal transition in MCF7 human breast cancer cells by paracrine and induced autocrine TGF-β. Int J Oncol. 2012 Sep;41(3):959–68.

150. J H Levine HLMLIGLBN. Spatial and temporal patterns of immunoreactive transforming growth factor beta 1, beta 2, and beta 3 during excisional wound repair. Am J Pathol. American Society for Investigative Pathology; 1993 Aug 1;143(2):368.

151. Shah M, Shah M, Foreman DM, Foreman DM, Ferguson M, Ferguson M. Control of scarring in adult wounds by neutralising antibody to transforming growth factor β. The Lancet. Elsevier; 1992;339(8787):213–4.

152. ROBERTS A, ROBERTS A, TIAN F, TIAN F, BYFIELD S, BYFIELD S, et al. Smad3 is key to TGF-β-mediated epithelial-to-mesenchymal transition, fibrosis, tumor suppression and metastasis. Cytokine & Growth Factor Reviews. 2006 Feb;17(1-2):19–27.

153. Amendt C, Mann A, Schirmacher P, Blessing M. Resistance of keratinocytes to TGFbeta-mediated growth restriction and apoptosis induction accelerates re-epithelialization in skin wounds. J Cell Sci. 2002 May 15;115(Pt 10):2189–98.

154. Kleibeuker EA, Griffioen AW, Verheul HM, Ben J Slotman, Thijssen VL. Combining angiogenesis inhibition and radiotherapy: A double-edged sword. Drug Resistance Updates. Elsevier Ltd; 2012 Jun 1;15(3):173–82.

155. Imaizumi N, Imaizumi N, Monnier Y, Monnier Y, Hegi M, Hegi M, et al. Radiotherapy Suppresses Angiogenesis in Mice through TGF-

βRI/ALK5-Dependent Inhibition of Endothelial Cell Sprouting. PLoS ONE. Public Library of Science; 2010 Jun 11;5(6):e11084.

156. Gabriels K, Hoving S, Seemann I, Visser NL, Gijbels MJ, Pol JF, et al. Local heart irradiation of ApoE−/− mice induces microvascular and endocardial damage and accelerates coronary atherosclerosis. Radiotherapy and Oncology. 2012 Dec;105(3):358–64.

157. Fajardo LF. Fajardo: Morphology of radiation effects on normal tissues - Google Scholar. Principles and Practices of Radiation Oncology. 1992.

158. Fajardo LF. The pathology of ionizing radiation as defined by morphologic patterns*. Acta Oncol. 2005 Jan;44(1):13–22.

159. Sams A. Histological Changes in the Larger Blood Vessels of the Hind Limb of the Mouse after X-irradiation. Int J Radiat Biol. Informa UK Ltd UK; 1965 Jan;9(2):165–74.

160. Stewart FA, Heeneman S, Poele Te J, Kruse J, Russell NS, Gijbels M, et al. Ionizing radiation accelerates the development of atherosclerotic lesions in ApoE-/- mice and predisposes to an inflammatory plaque phenotype prone to hemorrhage. Am J Pathol. 2006 Feb;168(2):649–58.

161. Halle M, Gabrielsen A, Paulsson-Berne G, Gahm C, Agardh HE, Farnebo F, et al. Sustained inflammation due to nuclear factor-kappa B activation in irradiated human arteries. J Am Coll Cardiol. 2010 Mar 23;55(12):1227–36.

162. Li J, De Leon H, Ebato B, Cui J, Todd J, Chronos NAF, et al. Endovascular irradiation impairs vascular functional responses in noninjured pig coronary arteries. Cardiovascular Radiation Medicine. 2002 Jul;3(3-4):152–62.

163. Kirkpatrick JB. Pathogenesis of foam cell lesions in irradiated arteries. Am J Pathol. American Society for Investigative Pathology; 1967;50(2):291.

164. Milliat F, François A, Isoir M, Deutsch E, Tamarat R, Tarlet G, et al. Influence of Endothelial Cells on Vascular Smooth Muscle Cells Phenotype after Irradiation. Am J Pathol. American Society for Investigative Pathology; 2010 Dec 9;169(4):1484–95.

165. Durand E, Durand E. In Vivo Induction of Endothelial Apoptosis Leads to Vessel Thrombosis and Endothelial Denudation: A Clue to the Understanding of the Mechanisms of Thrombotic Plaque Erosion. Circulation. 2004 Jun 1;109(21):2503–6.

166. Jahroudi N, Ardekani AM, Greenberger JS. Ionizing irradiation increases transcription of the von Willebrand factor gene in endothelial cells. Blood. 1996 Nov 15;88(10):3801–14.

167. Zhou Q, Zhao Y, Li P, Bai X, Ruan C. Thrombomodulin as a marker of

radiation-induced endothelial cell injury. Radiation Research. 1992 Sep;131(3):285–9.

168. DeMichele MA, Minnear FL. Modulation of vascular endothelial permeability by thrombin. Semin Thromb Hemost. 1992;18(3):287–95.

169. Noda-Heiny H, Noda-Heiny H, Sobel BE, Sobel BE. Vascular smooth muscle cell migration mediated by thrombin and urokinase receptor. Am J Physiol. 1995 May;268(5 Pt 1):C1195–201.

170. Gillibert-Duplantier J, Neaud V, Blanc J-F, Bioulac-Sage P, Rosenbaum J. Thrombin inhibits migration of human hepatic myofibroblasts. ajpgiphysiologyorg.

171. Arciniegas E, Frid MG, Douglas IS, Stenmark KR. Perspectives on endothelial-to-mesenchymal transition: potential contribution to vascular remodeling in chronic pulmonary hypertension. AJP: Lung Cellular and Molecular Physiology. 2007 Apr 6;293(1):L1–L8.

172. Alitalo K. The lymphatic vasculature in disease. Nature Medicine. Nature Publishing Group; 2011 Nov 1;17(11):1371–80.

173. Ji RC. Lymphatic Endothelial Cells, Inflammatory Lymphangiogenesis, and Prospective Players. 2007 Sep 5;:1–11.

174. Ji RC. Characteristics of lymphatic endothelial cells in physiological and pathological conditions. Histol Histopathol. 2005 Jan;20(1):155–75.

175. Norrmén C, Tammela T, Petrova TV, Alitalo K. Biological Basis of Therapeutic Lymphangiogenesis. Circulation. 2011 Mar 28;123(12):1335–51.

176. Detry B, Bruyère F, Erpicum C, Paupert J, Lamaye F, Maillard C, et al. Digging deeper into lymphatic vessel formation in vitro and in vivo. BMC Cell Biology. BioMed Central Ltd; 2011 Jun 24;12(1):29.

177. James JM, Nalbandian A, Mukouyama Y-S. TGFβ signaling is required for sprouting lymphangiogenesis during lymphatic network development in the skin. Development. 2013 Aug 14.

178. Clavin NW, Avraham T, Fernandez J, Daluvoy SV, Soares MA, Chaudhry A, et al. TGF-beta1 is a negative regulator of lymphatic regeneration during wound repair. Am J Physiol Heart Circ Physiol. 2008 Nov;295(5):H2113–27.

179. Avraham T, Yan A, Zampell JC, Daluvoy SV, Haimovitz-Friedman A, Cordeiro AP, et al. Radiation therapy causes loss of dermal lymphatic vessels and interferes with lymphatic function by TGF-beta1-mediated tissue fibrosis. American Journal of Physiology - Cell Physiology. 2010 Sep;299(3):C589–605.

180. Shayan R, Inder R, Karnezis T, Caesar C, Paavonen K, Ashton MW, et

al. Tumor location and nature of lymphatic vessels are key determinants of cancer metastasis. Clin Exp Metastasis. 2013 Mar;30(3):345–56.

181. Kajiya K, Sawane M, Huggenberger R, Detmar M. Activation of the VEGFR-3 Pathway by VEGF-CAttenuates UVB-Induced Edema Formation and SkinInflammation by Promoting Lymphangiogenesis. Nature Publishing Group; 2008 Nov 13;129(5):1292–8.

182. Cui Y, Wilder J, Rietz C, Gigliotti A, Tang X, Shi Y, et al. Radiation-induced impairment in lung lymphatic vasculature. Lymphatic Research and Biology. 2014 Dec;12(4):238–50.

183. Baker A, Semple JL, Moore S, Johnston M. Lymphatic Function Is Impaired Following Irradiation of a Single Lymph Node. Lymphatic Research and Biology. 2014 Jun;12(2):76–88.

184. Jackowski S, Janusch M, Fiedler E, Marsch WC, Ulbrich EJ, Gaisbauer G, et al. Radiogenic Lymphangiogenesis in the Skin. AJPA. American Society for Investigative Pathology; 2010 Dec 8;171(1):338–48.

185. Cheung L, Han J, Beilhack A, Joshi S, Wilburn P, Dua A, et al. An experimental model for the study of lymphedema and its response to therapeutic lymphangiogenesis. BioDrugs. 2006;20(6):363–70.

186. de Toledo SM, Asaad N, Venkatachalam P, Li L, Howell RW, Spitz DR, et al. Adaptive Responses to Low-Dose/Low-Dose-Rate γ Rays in Normal Human Fibroblasts: The Role of Growth Architecture and Oxidative Metabolism. Radiation …. 2006.

187. Mortimer PS, Simmonds RH, Rezvani M, Robbins ME, Ryan TJ, Hopewell JW. Time-related changes in lymphatic clearance in pig skin after a single dose of 18 Gy of X rays. Br J Radiol. 1991 Dec;64(768):1140–6.

188. Edwards JM, Kinmonth JB. Lymphovenous shunts in man. Br Med J. 1969 Dec 6;4(5683):579–81.

189. Aebischer D, Iolyeva M, Halin C. The inflammatory response of lymphatic endothelium. Angiogenesis. 2013 Oct 24;17(2):383–93.

190. Michalowski A, Wheldon TE, Kirk J. Can cell survival parameters be deduced from non clonogenic assays of radiation damage to normal tissues? The British Journal of Cancer Supplement. Nature Publishing Group; 1984;6:257.

191. Hymes SR, Hymes SR, Strom EA, Strom EA, Fife C, Fife C. Radiation dermatitis: Clinical presentation, pathophysiology, and treatment 2006. Journal of the American Academy of Dermatology. 2006 Jan;54(1):28–46.

192. Michalowski A, Michalowski A. Effects of radiation on normal tissues: hypothetical mechanisms and limitations of in situ assays of

clonogenicity. Radiat Environ Biophys. 1981;19(3):157–72.

193. Wheldon TE, Michalowski AS, Kirk J. The effect of irradiation on function in self-renewing normal tissues with differing proliferative organisation. British Journal of Radiology. 1982 Oct 1;55(658):759–66.

194. Zacharias T, Dörr W, Enghardt W, Haberer T. Acute response of pig skin to irradiation with 12C-ions or 200 kV X-rays. Acta …. 1997.

195. Mohanti BK, Bansal M. Late sequelae of radiotherapy in adults. Support Care Cancer. 2005 Oct;13(10):775–80.

196. Dörr W, Hendry JH. Consequential late effects in normal tissues. Radiother Oncol. Elsevier; 2001;61(3):223–31.

197. Maciejewski B, Maciejewski B, Withers HR, Withers HR, Taylor JM, Taylor JM, et al. Dose fractionation and regeneration in radiotherapy for cancer of the oral cavity and oropharynx. Part 2. Normal tissue responses: acute and late effects. Int J Radiat Oncol Biol Phys. 1990 Jan;18(1):101–11.

198. Field SB, Law MP. The relationship between early and late radiation damage in rodents' skin. Int J Radiat Biol. Informa UK Ltd UK; 1976;30(6):557–64.

199. Denekamp J. Early and late radiation reactions in mouse feet. British Journal of Cancer. Nature Publishing Group; 1977;36(3):322.

200. Emami B. Tolerance of Normal Tissue to Therapeutic Radiation. Reports of Radiotherapy and Oncology [Internet]. 2013 ed. 2013 Apr 9;1(1):35–48. Available from: https://www.google.com.au/

201. Ryan JL. Ionizing Radiation: The Good, the Bad, and the Ugly. J Investig Dermatol. Nature Publishing Group; 2012 Jan 5;132(3):985–93.

202. Hoskin P. Secondary malignancies after radiotherapy. The Lancet Oncology , 3 (9) pp 577-578 (2002). The Lancet Oncology; 2002.

203. Epstein R, Hanham I, Dale R. Radiotherapy-induced second cancers: are we doing enough to protect young patients? Eur J Cancer. 1997 Apr;33(4):526–30.

204. Moskowitz CS, Chou JF, Wolden SL, Bernstein JL, Malhotra J, Novetsky Friedman D, et al. Breast cancer after chest radiation therapy for childhood cancer. J Clin Oncol. 2014 Jul 20;32(21):2217–23.

205. Rubin P, Casarett G. Clinical Radiation Pathology As Applied To Curative Radiotherapy. Cancer. 1968 Oct 1;22:767–78.

206. Milano MT, Constine LS, Okunieff P. Normal Tissue Tolerance Dose Metrics for Radiation Therapy of Major Organs. Seminars in Radiation Oncology. 2007 Apr;17(2):131–40.

207. Bentzen SM, Constine LS, Deasy JO, Eisbruch A, Jackson A, Marks LB, et al. Quantitative Analyses of Normal Tissue Effects in the Clinic (QUANTEC): An Introduction to the Scientific Issues. International Journal of Radiation Oncology*Biology*Physics. 2010 Mar;76(3):S3–S9.

208. Pavy JJ, Denekamp J, Letschert J, Littbrand B, Mornex F, Bernier J, et al. EORTC Late Effects Working Group. Late Effects toxicity scoring: the SOMA scale. Int J Radiat Oncol Biol Phys. 1995 Mar 30;31(5):1043–7.

209. National Cancer Institute. Cancer Therapy Evaluation Program, Common Terminology Criteria for Adverse Events, Version 3.0. 2006 Aug 9;:1–72. Available from: http://ctep.cancer.gov

210. Koenig TR, Wolff D, Mettler FA, Wagner LK. Skin injuries from fluoroscopically guided procedures: part 1, characteristics of radiation injury. AJR Am J Roentgenol. 2001 Jul;177(1):3–11.

211. Schultze-Mosgau S, Schultze-Mosgau S, Grabenbauer GG, Grabenbauer GG, Radespiel-Tröger M, Radespiel-Tröger M, et al. Vascularization in the transition area between free grafted soft tissues and pre-irradiated graft bed tissues following preoperative radiotherapy in the head and neck region. Head Neck. 2002 Jan;24(1):42–51.

212. Lee S, Thiele C. Factors associated with free flap complications after head and neck reconstruction and the molecular basis of fibrotic tissue rearrangement in preirradiated soft tissue. J Oral Maxillofac Surg. 2010 Sep;68(9):2169–78.

213. Mueller CK, Schultze-Mosgau S. Radiation-induced microenvironments – The molecular basis for free flap complications in the pre-irradiated field? Radiotherapy and Oncology. 2009 Dec;93(3):581–5.

214. Gurtner GC, Werner S, Barrandon Y, Longaker MT. Wound repair and regeneration. Nature. Nature Publishing Group; 2008;453(7193):314–21.

215. Lee WH, Lee WH, Warrington JP, Warrington JP, Sonntag WE, Sonntag WE, et al. Irradiation Alters MMP-2/TIMP-2 System and Collagen Type IV Degradation in Brain. International Journal of Radiation Oncology*Biology*Physics. 2012 Apr;82(5):1559–66.

216. Gu Q, Gu Q, Wang D, Wang D, Gao Y, Gao Y, et al. Expression of MMP1 in surgical and radiation-impaired wound healing and its effects on the healing process. J Environ Pathol Toxicol Oncol. 2002;21(1):71–8.

217. Wiltfang J, Wiltfang J, Ries J, Ries J, Neukam FW, Neukam FW, et al. Vascularization in the transition area between free grafted soft tissues and pre-irradiated graft bed tissues following preoperative radiotherapy in the head and neck …. Head Neck. 2002.

218. Chin MS, Freniere BB, Bonney CF, Lancerotto L, Saleeby JH, Lo Y-C,

et al. Skin Perfusion and Oxygenation Changes in Radiation Fibrosis. Plast Reconstr Surg. 2013 Apr;131(4):707–16.

219. Hoppe IC, Patel PP, Datiashvili RO. The Radial Forearm Fasciocutaneous Free Flap for Head and Neck Reconstruction. Plast Reconstr Surg. 2012 Feb;129(2):379e–380e.

220. Tibbs MK. Wound healing following radiation therapy: a review. Radiother Oncol. 1997 Mar 10;42(2):99–106.

221. Weintraub NL, Jones WK, Manka D. Understanding Radiation- Induced Vascular Disease*. J Am Coll Cardiol. Elsevier Inc; 2010 Mar 23;55(12):1237–9.

222. Dorresteijn LDA, Dorresteijn LDA, Kappelle AC, Kappelle AC, Scholz NMJ, Scholz NMJ, et al. Increased carotid wall thickening after radiotherapy on the neck. Eur J Cancer. 2005 May;41(7):1026–30.

223. Hooning MJ, Botma A, Aleman BMP, Baaijens MHA, Bartelink H, Klijn JGM, et al. Long-term risk of cardiovascular disease in 10-year survivors of breast cancer. J Natl Cancer Inst. 2007 Mar 7;99(5):365–75.

224. Hilbers FSM, Hilbers FSM, Boekel NB, Boekel NB, van den Broek AJ, van den Broek AJ, et al. Genetic variants in TGFβ-1 and PAI-1 as possible risk factors for cardiovascular disease after radiotherapy for breast cancer. Radiother Oncol. 2012 Jan;102(1):115–21.

225. Darby SC, Ewertz M, McGale P, Bennet AM, Blom-Goldman U, Brønnum D, et al. Risk of Ischemic Heart Disease in Women after Radiotherapy for Breast Cancer. N Engl J Med. 2013 Mar 14;368(11):987–98.

226. Adams MJ, Hardenbergh PH, Constine LS, Lipshultz SE. Radiation-associated cardiovascular disease. Crit Rev Oncol Hematol. 2003 Jan;45(1):55–75.

227. Jurado JA, Bashir R, Burket MW. Radiation-induced peripheral artery disease. Catheter Cardiovasc Interv. 2008 Oct 1;72(4):563–8.

228. Orklund TCB, Jiang D, Reilly S-J, Qi Y, Gahm C, Walker NG, et al. Increased long-term expression of pentraxin 3 in irradiated human arteries and veins compared to internal controls from free tissue transfers. Journal of Translational Medicine. Journal of Translational Medicine; 2013 Sep 23;11(1):1–1.

229. Whelan TJ, Julian J, Wright J, Jadad AR, Levine ML. Does Locoregional Radiation Therapy Improve Survival in Breast Cancer? A Meta-Analysis. Journal of Clinical …. 2000.

230. Group EBCTC. Favourable and unfavourable effects on long-term survival of radiotherapy for early breast cancer: an overview of the randomised trials. Lancet. 2000 May 20;355(9217):1757–70.

231. Carver JR, Shapiro CL, Ng A, Jacobs L, Schwartz C, Virgo KS, et al. American Society of Clinical Oncology clinical evidence review on the ongoing care of adult cancer survivors: cardiac and pulmonary late effects. J Clin Oncol. 2007 Sep 1;25(25):3991–4008.

232. Aleman BMP, van den Belt-Dusebout AW, Klokman WJ, Van't Veer MB, Bartelink H, van Leeuwen FE. Long-term cause-specific mortality of patients treated for Hodgkin's disease. J Clin Oncol. 2003 Sep 15;21(18):3431–9.

233. Hayes SC. Review of Research Evidence on Secondary Lymphoedema--Incidence, Prevention, Risk Factors and Treatment. 2008.

234. Szuba A, Rockson SG. Lymphedema: classification, diagnosis and therapy. Vascular medicine. 1998.

235. Rebegea L, Firescu D, Dumitru M, Anghel R. The incidence and risk factors for occurrence of arm lymphedema after treatment of breast cancer. Chirurgia (Bucur). 2015 Jan;110(1):33–7.

236. Warren LEG, Miller CL, Horick N, Skolny MN, Jammallo LS, Sadek BT, et al. The impact of radiation therapy on the risk of lymphedema after treatment for breast cancer: a prospective cohort study. Int J Radiat Oncol Biol Phys. 2014 Mar 1;88(3):565–71.

237. Committee MSA. Review of current practices and future directions in the diagnosis, prevention and treatment of lymphoedema in Australia (February 2004). Canberra: The Department of Health and …; 2006.

238. Armer JM, Stewart BR. Post-breast cancer lymphedema: incidence increases from 12 to 30 to 60 months. Lymphology. 2010 Sep;43(3):118–27.

239. DiSipio T, Rye S, Newman B, Hayes S. Incidence of unilateral arm lymphoedema after breast cancer: a systematic review and meta-analysis. The Lancet Oncology. 2013 May;14(6):500–15.

240. Tsai RJ, Dennis LK, Lynch CF, Snetselaar LG, Zamba GKD, Scott-Conner C. The risk of developing arm lymphedema among breast cancer survivors: a meta-analysis of treatment factors. Ann Surg Oncol. 2009 Jul;16(7):1959–72.

241. Tran T, Tran T, Miles D, Hill M, Lum SS. The impact of radiation on surgical outcomes of immediate breast reconstruction. Am Surg. 2011 Oct;77(10):1349–52.

242. Henderson MA, Burmeister BH, Ainslie J, Fisher R, Di Iulio J, Smithers BM, et al. Adjuvant lymph-node field radiotherapy versus observation only in patients with melanoma at high risk of further lymph-node field relapse after lymphadenectomy (ANZMTG 01.02/TROG 02.01): 6-year follow-up of a phase 3, randomised controlled trial. The Lancet Oncology. 2015 Sep;16(9):1049–60.

243. Cormier JN, Askew RL, Mungovan KS, Xing Y, Ross MI, Armer JM. Lymphedema beyond breast cancer: a systematic review and meta-analysis of cancer-related secondary lymphedema. Cancer. 2010 Nov 15;116(22):5138–49.

244. Chang DW, Kim S. Breast Reconstruction and Lymphedema. Plast Reconstr Surg. 2010 Jan;125(1):19–23.

245. Cummings RJ, Mitra S, Foster TH, Lord EM. Migration of skin dendritic cells in response to ionizing radiation exposure. Radiation Research. 2009 Jun;171(6):687–97.

246. Ji R-C. Lymphatic endothelial cells, lymphangiogenesis, and extracellular matrix. Lymphatic Research and Biology. 2006;4(2):83–100.

247. Mozes M, Papa MZ, Karasik A, Reshef A, Adar R. The role of infection in post-mastectomy lymphedema. - PubMed - NCBI. Surgery annual; 1982.

248. Kronowitz SJ, Robb GL. Radiation Therapy and Breast Reconstruction: A Critical Review of the Literature. Plast Reconstr Surg. 2009 Aug;124(2):395–408.

249. Kronowitz SJ. Current Status of Autologous Tissue–Based Breast Reconstruction in Patients Receiving Postmastectomy Radiation Therapy. Plast Reconstr Surg. 2012 Aug;130(2):282–92.

250. Momoh AO, Momoh AO, Ahmed R, Ahmed R, Kelley BP, Kelley BP, et al. A Systematic Review of Complications of Implant-based Breast Reconstruction with Prereconstruction and Postreconstruction Radiotherapy. Ann Surg Oncol. 2013 Oct 1.

251. Korwar V, Skillman J, Matey P. Skin reducing mastectomy and immediate reconstruction: the effect of radiotherapy on complications and patient reported outcomes. Eur J Surg Oncol. 2014 Apr;40(4):442–8.

252. Spear SL, Onyewu C. Staged breast reconstruction with saline-filled implants in the irradiated breast: recent trends and therapeutic implications. Plast Reconstr Surg. 2000 Mar;105(3):930–42.

253. Evans GR, Schusterman MA, Kroll SS, Miller MJ, Reece GP, Robb GL, et al. Reconstruction and the radiated breast: is there a role for implants? Plast Reconstr Surg. 1995;96(5):1111.

254. Whitfield GA, Whitfield GA, Horan G, Horan G, Irwin MS, Irwin MS, et al. Incidence of severe capsular contracture following implant-based immediate breast reconstruction with or without postoperative chest wall radiotherapy using 40 Gray in 15 fractions. Radiotherapy and Oncology. Elsevier Ireland Ltd; 2009 Jan 1;90(1):141–7.

255. Fischer JP, Basta MN, Shubinets V, Serletti JM, Fosnot J. A Systematic Meta-analysis of Prosthetic-Based Breast Reconstruction in Irradiated

Fields With or Without Autologous Muscle Flap Coverage. Annals of Plastic Surgery. 2014 Dec 19.

256. Lee K-T, Mun G-H. Prosthetic breast reconstruction in previously irradiated breasts: A meta-analysis. J Surg Oncol. 2015 Sep 16.

257. Rochlin DH, Jeong A-R, Goldberg L, Harris T, Mohan K, Seal S, et al. Postmastectomy radiation therapy and immediate autologous breast reconstruction: integrating perspectives from surgical oncology, radiation oncology, and plastic and reconstructive surgery. J Surg Oncol. 2015 Mar;111(3):251–7.

258. Gill PS, Hunt JP, Guerra AB, Dellacroce FJ, Sullivan SK, Boraski J, et al. A 10-year retrospective review of 758 DIEP flaps for breast reconstruction. Plast Reconstr Surg. 2004 Apr 1;113(4):1153–60.

259. Schaverien MV, Schaverien MV, Macmillan RD, Macmillan RD, McCulley SJ, McCulley SJ. Is immediate autologous breast reconstruction with postoperative radiotherapy good practice?: A systematic review of the literature. British Journal of Plastic Surgery. Elsevier Ltd; 2013 Jul 22;:1–15.

260. Tran NV, Tran NV, Chang DW, Chang DW, Gupta A, Gupta A, et al. Comparison of Immediate and Delayed Free TRAM Flap Breast Reconstruction in Patients Receiving Postmastectomy Radiation Therapy. Plast Reconstr Surg. 2001 Jul 1;108(1):78.

261. Kronowitz SJ, Kronowitz SJ, Robb GL, Robb GL. Breast Reconstruction with Postmastectomy Radiation Therapy: Current Issues. Plast Reconstr Surg. 2004 Sep;114(4):950–60.

262. Schechter NR, Strom EA, Perkins GH, Arzu I, McNeese MD, Langstein HN, et al. Immediate breast reconstruction can impact postmastectomy irradiation. Am J Clin Oncol. 2005 Oct;28(5):485–94.

263. Fosnot J, Fischer JP, Smartt JM, Low DW, Kovach SJ, Wu LC, et al. Does previous chest wall irradiation increase vascular complications in free autologous breast reconstruction? Plast Reconstr Surg. 2011 Feb;127(2):496–504.

264. Lee BT, Duggan MM, Keenan MT, Kamatkar S, Quinlan RM, Hergrueter CA, et al. Commonwealth of Massachusetts Board of Registration in Medicine Expert Panel on Immediate Implant-Based Breast Reconstruction Following Mastectomy for Cancer: Executive Summary, June 2011. ACS. Elsevier Inc; 2011 Dec 1;213(6):800–5.

265. Levendag PC, Braaksma M, Boonzaaijer M. Patients with head and neck cancer cured by radiation therapy: A survey of the dry mouth syndrome in long-term survivors. Head & …. 2002.

266. Mendenhall WM. Mandibular Osteoradionecrosis. J Clin Oncol. 2004

Dec 15;22(24):4867–8.

267. Bhandare N, Eisbruch A, Antonelli PJ, Mendenhall WM. Radiation-Induced Ototoxicity. In: … Late Effects of Cancer …. Berlin, Heidelberg: Springer Berlin Heidelberg; 2013. pp. 109–39. (Medical Radiology).

268. Russell NS, Hoving S, Heeneman S, Hage JJ, Woerdeman LAE, de Bree R, et al. Novel insights into pathological changes in muscular arteries of radiotherapy patients. Radiother Oncol. 2009 Sep;92(3):477–83.

269. Cunha SSD, Cunha SSD, Sarmento VA, Sarmento VA, Ramalho LMP, Ramalho LMP, et al. Effects of Radiotherapy on Bone Tissue. Radiol Bras. 2007;40(3):189–92.

270. Herle P, Shukla L, Morrison WA, Shayan R. Preoperative radiation and free flap outcomes for head and neck reconstruction: a systematic review and meta-analysis. ANZ Journal of Surgery. 2015 Mar 1;85(3):121–7.

271. Strander H, Turesson I, Cavallin-ståhl E. A Systematic Overview of Radiation Therapy Effects in Soft Tissue Sarcomas. Acta Oncol. 2003 Jan;42(5-6):516–31.

272. Bujko K, Suit HD, Springfield DS, Convery K. Wound healing after preoperative radiation for sarcoma of soft tissues. Surg Gynecol Obstet. 1993 Feb;176(2):124–34.

273. Davis AM, O'Sullivan B, Turcotte R, Bell R, Catton C, Chabot P, et al. Late radiation morbidity following randomization to preoperative versus postoperative radiotherapy in extremity soft tissue sarcoma. Radiother Oncol. 2005 Apr;75(1):48–53.

274. Akudugu JM, Akudugu JM, Bell RS, Bell RS, Catton C, Catton C, et al. Wound healing morbidity in STS patients treated with preoperative radiotherapy in relation to in vitro skin fibroblast radiosensitivity, proliferative capacity and TGF-β activity. Radiotherapy and Oncology. 2006 Jan;78(1):17–26.

275. Begg AC, Stewart FA, Vens C. Strategies to improve radiotherapy with targeted drugs. Nature Reviews Cancer. 2011 Apr;11(4):239–53.

276. Marchetti F, Coleman MA, Jones IM, Wyrobek AJ. Candidate protein biodosimeters of human exposure to ionizing radiation. Int J Radiat Biol. 2006 Jan;82(9):605–39.

277. Müller K, Meineke V. Radiation-induced alterations in cytokine production by skin cells. Strahlenther Onkol [Internet]. 2007 Apr;35(4 Suppl 1):96–104. Available from: http://eutils.ncbi.nlm.nih.gov/entrez/eutils/elink.fcgi?dbfrom=pubmed&id=17379094&retmode=ref&cmd=prlinks

278. Haydont V, Riser BL, Aigueperse J, Vozenin-Brotons MC. Specific

signals involved in the long-term maintenance of radiation-induced fibrogenic differentiation: a role for CCN2 and low concentration of TGF- 1. AJP: Cell Physiology. 2008 Apr 9;294(6):C1332–41.

279. Haydont V, Mathé D, Bourgier C, Abdelali J, Aigueperse J, Bourhis J, et al. Induction of CTGF by TGF-β1 in normal and radiation enteritis human smooth muscle cells: Smad/Rho balance and therapeutic perspectives. Radiotherapy and Oncology. 2005 Aug;76(2):219–25.

280. Grose R, Werner S. Wound-Healing Studies in Transgenic and Knockout Mice. Molecular Biotechnology. 2004;28(2):147–66.

281. AIHW. an overview 2012. 2012 Nov 13;:1–215.

282. Randall K, Coggle JE. Expression of transforming growth factor-beta 1 in mouse skin during the acute phase of radiation damage. Int J Radiat Biol. 1995 Sep;68(3):301–9.

283. IMHE. Institute for Health Metrics and Evaluation. 2014 ed. IMHE, University of Washington, Seattle, WA; 2014 Jan 1. Available from: http://www.healthdata.org

284. Lin C-S, Xin Z-C, Deng C-H, Ning H, Lin G, Lue TF. Defining adipose tissue-derived stem cells in tissue and in culture. Histol Histopathol. 2010 Jun;25(6):807–15.

285. Tan AR, Alexe G, Reiss M. Transforming growth factor-β signaling: emerging stem cell target in metastatic breast cancer? Breast Cancer Res Treat. Springer; 2009;115(3):453–95.

286. Bernstein EF, Harisiadis L, Salomon G, Norton J, Sollberg S, UITTO J, et al. Transforming Growth Factor-beta Improves Healing of Radiation-Impaired Wounds. J Investig Dermatol. 1991 Sep;97(3):430–4.

287. Yan A, Avraham T, Zampell JC, Haviv YS, Weitman E, Mehrara BJ. Adipose-derived stem cells promote lymphangiogenesis in response to VEGF-C stimulation or TGF-β1 inhibition. Future Oncology. 2011 Dec;7(12):1457–73.

288. Cawthorn WP, Scheller EL, MacDougald OA. Adipose tissue stem cells meet preadipocyte commitment: going back to the future. The Journal of Lipid Research. 2012 Jan 9;53(2):227–46.

289. Harburger DS, Calderwood DA. Integrin signalling at a glance. 2009.

290. White DP, White DP, Caswell PT, Caswell PT, Norman JC, Norman JC. v 3 and 5 1 integrin recycling pathways dictate downstream Rho kinase signaling to regulate persistent cell migration. J Cell Biol. 2007 May 7;177(3):515–25.

291. Cordes N, Cordes N, Seidler J, Seidler J, Durzok R, Durzok R, et al. β1-integrin-mediated signaling essentially contributes to cell survival after

radiation-induced genotoxic injury. Oncogene. 2005 Oct 10;25(9):1378–90.

292. Tayeb MA, Skalski M, Cha MC, Kean MJ, Scaife M, Coppolino MG. Inhibition of SNARE-mediated membrane traffic impairs cell migration. Exp Cell Res. 2005 Apr 15;305(1):63–73.

293. Raftopoulou M, Hall A. Cell migration: Rho GTPases lead the way. Dev Biol. 2004.

294. Avraamides CJ, Garmy-Susini B, Varner JA. Integrins in angiogenesis and lymphangiogenesis. Nature Reviews Cancer. 2008 May 22;8(8):604–17.

295. Zhang X, Groopman JE, Wang JF. Extracellular matrix regulates endothelial functions through interaction of VEGFR-3 and integrin alpha5beta1. J Cell Physiol. 2005 Jan;202(1):205–14.

296. Vlahakis NE, Young BA, Atakilit A, Sheppard D. The Lymphangiogenic Vascular Endothelial Growth Factors VEGF-C and -D Are Ligands for the Integrin α9β1. Journal of Biological Chemistry. 2005 Feb 4;280(6):4544–52.

297. Abdollahi A. Inhibition of v 3 Integrin Survival Signaling Enhances Antiangiogenic and Antitumor Effects of Radiotherapy. Clinical Cancer Research. 2005 Sep 1;11(17):6270–9.

298. Hynes RO. Integrins: bidirectional, allosteric signaling machines. Cell. 2002 Sep 20;110(6):673–87.

299. Lafuma C, Nabout El RA, Crechet F, Hovnanian A, Martin M. Expression of 72-kDa Gelatinase (MMP-2), Collagenase (MMP-1), and Tissue Metalloproteinase Inhibitor (TIMP) in Primary Pig Skin Fibroblast Cultures Derived from Radiation-Induced Skin Fibrosis. J Investig Dermatol. 1994 Jun;102(6):945–50.

300. Haubner F, Ohmann E, Pohl F, Pohl F, Strutz JR, Gassner HG. Wound healing after radiation therapy: Review of the literature. Radiation Oncology [Internet]. Radiation Oncology; 2012 Sep 24;7(1):1–1. Available from: http://www.ro-journal.com/content/pdf/1748-717X-7-162.pdf

301. Gieringer M. Radiotherapy and wound healing: Principles, management and prospects (Review). Oncol Rep. 2011 May 25.

302. Yoo HG, Shin BA, Park JS, Lee KH, Chay KO. IL-1β induces MMP-9 via reactive oxygen species and NF-κB in murine macrophage RAW 264.7 cells. Biochemical and …. 2002.

303. Ebrahimian TG, Squiban C, Roque T, Lugo-Martinez H, Hneino M, Buard V, et al. Plasminogen activator inhibitor-1 controls bone marrow-derived cells therapeutic effect through MMP9 signaling: role in

physiological and pathological wound healing. Stem Cells. 2012 Jul;30(7):1436–46.

304. Rutkowski JM, Moya M, Johannes J, Goldman J, Swartz MA. Secondary lymphedema in the mouse tail: Lymphatic hyperplasia, VEGF-C up-regulation, and the protective role of MMP-9. Microvascular Research. 2006 Nov;72(3):161–71.

305. Hallahan D, Kuchibhotla J, Wyble C. Cell adhesion molecules mediate radiation-induced leukocyte adhesion to the vascular endothelium. Cancer Research. 1996 Nov 15;56(22):5150–5.

306. Handschel J, Prott FJ, Sunderkötter C, Metze D, Meyer U, Joos U, et al. Irradiation induces increase of adhesion molecules and accumulation of beta2-integrin-expressing cells in humans. Int J Radiat Oncol Biol Phys. 1999 Sep 1;45(2):475–81.

307. Heckmann M, Douwes K, Peter R, Degitz K. Vascular activation of adhesion molecule mRNA and cell surface expression by ionizing radiation. Exp Cell Res. 1998 Jan 10;238(1):148–54.

308. Prabhakarpandian B, Goetz DJ, Swerlick RA, Chen X, Kiani MF. Expression and functional significance of adhesion molecules on cultured endothelial cells in response to ionizing radiation. Microcirculation. 2001 Oct;8(5):355–64.

309. Jang Y, Lincoff AM, Plow EF, Topol EJ. Cell adhesion molecules in coronary artery disease. J Am Coll Cardiol. Journal of the American College of Cardiology; 1994 Dec 1;24(7):1591–601.

310. Balbay Y, Tikiz H, Baptiste RJ, Ayaz S, Saşmaz H, Korkmaz S. Circulating interleukin-1 beta, interleukin-6, tumor necrosis factor-alpha, and soluble ICAM-1 in patients with chronic stable angina and myocardial infarction. Angiology. 2001 Feb;52(2):109–14.

311. Gaugler M-H, Vereycken-Holler V, Squiban C, Vandamme M, Vozenin-Brotons M-C, Benderitter M. Pravastatin limits endothelial activation after irradiation and decreases the resulting inflammatory and thrombotic responses. Radiation Research. 2005 May;163(5):479–87.

312. Hallahan DE, Virudachalam S. Intercellular adhesion molecule 1 knockout abrogates radiation induced pulmonary inflammation. 1997.

313. Panés J, Anderson DC, Miyasaka M, Neil Granger D. Role of leukocyte-endothelial cell adhesion in radiation-induced microvascular dysfunction in rats. Gastroenterology. 1995 Jun;108(6):1761–9.

314. Chang Y-L, Chen C-L, Kuo C-L, Chen B-C, You J-S. Glycyrrhetinic acid inhibits ICAM-1 expression via blocking JNK and NF-κB pathways in TNF-α-activated endothelial cells. Nature Publishing Group. Nature Publishing Group; 2010 Apr 26;31(5):546–53.

315. Achen MG, Jeltsch M, Kukk E, Mäkinen T, Vitali A, Wilks AF, et al. Vascular endothelial growth factor D (VEGF-D) is a ligand for the tyrosine kinases VEGF receptor 2 (Flk1) and VEGF receptor 3 (Flt4). Proc Natl Acad Sci USA. 1998 Jan 20;95(2):548–53.

316. Joukov V, Pajusola K, Kaipainen A, Chilov D, Lahtinen I, Kukk E, et al. A novel vascular endothelial growth factor, VEGF-C, is a ligand for the Flt4 (VEGFR-3) and KDR (VEGFR-2) receptor tyrosine kinases. EMBO J. 1996 Jan 15;15(2):290–8.

317. Iyer S, Leonidas DD, Swaminathan GJ. The crystal structure of human placenta growth factor-1 (PlGF-1), an angiogenic protein, at 2.0 Å resolution. Journal of Biological …. 2001.

318. Muller YA, Li B, Christinger HW, Wells JA, Cunningham BC, de Vos AM. Vascular endothelial growth factor: crystal structure and functional mapping of the kinase domain receptor binding site. Proc Natl Acad Sci USA. 1997 Jul 8;94(14):7192–7.

319. Achen MG, Gad JM, Stacker SA, Wilks AF. Placenta growth factor and vascular endothelial growth factor are co-expressed during early embryonic development. Growth Factors. 1997;15(1):69–80.

320. De Falco S, Gigante B, Persico MG. Structure and Function of Placental Growth Factor. Trends in cardiovascular medicine. 2002.

321. Joukov V, Sorsa T, Kumar V, Jeltsch M, Claesson-Welsh L, Cao Y, et al. Proteolytic processing regulates receptor specificity and activity of VEGF-C. EMBO J. 1997 Jul 1;16(13):3898–911.

322. Stacker SA, Stenvers K, Caesar C, Vitali A, Domagala T, Nice E, et al. Biosynthesis of Vascular Endothelial Growth Factor-D Involves Proteolytic Processing Which Generates Non-covalent Homodimers. Journal of Biological Chemistry. 1999 Nov 5;274(45):32127–36.

323. McColl BK, Stacker SA, Achen MG. Molecular regulation of the VEGF family -- inducers of angiogenesis and lymphangiogenesis. APMIS. 2004 Jul;112(7-8):463–80.

324. Harris NC, Paavonen K, Davydova N, Roufail S, Sato T, Zhang Y-F, et al. Proteolytic processing of vascular endothelial growth factor-D is essential for its capacity to promote the growth and spread of cancer. FASEB J. 2011 Aug;25(8):2615–25.

325. Ji R-C. Lymphatic Endothelial Cells, Lymphedematous Lymphangiogenesis, and Molecular Control of Edema Formation. Lymphatic Research and Biology. 2008 Dec;6(3-4):123–37.

326. Skobe M, Hawighorst T, Jackson DG, Prevo R, Janes L, Velasco P, et al. Induction of tumor lymphangiogenesis by VEGF-C promotes breast cancer metastasis. Nature Medicine. 2001 Feb;7(2):192–8.

327. Goldman J, Le TX, Skobe M, Swartz MA. Overexpression of VEGF-C causes transient lymphatic hyperplasia but not increased lymphangiogenesis in regenerating skin. Circ Res. 2005 Jun 10;96(11):1193–9.

328. Zampell JC, Zampell JC, Avraham T, Avraham T, Yoder N, Yoder N, et al. Lymphatic function is regulated by a coordinated expression of lymphangiogenic and anti-lymphangiogenic cytokines. American Journal of …. 2012.

329. Nakamura K, Rockson SG. Molecular Targets for Therapeutic Lymphangiogenesis in Lymphatic Dysfunction and Disease. Lymphatic Research and Biology. 2008 Dec;6(3-4):181–9.

330. MD MY, MD NI, Date F, Shibata N, MD HM, MD KY, et al. Macrophages participate in lymphangiogenesis in idiopathic diffuse alveolar damage through CCL19-CCR7 signal. Human Pathology. Elsevier Inc; 2009 Nov 1;40(11):1553–63.

331. Ran S, Montgomery KE. Macrophage-Mediated Lymphangiogenesis: The Emerging Role of Macrophages as Lymphatic Endothelial Progenitors. Cancers. 2012 Dec;4(4):618–57.

332. Marigo I, Dazzi F. The immunomodulatory properties of mesenchymal stem cells. Semin Immunopathol. 2011 Apr 19;33(6):593–602.

333. Meeren AV, Bertho JM, Vandamme M, Gaugler MH. Ionizing radiation enhances IL-6 and IL-8 production by human endothelial cells. Mediators Inflamm. 1997;6(3):185–93.

334. Koike M, Shiomi T, Koike A. Identification of Skin injury-related genes induced by ionizing radiation in human keratinocytes using cDNA microarray. Journal of Radiation Research. 2005 Jun;46(2):173–84.

335. Liu W, Ding I, Chen K, Olschowka J, Xu J, Hu D, et al. Interleukin 1β (IL1B) Signaling is a Critical Component of Radiation-Induced Skin Fibrosis. Radiation Research. 2006 Feb;165(2):181–91.

336. Di Maggio FM, Minafra L, Forte GI, Cammarata FP, Lio D, Messa C, et al. Portrait of inflammatory response to ionizing radiation treatment. J Inflamm (Lond). 2015;12:14.

337. Janko M, Ontiveros F, Fitzgerald TJ, Deng A, DeCicco M, Rock KL. IL-1 Generated Subsequent to Radiation-Induced Tissue Injury Contributes to the Pathogenesis of Radiodermatitis. Radiation Research. 2012 Sep;178(3):166–72.

338. Brach MA, Gruss HJ, Kaisho T, Asano Y, Hirano T, Herrmann F. Ionizing radiation induces expression of interleukin 6 by human fibroblasts involving activation of nuclear factor-kappa B. J Biol Chem. 1993 Apr 25;268(12):8466–72.

339. Siva S, MacManus M, Kron T, Best N, Smith J, Lobachevsky P, et al. A pattern of early radiation-induced inflammatory cytokine expression is associated with lung toxicity in patients with non-small cell lung cancer. PLoS ONE. 2014;9(10):e109560.

340. Martin D, Galisteo R, Gutkind JS. CXCL8/IL8 stimulates vascular endothelial growth factor (VEGF) expression and the autocrine activation of VEGFR2 in endothelial cells by activating NFkappaB through the CBM (Carma3/Bcl10/Malt1) complex. J Biol Chem. 2009 Mar 6;284(10):6038–42.

341. Choi I, Lee YS, Chung HK, Choi D, Ecoiffier T, Lee HN, et al. Interleukin-8 reduces post-surgical lymphedema formation by promoting lymphatic vessel regeneration. Angiogenesis. 2012 Sep 4;16(1):29–44.

342. Burns JM. A novel chemokine receptor for SDF-1 and I-TAC involved in cell survival, cell adhesion, and tumor development. Journal of Experimental Medicine. 2006 Sep 5;203(9):2201–13.

343. Sánchez-Martín L, Sánchez-Mateos P, Cabañas C. CXCR7 impact on CXCL12 biology and disease. Trends in Molecular Medicine. Elsevier Ltd; 2013 Jan 1;19(1):12–22.

344. Drury LJ, Ziarek JJ, Gravel S, Veldkamp CT, Takekoshi T, Hwang ST, et al. Monomeric and dimeric CXCL12 inhibit metastasis through distinct CXCR4 interactions and signaling pathways. Proceedings of the National Academy of Sciences. 2011 Oct 25;108(43):17655–60.

345. Sun X, Cheng G, Hao M, Zheng J, Zhou X, Zhang J, et al. CXCL12 / CXCR4 / CXCR7 chemokine axis and cancer progression. Cancer Metastasis Rev. 2010 Dec;29(4):709–22.

346. Ponomaryov T, Peled A, Petit I, Taichman RS, Habler L, Sandbank J, et al. Induction of the chemokine stromal-derived factor-1 following DNA damage improves human stem cell function. J Clin Invest. 2000 Dec;106(11):1331–9.

347. Libert F, Parmentier M, Lefort A, Dinsart C, Van Sande J, Maenhaut C, et al. Selective amplification and cloning of four new members of the G protein-coupled receptor family. Science. 1989 May 5;244(4904):569–72.

348. Thelen M, Thelen S. CXCR7, CXCR4 and CXCL12: an eccentric trio? Journal of Neuroimmunology. 2008 Jul 31;198(1-2):9–13.

349. Sánchez-Alcañiz JA, Haege S, Mueller W, Pla R, Mackay F, Schulz S, et al. Cxcr7 Controls Neuronal Migrationby Regulating Chemokine Responsiveness. Neuron. Elsevier Inc; 2011 Jan 13;69(1):77–90.

350. Singh RK, Lokeshwar BL. The IL-8-Regulated Chemokine Receptor CXCR7 Stimulates EGFR Signaling to Promote Prostate Cancer Growth. Cancer Research. 2011 Apr 29;71(9):3268–77.

351. Levoye A, Balabanian K, Baleux F, Bachelerie F, Lagane B. CXCR7 heterodimerizes with CXCR4 and regulates CXCL12-mediated G protein signaling. Blood. 2009 Jun 11;113(24):6085–93.

352. Dambly-Chaudière C, Cubedo N, Ghysen A. Control of cell migration in the development of the posterior lateral line: antagonistic interactions between the chemokine receptors CXCR4 and CXCR7/RDC1. BMC Dev Biol. 2007;7(1):23.

353. Boldajipour B, Mahabaleshwar H, Kardash E, Reichman-Fried M, Blaser H, Minina S, et al. Control of Chemokine-Guided Cell Migration by Ligand Sequestration. Cell. 2008 Feb;132(3):463–73.

354. Kraemer A, Kraemer A, Anastasov N, Anastasov N, Angermeier M, Angermeier M, et al. MicroRNA-Mediated Processes are Essential for the Cellular Radiation Response. Radiation Research. 2011 Nov;176(5):575–86.

355. Wagner-Ecker M, Wagner-Ecker M, Schwager C, Schwager C, Wirkner U, Wirkner U, et al. MicroRNA expression after ionizing radiation in human endothelial cells. Radiat Oncol. 2010;5(1):25.

356. Kapur SK, Katz AJ. Review of the adipose derived stem cell secretome. Biochimie. Elsevier Masson SAS; 2013 Dec 1;95(12):2222–8.

357. Skalnikova HK. Proteomic techniques for characterisation of mesenchymal stem cell secretome. Biochimie. Elsevier Masson SAS; 2013 Dec 1;95(12):2196–211.

358. Valadi H, Ekström K, Bossios A, Sjöstrand M, Lee JJ, Lötvall JO. Exosome-mediated transfer of mRNAs and microRNAs is a novel mechanism of genetic exchange between cells. Nat Cell Biol. 2007 Jun;9(6):654–9.

359. Bennett MH, Feldmeier J, Hampson NB, Smee R, Milross C. Hyperbaric oxygen therapy for late radiation tissue injury. Bennett MH, editor. Vol. 22. Chichester, UK: John Wiley & Sons, Ltd; 2016. 1 p.

360. Marx RE, Ehler WJ, Tayapongsak P, Pierce LW. Relationship of oxygen dose to angiogenesis induction in irradiated tissue. Am J Surg. 1990 Nov;160(5):519–24.

361. Delanian S, Porcher R, Balla-Mekias S. POST data. Journal of Clinical …. 2003.

362. Greenberger JS, Epperly M. Bone Marrow–Derived Stem Cells and Radiation Response. YSRAO. Elsevier Inc; 2009 Apr 1;19(2):133–9.

363. Lombaert IMA, Wierenga PK, Kok T, Kampinga HH, deHaan G, Coppes RP. Mobilization of bone marrow stem cells by granulocyte colony-stimulating factor ameliorates radiation-induced damage to salivary glands. Clin Cancer Res. 2006 Mar 15;12(6):1804–12.

364. Poglio S, Galvani S, Bour S, André M, Prunet-Marcassus B, Pénicaud L, et al. Adipose tissue sensitivity to radiation exposure. Am J Pathol. 2009 Jan;174(1):44–53.

365. Mizuno H, Tobita M, Uysal AC. Concise review: Adipose-derived stem cells as a novel tool for future regenerative medicine. Stem Cells. 2012 May;30(5):804–10.

366. Zuk PA, Zhu M, Ashjian P, De Ugarte DA, Huang JI, Mizuno H, et al. Human Adipose Tissue Is a Source of Multipotent Stem Cells. Molecular Biology of the Cell. 2002 Dec;13:4279–95.

367. Ross RJ, Shayan R, Mutimer KL, Ashton MW. Autologous Fat Grafting: Current State of the Art and Critical Review. Annals of Plastic Surgery. 2014 ed. 2014 Sep 1;73(3):352–7.

368. Serra-Renom JM, Muñoz-Olmo JL, Serra-Mestre JM. Fat grafting in postmastectomy breast reconstruction with expanders and prostheses in patients who have received radiotherapy: formation of new subcutaneous tissue. Plast Reconstr Surg. 2010 Jan;125(1):12–8.

369. Tremolada C, Palmieri G, Ricordi C. Adipocyte Transplantation and Stem Cells: Plastic Surgery Meets Regenerative Medicine. Cell Transplantation. Cognizant Communication Corporation; 2010 Oct 1;19(10):1217–23.

370. Coleman SR. Structural fat grafts: the ideal filler? Clin Plast Surg. 2001 Jan;28(1):111–9.

371. Zuk PA, Zhu M, Mizuno H, Huang J, Futrell JW, Katz AJ, et al. Multilineage cells from human adipose tissue: implications for cell-based therapies. Tissue Eng. 2001 Apr;7(2):211–28.

372. Tabit CJ, Slack GC, Fan K, Wan DC, Bradley JP. Fat Grafting Versus Adipose-Derived Stem Cell Therapy: Distinguishing Indications, Techniques, and Outcomes. Aesthetic Plast Surg. 2011 Nov 9;36(3):704–13.

373. Rigotti G, Marchi A, Galiè M, Baroni G, Benati D, Krampera M, et al. Clinical Treatment of Radiotherapy Tissue Damage by Lipoaspirate Transplant: A Healing Process Mediated by Adipose-Derived Adult Stem Cells. Plast Reconstr Surg. 2007 Apr;119(5):1409–22.

374. Mizuno H, Hyakusoku H. Fat Grafting to the Breast and Adipose-Derived Stem Cells: Recent Scientific Consensus and Controversy. Aesthetic Surgery Journal. 2010 Jul 2;30(3):381–7.

375. Akita S, Yoshimoto H, Ohtsuru A, Hirano A, Yamashita S. Autologous adipose-derived regenerative cells are effective for chronic intractable radiation injuries. Radiation Protection Dosimetry. 2012 Sep 28;151(4):656–60.

376. Suga H, Eto H, Aoi N, Kato H, Araki J, Doi K, et al. Adipose tissue remodeling under ischemia: death of adipocytes and activation of stem/progenitor cells. Plast Reconstr Surg. 2010 Dec;126(6):1911–23.

377. Heimburg DV, Hemmrich K, Zachariah S, Staiger H, Pallua N. Oxygen consumption in undifferentiated versus differentiated adipogenic mesenchymal precursor cells. Respiratory Physiology & Neurobiology. 2005 Apr;146(2-3):107–16.

378. Thanik VD, Chang CC, Lerman OZ, Allen RJ, Nguyen PD, Saadeh PB, et al. A murine model for studying diffusely injected human fat. Plast Reconstr Surg. 2009 Jul;124(1):74–81.

379. Zhu M, Zhou Z, Chen Y, Schreiber R, Ransom JT, Fraser JK, et al. Supplementation of Fat Grafts With Adipose-Derived Regenerative Cells Improves Long-Term Graft Retention. Annals of Plastic Surgery. 2010 Feb;64(2):222–8.

380. Butala P, Sultan SM, Davidson EH, Crawford JL, Szpalski C, Knobel D, et al. AUGMENTATION OF FAT GRAFT SURVIVAL WITH PROGENITOR CELL MOBILIZATION. Plast Reconstr Surg. 2010 Jun;125(Supplement):12.

381. Phinney DG, Prockop DJ. Concise Review: Mesenchymal Stem/Multipotent Stromal Cells: The State of Transdifferentiation and Modes of Tissue Repair-Current Views. Stem Cells. 2007 Nov;25(11):2896–902.

382. Haubner F, Eto H, Leyh M, Kato H, Ohmann E, Suga H, et al. The fate of adipocytes after nonvascularized fat grafting: evidence of early death and replacement of adipocytes. Plast Reconstr Surg. 2012 May;129(5):1081–92.

383. Sterodimas A, de Faria J, Nicaretta B, Pitanguy I. Tissue engineering with adipose-derived stem cells (ADSCs): Current and future applications. British Journal of Plastic Surgery. Elsevier Ltd; 2010 Nov 1;63(11):1886–92.

384. Wang WZ, Fang X-H, Williams SJ, Stephenson LL, Baynosa RC, Wong N, et al. Analysis for apoptosis and necrosis on adipocytes, stromal vascular fraction, and adipose-derived stem cells in human lipoaspirates after liposuction. Plast Reconstr Surg. 2013 Jan;131(1):77e–85e.

385. Martin-Padura I, Gregato G, Marighetti P, Mancuso P, Calleri A, Corsini C, et al. The white adipose tissue used in lipotransfer procedures is a rich reservoir of CD34+ progenitors able to promote cancer progression. Cancer Research. 2012 Jan 1;72(1):325–34.

386. Krumboeck A, Pietro Giovanoli, Plock JA. Fat grafting and stem cell enhanced fat grafting to the breast under oncological aspects - Recommendations for patient selection. The Breast. 2013 ed. Elsevier

Ltd; 2013 Jun 13;:1–6.

387. Yoshimura K, Sato K, Aoi N, Kurita M, Hirohi T, Harii K. Cell-Assisted Lipotransfer for Cosmetic Breast Augmentation: Supportive Use of Adipose-Derived Stem/Stromal Cells. Aesthetic Plast Surg. 2007 Sep 1;32(1):48–55.

388. Rigotti G, Marchi A, Stringhini P, Baroni G, Galiè M, Molino AM, et al. Determining the oncological risk of autologous lipoaspirate grafting for post-mastectomy breast reconstruction. Aesthetic Plast Surg. 2010 Aug;34(4):475–80.

389. Yoshimura K, Asano Y. Fat injection to the breasts: cosmetic augmentation, implant replacement, inborn deformity, and reconstruction after mastectomy. Aesthetic and reconstructive Surgery …. 2010.

390. Nishimura T, Hashimoto H, Nakanishi I, Furukawa M. Microvascular angiogenesis and apoptosis in the survival of free fat grafts. Laryngoscope. 2000 Aug;110(8):1333–8.

391. Matsumoto D, Sato K, Gonda K, Takaki Y, Shigeura T, Sato T, et al. Cell-Assisted Lipotransfer: Supportive Use of Human Adipose-Derived Cells for Soft Tissue Augmentation with Lipoinjection. Tissue Eng. Mary Ann Liebert, Inc. 2 Madison Avenue Larchmont, NY 10538 USA; 2006 Dec 12;12(12):3375–82.

392. Zhu Y, Liu T, Song K, Fan X, Ma X, Cui Z. Adipose-derived stem cell: a better stem cell than BMSC. Cell Biochem Funct. 2008 Aug;26(6):664–75.

393. Trojahn Kølle S-F, Oliveri RS, Glovinski PV, Elberg JJ, Fischer-Nielsen A, Drzewiecki KT. Importance of mesenchymal stem cells in autologous fat grafting: a systematic review of existing studies. J Plast Surg Hand Surg. 2012 Apr;46(2):59–68.

394. Haubner F, Leyh M, Ohmann E, Pohl F, Prantl L, Gassner HG. Effects of external radiation in a co-culture model of endothelial cells and adipose-derived stem cells. Radiat Oncol. BioMed Central Ltd; 2013;8(1):1–7.

395. Yoshimura K, Suga H, Eto H. Adipose-derived stem/progenitor cells: roles in adipose tissue remodeling and potential use for soft tissue augmentation. Regenerative Medicine. 2009 Mar;4(2):265–73.

396. Piccinno MS, Veronesi E, Loschi P, Pignatti M, Murgia A, Grisendi G, et al. Adipose stromal/stem cells assist fat transplantation reducing necrosis and increasing graft performance. Apoptosis [Internet]. 2013 Jul 5;18(10):1274–89. Available from: http://eutils.ncbi.nlm.nih.gov/entrez/eutils/elink.fcgi?dbfrom=pubmed&id=23828239&retmode=ref&cmd=prlinks

397. Lu F, Li J, Gao J, Ogawa R, Ou C, Yang B, et al. Improvement of the Survival of Human Autologous Fat Transplantation by Using VEGF-

Transfected Adipose-Derived Stem Cells. Plast Reconstr Surg. 2009 Nov;124(5):1437–46.

398. Shoshani O, Livne E, Armoni M, Shupak A, Berger J, Ramon Y, et al. The Effect of Interleukin-8 on the Viability of Injected Adipose Tissue in Nude Mice. Plast Reconstr Surg. 2005 Mar;115(3):853–9.

399. MD S-FTKL, PhD AF-N, MD ABM, MD JJRE, PhD RSO, MD PVG, et al. Enrichment of autologous fat grafts with ex-vivo expandedadipose tissue-derived stem cells for graft survival:a randomised placebo-controlled trial. Lancet. Elsevier Ltd; 2013 Sep 28;382(9898):1113–20.

400. Caplan AI, Dennis JE. Mesenchymal stem cells as trophic mediators. J Cell Biochem. 2006;98(5):1076–84.

401. Fraser JK, Wulur I, Alfonso Z, Hedrick MH. Fat tissue: an underappreciated source of stem cells for biotechnology. Trends in Biotechnology. Elsevier; 2006;24(4):150–4.

402. Mizuno H. Adipose-derived stem cells for tissue repair and regeneration: ten years of research and a literature review. Journal of Nippon Medical School. J-STAGE; 2009;76(2):56–66.

403. Hsiao ST-F, Asgari A, Lokmic Z, Sinclair R, Dusting GJ, Lim SY, et al. Comparative Analysis of Paracrine Factor Expression in Human Adult Mesenchymal Stem Cells Derived from Bone Marrow, Adipose, and Dermal Tissue. Stem Cells and Development. 2012 Aug 10;21(12):2189–203.

404. Kilroy GE, Foster SJ, Wu X, Ruiz J, Sherwood S, Heifetz A, et al. Cytokine profile of human adipose-derived stem cells: expression of angiogenic, hematopoietic, and pro-inflammatory factors. J Cell Physiol. 2007 Sep;212(3):702–9.

405. Blaber SP, Webster RA, Hill CJ, Breen EJ, Kuah D, Vesey G, et al. Analysis of in vitro secretion profiles from adipose-derived cell populations. Journal of Translational Medicine. Journal of Translational Medicine; 2012 Aug 22;10(1):1–1.

406. Neuhof H, Hirshfeld S. The transplantation of tissues. D. Appleton; 1923. 1 p.

407. Kim W-S, Park B-S, Sung J-H. The wound-healing and antioxidant effects of adipose-derived stem cells. Expert Opin Biol Ther. 2009 Jul;9(7):879–87.

408. Collawn SS, Banerjee NS, la Torre de J, Vasconez L, Chow LT. Adipose-Derived Stromal Cells Accelerate Wound Healing in an Organotypic Raft Culture Model. Annals of Plastic Surgery. 2012 May;68(5):501–4.

409. Forcheron F, Agay D, Scherthan H, Riccobono D, Herodin F, Meineke

V, et al. Autologous adipocyte derived stem cells favour healing in a minipig model of cutaneous radiation syndrome. PLoS ONE. Public Library of Science; 2012;7(2):e31694.

410. Bhang SH, Cho S-W, La W-G, Lee T-J, Yang HS, Sun A-Y, et al. Angiogenesis in ischemic tissue produced by spheroid grafting. Biomaterials. Elsevier Ltd; 2011 Apr 1;32(11):2734–47.

411. Yuan Y, Gao J, Liu L, Lu F. Role of adipose-derived stem cells in enhancing angiogenesis early after aspirated fat transplantation: induction or differentiation? Cell Biol Int. 2013 Apr 22;37(6):547–50.

412. Ebrahimian TG, Pouzoulet F, Squiban C, Buard V, Andre M, Cousin B, et al. Cell Therapy Based on Adipose Tissue-Derived Stromal Cells Promotes Physiological and Pathological Wound Healing. Arteriosclerosis, Thrombosis, and Vascular Biology. 2009 Mar 18;29(4):503–10.

413. Locke M, Windsor J, Dunbar P. Human adipose-derived stem cells: isolation, characterization and applications in surgery. Wiley Online Library; 2009;79(4):235–44.

414. Strioga M, Viswanathan S, Darinskas A, Slaby O, Michalek J. Same or Not the Same? Comparison of Adipose Tissue-Derived Versus Bone Marrow-Derived Mesenchymal Stem and Stromal Cells. Stem Cells and Development. 2012 Sep 20;21(14):2724–52.

415. Dominici M, Le Blanc K, Mueller I, Slaper-Cortenbach I, Marini F, Krause D, et al. Minimal criteria for defining multipotent mesenchymal stromal cells. The International Society for Cellular Therapy position statement. Cytotherapy. 2006 Jan;8(4):315–7.

416. Zuk P. Adipose-Derived Stem Cells in Tissue Regeneration: A Review. ISRN Stem Cells. Hindawi Publishing Corporation; 2013;2013(5):1–35.

417. Yoshimura K, Shigeura T, Matsumoto D, Sato T, Takaki Y, Aiba-Kojima E, et al. Characterization of freshly isolated and cultured cells derived from the fatty and fluid portions of liposuction aspirates. J Cell Physiol. 2006 Mar 23;208(1):64–76.

418. Gronthos S, Franklin DM, Leddy HA, Robey PG, Storms RW, Gimble JM. Surface protein characterization of human adipose tissue-derived stromal cells. J Cell Physiol. 2001 Oct;189(1):54–63.

419. Baer PC, Geiger H. Adipose-Derived Mesenchymal Stromal/Stem Cells: Tissue Localization, Characterization, and Heterogeneity. Stem Cells International. 2012;2012(3):1–11.

420. Matsuda K, Falkenberg KJ, Woods AA, Choi YS, Morrison WA, Dilley RJ. Adipose-derived stem cells promote angiogenesis and tissue formation for in vivo tissue engineering. Tissue Engineering Part A. 2013

Jun;19(11-12):1327–35.

421. Zimmerlin L, Donnenberg AD, Rubin JP, Basse P, Landreneau RJ, Donnenberg VS. Regenerative Therapy and Cancer: In Vitroand In VivoStudies of the Interaction Between Adipose-Derived Stem Cells and Breast Cancer Cells from Clinical Isolates. Tissue Engineering Part A. Mary Ann Liebert, Inc. 140 Huguenot Street, 3rd Floor New Rochelle, NY 10801 USA; 2011 Jan;17(1-2):93–106.

422. Delay E, Garson S, Tousson G, Sinna R. Fat Injection to the Breast: Technique, Results, and Indications Based on 880 Procedures Over 10 Years. Aesthetic Surgery Journal. American Society for Aesthetic Plastic Surgery, Inc; 2009 Sep 1;29(5):360–76.

423. mazzola RF, cantarella G, torretta S, sbarbati A, lazzari L, pignataro L. Autologous fat injection to face and neck: from soft tissue augmentation to regenerative medicine. Acta otorhinolaryngologica. 2011(31):59–69.

424. Zimmerlan. Regenerative Therapy and Cancer - In Vitro and In Vivo studies of interaction between ADSC and Breast Ca cells from clinical isolates - Zimmerlan 2011. 2013 Jun 16;:1–14.

425. Karnoub AE, Dash AB, Vo AP, Sullivan A, Brooks MW, Bell GW, et al. Mesenchymal stem cells within tumour stroma promote breast cancer metastasis. Nature. Nature Publishing Group; 2007 Oct 4;449(7162):557–63.

426. Uysal AC, Mizuno H, Tobita M, Ogawa R, Hyakusoku H. The effect of adipose-derived stem cells on ischemia-reperfusion injury: immunohistochemical and ultrastructural evaluation. Plast Reconstr Surg. 2009 Sep;124(3):804–15.

427. Karathanasis V, Petrakis S, Topouridou K, Koliakou E, Koliakos G, Demiri E. Intradermal injection of GFP-producing adipose stromal cells promotes survival of random-pattern skin flaps in rats. Eur J Plast Surg. 2013 Feb 22;36(5):281–8.

428. Eto H, Suga H, Inoue K, Aoi N, Kato H, Araki J, et al. Adipose Injury–Associated Factors Mitigate Hypoxia in Ischemic Tissues through Activation of Adipose-Derived Stem/Progenitor/Stromal Cells and Induction of Angiogenesis. AJPA. Elsevier Inc; 2011 May 1;178(5):2322–32.

429. Lu F, Varma MJO, Mizuno H, Breuls RGM, Uysal CA, Schouten TE, et al. Improved Viability of Random Pattern Skin Flaps through the Use of Adipose-Derived Stem Cells. Plast Reconstr Surg. 2008 Jan;121(1):50–8.

430. Rehman J. Secretion of Angiogenic and Antiapoptotic Factors by Human Adipose Stromal Cells. Circulation. 2004 Mar 16;109(10):1292–8.

431. Pallua N, Pulsfort AK, Suschek C, Wolter TP. Content of the Growth Factors bFGF, IGF-1, VEGF, and PDGF-BB in Freshly Harvested

Lipoaspirate after Centrifugation and Incubation. Plast Reconstr Surg. 2009 Mar;123(3):826–33.

432. Zografou A, Tsigris C, Papadopoulos O, Kavantzas N, Patsouris E, Donta I, et al. Improvement of skin-graft survival after autologous transplantation of adipose-derived stem cells in rats. J Plast Reconstr Aesthet Surg. 2011 Dec;64(12):1647–56.

433. Kim W-S, Park B-S, Kim H-K, Park J-S, Kim K-J, Choi J-S, et al. Evidence supporting antioxidant action of adipose-derived stem cells: Protection of human dermal fibroblasts from oxidative stress. Journal of Dermatological Science. 2008 Feb;49(2):133–42.

434. Jiang D, Qi Y, Walker NG, Sindrilaru A, Hainzl A, Wlaschek M, et al. The effect of adipose tissue derived MSCs delivered by a chemically defined carrier on full-thickness cutaneous wound healing. Biomaterials. Elsevier Ltd; 2013 Mar 1;34(10):2501–15.

435. Heo SC, Jeon ES, Lee IH, Kim HS, Kim MB, Kim JH. Tumor necrosis factor-α-activated human adipose tissue-derived mesenchymal stem cells accelerate cutaneous wound healing through paracrine mechanisms. J Investig Dermatol. 2011 Jul;131(7):1559–67.

436. Benvenuto F, Ferrari S, Gerdoni E, Gualandi F, Frassoni F, Pistoia V, et al. Human Mesenchymal Stem Cells Promote Survival of T Cells in a Quiescent State. Stem Cells. 2007 Jul;25(7):1753–60.

437. Chen L, Tredget EE, Wu PYG, Wu Y. Paracrine factors of mesenchymal stem cells recruit macrophages and endothelial lineage cells and enhance wound healing. PLoS ONE. 2008;3(4):e1886.

438. Chang P, Qu Y, Liu Y, Cui S, Zhu D, Wang H, et al. Multi-therapeutic effects of human adipose-derived mesenchymal stem cells on radiation-induced intestinal injury. Nature Publishing Group; 2013 Jun 14;4(6):e685–13.

439. Nambu M, Ishihara M, Kishimoto S, Yanagibayashi S, Yamamoto N, Azuma R, et al. Stimulatory Effect of Autologous Adipose Tissue-Derived Stromal Cells in an Atelocollagen Matrix on Wound Healing in Diabetic db/db Mice. Journal of Tissue Engineering. 2011 Sep 9.

440. Goh YY, Pal M, Chong HC, Zhu P, Tan MJ, Punugu L, et al. Angiopoietin-Like 4 Interacts with Integrins β1 and β5 to Modulate Keratinocyte Migration. Am J Pathol. American Society for Investigative Pathology; 2010 Dec 29;177(6):2791–803.

441. Ohnishi S, Sumiyoshi H, Kitamura S, Nagaya N. Mesenchymal stem cells attenuate cardiac fibroblast proliferation and collagen synthesis through paracrine actions. FEBS Lett. 2007 Aug 21;581(21):3961–6.

442. Rodriguez-Menocal L, Salgado M, Ford D, Van Badiavas E. Stimulation of Skin and Wound Fibroblast Migration by Mesenchymal Stem Cells

Derived from Normal Donors and Chronic Wound Patients. Stem Cells Translational Medicine. 2012 Mar 28;1(3):221–9.

443. Walters A, Hulkower KI, Gehler S. Comparison of Oris Cell Migration Assay to Scratch Assay [Internet]. platypustech.com. [cited 2014 Sep 7]. Available from: http://www.platypustech.com/ApNote_Platypus_Oris_Scratch.pdf

444. Zhang Y, Daquinag AC, Amaya-Manzanares F, Sirin O, Tseng C, Kolonin MG. Stromal Progenitor Cells from Endogenous Adipose Tissue Contribute to Pericytes and Adipocytes That Populate the Tumor Microenvironment. Cancer Research. 2012 Oct 15;72(20):5198–208.

445. Gimble JM, Guilak F, Bunnell BA. Clinical and preclinical translation of cell-based therapies using adipose tissue-derived cells. Stem Cell & Research Therapy.

446. Bensidhoum M, Gobin S, Chapel A, Lemaitre G, Bouet S, Waksman G, et al. Potentiel thérapeutique des cellules souches mésenchymateuses humaines dans les lésions cutanées radioinduites. J Soc Biol. 2005;199(4):337–41.

447. François S, Mouiseddine M, Mathieu N, Semont A, Monti P, Dudoignon N, et al. Human mesenchymal stem cells favour healing of the cutaneous radiation syndrome in a xenogenic transplant model. Ann Hematol. Springer-Verlag; 2006 Oct 17;86(1):1–8.

448. Mouiseddine M, Francois S, Semont A, Sache A, Allenet B, Mathieu N, et al. Human mesenchymal stem cells home specifically to radiation-injured tissues in a non-obese diabetes/severe combined immunodeficiency mouse model. British Journal of Radiology. British Institute of Radiology; 2007 Sep 1;80(Special Issue 1):S49–S55.

449. Lee MJ, Kim J, Kim MY, Bae Y-S, Ryu SH, Lee TG, et al. Proteomic Analysis of Tumor Necrosis Factor-α-Induced Secretome of Human Adipose Tissue-Derived Mesenchymal Stem Cells. J Proteome Res. American Chemical Society; 2010 Apr 5;9(4):1754–62.

450. Lee SH, Jin SY, Song JS, Seo KK, Cho KH. Paracrine effects of adipose-derived stem cells on keratinocytes and dermal fibroblasts. Ann Dermatol. 2012 May;24(2):136–43.

451. Frazier TP, Gimble JM, Kheterpal I, Rowan BG. Impact of low oxygen on the secretome of human adipose-derived stromal/stem cell primary cultures. Biochimie. Elsevier Masson SAS; 2013 Dec 1;95(12):2286–96.

452. Chen M-F, Lin C-T, Chen W-C, Yang C-T, Chen C-C, Liao S-K, et al. The sensitivity of human mesenchymal stem cells to ionizing radiation. Int J Radiat Oncol Biol Phys. 2006 Sep 1;66(1):244–53.

453. Bill CA, Grochan BM, Vrdoljak E, Mendoza EA, Tofilon PJ. Decreased Repair of Radiation-Induced DNA Double-Strand Breaks with Cellular

Differentiation. Radiation Research. The Radiation Research Society; 1992 Nov 1;132(2):254–8.

454. Suga H, Matsumoto D, Inoue K, Shigeura T, Eto H, Aoi N, et al. Numerical Measurement of Viable and Nonviable Adipocytes and Other Cellular Components in Aspirated Fat Tissue. Plast Reconstr Surg. 2008 Jul;122(1):103–14.

455. Wu Y, Chen L, Scott PG, Tredget EE. Mesenchymal stem cells enhance wound healing through differentiation and angiogenesis. Stem Cells. 2007 Oct;25(10):2648–59.

456. Li J, Kwong DLW, Chan GC-F. The effects of various irradiation doses on the growth and differentiation of marrow-derived human mesenchymal stromal cells. 2007 Apr 25;11(4):379–87.

457. Schönmeyr BH, Wong AK, Soares M, Fernandez J, Clavin N, Mehrara BJ. Ionizing Radiation of Mesenchymal Stem Cells Results in Diminution of the Precursor Pool and Limits Potential for Multilineage Differentiation. Plast Reconstr Surg. 2008 Jul;122(1):64–76.

458. Su W, Chen Y, Zeng W, Liu W, Sun H. Involvement of Wnt signaling in the injury of murine mesenchymal stem cells exposed to X-radiation. Int J Radiat Biol. 2012 Sep;88(9):635–41.

459. Hsiao ST, Dilley RJ, Dusting GJ, Lim SY. Ischemic preconditioning for cell-based therapy and tissue engineering. Pharmacology and Therapeutics. Elsevier Inc; 2013 Dec 18;:1–13.

460. Ong WK, Sugii S. The International Journal of Biochemistry & Cell Biology. International Journal of Biochemistry and Cell Biology. Elsevier Ltd; 2013 Jun 1;45(6):1083–6.

461. Hulkower KI, Herber RL. Cell Migration and Invasion Assays as Tools for Drug Discovery. Pharmaceutics. Molecular Diversity Preservation International; 2011 Dec;3(4):107–24.

462. Stubbs SL, Hsiao ST-F, Peshavariya HM, Lim SY, Dusting GJ, Dilley RJ. Hypoxic Preconditioning Enhances Survival of Human Adipose-Derived Stem Cells and Conditions Endothelial Cells In Vitro. Stem Cells and Development. 2012 Jul 20;21(11):1887–96.

463. Rudolph R, Tripuraneni P, Koziol JA, McKean-Matthews M, Frutos A. Normal transcutaneous oxygen pressure in skin after radiation therapy for cancer. Cancer. 1994 Dec 1;74(11):3063–70.

464. Vala IS, Martins LR, Imaizumi N, Nunes RJ, Rino J, Kuonen F, et al. Low doses of ionizing radiation promote tumor growth and metastasis by enhancing angiogenesis. PLoS ONE. Public Library of Science; 2010;5(6):e11222.

465. Traktuev DO, Prater DN, Merfeld-Clauss S, Sanjeevaiah AR,

Saadatzadeh MR, Murphy M, et al. Robust functional vascular network formation in vivo by cooperation of adipose progenitor and endothelial cells. Circ Res. 2009 Jun 19;104(12):1410–20.

466. Huang S-P, Huang C-H, Shyu J-F, Lee H-S, Chen S-G, Chan JY-H, et al. Promotion of wound healing using adipose-derived stem cells in radiation ulcer of a rat model. Journal of Biomedical Science. Journal of Biomedical Science; 2013 Jul 22;20(51).

467. Lim J-Y, Ra JC, Shin IS, Jang YH, An H-Y, Choi J-S, et al. Systemic Transplantation of Human Adipose Tissue-Derived Mesenchymal Stem Cells for the Regeneration of Irradiation-Induced Salivary Gland Damage. Lim J-Y, Ra JC, Shin IS, Jang YH, An H-Y, Choi J-S, et al., editors. PLoS ONE. 2013 Aug 9;8(8):e71167.

468. Kojima T, Kanemaru S-I, Hirano S, Tateya I, Ohno S, Nakamura T, et al. Regeneration of radiation damaged salivary glands with adipose-derived stromal cells. Laryngoscope. 2011 Sep;121(9):1864–9.

469. Sultan SM, Stern CS, Allen RJ Jr., Thanik VD, Chang CC, Nguyen PD, et al. Human Fat Grafting Alleviates Radiation Skin Damage in a Murine Model. Plast Reconstr Surg. 2011 Aug;128(2):363–72.

470. Chen Y, Niu Z, Xue Y, Yuan F, Fu Y, Bai N. Improvement in the repair of defects in maxillofacial soft tissue in irradiated minipigs by a mixture of adipose-derived stem cells and platelet-rich fibrin. Br J Oral Maxillofac Surg. 2014 Oct;52(8):740–5.

471. Manabe Y, Toda S, Miyazaki K, Sugihara H. Mature adipocytes, but not preadipocytes, promote the growth of breast carcinoma cells in collagen gel matrix culture through cancer-stromal cell interactions. J Pathol. 2003;201(2):221–8.

472. Prantl L, Muehlberg F, Navone NM, Song Y-H, Vykoukal J, Logothetis CJ, et al. Adipose tissue-derived stem cells promote prostate tumor growth. Prostate. 2010 Jun 16;70(15):1709–15.

473. Iyengar P, Combs TP, Shah SJ, Gouon-Evans V, Pollard JW, Albanese C, et al. Adipocyte-secreted factors synergistically promote mammary tumorigenesis through induction of anti-apoptotic transcriptional programs and proto-oncogene stabilization. Oncogene. 2003 Sep 25;22(41):6408–23.

474. Yu JM, Jun ES, Bae YC, Jung JS. Mesenchymal stem cells derived from human adipose tissues favor tumor cell growth in vivo. Stem Cells and Development. 2008 Jun;17(3):463–73.

475. Muehlberg FL, Song Y-H, Krohn A, Pinilla SP, Droll LH, Leng X, et al. Tissue-resident stem cells promote breast cancer growth and metastasis. Carcinogenesis. 2009 Apr;30(4):589–97.

476. Claro F Jr, Figueiredo JCA, Zampar AG, Pinto-Neto AM. Applicability

and safety of autologous fat for reconstruction of the breast. Br J Surg. 2012 Apr 4;99(6):768–80.

477. Gutowski KA, ASPS Fat Graft Task Force. Current applications and safety of autologous fat grafts: a report of the ASPS fat graft task force. Vol. 124, Plastic and reconstructive surgery. 2009. pp. 272–80.

478. Krastev TK, Jonasse Y, Kon M. Oncological Safety of Autologous Lipoaspirate Grafting in Breast Cancer Patients: A Systematic Review. Ann Surg Oncol. 2012 Aug 10;20(1):111–9.

479. Ong WK, Sugii S. The International Journal of Biochemistry & Cell Biology. International Journal of Biochemistry and Cell Biology. Elsevier Ltd; 2013 Jun 1;45(6):1083–6.

480. Agha RA, Goodacre T, Orgill DP. Use of autologous fat grafting for reconstruction postmastectomy and breast conserving surgery: a systematic review protocol. BMJ Open. 2013 ed. 3:e003709.

481. Shayan R, Shayan R, Karnezis T, Karnezis T, Tsantikos E, Tsantikos E, et al. A system for quantifying the patterning of the lymphatic vasculature. Growth Factors. 2007 Dec;25(6):417–25.

482. Liao Y, Smyth GK, Shi W. The Subread aligner: fast, accurate and scalable read mapping by seed-and-vote. Nucleic Acids Res. 2013 May 1;41(10):e108.

483. Robinson MD, Robinson MD, McCarthy DJ, McCarthy DJ, Smyth GK, Smyth GK. edgeR: a Bioconductor package for differential expression analysis of digital gene expression data. Bioinformatics. 2010 Jan 1;26(1):139–40.

484. Smyth GK. Linear models and empirical bayes methods for assessing differential expression in microarray experiments. Stat Appl Genet Mol Biol. 2004;3:Article3.

485. Smyth GK, Michaud J, Scott HS. Use of within-array replicate spots for assessing differential expression in microarray experiments. Bioinformatics. 2005 May 1;21(9):2067–75.

486. Subramanian A, Subramanian A, Tamayo P, Tamayo P, Mootha VK, Mootha VK, et al. Gene set enrichment analysis: a knowledge-based approach for interpreting genome-wide expression profiles. Proc Natl Acad Sci USA. 2005 Oct 25;102(43):15545–50.

487. Wu D, Lim E, Vaillant F, Asselin-Labat M-L, Visvader JE, Smyth GK. ROAST: rotation gene set tests for complex microarray experiments. Bioinformatics. 2010 Sep 1;26(17):2176–82.

488. Wu D, Smyth GK. Camera: a competitive gene set test accounting for inter-gene correlation. Nucleic Acids Res. 2012 Sep 1;40(17):e133.

489. Harris NC, Davydova N, Roufail S, Paquet-Fifield S, Paavonen K, Karnezis T, et al. The propeptides of VEGF-D determine heparin binding, receptor heterodimerization, and effects on tumor biology. Journal of Biological Chemistry. 2013 Mar 22;288(12):8176–86.

490. Stacker SA, Halford MM, Roufail S, Caesar C, Achen MG. A Simple Bioassay for the Evaluation of Vascular Endothelial Growth Factors. J Vis Exp [Internet]. 2016 Mar 15;(109). Available from: http://eutils.ncbi.nlm.nih.gov/entrez/eutils/elink.fcgi?dbfrom=pubmed&id=27022756&retmode=ref&cmd=prlinks

491. Kamburov A, Cavill R, Ebbels TMD, Herwig R, Keun HC. Integrated pathway-level analysis of transcriptomics and metabolomics data with IMPaLA. Bioinformatics. 2011 Oct 15;27(20):2917–8.

492. Arganda-Carreras I, Fernández-González R, Muñoz-Barrutia A, Ortiz-De-Solorzano C. 3D reconstruction of histological sections: Application to mammary gland tissue. Microsc Res Tech. 2010 Oct;73(11):1019–29.

493. Larsson O, Diebold D, Fan D, Peterson M, Nho RS, Bitterman PB, et al. Fibrotic Myofibroblasts Manifest Genome-Wide Derangements of Translational Control. Barnes PJ, editor. PLoS ONE. 2008 Sep 16;3(9):e3220.

494. Hellevik T, Hellevik T, Pettersen I, Pettersen I, Berg V, Berg V, et al. Cancer-associated fibroblasts from human NSCLC survive ablative doses of radiation but their invasive capacity is reduced. Radiat Oncol. 2012;7(1):59.

495. Shelton DN, Chang E, Whittier PS, Choi D, Funk WD. Microarray analysis of replicative senescence. Current Biology. 1999 Sep;9(17):939–45.

496. Papadopoulou A, Kletsas D. Human lung fibroblasts prematurely senescent after exposure to ionizing radiation enhance the growth of malignant lung epithelial cells in vitro and in vivo. Int J Oncol. 2011 Oct;39(4):989–99.

497. Tsai KKC, Chuang EY-Y, Little JB, Yuan Z-M. Cellular mechanisms for low-dose ionizing radiation-induced perturbation of the breast tissue microenvironment. Cancer Research. 2005 Aug 1;65(15):6734–44.

498. Liu D, Hornsby PJ. Senescent human fibroblasts increase the early growth of xenograft tumors via matrix metalloproteinase secretion. Cancer Research. 2007 Apr 1;67(7):3117–26.

499. Yarnold J, Brotons M-CV. Radiotherapy and Oncology. Radiotherapy and Oncology. Elsevier Ireland Ltd; 2010 Oct 1;97(1):149–61.

500. Hinz B, Phan SH, Thannickal VJ, Galli A, Bochaton-Piallat M-L, Gabbiani G. The Myofibroblast. Am J Pathol. 2007 Jun;170(6):1807–16.

501. Crisan M, Corselli M, Chen WCW, Péault B. Perivascular cells for regenerative medicine. Moldovan NI, editor. J Cell Mol Med. 2012 Dec 13;16(12):2851–60.

502. Dickey JS, Zemp FJ, Martin OA, Kovalchuk O. The role of miRNA in the direct and indirect effects of ionizing radiation. Radiat Environ Biophys. 2011 Sep 18;50(4):491–9.

503. Warters RL, Packard AT, Kramer GF, Gaffney DK, Moos PJ. Differential gene expression in primary human skin keratinocytes and fibroblasts in response to ionizing radiation. Radiation Research. The Radiation Research Society; 2009;172(1):82–95.

504. Zheng W, Zheng W, Tammela T, Tammela T, Yamamoto M, Yamamoto M, et al. Notch restricts lymphatic vessel sprouting induced by vascular endothelial growth factor. Blood. 2011 Jul 28;118(4):1154–62.

505. Chigurupati S, Arumugam TV, Son TG, Lathia JD, Jameel S, Mughal MR, et al. Involvement of Notch Signaling in Wound Healing. Hotchin N, editor. PLoS ONE. 2007 Nov 14;2(11):e1167.

506. Saad S, Stanners SR, Yong R, Tang O, Pollock CA. The International Journal of Biochemistry & Cell Biology. International Journal of Biochemistry and Cell Biology. Elsevier Ltd; 2010 Jul 1;42(7):1115–22.

507. Leask A. Targeting the jagged/notch pathway: a new treatment for fibrosis? J Cell Commun Signal. 2010 Oct 12;4(4):197–8.

508. Dees C, Zerr P, Tomcik M, Beyer C, Horn A, Akhmetshina A, et al. Inhibition of Notch signaling prevents experimental fibrosis and induces regression of established fibrosis. Arthritis & Rheumatism. 2011 Apr 27;63(5):1396–404.

509. Riekki, Riitta. thesis. 2006 Nov 15;:1–64.

510. Seluanov A, Gorbunova V, Falcovitz A, Sigal A, Milyavsky M, Zurer I, et al. Change of the Death Pathway in Senescent Human Fibroblasts in Response to DNA Damage Is Caused by an Inability To Stabilize p53. Molecular and Cellular Biology. 2001 Mar 1;21(5):1552–64.

511. Liu Z-J, Li Y, Tan Y, Xiao M, Zhang J, Radtke F, et al. Inhibition of Fibroblast Growth by Notch1 Signaling Is Mediated by Induction of Wnt11-Dependent WISP-1. Vooijs M, editor. PLoS ONE. 2012 Jun 8;7(6):e38811.

512. Ando K, Kanazawa S, Tetsuka T, Ohta S, Jiang X, Tada T, et al. Induction of Notch signaling by tumor necrosis factor in rheumatoid synovial fibroblasts. Oncogene. 2003 Oct 30;22(49):7796–803.

513. Syed F, Bayat A. Notch signaling pathway in keloid disease: enhanced fibroblast activity in a Jagged-1 peptide-dependent manner in lesional vs. extralesional fibroblasts. Wound Repair Regen. 2012 Sep;20(5):688–706.

514. Rangarajan A, Talora C, Okuyama R, Nicolas M, Mammucari C, Oh H, et al. Notch signaling is a direct determinant of keratinocyte growth arrest and entry into differentiation. EMBO J. 2001 Jul 2;20(13):3427–36.

515. Cox TR, Erler JT. Remodeling and homeostasis of the extracellular matrix: implications for fibrotic diseases and cancer. Dis Model Mech. 2011 Mar;4(2):165–78.

516. Nabout El R, Martin M, Remy J, Kern P, Robert L. Collagen synthesis and deposition in cultured fibroblasts from subcutaneous radiation-induced fibrosis. Modification as a function of cell aging. Matrix. 1989.

517. Abreu-Velez AM, Howard MS. Collagen IV in Normal Skin and in Pathological Processes. N Am J Med Sci. 2012 Jan;4(1):1–8.

518. Ricard-Blum S. The Collagen Family. Cold Spring Harbor Perspectives in Biology. 2011 Jan 4;3(1):a004978–8.

519. Villone D, Fritsch A, Koch M, Bruckner-Tuderman L, Hansen U, Bruckner P. Supramolecular interactions in the dermo-epidermal junction zone: anchoring fibril-collagen VII tightly binds to banded collagen fibrils. J Biol Chem. 2008 Sep 5;283(36):24506–13.

520. Miyazaki Y, Hara A, Kato K, Oyama T, Yamada Y, Mori H, et al. The effect of hypoxic microenvironment on matrix metalloproteinase expression in xenografts of human oral squamous cell carcinoma. Int J Oncol. 2008 Jan;32(1):145–51.

521. Thewes M, Worret WI, Engst R, Ring J. Stromelysin-3 (ST-3): immunohistochemical characterization of the matrix metalloproteinase (MMP)-11 in benign and malignant skin tumours and other skin disorders. Clin Exp Dermatol. 1999 Mar;24(2):122–6.

522. Yang YC, Piek E, Zavadil J, Liang D, Xie D, Heyer J, et al. Hierarchical model of gene regulation by transforming growth factor. Proceedings of the National Academy of Sciences. 2011 May 1;100(18):10269–74.

523. Boerma M, Hauer-Jensen M. Preclinical Research into Basic Mechanisms of Radiation-Induced Heart Disease. Cardiology Research and Practice. 2011;2011(4):1–8.

524. NHMRC. Clinical practice guidelines for the management of early breast cancer: Second edition 2nd ed. 2002 Apr 5;:1–210.

525. Pezner RD. Coronary Artery Disease and Breast Radiation Therapy. International Journal of Radiation Oncology*Biology*Physics. 2013 Aug;86(5):816–8.

526. Montazeri K, Unitt C, Foody JM, Harris JR, Partridge AH, Moslehi J. ABCDE Steps to Prevent Heart Disease in Breast Cancer Survivors: Table. Circulation. 2014 Oct 27;130(18):e157–9.

527. Cuzick J, Stewart HJ, Peto R, Baum M, Fisher B, Host H, et al. Overview of Randomized Trials of Postoperative Adjuvant Radiotherapy in Breast Cancer. In: Cancer Clinical …. Berlin, Heidelberg: Springer Berlin Heidelberg; 1988. pp. 108–29. (Recent Results in Cancer Research; vol. 111).

528. Stewart FA, Seemann I, Hoving S, Russell NS. Clinical Oncology. Clinical Oncology. Elsevier Ltd; 2013 Oct 1;25(10):617–24.

529. Harris EER, Correa C, Hwang WT, Liao J, Litt HI, Ferrari VA, et al. Late Cardiac Mortality and Morbidity in Early-Stage Breast Cancer Patients After Breast-Conservation Treatment. J Clin Oncol. 2006 Aug 14;24(25):4100–6.

530. Jagsi R, Griffith KA, Koelling T, Roberts R, Pierce LJ. Rates of myocardial infarction and coronary artery disease and risk factors in patients treated with radiation therapy for early-stage breast cancer. Cancer. 2007.

531. Paszat LF, Mackillop WJ, Groome PA, Boyd C, Schulze K, Holowaty E. Mortality from myocardial infarction after adjuvant radiotherapy for breast cancer in the surveillance, epidemiology, and end-results cancer registries. Journal of Clinical …. 1998.

532. Guan H, Dong Y-L, Ding L-J, Zhang Z-C, Huang W, Liu C-X, et al. Morphological factors and cardiac doses in whole breast radiation for left-sided breast cancer. Asian Pac J Cancer Prev. 2015;16(7):2889–94.

533. Sautter-Bihl M-L, Hültenschmidt B, Melcher U, Ulmer HU. Radiotherapy of internal mammary lymph nodes in breast cancer. Principle considerations on the basis of dosimetric data. Strahlenther Onkol. 2002 Jan;178(1):18–24.

534. Taylor CW, Povall JM, McGale P, Nisbet A, Dodwell D, Smith JT, et al. Cardiac Dose From Tangential Breast Cancer Radiotherapy in the Year 2006. International Journal of Radiation Oncology*Biology*Physics. 2008 Oct;72(2):501–7.

535. Fuller SA, Haybittle JL, Smith REA, Dobbs HJ. Cardiac doses in post-operative breast irradiation. Radiotherapy and Oncology. 1992 Sep;25(1):19–24.

536. Boero IJ, Paravati A, Triplett DP, Hwang L. Modern radiation therapy and cardiac outcomes in breast cancer. International Journal of …. 2015.

537. Henson KE, McGale P, Taylor C, Darby SC. Radiation-related mortality from heart disease and lung cancer more than 20 years after radiotherapy for breast cancer. British Journal of Cancer. 2013 Jan 15;108(1):179–82.

538. Laib AM, Laib AM, Bartol A, Bartol A, Alajati A, Alajati A, et al. Spheroid-based human endothelial cell microvessel formation in vivo.

Nat Protoc. 2009;4(8):1202–15.

539. Mollà M, Gironella M, Miquel R, Tovar V, Engel P, Biete A, et al. Relative roles of ICAM-1 and VCAM-1 in the pathogenesis of experimental radiation-induced intestinal inflammation. Int J Radiat Oncol Biol Phys. 2003 Sep 1;57(1):264–73.

540. Lee MO, Song SH, Jung S, Hur S, Asahara T, Kim H, et al. Effect of Ionizing Radiation Induced Damage of Endothelial Progenitor Cells in Vascular Regeneration. Arteriosclerosis, Thrombosis, and Vascular Biology. 2012 Jan 18;32(2):343–52.

541. Coates PJ, Rundle JK, Lorimore SA, Wright EG. Indirect macrophage responses to ionizing radiation: implications for genotype-dependent bystander signaling. Cancer Research. 2008 Jan 15;68(2):450–6.

542. Mills S, Cowin A, Kaur P. Pericytes, Mesenchymal Stem Cells and the Wound Healing Process. Cells. 2013 Sep;2(3):621–34.

543. Baker DG, Krochak RJ. The response of the microvascular system to radiation: a review. Cancer Investigation. Informa UK Ltd UK; 2007 Oct 12;7(3):287–94.

544. Yuan S-M, Jing H. Cystic medial necrosis: pathological findings and clinical implications. Rev Bras Cir Cardiovasc. 2011 Jan;26(1):107–15.

545. Hake U, Dienes H-P, Hilker M, Oelert H. Cystic medial necrosis of the internal thoracic artery: Case report. Scandinavian Cardiovascular Journal. Informa UK Ltd UK; 1996;30(3-4):163–5.

546. Segal GH, Ratliff NB, Cosgrove DM. Cystic Medionecrosis of the Coronary Arteries and. The Annals of Thoracic Surgery. The Society of Thoracic Surgeons; 1990 Oct 1;50(4):653–5.

547. Kay IP, Ligthart JMR, Virmani R, van Beusekom HMM, Kozuma K, Carter AJ, et al. The black hole: echolucent tissue observed following intracoronary radiation. Int J Cardiovasc Intervent. 2003;5(3):137–42.

548. Tall J, Björklund TC, Skogh A-CD, Arnander C, Halle M. Vascular Complications After Radiotherapy in Head and Neck Free Flap Reconstruction: Clinical Outcome Related to Vascular Biology. Annals of Plastic Surgery. 2015 Sep;75(3):309–15.

549. Otsuka F, Yahagi K, Sakakura K, Virmani R. Why is the mammary artery so special and what protects it from atherosclerosis? Ann Cardiothorac Surg. 2013 Jul;2(4):519–26.

550. Zulli A. The Resistance of the IMA to Atherosclerosis Might Be Associated With Its Higher eNOS, ACE and ET-A Receptor Immunoreactivity. Arteriosclerosis, Thrombosis, and Vascular Biology. 2003 Jul 1;23(7):1308–8.

551. Aitasalo K, Aro H. Irradiation-induced hypoxia in bones and soft tissues: an experimental study. Plast Reconstr Surg. 1986 Feb;77(2):256–67.

552. Svalestad J, Hellem S, Thorsen E, Johannessen AC. Effect of hyperbaric oxygen treatment on irradiated oral mucosa: microvessel density. Int J Oral Maxillofac Surg. 2015 Mar;44(3):301–7.

553. Korpela E, Liu SK. Endothelial perturbations and therapeutic strategies in normal tissue radiation damage. Radiation Oncology. 2014;9:266.

554. Jackson IL, Rubin P, Hadley C, Vujaskovic Z. Molecular Mechanisms of Radiation Induced Injury. In: ALERT-Adverse Late Effects …. Berlin, Heidelberg: Springer Berlin Heidelberg; 2013. pp. 41–51. (Medical Radiology).

555. Sievert W, Trott K-R, Azimzadeh O, Tapio S, Zitzelsberger H, Multhoff G. Late proliferating and inflammatory effects on murine microvascular heart and lung endothelial cells after irradiation. Radiother Oncol. 2015 Nov;117(2):376–81.

556. Stewart FA, Hoving S, Russell NS. Vascular damage as an underlying mechanism of cardiac and cerebral toxicity in irradiated cancer patients. Radiation Research. 2010 Dec;174(6):865–9.

557. Lowe DJ, Raj K. Quantitation of Endothelial Cell Adhesiveness In Vitro. J Vis Exp. 2015;(100):e52924.

558. Nakashima Y, Raines EW, Plump AS, Breslow JL, Ross R. Up-regulation of VCAM-1 and ICAM-1 at Atherosclerosis-Prone Sites on the Endothelium in the ApoE-Deficient Mouse. Arteriosclerosis, Thrombosis, and Vascular Biology. 1998 May 1;18(5):842–51.

559. Ikeda U. Monocyte-endothelial cell interaction in atherogenesis and thrombosis. Japanese Journal of Thrombosis and Hemostasis. 1998.

560. Funayama H, Sakata Y, Kitagawa SI, Ikeda U. Monocytes modulate the fibrinolytic balance of endothelial cells. Thrombosis research. 1997.

561. Walther M, Kaffenberger W, Van Beuningen D. Influence of clinically used antioxidants on radiation-induced expression of intercellular cell adhesion molecule-1 on HUVEC. Int J Radiat Biol. 1999 Oct;75(10):1317–25.

562. Patel SS, Thiagarajan R, Willerson JT, Yeh ET. Inhibition of alpha4 integrin and ICAM-1 markedly attenuate macrophage homing to atherosclerotic plaques in ApoE-deficient mice. Circulation. 1998 Jan;97(1):75–81.

563. Radiation Induced normal tissue injury - role of adhesion molecules in leukocyte-endothelial cell interacations - Quarmby 1999. 1999 Jun 16;:1–11.

564. Karnezis T, Shayan R, Caesar C, Roufail S, Harris NC, Ardipradja K, et al. VEGF-D promotes tumor metastasis by regulating prostaglandins produced by the collecting lymphatic endothelium. Cancer Cell. 2012 Feb 14;21(2):181–95.

565. Stacker SA, Williams SP, Karnezis T, Shayan R, Fox SB, Achen MG. Lymphangiogenesis and lymphatic vessel remodelling in cancer. Nature Reviews Cancer. 2014 Mar;14(3):159–72.

566. Neusser MA, Kraus AK, Regele H, Cohen CD, Fehr T, Kerjaschki D, et al. The chemokine receptor CXCR7 is expressedon lymphatic endothelial cellsduring renal allograft rejection. Kidney International. Nature Publishing Group; 2010 Feb 17;77(9):801–8.

567. Partanen TA, Alitalo K, Miettinen M. Lack of lymphatic vascular specificity of vascular endothelial growth factor receptor 3 in 185 vascular tumors. Cancer. 1999.

568. Day RM, Snow AL, Panganiban RAM. Radiation-induced accelerated senescence: a fate worse than death? Cell Cycle. 2014;13(13):2011–2.

569. Chen J, Goligorsky MS. Premature senescence of endothelial cells: Methusaleh's dilemma. Am J Physiol Heart Circ Physiol. 2006 May;290(5):H1729–39.

570. Hayes AW. Principles and Methods of Toxicology, Fifth Edition. CRC Press; 2007. 1 p.

571. Panganiban R-A, Snow A, Day R. Mechanisms of Radiation Toxicity in Transformed and Non-Transformed Cells. Int J Mol Sci. 2013 Aug;14(8):15931–58.

572. Li D, Fengqing Z, Xueguang Z. Experimental studies on evaluation of protection by IL-8mAb to brain irradiation injury in rabbit--《Chinese Journal of Stereotactic and Functional Neurosurgery》2001年01期. Chinese Journal of Stereotactic …. 2001.

573. Choi I, Lee S, Kyoung Chung H, Suk Lee Y, Eui Kim K, Choi D, et al. 9-cis retinoic acid promotes lymphangiogenesis and enhances lymphatic vessel regeneration: therapeutic implications of 9-cis retinoic acid for secondary lymphedema. Circulation. 2012 Feb 21;125(7):872–82.

574. Klein KR, Karpinich NO, Espenschied ST, Willcockson HH, Dunworth WP, Hoopes SL, et al. Decoy receptor CXCR7 modulates adrenomedullin-mediated cardiac and lymphatic vascular development. Dev Cell. 2014 Sep 8;30(5):528–40.

575. Wang Y, Nakayama M, Pitulescu ME, Schmidt TS, Bochenek ML, Sakakibara A, et al. Ephrin-B2 controls VEGF-induced angiogenesis and lymphangiogenesis. Nature. Nature Publishing Group; 2010 May 18;465(7297):483–6.

576. Zhang G, Brady J, Liang W-C, Wu Y, Henkemeyer M, Yan M. EphB4 forward signalling regulates lymphatic valve development. Nature Communications. Nature Publishing Group; 1AD;6:1–10.

577. MartIn-Fontecha A, Sebastiani S, Höpken UE, Uguccioni M, Lipp M, Lanzavecchia A, et al. Regulation of dendritic cell migration to the draining lymph node: impact on T lymphocyte traffic and priming. J Exp Med. 2003 Aug 18;198(4):615–21.

578. Nicolay NH, Sommer E, Lopez R, Wirkner U, Trinh T, Sisombath S, et al. Mesenchymal stem cells retain their defining stem cell characteristics after exposure to ionizing radiation. Int J Radiat Oncol Biol Phys. 2013 Dec 1;87(5):1171–8.

579. Islam MS, Stemig ME, Takahashi Y, Hui SK. Radiation response of mesenchymal stem cells derived from bone marrow and human pluripotent stem cells. Journal of Radiation Research. 2015 Mar 13;56(2):269–77.

580. J Salgado A, L Reis R, Sousa N, M Gimble J. Adipose tissue derived stem cells secretome: soluble factors and their roles in regenerative medicine. Current stem cell research & therapy. Bentham Science Publishers; 2010;5(2):103–10.

581. Li Q, Zhang A, Tao C, Li X, Jin P. Biochemical and Biophysical Research Communications. Biochemical and Biophysical Research Communications. Elsevier Inc; 2013 Nov 22;441(3):675–80.

582. Maksym RB, Tarnowski M, Grymula K, Tarnowska J, Wysoczynski M, Liu R, et al. European Journal of Pharmacology. European Journal of Pharmacology. Elsevier B.V; 2009 Dec 25;625(1-3):31–40.

583. Kaelin WG Jr, McKnight SL. Influence of Metabolismon Epigenetics and Disease. Cell. Elsevier Inc; 2013 Mar 28;153(1):56–69.

584. Kanehisa M, Goto S, Sato Y, Kawashima M, Furumichi M, Tanabe M. Data, information, knowledge and principle: back to metabolism in KEGG. Nucleic Acids Res. 2014 Jan;42(Database issue):D199–205.

585. Kanehisa M, Goto S. KEGG: kyoto encyclopedia of genes and genomes. Nucleic Acids Res. 2000 Jan 1;28(1):27–30.

586. Sándor N, Schilling-Tóth B, Kis E, Benedek A, Lumniczky K, Sáfrány G, et al. Growth Differentiation Factor-15 (GDF-15) is a potential marker of radiation response and radiation sensitivity. Mutat Res Genet Toxicol Environ Mutagen. 2015 Nov;793:142–9.

587. Uchiyama T, Kawabata H, Miura Y, Yoshioka S, Iwasa M, Yao H, et al. The role of growth differentiation factor 15 in the pathogenesis of primary myelofibrosis. Cancer Med. 2015 Oct;4(10):1558–72.

588. Schiegnitz E, Kämmerer PW, Rode K, Schorn T, Brieger J, Al-Nawas B.

Growth differentiation factor 15 as a radiation-induced marker in oral carcinoma increasing radiation resistance. J Oral Pathol Med. 2016 Jan;45(1):63–9.

589. Yatsuga S, Fujita Y, Ishii A, Fukumoto Y, Arahata H, Kakuma T, et al. Growth differentiation factor 15 as a useful biomarker for mitochondrial disorders. Ann Neurol. 2015 Nov;78(5):814–23.

590. San-Marina S, Voss S, Crespo-Diaz R, Wyles C, Behfar A, Stalboeger P, et al. Adipose-Derived Mesenchymal Stem Cell Features in Patients with a History of Head and Neck Radiation. Laryngoscope Investigative Otolaryngology. 2016 Jun 10;1(3):36–41.

591. Folmes CDL, Dzeja PP, Nelson TJ, Terzic A. Metabolic plasticity in stem cell homeostasis and differentiation. Cell Stem Cell. 2012 Nov 2;11(5):596–606.

592. McKnight SL. On Getting There from Here. Science. 2010 Dec 2;330(6009):1338–9.

593. Darling PB, Grunow J, Rafii M, Brookes S, Ball RO, Pencharz PB. Threonine dehydrogenase is a minor degradative pathway of threonine catabolism in adult humans. Am J Physiol Endocrinol Metab. 2000 May;278(5):E877–84.

594. Ryu JM, Han HJ. L-Threonine Regulates G1/S Phase Transition of Mouse Embryonic Stem Cells via PI3K/Akt, MAPKs, and mTORC Pathways. Journal of Biological Chemistry. 2011 Jul 1;286(27):23667–78.

595. Van Winkle LJ. Threonine appears to be essential for proliferation of human as well as mouse embryonic stem cells. 2014 May 15;:1–2.

596. Shyh-Chang N, Shyh-Chang N, Locasale JW, Locasale JW, Lyssiotis CA, Lyssiotis CA, et al. Influence of Threonine Metabolism on S-Adenosylmethionine and Histone Methylation. Science. 2013 Jan 10;339(6116):222–6.

597. Fraser JK, Wulur I, Alfonso Z, Hedrick MH. Fat tissue: an underappreciated source of stem cells for biotechnology. Trends in Biotechnology. 2006 Apr;24(4):150–4.

598. Zhang J, Li S, Li L, Li M, Guo C, Yao J, et al. Exosome and exosomal microRNA: trafficking, sorting, and function. Genomics Proteomics Bioinformatics. 2015 Feb;13(1):17–24.

599. Davydova N, Harris NC, Roufail S, Paquet-Fifield S, Ishaq M, Streltsov VA, et al. Differential Receptor Binding and Regulatory Mechanisms for the Lymphangiogenic Growth Factors Vascular Endothelial Growth Factor (VEGF)-C and -D. Journal of Biological Chemistry. 2016 Dec 30;291(53):27265–78.

600. Wang J, Alexander P, Wu L, Hammer R, Cleaver O, McKnight SL. Dependence of mouse embryonic stem cells on threonine catabolism. Science. 2009 Jul 24;325(5939):435–9.

601. Shimizu Y, Shibata R, Ishii M, Ohashi K, Kambara T, Uemura Y, et al. Adiponectin-mediated modulation of lymphatic vessel formation and lymphedema. J Am Heart Assoc. 2013 Oct;2(5):e000438.

602. Yoshida S, Hamuy R, Hamada Y, Yoshimoto H, Hirano A, Akita S. Adipose-derived stem cell transplantation for therapeutic lymphangiogenesis in a mouse secondary lymphedema model. Regenerative Medicine. 2015;10(5):549–62.

603. Hwang JH, Kim IG, Lee JY, Piao S, Lee DS, Lee TS, et al. Therapeutic lymphangiogenesis using stem cell and VEGF-C hydrogel. Biomaterials. 2011 Jul;32(19):4415–23.

604. Zhou H, Wang M, Hou C, Jin X, Wu X. Exogenous VEGF-C augments the efficacy of therapeutic lymphangiogenesis induced by allogenic bone marrow stromal cells in a rabbit model of limb secondary lymphedema. Jpn J Clin Oncol. 2011 Jul;41(7):841–6.

605. Hou C, Wu X, Jin X. Autologous bone marrow stromal cells transplantation for the treatment of secondary arm lymphedema: a prospective controlled study in patients with breast cancer related lymphedema. Jpn J Clin Oncol. 2008 Oct;38(10):670–4.

606. Maldonado GEM, Pérez CAA, Covarrubias EEA, Cabriales SAM, Leyva LA, Pérez JCJ, et al. Autologous stem cells for the treatment of post-mastectomy lymphedema: a pilot study. Cytotherapy. 2011 Nov;13(10):1249–55.

607. Tammela T, Petrova TV, Alitalo K. Molecular lymphangiogenesis: new players. Trends Cell Biol. 2005 Aug;15(8):434–41.

608. Haiko P, Mäkinen T, Keskitalo S, Taipale J, Karkkainen MJ, Baldwin ME, et al. Deletion of vascular endothelial growth factor C (VEGF-C) and VEGF-D is not equivalent to VEGF receptor 3 deletion in mouse embryos. Molecular and Cellular Biology. 2008 Aug;28(15):4843–50.

609. Xu Y, Yuan L, Mak J, Pardanaud L, Caunt M, Kasman I, et al. Neuropilin-2 mediates VEGF-C-induced lymphatic sprouting together with VEGFR3. J Cell Biol. 2010 Jan 11;188(1):115–30.

610. Yuan L, Moyon D, Pardanaud L, Bréant C, Karkkainen MJ, Alitalo K, et al. Abnormal lymphatic vessel development in neuropilin 2 mutant mice. Development. 2002 Oct;129(20):4797–806.

611. Deng Y, Zhang X, Simons M. Molecular controls of lymphatic VEGFR3 signaling. Arteriosclerosis, Thrombosis, and Vascular Biology. 2015 Feb;35(2):421–9.

10 Appendices

10.1 Human Ethics

St. Vincent's Public Hospital/St. Vincent's and Mercy Private Hospital

Information and Consent form for a Study on Tissue Engineering

Full Project Title: The role of adult stem cells and tissue derived extracellular matrices in tissue engineering.

Protocol HREC No. 52/03

Version 15 **dated 13 January 2015.**

Principal Investigator: Professor Wayne Morrison

Your Consent:

You are invited to take part in this research project. This Principal Information contains detailed information about the research project. Its purpose is to explain to you as openly and clearly as possible all the procedures involved in this project before you decide whether or not to take part in it.

Please read the Participant information carefully. Feel free to ask questions about any information in the document. You may also wish to discuss the project with a relative or friend or a local health worker. Feel free to do this. Once you understand what the project is about and if you agree to take part in it, you will be asked to sign the consent form. By signing the consent form you indicate that you understand the information and that you give your consent to participate in the research project. You will be given a copy of the Participant Information and Consent Form to keep as a record.

What is the nature of the study?

As part of a larger study we are developing new methods of growing tissues that could eventually be used for reconstructive surgery. You are about to undergo an operation in which there may be tissue which could be used for this research. We hope to see if it is possible to "grow" body tissues with the purpose of replacing injured or diseased body parts and restoring their function in the future. The study requires samples of various types of human tissue for testing. Depending on which aspect of the study we are using your tissue for we will extract the proteins that surround the tissue and use these to create a scaffold that can be used for supporting new tissue growth. Alternatively we will collect cells from your tissue to test these scaffolds or experiments working towards growing new tissues. Our eventual aim is to develop new ways of "engineering" tissue for clinical applications.

10.2 Animal Ethics

ST VINCENT'S HOSPITAL MELBOURNE
A FACILITY OF ST VINCENT'S HEALTH AUSTRALIA

St Vincent's Hospital
(Melbourne) Limited
ABN 22 052 110 755

41 Victoria Parade Fitzroy VIC 3065
PO Box 2900 Fitzroy VIC 3065

Telephone 03 9288 2211
Facsimile 03 9288 3399
www.svhm.org.au

St Vincent's Hospital (Melbourne)
Animal Ethics Committee (AEC)

PROJECT APPLICATION FORM

All research and teaching that involves the use of animals for scientific purposes must comply with 'The Prevention of Cruelty to Animals Act' (1986), the associated Regulations and the NHMRC 'Australian code for the care and use of animals for scientific purposes' (8th Edition 2013).

This entire application form must be written using lay language and where the use of scientific language is unavoidable it must be supported by a suitable lay description or glossary of terms.

An answer must be provided for every question

A maximum of three (3) years approval only can be given for each project

---

AEC Reference Number (assigned by AEC Secretary)

0	1	5	/	1	5	-	r	5

Project Title *Should be concise and expressed in lay language; where possible avoid abbreviations, scientific terms.*
Radiotherapy-induced tissue injury: Investigation of mechanisms and therapeutic options.

Scientific Procedure Premises Licence (SPPL) Number	
SPPL	025: St Vincent's Institute

Principal Investigator *Identification of the person with ultimate responsibility for the conduct of the project and/or the care of the animals*	
Name: (Title, First, Surname)	Dr Ramin SHAYAN
Qualifications	MBBS, PhD, FRACS (Plastic & Reconstructive Surgery), PGrad Dip Surg Anatomy
Position	Laboratory Head, Institute Director
Department	Regenerative Surgery
Institution	O'Brien Institute at St Vincent's Institute
Phone	9288 4018
Email	rshayan@svi.edu.au

BAW Purpose and Benefit Codes	
Overall Purpose of the Project	1. The understanding of human or animal biology
BAW Benefit Code	2. Diseases - human

Research Team

Please ensure a Research Team Member Form (in Researcher Roles and Experience Section) is completed for every researcher listed, including Principal Investigator.

Name	Phone	Email	Qualifications
Dr Ramin Shayan	9288 4018	rshayan@svi.edu.au	MBBS, PhD, FRACS, PGrad Dip Surg Anatomy
Dr Tara Karnezis	9288 3925	tkarnezis@svi.edu.au	BSc. Hons, PhD
Dr Pradyumna Herle	9288 4033	pherle@svi.edu.au	MBBS, B Med Sci, PGrad Dip Surg Anatomy, PhD Candidate
Dr Charlotte Bendon	9288 4033	cbendon@svi.edu.au	MA(Oxon), BM BCh, MRCS
Dr Lipi Shukla	9288 4031	lipi.shukla@gmail.com	MBBS, PGrad Dip Surg Anatomy, Surgical Fellow, PhD Candidate
Katie Ardipradja	9288 4033	kardipradja@svi.edu.au	BSc. Hons
Dr Nicole Harris	9288 4033	nharris@svi.edu.au	BSc. Hons, PhD
Prof. Robin Anderson	9656 5284	robin.anderson@petermac.org	PhD, Principal Research Fellow
Dr Jim Hagekyriakou	9656 1111	jim.hagekyriakou@petermac.org	PhD, Senior Physicist
Cameron Nowell	+61 422 882 700	cameron.nowell@monash.edu	BSc. Hons, MIPS Imaging Research Facilities Manager
Amanda Rixon	9288 2649	rixona@svhm.org.au	Animal technician
Dr Caroline Taylor	9288 4027	cj.taylor@unimelb.edu.au	BSc. Hons, PhD
Jason Palmer	9288 4045	jpalmer@svi.edu.au	BSc. Hons

Which researcher(s) will have responsibility for the day to day running of the project and emergency care of animals?

Name	Telephone (Work hours)	Telephone (After hours)
Dr Prad Herle	9288 4031	0457 120 999
Dr Nicole Harris	9288 4033	0412 999 626
Katie Ardipradja	9288 4033	0410 514 369

QUESTION 1
Lay Explanation

a) Provide a summary of the proposed project (Max 200 words)

Radiotherapy significantly improves cancer patient survival however damage to tissues surrounding tumours, or radiation-induced bystander effects (RIBE), is inevitable. Clinically, RIBE manifests as pain, contracture, tissue break-down, recurring infection and lymphoedema. Lymphoedema presents as a swelling of tissues in irradiated areas or in an adjacent limb as a result of reduced drainage by lymphatic vessels. Lymphoedema is a key feature of radiotherapy injury and fundamental to initiating the progressive self-perpetuating cycle of fibrosis experienced by patients. Fat grafting (from liposuction) is commonly employed by plastic surgeons to reconstruct tissue defects from trauma, deformities or cancer resection. When fat is injected into irradiated areas, it reversed aspects of RIBE, with irradiated soft-tissues becoming more compliant, less swollen and less lymphoedematous. Animal models and clinical studies show that adipose derived stem cells (ADSCs) from the fat graft are likely the active component of

these fat grafts and are responsible for these positive effects. These findings raise several questions: *1) What molecular changes does RIBE cause? 2) Can these be reversed by ADSCs and by what mechanism? 3) If radiotherapy causes the inactivation of local ADSCs and ADSC implantation reverses RIBE, why can't distant ADSCs outside the radiotherapy area be recruited to repair tissue? 4) Can we harness vital components of fat grafts to develop therapeutics to treat RIBE?*

b) Briefly state the aim/s of the project

In this project we aim to characterize soft-tissue injury induced by radiation treatment. We hope to determine the efficacy of fat grafting as a therapy to rescue cells that have been irradiated by harnessing the beneficial characteristics of ADSCs to heal tissue and resolve lymphoedema. Our early experiments have focused on the effects of radiation on the cells that make up the lymphatics – the lymphatic endothelial cells (LECs), ADSCs (the key active component in fat grafts) and fibroblasts (the cells that form scar tissue and heal wounds). These experiments suggest that ADSCs improve the regeneration of LECs after radiotherapy, while also reversing the injury changes to fibroblasts. We would like to determine the effects in vivo of radiation on these cell types. Further, we hope to investigate the role of components of ADSCs in reversing the injury to the lymphatic vessels in living animals, thus determining their potential to reduce lymphoedematous swelling and scar formation in patients that have undergone radiation treatment.

c) Briefly state the potential benefits of the project

Increasingly effective therapies for many types of cancer have resulted in a significant increase in cancer survivors in the population. Over half of the 120,000 Australian patients diagnosed with a solid tumour annually require radiotherapy. However, radiotherapy itself results in a number of chronic soft-tissue injuries that we currently have no effective treatment for. The increase in these 'diseases of survivorship' is an area of particular importance and an area of unmet clinical need. For the majority of cancer survivors who develop lymphoedema, the effects result in significant health problems such as chronic infection and reduced wound healing, as well as tissue swelling deformities, psychological suffering and financial burden for themselves and their family that may not resolve in their lifetime. In addition, these patients' represent a major financial burden on the public health system and a challenging group of patients to care for effectively long-term.

Study of the tissue injury that occurs post-radiotherapy in mouse models that accurately model patient illness will allow us to define the molecular basis of this injury in cell types at the sites of radiotherapy. The data generated from this project will be used to identify and test targeted ADSC and fat graft derived therapies that we hope will translate to the clinic and will greatly improve their quality of life after radiotherapy.

d) If this application is a continuation of an existing project?
If yes provide a summary of the results from the previous project and include scientific results and any other information that the Committee should be aware of.

N/A

QUESTION 2
Replacement, Reduction and Refinement

a) REPLACEMENT:

Please justify why animals are required to achieve the aims of this project.
List alternatives considered and how they are used in this project
[i.e. historical data, computer simulations, in vitro techniques etc.]
Include why this research cannot be conducted in vitro or using human alternatives.

To address our hypothesis, we have performed a number of vitro studies using cell culture, and cell-specific bioassays. This has demonstrated a significant impairment in LEC migration, proliferation and tube formation in response to radiation injury. All of these processes are crucial for the formation of new lymphatics. In addition, we have developed spheroid assays and Boyden chamber assays, both simplified 3D models based on the processes

of endothelial cell sprouting and migration towards a gradient of factors released during injury, processes crucial to the function of these cells and their role in tissue repair. These functions are significantly affected following radiation injury and together these experiments can be used as a simplified model to study injury of this cell type seen in patients in the clinic.

To supplement our findings, additional in vitro studies have utilized state of the art next generation sequencing to profile the changes at a genetic level of cells in culture that have or have not undergone radiation. Further, we have mapped changes in proteins produced by these irradiated cells, in addition to determining the metabolic alterations that occur post radiation. These analyses have allowed us to hone in on those signaling networks responsible for the damage and provided insight into ways we can target these molecules to repair the tissue

Our in vitro studies have so far provided a comprehensive picture of some of the mechanisms at play in different cell types following radiation therapy. However, a full complement of relevant cell types in their correct spatio-temporal setting is crucial to assess the interplay between different cell types and how they react to radiation and thus affect one another following injury. This is impossible to achieve in a tissue culture system. In addition, cells from the immune system are recruited to the injured site. It is difficult to incorporate these components from the immune system in an in vitro culture system accurately. Mouse models of human disease, (and additionally mice containing modifications to genes of interest) are crucial to validate our findings in a living system, to assess the effectiveness of our treatments and to determine how best to proceed with viable treatment options. In order to provide meaningful avenues for therapeutic intervention in patients, we aim to utilize all the information uncovered from our extensive in vitro approaches, described above, in mouse models that faithfully recapitulate human disease. We have determined the expression of some genes of interest in clinical samples of patient tissue. However the experiments we aim to conduct are of course not suitable to be undertaken in humans. We therefore propose to conduct the mouse experiments described in this application as a means of modeling human disease and validating therapeutic approaches that we aim to introduce in a clinical setting.

b) *REDUCTION**: The number of animals used in a project must be the minimum necessary to achieve the proposed aim(s) and to satisfy good statistical design.***

Please describe any efforts made to minimise the total animal numbers requested in this proposed project.

We have estimated our use of mice for these experiments based on robust statistical modelling of our conditions. We have utilised experiments published in the literature to determine, where possible, the variability seen in these tissues under a range of conditions and thus calculated the expected number of mice to ensure that each experiment will provide the required statistical power so as to determine whether a result is significant and therefore meaningful. The number of mice needed as given by our statistical modelling is the maximum number of mice we require for each study to achieve statistical power based on our known parameters. However, different study groups will be processed in groups of 6 or 12 at a time to keep the workload manageable and we will be quantitating the results of each group straightaway. As soon as statistical power is reached between study groups, or we can determine that there is no statistical difference, we will not use any further mice.

Further efforts have been made to minimize the animal numbers used, include rigorous study design and planning as well as incorporating conditions and time-points known to generate meaningful data. In addition, for those experiments conducted on the ears and legs, both ears and both hind legs of each mouse will be included in the studies to minimize the number of mice required. All samples will be harvested and stored appropriately, before processing and analysis as per established and published protocols, to ensure that all the relevant tissues of the animals are utilized and not wasted to effectively contribute to the study aims. All experiments will be conducted by or with experienced staff so as to avoid errors during the studies or in the analysis of the data.

c) *REFINEMENT**: Steps must be taken at all times to support and safeguard animal wellbeing.***

Please identify known and potential impact on the wellbeing of an animal in this project. [e.g. number of injections, route of injections, accumulated impact of procedures, surgical procedures, long term housing, singly housed animals]
How will such impacts will be avoided or minimised? [e.g. rotate injection site, use of analgesia, environmental enrichment]

The models we are undertaking are either well established techniques in the literature or will be conducted by experts in the field, allowing us to minimize excess use of mice. All staff involved in performing procedures are thoroughly trained. Radiation will be undertaken at the Peter MacCallum Cancer Centre in collaboration with

Professor Robin Anderson, and will be carried out by Senior Physicist Dr Jim Hagekyriakou, both have considerable experience in targeted irradiation of mice (past animal studies in breast cancer, AEC E481). Based on their experience we anticipate no problems in delivering these sub-lethal doses to the mouse. Tail surgery will be performed by trained surgeons and tail vein injections will be carried out by trained lab members with over 10 years animal experience.

Mice will be transported to the Peter MacCallum Cancer Centre for irradiation procedures in a personal vehicle. Clean hospital towels and lab coats will be used as padding to protect from car movement, to shield the micro-isolators from view and keep mice calm. Prior to transport, mice will be placed in clean micro-isolators with clean bedding and without their water bottles. Mice are expected to be without water for a maximum of one hour, which will have no adverse effects.

Following all irradiation procedures Baytril will be included in the water for 2 weeks post irradiation to minimise weight loss from radiation induced sickness and mice will be monitored as per AEC Clinical SOP 30 Mouse Health Monitoring. Temgesic analgesia will be utilized as per AEC Clinical SOP 27 Analgesia in Mice. Analgesia will be given prior to irradiation and for any invasive procedures conducted. Additionally, when a mouse shows any signs of pain during general health monitoring, analgesia will be given as per SOP. Further, Isoflurane gas anaesthetic will be given prior to foot pad injection or hole punch biopsy in the ear.

Following tail surgery mice will be singly housed so as to avoid disturbance of the surgery site by other mice. These mice will therefore receive additional environment enrichment for this time.

Final imaging studies will be performed under full anaesthesia at Monash Institute for Pharmalogical Sciences (MIPS) in conjunction with our collaborator Cameron Nowell, who has over 10 years experience with imaging live animals. This will be performed on anesthetized animals at the MIPS campus in Parkville. The journey from EMSU to MIPS will be undertaken with an approved animal shipping company eg. JetPets. With Cameron's extensive experience in imaging and MIPS, and the presence of at least one OBI/SVI member during imaging procedures, welfare of the mice will be constantly monitored during the entire imaging procedure.

QUESTION 3
Experimental Procedures and Monitoring

Experimental Procedure Form
This form must be completed for EVERY procedure listed in proposed project

Where possible refer to SOP's (state SOP number and title).
List of AEC approved Clinical SOP's can be found at:
http://www.svhm.org.au/research/governance/Pages/Operatingprocedures.aspx

Procedure #	1	Species	Prox-1 GFP mouse CXCR7-GFP mouse	# Animals	384 384
Location:	☒EMSU ☐BRC ☐ Other (please specify):				
Title	Radiotherapy-induced soft tissue injury: Investigation of mechanisms and therapeutic options - Ear model				
BAW Impact	4. Minor operative procedure with recovery				
BAW Part. Procedure	12. Ionising radiation exposure				
Level of Discomfort	Moderate				

Provide a clear step by step description of procedure to be carried out on each animal or group of animals, in relation to the aims, in this project.

Include the following information:
- Dose rate, volume and route of administration of any substance or treatment administered
- Volume, frequency and method of collection of any samples
- Surgical and related procedures, including analgesia and anaesthesia

- Post-operative or post-procedure care
- Experimental endpoints
- Methods of euthanasia

We would like to analyse lymphatics in the mice following radiation treatment. To do so we plan to utilize ears as a site of skin tissue containing a well-defined network of lymphatic vessels. To assess this tissue we will use established techniques to quantify and compare a range of parameters of lymphatic vessel formation - lymphatic endothelial cell sprouting (from existing vessels to form new vessels), sprout tip number, branching of vessels, blind ending sacs and loops (Shayan et al. Growth Factors 2007, Vol. 25, No. 6 , Pages 417-425).

EAR MODEL: Baseline characteristics.

Experimental groups

The experimental groups will be as follows.

1. Old mice (19-24 weeks) – Irradiation of right ear (45 Prox-1 GFP mice, 45 CXCR7-GFP mice)
2. Young mice (6-10 weeks) – Irradiation of right ear (45 Prox-1 GFP mice, 45 CXCR7-GFP mice)
3. Old mice (19-24 weeks) – No irradiation (45 Prox-1 GFP mice, 45 CXCR7-GFP mice)
4. Young mice (6-10 weeks) – No irradiation (45 Prox-1 GFP mice, 45 CXCR7-GFP mice)

Procedure notes

Mice will be transported to Peter MacCallum Cancer Centre and mouse ears will be irradiated by Dr Jim Hagekyriakou (PhD, Senior Physicist), with Professor Robin Anderson. Briefly, mice will be placed into a lead chamber specially designed by Dr Hagekyriakou which protects the head and body of the mouse from radiation, whilst exposing a single ear to radiation. Ketamine/Xylazine (100mg/kg and 10mg/kg respectively) will be administered via intraperitoneal injection to anaesthetize mice prior to irradiation/sham irradiation of mice ears as per AEC Clinical SOP 49 Injectable anaesthesia in mice and AEC Clinical SOP 52 Intra-peritoneal injection in the mouse. After irradiation, mice will be monitored for recovery in the OBI contamination room. Mouse body temperature will be maintained on warming mats until mice regain consciousness and show signs of responsiveness indicating adequate recovery. Post irradiation recovery will be carried out as per AEC Clinical SOP 23 Irradiation of mice to closely monitor mouse weight and general health as per AEC Clinical SOP 30 Mouse Health Monitoring. Mice will receive Baytril in their water post irradiation.

Endpoints

Mice will be sacrificed one, two or three weeks post irradiation / sham irradiation by cervical dislocation carried out by experienced animal technicians as per AEC Clinical SOP 26 Euthanasia of laboratory animals. Alternatively if tissues are to be collected for electron microscopy, transcardiac perfusion will be performed on terminally anaesthetized animals. Mice which will have transcardiac perfusion will be anaesthesised with an overdose of isoflourane or ketamine/xylazine, when animal has stopped breathing, blood from the vasculature will be flushed using a PBS solution injected into the left ventricle of the heart followed by fixative. This perfusion of fixative will allow us to image small subcellular structures of the fixed tissue by electron microscopy. Whole ears will be harvested, the volar surface will be dissected and cartilage peeled off the posterior surface. Ears will be mounted and imaged, followed by quantitation of lymphatic vessel parameters using custom designed analysis software. Additionally a number of mice from each group will be transported to MIPS as described in question 2 for final imaging studies prior to being sacrificed. Final imaging studies will be conducted on the mice under full anaesthesia without recovery. Once unconscious, a small volume (less than 50 µl) of fluorescent particles will be injected into the skin of the ear. These particles naturally traffic to the lymphatic system of the ear. Using intravital microscopy, lymphatic flow can be easily quantitated based on the observed rate of movement of these particles. After these assessments, mice will be given an overdose of Ketamine/Xylazine and tissues will be collected at MIPS.

EAR WOUNDING and TREATMENT MODEL

Experimental groups

1. Wounding both ears- irradiation of right ear (110 Prox-1 GFP mice, 110 CXCR7-GFP mice)
2. Wounding both ears – no irradiation of right ear (100 Prox-1 GFP mice, 110 CXCR7-GFP mice)
3. Wounding both ears – irradiation of right ear + ADSC-CM treatment (47 Prox-1 GFP mice, 47 CXCR7-GFP mice)
4. Wounding both ears – irradiation of right ear + vehicle control (47 Prox-1 GFP mice, 47 CXCR7-GFP mice)
5. Wounding both ears – no irradiation of right ear + ADSC-CM treatment (10 Prox-1 GFP mice)

Procedure notes

Anaesthetic procedures will be the same as described above for irradiation. Mice will receive irradiation on a single ear as described above. One, two or three weeks post irradiation the mice will undergo ear wounding using a punch biopsy, which is commonly used as a numbering system to easily identify individual mice. Ear wounding of both the irradiated and non-irradiated ears will be performed using a 3mm punch biopsy whilst mice are restrained, the punch will be placed in a central location in the ears. During the punch biopsy mice will receive isoflurane gas anaesthetic, post procedure the mice will receive Temgesic analgesia to reduce pain from the procedure. Mice will be monitored post-procedure for signs of distress or infection as per AEC Clinical SOP 30 Mouse Health Monitoring.

Mice in groups 3 – 4 will undergo ear punch wounding 1 week post irradiation and receive treatment with ADSC-CM or vehicle control once daily until they have received 4 treatments total. Treatment will begin once the punch wound has been determined to have healed sufficiently for the injections to be most effective, 4 days post punch wounding, therefore treatments will be administered on day 4, 5, 6 and 7 post wounding (see attached flow chart). For each treatment 0.025 ml of ADSC-CM or vehicle will be delivered via intra-dermal injection using a 0.5 ml syringe and 30 gauge needle to both the irradiated and non-irradiated ear once a day until 4 treatments, a total volume of 0.1 ml, are completed. The injection sites will be rotated around the wound to reduce discomfort. The wound will be allowed to heal for 3 weeks after the treatment has ended and the mice will be euthanized on Day 35. For each treatment injection the mice will receive isoflurane gas anaesthetic for a maximum of 10 minutes (including anaesthetic induction chamber) and are expected to recover 1 min after injection. Post procedure the mice will receive Temgesic analgesia. Mice will be monitored post-procedure for signs of distress or infection as per AEC Clinical SOP 30 Mouse Health Monitoring. Due to a number of blood vessels in the ear, mice may suffer from a haematoma and swelling as an effect from the injection. If this occurs in any of the mice, precluding safe injection, intradermal injections will be stopped for one day until ear skin shows signs of recovery (normal redness, decreased swelling and healing). If the haematoma is not resolved after the 24 hour rest period, the animal will be removed from the study.

End points

Mice will be sacrificed one week, two weeks or three weeks after ear wounding by cervical dislocation carried out by experienced animal technicians as per AEC Clinical SOP 26 Euthanasia of laboratory animals**.** Alternatively if tissues are to be collected for electron microscopy, transcardiac perfusion will be performed on terminally anaesthetized animals. Briefly: mice which will have transcardiac perfusion will be anaesthesised with an overdose of isoflourane or ketamine/xylazine, when animal has stopped breathing, blood from the vasculature will be flushed using a PBS solution injected into the left ventricle of the heart followed by fixative. This perfusion of fixative will allow us to image small subcellular structures of the fixed tissue microscopy. A new SOP for transcardiac perfusion has been written and submitted for approval. Whole ears (both) will be harvested, the volar surface will be dissected and cartilage peeled off the posterior surface. Ears will be mounted and imaged and lymphatic parameters as discussed above.

Additionally a number of mice from each group will be transported to MIPS as described in question 2 for final imaging studies prior to being sacrificed. Final imaging studies will be conducted on the mice under full anaesthesia without recovery. Once unconcious, a small volume (less than 50 µl) of fluorescent particles will be injected into the

base of the ear. These particles naturally traffic to the lymphatic system of the ear. Using a microscope, lymphatic flow can be easily quantitated based on the observed rate of movement of these particles. After these assessments, mice will be given an overdose of Ketamine/Xylazine and tissues will be collected at MIPS.

Provide details of how the wellbeing of animals will be monitored and assessed.

Describe the:

- Frequency of monitoring and assessment
- Actions to be taken if problems are identified
- Criteria for intervention points and humane endpoints.

Attach relevant monitoring sheets or checklists.

Post-anaesthesia mice will be kept warm on a warming pad with close monitoring of breathing, responsiveness and temperature for 30 minutes. The mice are monitored until they are fully recovered. Ongoing monitoring of mouse weight post irradiation as per AEC Clinical SOP 23 Irradiation of Mice.

Animal general health and signs of pain will be monitored as per AEC SOP 30. Temgesic analgesia will be given as per SOP 27 analgesia in mice to minimize pain from the procedure. Isoflurane gas anaesthetic will be used during the punch biopsy procedure and for intra dermal injections. The wound site will be monitored for signs of infection in the following weeks of study as per AEC SOP 30.

Investigators will monitor these animals every 2-3 days for the duration of the experiments in addition to animal technician care and monitoring. Investigators will be contacted by animal technician in case of any urgent matters regarding animal health and animals will be euthanized if a vet deems this necessary. See attached monitoring sheet, at the end of this document.

Procedure #	2	Species	Prox-1 GFP mouse CXCR7Tie2 mouse	# Animals	336 336
Location:	☒EMSU ☐BRC ☐ Other (please specify):				
Title	Radiotherapy-induced soft tissue injury: Investigation of mechanisms and therapeutic options - Tail model				
BAW Impact	4. Minor operative procedure with recovery				
BAW Part. Procedure	12. Ionising radiation exposure				
Level of Discomfort	Moderate				

Provide a clear step by step description of procedure to be carried out on each animal or group of animals, in relation to the aims, in this project.

Include the following information:

- Dose rate, volume and route of administration of any substance or treatment administered
- Volume, frequency and method of collection of any samples
- Surgical and related procedures, including analgesia and anaesthesia
- Post-operative or post-procedure care
- Experimental endpoints
- Methods of euthanasia

We plan to mimic patient lymphoedema by investigating the effects of radiation and surgery on the mouse tail lymphatic drainage by tail diameter/volume measurements. The mouse tail is an established tissue to investigate lymphoedema and is well characterized in the literature The lymphatic vasculature present can be divided into dermal lymphatics (present in the skin) and the deeper, subcutaneous collecting lymphatic vessels, both of which are amenable to surgical techniques.

LYMPHOEDEMA MODEL – TAIL

Experimental Groups

In this portion we aim to define the roles of the different lymphatic vessel types (dermal and deeper subcutaneous) anatomically in their contribution to lymphoedema. We will combine surgery and radiation, radiation alone and different anatomical structures affected by surgery. Trained surgeons will complete all surgery without disrupting the blood supply.
Group 1 - 8 week old mice - Radiation vs no radiation 84 Prox-1 GFP mice and 84 CXCR7Tie2 mice
Group 2 - 8 week old mice – Comparison between 3 surgical procedures with radiation: dermal surgery (dermal lymphatics removal) + radiation, collecting surgery (collecting lymphatics removal) + radiation, and dermal and collecting surgery (dermal and collecting lymphatics removal) + radiation 126 Prox-1 GFP mice and 126 CXCR7Tie2 mice
Group 3 - 8 week old mice - Comparison between 3 surgical procedures alone: dermal surgery (dermal lymphatics removal) + no radiation, collecting surgery (collecting lymphatics removal) + no radiation, and dermal and collecting surgery (dermal and collecting lymphatics removal) + no radiation 126 Prox-1 GFP mice and 126 CXCR7Tie2 mice

Procedure notes
Anaesthetic procedures will be the same as previously described for radiation. Temgesic analgesia will be administered post procedure. Irradiation will be carried out as described above at the Peter MacCallum Cancer Centre.
Group 1

- The mice will be transported to Peter MacCallum Cancer Centre, anaesthetized as described above and receive radiation or sham radiation to their tail. Mice will then be monitored and tail diameter will be measured from standardized images taken of the tail at regular time-points for 4-6 weeks. Standardized images will be generated by placing mice on graph paper with a ruler for scale, pictures will be taken with a camera on a tripod at a defined distance. This method will be consistent for all groups. Tail images will be analysed using ImageJ software.

Group 2 and 3 procedures (under anaesthetic). Mice will receive radiation to the tail one week prior to surgery as described for Group 1. One week post radiation mice will undergo surgery:

- Dermal lymphatic surgery – a circumferential patch of skin and immediate subcutaneous tissue of up to 10 mm in diameter will be removed from the proximal end of the mouse tail to disrupt the dermal lymphatics. Deeper collecting vessels will be left intact. Gauze and surgical tape will be placed over the wound. Mice will then be monitored and tail diameter will be measured from standardized images taken of the tail at regular time-points for 4-6 weeks.
- Deeper collecting vessel surgery – the collecting lymphatic vessels will be identified by patent blue injection into the mouse tail tip. This procedure will be conducted as per AEC Clinical SOP 53 Subcutaneous injection in mice. These vessels will then be dissected and the wound closed. Gauze and surgical tape will be placed over the wound. Mice will then be monitored and tail diameter will be measured from standardized images taken of the tail at regular time-points for 4-6 weeks.
- Dermal surgery and collecting vessel surgery – both dermal surgery and deeper collecting vessel surgery will be performed in the one procedure as described above. Gauze and surgical tape will be placed over the wound. Mice will then be monitored and tail diameter will be measured from standardized images taken of the tail at regular time-points for 4-6 weeks.

End points

- Group 1 - Mice will be sacrificed from 4 hrs and up to 6 weeks post irradiation.
- Group 2- Post-surgery the mice will be as in Group 1, monitored for tail diameter up until they are sacrificed 4-6 weeks post-procedure.
- Group 3 – Animals will be sham irradiated 1 week prior to surgery. Post-surgery the endpoint is the same as group 2, 4-6 weeks post-procedure
- Additionally a number of mice from each group will be transported to MIPS as described in question 2 for final imaging studies prior to being sacrificed. Final imaging studies will be conducted on the mice under full anaesthesia without recovery. Once unconscious, a small volume (less than 50 µl) of fluorescent

particles will be injected into the base of the tail. These particles naturally traffic to the lymphatic system. After injection, a flap of skin on the tail will be raised to expose the vessels in the skin. Using a microscope, lymphatic flow within these vessels will be quantified based on the observed rate of movement of the fluorescent particles. After these assessments, mice will be given an overdose of Ketamine/Xylazine and tissues will be collected at MIPS.

- Some of the tissues will be collected for electron microscopy, which requires transcardiac perfusion of fixative. Mice which will have transcardiac perfusion will be anaesthesised with an overdose of isoflourane or ketamine/xylazine, when animal has stopped breathing, blood from the vasculature will be flushed using a PBS solution injected into the left ventricle of the heart followed by fixative. This perfusion of fixative will allow us to image small subcellular structures of the fixed tissue by electron microscopy. A new SOP for transcardiac perfusion has been written and submitted for approval.

Provide details of how the wellbeing of animals will be monitored and assessed.

Describe the:

- Frequency of monitoring and assessment
- Actions to be taken if problems are identified
- Criteria for intervention points and humane endpoints**.**

Attach relevant monitoring sheets or checklists.

Post anaesthesia mice will be kept warm on a warming pad with close monitoring of breathing, responsiveness and temperature for 30 minutes. The mice will be monitored until they are fully recovered. Post radiation ongoing monitoring of mouse weight, and Baytril in the water for 2 weeks post irradiation as per AEC Clinical SOP 23 Irradiation of Mice.

Animal general health and signs of pain will be monitored as per AEC SOP 30. Analgesia will be given as per SOP 27 analgesia in mice. Surgical sites on the mice will then be monitored closely for 1 hour post procedure, and adequate Temgesic analgesia will be given to minimize pain at the surgical site. The site of the wound will be covered with gauze and Tegaderm surgical tape to aid in healing, reduce site infection and minimise mouse interference. The mice will be monitored for signs of infection in the following weeks of study as per AEC SOP 30 and singly housed following surgery with additional environmental enrichment.

Investigators will monitor these animals every 2-3 days for 2 weeks and once weekly after two weeks in addition to animal technician care and monitoring. Investigators will be contacted by animal technician in case of any urgent matters regarding animal health and animals will be euthanized if a vet deems this necessary.

Procedure #	3	Species	Prox-1 GFP mouse CXCR7Tie2 mouse	# Animals	140 140

Location:	☒EMSU ☐BRC ☐ Other (please specify):
Title	Radiotherapy-induced soft tissue injury: Investigation of mechanisms and therapeutic options - Leg model
BAW Impact	4. Minor operative procedure with recovery
BAW Part. Procedure	12. Ionising radiation exposure
Level of Discomfort	Moderate

Provide a clear step by step description of procedure to be carried out on each animal or group of animals, in relation to the aims, in this project.

Include the following information:

- Dose rate, volume and route of administration of any substance or treatment administered
- Volume, frequency and method of collection of any samples
- Surgical and related procedures, including analgesia and anaesthesia
- Post-operative or post-procedure care
- Experimental endpoints
- Methods of euthanasia

Approximately 30% of cancer patients that have received radiotherapy as part of their treatment later present in the

clinic with radiation tissue injury which has caused lymphoedema swelling. We plan to model this in the mouse by irradiating the lower limb (leg) and then assessing the induction of lymphoedema in the leg over time by diameter/volume measurements and foot pad thickness. Having established this as a model of radiation-induced lymphoedema, we will use this to test treatment options that arise from our in vitro studies.

LYMPHOEDEMA MODEL – LEG (THERAPEUTIC)

Experimental Groups

We will expose the mouse leg to radiation that results in cell injury and lymphoedema in collaboration with Professor Robin Anderson and Dr Jim Hagekyriakou. This will be followed by defining the role of factors released by adipose derived stem cells (ADSCs) in reversing radiation injury by treating irradiated tissue with whole conditioned media (containing everything secreted by ADSCs in vitro), in addition to treating with fractions of this media (containing selective components secreted by ADSCs) which have shown promising cell rescue in vitro. Control media will be cell culture media not exposed to ADSCs and therefore not containing any secreted components from these cells.

We plan to use the contralateral leg as an internal control in addition to negative control animals for reasons stated previously.

1. Group 1 Radiation (right leg) 28 Prox-1 GFP mice and 28 CXCR7Tie2 mice
    a. Treated with ADSC conditioned media injection in right leg
    b. ADSC conditioned media injection in left leg
2. Group 2 Radiation (right leg) 28 Prox-1 GFP mice and 28 CXCR7Tie2 mice
    a. Treated with ADSC conditioned media injection in right leg
    b. Control media in left leg.
3. Group 3 Radiation (right leg) 28 Prox-1 GFP mice and 28 CXCR7Tie2 mice
    a. Treated with control media in right leg
    b. Treated with control media in left leg.
4. Group 4 + 5 28 Prox-1 GFP mice and 28 CXCR7Tie2 mice per group
    a. Repeat experiments 1+2 with different fractions of ADSC media.

Procedure notes

Anaesthetic, radiation and euthanasia techniques will be the same as for previous procedures. Radiation will be delivered to the right leg of mice using a specially designed lead jig designed by Dr Jim Hagekyriakou.
Following radiation Control media or ADSC-conditioned media will be administered to treat the lymphoedema. Both will be administered at an equal volume (v=100µl) into the foot pad. Isoflurane gas anaesthetic will be utilized for the foot pad injection and Temgesic analgesia will be utilized post procedure. Mice will be monitored for 2-3 weeks post injection with Control media or ADSC-conditioned media to determine if a therapeutic effect is seen. Standardized images of the leg will be obtained as in Procedure 2 and the volume of the leg and foot pad thickness will be monitored.

Conditioned media is media that is used to culture cells in vitro. The media is added to tissue culture flasks containing un-irradiated adipose derived stem cells for 72 hours. Media is centrifuged and the supernatant filtered to ensure the media product being used is cell free and sterile. Conditioned media has shown promise in rescuing irradiated cells as it contains components secreted from ADSCs including growth factors and other beneficial molecules.

Fractionated media is media that has been separated based on particle size and charge from one complex mixture to several fractions with reduced complexity, the point of the fractionated media is to narrow down substances of interest that may be in conditioned media that are responsible for the rescue effects we have observed in vitro. Identification of the beneficial molecules of interest is then simplified to the reduced components present in each fraction. The capacity to rescue tissue in the mouse will be compared to the complete conditioned media to ensure all those molecules that promote cell rescue are defined by what is present in the fractions.

End points

- Group 1 - Mice will be sacrificed 2 -3 weeks after ADSC conditioned media injections are administered. Group 2 and 3 – Same as Group 1: 2 – 3 weeks post treatment with ADSC conditioned media samples or Control media.
- Group 4 and 5 - Mice will be sacrificed 2 -3 weeks after injection with fractions of ADSC conditioned media.

As discussed with the AEC, endpoints will be determined by a pilot study for Group 3 mice (Prox-1 GFP) that assesses the time it takes to achieve lymphoedema without impeding the movement of the mice, expected to be around 4 weeks post-irradiation. A report will be submitted to the AEC at the completion of this Pilot Study detailing the experimental results and wellbeing of the mice.

Provide details of how the wellbeing of animals will be monitored and assessed.

Describe the:

- Frequency of monitoring and assessment
- Actions to be taken if problems are identified
- Criteria for intervention points and humane endpoints.

Attach relevant monitoring sheets or checklists.

Post anaesthesia the body temperature of the mice will be maintained on a warming pad with close monitoring of breathing, responsiveness and temperature for 30 minutes. The mice are monitored until they are fully recovered. Ongoing monitoring of mouse weight for 4-6 weeks post irradiation as per AEC Clinical SOP 23 Irradiation of Mice.

Animal general health and signs of pain will be monitored as per AEC SOP 30. Isoflurane gas anaesthetic will be used for footpad injections, and Temgesic analgesia will be given as per SOP 27 analgesia in mice post foot pad injection. The site of irradiation will be monitored for signs of infection in the following weeks of study as per AEC SOP 30. Investigators will monitor these animals every 2-3 days for 2 weeks and once a week after 2 weeks in addition to animal technician care and monitoring. Investigators will be contacted by animal technician in case of any urgent matters regarding animal health and animals will be euthanized if a vet deems this necessary. Baytril will be added to the water of all mice following irradiation.

QUESTION 4

Who will monitor the animals during the proposed project?	
Weekdays	Dr Pradyumna Herle, Dr Nicole Harris, Amanda Rixon, Katie Ardipradja, Dr Charlotte Bendon
After hours (including weekends and public holidays)	Dr Pradyumna Herle, Dr Nicole Harris, Katie Ardipradja

QUESTION 5

Please provide a flow chart showing the sequence of events, from start to finish, for individuals or groups of animal.

See attached flow chart at the end of document

QUESTION 6

Please list all agents that will be administered to animals in the proposed project.
Include anaesthetics, analgesics, disease induction agents, antibiotics etc.

Agent	Route	Dose	Duration
Ketamine	Subcutaneous injection	100mg/kg	Single dose for surgical anaesthesia, total number of 3

			doses at maximum per mice
Xylazine	Subcutaneous injection	10mg/kg	Single dose of surgical anaesthesia, total number of 3 doses at maximum per mice
Radiation	Radiation	10-30 Gy	As a single dose over 10min
ADSC conditioned media	Intradermal injection	0.1ml	Single injection
Flourescent particles	Intradermal injection	50 µl	Single injection per ear or tail
Baytril	Drinking water	1.7ml/750ml water	For 5 days from the day of procedure
Temgesic	Subcutaneous injection	0.1mg/kg	Single dose at time of procedure
Isoflurane	Gas		Single dose to anaesthetize animal

QUESTION 7
Animal Use

Animals Requested				
Species	**Strain**	**Source***	**Housing Location**	**Total Number**
Mouse	Prox1-GFP BAC transgenic KY221 Gsat/Mmcd, on a FVB/N-Crl:CD1(ICR) background	Own Derivation (Refer IBC 246)	O'Brien Institute Mouse Room, EMSU	860
Mouse	*Tie2-Cre/+ Cxcr7$^{lox/lox}$* C57BL/6 background	Own Derivation (Refer IBC 246)	O'Brien Institute Mouse Room, EMSU	476
Mouse	CXCR7-GFP BAC transgenic HE28Gsat/Mmucd on a FVB/N-IcrTac:ICR background	Own Derivation (Refer IBC 246)	O'Brien Institute Mouse Room, EMSU	384
*Source: 1. Own derivation (breeding) 2. Victorian SABL Supplier 3. Interstate Licensed Supplier 4. Overseas Supplier or 5. Specify if another source			**GRAND TOTAL:**	1720

QUESTION 8

Justify why these species/strains will be used.
The Prox1-GFP mouse is a genetically modified mouse strain, incorporating a Prox-1 promoter-driven Green-Fluorescent-Protein (GFP) reporter gene, therefore the lymphatic vessels fluoresce green due to their expression of the Prox-1 gene. The GFP expression will allow us to easily visualize lymphatic vessels in tissue, and to isolate them for in vitro culture. This strain was obtained from the Institute of Molecular Biosciences Animal Facility, University of Queensland, by Mat Francois. We have a breeding protocol approved at St Vincent's Hospital (Ref. IBC 246, AEC-GNMBL 013/14) and are currently breeding these mice in the EMSU facility. Cxcr7Tie2, is a genetically modified strain created at the Garvan Institute in collaboration with New York University and St Vincent's Hospital. They are a conditional knock-out mice created using a Cre-LoxP technique. This conditional knock-out is linked with the gene Tie2, therefore the expression of cxcr7 is lost in endothelial tissues that

express Tie2. We will thus be able to investigate the role of Cxcr7 in lymphatic endothelial cells and how it contributes to lymphoedema post-radiation. In Cxcr7-GFP mice, the *Cxcr7* gene encoded by exon 2 was replaced by a GFP sequence, allowing expression of GFP at the sites of Cxcr7 expression. This labelling will be particularly useful to determine expression changes of Cxcr7 in tissues post radiation and to isolate tissue for in vitro analysis that are positive for Cxcr7. Both Cxcr7 strains will be obtained from Monash University, Melbourne from Professor Charles Mackay.

QUESTION 9

Justify the total number of animals that have been requested. Include a power calculation and/or description of the statistical method used to calculate the total animal number.

Given the numbers of animals requested we anticipate that we will complete the experiments over 2 – 3 years.

EAR MODEL – BASELINE CHARACTERISTICS

Based on assessments of patient tissue we suspect in the absence of wounding there is no more than 5% difference in the baseline characteristics of lymphatics. From a previous study by Shayan et al, the number of branch points on average is between 30-40 branch points per 10 × microscopic fields. The number needed for power calculation was determined using G*Power, a computer application for calculating power of statistical tests and number needed for power.

<u>To test for a 5% difference</u>

t tests - Means: Difference between two dependent means (matched pairs)

Analysis:	A priori: Compute required sample size			
Input:	Tail(s)	=	Two	
	Effect size dz	=	0.3000000	
	α err prob	=	0.05	
	Power (1-β err prob)	=	0.90	
Output:	Noncentrality parameter δ	=	3.2726136	
	Critical t	=	1.9802722	
	Df	=	118	
	Total sample size	=	119	
	Actual power	=	0.9007612	

I.e. in order to achieve a 90% power calculation with a significance of $p<0.05$ we would require 120 mice in order to determine the effects of radiotherapy (using the other ear as an internal control).
The effect of radiation would also need to be compared to negative controls (who have not received any radiation) in case there is any systemic effect from radiation or bystander radiation through the jig (which should be minimal). The calculation for this is shown below.

<u>To test for a 5% difference</u>

Analysis:	A priori: Compute required sample size			
Input:	Tail(s)	=	Two	
	Effect size d	=	0.3000000	
	α err prob	=	0.05	
	Power (1-β err prob)	=	0.90	
	Allocation ratio N2/N1	=	1	
Output:	Noncentrality parameter δ	=	3.2519225	
	Critical t	=	1.9650459	
	Df	=	468	
	Sample size group 1	=	235	

Sample size group 2 = 235
Total sample size = 470
Actual power = 0.9006525

The literature also has conflicting evidence regarding lymphatic density and changes of lymphatic vessel density with age. We estimate the difference to be at least in the magnitude of 2-5%. Utilising values for lymphatic density from previously published data, the number needed for power was calculated in G*Power with the values demonstrated below.

To test for a 5% difference

t tests - Means: Difference between two independent means (two groups)
Analysis: A priori: Compute required sample size
Input: Tail(s) = Two
Effect size d = 0.5000000
α err prob = 0.05
Power (1-β err prob) = 0.90
Allocation ratio N2/N1 = 1
Output: Noncentrality parameter δ = 3.2787193
Critical t = 1.9740167
Df = 170
Sample size group 1 = 86
Sample size group 2 = 86
Total sample size = 172
Actual power = 0.9032300

Number of Experimental mice:
The middle-ground figure therefore with all these values and limitations of resources in mind we request the following:
90 mice receiving irradiation
90 mice receiving sham irradiation for a total of 180 mice

In each group:
45 old mice
45 young mice

EAR WOUNDING MODEL
Statistical testing
A study by Shayan et al showed in a wounded ear imaged at 10×, there were approximately 3.5 +/- 0.5 sprouts per field in a wounded ear. We suspect radiation impairs lymphangiogenesis and therefore expect ~ 10% difference.

The number needed for power calculation values for the wounding model (using non-irradiated ear as an internal control) is shown below. As this experiment forms the crux of our theoretical basis behind radiation injury we will aim for a 95% power.

t tests - Means: Difference between two dependent means (matched pairs)
Analysis: A priori: Compute required sample size
Input: Tail(s) = Two
Effect size dz = 0.7000000
α err prob = 0.05
Power (1-β err prob) = 0.95

Output: Noncentrality parameter δ = 3.7696154
Critical t = 2.0484071
Df = 28
Total sample size = 29
Actual power = 0.9532752

Once again it is necessary to compare to completely non-irradiated mice and the calculation for this is also demonstrated.
t tests - Means: Difference between two independent means (two groups)
Analysis: A priori: Compute required sample size
Input: Tail(s) = Two
Effect size d = 0.7000000
α err prob = 0.05
Power (1-β err prob) = 0.95
Allocation ratio N2/N1 = 1
Output: Noncentrality parameter δ = 3.6708310
Critical t = 1.9821735
Df = 108
Sample size group 1 = 55
Sample size group 2 = 55
Total sample size = 110
Actual power = 0.9533297

I.e. Sample sizes of 55 in the wounded-irradiated and the wounded-non irradiated groups would deliver sufficient power for both purposes. Total number of mouse requested is 110.

Number of Experimental mice:
Given this is the main crux of our research goals we request 55 mice per group (irradiation versus no irradiation).

EAR WOUNDING TREATMENT MODEL
To calculate the animal number we have used G*Power, a computer application for calculating power of statistical tests and the number of animals needed for power. We have used experimental numbers from the studies we have already conducted so far in the ear wounding model, the numbers therefore are based on the degree of change we see in the vessels and how robust this result is between experiments. The numbers we have outlined are based on calculating the number of mice that would be required to observe a 10% difference between study groups with 80% confidence that the result is not due to chance. The total number of mice requested is only an estimate of the maximum required to achieve a significant, meaningful result. As soon as statistical significance is reached in this study it will end and no more mice will be used.

<u>Number of mice required to test a difference between treatment and vehicle control in IRRADIATED EARS:</u>
t-test – Means: Difference between two dependent means (matched pairs)
Analysis: A priori: Complete required sample size
Input: Tail(s) = one
Effect size dz = 0.5024954

Effect size calculated using 20% positive difference on current 10Gy ear sprout number values and Standard Deviation.

OUTPUT -
α err prob = 0.05

Power (1 – β err prob) = 0.95
Noncentrality parameter δ = 3.3664077
Critical t = 1.6803274
Df = 43.8816940
Total sample size = 47 pairs of ears (10Gy treated vs vehicle control)
Actual power = 0.9524378

LYMPHOEDEMA MODEL - TAIL

Statistical analysis.

Lymphoedema is defined in measurements as >10% volume difference compared to pre-operative state or other limbs. Given mice tail diameter at its base varies from 4-5mm diameter and assuming an inverted cone shape of a length of ~80mm, The assumed volume the tail can be considered to be approximately 424mm^3 +/- 80mm^3, A change of ~42mm^3 may be considered as lymphoedema.

The calculation values for numbers needed for each group to achieve a 90% power are shown below.

Analysis: A priori: Compute required sample size
Input: Tail(s) = Two
Effect size d = 0.525
α err prob = 0.05
Power (1-β err prob) = 0.90
Allocation ratio N2/N1 = 1
Output: Non-centrality parameter δ = 3.33616402
Critical t = 2.0210754
Df = 41
Matched experiments required = 42
Actual power = 0.9065

For each experimental group we request 42 matched experiments (2 conditions for the first Group – radiation vs no radiation and therefore 84 mice, and 3 conditions for the 2nd and 3rd experimental groups – i.e. 126 mice per group).

LYMPHOEDEMA MODEL – LEG (THERAPEUTIC)

Statistical analysis.

Given the foot is shaped like a flat cylinder in the mouse, the increase in volume would be directly proportional to the change of height. Clinical studies studying the effectiveness of surgical interventions have quoted volume improvements of ~55% with surgery that fuses a draining lymphatic vessel to a vein (lympho-venous anastomosis) or free tissue transfer compared with pre-operative state. We think therefore a reduction of 15-25% of the pre-intervention state would be clinically relevant. Given swollen mouse foot pads are approximately 6mm thickness, a reduction to the volume of ~5mm would be sought.

Using G*Power, the numbers needed for each group to achieve a 95% power, demonstrate a value of 28 per group for each group.

i.e. roughly 140 experimental mice are needed for this portion of the treatment.

CXCR7 mice

We would like to repeat the tail lymphoedema model and the leg lymphoedema and treatment model in the CXCR7Tie2 mouse to identify the role of CXCR7 of endothelial cells in contributing towards lymphoedema and prolonged soft tissue injury following irradiation. The experimental designs are detailed above. The number of mice

therefore would also be 252 for the tail model and 140 for the leg model of lymphoedema.

We would also like to perform a similar experiment to the ear models utilizing CXCR7-GFP mice, to quantify if CXCR7 is differentially expressed post irradiation. As this work is novel, exact numbers needed are hard to quantitate. As we have calculated the above values for Prox1-GFP mice using conservative expected differences of 5-10% and hence think they may also apply for these experiments. I.e. 180 mice to determine age and radiotherapy effect on CXCR7 expression and 110 mice for estimating the role of radiation in CXCR7 expression in wound healing.

Pages 19-32 Additional Research Member Forms not included.